

NASA Reference Publication 1376  
Volume III

# Clouds and the Earth's Radiant Energy System (CERES) Algorithm Theoretical Basis Document

*Volume III—Cloud Analyses and Determination of Improved  
Top of Atmosphere Fluxes (Subsystem 4)*

---

*CERES Science Team*

---

December 1995



# Clouds and the Earth's Radiant Energy System (CERES) Algorithm Theoretical Basis Document

## *Volume III—Cloud Analyses and Determination of Improved Top of Atmosphere Fluxes (Subsystem 4)*

---

*CERES Science Team  
Langley Research Center • Hampton, Virginia*

Available electronically at the following URL address: <http://techreports.larc.nasa.gov/ltrs/ltrs.html>

Printed copies available from the following:

NASA Center for AeroSpace Information  
800 Elkridge Landing Road  
Linthicum Heights, MD 21090-2934  
(301) 621-0390

National Technical Information Service (NTIS)  
5285 Port Royal Road  
Springfield, VA 22161-2171  
(703) 487-4650

## Contents

Preface .....	v
Nomenclature .....	ix
CERES Top Level Data Flow Diagram .....	xvii
Subsystem 4.0 Top Level Data Flow Diagram .....	xviii
Overview of Cloud Retrieval and Radiative Flux Inversion (Subsystem (4.0)) .....	1
Imager Clear-Sky Determination and Cloud Detection (Subsystem 4.1) .....	43
Imager Cloud Height Determination (Subsystem 4.2) .....	83
Cloud Optical Property Retrieval (Subsystem 4.3) .....	135
Convolution of Imager Cloud Properties With CERES Footprint Point Spread Function (Subsystem 4.4) .....	177
CERES Inversion to Instantaneous TOA Fluxes (Subsystem 4.5) .....	195
Empirical Estimates of Shortwave and Longwave Surface Radiation Budget Involving CERES Measurements (Subsystem 4.6.0) .....	207
Estimate of Shortwave Surface Radiation Budget From CERES (Subsystem 4.6.1) .....	213
Estimation of Longwave Surface Radiation Budget From CERES (Subsystem 4.6.2) .....	217
An Algorithm for Longwave Surface Radiation Budget for Total Skies (Subsystem 4.6.3) .....	235



## **Preface**

The Release-1 CERES Algorithm Theoretical Basis Document (ATBD) is a compilation of the techniques and processes that constitute the prototype data analysis scheme for the Clouds and the Earth's Radiant Energy System (CERES), a key component of NASA's Mission to Planet Earth. The scientific bases for this project and the methodologies used in the data analysis system are also explained in the ATBD. The CERES ATBD comprises 11 subsystems of various sizes and complexities. The ATBD for each subsystem has been reviewed by three or four independently selected university, NASA, and NOAA scientists. In addition to the written reviews, each subsystem ATBD was reviewed during oral presentations given to a six-member scientific peer review panel at Goddard Space Flight Center during May 1994. Both sets of reviews, oral and written, determined that the CERES ATBD was sufficiently mature for use in providing archived Earth Observing System (EOS) data products. The CERES Science Team completed revisions of the ATBD to satisfy all reviewer comments. Because the Release-1 CERES ATBD will serve as the reference for all of the initial CERES data analysis algorithms and product generation, it is published here as a NASA Reference Publication.

Due to its extreme length, this NASA Reference Publication comprises four volumes that divide the CERES ATBD at natural break points between particular subsystems. These four volumes are

### **I: Overviews**

CERES Algorithm Overview

Subsystem 0. CERES Data Processing System Objectives and Architecture

### **II: Geolocation, Calibration, and ERBE-Like Analyses**

Subsystem 1.0. Instrument Geolocate and Calibrate Earth Radiances

Subsystem 2.0. ERBE-Like Inversion to Instantaneous TOA and Surface Fluxes

Subsystem 3.0. ERBE-Like Averaging to Monthly TOA

### **III: Cloud Analyses and Determination of Improved Top of Atmosphere Fluxes**

Subsystem 4.0. Overview of Cloud Retrieval and Radiative Flux Inversion

Subsystem 4.1. Imager Clear-Sky Determination and Cloud Detection

Subsystem 4.2. Imager Cloud Height Determination

Subsystem 4.3. Cloud Optical Property Retrieval

Subsystem 4.4. Convolution of Imager Cloud Properties With CERES Footprint Point Spread Function

Subsystem 4.5. CERES Inversion to Instantaneous TOA Fluxes

Subsystem 4.6. Empirical Estimates of Shortwave and Longwave Surface Radiation Budget Involving CERES Measurements

### **IV: Determination of Surface and Atmosphere Fluxes and Temporally and Spatially Averaged Products**

Subsystem 5.0. Compute Surface and Atmospheric Fluxes

Subsystem 6.0. Grid Single Satellite Fluxes and Clouds and Compute Spatial Averages

Subsystem 7.0. Time Interpolation and Synoptic Flux Computation for Single and Multiple Satellites

Subsystem 8.0. Monthly Regional, Zonal, and Global Radiation Fluxes and Cloud Properties

Subsystem 9.0. Grid TOA and Surface Fluxes for Instantaneous Surface Product

Subsystem 10.0. Monthly Regional TOA and Surface Radiation Budget

Subsystem 11.0. Update Clear Reflectance, Temperature History (CHR)

Subsystem 12.0. Regrid Humidity and Temperature Fields

The CERES Science Team serves as the editor for the entire document. A complete list of Science Team members is given below. Different groups of individuals prepared the various subsections that constitute the CERES ATBD. Thus, references to a particular subsection of the ATBD should specify

the subsection number, authors, and page numbers. Questions regarding the content of a given subsection should be directed to the appropriate first or second author. No attempt was made to make the overall document stylistically consistent.

The CERES Science Team is an international group led by 2 principal investigators and 19 coinvestigators. The team members and their institutions are listed below.

### **CERES Science Team**

**Bruce A. Wielicki, Interdisciplinary Principal Investigator**  
**Bruce R. Barkstrom, Instrument Principal Investigator**

Atmospheric Sciences Division  
NASA Langley Research Center  
Hampton, Virginia 23681-0001

### **Coinvestigators**

**Bryan A. Baum**  
Atmospheric Sciences Division  
NASA Langley Research Center  
Hampton, Virginia 23681-0001

**Maurice Blackmon**  
Climate Research Division  
NOAA Research Laboratory  
Boulder, Colorado 80303

**Robert D. Cess**  
Institute for Terrestrial & Planetary Atmospheres  
Marine Sciences Research Center  
State University of New York  
Stony Brook, New York 11794-5000

**Thomas P. Charlock**  
Atmospheric Sciences Division  
NASA Langley Research Division  
Hampton, Virginia 23681-0001

**James A. Coakley**  
Oregon State University  
Department of Atmospheric Sciences  
Corvallis, Oregon 97331-2209

**Dominique A. Crommelynck**  
Institute Royal Meteorologique  
B-1180 Bruxelles  
Belgium

Richard N. Green  
Atmospheric Sciences Division  
NASA Langley Research Center  
Hampton, Virginia 23681-0001

Robert Kandel  
Laboratoire de Meteorologie Dynamique  
Ecole Polytechnique  
91128 Palaiseau  
France

Michael D. King  
Goddard Space Flight Center  
Greenbelt, Maryland 20771

Robert B. Lee III  
Atmospheric Sciences Division  
NASA Langley Research Center  
Hampton, Virginia 23681-0001

A. James Miller  
NOAA/NWS  
5200 Auth Road  
Camp Springs, Maryland 20233

Patrick Minnis  
Atmospheric Sciences Division  
NASA Langley Research Center  
Hampton, Virginia 23681-0001

Veerabhadran Ramanathan  
Scripps Institution of Oceanography  
University of California-San Diego  
La Jolla, California 92093-0239

David R. Randall  
Colorado State University  
Department of Atmospheric Science  
Foothills Campus, Laporte Avenue  
Fort Collins, Colorado 80523

G. Louis Smith  
Atmospheric Sciences Division  
NASA Langley Research Center  
Hampton, Virginia 23681-0001

Larry L. Stowe  
NOAA/NWS  
5200 Auth Road  
Camp Springs, Maryland 20233

Ronald M. Welch  
South Dakota School of Mines and Technology  
Institute of Atmospheric Sciences  
Rapid City, South Dakota 57701-3995

## Nomenclature

### Acronyms

ADEOS	Advanced Earth Observing System
ADM	Angular Distribution Model
AIRS	Atmospheric Infrared Sounder (EOS-AM)
AMSU	Advanced Microwave Sounding Unit (EOS-PM)
APD	Aerosol Profile Data
APID	Application Identifier
ARESE	ARM Enhanced Shortwave Experiment
ARM	Atmospheric Radiation Measurement
ASOS	Automated Surface Observing Sites
ASTER	Advanced Spaceborne Thermal Emission and Reflection Radiometer
ASTEX	Atlantic Stratocumulus Transition Experiment
ASTR	Atmospheric Structures
ATBD	Algorithm Theoretical Basis Document
AVG	Monthly Regional, Average Radiative Fluxes and Clouds (CERES Archival Data Product)
AVHRR	Advanced Very High Resolution Radiometer
BDS	Bidirectional Scan (CERES Archival Data Product)
BRIE	Best Regional Integral Estimate
BSRN	Baseline Surface Radiation Network
BTD	Brightness Temperature Difference(s)
CCD	Charge Coupled Device
CCSDS	Consultative Committee for Space Data Systems
CEPEX	Central Equatorial Pacific Experiment
CERES	Clouds and the Earth's Radiant Energy System
CID	Cloud Imager Data
CLAVR	Clouds from AVHRR
CLS	Constrained Least Squares
COPRS	Cloud Optical Property Retrieval System
CPR	Cloud Profiling Radar
CRH	Clear Reflectance, Temperature History (CERES Archival Data Product)
CRS	Single Satellite CERES Footprint, Radiative Fluxes and Clouds (CERES Archival Data Product)
DAAC	Distributed Active Archive Center
DAC	Digital-Analog Converter
DB	Database
DFD	Data Flow Diagram
DLF	Downward Longwave Flux

DMSP	Defense Meteorological Satellite Program
EADM	ERBE-Like Albedo Directional Model (CERES Input Data Product)
ECA	Earth Central Angle
ECLIPS	Experimental Cloud Lidar Pilot Study
ECMWF	European Centre for Medium-Range Weather Forecasts
EDDB	ERBE-Like Daily Data Base (CERES Archival Data Product)
EID9	ERBE-Like Internal Data Product 9 (CERES Internal Data Product)
EOS	Earth Observing System
EOSDIS	Earth Observing System Data Information System
EOS-AM	EOS Morning Crossing Mission
EOS-PM	EOS Afternoon Crossing Mission
ENSO	El Niño/Southern Oscillation
ENVISAT	Environmental Satellite
EPHANC	Ephemeris and Ancillary (CERES Input Data Product)
ERB	Earth Radiation Budget
ERBE	Earth Radiation Budget Experiment
ERBS	Earth Radiation Budget Satellite
ESA	European Space Agency
ES4	ERBE-Like S4 Data Product (CERES Archival Data Product)
ES4G	ERBE-Like S4G Data Product (CERES Archival Data Product)
ES8	ERBE-Like S8 Data Product (CERES Archival Data Product)
ES9	ERBE-Like S9 Data Product (CERES Archival Data Product)
FLOP	Floating Point Operation
FIRE	First ISCCP Regional Experiment
FIRE II IFO	First ISCCP Regional Experiment II Intensive Field Observations
FOV	Field of View
FSW	Hourly Gridded Single Satellite Fluxes and Clouds (CERES Archival Data Product)
FTM	Functional Test Model
GAC	Global Area Coverage (AVHRR data mode)
GAP	Gridded Atmospheric Product (CERES Input Data Product)
GCIP	GEWEX Continental-Phase International Project
GCM	General Circulation Model
GEBA	Global Energy Balance Archive
GEO	ISCCP Radiances (CERES Input Data Product)
GEWEX	Global Energy and Water Cycle Experiment
GLAS	Geoscience Laser Altimetry System
GMS	Geostationary Meteorological Satellite
GOES	Geostationary Operational Environmental Satellite
HBTM	Hybrid Bispectral Threshold Method

HIRS	High-Resolution Infrared Radiation Sounder
HIS	High-Resolution Interferometer Sounder
ICM	Internal Calibration Module
ICRCCM	Intercomparison of Radiation Codes in Climate Models
ID	Identification
IEEE	Institute of Electrical and Electronics Engineers
IES	Instrument Earth Scans (CERES Internal Data Product)
IFO	Intensive Field Observation
INSAT	Indian Satellite
IOP	Intensive Observing Period
IR	Infrared
IRIS	Infrared Interferometer Spectrometer
ISCCP	International Satellite Cloud Climatology Project
ISS	Integrated Sounding System
IWP	Ice Water Path
LAC	Local Area Coverage (AVHRR data mode)
LaRC	Langley Research Center
LBC	Laser Beam Ceilometer
LBTM	Layer Bispectral Threshold Method
Lidar	Light Detection and Ranging
LITE	Lidar In-Space Technology Experiment
Lowtran 7	Low-Resolution Transmittance (Radiative Transfer Code)
LW	Longwave
LWP	Liquid Water Path
LWRE	Longwave Radiant Excitance
MAM	Mirror Attenuator Mosaic
MC	Mostly Cloudy
MCR	Microwave Cloud Radiometer
METEOSAT	Meteorological Operational Satellite (European)
METSAT	Meteorological Satellite
MFLOP	Million FLOP
MIMR	Multifrequency Imaging Microwave Radiometer
MISR	Multiangle Imaging Spectroradiometer
MLE	Maximum Likelihood Estimate
MOA	Meteorology Ozone and Aerosol
MODIS	Moderate-Resolution Imaging Spectroradiometer
MSMR	Multispectral, multiresolution
MTSA	Monthly Time and Space Averaging
MWH	Microwave Humidity

MWP	Microwave Water Path
NASA	National Aeronautics and Space Administration
NCAR	National Center for Atmospheric Research
NESDIS	National Environmental Satellite, Data, and Information Service
NIR	Near Infrared
NMC	National Meteorological Center
NOAA	National Oceanic and Atmospheric Administration
NWP	Numerical Weather Prediction
OLR	Outgoing Longwave Radiation
OPD	Ozone Profile Data (CERES Input Data Product)
OV	Overcast
PC	Partly Cloudy
POLDER	Polarization of Directionality of Earth's Reflectances
PRT	Platinum Resistance Thermometer
PSF	Point Spread Function
PW	Precipitable Water
RAPS	Rotating Azimuth Plane Scan
RPM	Radiance Pairs Method
RTM	Radiometer Test Model
SAB	Sorting by Angular Bins
SAGE	Stratospheric Aerosol and Gas Experiment
SARB	Surface and Atmospheric Radiation Budget Working Group
SDCD	Solar Distance Correction and Declination
SFC	Hourly Gridded Single Satellite TOA and Surface Fluxes (CERES Archival Data Product)
SHEBA	Surface Heat Budget in the Arctic
SPECTRE	Spectral Radiance Experiment
SRB	Surface Radiation Budget
SRBAVG	Surface Radiation Budget Average (CERES Archival Data Product)
SSF	Single Satellite CERES Footprint TOA and Surface Fluxes, Clouds
SSMI	Special Sensor Microwave Imager
SST	Sea Surface Temperature
SURFMAP	Surface Properties and Maps (CERES Input Product)
SW	Shortwave
SWICS	Shortwave Internal Calibration Source
SWRE	Shortwave Radiant Excitance
SYN	Synoptic Radiative Fluxes and Clouds (CERES Archival Data Product)
SZA	Solar Zenith Angle
THIR	Temperature/Humidity Infrared Radiometer (Nimbus)

TIROS	Television Infrared Observation Satellite
TISA	Time Interpolation and Spatial Averaging Working Group
TMI	TRMM Microwave Imager
TOA	Top of the Atmosphere
TOGA	Tropical Ocean Global Atmosphere
TOMS	Total Ozone Mapping Spectrometer
TOVS	TIROS Operational Vertical Sounder
TRMM	Tropical Rainfall Measuring Mission
TSA	Time-Space Averaging
UAV	Unmanned Aerospace Vehicle
UT	Universal Time
UTC	Universal Time Code
VAS	VISSR Atmospheric Sounder (GOES)
VIRS	Visible Infrared Scanner
VISSR	Visible and Infrared Spin Scan Radiometer
WCRP	World Climate Research Program
WG	Working Group
Win	Window
WN	Window
WMO	World Meteorological Organization
ZAVG	Monthly Zonal and Global Average Radiative Fluxes and Clouds (CERES Archival Data Product)

### **Symbols**

$A$	atmospheric absorptance
$B_{\lambda}(T)$	Planck function
$C$	cloud fractional area coverage
$CF_2Cl_2$	dichlorofluorocarbon
$CFCl_3$	trichlorofluorocarbon
$CH_4$	methane
$CO_2$	carbon dioxide
$D$	total number of days in the month
$D_e$	cloud particle equivalent diameter (for ice clouds)
$E_o$	solar constant or solar irradiance
$F$	flux
$f$	fraction
$G_a$	atmospheric greenhouse effect
$g$	cloud asymmetry parameter
$H_2O$	water vapor

$I$	radiance
$i$	scene type
$m_i$	imaginary refractive index
$\hat{N}$	angular momentum vector
$N_2O$	nitrous oxide
$O_3$	ozone
$P$	point spread function
$p$	pressure
$Q_a$	absorption efficiency
$Q_e$	extinction efficiency
$Q_s$	scattering efficiency
$R$	anisotropic reflectance factor
$r_E$	radius of the Earth
$r_e$	effective cloud droplet radius (for water clouds)
$r_h$	column-averaged relative humidity
$S_o$	summed solar incident SW flux
$S'_o$	integrated solar incident SW flux
$T$	temperature
$T_B$	blackbody temperature
$t$	time or transmittance
$W_{liq}$	liquid water path
$w$	precipitable water
$\hat{x}_o$	satellite position at $t_o$
$x, y, z$	satellite position vector components
$\dot{x}, \dot{y}, \dot{z}$	satellite velocity vector components
$z$	altitude
$z_{top}$	altitude at top of atmosphere
$\alpha$	albedo or cone angle
$\beta$	cross-scan angle
$\gamma$	Earth central angle
$\gamma_{at}$	along-track angle
$\gamma_{ct}$	cross-track angle
$\delta$	along-scan angle
$\epsilon$	emittance
$\Theta$	colatitude of satellite
$\theta$	viewing zenith angle
$\theta_o$	solar zenith angle
$\lambda$	wavelength
$\mu$	viewing zenith angle cosine

$\mu_o$	solar zenith angle cosine
$\nu$	wave number
$\rho$	bidirectional reflectance
$\tau$	optical depth
$\tau_{aer}(p)$	spectral optical depth profiles of aerosols
$\tau_{H_2O\lambda}(p)$	spectral optical depth profiles of water vapor
$\tau_{O_3}(p)$	spectral optical depth profiles of ozone
$\Phi$	longitude of satellite
$\phi$	azimuth angle
$\tilde{\omega}_o$	single-scattering albedo

Subscripts:

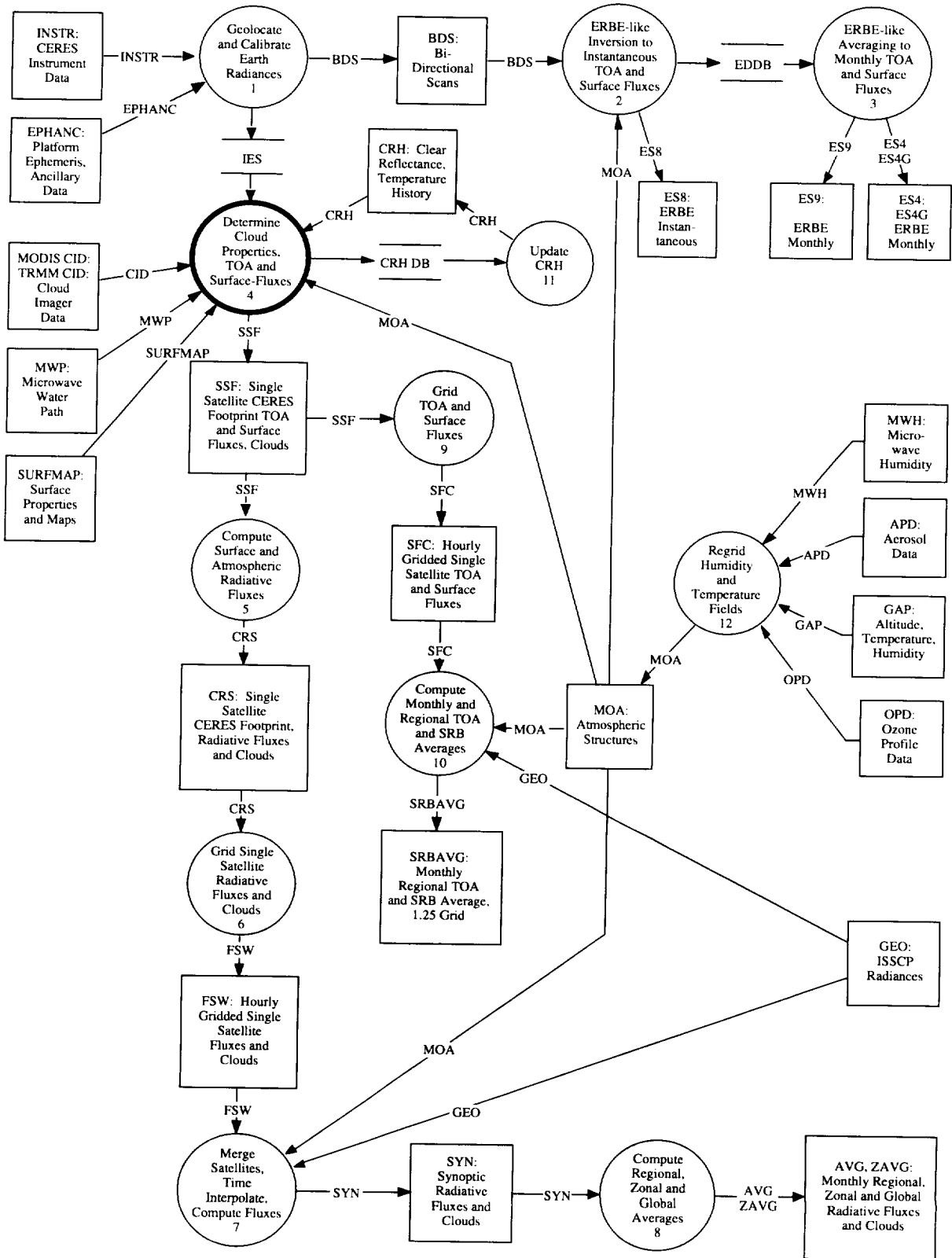
$c$	cloud
$cb$	cloud base
$ce$	cloud effective
$cld$	cloud
$cs$	clear sky
$ct$	cloud top
$ice$	ice water
$lc$	lower cloud
$liq$	liquid water
$s$	surface
$uc$	upper cloud
$\lambda$	spectral wavelength

Units

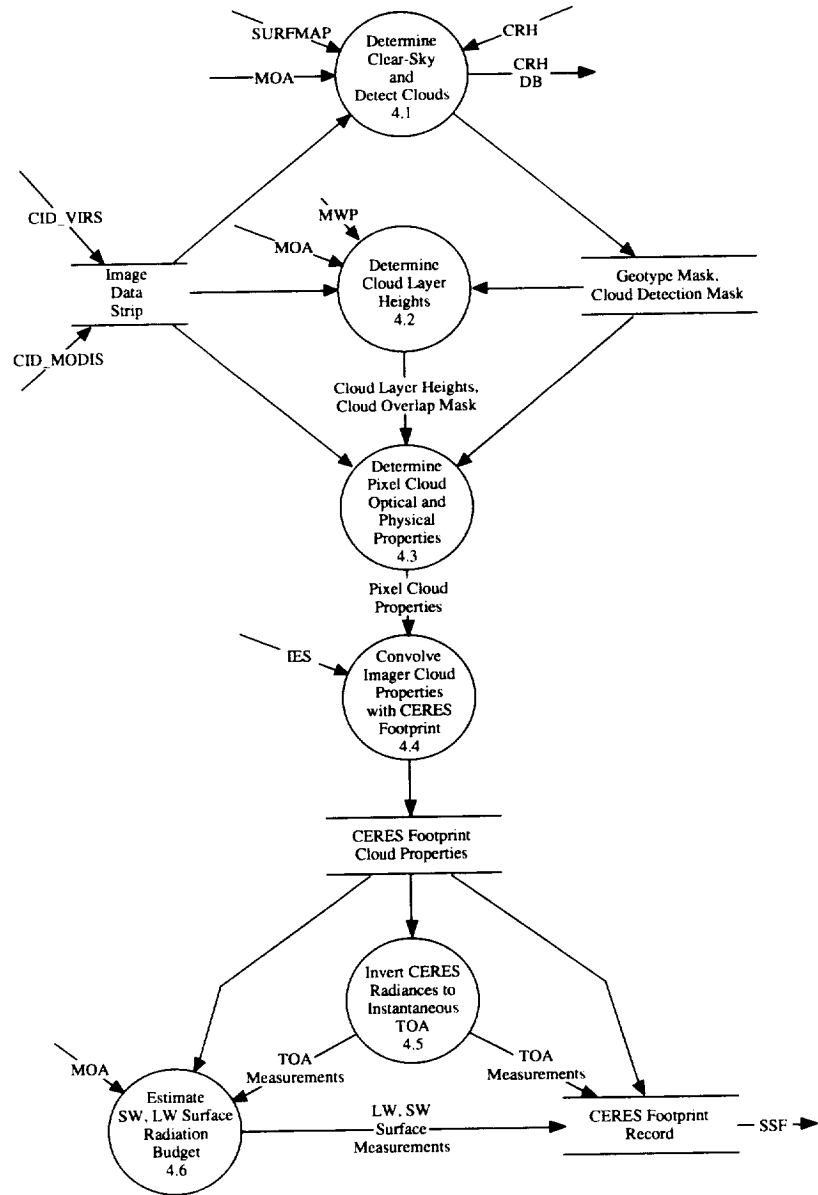
AU	astronomical unit
cm	centimeter
cm-sec <sup>-1</sup>	centimeter per second
count	count
day	day, Julian date
deg	degree
deg-sec <sup>-1</sup>	degree per second
DU	Dobson unit
erg-sec <sup>-1</sup>	erg per second
fraction	fraction (range of 0–1)
g	gram
g-cm <sup>-2</sup>	gram per square centimeter
g-g <sup>-1</sup>	gram per gram
g-m <sup>-2</sup>	gram per square meter

h	hour
hPa	hectopascal
K	Kelvin
kg	kilogram
kg-m <sup>-2</sup>	kilogram per square meter
km	kilometer
km-sec <sup>-1</sup>	kilometer per second
m	meter
mm	millimeter
μm	micrometer, micron
N/A	not applicable, none, unitless, dimensionless
ohm-cm <sup>-1</sup>	ohm per centimeter
percent	percent (range of 0–100)
rad	radian
rad-sec <sup>-1</sup>	radian per second
sec	second
sr <sup>-1</sup>	per steradian
W	watt
W-m <sup>-2</sup>	watt per square meter
W-m <sup>-2</sup> sr <sup>-1</sup>	watt per square meter per steradian
W-m <sup>-2</sup> sr <sup>-1</sup> μm <sup>-1</sup>	watt per square meter per steradian per micrometer

# CERES Top Level Data Flow Diagram



## Subsystem 4.0 Top Level Data Flow Diagram



**Clouds and the Earth's Radiant Energy System (CERES)**  
**Algorithm Theoretical Basis Document**

*Overview of Cloud Retrieval and Radiative Flux Inversion*  
*(Subsystem 4.0)*

**Cloud Working Group Chair**

B. A. Wielicki<sup>1</sup>

**Inversion Working Group Chair**

R. N. Green<sup>1</sup>

**Data Management Team**

C. J. Tolson<sup>2</sup>  
A. Fan<sup>2</sup>

<sup>1</sup>Atmospheric Sciences Division, NASA Langley Research Center, Hampton, Virginia 23681-0001

<sup>2</sup>Science Applications International Corporation (SAIC), Hampton, Virginia 23666

## Abstract

*One of the major advances of the CERES (Clouds and the Earth's Radiant Energy System) radiation budget analysis over the ERBE (Earth Radiation Budget Experiment) is the ability to use high spectral and spatial resolution cloud imager data to determine cloud and surface properties within the relatively large CERES field of view [20-km diameter for the Earth Observing System (EOS)-AM and EOS-PM, 10 km diameter for TRMM (Tropical Rainfall Measuring Mission)]. For the first launch of the CERES broadband radiometer on TRMM in 1997, CERES will use the VIRS (Visible Infrared Scanner) cloud imager as input. For the next launches on EOS-AM (1998) and EOS-PM (2000), CERES will use the MODIS (Moderate-Resolution Imaging Spectroradiometer) cloud imager data as input.*

*This overview summarizes the Subsystem 4 CERES algorithms which*

- 1. Determine clear-sky radiances and detect pixels containing clouds*
- 2. Determine well-defined cloud layers and identify multilayer pixels*
- 3. Determine cloud properties for each imager pixel*
- 4. Map the imager cloud properties to the CERES broadband radiance footprint*
- 5. Use the CERES footprint cloud properties to determine an angular distribution model for the conversion of radiance to top-of-atmosphere (TOA) flux*
- 6. Use the TOA fluxes and parameterizations to estimate surface radiative fluxes*

*Angular sampling errors were determined to be the largest error source for ERBE shortwave fluxes. The increased accuracy of CERES cloud property determination and the new angular models are expected to reduce these errors by a factor of 3 to 4. The cloud properties and radiative fluxes for each CERES footprint are also key to providing more accurate estimates of in-atmosphere radiative fluxes. These in-atmosphere radiative flux calculations are discussed in Subsystem 5.*

## 4.0. Overview of Cloud Retrieval and Radiative Flux Inversion

### 4.0.1. Introduction

This documentation is intended as an overview of the CERES cloud retrieval algorithm. The cloud retrieval algorithm has two major objectives.

The first objective is to derive surface and cloud properties sufficient to classify a unique set of targets with distinctly different anisotropic radiation fields. This is required so that the CERES rotating azimuth plane scanner can observe a complete range of surface and cloud targets for all typical viewing and solar angle geometries for a given satellite orbital geometry. These cloud determinations are then combined with the CERES broadband scanner radiance data to derive empirical models of shortwave (SW) and longwave (LW) anisotropy required to accurately convert the CERES-measured radiances

into unbiased estimates of radiative fluxes. For example, we would combine observations of boundary layer cumulus with cloud fractions between 20 and 30% over a tropical forest background. In turn, this cumulus cloud class might further be broken into several optical depth classes. In this manner, even the potentially large but uncertain effect of 3-D cloud structure can be implicitly included in the anisotropic models. Testing of these concepts has begun by using the Nimbus-7 THIR (Temperature-Humidity Infrared Radiometer) and TOMS (Total Ozone Mapping Spectrometer) cloud properties (Stowe et al. 1988) and ERB (Earth Radiation Budget) broadband radiances (Jacobowitz et al. 1984). The testing will continue with the Release 1 CERES cloud algorithm using AVHRR (Advanced Very High Resolution Radiometer), HIRS (High-Resolution Infrared Sounder), and ERBE global radiance data sets.

The second objective is to provide a set of cloud properties optimally designed for studies of the role of clouds in the Earth's radiation budget. In particular, cloud properties determined using high spatial (0.25–2 km at nadir) and spectral resolution cloud imager data will be matched to each CERES footprint (10–20 km at nadir) to as consistently as possible tie the cloud physical and cloud broadband radiative properties. These cloud properties will be used in calculations of the surface and in-atmosphere radiative fluxes. Because all current cloud remote sensing methods use 1-D radiative transfer models, which are not appropriate for optically thick cumulus clouds, the close tie of CERES TOA fluxes to imager cloud properties allows a first-order correction for 3-D cloud effects. For example, TOA reflected SW flux computed using the 1-D-determined imager cloud optical depth and cloud particle size may differ greatly from the observed TOA flux. The observed flux used empirical models of cloud anisotropy to correctly convert radiance into flux even for 3-D cloud structure. This flux can then be used to determine an “equivalent” plane-parallel cloud optical depth or to specify a 3-D cloud parameter such as cloud aspect ratio. In this sense, the CERES cloud algorithm will produce an initial estimate of cloud properties. This estimate will then be modified to obtain consistency in cloud properties and TOA broadband radiative fluxes. This consistency will be essentially that required to examine global climate models, which use 1-D radiative flux computations similar to those performed by CERES.

#### 4.0.2. Input and Output Data

The primary input data sets for Subsystem 4 are the CERES broadband radiance data and the cloud imager data. Other auxiliary input data sets are discussed more fully in Subsystems 4.1–4.3 and in the input data descriptions in appendix A. The CERES instrument data are described in Subsystem 1. The cloud imager data vary between prelaunch studies, TRMM, and EOS, and a brief overview is given below.

VIRS is a next generation version of the AVHRR scanning radiometer with a 2-km diameter nadir field of view and five spectral channels (0.65, 1.6, 3.75, 10.8, and 12.0  $\mu\text{m}$ ). The major advances over the current AVHRR are the addition of a 1.6- $\mu$  channel and onboard solar channel calibration. The AVHRR instrument has shown large changes in instrument gain with time (Staylor, 1990; NESDIS, 1993).

MODIS (King et al. 1992) will be a major improvement over both AVHRR and VIRS. Onboard calibration will be greatly improved for solar reflectance channels by including onboard lamps, solar diffuser plate, and the ability to use the moon as a stable target. Channel spectral wavelengths will also be monitored in flight. MODIS provides 11 spectral channels of prime use for cloud analysis, including

- 13.3, 13.6, and 13.9  $\mu\text{m}$  for determining thin cirrus cloud height
- 1.38  $\mu\text{m}$  for detecting very thin cirrus, even in the presence of low cloud
- 3.7, 8.5, 11, and 12  $\mu\text{m}$  for determining nighttime cloud particle size/phase
- 0.65, 1.6, and 2.1  $\mu\text{m}$  for determining daytime optical depth, particle size/phase

The thermal infrared channels have a field of view diameter of 1 km, the near infrared are 0.5 km, and the visible channel is 0.25 km. The high spatial resolution visible channel eliminates the problem of

partially cloud filled fields of view even for boundary layer clouds such as cumulus (Wielicki and Parker, 1992).

The CERES cloud retrieval algorithm will use the cloud imager data to produce estimates of basic cloud physical and optical properties within each CERES footprint including

- Fractional coverage
- Temperature/height/pressure
- Optical depth (0.65  $\mu\text{m}$ )
- Emissivity (11  $\mu\text{m}$ )
- Particle size and phase
- Liquid/ice water path
- Vertical thickness
- Vertical aspect ratio

The cloud properties are listed roughly in the order of expected accuracy and current understanding of their retrieval. The first four properties are reasonably well understood, the next two are in advanced stages of development, and the last two are only in the beginning stages of development, and may only provide useful information for a limited range of cloud conditions. These properties cover a reasonably complete set of variables to describe the effect of clouds on the radiative fluxes at the surface, within the atmosphere, and at the top of the atmosphere. They are not a rigorously exhaustive set. For example, cloud vertical aspect ratio is a variable which is intended (along with cloud fraction and cloud optical depth) to allow at least a limited investigation of the effects of 3-D radiative transfer issues.

Surface observers indicate that about half of cloud observations are multilayered (Warren et al. 1985), and that multilayered clouds are much more likely over ocean than land. Over ocean, 52% of all observations are multilayered while 43% are single-layered. Over land, 31% are multilayered while 47% are single-layered. Tian and Curry (1989) used the combined satellite, aircraft, and surface cloud observations in the Air Force 3DNEPH data to examine cloud overlap assumptions over the North Atlantic Ocean, and concluded that for cloud layers within 1 km in altitude, maximum overlap is most accurate, while for cloud altitudes separated by 3 km or more, random overlap is the best assumption. Their study further concluded that at a spatial scale of 45 km (similar to the CERES footprint) 75% of the multilayered cases consisted of two-layer cloud systems. As the spatial scale of interest increases to 220 km, three-layer cases dominate. We conclude that the CERES cloud analysis must commonly address the issue of two-layer cloud systems.

All current global satellite cloud climatologies assume a single cloud layer to occur in each imager pixel, although multiple cloud layers are allowed in large regions. For example, subtropical optically thin cirrus overlying a lower boundary layer cloud gives cloud height properties dominated by the cold cirrus and cloud optical depth dominated by the optically thicker stratus cloud. Recent studies of the sensitivity of the LW surface radiation budget to cloud overlap assumptions show that knowledge of cloud overlap is more important than accurate knowledge of the thickness of individual cloud layers (Subsystem 5.0).

CERES will employ two strategies to improve the remote sensing of multilayer clouds. For an optically thin high cloud over low clouds, the MODIS  $\text{CO}_2$  sounding channels will be used to establish the upper cloud height and optical depth, while the spectral window visible and infrared channels will be used for the low clouds (Baum et al. 1994). For an optically thick high cloud over a low cloud, the cloud imager channels will be used for the high cloud properties, while passive microwave liquid water path (LWP) measurement (Greenwald et al. 1993) is used to indicate the presence of the lower cloud layer over ocean backgrounds. These two improvements for sensing multilevel clouds should provide substantially better estimates of LW surface and in-atmosphere radiation budget.

### 4.0.3. Algorithm Assumptions

Any algorithm to remotely sense physical or radiative properties is based on an assumed physical model. This conceptual model may be explicit (plane-parallel radiative calculations) or implicit (piecewise constant spatial averaging). The more explicit the conceptual model, the more precisely the algorithm strengths and weaknesses can be understood. This is particularly the case in validating the algorithm results. The most fruitful validation is not simply the comparison of end results, but rather the validation of underlying assumptions. The successes and failures of these assumptions lead to critical new results and methods.

The CERES cloud identification and radiative flux determination algorithms are based on the following assumptions.

**1. *Cloud-filled pixel assumption: Clouds are much larger than a cloud imager pixel, so that cloud cover in a pixel is 0 or 1.***

This assumption is the subject of much debate. While no data have conclusively answered this question, initial answers are beginning to arrive. The cloud types most subject to error are those with the smallest cloud cells such as cumulus. Figure 4.0-1 shows the accuracy of detecting oceanic boundary layer cloud amount with different spatial resolution sensors (8, 4, 2, 1, 0.5, and 0.25 km). The results are an extension of the results of Wielicki and Parker (1992) to a much larger number of cases. The results shown here are for 52 cloud fields (each 58.4 km square), but show similar results to those found earlier, although now the bias can be shown to be a systematic function of cloud amount.

Each point in the scatter plot gives the regional cloud fraction in one of the 58.4-km regions. Note that the current ISCCP (International Satellite Cloud Climatology Project) data use 4–8 km resolution data, depending on the satellite [GOES (Geostationary Operational Environmental Satellite) is 8 km, GMS (Geosynchronous Meteorological Satellite) and METEOSAT are 5 km, and AVHRR is 4 km]. Figure 4.0-1 shows that the maximum “beam filling” error is at a cloud amount of 0.5, where partially cloud-filled pixels are sufficiently bright to trigger the cloud threshold, but are treated as cloud filled. For cloud amounts less than about 0.2, the large pixel data underestimate cloud amount, since few of the pixels have sufficient cloud cover to exceed the cloud threshold.

For 8-km data, average cloud fraction for the 52 cases is biased too large by 0.06, with a 1s rms error of about 0.11. The use of AVHRR 4-km data reduces this error by about 30% to 0.04 bias and 0.08 (1s). The VIRS 2-km data have a bias of 0.02 and a 1s of 0.06 (less than half the ISCCP error). The 0.5 km and 0.25 km results typical of MODIS resolution show a small bias of about  $-0.02$  and 1s of 0.04. The bias for these last two cases is dominated by the difference in reflectance threshold between the reference data ( $R_{clr} + 1.5\%$ ) and the ISCCP radiance threshold, which for the cases here is equivalent to approximately  $R_{clr} + 4.5\%$ , where  $R_{clr}$  is the nadir bidirectional reflectance as defined in Wielicki and Parker (1992). Given very high spatial resolution data, the ISCCP threshold misses significant amounts of optically thin clouds, even for boundary layer clouds. Note that for these cases, the reference threshold would detect a cloud with 10- m water droplets at a visible optical depth of about 0.3. If the reflectance threshold of the 0.25-km pixel analysis is set equal to the reference case, the two agree to better than 0.01 in cloud fraction. We conclude that the MODIS 0.25-km visible channel is sufficient to derive cloud cover for oceanic boundary layer clouds with errors of a few percent or less.

Cirrus clouds have also been examined using numerous Landsat scenes. For cirrus, the thermal threshold dominates, so that the MODIS 1-km and VIRS 2-km resolutions are pertinent to the CERES algorithm. Figure 4.0-2 gives a similar result for cirrus cloud fields. As in Wielicki and Parker (1992), the cirrus clouds show very little spatial resolution effects for pixel sizes of 1–8 km. We conclude that the cloud-filled pixel assumption is reasonable for AVHRR, VIRS, and MODIS for cirrus clouds. While these results are encouraging, further work is needed, especially for land cumulus. Studies to verify the accuracy of this approximation are underway using cumulus cloud fields over the Amazon.

## 52 Boundary Layer Cloud Fields ( 58 km )

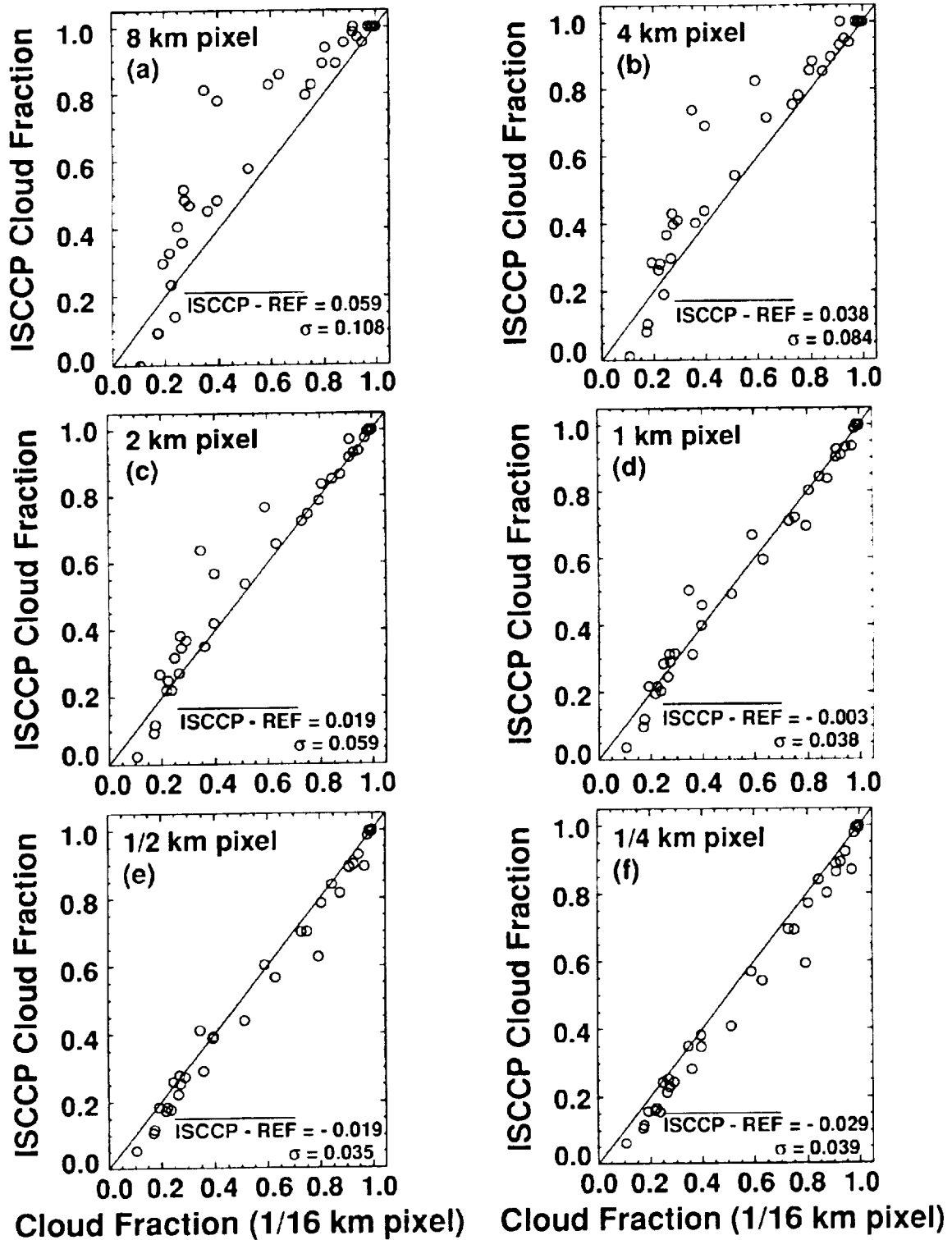


Figure 4.0-1. Effect of sensor spatial resolution on ISCCP threshold estimate of boundary layer cloud fraction. Reference is 57-m spatial resolution Landsat data. Each point represents cloud fraction for a 58-km region.

The most difficult problem may be the detection of boundary layer clouds at night, when even the MODIS retrievals will require the use of 1-km data. The thermal contrast of these clouds at night is much less than the visible reflectance contrast during the day. The problem of missing optically thin clouds may become more severe. Verification of the accuracy of nighttime detection must be performed with coincident lidar and cloud imager data, or with very high spatial resolution data from the MAS (MODIS Airborne Simulator) on the ER-2 aircraft.

CERES will examine the use of spatial coherence to infer subpixel cloud fraction using techniques to correct for emittances less than 1 (Lin and Coakley, 1993). This would allow the Release 2 algorithm to eliminate the cloud-filled pixel assumption for VIRS data and nighttime MODIS data.

***2. Independent pixel assumption: Clouds can be modeled as plane-parallel, even though they exhibit large horizontal variability in optical depth.***

An excellent discussion of this assumption can be found in Cahalan et al. (1994). They demonstrate that the assumption is accurate to a few percent for narrowband flux calculations with overcast marine boundary layer clouds. Wielicki and Parker (1992) found support for the plane-parallel assumption using Landsat nadir radiances at 0.83  $\mu\text{m}$  and 11  $\mu\text{m}$  for broken and solid boundary layer clouds. Stackhouse and Stephens (1994) found rms errors of up to 20% in derived optical depths using plane-parallel radiance calculations, although bias errors were much smaller. In general, this assumption will be less accurate for radiances than for fluxes.

The relatively small errors of this assumption seem to be caused by three properties of the clouds examined:

- A red spectrum of radiance variability, typical of most meteorological fields. This means that as spatial scale decreases, cloud optical property variability decreases. A red spectrum limits the “sharpness” of cloud edges.
- Low to moderate optical depths for the cirrus and marine boundary layer clouds, especially for broken clouds (Harshvardhan et al. 1994; Wielicki and Parker, 1992; Luo et al. 1994). Welch et al. (1980) used Monte Carlo radiative model calculations to show that the effect of horizontal inhomogeneity on fluxes became pronounced only for cloud optical depths above about 8. Most of the cirrus and broken marine boundary layer clouds appear to be at lower optical depths, thereby minimizing the effects.
- Cloud vertical aspect ratios (vertical/horizontal) are typically much less than 1 for cirrus and inversion-capped boundary layer clouds.

The most severe test of this assumption will come with examination of boundary layer cumulus over land (Wielicki and Welch, 1986), and deep convection over land and ocean, which will have large optical depths and large aspect ratios. One of the complications caused by deep convection, or any high optically thick cloud with sharp edges, is the problem of cloud shadowing. Subsystem 4.3 discusses the effect of shadowing on cloud optical property retrieval and suggests strategies for minimizing the effect.

Even if the independent pixel assumption is without error, Cahalan et al. (1994) and Stephens (1988) showed that optical depths cannot be spatially or temporally averaged without causing large errors in radiative flux calculations. This error is simply caused by the nonlinear relationship between albedo and optical depth. CERES cloud retrievals will minimize this problem by saving 1-D histograms of cloud visible (0.65  $\mu\text{m}$ ) optical depth calculated using the highest resolution cloud imager data available (Subsystem 4.5). These histograms will be carried through the spatial gridding and time ( $t$ ) averaging processes as well as averaging to instantaneous CERES footprints. One step to minimize this error is to average  $\ln(t)$  as opposed to a linear average of  $t$  (Rossow et al. 1991). The advantage of this process is that cloud spherical albedo is roughly linear in  $\ln(t)$ , so that this variable comes closer to conserving the cloud albedo. In fact, the errors showed by Cahalan et al. (1994) would have been significantly reduced if this averaging had been used.

## 24 Cirrus Cloud Fields ( 58 km )

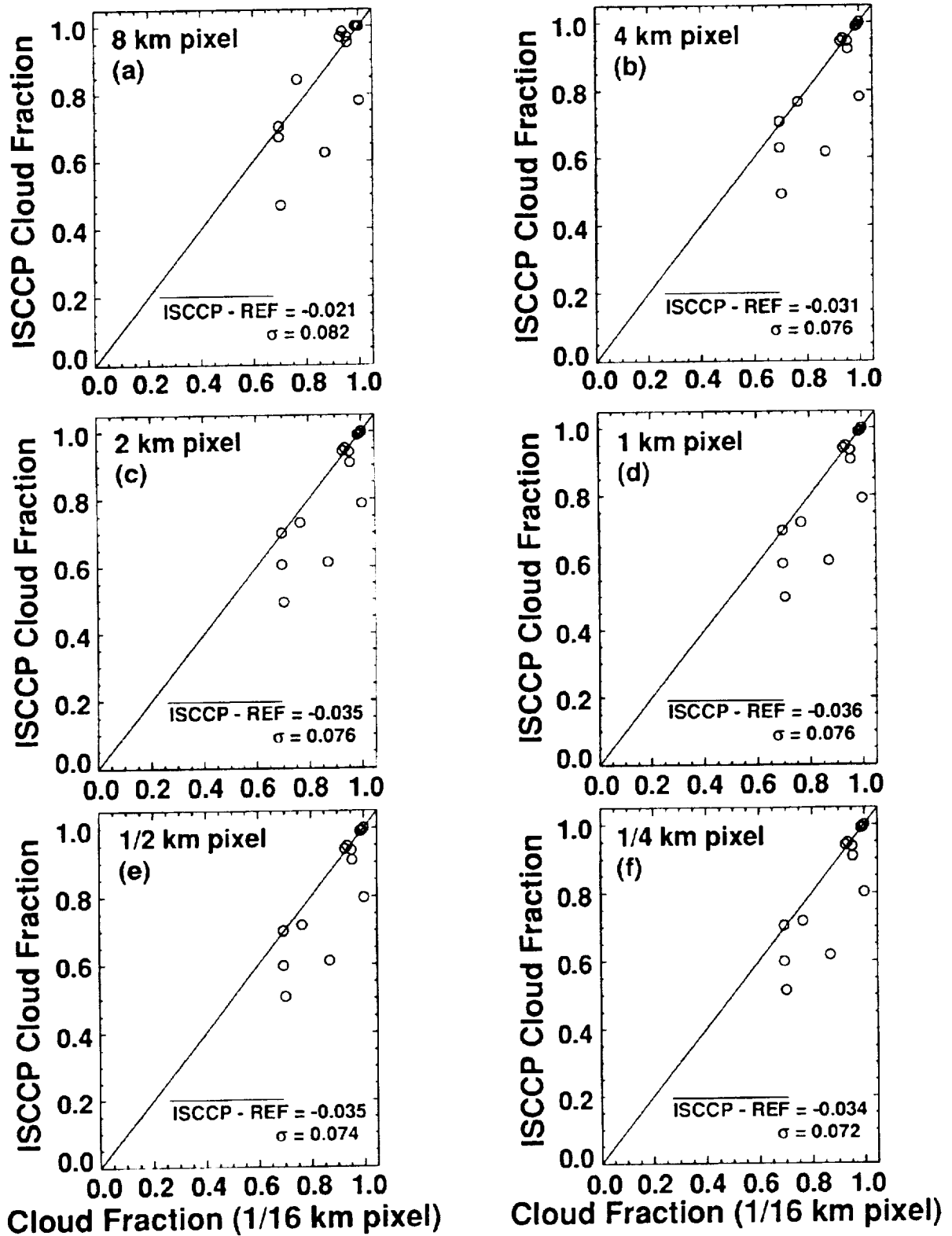


Figure 4.0-2. Effect of sensor spatial resolution on ISCCP threshold estimate of cirrus cloud fraction. Reference is 57-m spatial resolution Landsat data. Each point represents cloud fraction for a single 58-km region over ocean.

Although we discussed the impact of the cloud-filled pixel assumption on cloud fraction, what is its impact on cloud optical depth? Figure 4.0-3 shows the effect of varying pixel size on the derived average optical depth in the 58.4 km region. The results shown are for linear-averaged optical depth, and therefore are more typical of spatially averaged error in LWP which for a fixed cloud particle size is linear in optical depth (Subsystem 4.3). For 8-km pixels, the bias error is an underestimate of 23%, with a  $1\sigma$  of 25%. The fractional error is much larger than cloud amount errors because both the spatial averaging error discussed above (using a spatially averaged reflectance) will always underestimate the true average optical depth (Cahalan et al. 1994) and the cloud filled-pixel error (clear regions in cloudy pixels lower the mean reflectance) contrive to underestimate the optical depth. For the 2-km VIRS data, the error drops to a bias of 12%, while finally for 0.25-km data, the bias becomes an overestimate of 8% with a  $1\sigma$  of 12%. Why the overestimate for small pixels? This shows the effect of changing from the reference threshold at  $R_{clr} + 1.5\%$  to the ISCCP value of approximately  $R_{clr} + 4.5\%$ . The ISCCP threshold misses some of the optically thin clouds picked up by the smaller threshold. This is confirmed by the fact that the bias is largest for the smallest optical depth clouds.

Further studies are needed to examine the errors for logarithmic averaging of optical depth, and the determination of optimal thresholds as a function of spatial resolution. Finally, as discussed by Stephens (1988) and Rossow (1989), the optimal methods for spatial and temporal averaging of cloud physical and optical properties have yet to be established. CERES will perform studies using the broadband radiative models discussed in Subsystem 5 along with imager pixel-level cloud properties to examine the effect of spatial averaging on relationships between cloud properties and optical properties in time- and space-averaged data.

***3. Cloud height has the smallest horizontal spatial variability, followed by cloud particle phase/size. Finally, cloud visible optical depth has the largest spatial variability.***

If all cloud properties are equally variable in space, then we must treat every cloud imager pixel as a unique cloud retrieval, totally independent of its neighbors. Neighboring pixels in this case do not impart any new information. At best they may be used in larger groups only to decrease the amount of instrument noise.

If, on the other hand, one or more of the cloud properties exhibits much larger spatial scales or less variability than the other cloud properties, then it is possible to group the data and derive additional information from collections of pixels that would not be feasible, or would be ambiguous, using a single pixel. Many cloud algorithms use exactly this assumption, but for different cloud properties. The spatial coherence algorithm (Coakley and Bretherton, 1982) relies on the uniformity of cloud height to derive estimates of overcast cloud layer properties, to separate these overcast pixels from broken cloud or variable emissivity pixels, and to ascribe an effective cloud amount to each variable pixel. Some recent studies of cloud particle size (Lin and Coakley, 1993) further assume that both cloud height and cloud particle size are constant over a distribution of pixels. The method of Arking and Childs (1985) assumed that cloud height and cloud visible optical depth were constant and adjusted cloud amount to achieve a consistent cloud retrieval.

Rigorous proof of these assumptions is not yet available, although for cloud height, the recent availability of ECLIPS (Experimental Cloud Lidar Pilot Study) lidar data for cloud base, and 3-mm radar data from FIRE (First ISCCP Regional Experiment) provide data sets adequate to begin a more thorough examination of this assumption. Uplooking LWP data such as taken during the FIRE experiments can be used to infer the variability of optical depth. We conducted an initial examination of this variability using the 1987 FIRE data from San Nicolas Island for LWP over a 19-day period, and cloud base altitude from ECLIPS lidar for a 5-day period. These initial data confirmed the usual qualitative assumption that cloud height is much less variable. These data sets are too limited to base global analysis on, however, and further work is needed in this area for a wider range of cloud types. The answer is likely to be a function of cloud type and whether cloud base or cloud top is most important. A very

### 52 Boundary Layer Cloud Fields ( 58 km )

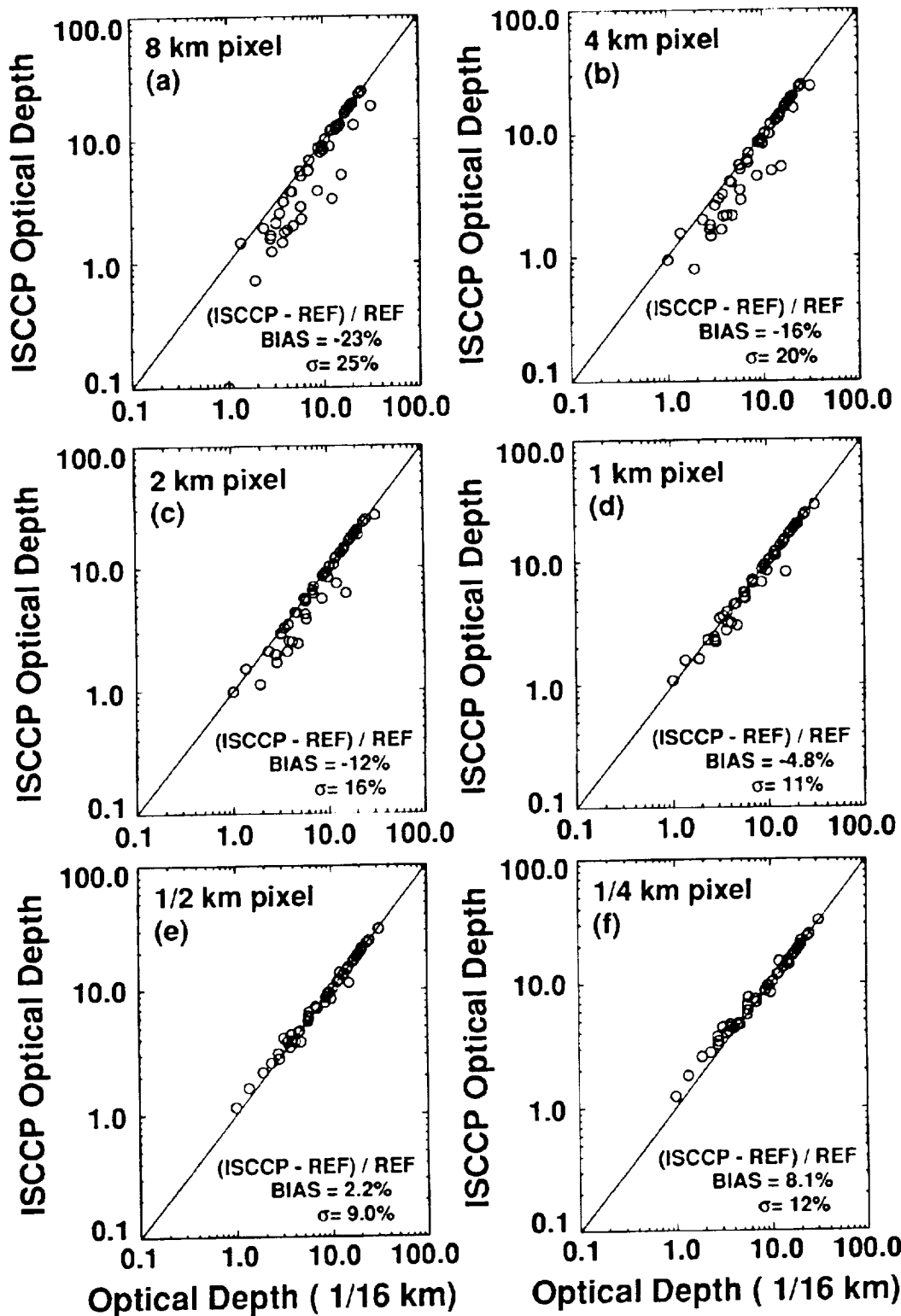


Figure 4.0-3. Effect of sensor spatial resolution on ISCCP-like estimate of cloud optical depth for boundary layer cloud cases. Reference is 57-m spatial resolution Landsat data. Each point is a linear average of optical depth for cloudy pixels in a 58-km region.

interesting data set in this regard is the global lidar data taken from the space shuttle in late 1994 by the Langley Lidar In-Space Technology Experiment (LITE). Other critical future data sets will be long time series from 3-mm radar at ARM (Atmospheric Radiation Measurement) sites in the tropics, mid latitudes, and polar regions. The assumption used here that cloud particle size is more spatially contiguous than visible optical depth is based on aircraft reports that cloud liquid water content seems to vary more with cloud particle number than with cloud particle size. This assumption is also supported by initial analysis of satellite inferred cloud properties using the AVHRR visible channel (optical depth variability) and 3.7- $\mu\text{m}$  channel (cloud particle size) as shown in Coakley et al. (1987) and Coakley and Davies (1986). A rigorous study of this conclusion over a large data set has not been carried out to our knowledge. Much of this data exists, at least for boundary layer clouds, convective clouds, and cirrus.

Given the importance of multilayer clouds to the LW surface radiation balance, and to the in-atmosphere radiative fluxes, the CERES algorithms will begin to address the issue of remote sensing of multilayer cloud systems. One of the key proposals for unscrambling complex cloud overlap cases is to allow cloud height information to propagate horizontally from single-layer to multilayer cloud observations. A key assumption is that the layers are reasonably independent, so that cloud heights in single-layer regions are similar to cloud heights in multilayer overlapped cloud regions. Clearly if the cloud layers are vertically close (1 km or less) they are likely to be strongly correlated. If they are vertically separated by more than 6 km, they are probably poorly correlated (cirrus over boundary layer stratus). An exception to this would obviously be storm fronts, where large systematic cloud height changes occur over several hundred km. As a first approximation, CERES will assume that cloud layers are uncorrelated when separated by more than about 3 km. In Release 1, CERES will only consider the overlap case of nonblack cloud over lower cloud, with the layers separated by at least 3 km. The 3-km separation is also required to get a sufficient signal in the thermal infrared to attempt separation of two cloud layers overlapped in a imager pixel (Baum et al. 1994). Note that variations in the height of nonoverlapped cloud layers can be detected for much smaller changes in cloud height, down to perhaps 0.25 km. The restriction here is for initial attempts to unscramble the signal from an optically thin upper cloud over a lower cloud.

In Release 2, CERES will add the ability over oceans to use passive microwave data to estimate cloud LWP beneath an optically thick ice cloud. For other regions of optically thick high- or middle-level cloud, assumptions must be made about cloud overlap: random, maximum, or minimum overlap. Further discussions of this issue can be found in Hahn et al. (1982) and Tian and Curry (1989). Finally, we assume that no more than two cloud layers are present at the same time. A great deal of work needs to be done on the cloud layering assumptions, and the best data set appears to be the recent field observations using 3-mm or 8-mm cloud radar. There is also an urgent need for a spaceborne cloud radar to achieve global measurements of cloud height and cloud overlap. Cloud lidar will work for some systems, but only if the total cloud optical depth of both layers is less than about 3.

#### ***4. Cloud layers separated by more than 3 km in height are independent.***

The initial reason for this assumption is to allow the use of nearby single-layer cloud height observations to constrain the solution of optical properties for two-layer cloud overlap conditions. This assumption also enters into how to handle the time and space averaging of cloud overlap conditions. If the layers are independent, then cloud physical and optical properties can be saved in cloud height categories, where cloud properties for an imager pixel are categorized based on the effective cloud pressure,  $p_e$ :

High Cloud:	$p_e < 300$ hPa
Upper Middle:	$300 < p_e < 500$ hPa
Lower Middle:	$500 < p_e < 700$ hPa
Low:	$700 < p_e < 1000$ hPa

$p_e$  is the pressure in the atmospheric temperature profile which corresponds to the effective radiating temperature of the cloud. For a thin cloud this is the cloud center; for a thick cloud it is the cloud top. This can be thought of as the radiative center of mass for the cloud as viewed from the TOA in the thermal infrared part of the spectrum. Given the independence of cloud layers, we do not require that separate cloud properties be saved for every overlap combination of two cloud height categories. Instead, we simply save the fraction of space or time covered by each of the 11 cloud overlap conditions:

1. No cloud
2. Low cloud only
3. Lower middle cloud only
4. Upper middle cloud only
5. High cloud only
6. High cloud over upper middle cloud
7. High cloud over lower middle cloud
8. High cloud over low cloud
9. Upper middle cloud over lower middle cloud
10. Upper middle cloud over low cloud
11. Lower middle cloud over low cloud.

The selection of category pressure boundaries is somewhat arbitrary. The current selection is based on the following criteria:

- A minimum of three cloud layers to distinguish major cloud types: high/middle/low clouds
- A pressure boundary at 500 hPa, the level chosen for CERES initial atmospheric radiative flux analysis, thereby separating the troposphere into two parts for radiative heating
- Pressure boundaries which are a subset of those used by ISCCP, so that direct comparisons can be made to the ISCCP data; ISCCP has boundaries which include 680 and 310 hPa
- Maintain a minimum of about 3-km separation between height categories, so that layers are often independent

These criteria led to the selection of four cloud height categories and boundaries at 700, 500, and 300 hPa. In the tropics, the 300-hPa boundary occurs at a temperature of about 240K, similar to the 235K threshold often used to distinguish precipitating clouds. This selection should prove useful when comparing radiative and latent heating profiles estimated using TRMM data.

A schematic diagram summarizing the cloud height categories and layering assumptions is shown in Figure 4.0-4 which is taken from Subsystem 4.4.

***5. Clouds are sufficiently varied in time and space that there is currently no single cloud algorithm that works well for the all cloud types and cloud properties.***

As is often the case when attacking a formidable problem, each cloud algorithm has commonly examined a small piece of the whole cloud retrieval problem. ISCCP has developed the most complete analysis to date, although the ISCCP algorithm is severely limited by the restriction to use only two spectral bands, a visible and an infrared window channel. The CERES cloud analysis will have a more complete set of measurements to use, including all five of the AVHRR channels, the 1.6- $\mu\text{m}$  channel on VIRS and MODIS, new channels on MODIS, as well as passive microwave data. In spite of this additional information, there is still no single algorithm available to handle the wide diversity of cloud properties observed over the globe. Instead, a robust cloud analysis which gains the best information from each spectral channel and instrument will by nature be forced to combine multiple cloud algorithms.

Clear and accurate combination of diverse algorithms is a difficult task. In order to achieve this strategy, CERES has a team which includes experts in many of these different approaches. This

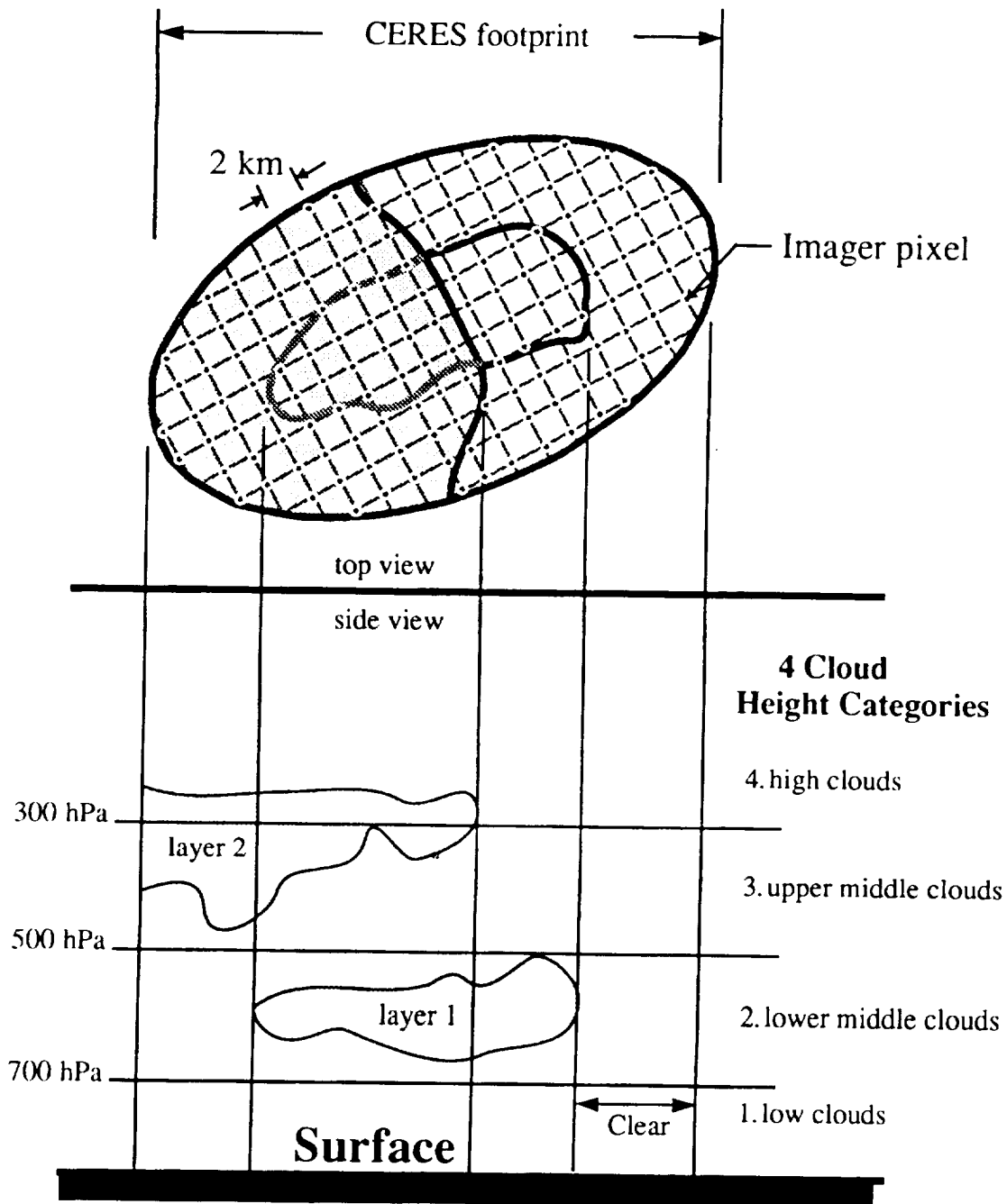


Figure 4.0-4. Schematic diagram of vertical and horizontal cross sections of imager pixel cloud properties matched to CERES field of view. 2-km imager pixel spacing is typical of VIRS on TRMM. Data tables can be found in Subsystem 4.4.

document describes the current understanding of the best way to implement such a combined algorithm. Like ISCCP, the cloud algorithm is divided into a cloud detection and a cloud optical property stage. Unlike ISCCP, the algorithm also includes an additional stage for the determination of well-defined cloud layers. Sections 4.1, 4.2, and 4.3 of this document summarize the current strategy for these three tasks. In each area, multiple algorithms are brought to bear, usually in a hierarchy which depends on either the surface background (ocean, land, mountain, desert, snow/ice) or on the clouds themselves

(low, high, thick, thin, single layer, multiple layer). Initially, this combination is likely to cause significant problems. As the CERES team works through the first month of global data in the next year, a better understanding will emerge of our ability to combine the algorithm capabilities.

**6. Accurate relationships between cloud and radiative fluxes require accurate spatial and time matching of both imager-derived cloud properties and CERES broadband radiation data.**

There are three primary reasons to closely link the instantaneous CERES radiances to cloud imager derived cloud properties.

First, the development of anisotropic models from CERES rotating azimuth plane scanner data requires that CERES broadband radiances be accurately classified as a function of cloud and surface properties. A particularly critical cloud property for SW and LW anisotropy is cloud optical depth. Tests were made using FIRE stratocumulus uplooking passive microwave observations of LWP (e.g., Cahalan et al. 1994) taken every minute for 19 days in July 1987 at San Nicolas Island. At a mean wind speed over the period of 5 m/s, the 1-minute sampling corresponds to a cloud advection of about 300 m. A running time average was then applied to the data to simulate the 20-km CERES footprint scale (roughly a 60-minute running average). Finally, the time-averaged CERES footprint data were time lagged to simulate the effect of a spatial (or temporal) mismatch in the cloud imager data (providing LWP or cloud optical depth) and the broadband radiation data. If the lagged rms difference in LWP is required to be 5% or less, then the 20-km average can be mismatched by no more than 1 km (or about 3 minutes). The rms LWP error was roughly linear in the lag time or distance. We conclude that accurate angular models are likely to require close matching of cloud and radiation data. Further tests will be conducted using Landsat data to extend these 1-D results to two dimensions.

Second, if TOA flux measurements are to be used to constrain the radiative fluxes calculated using cloud imager derived cloud properties, then a close match of these properties must be obtained. Because cloud physical and optical properties are nonlinearly related to radiative fluxes, rms errors in matching cloud and radiation data should be kept to less than 10% to avoid bias errors. Tests of this sensitivity will be conducted using simulations similar to those above, but including radiative flux calculations on high resolution cloud imager properties such as AVHRR Local Area Coverage data.

Third, the complexity of relationships between cloud properties and radiative properties increases as clouds become multilayered. Tian and Curry (1989) found that while single-layer clouds dominated observations at a 45-km scale (similar to a single CERES footprint), multiple-layer clouds dominated at 220 km (similar to an ERBE grid box). This suggests that for some studies, there is an advantage to close ties of cloud properties and radiative fluxes at not only the scale of large grid boxes, but also at the scale of individual CERES footprints.

The CERES strategy is to represent the distribution of energy received at the CERES broadband detectors by the point spread function (Subsystem 4.4). The point spread function includes the effects of detector response, optical field of view, and electronic filters (Subsystem 1). Cloud imager derived cloud properties will be convolved with the CERES point spread function to derive properties appropriately weighted and matched to the CERES fields of view. Note that the nominal  $2\sigma$  accuracy of the navigation for the EOS and TRMM platforms is less than 1 km, sufficient to allow an accurate mapping of imager pixel data into CERES fields of view.

**7. Anisotropy of cloud and surface scenes can be determined by compositing a large ensemble of scenes where each scene is viewed at one instant of time from only 1 or 2 directions.**

The rapid variability of clouds in space and time places a fundamental limitation on measuring radiative flux from space. There are no sufficiently homogeneous targets for which a satellite can view all  $2\pi$  steradians of a "target" at the same time. The flat plate or active cavity instruments which view  $2\pi$  steradians from satellite altitude respond to about a 2000-km region on the Earth, guaranteeing inhomogeneity. Therefore, all measurements of flux from space require compositing over time. The scanning

radiometers such as the Nimbus-7 ERB or ERBE scanners select a small angular field of view in order to measure individual scene types (forest, cumulus, stratus, cirrus, etc.). This requires the conversion of the radiance measured in a single direction to the desired radiative flux. In order to improve spatial sampling over the globe, scanning radiometers usually scan in a cross-track pattern, limiting angle views to a small systematic subset of the full angular space.

For SW radiation, anisotropy is a function of viewing zenith angle, viewing azimuth angle, and solar zenith angle (Suttles et al. 1988; Wielicki and Green, 1989). Typical scanning instruments measure only a small portion of this 3-D angular space. The Nimbus-7 ERB instrument was designed to sacrifice spatial sampling to obtain improved angular sampling over the entire  $2\pi$  hemisphere (Taylor and Stowe, 1984). ERBE used these observations to develop the 12 ERBE angular distribution models (ADM's) as a function of cloud fraction and surface type (ocean, land, desert, snow/ice) (Suttles et al. 1988).

Unfortunately, the ERBE models are unsatisfactory for CERES for three reasons. First, postflight analysis (Suttles et al. 1992) has shown that the estimated SW albedo systematically increases with viewing zenith angle and the estimated LW flux decreases with viewing zenith angle. The ERBE models based on Nimbus-7 observations underestimate the amount of anisotropy. Second, the albedo bias is a function of solar zenith angle, and therefore a function of latitude (Suttles et al. 1992), which will affect the inference of equator-to-pole heat transport. Third, the models only depend on cloud amount, so that the rms error in deriving instantaneous fluxes is estimated as roughly 12%. This instantaneous noise is primarily caused by the inability of ERBE and Nimbus 7 to measure cloud optical depth, the largest source of varying anisotropy (Wielicki and Barkstrom, 1991).

Tests of the ADM bias have examined three possible causes: incorrect scene identification by the ERBE maximum likelihood estimation technique (Suttles et al. 1992; Ye, 1993), incorrect assumptions in building the ERBE ADM's, and the dependence of ADM's on spatial scale (Ye, 1993; Payette, 1989). CERES will fly a scanner which will rotate in azimuth angle as it scans in elevation, allowing the development of a new set of ADM's. All three candidate problems are being examined with current data in preparation for designing the CERES ADM's.

First, scene identification will be greatly improved by matching VIRS- and MODIS-derived cloud properties to each CERES field of view. This will provide the basic cloud typing for development of new ADM's. ADM's will be derived as a function of cloud amount, cloud optical depth/emittance, cloud height, particle phase, and cloud particle size. Second, one of the critical assumptions of the Nimbus-7 and ERBE ADM's was that cloud anisotropy and cloud albedo are uncorrelated. For the case of increasing cloud optical depth, this is clearly a questionable assumption. This assumption will be removed for CERES by using the radiance pair method discussed in Subsystem 4.5. This method uses the rotating azimuth plane CERES scanner to obtain views of the same target at nearly the same time from two different viewing angles. The pairs are used to obtain reflectance ratios which eliminate the dependence on target albedo. Finally, studies will examine the dependence of field of view spatial scale in testing of new CERES ADM's.

#### 4.0.4. Algorithm Outline

Because cloud fields are highly variable in space and time, the process of both cloud detection and cloud property determination from space can become very complex. This is true especially over variable backgrounds such as mountains, desert, or snow and ice. As a result, no single cloud algorithm works well for all cloud types over all backgrounds. In order to deal with this complexity, the CERES cloud algorithm has broken this task into three relatively independent functions:

Subsystem 4.1—Imager clear-sky determination and cloud detection.

Subsystem 4.2—Imager cloud height determination.

Subsystem 4.3—Cloud optical property retrieval.

Following the cloud retrieval over a swath of cloud imager data, three final steps are carried out to obtain TOA and surface radiative fluxes for each CERES broadband measurement.

Subsystem 4.4—Convolution of imager cloud properties with CERES footprint point spread function.

Subsystem 4.5—CERES inversion to instantaneous TOA fluxes.

Subsystem 4.6—Empirical estimates of shortwave and longwave surface radiation budget involving CERES measurements.

The final result is a set of cloud properties and radiative fluxes for each CERES footprint. The final cloud properties are grouped into four cloud height categories with height boundaries at pressures of 700, 500, and 300 hPa. Since more than one cloud layer is allowed in a CERES footprint, we also save the fraction of the footprint covered by cloud imager pixels which showed evidence of overlap of any two of the four cloud height categories. Only two of the four cloud height categories are allowed to overlap in a single cloud imager pixel. For Release 1, we assume that the four cloud height categories are independent, so that cloud properties in any given height category are independent of whether or not they were overlapped with any other height category. This simplification allows us to keep cloud properties for only four categories, as opposed to all possible combinations of cloud height categories. Cloud overlap is only saved as the fractional area of overlap between all combinations of two of the four cloud height categories. Note that while ISCCP saved frequency distributions of a bispectral histogram of cloud optical depth classes and cloud height classes, this leads to a substantial discretization error in determination of average cloud height within a height class. CERES saves not only the frequency of occurrence, but also the average and standard deviation of all cloud properties separately for each cloud height category. In this case, even very small cloud height shifts can be detected within each cloud height category.

All cloud properties are weighted with the CERES point spread function so that CERES-measured broadband TOA fluxes can be used to directly constrain radiative calculations of surface and in-atmosphere fluxes produced using the cloud imager cloud properties. These CERES footprint averages represent a very specific view or composite of cloud physical and optical properties designed to facilitate studies of the role of clouds in the Earth's radiation budget. A table of the CERES cloud products for each CERES footprint can be found in Subsystem 4.4.

Finally, where possible, direct parameterizations of TOA radiative fluxes to surface radiative fluxes are derived. These surface flux estimates for each CERES footprint are saved in the SSF output product of Subsystem 4, as well as in spatially gridded and time-averaged forms in the SURFACE products (Subsystems 9 and 10). Direct parameterization of TOA to surface fluxes is used as an alternative approach to the calculation of surface radiative fluxes using cloud properties and radiative models used in the ATMOSPHERE data products (Subsystems 6, 7, and 8).

A full description of the Subsystem 4 input and output products can be found in appendixes A and B.

#### **4.0.5. Algorithm Releases**

The CERES algorithm will be designed in four phases or "releases." Version 0 is an experimental version to test initial concepts in an informal way. Version 0 was a layer bispectral threshold method (Minnis et al. 1993) which determined cloud fraction in three vertical layers. It is similar to the ISCCP technique in that fixed differentials are added to the expected clear-sky visible (0.65  $\mu\text{m}$ ) and infrared (10.8  $\mu\text{m}$ ) radiances to set thresholds for cloud detection. Data from the 3.7- $\mu\text{m}$  channel are used to detect snow. Optical depth is calculated (section 4.3.4.1.1) using the visible channel and one of two microphysical models: 10- $\mu\text{m}$  water spheres for cloud temperatures warmer than 253K, and cirrostratus hexagonal ice crystals (Takano and Liou, 1989) for colder clouds. Visible optical depth is converted to 10.8- $\mu\text{m}$  absorption optical depth and then used to correct cloud altitudes for emittances less than 1

(section 4.3.4.4). The version 0 code was applied to NOAA-9 October 1986 AVHRR and ERBE data. The AVHRR global area coverage (GAC) pixels were matched to ERBE footprints using an  $8 \times 8$  array of GAC data centered on the ERBE footprint. The analysis incorporated many of the same inputs that will be used in the later CERES cloud algorithm versions. Analysis results were provided for use in initial testing of the calculation of in-atmosphere fluxes in Subsystem 5.

Release 1 will be operational by 1995, and is designed to process global data from the existing NOAA-9 and NOAA-10 ERBE/AVHRR/HIRS data. This release will be used to test algorithm concepts on global data, and for comparing multiple algorithms for cloud parameters such as cloud height. This is a critical step, since most of the algorithms have only been used for specific regional studies. This step will expose much of the exception handling required to run a global analysis. In addition, many of the sensitivity studies needed to test time interpolation/averaging algorithms in Subsystems 7, 8, and 10 require geostationary data analyzed at hourly intervals. Data from GOES-8, launched in the Spring of 1994, will provide the opportunity to test the CERES Release 1 algorithms on geostationary data very similar in spatial resolution and spectral channels to the AVHRR/HIRS combination on NOAA 9 and 10.

Release 2 will be ready by early 1997, in time to integrate into the Langley DAAC (Distributed Active Archive Center) before the TRMM launch of the first CERES instrument planned for August, 1997. Release 2 will be designed to operate on TRMM data, including the CERES broadband scanner data and the VIRS cloud imager data. Release 2 will also incorporate the use of the TMI (TRMM Microwave Imager) LWP measurements for multilayer clouds over ocean. This release will not use any infrared sounder channel analysis (these channels are missing from VIRS) but will incorporate the VIRS 1.6- $\mu\text{m}$  channel for improved particle size determination. In addition, this release may use the VIRS 0.65- and 1.6- $\mu\text{m}$  channels to obtain estimates of aerosol optical depth based on the NOAA AVHRR operational algorithm. The advanced NOAA aerosol algorithm using the 0.65- and 1.6- $\mu\text{m}$  channels of AVHRR should have been tested for 2 years prior to the TRMM launch.

Release 3 will be designed to use the MODIS cloud imager data, as well as the CERES rotating azimuth plane scanner which will be used to develop new empirical models of the anisotropy of SW and LW radiances. This release will be used to process EOS-AM and EOS-PM data. Until new angular models are developed, the CERES analysis will rely on the ERBE models (Suttles et al. 1988) to convert the measured broadband radiance to a TOA broadband flux. Note that the MIMR (Multifrequency Imaging Microwave Radiometer) passive microwave instrument will be available on the EOS-PM platform and on an ESA (European Space Agency) polar-orbiting platform in the same orbit at EOS-AM. These MIMR instruments will provide the estimates of cloud liquid water path.

#### 4.0.6. Validation

The CERES investigation directly funds CERES science team members and support staff to carry out validation investigations. These investigations typically involve tests of various algorithm components (cloud height, particle size, etc.) against field experiment data such as that obtained by the FIRE and ARM projects.

Current data used for *simulation* of CERES cloud and flux inversion algorithm capabilities include Satellite data:

- AVHRR/HIRS to simulate most of the VIRS and MODIS channels
- Landsat to simulate the higher spatial resolution of MODIS, as well as measurements of 1.6 and 2.1- $\mu\text{m}$  channels not on AVHRR or HIRS.
- GOES radiance and ISCCP cloud data to test time sampling of cloud properties
- Nimbus-7 ERB and ERBE broadband data to test angular modeling
- GOES-8 (similar to AVHRR/HIRS channels)

Aircraft data:

- MAS on the ER-2 in FIRE, ARM, SCAR (Sulfates, Clouds, and Radiation), etc.
- Thematic Mapper Simulator on the ER-2

Current data used to *validate* the satellite cloud and flux inversion algorithms include

- ER-2 lidar collocated with Landsat, AVHRR, HIRS, and MAS data (cloud top)
- Surface-based lidar (cloud base, tops for thin clouds)
- Surface-based 3-mm and 8-mm radar (cloud base and top)
- Surface- and ER-2-based passive microwave for LWP (cloud LWP)
- Landsat and ER-2 data for cloud detection accuracy (cloud area)
- Aircraft microphysical probes (cloud particle size, phase, habit)
- Multi-instrument comparisons: AVHRR vs. HIRS cloud height for thin cirrus
- ER-2 CCD (charged coupled device) array imager to examine cloud anisotropy at solar wavelengths
- CAR (Cloud Absorption Radiometer) to examine cloud single scattering albedo, and angular reflectance patterns (scans from nadir to zenith, 0.5 to 2.5 m channels)
- LITE on space shuttle for 5 days in September 1994: First global measurement of lidar cloud height; space scales and AVHRR underflights

Future data sets used to *validate* satellite cloud and flux inversion algorithms include

- NOAA U.S. ceilometer network (cloud base to 4-km altitude)
- LITE (future missions)
- ADEOS (Advanced Earth Observing System; ESA, Japan 1996 a.m. sun-synchronous) POLDER (Polarization and Directionality of Earth's Reflectances) instrument for polarization and multiangle CCD array measurements at solar wavelengths
- EOS-AM platform (1998) ASTER (Advanced Spaceborne Thermal Emission and Reflection Radiometer) instrument (Landsat-like spatial resolution, but adds thermal channels at 3.7, 8.5, 11, and 12 m similar to MODIS)
- EOS-AM platform MISR (Multiangle Imaging Spectroradiometer) multiangle CCD array cameras for SW anisotropy at spatial scales from 200 m to 300 km, and stereo cloud height
- EOS-PM platform (2000) MIMR passive microwave instrument [improved Special Sensor Microwave/Imager (SSM/I) for LWP]
- EOS GLAS (Geoscience Laser Altimeter System; 2002) a nadir pointing space-based lidar for validation of global cloud height observations
- Space-based 3 mm radar (under discussion but not scheduled for flight: Cloud top and cloud base, plus multilevel cloud validation)
- Field experiment data including
  - FIRE: Expected to examine polar boundary layer cloud and tropical cirrus (1997, 1998). Includes in-cloud and surface radiative flux data
  - CEPEX (Central Equatorial Pacific Experiment) and TOGA-COARE (Tropical Ocean Global Atmosphere Coupled Ocean-Atmosphere Response Experiment): 1992/1993 tropical cloud experiments
  - GCIP [GEWEX (Global Energy and Water Cycle Experiment) Continental-Phase International Project]: Expected to examine continental U.S. clouds; Mississippi basin (1996 and later). Primarily ceilometers and surface radiative fluxes
  - ARM: Oklahoma, western Pacific Ocean, and Alaskan north slope surface sites. These sites include surface radiation, lidar, cloud radar, and profilers. Data available over next few years and extending over a 10-year period
  - SHEBA (Surface Heat and Energy Balance of the Arctic): A surface site on the polar ice cap for 18 months (1997). Includes lidar and surface radiation budget data

WBSRN (World Baseline Surface Radiation Network): Surface radiative fluxes  
 Other field experiments of opportunity: BOREAS (Boreal Ecosystem Atmosphere Study),  
 SCAR, etc.

CERES science team members are active members of many of the field experiment programs including FIRE, ARM, GCIP, WBSRN, CEPEX, TOGA-COARE, and SCAR programs. These relationships, along with CERES investigator funding will be used to develop and carry out validation plans for specific components of the CERES cloud and radiative flux inversion algorithms discussed in Subsystems 4.1–4.6. CERES does not, however, have funding to carry out its own field experiments. CERES is dependent on these other programs for validation data. Many of the results shown in the subsystem ATBDs and used to plan the current CERES algorithms are a result of CERES science team participation in these programs to date.

#### 4.0.7. Processing Estimates

Processing resources required have been estimated by scaling existing satellite analysis codes including the ERBE inversion subsystem (Wielicki and Green, 1989) processing global ERBE data, the Spatial Coherence cloud algorithm running on 4-km AVHRR data, the HBTM (Hybrid Bispectral Threshold Method) running on 4-km AVHRR data (Minnis et al. 1993), a two-channel ISCCP-like (CERES version 0) algorithm running on 4-km AVHRR data, and finally a newly developed research code incorporating more of the CERES algorithms, but without optimization (see Subsystem 4.3).

In order to estimate the requirements for VIRS and MODIS processing, these processing times were scaled linearly by

- Number of imager pixels to be processed
- Number of imager spectral bands to be processed
- An increased total algorithm complexity of a factor of 4 times the ERBE, spatial coherence, and ISCCP-like V0 algorithms, and a factor of 2 times the new research algorithm
- A requirement for the algorithm to run three times faster than real time (i.e., 3 days of global data for one instrument processed in 1 day)

All algorithms were run on Sun Sparc 2 systems with an assumed floating point computational power of 4.0 million floating point operations per second.

We scaled the timings to process five spectral bands on VIRS (2-km spatial resolution), and to process 11 spectral bands on MODIS, including two 250-m spatial resolution spectral bands (day only), two 500-m bands (day only), and seven 1-km bands (day and night). The timing estimates in Gflops (billions of floating point operations per second) were:

	<u>ERBE</u>	<u>ISCCP V0</u>	<u>Spatial Coherence</u>	<u>New Research Algorithm</u>
VIRS:	0.5	0.7	0.7	4.5
MODIS:	7.5	12.2	12.2	78.

The highest processing loads were from a new unoptimized research code, and should reduce by a factor of 2–10 with optimization. Overall, estimates appear to be about 0.7 Gflop for VIRS and 10 Gflops for MODIS full resolution data. We will examine the accuracy degradation in subsampling the MODIS data to 1/4 of the MODIS pixels. This accuracy issue is primarily for matching instantaneous cloud property data to CERES fields of view for the radiative flux calculations performed in Subsystem 5. If cloud properties include too high a spatial sampling noise, then constraints against TOA measured fluxes are more difficult and less accurate. This subsampling issue will be examined using 1-km AVHRR data and simulating the CERES point spread function.

For large data volumes, there is a common conception that processing is I/O (input/output) bound, even for hard disk I/O. To test this, we examined the time to perform the following processes on a 10-Mbyte Landsat data file:

- 10 seconds = Read data from hard disk (SCSI-1 on a Sun Sparc 2) to memory
- 43 seconds = Unpack the data from scan line records to pixel byte data (16-bit digital count) using an optimized routine for unpacking data
- 24 seconds = Convert the digital count data to real radiance values (32 bit) using a simple look-up table

We found that for even this simple process, that only 13% of the total time was spent in reading the data, while the processing burden of unpacking and calibrating dominated the processing time. For a complete cloud algorithm which then analyzes the radiance data, the I/O fraction will be 1% or less. This trade-off will be examined further with much higher power processors such as an SGI machine using a 4400 processor at greater than 30 million floating point operations per second. The critical I/O issue is more likely to occur in reading the archive media.

Given the rapid improvement in microprocessor speeds, it is likely that super workstations will be capable of processing the VIRS and later MODIS data streams. The larger problem may well be data storage. For the MODIS and VIRS data, the Langley DAAC will not keep a separate level 1b archive, but will only keep data for the last month or two to simplify data storage. Any later reprocessing would return to the GSFC DAAC to obtain the required MODIS level 1b data.

#### **4.0.8. Relationship of MODIS and CERES Cloud Data Products**

**4.0.8.1. Background.** One of the comments of the peer review panel was that CERES and MODIS Science Teams are both producing estimates of cloud properties. Is this a duplication of effort? Can't one cloud product satisfy all users?

If we view clouds as large (relative to satellite image pixels), well-defined, and well-behaved sheets of paper floating in the atmosphere, then one cloud definition will suffice for all users. We simply define whether the sheet is present or not, the altitude of cloud occurrence, and the properties of the cloud sheet.

Field experiments show that actual clouds

- Change on time scales of seconds to hours (much less than satellite revisit time)
- Change on space scales from meters to 10 000 km (much less than to much greater than satellite pixel size)
- Have highly variable shapes and configurations
- Occur at least half the time in multiple overlapping cloud layers
- Often have optically thin cloud edges; no sharp cloud/clear boundary (boundary layer clouds)
- Are often sufficiently optically thin to be at the edge of detectability with passive radiometers (cirrus clouds)

Given this extreme variability, and the associated difficulty in accurately remotely sensing cloud properties, it is unlikely that a single approach to cloud measurement will meet all needs.

**4.0.8.2. EOS cloud products.** In particular there are three major categories of cloud data required: cloud masking, cloud physical properties, and cloud radiative properties. For each of these areas, the MODIS and CERES teams are cooperatively examining a range of strategies to derive cloud properties. A comparison of MODIS and CERES cloud products is given in Table 4.0-1. The table gives the primary *focus* of each product, *not* its only use. The focus, or top priority, however, controls the future processing strategies and adjustments as we learn more about clouds using the EOS and field experiment observations.

Table 4.0-1. Comparison of MODIS and CERES Cloud Products

MODIS: Daytime solar channels (King)	MODIS: Day/night infrared HIRS-like clouds (Menzel)	CERES: Day/night, solar/Infrared VIRS-like clouds (Barkstrom)
Cloud dynamics	Cloud dynamics	Cloud radiative effects
Daytime only	Daytime and nighttime	Daytime and nighttime
Instantaneous	Time averaged	Time averaged
Pixel to global scale	Regional to global scale	Regional to global scale
Rapid algorithm improvement	Infrequent algorithm improvement	Slow algorithm improvement
Time series inconsistency allowed	Time series must be consistent	Time series must be consistent
Algorithm change MIGHT = Reprocessing	Algorithm change MUST = Reprocessing	Algorithm change MUST = Reprocessing
Subset of cloud properties OK (all retrieved properties high accuracy)	Subset of cloud properties OK (all retrieved properties high accuracy)	Complete cloud properties required (some cloud properties low accuracy such as cloud thickness and base)
Cloud properties stand alone	Cloud properties must be consistent with existing HIRS data	MODIS/VIRS must be consistent (at least in early years of EOS)
Avoid marginal cloudy/clear data in time and space averaged data	Include marginal cloudy/clear data in time and space averaged data	Include marginal cloudy/clear data in time and space averaged data

**1. Cloud masking: Determination of each satellite pixel as either cloud-free or cloud contaminated.**

Masking determines if a satellite pixel is a candidate for use in observing surface properties after correction for atmospheric effects. For example

- SST (sea surface temperature) observations: optically thin boundary layer cloud is acceptable (small thermal infrared impact) while optically thin cirrus is damaging (relatively large thermal infrared effect). Cloud shadows have no effect.
- Vegetation canopy studies: More thin cirrus is allowable, but need to avoid cloud shadows.
- Fields of view which are uncertain (could be clouds or clear) will usually be ignored in MODIS time and space averages of cloud and surface properties. These data will be included in the CERES time and space averages of cloud properties for radiation budget purposes.

**2. Cloud physical properties: Cloud property estimates for use in characterizing cloud properties over the globe, and for testing dynamical models of clouds.**

Emphasis is on getting accurate cloud water budget: liquid water, ice water, cloud amount, height, and particle size/phase. Statistics in a grid cell, or over a type of cloud, are most critical, since a simulated cloud field can never be expected to match real clouds cell for cell (predictability problem and inadequate model initialization at cloud scale). Primary emphasis is on provision of regional cloud properties with highest accuracy, but availability depends on actual cloud conditions. Secondary emphasis is on global scale properties. As improvements in cloud remote sensing are developed using MODIS, they are implemented, with improvements every 3–6 months shortly after launch and at 1–2 year intervals thereafter. Reprocessing of the previous data is decided on a case by case basis. Accuracy of current data is more important than a single consistent time record.

Cloud properties vary greatly in their effect on solar radiation (scattering dominated) as opposed to thermal infrared radiation (absorption and emission dominated). MODIS will exploit this difference to pursue two different strategies for determining cloud physical properties. One set of cloud data (King; see Table 4.0-1) will focus on information retrieved using solar reflectance channels on MODIS to derive cloud particle size and cloud optical depth during daytime observations. A second set of cloud data (Menzel; see Table 4.0-1) will focus on information retrieved using the thermal infrared channels on MODIS to derive cloud effective emittance, cloud height, and cloud particle size. Each technique has advantages and disadvantages that will be useful in studies of clouds. The thermal infrared cloud data will also extend in time a global cloud data set started using the NOAA HIRS/2 data. For climate record analysis, the infrared cloud analysis technique will be consistent for the HIRS and MODIS data sets.

**3. *Cloud radiative properties: Cloud property estimates for use in determining the radiation budget at the top of the atmosphere, within the atmosphere, and at the surface, and for studying the role of clouds and radiation in the climate system.***

Many studies of cloud/climate feedback mechanisms will require cloud and radiation budget data which are internally consistent. For CERES (Barkstrom; see Table 4.0-1), the emphasis is on radiatively effective cloud data. Emphasis is also on global data available at all times and places. Secondary emphasis is on regional studies. Because climate data must be stable for long periods of time, algorithms are updated very infrequently, perhaps once every 3–5 years. When algorithms are updated, all previous data are reprocessed with the new algorithms. A single consistent time record is of primary importance; accuracy of current data is of secondary importance. As an example, CERES will have flown on the TRMM spacecraft 1 year before the launch of EOS-AM. Accurate determination of the diurnal cycle of radiation will require combination of TRMM, EOS-AM, and EOS-PM data. But the TRMM cloud imager (VIRS) is not as capable as the MODIS instrument on EOS-AM and EOS-PM. VIRS has a larger footprint, and has only half of the MODIS channels useful for cloud property analysis. CERES will need to maximize the consistency between VIRS and MODIS cloud properties, thereby maximizing the time sampling information provided by the TRMM precessing orbit. A trade-off will result; the CERES analysis of MODIS data will strive for consistency with VIRS on the one hand, and full utilization of MODIS on the other. The trade-off will be decided by examining the impact of the decision on derived CERES radiative fluxes. The likely result is that CERES will sacrifice some of the MODIS cloud property accuracy for consistency with TRMM cloud data from VIRS. The MODIS team, in contrast, will seek to utilize the full capability of the MODIS data for cloud physical properties.

**4.0.8.3. *Data processing cost issues.*** At a recent workshop on the future projections for computing capabilities in the late 1990's (Skamania, October 1994), two conclusions were reached:

- Flops and baud will be free [i.e., processing power and data transfer rates (bits per second for sequential data transfer) will get very cheap].
- Data storage costs will not fall nearly as fast. Data random access times will also fall much slower.

The conclusion is that the additional cost of processing data twice in a global streaming mode (process all data in time-ordered fashion) will be inexpensive. The cost to send the full MODIS level 1b data stream (about 20 Mbps) to LaRC in 1998 is estimated to be less than \$10K per year in line charges, and would require about 1/7 the bandwidth of a common 155 Mbps ATM (asynchronous transfer mode) data line in 1998. Further, since CERES is processing climate data, there is no need for immediate MODIS processing. Up to a 1-month delay is acceptable. In this case, even if ATM data line availability is delayed beyond 1998, the MODIS data could be copied to high density tape and transported between the GSFC and Langley DAAC's until the ATM lines are available. There is also no need to archive the MODIS level 1b data at Langley. LaRC would keep the last 2 months of data on a revolving archive for current processing. Over 5 years of MODIS data, this archive cost is 3% of the total MODIS archive at GSFC. Reprocessing the CERES data is seldom done (say every 5 years) so that frequent access to

MODIS data is not required by the operational CERES processing. When MODIS level 1b data are required for reprocessing of CERES data, reprocessing is efficiently done in a streaming mode with the newest, perhaps recalibrated, MODIS level 1b data retransmitted from the GSFC archive.

**4.0.8.4. Summary.** The role of clouds and radiation in the climate system is the highest priority science issue in the U.S. Global Change Research Program. Solutions to this problem will be very difficult, and therefore should be approached from distinctly different perspectives to maintain program robustness. The cost of processing two different views (dynamical and radiative) of cloud properties using the MODIS data is a very small fraction of the cost of building, flying, and operating the MODIS instrument and processing the data.

Any single cloud algorithm team will be subject to a “one size fits all” approach. This approach will not be optimal for any cloud data use and will suppress new creative solutions to problems. On the other hand, the current uncertainties are sufficiently large that in a room of 12 cloud researchers one is likely to find 12 different proposed cloud algorithms. EOS cannot afford to support all possibilities, but must, however, support a few key strategies best suited to the EOS observational capabilities.

We propose that CERES provide a cloud data set focused on the needs of the cloud radiation budget science issues and that MODIS provide a data set focused on the needs of cloud dynamics and cloud processes science issues.

Note that MODIS and CERES are not the only investigations which will provide critical contributions needed for cloud/climate research. In particular

- MISR will provide unique simultaneous multiangle solar reflectance observations to verify the radiative modeling of inhomogeneous cloud cells and cloud fields. MISR will also provide independent verification of cloud heights using stereo viewing techniques.
- AIRS (Atmospheric Infrared Sounder) will provide unique high spectral resolution infrared observations of clouds that will allow more complete examination of cloud microphysics at night, and a consistent day/night subset of cloud properties.
- ASTER will provide very high spatial resolution data (15–90 m) for verification of the effects of beam filling on global data derived using coarser resolution sensors such as MODIS and VIRS.
- EOSP (Earth Observing Scanning Polarimeter) polarization measurements offer the best hope of distinguishing ice particle shape.
- Eventually, cloud lidar (thin clouds) and cloud radar (thick clouds) will be required to verify the EOS capabilities for overlapped multilevel cloud conditions.

MODIS and CERES provide the two most comprehensive global cloud data sets for global change studies. But there are additional critical contributions made by other instruments that also will be necessary to solve the role of clouds in the climate system.

## Appendix A

### Input Data Products

#### Determine Cloud Properties, TOA and Surface Fluxes (Subsystem 4.0)

This appendix describes the data products which are used by the algorithms in this subsystem. Table A-1 below summarizes these products, listing the CERES and EOSDIS product codes or abbreviations, a short product name, the product type, the production frequency, and volume estimates for each individual product as well as a complete data month of production. The product types are defined as follows:

Archival products:	Assumed to be permanently stored by EOSDIS
Internal products:	Temporary storage by EOSDIS (days to years)
Ancillary products:	Non-CERES data needed to interpret measurements

The following pages describe each product. An introductory page provides an overall description of the product and specifies the temporal and spatial coverage. The table which follows the introductory page briefly describes every parameter which is contained in the product. Each product may be thought of as metadata followed by data records. The metadata (or header data) is not well-defined yet and is included mainly as a placeholder. The description of parameters which are present in each data record includes parameter number (a unique number for each distinct parameter), units, dynamic range, the number of elements per record, an estimate of the number of bits required to represent each parameter, and an element number (a unique number for each instance of every parameter). A summary at the bottom of each table shows the current estimated sizes of metadata, each data record, and the total data product. A more detailed description of each data product will be contained in a User's Guide to be published before the first CERES launch.

Table A1. Input Products Summary

Product Code		Name	Type	Frequency	Size, MB	Monthly Size, MB
CERES	EOSDIS					
CID_MODIS	CERX04	MODIS Cloud Imager Data	Ancillary	1/Hour	2491.0	1853304
CID_VIRS	CERX05	VIRS Cloud Imager Data	Ancillary	1/Hour	71.1	52898
CRH	CER16	Clear Reflectance History	Archival	Every 10 Days	91.1	282
IES	CER09	Instrument Earth Scans	Internal	1/Hour	16.7	12425
MOA	CERX06	Meteorological, Ozone and Aerosols	Archival	1/Hour	10.5	7797
MWP	CERX08	Microwave Liquid Water Path	Ancillary	1/Day	25.0	775
SURFMAP	CERX07	Surface Map	Ancillary	1/Week	82.8	367

#### MODIS Cloud Imager Data (CID\_MODIS)

The MODIS cloud imager data (CID\_MODIS) from the EOS spacecraft is level 1b data from 11 of the MODIS channels. The data coverage is 1 hour. The product has a header record followed by multiple scan line records. The organizational details of this product are not finalized yet. Each pixel in the scan line record has radiance values for each of the channels. In addition, each scan line record contains time, location, and solar angle data. It is assumed that the data are organized in the scan lines that appear to scan in the same direction for each scan.

The channels requested by the CERES Science Team are

Channels	Wavelength, $\mu\text{m}$	Resolution (km)
Channel 1	0.645	0.25
Channel 6	1.64	0.50
Channel 7	2.13	0.50
Channel 20	3.75	1.0
Channel 26	1.375	1.0
Channel 29	8.55	1.0
Channel 31	11.03	1.0
Channel 32	12.02	1.0
Channel 33	13.335	1.0
Channel 34	13.635	1.0
Channel 35	13.935	1.0

The CERES Science Team has requested averaged data from the 1/4-km resolution channel to 1/2 km and 1 km, and the two 1/2-km resolution channels averaged to 1-km resolution. The cloud system thus requires input data from the 11 channels and the 4 averaged data sets for a total of 15 sets of “channel” data.

The CID\_MODIS product is external to the CERES processing and is released after CERES processing is completed. It is assumed that the responsible EOSDIS DAAC would retain a copy of this product should it be needed by CERES for a rerun.

**Level:** 1b  
**Type:** Ancillary  
**Frequency:** 1/Hour

**Portion of Globe Covered**  
**File:** Satellite Swath  
**Record:** 1 Scan

**Time Interval Covered**  
**File:** 1 Hour  
**Record:** 1 MODIS Scan

**Portion of Atmosphere Covered**  
**File:** Satellite Altitude

Table A2. MODIS Cloud Imager Data (CID\_MODIS)

Description	Parameter Number	Units	Range	Elements/Record	Bits/Elem	Elem Num
CID_MODIS						
MODIS header record		N/A	N/A	1	2048	
<b>MODIS_Record</b> is Array[25000] of: <b>MODIS_Scanline</b>						
<b>MODIS_Pixels</b> is Array[52240] of: MODIS channel and FOV data	1	N/A	TBD	52240	16	1
<b>Total Meta Bits/File:</b>	2048					
<b>Total Data Bits/Record:</b>	835840					
<b>Total Records/File:</b>	25000					
<b>Total Data Bits/File:</b>	20,896,000,000					
<b>Total Bits/File :</b>	20,896,002,048					

### VIRS Cloud Imager Data (CID\_VIRS)

The VIRS cloud imager data (CID\_VIRS) is received from the VIRS instrument on the TRMM spacecraft. We are requesting level 1b data from the five VIRS channels. The data coverage is 1 hour. The product has a header record followed by multiple scan line records. Each scan line has

Pixel location  
 Spacecraft position  
 Channel data  
 VIRS pixel data  
 Solar viewing angles

Each pixel in the scan line record has radiance values for each of the channels. It is assumed that the data are organized in scan lines that appear to scan in the same direction for each scan.

The CID\_VIRS product is external to the CERES processing and is released after CERES processing is completed. It is assumed that the responsible EOSDIS DAAC would retain a copy of this product should it be needed by CERES for a rerun.

**Level:** 1b  
**Type:** Ancillary  
**Frequency:** 1/Hour

**Portion of Globe Covered**  
**File:** Satellite Swath  
**Record:** 1 Scanline

**Time Interval Covered**  
**File:** 1 Hour  
**Record:** 1 Scan each 3.4 sec

**Portion of Atmosphere Covered**  
**File:** Satellite Altitude

Table A3. VIRS Cloud Imager Data (CID\_VIRS)

Description	Parameter Number	Units	Range	Elements/Record	Bits/Elem	Elem Num
<b>CID_VIRS</b>						
<b>VIRS_Header</b>						
Julian date of product start day		day	TBD	1	32	
Fractional Julian time of product start time		day	0.0 - .999999999	1	32	
Name of spacecraft carrying imager instrument		N/A	N/A	1	32	
Observing imager name		N/A	N/A	1	32	
Number of imager channels considered		N/A	1 .. 5	1	16	
Number of scan lines		N/A	0 .. 11,808	1	32	
<b>VIRS_Scanline</b> is Array[11808] of:						
<b>VIRS_Scan_Line_Definition</b>						
Year, day, hour, minute, second time code	1	count	TBD	1	48	1
Angular velocity	2	rad sec <sup>-1</sup>	TBD	1	32	2
<b>Location</b> is Array[261] of:						
<b>Pixel_Location</b>						
Latitude of imager pixel	3	deg	-90 .. 90	261	32	3
Longitude of imager pixel	4	deg	-90 .. 90	261	32	264
Scan angle of imager pixel	5	deg	TBD	261	16	525
<b>Spacecraft_Dynamic_Parameters</b> is Array[3] of:						
<b>Spacecraft_Position</b>						
xdot, ydot, zdot	6	m sec <sup>-1</sup>	TBD	3	32	786
pitch, roll, yaw	7	deg	TBD	3	32	789
x, y, z position	8	m	TBD	3	32	792
<b>Additional_Requirements</b>						
Scan number	9	N/A	0 .. 11,808	1	16	795
Quality flag	10	N/A	TBD	1	32	796
Number of meaningful viewing angles appended to scan	11	N/A	TBD	1	8	797
<b>Angles_VIRS</b> is Array[261] of:						
<b>Angles</b>						
Solar zenith angles from imager	12	deg	0 .. 90	261	8	798
Viewing zenith angles from imager	13	deg	0 .. 90	261	16	1059
Viewing azimuth angles from imager	14	deg	0 .. 180	261	8	1320

Table A3. Concluded

Description	Parameter Number	Units	Range	Elements/Record	Bits/Elem	Elem Num
<b>VIRS_Pixels</b> is Array[261] of:						
<b>Channel Data</b>						
Channel 1, .63 micrometers (visible), day only	15	W-m <sup>-2</sup> sr <sup>-1</sup> μm <sup>-1</sup>	TBD	261	16	1581
Channel 2, 1.6 micrometers (near infrared), day only	16	W-m <sup>-2</sup> sr <sup>-1</sup> μm <sup>-1</sup>	TBD	261	16	1842
Channel 3, 3.75 micrometers (infrared), day and night	17	W-m <sup>-2</sup> sr <sup>-1</sup> μm <sup>-1</sup>	TBD	261	16	2103
Channel 4, 10.7 micrometers (infrared, clouds), day and night	18	W-m <sup>-2</sup> sr <sup>-1</sup> μm <sup>-1</sup>	TBD	261	16	2364
Channel 5, 12.0 micrometers (infrared, moisture), day and night	19	W-m <sup>-2</sup> sr <sup>-1</sup> μm <sup>-1</sup>	TBD	261	16	2625
<b>Total Meta Bits/File:</b>	176					
<b>Total Data Bits/Record:</b>	50536					
<b>Total Records/File:</b>	11808					
<b>Total Data Bits/File:</b>	596729088					
<b>Total Bits/File :</b>	596729264					

### Clear Reflectance History (CRH)

The clear reflectance/temperature history (CRH) data are organized on a global equal-area grid that is approximately 10 km by 10 km. The data coverage is 24 hours, and is updated every 10 days from the clear reflectance/temperature history database (CRH\_DB). The CRH\_DB has the same structure as CRH, and is updated twice a day if clear-sky conditions exist for the particular grid cell. The data product consists of a product header followed by fixed-length records organized according to the grid pattern. Each record has

Visible albedo  
Temperature  
Viewing angles

The parameters are derived from cloud imager measurements by Subsystem 4. The CRH product is the same structure for both MODIS values and VIRS values. There is a source indication on the header record. The CRH is archived so that the CERES investigation will have access to any particular day throughout the life of the mission, and it is needed for reprocessing.

**Level:** 3

**Type:** Archival

**Frequency:** Every 10 Days

**Portion of Globe Covered**

**File:** Entire Globe

**Record:** 10km by 10km grid

**Time Interval Covered**

**File:** Life of Mission

**Record:** Every 10 Days

**Portion of Atmosphere Covered**

**File:** Surface Reference

Table A4. Clear Reflectance History (CRH)

Description	Parameter Number	Units	Range	Elements/Record	Bits/Elem	Elem Num
CRH						
CRH header record		N/A	N/A	1	2048	
<b>Record_CRH</b> is Array[4341600] of:						
<b>Grid_CRH</b>						
Day of observation	1	day	Mission Life	1	32	1
Time of observation	2	day	0..1	1	32	2
Visible albedo for collimated, overhead sun illumination	3	N/A	0 .. 1	1	16	3
Temperature derived from 3.7 μm imager channel	4	K	TBD	1	16	4
Temperature derived from 11 μm imager channel	5	K	TBD	1	16	5
Solar zenith angle from imager	6	deg	0 .. 90	1	16	6

Table A4. Concluded

Description	Parameter Number	Units	Range	Elements/Record	Bits/Elem	Elem Num
Mean imager viewing zenith over CERES FOV	7	deg	0 .. 90	1	16	7
Mean imager relative azimuth angle over CERES FOV	8	deg	0 .. 360	1	16	8
Narrowband ADM Type	9	N/A	TBD	1	16	9
<b>Total Meta Bits/File:</b>					2048	
<b>Total Data Bits/Record:</b>					176	
<b>Total Records/File:</b>				4341600		
<b>Total Data Bits/File:</b>					764121600	
<b>Total Bits/File :</b>					764123648	

**Instrument Earth Scans (IES)**

The IES data product contains the equivalent of 1 hour of data from a single CERES scanner. The data records are ordered along the orbital ground track, with each footprint position related to the spacecraft’s suborbital point at the start of the hour. The spatial ordering of records within this product will ease the comparison of CERES data with cloud imager data in subsystem 4. The footprint record is the basic data structure for this data product. This record contains the following kinds of information:

1. Time of observation
2. Geolocation data (at both the top of atmosphere (TOA) and at Earth's surface)
3. Filtered radiances (at satellite altitude), with associated quality measures
4. Spacecraft orbital data
5. Footprint viewing geometric data

The IES data product contains only measurements that view the Earth. For the TRMM mission, this means that approximately 225 Earth-viewing footprints (records) are stored on the IES from each 3.3-second half-scan. Because the Earth scan pattern of the CERES instrument in the biaxial scan mode is irregular, the exact number of pixels in each IES data product varies. This variation is caused by the lack of predictability of the azimuth position at both the start and end of the hour. If the azimuth angle near the start (or end) of an hour is near the crosstrack position, then the number of footprints in the IES product is near the estimated value given below. If the azimuth angle is near the alongtrack position, some of the footprints are instead spatially located within the previous (or next) hours IES. Thus, we have used an estimate of the number of 3.3-second half-scans per hour (approximately 1091) times the number of Earth-viewing measurements in a half-scan (TRMM estimate is 225, EOS estimate is 195) to arrive at our IES product sizing. For TRMM, this is estimated as 245 475 measurements per IES data product and for EOS the estimate is 212 745 measurements. The larger of these two measures is used to determine product sizing.

**Level:** 1b  
**Type:** Internal  
**Frequency:** 1/Hour

**Portion of Globe Covered**  
**File:** Satellite Swath  
**Record:** One CERES footprint

Time Interval Covered  
**File:** 1 Hour  
**Record:** 100 Hz

**Portion of Atmosphere Covered**  
**File:** Satellite Altitude

Table A5. Instrument Earth Scans (IES)

Description	Parameter Number	Units	Range	Elements/Record	Bits/Elem	Elem Num
<b>IES</b>						
IES File Header		N/A		1	256	
<b>IES_Start_Info</b>						
Julian Day at Hour Start		day	2449353..2458500	1	32	
Julian Time at Hour Start		day	0..1	1	32	
Colatitude of satellite at IES start		deg	0..180	1	16	
Longitude of satellite at IES start		deg	0..360	1	16	
Number of footprints in IES product		N/A	1..245475	1	32	
Number of orbits		N/A	TBD	1	16	
IES_Footprints is Array[245475] of:						
<b>IES_Footprint_Records</b>						
<b>FOV_Centroid_Info</b>						
<b>TOA_CoLat_&amp;_Long</b>						
Colatitude of CERES FOV at TOA	1	deg	0..180	1	16	1
Longitude of CERES FOV at TOA	2	deg	0..360	1	16	2
<b>Surface_CoLat_&amp;_Long</b>						
Colatitude of CERES FOV at surface	3	deg	0..180	1	16	3
Longitude of CERES FOV at surface	4	deg	0..360	1	16	4
<b>Zenith_Angles</b>						
CERES viewing zenith at TOA	5	deg	0..90	1	16	5
CERES solar zenith at TOA	6	deg	0..180	1	16	6
CERES relative azimuth at TOA	7	deg	0..360	1	16	7
CERES viewing azimuth at TOA wrt North	8	deg	0..360	1	16	8
<b>Miscellaneous_Angles</b>						
Cross-track angle of CERES FOV at TOA	9	deg	-90..90	1	16	9
Along-track angle of CERES FOV at TOA	10	deg	0..360	1	16	10
<b>Clock_&amp;_Cone_Angles</b>						
Cone angle of CERES FOV at satellite	11	deg	0..180	1	16	11
Clock angle of CERES FOV at satellite wrt inertial velocity	12	deg	0..180	1	16	12
Rate of change of cone angle	13	deg sec <sup>-1</sup>	-100..100	1	16	13
Rate of change of clock angle	14	deg sec <sup>-1</sup>	-10..10	1	16	14
<b>SC_Velocity</b>						
X component of satellite inertial velocity	15	km sec <sup>-1</sup>	-10..10	1	16	15
Y component of satellite inertial velocity	16	km sec <sup>-1</sup>	-10..10	1	16	16
Z component of satellite inertial velocity	17	km sec <sup>-1</sup>	-10..10	1	16	17
<b>Filtered_Radiances</b>						
CERES total filtered radiance, upwards	18	W m <sup>-2</sup> sr <sup>-1</sup>	0..700	1	16	18
CERES shortwave filtered radiance, upwards	19	W m <sup>-2</sup> sr <sup>-1</sup>	-10..510	1	16	19
CERES window filtered radiance, upwards	20	W m <sup>-2</sup> sr <sup>-1</sup>	0..50	1	16	20
<b>Satellite_&amp;_Sun_Info</b>						
Colatitude of satellite at observation	21	deg	0..180	1	16	21
Longitude of satellite at observation	22	deg	0..360	1	16	22
Radius of satellite from center of Earth at observation	23	km	6000..8000	1	32	23
Colatitude of Sun at observation	24	deg	0..180	1	16	24
Longitude of Sun at observation	25	deg	0..360	1	16	25
Earth-Sun distance	26	AU	0.98 .. 1.02	1	16	26
<b>Observation_References</b>						
Scan sample number	27	N/A	1..660	1	16	27
IES quality flags	28	N/A	0..255	1	16	28
Time of observation	29	day	0..1	1	32	29
<b>Total Meta Bits/File:</b>		400				
<b>Total Data Bits/Record:</b>		544				
<b>Total Records/File:</b>		245475				
<b>Total Data Bits/File:</b>		133538400				
<b>Total Bits/File:</b>		133538800				

**Meteorological, Ozone, and Aerosols (MOA)**

The CERES archival product, meteorological, ozone, and aerosols (MOA), is produced by the CERES Regrid Humidity and Temperature Subsystem. Each MOA file contains meteorological data for 1 hour, and is used by several of the CERES subsystems. Data on the MOA are derived from several data sources external to the CERES system, such as NMC, MODIS, SAGE, and various other meteorological satellites. These data arrive anywhere from four times daily to once a month. These data are also horizontally and vertically organized differently from what the CERES system requires. The Regrid Humidity and Temperature Subsystem interpolates these data temporally, horizontally, and vertically to conform with CERES processing requirements.

The MOA contains

- Surface temperature and pressure
- Vertical profiles for up to 38 internal atmospheric levels of temperature, humidity, pressure, and geopotential height
- Column precipitable water
- Vertical ozone profiles for 26 (of the 38) internal atmospheric levels
- Column ozone
- Total column aerosol
- Stratospheric aerosol

The 38 internal atmospheric levels, in hPa, as requested by the CERES clouds and SARB working groups are

Surface	925	775	550	275	125	5
Surface - 10	900	750	500	250	100	1
Surface - 20	875	725	450	225	70	
1000	850	700	400	200	50	
975	825	650	350	175	30	
950	800	600	300	150	10	

**Level:** 3

**Type:** Archival

**Frequency:** 1/Hour

**Portion of Globe Covered**

**File:** Global

**Record:** 1.25-deg equal area region

**Time Interval Covered**

**File:** 1 hour

**Record:** 1 hour

**Portion of Atmosphere Covered**

**File:** Surface and Internal

Table A6. Meteorological, Ozone, and Aerosols (MOA)

Description	Parameter Number	Units	Range	Elements/Record	Bits/Elem	Elem Num
<b>Meta Data</b>						
Header				1	320	
<b>Regional Data</b>						
Region Number	1	N/A	1..26542	1	16	1
<b>Surface Data</b>						
Surface Temperature	2	K	175..375	1	16	2
Surface Pressure	3	hPa	1100..400	1	16	3
Flag, Source Surface Data	4	N/A	TBD	1	16	4

Table A6. Concluded

Description	Parameter Number	Units	Range	Elements/Record	Bits/Elem	Elem Num
<b>Temperature and Humidity Profiles</b>						
Geopotential Height Profiles	5	km	0..50	38	16	5
Pressure Profiles	6	hPa	1100..0	38	16	43
Temperature Profiles	7	K	175..375	38	16	81
Humidity Profiles	8	N/A	0..100	38	16	119
Flag, Source Temp. and Humidity Profiles	9	N/A	TBD	1	16	157
<b>Column Precipitable Water</b>						
Precipitable Water	10	cm	0.001..8.000	1	16	158
Precipitable Water, std	11	cm	TBD	1	16	159
Flag, Source Column Precipitable Water	12	N/A	TBD	1	16	160
<b>Ozone Profile Data</b>						
Ozone Profiles	13	g kg <sup>-1</sup>	0.00002..0.02	26	16	161
Flag, Source Ozone Profile Data	14	N/A	TBD	1	16	187
<b>Column Ozone</b>						
Column Ozone	15	du	200..500	1	16	188
Flag, Source Column Ozone	16	N/A	TBD	1	16	189
<b>Total Column Aerosol</b>						
Aerosol Mass Loading, Total Column	17	g m <sup>-2</sup>	TBD	1	16	190
Flag, Source Aerosol Mass Loading, Total Column	18	N/A	TBD	1	16	191
Optical Depth, Total Column	19	N/A	0.0..2.0	1	16	192
Flag, Source Optical Depth, Total Column	20	N/A	TBD	1	16	193
Asymmetry Factor, Total Column	21	N/A	0.0..1.0	1	16	194
Flag, Source Asymmetry Factor, Total Column	22	N/A	TBD	1	16	195
Single Scattering Albedo, Total Column	23	N/A	0.0..1.0	1	16	196
Flag, Source Single Scattering Albedo, Total Column	24	N/A	TBD	1	16	197
Effective Particle Size, Total Column	25	μm	0.0..20.0	1	16	198
Flag, Source Effective Particle Size, Total Column	26	N/A	TBD	1	16	199
Mean Aerosol Layer Temperature, Total Column	27	K	150..280	1	16	200
Flag, Source Mean Aerosol Layer Temperature, Total Column	28	N/A	TBD	1	16	201
<b>Stratospheric Aerosol</b>						
Optical Depth, Stratosphere	29	N/A	0.0..0.5	1	16	202
Asymmetry Factor, Stratosphere	30	N/A	0.0..1.0	1	16	203
Single Scattering Albedo, Stratosphere	31	N/A	0.0..1.0	1	16	204
Effective Particle Size, Stratosphere	32	μm	0.0..10.0	1	16	205
Mean Aerosol Layer Temperature, Stratosphere	33	K	150..280	1	16	206
Flag, Source Stratospheric Aerosol	34	N/A	TBD	1	16	207
Total Meta Bits/File:	320					
Total Data Bits/Record:	3312					
Total Records/File:	26542					
Total Data Bits/File:	87907104					
Total Bits/File:	87907424					

### Microwave Liquid Water Path (MWP)

The microwave liquid water path (MWP) product is a daily, level 2 product. The product contains a product header followed by the microwave water path parameter values, which are total atmospheric column integrated. The TRMM microwave imager (TMI) data swath on TRMM is approximately 700 km, while the multifrequency imaging microwave radiometer (MIMR) data swath used for EOS is approximately 1 400 km. The FOV of MIMR and TMI is approximately 20 km at nadir, so an estimate of the number of MIMR pixels in a scan line is about 75 and the number of scan lines in a day is about 250 000.

The MWP Product is a non-EOS ancillary product, external to the CERES processing system, that the CERES project plans to keep in the LaRC DAAC for reprocessing.

**Level: 2**  
**Type: Ancillary**  
**Frequency: 1/Day**

**Portion of Globe Covered**  
**File: Global**  
**Record: Swath**

**Time Interval Covered**  
**File: 24 Hours**  
**Record: One scan**

**Portion of Atmosphere Covered**  
**File: Total atmospheric column**

Table A7. Microwave Liquid Water Path (MWP)

Description	Parameter Number	Units	Range	Elements/Record	Bits/Elem	Elem Num
MWP		N/A	N/A	1	2048	
MWP header record - TBD						
<b>Records_MWP</b> is Array[25000] of:						
<b>Scan_lines_MWP</b>						
<b>Pixels_MWP</b> is Array[75] of:						
<b>H2OC_Path</b>						
Time of observation	1	day	0..1	75	32	1
Latitude of MWP pixel	2	deg	-90 .. 90	75	32	76
Longitude of MWP pixel	3	deg	-90 .. 90	75	32	151
Microwave water path data	4	kg m <sup>-2</sup>	TBD	75	16	226
<b>Total Meta Bits/File:</b>				2048		
<b>Total Data Bits/Record:</b>				8400		
<b>Total Records/File:</b>				25000		
<b>Total Data Bits/File:</b>				210000000		
<b>Total Bits/File :</b>				210002048		

**Surface Map (SURFMAP)**

The surface map and properties (SURFMAP) product is a composite product of different types of surface conditions, arranged on a global 10 km by 10 km equal-area grid. The individual products received from different non-EOS sources are

SURFMAP(DEM)	Digital elevation map
SURFMAP(H2O)	Water map
SURFMAP(ICE)	Ice map
SURFMAP(SNOW)	Snow map
SURFMAP(VEGE)	Vegetation map

The remaining surface data are compiled by the CERES science team from various clear-sky models into the SURFMAP(STD) product.

SURFMAP(STD)	Science thermophysical data
--------------	-----------------------------

The STD product consists of

- Surface type indicator
- Broadband shortwave surface ADM type
- Visible albedo for collimated, overhead sun illumination
- Spectral emissivity from 3.7-micron channel imager data
- Spectral emissivity from 11.0-micron channel imager data

The surface type indicator specifies which of the surface conditions best describes the grid cell (land, water, snow, or ice). Snow/ice takes precedence over land/water.

Each of the above products contain a product header and parameters for each 10 km by 10 km equal area grid cell. The SURFMAP is updated at different frequencies, depending on the type of data. For

example, the snow and ice map are updated weekly, whereas the elevation map may be used for the life of the mission.

The SURFMAP product will be retained at the LaRC DAAC permanently. EOSDIS may provide the data for some of the required surface conditions, which the CERES software would access through the product generation system toolkit.

**Level: 3**  
**Type: Ancillary**  
**Frequency: 1/Week**

**Portion of Globe Covered**  
**File: Entire globe**  
**Record: 10 km equal area grid**

**Time Interval Covered**  
**File: 1 Week**  
**Record: 1 Week**

**Portion of Atmosphere Covered**  
**File: Surface**

Table A8. Surface Map (SURFMAP)

Description	Parameter Number	Units	Range	Elements/Record	Bits/Elem	Elem Num
<b>SURFMAP</b>						
SURFMAP_Composite_Product is Array[1] of:						
SURFMAP_Individual_Products						
<b>DEM</b>						
Header record		N/A	N/A	1	2048	
Record_DEM is Array[4341600] of:						
Digital Elevation Model	1	km	-12..10	4341600	16	1
<b>H2O</b>						
Header record		N/A	N/A	1	2048	
Record_H2O is Array[4341600] of:						
Water map	2	percent	0 .. 100	4341600	16	4341601
<b>ICE</b>						
Header record		N/A	N/A	1	2048	
Record_ICE is Array[4341600] of:						
Ice map	3	percent	0 .. 100	4341600	16	8683201
<b>SNOW</b>						
Header record		N/A	N/A	1	2048	
Record_SNOW is Array[4341600] of:						
Snow map	4	percent	0 .. 100	4341600	16	13024801
<b>VEGE</b>						
Header record		N/A	N/A	1	2048	
Record_VEGE is Array[4341600] of:						
Vegetation map	5	TBD	TBD	4341600	16	17366401
<b>STD</b>						
Header record		N/A	N/A	1	2048	
Record_STD is Array[4341600] of:						
<b>Science_Thermophysical_Data</b>						
Surface type indicator for each grid	6	N/A	1 .. 13	4341600	16	21708001
Broadband shortwave surface ADM type	7	N/A	TBD	4341600	16	26049601
Visible albedo for collimated, overhead sun illumination	8	N/A	0 .. 1	4341600	16	30391201
Spectral emissivity at 3.7 micrometers	9	N/A	TBD	4341600	16	34732801
Spectral emissivity at 11 micrometers	10	N/A	TBD	4341600	16	39074401
<b>Total Meta Bits/File:</b>						12288
<b>Total Data Bits/Record:</b>						694656000
<b>Total Records/File:</b>						1
<b>Total Data Bits/File:</b>						694656000
<b>Total Bits/File :</b>						694668288

## Appendix B

### Output Data Products

#### Determine Cloud Properties, TOA and Surface Fluxes (Subsystem 4.0)

This appendix describes the data products which are produced by the algorithms in this subsystem. Table B-1 below summarizes these products, listing the CERES and EOSDIS product codes or abbreviations, a short product name, the product type, the production frequency, and volume estimates for each individual product as well as a complete data month of production. The product types are defined as follows:

Archival products:	Assumed to be permanently stored by EOSDIS
Internal products:	Temporary storage by EOSDIS (days to years)

The following pages describe each product. An introductory page provides an overall description of the product and specifies the temporal and spatial coverage. The table which follows the introductory page briefly describes every parameter which is contained in the product. Each product may be thought of as metadata followed by data records. The metadata (or header data) is not well-defined yet and is included mainly as a placeholder. The description of parameters which are present in each data record includes parameter number (a unique number for each distinct parameter), units, dynamic range, the number of elements per record, an estimate of the number of bits required to represent each parameter, and an element number (a unique number for each instance of every parameter). A summary at the bottom of each table shows the current estimated sizes of metadata, each data record, and the total data product. A more detailed description of each data product will be contained in a user's guide to be published before the first CERES launch.

Table B1. Output Products Summary

Product Code		Name	Type	Frequency	Size, MB	Monthly Size, MB
CERES	EOSDIS					
CRH_DB	CERX03	Clear reflectance history	archival	Every 10 days	91.1	91
SSF	CER11	Single satellite footprint, and surface flux, clouds	archival	1/hour	154.0	114576

#### Clear Reflectance History (CRH\_DB)

The clear reflectance/temperature history (CRH) data are organized on a global equal-area grid that is approximately 10 km by 10 km. The data coverage is 24 hours, and is updated twice a day if clear-sky conditions exist for the particular grid cell. The data product consists of a product header followed by fixed-length records organized according to the grid pattern. The parameters are derived from cloud imager measurements by subsystem 4. The CRH\_DB product is the same structure for both MODIS values and VIRS values. There is a source indication on the header record.

The CRH\_DB is used in subsystem 11 to update the CRH archival product about every 10 days. The CRH product retains clear-sky information for the life of the mission, whereas the CRH\_DB contains only the most recent 10 day clear-sky data.

**Level: 3**  
**Type: Internal**  
**Frequency: Every 10 Days**

**Portion of Globe Covered**  
**File: Entire Globe**  
**Record: 10km by 10km grid**

**Time Interval Covered**  
**File: 10 Days**  
**Record: 2/Day**

**Portion of Atmosphere Covered**  
**File: Surface Reference**

Table B2. Clear Reflectance History (CRH\_DB)

Description	Parameter Number	Units	Range	Elements/Record	Bits/Elem	Elem Num
CRH_DB						
CRH header record		N/A	N/A	1	2048	
<b>Record CRH_DB is Array[4341600] of:</b>						
<b>Grid_CRH_DB</b>						
Day of observation	1	day	Mission Life	1	32	1
Time of observation	2	day	0..1	1	32	2
Visible albedo for collimated, overhead sun illumination	3	N/A	0 .. 1	1	16	3
Temperature derived from 3.7 $\mu$ m imager channel	4	K	TBD	1	16	4
Temperature derived from 11 $\mu$ m imager channel	5	K	TBD	1	16	5
Solar zenith angle from imager	6	deg	0 .. 90	1	16	6
Mean imager viewing zenith over CERES FOV	7	deg	0 .. 90	1	16	7
Mean imager relative azimuth angle over CERES FOV	8	deg	0 .. 360	1	16	8
Narrowband ADM Type	9	N/A	TBD	1	16	9
<b>Total Meta Bits/File:</b>			2048			
<b>Total Data Bits/Record:</b>			176			
<b>Total Records/File:</b>			4341600			
<b>Total Data Bits/File:</b>			764121600			
<b>Total Bits/File :</b>			764123648			

### Single Satellite Footprint, TOA and Surface Flux, Clouds (SSF)

The single satellite flux and cloud swaths (SSF) is produced from the cloud identification, inversion, and surface processing for CERES. Each SSF covers a single hour swath from a single CERES instrument mounted on one satellite. The product has a product header and multiple records of approximately 125 parameters or 315 elements for each pixel.

The major categories of data output on the SSF are

- CERES footprint geometry and CERES viewing angles
- CERES footprint radiance and flux (TOA and Surface)
- CERES footprint cloud statistics and imager viewing angles
- CERES footprint clear area statistics
- CERES footprint cloudy area statistics for each of four cloud height categories
  - Visible optical depth (mean and standard deviation)
  - Infrared emissivity (mean and standard deviation)
  - Liquid water path (mean and standard deviation)
  - Ice water path (mean and standard deviation)
  - Cloud top pressure (mean and standard deviation)
  - Cloud effective pressure (mean and standard deviation)
  - Cloud effective temperature (mean and standard deviation)
  - Cloud effective height (mean and standard deviation)
  - Cloud bottom pressure (mean and standard deviation)
  - Water particle radius (mean and standard deviation)
  - Ice particle radius (mean and standard deviation)

Particle phase (mean and standard deviation)  
 Vertical aspect ratio (mean and standard deviation)  
 Visible optical depth/IR emissivity (13 percentiles)  
 CERES footprint cloud overlap conditions (11 conditions)

The SSF is an archival product that will be run daily in validation mode starting with the TRMM launch until sufficient data have been collected and analyzed to produce a production quality set of CERES angular distribution models (ADM). It is estimated that at TRMM launch plus 18 months, the SSF product will be produced on a routine basis and will be archived within EOSDIS for distribution. The inversion process will be rerun starting from the TRMM launch and a new SSF produced, in which case, only the TOA fluxes and surface parameters will be replaced in the inversion rerun process. If the cloud algorithms are rerun, the SSF product itself will be input into the cloud identification process in order to retrieve the CERES radiance and location data input data needed.

**Level: 2**  
**Type: Archival**  
**Frequency: 1/Hour**

**Portion of Globe Covered**  
**File: Satellite Swath**  
**Record: One Footprint**

**Time Interval Covered**  
**File: 1 Hour**  
**Record: 1/100 Second**

**Portion of Atmosphere Covered**  
**File: Surface to TOA**

Table B3. Single Satellite Footprint, TOA and Surface Flux, Clouds (SSF)

Description	Parameter Number	Units	Range	Elements/Record	Bits/Elem	Elem Num
<b>SSF</b>						
<b>SSF_Header</b>						
Julian Day at Hour Start		day	2449353..2458500	1	32	
Julian Time at Hour Start		day	0..1	1	32	
Character name of satellite		N/A		1	16	
Number of orbits		N/A	TBD	1	16	
Name of high resolution imager instrument		N/A	N/A	1	16	
Number of footprints in IES product		count	1..245475	1	32	
Number of imager channels used		N/A	1 .. 11	1	16	
<b>WavLen_Array</b> is Array[11] of:						
Central wavelengths of imager channels		µm	0.4 .. 15.0	11	16	
<b>SSF_Record</b> is Array[245475] of:						
<b>SSF_Footprints</b>						
<b>Footprint_Geometry</b>						
<b>Time_and_Position</b>						
Time of observation	1	day	0..1	1	32	1
Earth-Sun distance	2	AU	0.98 .. 1.02	1	16	2
Radius of satellite from center of Earth at observation	3	km	6000..8000	1	32	3
Colatitude of satellite at observation	4	deg	0..180	1	16	4
Longitude of satellite at observation	5	deg	0..360	1	16	5
Colatitude of Sun at observation	6	deg	0..180	1	16	6
Longitude of Sun at observation	7	deg	0..360	1	16	7
Colatitude of CERES FOV at TOA	8	deg	0..180	1	16	8
Longitude of CERES FOV at TOA	9	deg	0..360	1	16	9
Colatitude of CERES FOV at surface	10	deg	0..180	1	16	10
Longitude of CERES FOV at surface	11	deg	0..360	1	16	11
Scan sample number	12	N/A	1..660	1	16	12
Cone angle of CERES FOV at satellite	13	deg	0..180	1	16	13
Clock angle of CERES FOV at satellite wrt inertial velocity	14	deg	0..180	1	16	14
Rate of change of cone angle	15	deg sec <sup>-1</sup>	-100..100	1	16	15
Rate of change of clock angle	16	deg sec <sup>-1</sup>	-10..10	1	16	16
Along-track angle of CERES FOV at TOA	17	deg	0..360	1	16	17
Cross-track angle of CERES FOV at TOA	18	deg	-90..90	1	16	18

Table B3. Continued

Description	Parameter Number	Units	Range	Elements/Record	Bits/Elem	Elem Num
X component of satellite inertial velocity	19	km sec <sup>-1</sup>	-10..10	1	16	19
Y component of satellite inertial velocity	20	km sec <sup>-1</sup>	-10..10	1	16	20
Z component of satellite inertial velocity	21	km sec <sup>-1</sup>	-10..10	1	16	21
<b>CERES_Viewing_Angles</b>						
CERES viewing zenith at TOA	22	deg	0..90	1	16	22
CERES solar zenith at TOA	23	deg	0..180	1	16	23
CERES relative azimuth at TOA	24	deg	0..360	1	16	24
CERES viewing azimuth at TOA wrt North	25	deg	0..360	1	16	25
<b>Surface_Map_Parameters</b>						
Mean altitude of surface above sea level	26	km	-12 .. 10	1	16	26
<b>LandTypes</b> is Array[10] of:						
Area fraction of land types in percent	27	N/A	0 .. 100	10	16	27
<b>SeaTypes</b> is Array[3] of:						
Area fraction of sea types in percent	28	N/A	0 .. 100	3	16	37
<b>Scene_Type</b>						
CERES clear sky or full sky indicator	29	N/A	N/A	1	16	40
CERES scene type for Inversion process	30	N/A	0 .. 200	1	16	41
<b>Footprint_Radiation</b>						
<b>CERES_Filtered_Radiances</b>						
CERES total filtered radiance, upwards	31	W-m <sup>-2</sup> sr <sup>-1</sup>	0..700	1	16	42
CERES shortwave filtered radiance, upwards	32	W-m <sup>-2</sup> sr <sup>-1</sup>	-10..510	1	16	43
CERES window-filtered radiance, upwards	33	W-m <sup>-2</sup> sr <sup>-1</sup>	0..50	1	16	44
Quality flag for total radiance value	34	N/A	N/A	1	16	45
Quality flag for SW radiance value	35	N/A	N/A	1	16	46
Quality flag for window radiance value	36	N/A	N/A	1	16	47
<b>CERES_Unfiltered_Radiances</b>						
CERES shortwave radiance, upwards	37	W-m <sup>-2</sup> sr <sup>-1</sup>	-10..510	1	16	48
CERES longwave radiance, upwards	38	W-m <sup>-2</sup> sr <sup>-1</sup>	0..200	1	16	49
CERES window radiance, upwards	39	W-m <sup>-2</sup> sr <sup>-1</sup>	0..50	1	16	50
<b>TOA_and_Surface_Flux</b>						
CERES shortwave flux at TOA, upwards	40	W-m <sup>-2</sup>	0..1400	1	16	51
CERES longwave flux at TOA, upwards	41	W-m <sup>-2</sup>	0..500	1	16	52
CERES window flux at TOA, upwards	42	W-m <sup>-2</sup>	10..400	1	16	53
CERES shortwave flux at surface, downwards	43	W-m <sup>-2</sup>	0..1400	1	16	54
CERES longwave flux at surface, downwards	44	W-m <sup>-2</sup>	0..500	1	16	55
CERES net shortwave flux at surface	45	W-m <sup>-2</sup>	0..1400	1	16	56
CERES net longwave flux at surface	46	W-m <sup>-2</sup>	0..500	1	16	57
CERES surface emissivity	47	N/A	0..1	1	16	58
Photosynthetically active radiation at surface	48	W-m <sup>-2</sup>	0..780	1	16	59
Direct/diffuse ratio at the surface	49	TBD	0..30	1	16	60
<b>Full_Footprint_Area</b>						
Mean imager viewing zenith over CERES FOV	50	deg	0 .. 90	1	16	61
Mean imager relative azimuth angle over CERES FOV	51	deg	0 .. 360	1	16	62
Number of cloud height categories	52	N/A	-1 .. 4	1	16	63
Number of imager pixels in CERES FOV	53	N/A	0 .. 9000	1	16	64
<b>BDRF_Image</b> is Array[11] of:						
Bidirectional reflectance or brightness temperature	54	TBD	TBD	11	16	65
Precipitable water	55	cm	0.001 .. 8	1	16	76
5th percentile of 0.6- $\mu$ m imager radiances over CERES FOV	56	W-m <sup>-2</sup> sr <sup>-1</sup> $\mu$ m <sup>-1</sup>	TBD	1	16	77
Mean of 0.6 $\mu$ m imager radiances over CERES FOV	57	W-m <sup>-2</sup> sr <sup>-1</sup> $\mu$ m <sup>-1</sup>	TBD	1	16	78
95th percentile of 0.6- $\mu$ m imager radiances over CERES FOV	58	W-m <sup>-2</sup> sr <sup>-1</sup> $\mu$ m <sup>-1</sup>	TBD	1	16	79
5th percentile of 3.7- $\mu$ m imager radiances over CERES FOV	59	W-m <sup>-2</sup> sr <sup>-1</sup> $\mu$ m <sup>-1</sup>	TBD	1	16	80
Mean of the 3.7- $\mu$ m imager radiances over CERES FOV	60	W-m <sup>-2</sup> sr <sup>-1</sup> $\mu$ m <sup>-1</sup>	TBD	1	16	81
95th percentile of 3.7- $\mu$ m imager radiances over CERES FOV	61	W-m <sup>-2</sup> sr <sup>-1</sup> $\mu$ m <sup>-1</sup>	TBD	1	16	82
5th percentile of 11- $\mu$ m imager radiances over CERES FOV	62	W-m <sup>-2</sup> sr <sup>-1</sup> $\mu$ m <sup>-1</sup>	TBD	1	16	83
Mean of the 11- $\mu$ m imager radiances over CERES FOV	63	W-m <sup>-2</sup> sr <sup>-1</sup> $\mu$ m <sup>-1</sup>	TBD	1	16	84

Table B3. Continued

Description	Parameter Number	Units	Range	Elements/ Record	Bits/ Elem	Elem Num
95th percentile of 11- $\mu\text{m}$ imager radiances over CERES FOV	64	$\text{W}\cdot\text{m}^{-2}\text{sr}^{-1}\mu\text{m}^{-1}$	TBD	1	16	85
Notes on general procedures	65	N/A	TBD	1	16	86
Texture algorithm flag	66	N/A	TBD	1	16	87
Multilevel cloud algorithm flag	67	N/A	TBD	1	16	88
Spatial coherence algorithm flag	68	N/A	TBD	1	16	89
Infrared sounder algorithm flag	69	N/A	TBD	1	16	90
Threshold algorithm flag	70	N/A	TBD	1	16	91
Visible optical depth algorithm flag	71	N/A	TBD	1	16	92
Infrared emissivity algorithm flag	72	N/A	TBD	1	16	93
Cloud particle size algorithm flag	73	N/A	TBD	1	16	94
Cloud water path algorithm flag	74	N/A	TBD	1	16	95
<b>Clear_Footprint_Area</b>						
Mean of 0.6- $\mu\text{m}$ imager radiances over clear area	75	$\text{W}\cdot\text{m}^{-2}\text{sr}^{-1}\mu\text{m}^{-1}$	TBD	1	16	96
Stddev of the 0.6- $\mu\text{m}$ imager radiances over clear area	76	$\text{W}\cdot\text{m}^{-2}\text{sr}^{-1}\mu\text{m}^{-1}$	TBD	1	16	97
Mean of the 3.7- $\mu\text{m}$ imager radiances over clear area	77	$\text{W}\cdot\text{m}^{-2}\text{sr}^{-1}\mu\text{m}^{-1}$	TBD	1	16	98
Stddev of 3.7- $\mu\text{m}$ imager radiances over clear area	78	$\text{W}\cdot\text{m}^{-2}\text{sr}^{-1}\mu\text{m}^{-1}$	TBD	1	16	99
Mean of the 11- $\mu\text{m}$ imager radiances over clear area	79	$\text{W}\cdot\text{m}^{-2}\text{sr}^{-1}\mu\text{m}^{-1}$	TBD	1	16	100
Stddev of the 11- $\mu\text{m}$ imager radiances over clear area	80	$\text{W}\cdot\text{m}^{-2}\text{sr}^{-1}\mu\text{m}^{-1}$	TBD	1	16	101
Stratospheric aerosol visible optical depth in clear area	81	N/A	0 .. 0.5	1	16	102
Stratospheric aerosol effective radius in clear area	82	$\mu\text{m}$	0 .. 10	1	16	103
Total aerosol visible optical depth in clear area	83	N/A	0 .. 2	1	16	104
Total aerosol effective radius in clear area	84	$\mu\text{m}$	0 .. 20	1	16	105
<b>Cloudy_Footprint_Area</b> is Array[4] of:						
<b>Cloud_Cat_Arrays</b>						
Number of imager pixels for cloud category	85	N/A	0 .. 9000	4	16	106
Number of overcast pixels for cloud category	86	N/A	0 .. 9000	4	16	110
Cloud category weighted area fraction	87	N/A	0 .. 1	4	16	114
Cloud category weighted overcast fraction	88	N/A	0 .. 1	4	16	118
Cloud category weighted broken fraction	89	N/A	0 .. 1	4	16	122
Mean of 0.6- $\mu\text{m}$ imager radiances for cloud category	90	$\text{W}\cdot\text{m}^{-2}\text{sr}^{-1}\mu\text{m}^{-1}$	TBD	4	16	126
Stddev of 0.6- $\mu\text{m}$ imager radiance for cloud category	91	$\text{W}\cdot\text{m}^{-2}\text{sr}^{-1}\mu\text{m}^{-1}$	TBD	4	16	130
Mean of 3.7- $\mu\text{m}$ imager radiances for cloud category	92	$\text{W}\cdot\text{m}^{-2}\text{sr}^{-1}\mu\text{m}^{-1}$	TBD	4	16	134
Stddev of 3.7- $\mu\text{m}$ imager radiances for cloud category	93	$\text{W}\cdot\text{m}^{-2}\text{sr}^{-1}\mu\text{m}^{-1}$	TBD	4	16	138
Mean of 11- $\mu\text{m}$ imager radiances for cloud category	94	$\text{W}\cdot\text{m}^{-2}\text{sr}^{-1}\mu\text{m}^{-1}$	TBD	4	16	142
Stddev of 11- $\mu\text{m}$ imager radiances for cloud category	95	$\text{W}\cdot\text{m}^{-2}\text{sr}^{-1}\mu\text{m}^{-1}$	TBD	4	16	146
Mean cloud visible optical depth for cloud category	96	N/A	0 .. 400	4	16	150
Stddev of visible optical depth for cloud category	97	N/A	TBD	4	16	154
Mean cloud infrared emissivity for cloud category	98	N/A	0 .. 1	4	16	158
Stddev of cloud infrared emissivity for cloud category	99	N/A	TBD	4	16	162
Mean liquid water path for cloud category	100	$\text{kg m}^{-2}$	TBD	4	16	166
Stddev of liquid water path for cloud category	101	$\text{kg m}^{-2}$	TBD	4	16	170
Mean ice water path for cloud category	102	$\text{kg m}^{-2}$	TBD	4	16	174
Stdev of ice water path for cloud category	103	$\text{kg m}^{-2}$	TBD	4	16	178
Mean cloud top pressure for cloud category	104	hPa	0 .. 1100	4	16	182
Stddev of cloud top pressure for cloud category	105	hPa	TBD	4	16	186
Mean cloud effective pressure for cloud category	106	hPa	0 .. 1100	4	16	190
Stddev of cloud effective pressure for cloud category	107	hPa	TBD	4	16	194
Mean cloud effective temperature for cloud category	108	K	100 .. 350	4	16	198
Stddev of cloud effective temperature for cloud category	109	K	TBD	4	16	202
Mean cloud effective height for cloud category	110	km	0 .. 20	4	16	206
Stddev of cloud effective height for cloud category	111	km	TBD	4	16	210
Mean cloud bottom pressure for cloud category	112	hPa	0 .. 1100	4	16	214
Stddev of cloud bottom pressure for cloud category	113	hPa	TBD	4	16	218
Mean water particle radius for cloud category	114	TBD	TBD	4	16	222
Stddev of water particle radius for cloud category	115	TBD	TBD	4	16	226
Mean ice particle radius for cloud category	116	TBD	TBD	4	16	230

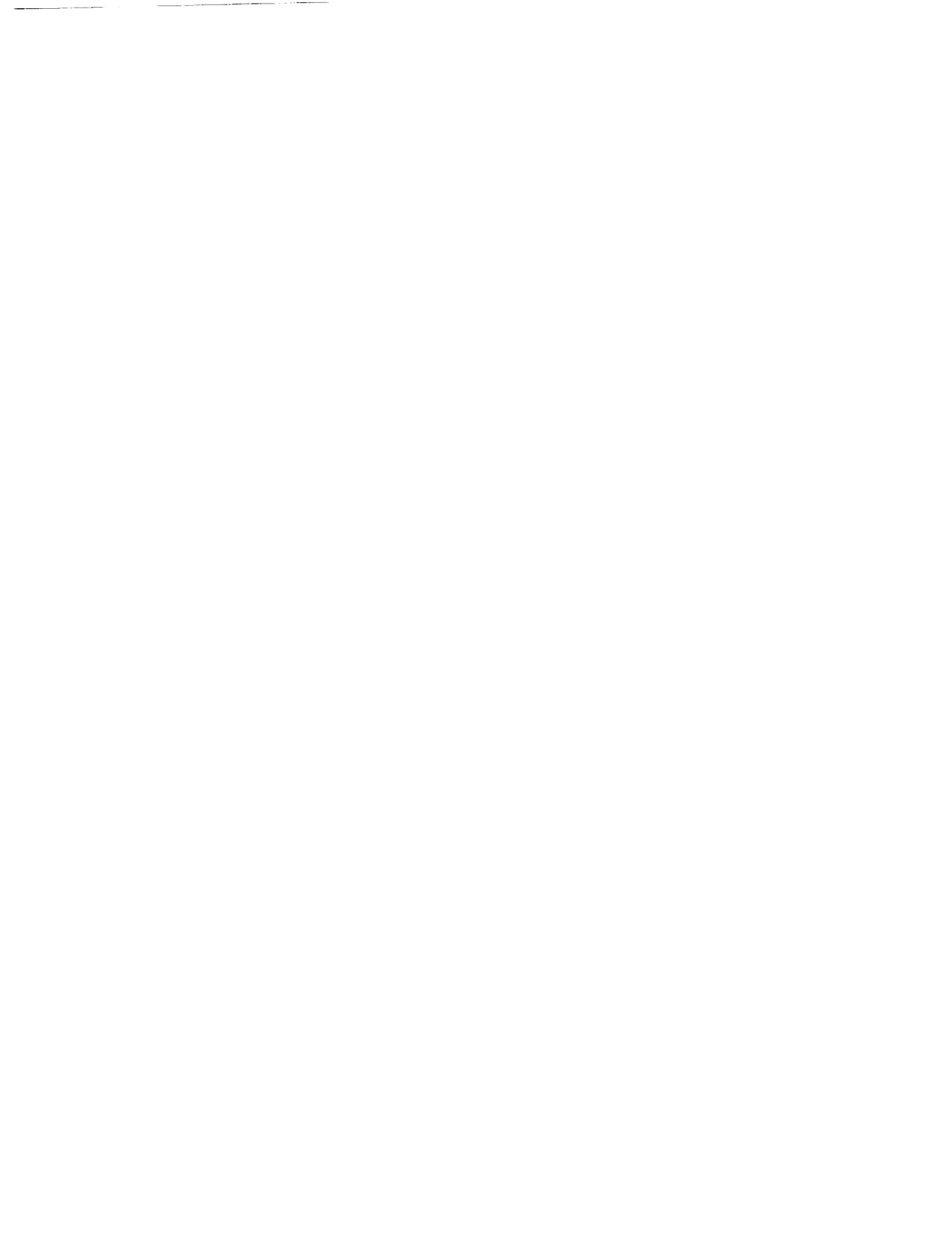
Table B3. Concluded

Description	Parameter Number	Units	Range	Elements/Record	Bits/Elem	Elem Num
Stddev of ice particle radius for cloud category	117	TBD	TBD	4	16	234
Mean cloud particle phase for cloud category	118	N/A	0 .. 1	4	16	238
Stddev of cloud particle phase for cloud category	119	N/A	0 .. 1	4	16	242
Mean vertical aspect ratio for cloud category	120	N/A	0 .. 1	4	16	246
Stddev of vertical aspect ratio for cloud category	121	N/A	TBD	4	16	250
<b>Optical_Depth_Percentile</b> is Array[13] of:						
Percentiles of visible optical depth/IR emissivity for cloud category	122	N/A	TBD	52	16	254
<b>Overlap_Footprint_Area</b> is Array[11] of:						
<b>Overlap_Conditions</b>						
Number of imager pixels for overlap condition	123	N/A	0 .. 9000	11	16	306
Overlap condition weighted area fraction	124	N/A	0 .. 1	11	16	317
<b>Total Meta Bits/File:</b>	336					
<b>Total Data Bits/Record:</b>	5264					
<b>Total Records/File:</b>	245475					
<b>Total Data Bits/File:</b>	1292180400					
<b>Total Bits/File :</b>	1292180736					

## 4.0.9. References

- Arking, A.; and Childs, J. D. 1985: Retrieval of Cloud Cover Parameters From Multispectral Satellite. *J. Climat. & Appl. Meteorol.*, vol. 24, pp. 322–333.
- Baum, Bryan A.; Arduini, Robert F.; Wielicki, Bruce A.; Minnis, Patrick; and Si-Chee, Tsay 1994: Multilevel Cloud Retrieval Using Multispectral HIRS and AVHRR Data: Nighttime Oceanic Analysis. *J. Geophys. Res.*, vol. 99, no. D3, pp. 5499–5514.
- Cahalan, Robert F.; Ridgway, William; Wiscombe, Warren J.; Gollmer, Steven; and Harshvardhan 1994: Independent Pixel and Monte Carlo Estimates of Stratocumulus Albedo. *J. Atmos. Sci.*, vol. 51, no. 24, pp. 3776–3790.
- Coakley, J. A., Jr.; and Bretherton, F. P. 1982: Cloud Cover From High-Resolution Scanner Data: Detecting and Allowing for Partially Filled Fields of View. *J. Geophys. Res.*, vol. 87, pp. 4917–4932.
- Coakley, J. A., Jr.; and Davies, R. 1986: The Effect of Cloud Sides on Reflected Solar Radiation as Deduced from Satellite Observations. *J. Atmos. Sci.*, vol. 43, pp. 1025–1035.
- Coakley, James A., Jr.; Bernstein, Robert L.; and Durkee, Philip A. 1987: Effect of Ship-Stack Effluents on Cloud Reflectivity. *Science*, vol. 237, pp. 1020–1022.
- Greenwald, Thomas J.; Stephens, Graeme, L.; Vonder Haar, Thomas H.; and Jackson, Darren L. 1993: A Physical Retrieval of Cloud Liquid Water Over the Global Oceans Using Special Sensor Microwave/Imager (SSM/I) Observations. *J. Geophys. Res.*, vol. 98, no. D10, pp. 18471–18488.
- Hahn, C. J.; Warren, S. G.; London, J.; Chervin, R. M.; and Jenne, R. 1982: *Atlas of Simultaneous Occurrence of Different Cloud Types Over the Ocean*. NCAR TN-201.
- Harshvardhan; Ginger, K.; and Wielicki, B. A. 1994: The Interpretation of Remotely Sensed Cloud Properties From a Model Parameterization Perspective. *Eighth Conference on Atmospheric Radiation*, pp. 443–445.
- Jacobowitz, H.; Soule, H. V.; Kyle, H. L.; and House, F. B. 1984: The Earth Radiation Budget (ERB) Experiment—An Overview. *J. Geophys. Res.*, vol. 89, pp. 5021–5038.
- King, M. D.; Kaufman, Y. J.; Menzel, W. P.; and Tanre, D. 1992: Remote Sensing of Cloud, Aerosol, and Water Vapor Properties from the Moderate Resolution Imaging Spectrometer (MODIS). *IEEE Trans. Geosci. & Remote Sens.*, vol. 30, no. 1, pp. 2–27.
- Lin, X.; and Coakley, J. A., Jr. 1993: Retrieval of Properties for Semitransparent Clouds From Multispectral Infrared Imagery Data. *J. Geophys. Res.*, vol. 98, pp. 18,501–18,514.
- Luo, G.; Lin, X.; and Coakley, J. A. 1994: 11- $\mu\text{m}$  Emissivities and Droplet Radii for Marine Stratocumulus. *J. Geophys. Res.*, vol. 99, pp. 3685–3698.
- Minnis, Patrick; Heck, Patrick W.; and Young, David 1993: Inference of Cirrus Cloud Properties Using Satellite-Observed and Infrared Radiances. Part II: Verification of Theoretical Cirrus Radiative Properties. *J. Atmos. Sci.*, vol. 50, no. 9, p. 1322.
- Nagarajarao, C. R., ed. 1993: *Degradation of the Visible and Near-Infrared Channels of the Advanced Very High Resolution Radiometer on the NOAA-9 Spacecraft—Assessment and Recommendations for Corrections*. NOAA-TR-NESDIS-70.
- Payette, F. 1989: Application of a Sampling Strategy for the ERBE Scanner Data. M.S. Thesis, McGill Univ.
- Rossow, William B. 1989: Measuring Cloud Properties From Space—A Review. *J. Climat.*, vol. 2, pp. 201–213.
- Rossow, William B.; Garder, Leonid, C.; Lu, Pei-Jane; and Walker, Alison 1992: *International Satellite Cloud Climatology Project (ISCCP): Documentation of Cloud Data*. World Meteorol. Org.
- Staylor, W. Frank 1990: Degradation Rates of the AVHRR Visible Channel for the NOAA 6, 7, and 9 Spacecraft. *J. Atmos. & Ocean. Technol.*, vol. 7, pp. 411–423.
- Stackhouse, P. W.; and Stephens, G. L. 1994: Investigation of the Effects of Macrophysical and Microphysical Properties of Cirrus Clouds on the Retrieval of Optical Properties—Result from FIRE II. *Eighth Conference on Atmospheric Radiation*, pp. 225–227.
- Stephens, Graeme L. 1988: Radiative Transfer Through Arbitrarily Shaped Optical Media. II—Group Theory and Simple Closures. *J. Atmos. Sci.*, vol. 45, pp. 1818–1848.
- Stephens, G. L.; Paltridge, G. W.; and Platt, C. M. R. 1978: Radiation Profiles in Extended Water Clouds. III—Observation. *J. Atmos. Sci.*, vol. 35, pp. 2133–2141.

- Stowe, L. L.; Wellemeyer, C. G.; Eck, T. F.; and Yeh, H. Y. M.; and Nimbus-7 Cloud Data Processing Team 1988: Nimbus-7 Global Cloud Climatology. I—Algorithms and Validation. *J. Climat.*, vol. 1, no. 5, pp. 445–470.
- Suttles, J. T.; Green, R. N.; Minnis, P.; Smith, G. L.; Staylor, W. F.; Wielicki, B. A.; Walker, I. J.; Young, D. F.; Taylor, V. R.; and Stowe, L. L. 1988: *Angular Radiation Models for Earth-Atmosphere System. Volume I: Shortwave Radiation*. NASA RP-1184.
- Suttles, John T.; Wielicki, Bruce A.; and Vemury, Sastri 1992: Top-of-Atmosphere Radiative Fluxes—Validation of ERBE Scanner Inversion Algorithm Using Nimbus-7 ERB Data. *J. Appl. Meteorol.*, vol. 31, no. 7, pp. 784–796.
- Takano, Yoshihide; and Liou, Kuo-Nan 1989: Solar Radiative Transfer in Cirrus Clouds. I—Single-Scattering and Optical Properties of Hexagonal Ice Crystals. *J. Atmos. Sci.*, vol. 46, pp. 3–36.
- Tian, Lin; and Curry, Judith A. 1989: Cloud Overlap Statistics. *J. Geophys. Res.*, vol. 94, pp. 9925–9935.
- Taylor, V. Ray; and Stowe, Larry L. 1984: Reflectance Characteristics of Uniform Earth and Cloud Surfaces Derived from NIMBUS 7 ERB. *J. Geophys. Res.*, vol. 89, no. D4, pp. 4987–4996.
- Warren, S. G.; Hahn, C. J.; and London, J. 1985: Simultaneous Occurrence of Different Cloud Types. *J. Climat. and Appl. Meteorol.*, vol. 24, pp. 658–667.
- Welch, Ronald M.; Cox, Stephen K.; and Davis, John M. 1980: Solar Radiation and Clouds. *Meteorol. Monogr.*, vol. 17, no. 39.
- Wielicki, Bruce A.; and Green, Richard N. 1989: Cloud Identification for ERBE Radiative Flux Retrieval. *J. Appl. Meteorol.*, vol. 28, pp. 1133–1146.
- Wielicki, Bruce A.; and Barkstrom, Bruce R. 1991: Clouds and the Earth's Radiant Energy System (CERES)—An Earth Observing System Experiment. *Second Symposium on Global Change Studies—Preprints*, American Meteorol. Soc., pp. 11–16.
- Wielicki, Bruce A.; and Parker, Lindsay 1992: On the Determination of Cloud Cover from Satellite Sensors—The Effect of Sensor Spatial Resolution. *J. Geophys. Res.*, vol. 97, no. D12, pp. 12799–12823.
- Wielicki, B. A.; and Welch, R. M. 1986: Cumulus Cloud Properties Derived Using Landsat Satellite Data. *J. Climat. & Appl. Meteorol.*, vol. 25, pp. 261–276.
- Ye, Qian 1993: The Spatial-Scale Dependence of the Observed Anisotropy of Reflected and Emitted Radiation. PH.D Diss., Ohio State Univ.



# **Clouds and the Earth's Radiant Energy System (CERES)**

## **Algorithm Theoretical Basis Document**

### ***Imager Clear-Sky Determination and Cloud Detection***

#### ***(Subsystem 4.1)***

#### **CERES Science Team Cloud Retrieval Working Group**

Bryan A. Baum<sup>1</sup>  
Ronald M. Welch<sup>2</sup>  
Pat Minnis<sup>1</sup>  
Larry L. Stowe<sup>3</sup>  
James A. Coakley, Jr.<sup>4</sup>

#### **Algorithm Implementation, Data Analysis, and Data Management**

James Titlow<sup>5</sup>  
Vasanth Tovinkere<sup>5</sup>  
Pat Heck<sup>6</sup>  
Qing Trepte<sup>5</sup>  
Dave Doelling<sup>6</sup>  
Shalini Mayor<sup>6</sup>

#### **Automated Classification Techniques and Algorithm Development**

Todd Berendes<sup>2</sup>  
Qingyuan Han<sup>1</sup>  
Sundar A. Christopher<sup>1</sup>  
Kwo-Sen Kuo<sup>1</sup>  
Manuel Penaloza<sup>1</sup>  
Antonette Logar<sup>1</sup>  
Paul Davis<sup>3</sup>

<sup>1</sup>Atmospheric Sciences Division, NASA Langley Research Center, Hampton, Virginia 23681-0001

<sup>2</sup>South Dakota School of Mines and Technology, Rapid City, South Dakota 57701-3995

<sup>3</sup>Satellite Research Laboratory, National Oceanic and Atmospheric Administration, 5200 Auth Road, Camp Springs, Maryland 20746

<sup>4</sup>Department of Atmospheric Sciences, Oregon State University, Corvallis, Oregon 97331-2209

<sup>5</sup>Science Applications International Corporation (SAIC), Hampton, Virginia 23666

<sup>6</sup>Analytical Services & Materials, Inc., Hampton, Virginia 23666

## 4.1. Imager Clear-Sky Determination and Cloud Detection

### 4.1.1. Overview

This document outlines the methodology for the CERES Release 1 global cloud mask. The cloud mask will be applied to the appropriate imager data stream for TRMM or EOS (VIRS or MODIS, respectively). More precisely, the goal of this effort is to determine those imager pixels that are unobstructed between the top of atmosphere (TOA) and the surface. The output from this algorithm is a pixel-level mask that includes information about which cloud masking tests were applied, whether each test did or did not indicate cloud, and a final decision of whether cloud was or was not present for each pixel.

The cloud mask is being designed for the narrowband channels on both the AVHRR and VIRS instruments. The additional capabilities afforded by the MODIS instrument will be addressed in Release 2 of this document. The members of the CERES cloud mask development team are closely coordinating their activities with the MODIS cloud mask algorithm development. Therefore, close coordination between the CERES and MODIS efforts will be maintained.

The CERES cloud masking algorithm will rely heavily upon a rich heritage of both NASA and NOAA experience with global data analysis. Initial algorithm design will incorporate the approaches used by ISCCP (International Satellite Cloud Climatology Project) (Rossow and Garder 1993), CLAVR (Clouds from AVHRR) (Stowe et al. 1991), and SERCAA (Support of Environmental Requirements for Cloud Analysis and Archive). The ISCCP algorithms are based upon two channels, one in the visible wavelength region and one in the infrared. The CLAVR approach uses all five channels of the AVHRR instrument. The CLAVR multispectral threshold approach with narrowband channel difference and ratio tests will be used, including dynamic threshold specification with clear-sky radiation statistics. The SERCAA algorithm is operational at the Phillips Laboratory, Hanscom Air Force Base, and uses all five AVHRR radiometric channels. The SERCAA is sponsored jointly by the Department of Defense, Department of Energy, and Environmental Protection Agency Strategic Environmental Research and Development Program. When appropriate, the spatial coherence method (Coakley and Bretherton 1982) will be used to improve the clear-sky spectral values. Artificial intelligence classification approaches will be applied for complex scene analysis, especially in polar, rugged terrain, and coastal regions.

The cloud mask algorithm will be tested on two months of global AVHRR GAC data. It will be modified as needed for Release 2 and then delivered for use with VIRS data on the TRMM mission.

### 4.1.2. Data and Assumptions

#### 4.1.2.1. Assumptions

Anyone who has worked with data measured in the field quickly comes to realize that the real world is less than perfect. A number of assumptions may be listed that attempt to place boundaries on the cloud mask task.

1. Satellite data used as input to the cloud mask algorithm is calibrated.
2. Satellite level 1-B data, for some imaging instruments, may be striped (like the GOES scanner) or have some "smearing" at high viewing scan angles. We assume that the data contains no striping or smearing.
3. The mask will be provided for "good" data only, i.e., for those narrowband channels that have radiometric integrity. For instance, the AVHRR 3.7- $\mu\text{m}$  channel is sometimes too noisy to permit accurate analysis of the radiometric data. This assumption implies that there may be holes in the mask if the data are incomplete.
4. The system level integration issues associated with implementation of this algorithm will not be raised in this subsystem document.

5. Sea surface temperature, surface snow/ice coverage, and operational National Meteorological Center gridded analysis products are assumed to be available for the operational cloud mask algorithm.
6. Smoke from forest fires, dust storms over deserts, and other surface phenomena that result in obstructing the field of view between the surface and the satellite will be considered as “cloud” if such pixels pass the threshold tests. When new tests are developed that distinguish between these phenomena, they will be incorporated into the algorithm.

**4.1.2.1.1. Input data.** The primary input data sets for subsystem 4.1 are the AVHRR GAC (global area coverage) satellite data and the following ancillary data sets:

- 1-min resolution coastline map, with lakes, rivers, islands, state/country boundaries
- 10-min resolution topographical map (see section 4.1.5.1. for further information)
- 10-min resolution ecosystem map
- 18-km resolution U.S. Navy/NOAA weekly Sea Ice Product
- 150-km or better resolution weekly NOAA Snow Data Product
- NMC gridded meteorological analysis product
- NOAA gridded weekly sea surface temperature product

The spatial resolution of the AVHRR GAC data is about 4 km at nadir. The spectral data include AVHRR channels 1 (0.55–0.68  $\mu\text{m}$ ), 2 (0.725–1.1  $\mu\text{m}$ ), 3 (3.55–3.93  $\mu\text{m}$ ), 4 (10.5–11.5  $\mu\text{m}$ ), and 5 (11.5–12.5  $\mu\text{m}$ ), which include visible, near-infrared, and infrared window regions. The NOAA-11 central wave numbers for the AVHRR IR channels are (see Kidwell 1991)

Table 4.1-1. Central Wave Numbers as a Function of Temperature for the NOAA-11 AVHRR NIR and IR Channels

Temperature Range (K)	Ch 3 ( $\text{cm}^{-1}$ )	Ch 4 ( $\text{cm}^{-1}$ )	Ch 5 ( $\text{cm}^{-1}$ )
180-225	2663.50	926.80	837.75
225-275	2668.15	927.34	838.08
275-320	2671.40	927.80	838.40
270-310	2670.95	927.73	838.35

The values shown in Table 4.1-1 are slightly different for other sensors in this series of instruments. The VIRS instrument has a 720-km swath width with spectral measurements at channels 1 (0.63  $\pm$  0.05  $\mu\text{m}$ ), 2 (1.60  $\pm$  0.03  $\mu\text{m}$ ), 3 (3.75  $\pm$  0.19  $\mu\text{m}$ ), 4 (10.80  $\pm$  0.5  $\mu\text{m}$ ), and 5 (12.00  $\pm$  0.5  $\mu\text{m}$ ).

**4.1.2.1.2. Output data.** The output from the cloud mask algorithm will be a pixel by pixel product; i.e., a cloud mask will be derived for each imager pixel. The mask will be derived for the highest spatial resolution data available. There will be a final decision as to whether the pixel was obstructed or not that will be based upon the various cloud mask tests applied during the course of the algorithm. The final obstruction/no obstruction decision is stored in the variable denoted by “cloud fraction” in the imager pixel output data structure (Table 4.4-4). For the VIRS instrument, the cloud fraction will be either a “0” or a “1.” For validation purposes only, a separate output data structure will be implemented that stores the results from the individual tests. If there are 10 tests applied to identify cloud, there will be 10 results saved for each pixel.

### 4.1.3. Cloud Masking Algorithms

#### 4.1.3.1. Overview

Clouds generally are characterized by higher albedos and lower temperatures than the underlying surface. However, there are numerous conditions when this characterization is inappropriate, most notably over snow and ice. Of the cloud types, cirrus, low stratus, and small cumulus are the most difficult to detect. Likewise, cloud edges are difficult to recognize when they do not completely fill the field of view (FOV) of the imager pixel. The cloud mask effort builds upon operational experience of several groups that will now be discussed.

The NOAA CLAVR algorithm (Phase I) uses all five channels of AVHRR to derive a global cloud mask (Stowe et al. 1991). It examines multispectral information, channel differences, and spatial differences and then employs a series of sequential decision tree tests. Cloud-free, mixed (variable cloudy), and cloudy regions are identified for  $2 \times 2$  GAC pixel arrays. If all four pixels in the array fail all the cloud tests, then the array is labeled as cloud-free (0% cloudy); if all four pixels satisfy just one of the cloud tests, then the array is labeled as 100% cloudy. If one to three pixels satisfy a cloud test, then the array is labeled as mixed and assigned an arbitrary value of 50% cloudy. If all four pixels of a mixed or cloudy array satisfy a clear-restoral test (required for snow/ice, ocean specular reflection, and bright desert surfaces) then the pixel array is reclassified as "restored-clear" (0% cloudy). The set of cloud tests is subdivided into daytime ocean scenes, daytime land scenes, nighttime ocean scenes, and nighttime land scenes.

Subsequent phases of CLAVR, now under development, will use dynamic clear/cloud thresholds predicted from the angular pattern observed from the clear sky radiance statistics of the previous 9-day repeat cycle of the NOAA satellite for a mapped  $1^\circ$  equal area grid cell (Stowe et al. 1994). As a further modification, CLAVR will include pixel by pixel classification based upon different threshold tests to separate clear from cloud contaminated pixels, and to separate cloud contaminated pixels into partial and total (overcast) cover. Cloud contaminated pixels will be radiatively "typed" as belonging to low stratus, thin cirrus, and deep convective cloud systems. A fourth type is middle mixed which includes all other cloud types.

The International Satellite Cloud Climatology Project (ISCCP) cloud masking algorithm is described by Rossow (1989), Rossow and Gardner (1993), and Seze and Rossow (1991a, b). Only two channels are used, the narrowband VIS ( $0.6 \mu\text{m}$ ) and the IR ( $11 \mu\text{m}$ ). Each observed radiance value is compared against its corresponding Clear-Sky Composite value. This step uses VIS radiances, not VIS reflectances. Clouds are assumed to be detected only when they alter the radiances by more than the uncertainty in the clear values. In this way the "threshold" for cloud detection is the magnitude of the uncertainty in the clear radiance estimates. As such this algorithm is not a constant threshold method such as used in Phase I of the CLAVR algorithm.

The ISCCP algorithm is based on the premise that the observed VIS and IR radiances are caused by only two types of conditions, "cloudy" and "clear," and that the ranges of radiances and their variability that are associated with these two conditions do not overlap (Rossow and Garder 1993). As a result, the algorithm is based upon thresholds, where a pixel is classified as "cloudy" only if at least one radiance value is distinct from the inferred "clear" value by an amount larger than the uncertainty in that "clear" value. The uncertainty can be caused both by measurement errors and by natural variability. This algorithm is constructed to be "cloud-conservative," minimizing false cloud detections but missing clouds that resemble clear conditions.

The ISCCP cloud-detection algorithm consists of five steps (Rossow and Garder 1993):

1. Space contrast test on a single IR image
2. Time contrast test on three consecutive IR images at constant diurnal phase

3. Cumulation of space/time statistics for IR and VIS images
4. Construction of clear-sky composites for IR and VIS every 5 days at each diurnal phase and location
5. Radiance threshold for IR and VIS for each pixel

Parts of the ISCCP scheme will be incorporated into the CERES cloud mask. Some modifications are necessary since all the AVHRR channels will be used, not just the visible and infrared channels (AVHRR channels 1 and 4).

The Support of Environmental Requirements for Cloud Analysis and Archive (SERCAA) algorithm from the Air Force uses multispectral AVHRR data to derive a global cloud mask. The SERCAA cloud decision tree consists of a series of cloud tests and background filter tests to identify cloudy and clear scenes using multispectral data and empirical thresholds. The algorithm is performed on a pixel-by-pixel basis. Percent albedo of channel 1 and channel 2 used in SERCAA has been changed to reflectance for CERES analysis.

The spatial coherence method (Coakley and Bretherton 1982) is especially useful in determining clear and cloudy sky radiances. It is applicable to single-layered and sometimes multilayered cloud systems that extend over moderately large regions, greater than  $250 \text{ km} \times 250 \text{ km}$ , and which have completely cloudy and completely clear pixels. Using the local spatial structure of the IR radiances, difficulties arise when interpreting situations involving multilayered cloud systems, subpixel-sized clouds, and clouds with variable emissivities.

#### 4.1.3.2. ISCCP Space Contrast Test

This test, described in Rossow and Garder (1993), is similar to that of spatial coherence in that it is applied only to IR brightness temperatures. It is based upon the fact that clear pixels tend to have higher temperatures than cloudy pixels and to exhibit less spatial variability. First a small local region is defined, composed of pixels with the same ecosystem. The spatial domain is approximately  $450 \text{ km} \times 450 \text{ km}$  over ocean,  $90 \text{ km} \times 90 \text{ km}$  over ice-covered water, and  $90 \text{ km} \times 90 \text{ km}$  over land. The pixel in the local region with the largest IR ( $11\text{-}\mu\text{m}$ ) brightness temperature ( $T_{B\text{max}}$ ) is found, consistent with the spatial coherence test. All pixels with temperatures lower than the spatial contrast threshold defined by

$$T_B < T_{B\text{max}} - \text{Threshold}_{cs} \quad (4.1-1)$$

are labeled as cloudy; all others are labeled as "undecided." Since cloud variability can be as small as surface variability, values of  $\text{Threshold}_{cs} = 3.5 \text{ K}$  are chosen over ocean and  $\text{Threshold}_{cs} = 6.5 \text{ K}$  over both ice-covered water and land. Note that not only is it important that the class of pixels be identical (land or ocean), but also that the size of the region be chosen carefully. All coastal regions and all land regions containing mixed land and water pixels are excluded from this test, since the inherent contrast between land and water surface radiances would dominate the results. For regions that are too large, there is increased likelihood of spatial variations in surface parameters. The shape of the test regions also can be important, since meridional gradients in surface temperature generally are larger than zonal gradients. The size of the contrast threshold must be larger than the magnitude of natural variations at the surface and smaller than that caused by clouds.

#### 4.1.3.3. ISCCP Spatial/Temporal Analysis

In decreasing order of magnitude, temporal variations of IR and VIS radiances are caused by: (1) formation/dissipation of clouds, or advection of clouds, (2) diurnal heating and cooling (IR) and changes in solar illumination (VIS), (3) variations of surface parameters at synoptic and seasonal time scales, and (4) atmospheric conditions. Investigations of temporal variability and regional variations are reported by Minnis and Harrison (1984a, b), Seze and Desbois (1987), Gutman et al. (1987) and Seze

and Rossow (1991a, b). Diurnal variations of surface temperature on land can be large enough to prevent a sensitive test. However, this can be partially overcome by modeling the full diurnal cycle based on the clear measurements in daytime (Minnis and Harrison, 1984a). The IR radiances are corrected to an approximate nadir view by using a radiative transfer model based upon zonal, monthly mean atmospheric conditions derived from TOVS data.

The following has been adapted from Rossow and Garder (1993); in this implementation, we have included tests for AVHRR channel 2 and 3 reflectances. The first test in this set examines the temperature and channels 1 through 3 reflectance values on the present and previous clear days. If

$$|T_B(i) - T_B(cs)| < \text{Threshold}_T^{\min} = 2.5 \text{ K} \quad (4.1-2)$$

$$|\rho_1(i) - \rho_1(cs)| < \text{Threshold}_1^{\min} \quad (4.1-3)$$

$$|\rho_2(i) - \rho_2(cs)| < \text{Threshold}_2^{\min} \quad (4.1-4)$$

$$|\rho_3(i) - \rho_3(cs)| < \text{Threshold}_3^{\min} \quad (4.1-5)$$

then the pixel is labeled as probably clear, where  $T(i)$  and  $T(cs)$  are the measured ( $i$ ) and clear sky ( $cs$ ) temperatures, respectively, and  $\rho(i)$  and  $\rho(cs)$  are measured and clear sky reflectance values for each of the three channels. Obviously,  $\text{Threshold}_T^{\min}$ ,  $\text{Threshold}_1^{\min}$ ,  $\text{Threshold}_2^{\min}$ , and  $\text{Threshold}_3^{\min}$  must be larger than the natural surface variability. On the other hand, if these values are set too low, then relatively smooth low-level broken cloudiness will be classified as clear.

Likewise, if

$$|T_B(i) - T_B(cs)| > \text{Threshold}_T^{\max} = 6 \text{ K} \quad (4.1-6)$$

$$|\rho_1(i) - \rho_1(cs)| > \text{Threshold}_1^{\max} \quad (4.1-7)$$

$$|\rho_2(i) - \rho_2(cs)| > \Delta \text{Threshold}_2^{\max} \quad (4.1-8)$$

$$|\rho_3(i) - \rho_3(cs)| > \text{Threshold}_3^{\max} \quad (4.1-9)$$

then the pixel is labeled as probably cloudy. Pixels which do not satisfy either of the above two tests are labeled as undecided. The reflectance values defined above are different for different ecosystems.

Events associated with storms may cause large changes in surface temperature. Snow and precipitation and wetting the ground cause large changes in surface reflectances. Therefore, if the previous day was cloudy and all of the neighboring pixels of the same ecosystem were cloudy, then it is assumed that a major storm may have occurred and that the above tests are suspect. If some of the neighboring pixels of the same ecosystem were clear on the previous day, then no major storm event took place. In this case, the average values of the neighboring clear pixels for the previous day are used in these tests.

A final spatial/temporal test examines characteristic variations of clear conditions of the same ecosystem type over larger spatial scales and at longer periods of time. The short-term (ST) period of time is approximately 9 days; the long-term (LT) period of time is approximately 25 days. The actual ST and LT time scales vary according to ecosystem (see Table 4.1-11). The short-term period of time approximates the natural time scale for significant variability of the local surface temperature and reflectances and is the repeat cycle for the AVHRR sensor. The long-term period of time is consistent with variations of more persistent cloud cover and covers three AVHRR cycles. Statistics of the mean ( $M$ ) and standard deviation ( $\sigma$ ) are computed for both ST and LT over approximately  $32 \times 32$  pixel regions of

the same ecosystem. The minimum and maximum values of ST and LT over this region also are found. If the present-day values are labeled as clear and if these values lie within one standard deviation of the ST and LT values, then the pixel is labeled as definitely clear. If the present day mean value lies between  $M + \sigma$  and the maximum value or between  $M - \sigma$  and the minimum value, then the pixel is labeled as probably clear. A similar test is made if the present day pixel is labeled as cloudy. Otherwise the pixel is labeled as undecided.

#### 4.1.3.4. CLAVR Reflectance Uniformity Test

The reflectance uniformity test is applied by computing the maximum and minimum values of AVHRR channel 1 or channel 2 reflectances within a  $2 \times 2$  pixel array. Pixel arrays with channel 1 reflectance differences greater than 9% over land or channel 2 reflectance differences greater than 0.3% over ocean are labeled as mixed (Davis et al. 1993). The value over ocean is low because a cloud-free ocean is almost uniformly reflective, while nonuniformity is assumed to be caused by cloudiness.

Note that this test is being refined; first, by requiring that the ecosystem be the same for the pixel array. Second, the mean and standard deviation of reflectance values for each of the 59 ecosystems (see section 4.1.4.1.) will be computed for channels 1 through 3 as a function of season. It is expected that this test can be substantially improved.

#### 4.1.3.5. Cirrus Cloud Tests

a. *SERCAA*. The brightness temperature difference between channel 4 and channel 5 ( $T_{B4} - T_{B5}$ , or  $BTD^{45}$ ) exhibits a persistent cirrus cloud signature based on the fact that cirrus cloud brightness temperatures are consistently higher at  $10.7 \mu\text{m}$  than at  $11.8 \mu\text{m}$ . However, in the absence of cloud, water vapor attenuation can cause a positive  $BTD^{45}$  that could be mistaken for a cloud signature. Thus, the cloud detection threshold is defined as a function of the channel 4 brightness temperature  $T_{B4}$  (as a surrogate for water vapor loading) and viewing zenith angle  $\theta$  (to count for atmospheric path length). Table 4.1-2 contains the threshold values for a range of  $T_{B4}$  and  $\theta$  developed by Saunders and Kriebel (1988) is used as the basis in the Cirrus Cloud Test.

Table 4.1-2. Thresholds for SERCAA Cirrus Cloud Test

$T_{B4}$	Threshold for $\sec(\theta)$ of—				
	1.00	1.25	1.50	1.75	2.00
260	0.55	0.60	0.65	0.90	1.10
270	0.58	0.63	0.81	1.03	1.13
280	1.30	1.61	1.88	2.14	2.30
290	3.06	3.72	3.95	4.27	4.73
300	5.77	6.92	7.00	7.42	8.43
310	9.41	10.74	11.03	11.60	13.39

The cirrus cloud test is defined as

$$T_{B4} - T_{B5} > \text{Threshold}(T_{B4}, \theta) \quad (4.1-10)$$

It can apply to both daytime and nighttime.

When the background is classified as snow or ice covered, an additional test is required based on the assumption that channel 4 brightness temperatures measured from cirrus clouds are lower than the terrestrial background temperature. This test is defined as:

$$T_{cs} - T_{B4} > \text{Threshold}_{ci} \quad (4.1-11)$$

where  $T_{cs}$  is the clear sky brightness temperature, and  $\text{Threshold}_{ci} = 5.0 \text{ K}$ , is the cirrus cloud snow/ice filter threshold.

**b. CLAVR.** The CLAVR brightness temperature difference between channels 4 and 5 (BTD<sup>45</sup>) (Stowe et al. 1993; Inoue 1987, 1989) is particularly effective in detecting cirrus clouds. Stowe et al. suggest the following thresholds for oceans and land:

$$\text{Threshold}_{45}(\text{oceans}) = \sum_{i=0}^5 a_i T_{B4}^i \quad (4.1-12)$$

$$\text{Threshold}_{45}(\text{land}) = \sum_{i=0}^4 a_i T_{B4}^i \quad (4.1-13)$$

where the coefficients  $a_i$  are given in Table 4.1-3. If the value for  $\text{Threshold}_{45}$  is greater than the threshold determined from equations (4.1-12) or (4.1-13), the pixel is labelled as being cloudy. If  $T_{B4}$  is less than 260 K over a water surface, the threshold is set to zero.

Table 4.1-3. Coefficients Used to Determine Thresholds for CLAVR Cirrus Test

Coefficient	Ocean	Land
$a_0$	$9.27066 \times 10^4$	$-1.34436 \times 10^4$
$a_1$	$-1.79203 \times 10^3$	194.945
$a_2$	13.8305	-1.05635
$a_3$	-0.0532679	$2.53361 \times 10^{-3}$
$a_4$	$1.02374 \times 10^{-4}$	$-2.26786 \times 10^{-6}$
$a_5$	$-7.85333 \times 10^{-8}$	0

#### 4.1.3.6. Cold Cloud Test

The Cold Cloud Test uses a single IR channel to discriminate the thermal signature of midlevel clouds from the terrestrial background. A cloud decision is made by comparing the channel 4 brightness temperature  $T_{B4}$ , with the clear scene brightness temperature  $T_{cs}$ . When  $T_{B4}$  is lower than  $T_{cs}$  by a amount greater than a preset threshold, the pixel is classified as cloudy. The test is defined as:

$$T_{cs} - T_{B4} > \text{Threshold}_{\text{cold}} \quad (4.1-14)$$

where  $\text{Threshold}_{\text{cold}}$  is the surface-dependent threshold shown in the following table:

Table 4.1-4. Thresholds for Cold Cloud Test

Surface background	Threshold (K)
Water	9.0
Land	10.0
Coast	20.0
Desert	10.0
Snow	15.0

#### 4.1.3.7. Daytime Low Cloud and Fog Test

The Low Cloud and Fog Test is based on the different radiative characteristics of liquid water clouds at AVHRR channel 3 (3.7  $\mu\text{m}$ ) and channel 4 (10.8  $\mu\text{m}$ ) wavelengths. During daytime, the radiance from channel 3 is a combination of both emitted and reflected energy, while channel 4 is only emitted energy. The test assumes that a liquid water cloud will reflect enough solar energy at 3.7  $\mu\text{m}$  to make the channel 3 brightness temperature,  $T_{B3}$ , significantly higher than  $T_{B4}$ . The test is defined as the difference between the 3.7- and 10.8- $\mu\text{m}$  brightness temperatures ( $\text{BTD}_{34}$ ):

$$T_{B3} - T_{B4} > \text{Threshold}_{lcf} \quad (4.1-15)$$

where  $\text{Threshold}_{lcf}$  is a surface-dependent cloud detection threshold given in Table 4.1-5.

Table 4.1-5. Thresholds for Daytime Low Cloud and Fog Test

Surface background	Threshold (K)
Nondesert	12.0
Desert	20.0
Sun glint regions	54.0

The test is extremely sensitive to desert surface and Sun glint, since they increase the 3.7- $\mu\text{m}$  radiance relative to the 10.8- $\mu\text{m}$  radiance. Potential sun glint areas are identified prior to testing for cloud contamination and a larger threshold is applied at sun glint regions.

#### 4.1.3.8. Daytime Precipitating Cloud Test

The Precipitating Cloud Test exploits the reflective nature of thick ice clouds at 3.7  $\mu\text{m}$ . Optically thick ice clouds, such as towering cumulonimbus, reflect more strongly than optically thin cirrus. Therefore, the brightness temperature from channel 3,  $T_{B3}$ , is much higher than the true physical temperature of clouds, represented by  $T_{B4}$ . The test is defined as

$$T_{B3} - T_{B4} > \text{Threshold}_{\text{precip}(1)} \quad (4.1-16)$$

where  $\text{Threshold}_{\text{precip}(1)} = 20.0$  K is a cloud detection threshold.

Two additional checks should also be performed to discriminate cumulonimbus clouds from low liquid water clouds and optical thin ice clouds, such as cirrostratus.

$$T_{\text{clear sky}} - T_{B4} > \text{Threshold}_{\text{precip}(2)} \quad (4.1-17)$$

$$\rho_2 > \text{Threshold}_{\text{precip}(3)} \quad (4.1-18)$$

where  $T_{\text{clear sky}}$  is the clear sky brightness temperature,  $\rho_2$  is reflectance of channel 2, and  $\text{Threshold}_{\text{precip}(2)}$  and  $\text{Threshold}_{\text{precip}(3)}$  are precipitating cloud detection thresholds.  $\text{Threshold}_{\text{precip}(2)} = 30.0$  K and  $\text{Threshold}_{\text{precip}(3)} = 0.45$ .

The  $T_{\text{clear sky}} - T_{B4}$  test eliminates any low clouds that pass the  $T_{B3} - T_{B4}$  test by ensuring that the true physical cloud top temperature is significantly lower than the clear scene brightness temperature. The  $\rho_2$  test eliminates ice clouds that are not optically thick, and hence not as bright as precipitating clouds.

#### 4.1.3.9. Daytime Thin Cirrus Cloud Test

The Daytime SERCAAThin Cirrus Cloud Test utilizes the results from the solar independent Cirrus Cloud Test and the reflectance of channel 1 and channel 2. Recall the Cirrus Cloud Test requires the following conditions to be met:

$$T_{B4} - T_{B5} > \text{Threshold}(T_{B4}, \theta) \quad (4.1-19)$$

where  $\text{Threshold}(T_{B4}, \theta)$  is the cloud detection threshold obtained through interpolation from Table 4.1-2.

If the background is classified as snow or ice covered, an additional test is required:

$$T_{\text{clear sky}} - T_{B4} > \text{Threshold}_{ci} \quad (4.1-20)$$

where  $T_{\text{clear sky}}$  is the clear sky brightness temperature, and  $\text{Threshold}_{ci} = 5.0 \text{ K}$  is the cirrus cloud snow/ice filter threshold.

In addition to the tests listed above, the Daytime Thin Cirrus Cloud Test uses reflectance of channel 1 ( $\rho_1$ ) and channel 2 ( $\rho_2$ ) to discriminate thin cirrus. The criterion used is dependent on the background surface type:

$$\rho_2 < \text{Threshold}_{dci\_w} \quad (\text{Over water}) \quad (4.1-21)$$

$$\rho_1 < \text{Threshold}_{dci\_l} \quad (\text{Over land}) \quad (4.1-22)$$

where  $\text{Threshold}_{dci\_w}$  and  $\text{Threshold}_{dci\_l}$  are the cloud detection threshold values over water and land, respectively,  $\text{Threshold}_{dci\_w} = 0.2$  and  $\text{Threshold}_{dci\_l} = 0.2$ .

#### 4.1.3.10. Visible Reflectance Ratio Test

The Visible Reflectance Ratio Test is based on the fact that for clouds, the spectral signature in channel 1 and channel 2 are very close to each other so that the ratio  $\rho_2/\rho_1$  is approximately equal to 1. For clear land surfaces, the ratio is greater than 1.0 and for water surfaces, the ratio is less than 1.0. Thus, the cloud test is applied by testing the  $\rho_2/\rho_1$  ratio against upper and lower limit cloud thresholds.

The test is only used in the absence of sun glint, desert, snow/ice background, and coast regions, all of which can produce a false cloud signal.

High humidity causes increased concentrations of aerosols and haze, resulting in a preferential increase in atmospheric scattering at visible wavelengths relative to the near-IR, which results in a higher measured channel 1 reflectance to channel 2 for cloud-free areas and produces a false cloud signature. To account for this, the value for upper and lower thresholds are lowered to account for lower clear scene channel ratio values. Regions of potentially high humidity are identified by testing the magnitude of the clear sky brightness temperature against a threshold:

$$T_{\text{clear sky}} > \text{Threshold}_{\text{ratio\_humid}} \quad (4.1-23)$$

where  $\text{Threshold}_{\text{ratio\_humid}} = 295 \text{ K}$  is the high humidity threshold. In regions where this test evaluates as true, the Visible Brightness Ratio Test is defined as

$$\text{Threshold}_{\text{ratio\_lo\_wet}} < \rho_2/\rho_1 < \text{Threshold}_{\text{ratio\_up\_wet}} \quad (4.1-24)$$

where  $\text{Threshold}_{\text{ratio\_lo\_wet}}$  and  $\text{Threshold}_{\text{ratio\_up\_wet}}$  are the lower and upper limit ratio thresholds for high humidity. In regions where the humidity test evaluates as false, the Visible Brightness Ratio Test uses a different set of thresholds:

$$\text{Threshold}_{\text{ratio\_lo\_dry}} < \rho_2 / \rho_1 < \text{Threshold}_{\text{ratio\_up\_dry}} \quad (4.1-25)$$

where  $\text{Threshold}_{\text{ratio\_lo\_dry}}$  and  $\text{Threshold}_{\text{ratio\_up\_dry}}$  are the lower and upper limit ratio thresholds for lower humidity given in Table 4.1-6.

Table 4.1-6. Thresholds Based on Humidity for Visible Reflectance Ratio Test

$\text{Threshold}_{\text{ratio\_lo\_wet}}$	0.7
$\text{Threshold}_{\text{ratio\_up\_wet}}$	1.0
$\text{Threshold}_{\text{ratio\_lo\_dry}}$	0.75
$\text{Threshold}_{\text{ratio\_up\_dry}}$	1.1

#### 4.1.3.11. Reflectance Threshold Test

The test described here is used in CLAVR, SERCAA, and ISCCP, and uses a visible wavelength channel threshold to discriminate high cloud reflectance from a low background reflectance. This test works well in discriminating most cloud types with the exception of thin cirrus. The clear sky background reflectance ( $\rho_{cs}$ ) is calculated from clear sky albedo ( $\alpha_{cs}$ ) and the bidirectional reflectance function (BDRF). The clear-sky albedo is obtained by spatial and temporal interpolation from ISCCP's 3-hour 2.5° map. The BDRF's for ocean and land were developed from GOES East and GOES West data (Minnis and Harrison 1984a, b, c); BDRF's for other surface types are taken from the ERBE broadband bidirectional models until other models can be developed and tested.

The clear sky reflectance is shown as follows:

$$\rho_{cs} = \alpha_{cs} / \text{BDRF}(\theta_o, \theta, \phi, M) \quad (4.1-26)$$

where  $\theta_o$ ,  $\theta$ , and  $\phi$  are solar zenith, viewing zenith, and relative azimuth angles, and  $M$  is scene type.

A pixel is classified as cloudy if the satellite measured reflectance exceeds the expected clear-scene background value by an amount greater than a threshold. The test is only applied for the pixels with  $\theta_o < 70^\circ$  and not applied for regions containing sun glint, desert, or snow/ice background. Separate thresholds and different channels are used for land and water backgrounds. Over land, channel 1 reflectance is used, while over water channel 2 data is used. The test is defined as

$$\rho_1 - \rho_{cs} > \text{Threshold}_{\text{land}} \quad (\text{Over land}) \quad (4.1-27)$$

$$\rho_2 > \text{Threshold}_{\text{water}} \quad (\text{Over water}) \quad (4.1-28)$$

where  $\text{Threshold}_{\text{land}} = 0.25$  and  $\text{Threshold}_{\text{water}} = 0.16$  are cloud detection thresholds over land and water background, respectively.

#### 4.1.3.12. Channel 3 Reflectance Test

Likewise channel 3 reflectance values  $> 6\%$  are considered to be cloudy. However, "cloudy" pixels with channel 3 reflectance values  $< 3\%$  are considered to be snow/ice (Davis et al. 1993). Note that the channel 3 reflectance tests are not applied over deserts. This is because bright desert regions with highly variable emissivities tend to be misclassified as cloudy with this test. Thermal contrast needs to be examined in conjunction with channel 3 reflectivity. As we gain experience with these approaches, the actual thresholds will be adjusted to ecosystem type.

#### 4.1.3.13. Nighttime Low Stratus Test

Both SERCAA and CLAVR describe low stratus tests (LST) based upon the brightness temperature differences between the 3.7- and 11- $\mu\text{m}$  channels. The test assumes that for water droplet clouds, the emissivity at 3.7  $\mu\text{m}$  (channel 3) is general lower than at 10.8  $\mu\text{m}$  (channel 4). For the CLAVR test, the threshold for the LST test ( $\text{Threshold}_{LST}$ ) is described as:

$$\text{Threshold}_{LST} = \exp\{A + BT_{B4}\} - C \quad (4.1-29)$$

where  $A = -9.37528$ ,  $B = 0.0341962$ , and  $C = 1.0$  (oceans) and  $C = 3.0$  (land). The constant  $C$  increases for land from the ocean value and depends on surface type. This test is applicable for the temperature range 264 K to clear-sky  $T_{B4}$ . If the threshold is exceeded, then low stratus is said to exist. The specific values of the coefficients may vary in the CERES implementation, depending on the results of testing with global GAC data.

The SERCAA test assumes that clouds are detected if  $T_{B4}$  is greater than  $T_{B3}$  by an amount greater than a cloud detection threshold:

$$T_{B4} - T_{B3} > \text{Threshold}_{LST} \quad (4.1-30)$$

where  $\text{Threshold}_{LST}$  is a surface-dependent cloud detection threshold:

$$\begin{aligned} \text{Threshold}_{LST} &= 1.0 \text{ K} && \text{(Over nondesert)} \\ \text{Threshold}_{LST} &= 2.0 \text{ K} && \text{(Over desert)} \end{aligned}$$

The final determination of thresholds to use for the CERES algorithm will be determined through global analysis of AVHRR data.

#### 4.1.4.14. Nighttime Thin Cirrus Test

Both the SERCAA and CLAVR methods use a similar test based upon the difference in brightness temperatures between the 3.7- and 12-micron channels ( $T_{B3} - T_{B5}$ , or  $\text{BTD}_{35}$ ). The test is based on the idea that cirrus cloud transmissivity at 3.7  $\mu\text{m}$  (channel 3) is generally greater than at 12  $\mu\text{m}$  (channel 5), causing some radiation from warmer backgrounds to be included in the channel 3 measurement. If the difference exceeds a given threshold, then cirrus is said to exist in the pixel.

The CLAVR Cirrus Test (CIRT) is applied at night over both land and ocean. The threshold is determined by the brightness temperature of channel 4 (11 micron). This threshold was defined by using a simulation database to plot cloud-free CIRT values against the associated channel 4 temperatures. The relatively high optical transmittance of most cirrus clouds, along with the spectrally different Planck blackbody radiance dependence on temperature, can identify cirrus clouds. The CIRT threshold is given by

$$\text{Threshold}_{\text{CIRT}} = -0.485 + 1.775 \times 10^{-3} T_{B4} \quad (4.1-31)$$

When  $T_{B4} < 273$  K, this threshold is set to zero; when  $T_{B4} > 292$  K, it is set to 0.033. If the threshold is exceeded, then thin cirrus is said to exist in the pixel.

The SERCAA Nighttime Thin Cirrus Cloud Test is defined as:

$$T_{B3} - T_{B5} > \text{Threshold}_{ici} \quad (4.1-32)$$

where  $\text{Threshold}_{ici} = 4.0$  K is the nighttime thin cirrus cloud detection threshold.

Empirical study has found that in regions of high humidity, the water vapor can attenuate the channel 5 signal by several degrees K. As a result, clear background surfaces will appear significantly cooler in channel 5, and if the clear sky brightness temperature does not take the humidity into account, the

result could be a false detection of cloud. The high humidity regions are identified if the clear sky brightness temperature is greater than a defined threshold:

$$T_{cs} > \text{Threshold}_{tci\_humid} \quad (4.1-33)$$

where  $\text{Threshold}_{tci\_humid} = 290$  K is the high humidity threshold. If the humidity test is true, then AVHRR channel 4, which is less sensitive to water vapor attenuation, is used instead of channel 5 in the test:

$$T_{B3} - T_{B4} > \text{Threshold}_{tci} \quad (4.1-34)$$

where  $\text{Threshold}_{tci}$  is the same threshold used with channel 5.

#### 4.1.4. Artificial Intelligence Cloud Classification Techniques

There are regions in which simple cloud mask algorithms have been shown to perform inadequately, such as in polar, rugged terrain, and coastal regions. For these areas, or when the cloud masks indicate no clear decision on whether cloud is present, artificial intelligence (AI) classification approaches will be applied. The AI classification approaches use a number of textural and spectral features, or measures, that are derived from the satellite data. The following discussion outlines the methods that will be employed in the Release 1 algorithm. We should note that if the reader wishes to skip this discussion, section 4.1.5. begins the actual description of the cloud mask implementation.

##### 4.1.4.1. Texture Features

Texture is often interpreted in the literature as a set of statistical measures of the spatial distribution of gray levels in an image. Here it is assumed that textural information is contained in the average spatial relationships that gray levels have with one another (Haralick et al. 1973). The gray level difference-vector (GLDV) approach is based on the absolute differences between pairs of gray levels  $I$  and  $J$  found at a distance  $d$  apart at angle  $\phi$  with a fixed direction. The GLDV difference-vector probability density function  $P(m)_{d,\phi}$  is defined for  $m = I - J$ , where  $I$  and  $J$  are the corresponding gray levels having a value between 0 and 255. The gray level range may vary, but we will use  $2^8$  gray levels in our analysis. The density function  $P(m)_{d,\phi}$  (henceforth  $P(m)$ , where the dependence of  $P(m)$  on  $d$  and  $\phi$  is implicitly assumed) is obtained by normalizing the GLDV difference vector by the total number of difference pairs. Once  $P(m)$  has been formed, textural measures are computed for each of the five AVHRR spectral channels assuming a pixel separation distance of  $d = 1$  and at an angle  $\phi = 0^\circ$  and  $90^\circ$ . The following textural features are computed for use in the classification system, and are calculated individually for each  $N \times N$  pixel subarray.

Mean:

$$u = \sum_m mP(m) \quad (4.1-35)$$

Standard deviation:

$$\sigma = \left[ \sum_m (m - u)^2 P(m) \right]^{1/2} \quad (4.1-36)$$

*Contrast* is a natural measure of the degree of spread in the gray levels. A small contrast value indicates high concentration of occurrences on the main diagonal and represents a coarse texture. Larger values of contrast indicate that the occurrences are spread out about the main diagonal and represent a finer structure:

$$CON = \sum_m m^2 P(m) \quad (4.1-37)$$

*Angular second moment* is a measure of homogeneity in the subscene. The measure is smallest when the gray levels are equally probable, and large values indicate that there are dominant gray levels present.

$$ASM = \sum_m [P(m)]^2 \quad (4.1-38)$$

*Entropy* is a measure of disorder in the scene, and is largest for equally distributed gray levels and smallest when they are unequally distributed.

$$ENT = \sum_m P(m) \log P(m) \quad (4.1-39)$$

*Local homogeneity* is a measure of local similarity and has a larger value for coarse textures than for finer textures.

$$HOM = \sum_m \frac{P(m)}{(1 + m^2)} \quad (4.1-40)$$

*Cluster shade* is a measure of the degree to which the outliers in the histogram favor one side or another of the mean.

$$SHADE = \frac{\left[ \sum_m (m - u)^3 P(m) \right]}{\sigma^3} \quad (4.1-41)$$

*Cluster prominence* measures the effect of the outliers on the peak of the distribution.

$$PROM = \frac{\left[ \sum_m (m - u)^4 P(m) \right]}{\sigma^4} \quad (4.1-42)$$

These features are described by Chen et al. (1989) in greater detail. Plots of representative cloud texture measures as a function of pixel separation distance and angle are shown in Welch et al. (1989) and for a variety of ice and snow backgrounds in Welch et al. (1990).

#### 4.1.4.2. Spectral Features

The spectral features are formed from the gray level representation of the bidirectional reflectances for AVHRR channels 1 and 2 and from the gray level representation of brightness temperatures for the NIR and IR channels. The reflectances are calculated using the solar zenith angle  $\theta_0$  at each pixel and then scaled to gray levels 0–255, representing 0%–100%, respectively. Gray level representation means that the range of possible values is scaled between 0–255. The daytime 3.7- $\mu\text{m}$  measured radiance contains contributions from both solar reflection and thermal emission. For classification purposes only, the AVHRR 3.7- $\mu\text{m}$  radiometric data (channel 3) are converted to bidirectional reflectance through a relationship commonly used for optically thick clouds (e.g., Allen et al. 1990; Ebert 1987; Key and Barry 1989):

$$\rho_3 = \frac{I_3 - B_3(T_{B4})}{\pi^{-1} F_3 \cos \theta_0 - B_3(T_{B4})} \quad (4.1-43)$$

where  $I_3$  and  $F_3$  are the radiance and incoming solar flux for channel 3, respectively. The 3.7- $\mu\text{m}$  thermal emission is estimated by using the 10.8- $\mu\text{m}$  brightness temperature ( $T_{B4}$ ) to calculate the Planck emission at the central wavelength of channel 3,  $B_3(T_{B4})$ . The reflectance calculated in this fashion is used as a spectral feature because it has been shown to be effective in distinguishing between water and ice clouds (Allen et al. 1990). Note that this is a rough approximation to the true channel 3 reflectance and does not account for differences in emissivity between channels 3 and 4 or for nonblack clouds.

Additional spectral features are formed from combinations of the five AVHRR channels. Spectral features are formed from the gray-level representation of reflectances, brightness temperatures, or combinations of quantities, such as brightness temperature differences between two channels. The spectral features are calculated for a single channel quantity  $X$  (where a quantity is either a reflectance or a brightness temperature), for two different quantities  $X$  and  $Y$ , or for three quantities  $X$ ,  $Y$ , and  $Z$ , as follows.

1. Mean  $X$ : This spectral feature is the mean gray level value of either reflectance or brightness temperature calculated from the array.
2. Band Difference [ $X - Y$ ]: This spectral feature is the difference of the gray-level means of two channels.
3. Band Ratio [ $X/Y$ ]: This feature is formed from taking the ratio of mean gray-level values between two channels.
4. Overlay [ $X, Y, Z$ ]: This spectral feature forms a packed integer from the mean gray-level value of three quantities  $X$ ,  $Y$ , and  $Z$ . It is similar in nature to the idea of using 24-bit color graphics to form false-color imagery. With the proper channel combination, warm reflective stratus clouds would have different values than cold, thin, less-reflective cirrus. The overlay of  $X$ ,  $Y$ , and  $Z$  is calculated from  $\text{OVERLAY} = Z * 2^{16} + Y * 2^8 + X$ . This particular feature is useful in separating the clear-sky land, low-level cloud, mid-level cloud, and high-level cloud classes.
5. Low  $X$ : This feature is the percentage of pixels in the array that have a reflectance less than 10%. It is calculated only for AVHRR channels 1, 2, or 3, and is not calculated from gray-scale values. For channel 3, the reflectance is determined by Equation 4.1-43.
6. High  $X$ : This feature is essentially the complement of LOW  $X$ . It is the percentage of pixels where the reflectance is greater than 10% (again, only for AVHRR channels 1–3). For channel 3, the reflectance is determined by Equation 4.1-43.
7. Spatial coherence: For a given array, means and standard deviations are calculated for all local ( $2 \times 2$  or  $4 \times 4$ ) pixel groups within the  $32 \times 32$  array. The spatial coherence feature is the mean of those local pixel groups that have a standard deviation less than 2.5.

This list of spectral features demonstrates a sampling of the nature of features currently in use and will be added to in future work.

#### **4.1.4.3. Subregion ( $N \times N$ array) Labeling**

A critical aspect of the algorithm development is subarray labeling. To train and test classifiers, a large number of labeled samples for each class are required. A sample is defined here as an  $N \times N$  array of AVHRR data. Accurate labeling is the key to accurate classification. Therefore, it is important to provide the analyst with as much information as possible. The actual labeling process involves more than choosing samples directly from a screen image. For each scene, the analyst uses a variety of ancillary data sets to aid in gaining more information on the scene. For instance, for sample labeling over North America, we also study NMC analyses or rawinsonde temperature and humidity profiles and National Weather Service 6-hourly surface synoptic observations to gain a better understanding of the overall scene.

Figure 4.1-1 shows an example of the Satellite Image Visualization System (SIVIS) which displays three-band color overlays. A series of pull-down menus are available to the analyst which allow a wide

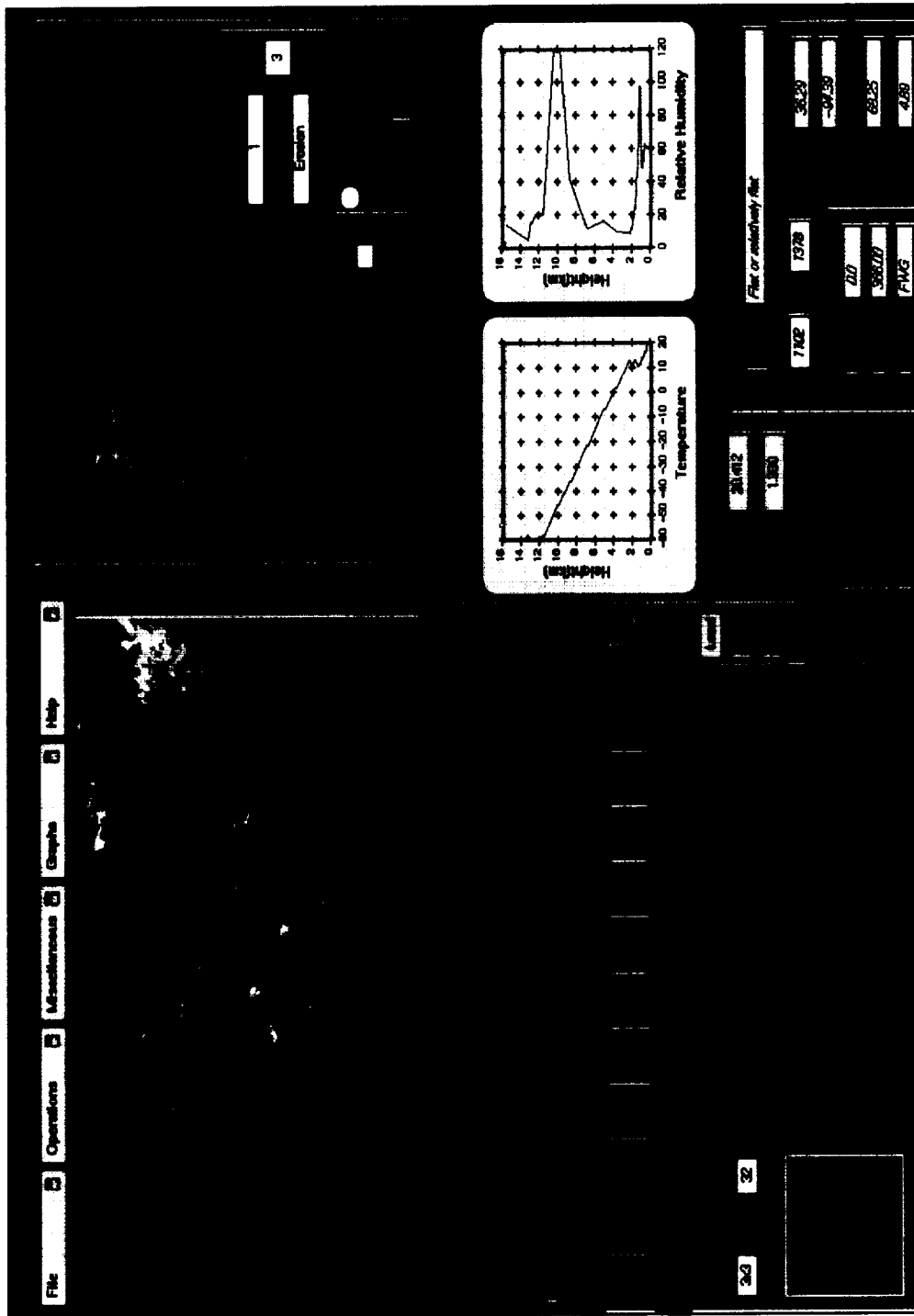


Figure 4.1-1. The Satellite Image Visualization System (SIVIS), Version 1.2.1, is a visualization analysis tool under development to perform both classification, cloud masking, image processing, and other functionality for satellite data analysis. Shown in the upper left hand corner is a segment of a 1.1-km AVHRR image over the southwestern United States. Image processing functions such as histograms, dilation, and density slicing are shown to the right of the image for the boxed region outlined in red in the image to the left. From left to right along the bottom, the boxed region in the image is shown in the bottom left corner, followed by spatial coherence analysis and brightness temperature differences between the 3.7- and 10.8- $\mu\text{m}$  channels. Other functionality includes the ability to overlay coastlines, political boundaries, cloud masks, and navigation information.

range of channel displays and image processing functions. By default all bands are histogram equalized for contrast enhancement. However, any combination of band differences and band ratios can be designed and displayed on command. Additional display features such as principal components, decorrelation stretch, canonical transformations, and edge finding are being implemented.

#### **4.1.4.4. Automated Classification Methods**

**4.1.4.4.1. Overview.** The tests described in section 4.1.3. are to one degree or another based upon thresholds. The NOAA CLAVR algorithm is a decision tree based upon thresholds. The NASA ISCCP algorithm combines uncertainties from multiple tests in a similar fashion.

Texture is a powerful tool for defining the context of a region. Textures were not invoked in the previous analysis because they about double the cpu requirements of the algorithm. However, they are applied to regions which are uncertain. It is probably desirable to apply textures from the outset for difficult regions such as coastlines, deserts, snow covered regions, and areas of variable topography. A texture-flag is set to inform the algorithm manager that texture is to be used.

The textures, along with the results from the previous tests, are then passed to an artificial intelligence classifier. It is a common misconception that AI techniques are operationally more cpu intensive. While AI techniques often do take longer to train, they are no more cpu intensive than are traditional approaches such as Maximum Likelihood. Indeed, many of these AI classifiers are more cpu efficient in the operational mode.

Thresholds are never global. There are always exceptions. For example, the  $\rho_2/\rho_1$  ratio test (section 4.1.3.10.) identifies cloud for values in the range  $0.9 < \rho_2/\rho_1 < 1.1$ . However, new analyses (McClain 1993) suggest that the lower value may need to be lowered to about 0.8, at least for some cases. The same is true for the other tests. Indeed, it seems unrealistic to label a pixel with  $\rho_2/\rho_1 = 1.1$  as cloudy, and a neighboring pixel with the ratio of 1.11 as noncloudy. Rather, as one approaches the threshold limits, the certainty of the labeling becomes more and more uncertain, or "fuzzy." In situations where the threshold results are uncertain, we will use test the use of either a neural network or fuzzy logic based classification system. In a nutshell, fuzzy logic may be thought of as following the entire decision tree, keeping a running total of the uncertainty accumulated along each path. Instead of hard-and-fast thresholds, fuzzy membership functions are used. Then, at the termination of the decision tree, a "defuzzication" function is applied to the results. Uncertainty estimates of clear and cloudy at each pixel are the outcome.

**4.1.4.4.2. Don't care neural network classifier.** A perceptron network consists of an input layer, an output layer, and weights which define linear separating surfaces. Each pattern class  $C_i$  is separated by hyperplanes from all other surfaces. It has long been known that this network has very limited capabilities. Consider three tangent circles, each of which represents a class in 2-space. Neither traditional classifiers nor the perceptron network can find separating surfaces to correctly classify the points in the circles. However, the problem can be solved by a three-layer network or by training the network to find pairwise linear separating surfaces. Training a network to produce pairwise linear separating surfaces requires that for any class  $C_m$ , the linear function corresponding to the separating hyperplane  $C_i/C_j$  will have the value 1 if  $m = i$ , a value of 0 if  $m = j$ , and a "don't care"  $x$  output otherwise.

For a two-layer network, the surfaces separating the various classes are linear. Similarly, in a multi-layer network, nonlinear surfaces separate the classes. Again, pairwise separating surfaces can be constructed using "don't care" outputs. In the perceptron case, the addition of "don't care" outputs broadens the repertoire of problems the network can solve. For multilayer networks, a different benefit results. The hidden layer allows the decision surfaces to be formed into arbitrarily complex shapes. The surfaces initially are "simple," and additional training (i.e., iterations) introduces the more complex elements into the separating surface. The network can be trained to find the simpler pairwise separator surfaces

and then construct a more complicated separating surface from pieces of these simpler curves. As a result, fewer iterations are required to train the network. Our studies show that this approach can simplify the training significantly and reduce the training time by two orders of magnitude.

The steps in the algorithm can be summarized as

*Step 1:* Determine the number of output nodes needed to represent the pattern classes.

Since the network will produce pairwise separating surfaces, the number of output nodes required for this technique is:

$$\binom{N}{2} = \frac{N(N-1)}{2} \quad (4.1-44)$$

where  $N$  is the number of classes. In contrast, traditional approaches only require  $N$  output nodes.

*Step 2:* Build the class representations.

Consider the desired node outputs for a class to be a bit string, where each position in the bit string serves as a discriminator between two classes. For each pair of classes, select a bit not previously chosen to be the discriminator and set that bit in one string to 0; set that same bit to 1 in the second string. After all pairs have been processed, fill the remaining positions with "don't care" symbols. This simple process can be easily automated and introduces only a small overhead penalty to the training algorithm.

For example, a 4-class problem requires six output nodes. Using the above algorithm, one possible assignment of output values to classes can be found in the following table.

Table 4.1-7. Possible Assignment of Output Values

Class	Bit number—					
	1	2	3	4	5	6
1	1	1	1	x	x	x
2	0	x	x	1	1	x
3	x	0	x	0	x	1
4	x	x	0	x	0	0

Note that bit 1 discriminates between class 1 and 2, bit 2 discriminates between class 1 and 3, and so on. The symbol "x" denotes a don't care value.

*Step 3:* Train the network.

During training, error is measured at the output nodes and used to adjust the network weights using back-propagation. In our experiments, the error measure

$$\text{Network - Error} = \sum_k (\text{Actual}_k - \text{Desired}_k)^2 \quad (4.1-45)$$

was used. However, unlike the standard back-propagation algorithm, the above error is not calculated at the nodes which have a don't care designation. The set of weights that will be adjusted during a particular training episode is, therefore, a function of the input pattern. Note, however, that all input to hidden weights are updated.

*Step 4:* Classify the pattern.

To classify the pattern, simply compare the outputs to the bit strings for each class. Note that an output pattern can match at most one class since there is a discrimination bit for each pair of classes. However, it is possible that an output pattern will not match any class. As with standard back-propagation,

the option exists to force a match by selecting the class to which the output pattern is in closest agreement.

**4.1.4.4.3. Cloud mask using a fuzzy logic classifier.** The “fuzzy logic” classifier methodology is described in Tovinkere et al. (1993). The classifier uses the concept of class membership to determine what classes are present within a given data array. For the cloud mask process, the initial set of classes will be cloud, land, snow, and water. Since the Tovinkere et al. (1993) study addresses only cloud classification in the Arctic, modifications to the methodology will be necessary for use in a global algorithm. This approach is moving from the conceptual stage to a test stage at the current time.

Class mixtures are often classified as a single class, thereby leading to poor information extraction. This is due to uncertainty in the membership concept of the classical set theory. This representation scheme has difficulty in dealing with elements that partially belong to two or more sets. In order to improve the information representation, the concept of fuzzy set theory has been used. Fuzzy logic is concerned with formal principles of approximate reasoning; i.e., it aims at modeling imprecise modes of reasoning to make decisions in an environment of uncertainty.

The greater expressive power of fuzzy logic derives from the fact that it contains, as special cases, not only the classical two-value and multivalued logical systems but also probability theory and probabilistic logic. The main features of fuzzy logic that differentiate it from traditional logical systems are the following:

1. In two-valued logical systems, a proposition  $p$  is either true or false. In multivalued logical systems, a proposition may be true or false or have an intermediate truth value.
2. The predicates in two-valued logic are constrained to be crisp in infinite truth value set  $T$ . In fuzzy logic, truth values are allowed to range over the fuzzy subsets of  $T$ . Predicates may be either crisp (e.g., “mortal,” “even”) or fuzzy (e.g., “tired,” “tall,” “cold”).
3. Two-valued as well as multivalued logics allow only two quantifiers: “all” and “none.” By contrast, fuzzy logic allows the use of fuzzy quantifiers exemplified by “most,” “many,” “several,” and so on. Such quantifiers may be interpreted as fuzzy numbers that provide an imprecise characterization of the cardinality of one or more fuzzy or nonfuzzy sets. In this way, a fuzzy quantifier may be viewed as a second-order fuzzy predicate. On the basis of this view, fuzzy quantifiers may be used to represent the meaning of propositions containing fuzzy probabilities and thereby make it possible to manipulate probabilities within fuzzy logic.

**4.1.4.4.4. The fuzzy expert system (ES).** A fuzzy ES includes two other elements, in addition to the components of a conventional system, “fuzzifiers” which convert inputs into their fuzzy representations, and “defuzzifiers” which convert the output of the inference process into a single numerical value within the range of values of the output variable. The numerical output is used to adjust the state of the system being controlled.

A fuzzy control variable may have several states, each state being represented by a membership function. Suppose we are able to classify cloud from clear land and open water by just using the reflectances computed from channel one (CH1) and temperature from channel four (CH4). Figure 4.1-2 shows the different states for these two measures. CH1 is defined by the five albedo states: very low, low, medium, high, and very high. CH4 is defined by the three temperature states: cold, normal, and warm. The albedo measured in CH1 generally is higher for clouds than for land and water. CH4 generally is warm for land and cold for clouds. The above reasoning might lead to the following set of fuzzy rules:

- Rule 1: IF CH1 is very low and CH4 is normal THEN class is water
- Rule 2: IF CH1 is low and CH4 is warm THEN class is land
- Rule 3: IF CH1 is medium and CH4 is cold THEN class is cloud

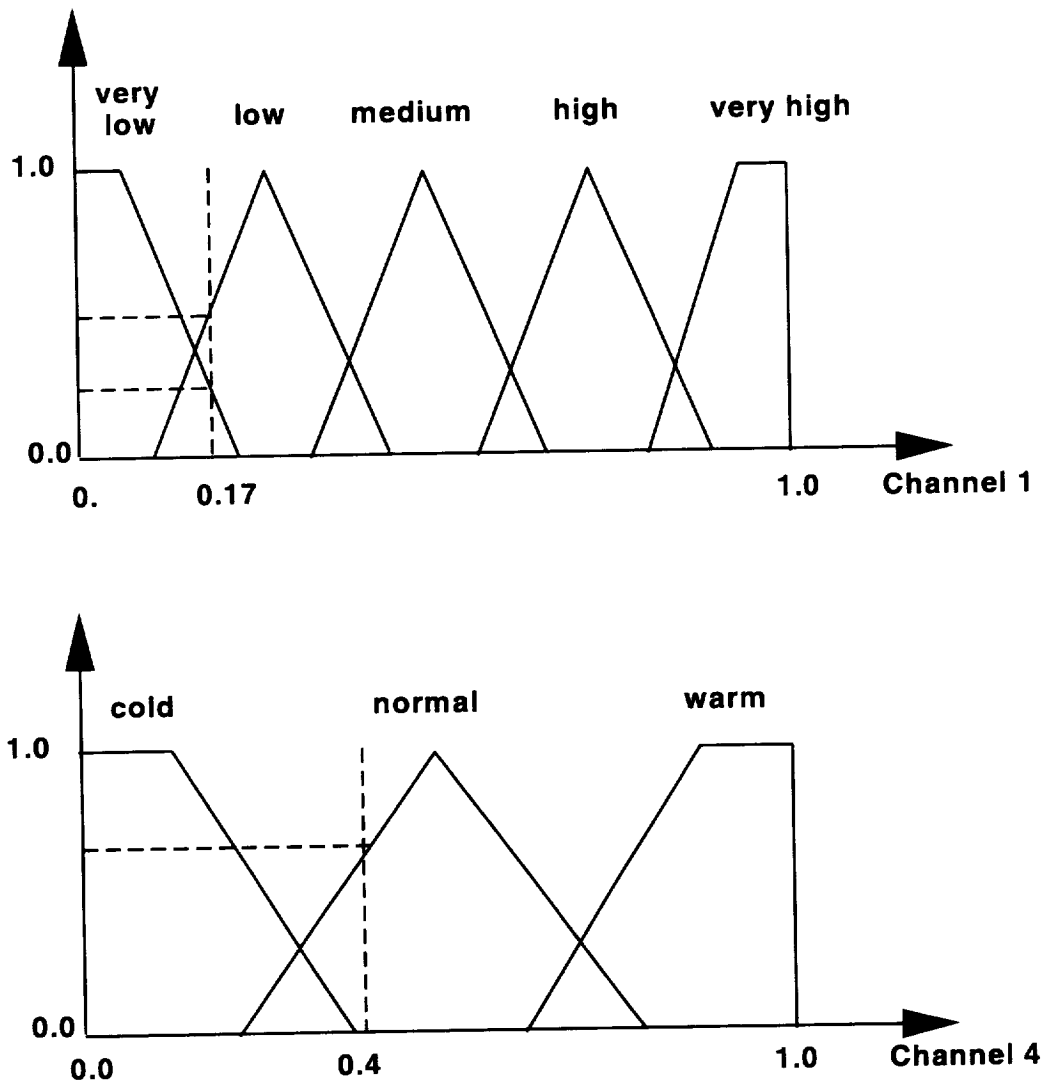


Figure 4.1-2. Schematic showing the concept of class membership in the fuzzy logic classification approach as discussed in section 4.1.4.4.3.

The CH1 reflectance and CH4 temperature values are rescaled to an integer ranging from 0 to 255. As shown in Figure 4.1-2, for a given image sample, the input value for CH1 is 0.17 and 0.4 for CH4; the fuzzifier then computes the degree of membership (DM) for one or more of these fuzzy states. In this case, the states "very low" and "low" of CH1 have membership values of 0.25 and 0.5, respectively. The other states for CH1 are zero. Similarly, the only state of CH4 with a value different from zero is "normal," with a value of 0.60. The confidence level (CL) for each rule is computed by combining the DM's associated with each condition using the following certainty theory formula (Luger and Stubblefield 1989):

$$CL(C1;C2) = \min[DM(C1);DM(C2)] \quad (4.1-46)$$

where C1 and C2 are the conditions of the rule. The CL for rules 1, 2 and 3 are

- Rule 1:  $\min(0.25, 0.60) = 0.25$
- Rule 2:  $\min(0.5, 0.0) = 0.0$
- Rule 3:  $\min(0.0, 0.0) = 0.0$

Since rule 1 has the higher confidence level, the class selected is “water,” which corresponds to the action of rule 1.

The classification process is performed with the aid of a general fuzzy expert system (GFES). GFES can handle different membership functions for describing the different states of the control variables. These functions are triangular; trapezoidal; one-, two-, and three-dimensional normal distributions; PI function; S function; and elliptical cones. The height for all these functions is equal to 1, since any membership function can have any real value between 0 and 1. The multivariate normal distribution is an extension of the one-dimensional normal distribution.

Usually, triangular, trapezoidal, PI, and S functions (Giarratano and Riley 1990) are used for the definition of fuzzy ES's. Since our classifier uses control variables which are often assumed to belong to normal distributions, we have extended the usual set of function types to accommodate the definition of fuzzy states with one- and multi-dimensional normal distributions. Our experiments show that by increasing the number of dimensions, the classifier is able to separate better the different classes.

Three input files are required to run GFES: a control variable file, a rule file, and a facts file. The control variable file requires the following information for each control variable: the name of the variable (e.g., temperature), the type of membership function used to approximate the mean and standard deviation of the feature vector, the number of states, the state names (e.g., hot, cold), and the values that define each state's membership function. The output consists of the class or classes present in the region or pixel with an associated value representing the percentage of the class within the region or pixel.

#### 4.1.5. Cloud Mask Algorithm Description

##### 4.1.5.1. Ancillary Data Set Requirements

A number of preprocessing steps will be made to the AVHRR GAC data before the cloud masking algorithm is applied. An example of navigated GAC data is shown in Figure 4.1-3. These preprocessing steps are described below:

1. The NAVY 10-min database is a  $1080 \times 2160$  array covering  $180^\circ$  in latitude from North to South Pole and  $360^\circ$  in longitude (Fig. 4.1-4). This database provides surface elevation (Fig. 4.1-4), the percentage (an integer between 0 and 100) of water in the 10-min box, and character type as shown in Table 4.1-8 and Figure 4.1-5. Note that multiple characteristics are defined in this system; an example is code 14 = flat lake country or atoll.

Table 4.1-8. Navy Character Map that Provides a General Surface Classification

Code	Feature
0	Salt or lake bed
1	Flat or relatively flat
2	Desert (or for high latitudes, glaciers, or permanent ice)
3	Marsh
4	Lake country or atoll
5	Major valleys or river beds
6	Isolated mountains, ridge, or peak
7	Low mountains
8	Mountainous
9	Extremely rugged mountains
62	Ocean

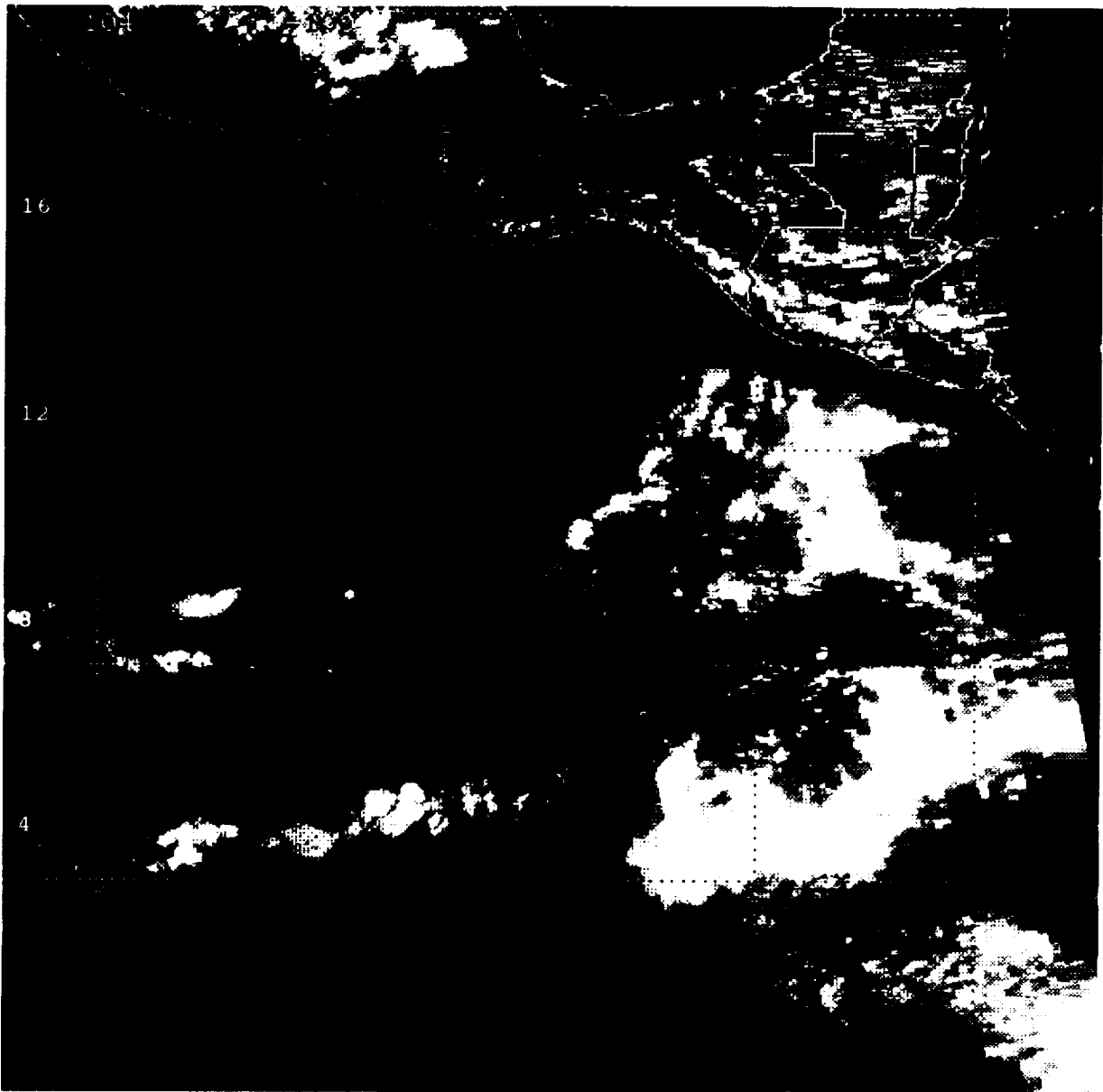


Figure 4.1-3. A navigated AVHRR GAC (~4 km resolution) image from 88°W to 104°W longitude and 2°N to 20°N latitude. Overlaid upon the satellite radiometric data are the coastline boundaries.

2. The EPA Global Ecosystem (WE1.4D) Database also is a 1080 × 2160 byte array which contains 59 different ecosystems classes (Fig. 4.1-6).
3. The US NAVY/NOAA Sea Ice Product provides weekly reports of fractional ice coverage at spatial resolution of about 18 km.
4. The NOAA Snow Data Product provides weekly report of snow cover at a spatial resolution of 150–200 km; snow is reported if the grid cell is more than 50% covered.
5. The NMC 3-hour surface analyses of temperature and wind speed.

Ancillary data will be subset into scenes of about 1000 lines each consisting of 409 pixels (the full swath of AVHRR GAC data). First each pixel in the scene will be tagged as being land or water, and if land, a land/water percentage. Second, each land pixel will be designated as relatively flat, valley,

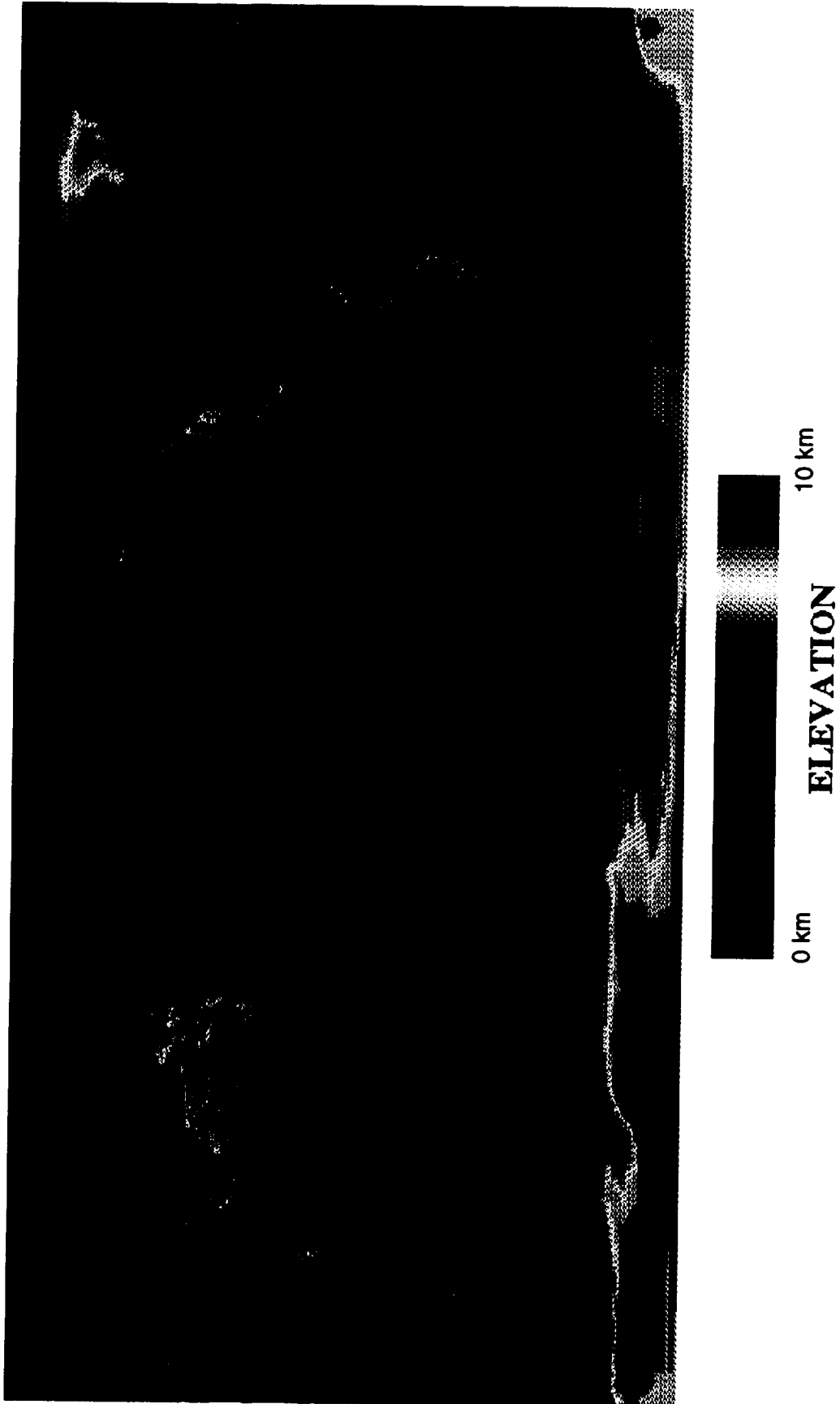


Figure 4.1-4. False color image of the global elevation map derived from the Navy 10-min database discussed in section 4.1.5.1.

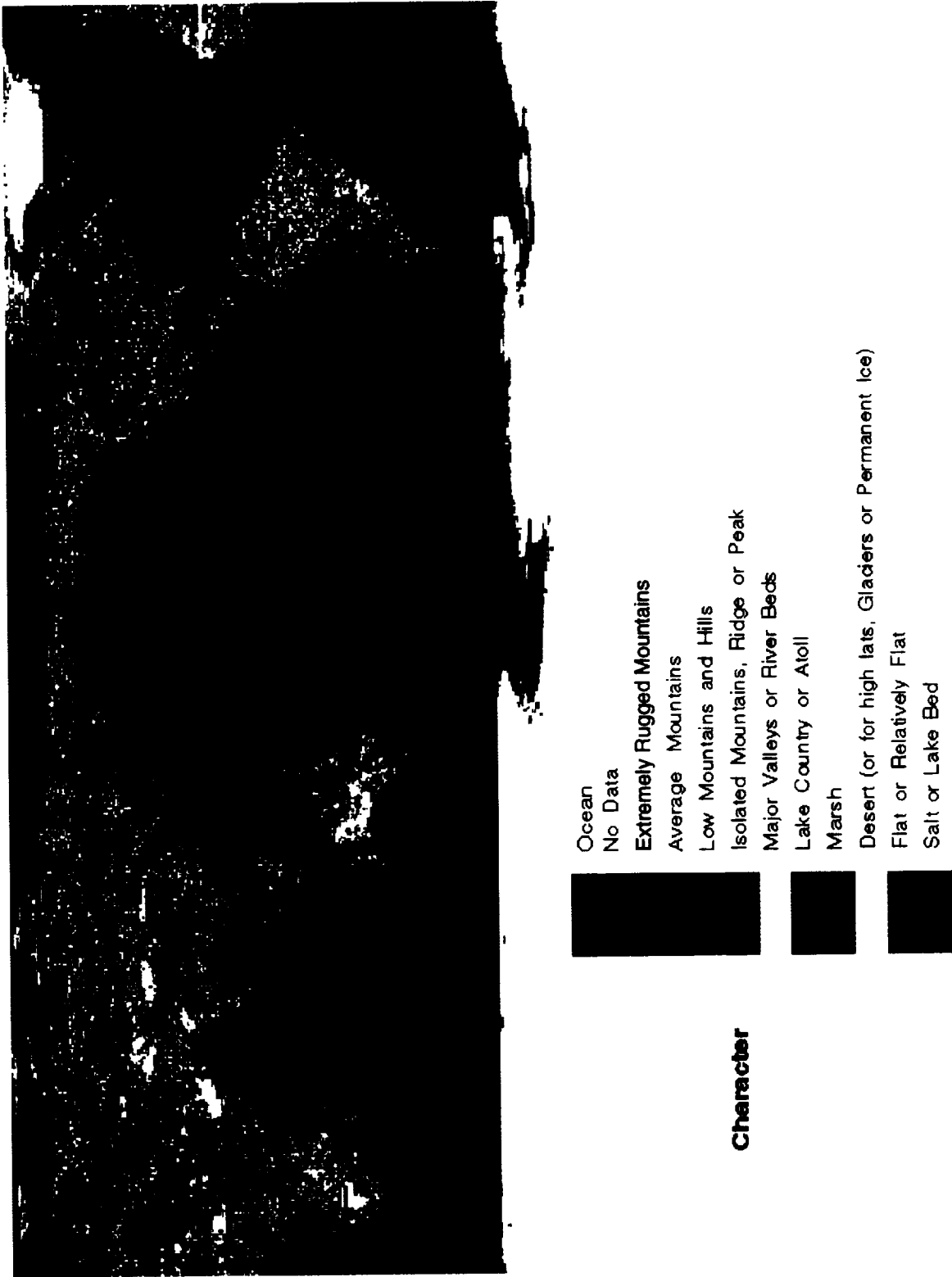


Figure 4.1-5. False-color image of the global surface character type derived from the Navy database discussed in section 4.1.5.1.

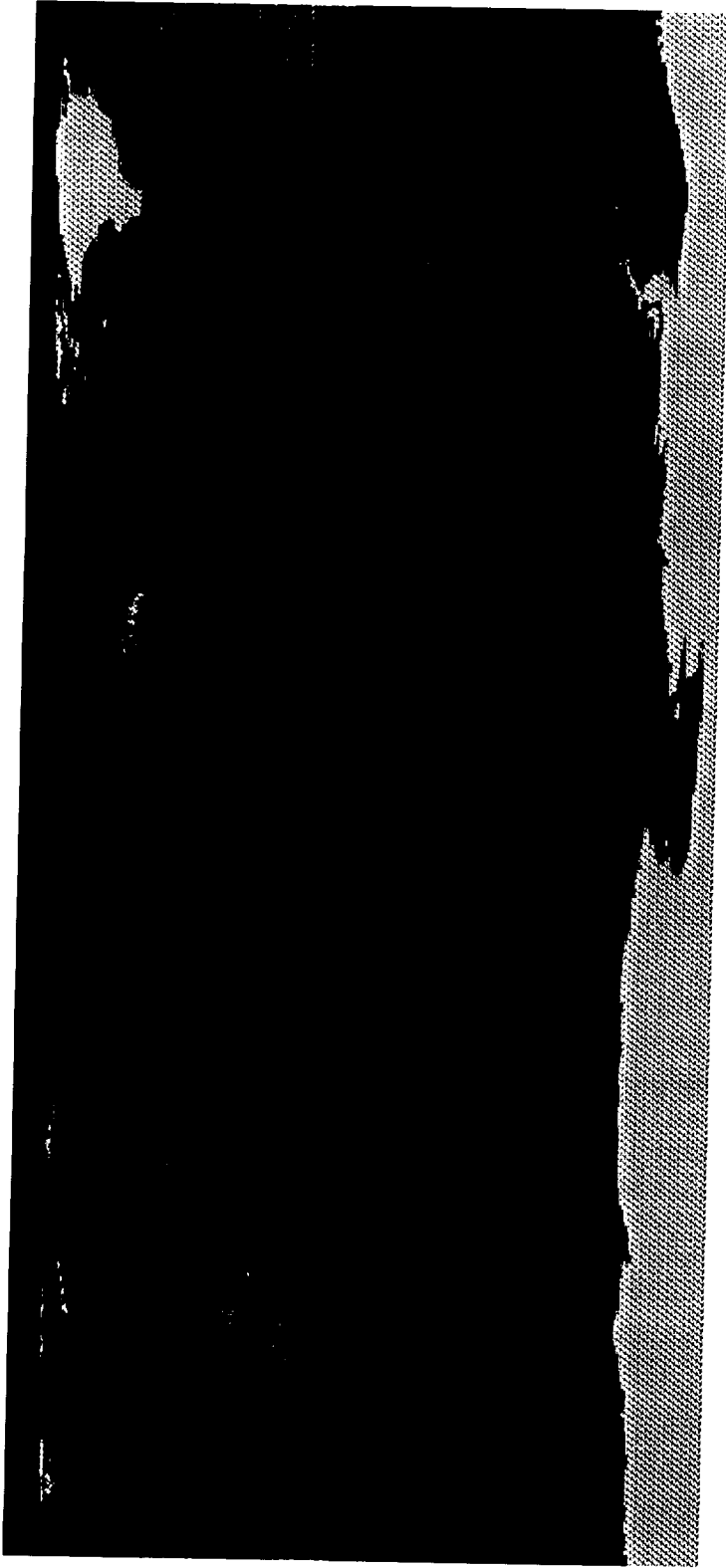


Figure 4.1-6. False-color image of the EPA global ecosystem map as discussed in section 4.1.5.1. The number of classes has been reduced to facilitate ease of interpretation in this image.

isolated mountainous region, low mountains or hills, generally mountainous, or extremely rugged mountains. From the NOAA Snow Data Product each pixel will be designated as probably/probably not snow covered. Each land pixel will be classified as to its ecosystem, along with a more general ecosystem classification of urban, forest, woodland, grassland, shrubland, tundra, arid vegetation and highland vegetation. Ocean regions will be classified as water, coastline (including islands), possibility of isolated icebergs, marginal ice zone, and nearly solid sea ice (leads may be present).

#### **4.1.5.2. Cloud Mask for Daylight Oceanic Areas**

The procedures outlined here will be applied between 60°N and 60°S for oceanic regions and seasonally for large lakes (for which ice is very unlikely). Solar zenith angles are constrained to be less than 85°. The nighttime algorithm is used for sun glint areas.

**4.1.5.2.1. SERCAA Sun glint test.** The Sun glint test is applied over water surfaces. Reflectance over open water is strongly influenced by illumination and viewing geometry. Sun glint is also a function of surface wind. To determine whether sun glint is present, we will implement a series of tests that are used operationally by SERCAA. Two sets of tests are run. The first set of three tests determine if the background surface type and solar/satellite geometry will support sun glint. The three tests are

1. Surface type must be water
2.  $|\theta_o - \theta| < \text{Threshold}_{\text{zenith}}$
3. Azimuthal angle must fall within a certain range

If pixels passed the first set of tests, a second set of spectral tests is applied:

4. The reflectance must be high in the visible channels
5. The 3.7- $\mu\text{m}$  brightness temperature must be high (near saturation)
6. The IR brightness temperature must be relatively high (not indicative of cold clouds)

Pixels that pass the sun glint test but have little illumination due to high solar zenith angle ( $\theta_o > 85^\circ$ ) will be passed to the nighttime ocean algorithm.

**4.1.5.2.2. Cloud mask tests.** The hierarchical approach we will use in the Version 1 code has six stages:

1. Filter pixels that have sun glint
2. Filter pixels that have high solar zenith angle
3. Spatial coherence (to identify clear and cloudy pixels in a 256-km by 256-km region)
4. Apply masking tests to individual pixels in the following order:
  - Imager pixel IR channel threshold test
  - Imager pixel NIR-IR brightness temperature difference threshold tests
  - Imager pixel visible channel reflectance threshold tests
  - Imager pixel visible channel ratio test
5. Apply masking tests to pixel arrays, or tiles, in the following order
  - Spatial contrast
  - Spatial/temporal uniformity
  - Artificial intelligence classification
  - IR clear-sky composite consistency test
  - VIS clear-sky composite consistency test
6. Determine final result of mask tests for each pixel

#### **4.1.5.3. Cloud Mask for Daylight Land Areas**

This portion of the algorithm is applied to land areas at latitudes from 60°N to 60°S, including islands. The hierarchy of cloud mask algorithm application is as follows.

1. Check ecosystem (vegetation) map and land/water percentages data bases. Determine land/water percentage and vegetation for every pixel.
- 2a. Compute sun glint angles for every pixel. Within the sun glint region the percent water database is examined (at 10-min resolution). If water is present, then a flag is set indicating possible sun glint. Eliminate use of visible channels for sun glint pixels and apply nighttime algorithm to those pixels.
- 2b. Over land pixels that are vegetated, compute scattering angle. If the scattering angle is close to 0°, there may be enhancements in the visible channel reflectances (hot spots). The scattering angle is computed from

$$\cos\gamma = \sin\theta\sin\theta_o\cos\phi - \cos\theta\cos\theta_o$$

3. Check surface elevation, clear-sky radiance/temperature data base, and snow-cover data base.
4. If the pixel or subregion is snow-covered, rugged terrain, coastline, or other special cases, pass imager data to automated classification algorithms.
5. Apply spatial coherence to large-scale 256-km by 256-km regions.
6. Apply masking tests to individual pixels in the following order
  - Imager pixel IR channel threshold tests
  - Imager pixel NIR-IR brightness temperature difference threshold tests
  - Imager pixel visible channel reflectance threshold tests.
7. Apply masking tests to pixel arrays, or tiles, in the following order
  - Spatial contrast
  - Spatial/temporal uniformity
  - IR clear-sky composite consistency test
  - VIS clear-sky composite consistency test
  - Artificial intelligence classification
8. Determine final result of mask tests for each pixel.

The databases are examined for elevation characteristics and ecosystem type. A separate database is examined for probability of snow. The snow probability index is set high if either the NOAA Snow Data Product is positive or if snow was indicated on the previous clear day. If the previous day was not clear, then local regions of the same ecosystem type are examined. If these regions also were cloudy on the previous day, then the pixel and its local regions are examined for two additional prior days. If these tests fail, then the snow flag is set to a low value. This test is seasonal; it is not run for tropical regions (except for regions of high elevation) or during summer months. NMC analyses also are examined. Prior days with surface temperatures > 50°C decrease the snow probability index values. On the other hand, during the late fall to early spring in the mid- to high-latitudes, cloud cover on the previous day coupled with surface temperatures in the NMC surface analysis increases the snow probability index. Note that this index has values between 0 and 100. As explained in section 4.2.3., artificial intelligence and texture analysis are applied to regions which are uncertain. The fuzzy logic algorithm directly uses the snow probability index values.

#### **4.1.5.4. Cloud Mask for Nighttime Ocean and Land Scenes**

These algorithms are applied to all surface regions between 60°N and 60°S, for solar zenith angles greater than 85°, and for daytime pixels labeled as having sun glint, vegetation hot spots, or low illumination angles. Spatial coherence is used over oceans and over land areas of the same ecosystem.

1. The initial step is to label each pixel with ecosystem, elevation, surface characteristics, snow/ice, and land/water percentage. If snow-covered, set flag.
2. Retrieve short-term clear night (within last 72 hours) and radiance values for channels 3, 4, and 5. If there are no short-term clear night data available, use longer-term values. If the subregion is

- snow-covered, rugged terrain, coastline, or under the heading of other special cases, pass the sub-region to automated classification algorithms.
3. Apply spatial coherence to large-scale 256-km by 256-km regions, noting that the algorithm will be applied only to areas having the same ecosystem (e.g. water or ocean).
  4. Apply masking tests in the following order.
  5. Apply masking tests to individual pixels in the following order
    - Imager pixel IR channel threshold tests
    - Imager pixel NIR-IR brightness temperature difference threshold tests
  6. Apply masking tests to pixel arrays, or tiles, in the following order
    - Spatial contrast
    - Spatial/temporal uniformity
    - IR clear-sky composite consistency test
    - Artificial intelligence classification

#### 4.1.5.5. Daytime Polar Region Cloud Mask Analysis

A daytime polar region cloud mask algorithm is currently under development. The daytime polar scene classification system currently separates pixel subarrays into the following classes:

1. Water
2. Solid sea ice or snow-covered land
3. Broken sea ice
4. Snow-covered mountains (or regions of high relief)
5. Stratus-type clouds over water
6. Stratus-type cloud over ice
7. Cirrus clouds over ice
8. Cumulus clouds over water
9. Multilayer cloudiness
10. Nonsnow-covered land

These classes need to be expanded somewhat to include, for example, cirrus clouds over water. To date, high accuracies are achieved for pure classes. However, additional work is in progress to extend the classes and to include a broader range of textural measures.

The current algorithm is applied poleward of 60°N and 60°S and is based upon Ebert (1987, 1989), Key and Barry (1989), Welch et al. (1992) and Tovinkere et al. (1993). The following eight spectral and textural measures were used in a polar scene identification study by Tovinkere et al. (1993):

1.  $\rho_1 - \rho_2$
2. Low 3
3.  $\rho_3/\rho_1$
4. Mean ASM 3
5. Mean 1
6. Mean 4
7. Max Ent1
8. Max Ent4

*Measure 1.*  $\rho_1 - \rho_2$ : The reflectance difference between channels 1 and 2. This measure is positive for classes with snow and ice surfaces and negative for land. The reflectance difference  $\rho_1 - \rho_2$  tends to have a positive value for the cloud classes and for water and snow and negative for land.

*Measure 2.* Low 3: This is the percentage of pixels in channel 3 that have a reflectance less than 10%. This is the greatest for water and snow and least for stratus and stratocumulus cloudiness.

*Measure 3.*  $\rho_3/\rho_1$ : The mean reflectances of channels 1 and 3 are computed, and the ratio is calculated using these values. This value is low for ice covered surfaces and cirrus cloudiness.

*Measure 4.* Mean ASM3: Angular second moment of channel 3. This textural feature is a measure of homogeneity in the scene. This measure is smallest when all the gray levels occur with equal probability.

*Measure 5.* Mean 1: This is the mean reflectance of channel 1.

*Measure 6.* Mean 4: This is the mean brightness temperature computed from channel 4.

*Measure 7.* Max Ent1: This is a measure of disorder in the scene. The entropy measure is calculated from channel 1. It has low values for water, solid sea ice, and land.

*Measure 8.* Max Ent4: This is the entropy measure of the region in channel 4. Max Ent4 has low values for classes which have display distinct scales of organization and relatively uniform temperatures.

These features are defined for daylight ( $\theta_o < 85^\circ$ ). Also, the pixel arrays are defined over a single ecosystem type. The pixel array may be modified to suit individual regions, by altering the size the array to be larger or smaller and by altering the shape of the region as necessary. If a single ecosystem type cannot be defined for a given region, then a broader categorization of forest, tundra, etc., is used.

The Navy weekly 18-km sea ice product is utilized to define the marginal ice zone. Oceanic regions within 100 km of the ice edge are labeled as probably broken sea ice. Regions further poleward are labeled with distance as more and more probable of being solid sea ice. Regions in the opposite direction are labeled with distance as less and less probable of being broken sea ice.

The NMC surface temperature analysis is used for consistency checks. For example, high surface temperatures ( $>273$  K) indicate ice melt, probable melt ponds, and lower ice/snow reflectivities. On the other hand, very low surface temperatures generally are consistent with the lack of open water and with higher surface reflectivities. Such low surface temperatures also mean that the various thermal tests need to be applied over more restricted domains.

Artificial intelligence classifiers may be applied from the outset to provide the context of the local region. Once the surface is known (water, solid sea ice or snow-covered land, broken sea ice, land, patchy snow over land, frozen lakes and rivers) and once the basic cloud cover is known (stratus, stratocumulus, cumulus, cirrus, or multilayer), then the previously defined tests may be used at the pixel level. Somewhat different sets of the tests described previously are used for each of the various scenarios.

In the near future (F.Y. 95), we will be deriving and applying new polar cloud mask algorithms. The polar algorithm will be exercised using both AVHRR 1-km and 4-km data over both poles. The final Version 1 algorithm is expected to be modified extensively over the next year.

#### **4.1.6. Short-Term and Long-Term Clear-Sky Composite Maps**

##### **4.1.6.1. ISCCP Clear-Sky Composite**

The ISCCP developed clear-sky reflectance and temperature composites to detect clouds over a given 32-km square area by comparing the pixel radiances to the clear-sky composite values with some added thresholds (Rossow and Garder 1993). These composites are based on the observation that variations in VIS clear reflectances usually are smaller in time than in space, especially over land. Variations of surface VIS reflectances generally are smaller than variations of cloud reflectances. Therefore, it is assumed that the characteristic shape of the darker part of the VIS radiance distribution is at most weakly dependent upon surface type (Seze and Rossow 1991a, b). The minimum reflectance value for channel 1 is used to estimate clear values. Corrections to the minimum values are inferred from the shapes of the visible reflectance distribution associated with different surface types.

Rossow and Garder (1993) classify the surface into nine types depending on the time scale and magnitude of the reflectance variations (see Tables 5 and 6). The clear sky reflectance values for land and ocean regions whose surface characteristics vary the most rapidly are estimated using short-term values of  $\rho_{min}$  such that  $\rho_{cs} = \rho_{min}(ST) + DEL2$ . Sparsely vegetated surfaces generally exhibit more spatial variability than heavily vegetated surfaces (cf. Matthews and Rossow 1987), but are also generally less cloudy. For these,  $\rho_{cs} = \rho_{min}(LT) + DEL2$ . Vegetated areas show less small-scale spatial variability. They also tend to be more uniform from one geographic location to another. For vegetated regions, the clear-sky reflectance is determined by first calculating  $\rho_{cs} = \rho_{min}(ST) + DEL2$ . Then the individual pixel reflectance values within each latitude zone are compared to the distribution of  $\rho_{cs}$  values for the same ecosystem type; they are required to be within DEL1 of the distribution mode value,  $\rho_{mode}$ .

Similar assumptions are used for the determination of  $T_{cs}$  fields. The time scales of VIS and IR variability for different classes and the associated ISCCP thresholds are shown in Tables 4.1-9 through 4.1-12.

Table 4.1-9. Time Scales of Variability for Different Surface Types for Visible Channel

VIS classes	Short term (ST)	Long term (LT)
Ocean	-	30 days
Lakes	-	15 days
Polar ocean (open water)	-	15 days
Ice-covered water	5 days	-
Forests, woodlands, shrublands	-	30 days
Grasslands, tundra	-	30 days
Arid vegetation, deserts	-	30 days
Polar land (snow free)	-	15 days
Snow- or ice-covered land	5 days	-

Table 4.1-10. Values Used in VIS Clear-Sky Composite Logic (after Rossow and Garder 1993); VIS Threshold Values are in Percent Reflectance

IR surface types	DEL1	DEL2
Ocean, near-coastal, lakes	3.0	1.5
Forests, woodlands, shrubland	6.0	3.5
Grasslands, tundra	-	3.5
Arid vegetation, deserts	-	3.5
Ice-covered water	-	5.0
Ice- or snow-covered land	-	5.0

Table 4.1-11. Time Scales of Variability for Different Surface Types for IR Channels (after Rossow and Garder 1993)

IR classes	Short term (ST)	Long Term (LT)
Open ocean	15 days	30 days
Near-coastal ocean and lakes	5 days	15 days
Polar seas and ice-covered water	5 days	15 days
Land	5 days	15 days
High and rough topography land	5 days	15 days
Ice- or snow-covered land	5 days	15 days

Table 4.1-12. Test Values Used in IR Composite Logic (after Rossow and Garder 1993);  
IR Values are in Kelvins

IR surface types	DEL1	DEL2	DEL3
Ocean	2.0	2.0	2.5
Near-coastal ocean, lakes	3.0	3.0	4.0
Ice-covered water	3.0	3.0	4.0
Land	6.0	5.0	8.0
High and rough topography	9.0	7.0	11.0
Ice- or snow-covered land	9.0	7.0	11.0

One of the primary difficulties in using the ISCCP approach as currently formulated is the angular dependence of clear-sky reflectance. Although cross-track scanning Sun-synchronous satellites such as the NOAA-AVHRR repeat the angular viewing conditions on a regular cycle, the solar zenith angle slowly varies and the cloudiness conditions may prevent the determination of clear-sky reflectance at some points in cycle. The ISCCP relies on an empirical bidirectional reflectance model for clear-sky ocean reflectance (Minnis and Harrison 1984a). Thus, over ocean, the angular problems are minimized. Over land, the ISCCP assumes isotropic clear-sky reflectance, although it has been established that the anisotropy of land scenes is significant (e.g., Kriebel 1978; Tarpley 1979; Minnis and Harrison 1984c; Suttles et al. 1988). For  $\theta_o < 85^\circ$ , the vegetated land clear-sky anisotropic reflectance factor  $R(k, \theta_o, \theta, \phi)$ , where  $k$  is a surface type that can vary from 0.6 to 1.6 (e.g., Suttles et al. 1988) for  $\theta < 70^\circ$ . Thus, there is the potential for clear-sky reflectance errors as great as 300% if one assumes that the measurement taken at a particular set of viewing conditions represents the reflectance at all viewing angles for a given value of  $\theta_o$ . Systematic changes of albedo with  $\theta_o$  are also not considered for land surfaces. The reflectance anisotropy over snow and desert scenes is generally not as great as that over vegetated surfaces, but the absolute changes in reflectance are as great because of the higher albedos over these surfaces.

The CERES processing will begin with a set of global clear-sky radiances matched to the Navy 10-min database at a 3-hourly resolution. Thus, a relatively high-resolution clear-sky field is required. The clear-sky radiance maps currently available from the ISCCP are the C1 datasets that have a 250-km and 3-hour resolution and that lack the anisotropy corrections noted above. The following processing steps using the ISCCP data are applied to historical AVHRR data to obtain the clear-sky radiances at the higher spatial resolution and to account for reflectance anisotropy.

From the ISCCP C1 data, the clear-sky reflectance at a given day  $d$ , synoptic hour  $h$ , nominal regional latitude  $\Theta_{C1}$ , and longitude  $\Phi_{C1}$  is  $\rho_{csC1}(\theta_o, \theta, \phi, \Theta_{C1}, \Phi_{C1}, h, d)$ . The corresponding clear-sky albedo is

$$\alpha_{csC1}(k, \theta_o, \Theta_{C1}, h, d) = \frac{\rho_{csC1}(k, \theta_o, \theta, \phi, \Theta_{C1}, \Phi_{C1}, h, d)}{R(k, \theta_o, \theta, \phi)} \quad (4.1-47)$$

where the value of  $R$  is taken from Minnis and Harrison (1984a) for vegetated land and from Suttles et al. (1988) for snow and desert. Over ocean,  $\alpha_{csC1}$  is estimated using an updated version of the clear ocean bidirectional reflectance model of Minnis and Harrison (1984a). The updated version includes calibrated data from more angles than the original model. The value of  $\alpha_{csC1}(\text{ocean}, \theta_o = 0) = 0.045$ . The standard deviation of  $\alpha_{csC1}$  is  $\sigma_{\alpha C1}(k, \theta_o, \theta, \Theta_{C1}, \Phi_{C1}, h, d)$ . For mixed land-water regions, the reflectance for the land portion is, leaving off the dependence on the parameters  $\theta_o, \theta, \phi, \Theta_{C1}, \Phi_{C1}, h$ , and  $d$ :

$$\rho_{csC1}(\text{land}) = \frac{[\rho_{csC1} - (1 - f_{\text{land}})\rho_{csC1}(\text{ocean})]}{f_{\text{land}}} \quad (4.1-48)$$

where  $f_{\text{land}}$  is the land fraction in the C1 region. The standard deviation of  $\alpha_{csC1}$  is  $\sigma_{\alpha C1}(k, \theta_o, \theta, \Theta_{C1}, \Phi_{C1}, h, d)$ . Average values of these parameters,  $\langle \alpha_{csC1}(k, \Theta_{C1}, \Phi_{C1}, h) \rangle$  and  $\langle \sigma_{\alpha C1}(k, \Theta_{C1}, \Phi_{C1}, h) \rangle$  are computed for each region and month.

The corresponding ISCCP clear-sky, 11- $\mu\text{m}$  temperatures and their standard deviations are  $T_{csC1}(k, \Theta_{C1}, \Phi_{C1}, h, d)$  and  $\sigma_{TC1}(k, \Theta_{C1}, \Phi_{C1}, h, d)$ , respectively. Monthly mean values,  $\langle T_{csC1}(k, \Theta_{C1}, \Phi_{C1}, h) \rangle$  and  $\langle \sigma_{TC1}(k, \Theta_{C1}, \Phi_{C1}, h) \rangle$ , are also computed for these parameters. All 10-min regions falling within the 250-km C1 region are initially assigned the clear-sky radiances for the ISCCP region if the C1 region is all land or water. If the C1 region is mixed, the 10-min boxes that are entirely water are assigned the empirical model values for ocean albedo and the land boxes are given the land clear-sky albedos computed from (4.1-48) and (4.1-47). The coastal boxes retain the nominal C1 albedo. The C1 temperature is assigned to the 10-min box regardless of the geotype. These mean values constitute the starting point for the development of the high-resolution clear-sky radiance set.

To derive the high-resolution dataset, AVHRR GAC data are analyzed to determine if the pixels belonging to a particular 10-min box are clear. During a given AVHRR orbit at time  $t$ , the reflectance  $\rho$ , and 11- $\mu\text{m}$  brightness temperature  $T_{B4}$  of all pixels located within a given 10-min box are compared to the monthly mean dataset. The pixels are assumed to be clear if, again leaving off the dependence on the parameters  $k, \theta_o, \theta, \phi, \Theta_{C1}, \Phi_{C1}, h$ , and  $d$ :

$$\rho(t) < \rho_{csC1}(t) + 2\sigma_{\alpha C1} \quad (4.1-49)$$

and

$$T_{B4} > T_{csC1} - 2\sigma_{TC1} \quad (4.1-50)$$

where  $h < t < h + 1$ , and

$$\rho_{csC1}(k, \theta_o, \theta, \phi, \Theta_{C1}, \Phi_{C1}, t) = R(k, \theta_o, \theta, \phi) \alpha_{csC1}(k, \theta_o, \Theta_{C1}, \Phi_{C1}, t) \quad (4.1-51)$$

The last term in (4.1-51) is the albedo at time  $t$  found by linearly interpolating the C1 albedos in time. First, the albedos are extended to  $\theta_o$  using the directional reflectance models derived from the results of Minnis and Harrison (1984a, c) based on the mean  $\theta_o$  at the synoptic times. This approach is the same employed by the ERBE time-space averaging subsystem (see Brooks et al. 1986). Simple linear interpolation is used to determine the expected standard deviation. When albedos do not exist at  $h$  or  $h + 1$ , the available albedo is extrapolated to  $t$  using the directional reflectance models. Over snow scenes, additional tests using the  $T_{B3} - T_{B4}$  differences supplement the standard clear-sky tests to insure that the scene is cloud free. The expected clear-sky temperature,  $T_{csC1}(k, \theta_o, \Theta_{C1}, \Phi_{C1}, t)$  and its standard deviation are interpolated using linear interpolation.

For some areas, such as deserts, the surface emittance at 3.7  $\mu\text{m}$  will not be unity. When the surface emittance is less than unity, the task of determining the expected clear-sky 3.7- $\mu\text{m}$  brightness temperature will be difficult. For this reason, we will develop a surface emittance map at 3.7  $\mu\text{m}$  using nighttime data so that there is no solar contribution. The effective surface emittance  $\epsilon_{3s}$  for channel 3 is also estimated for each 10-min box by first correcting the nighttime clear-sky values of  $T_{B3}$  and  $T_{B4}$  for water vapor attenuation. Assuming that the clear-sky downwelling radiance is zero for channel 3 and  $\epsilon_{4s} = 1$ , then  $\epsilon_{3s} = [B_3(T_{B4s}) - B_3(T_{B3s})] / B_3(T_{B4s})$ , where the subscript  $s$  indicates values at the surface.

The pixel values selected as clear are then analyzed as in Minnis et al. (1987) to determine an estimate of  $\rho_{cs}$  and  $T_{cs}$  for the 10-min box and new values for their standard deviations. The procedure is reversed to estimate the clear albedo and temperature at the nearest synoptic hour. These new values plus the mean channel-3 emittances are then used to construct a new clear-sky map. The results from different days at a given  $h$  are averaged to yield the new detailed clear-sky fields that will become the initial CERES clear-sky radiance fields.

Examples of applying this procedure to a day of October 1986 NOAA-9 AVHRR data are shown in Figs. 4.1-7–4.1-10. The initial clear-sky reflectance field based solely on the ISCCP land “albedos” and the ocean reflectance model have a somewhat blocky appearance due to the low-resolution of the C1 dataset. The scattering of some of the data values near the orbit overlaps is due to overwriting of previous results by pixels in the following orbit. The ocean model produces a realistic pattern of reflectance including the distinct sun glint areas. Application of the clear-sky procedure yields a somewhat finer resolution of various features such as the Arabian Peninsula and the Pampas region in South America. Bright areas of sun glint appear in the middle of the predicted sun glint during some orbits. Changes did not occur in many areas because of clouds. The clear-sky temperature fields (Figs. 4.1-9 and 4.1-10) show even more dramatic changes because of more local variability, especially over land.

The procedure used to produce the results in Figures 4.1-8 and 4.1-10 will be applied to the AVHRR data for months during four different seasons. Over some particularly clear areas, the resulting means for a given hour will be examined closely to determine the sensitivity of the technique to the values of  $R$ . New anisotropic reflectance and thermal infrared limb-darkening models will be tested as they are developed. This methodology will be continuously refined prior to the TRMM launch.

The logic employed here will be combined with the other clear-sky detection methods and with a modified version of the ISCCP approach to provide updates of clear-sky radiances during CERES on the time scales suggested in the ISCCP method. The CERES clear-sky composite relies on high-resolution data applied to a higher-resolution grid than that employed by the ISCCP. Thus, accounting for local variability becomes very important. The ISCCP thresholds that bound the clear-sky domain for a particular surface category will be used as guidelines and as default values for the CERES clear-sky composite development. The local standard deviations in the clear-sky radiances computed using the above analysis procedure on preflight AVHRR data will be used to set the thresholds for cloud detection during CERES.

#### **4.1.7. Version 2: Future Directions**

##### ***4.1.7.1. Detection of Cloud Shadows***

The detection of cloud shadows is a problem that has not been addressed adequately in the literature. The following strategy is the first method we will employ to begin determining cloud shadows. The following discussion is only meant to provide an idea of the approach. Further work in this area has been initiated on this problem.

A  $3 \times 3$  median filter first is applied to reduce noise in the image. It has the following desirable properties: (1) it does not affect the presence or position of the shadow edges, (2) no new brightness values are created, and (3) performance of the Laplace of Gaussian (LOG) zero crossing edge detection algorithm is improved.

**4.1.7.1.1. Oceans.** Histogram equalization of the AVHRR channel 1 image is made first. The histogram equalization transform produces a histogram that is quasi-uniform on the average. It is based upon the discrete cumulative histogram with quantized brightness values. The dark values on the histogram equalized image are those due to cloud shadows.

**4.1.7.1.2. Land.** The algorithm over land is more complex because shadows may fall upon both land surfaces of varying reflectances as well as water surfaces such as lakes, rivers, and marshes. The application of a Laplacian filter to a Gaussian filter image is made first. This operation aids in the recognition of shadow and cloud regions. Edge locations are determined by the zero-crossings of the LOG-filtered image. Details are given in Berendes et al. (1992). Many more edges are produced than just cloud and shadow ones. These are due to background variations and to noise.

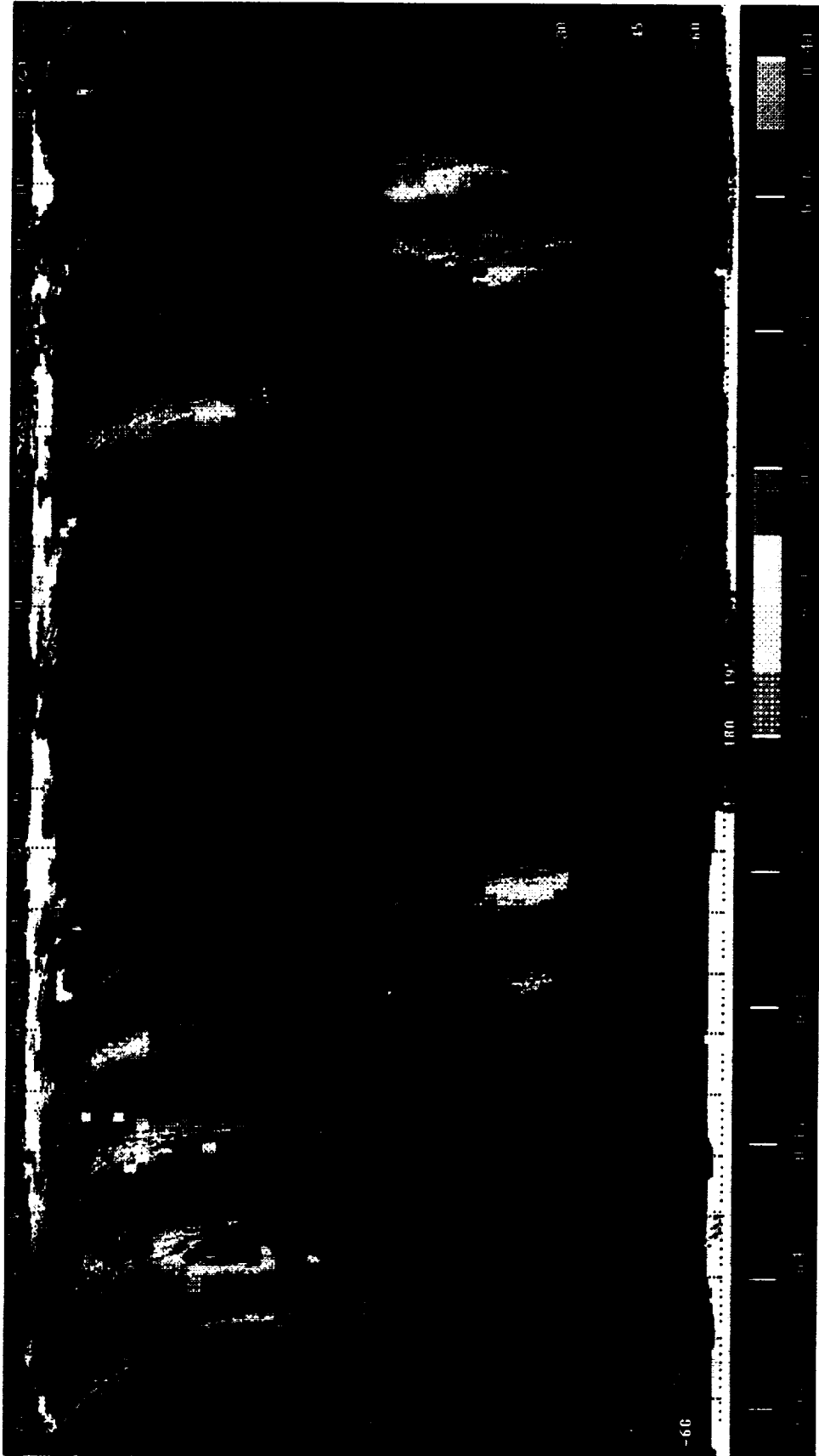


Figure 4.1-7. ISCCP clear-sky reflectance, Oct. 22, 1986. (See section 4.1.6.1.)

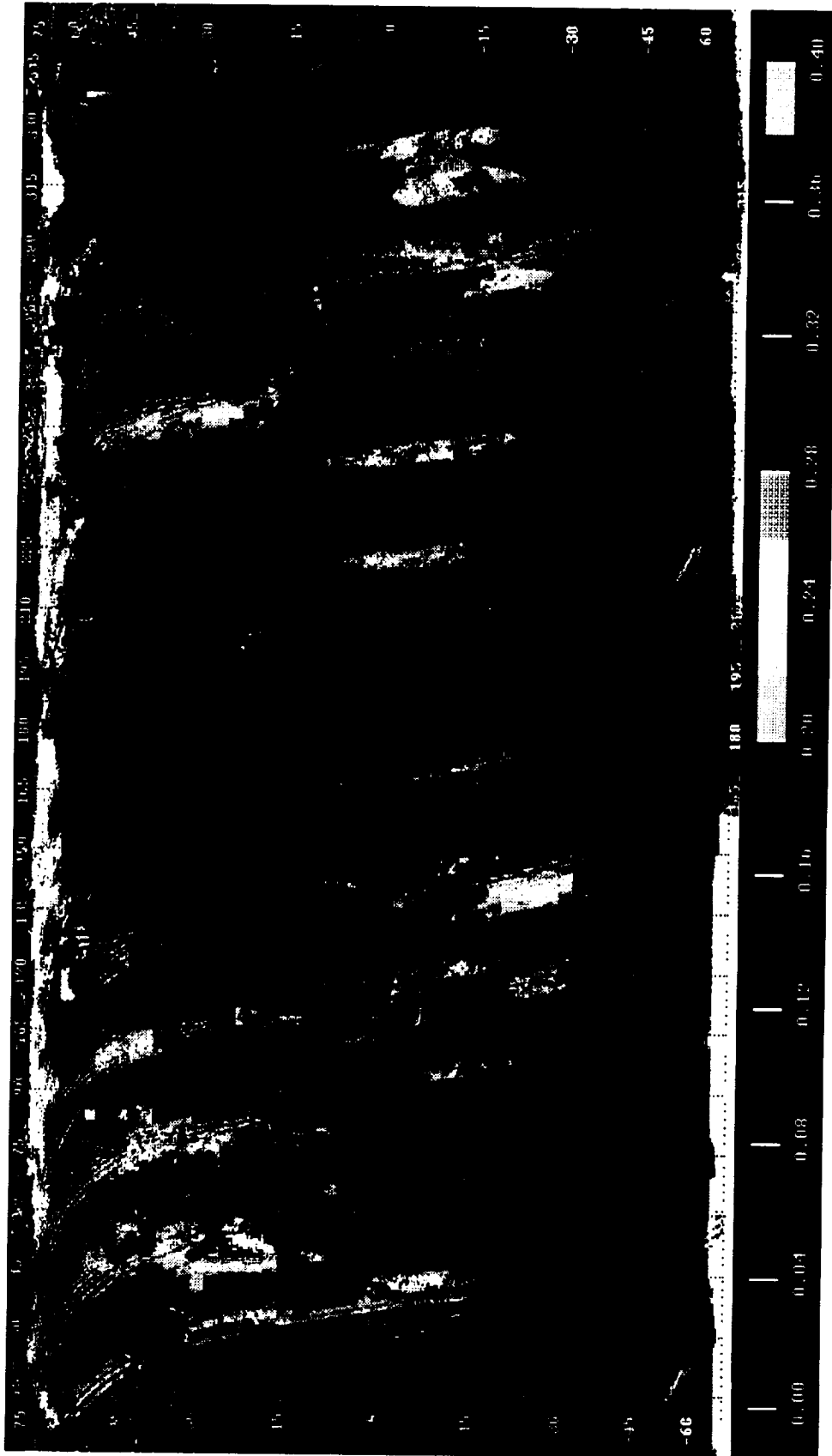


Figure 4.1-8. Revised clear-sky reflectance, Oct. 22, 1986. (See section 4.1.6.1.)

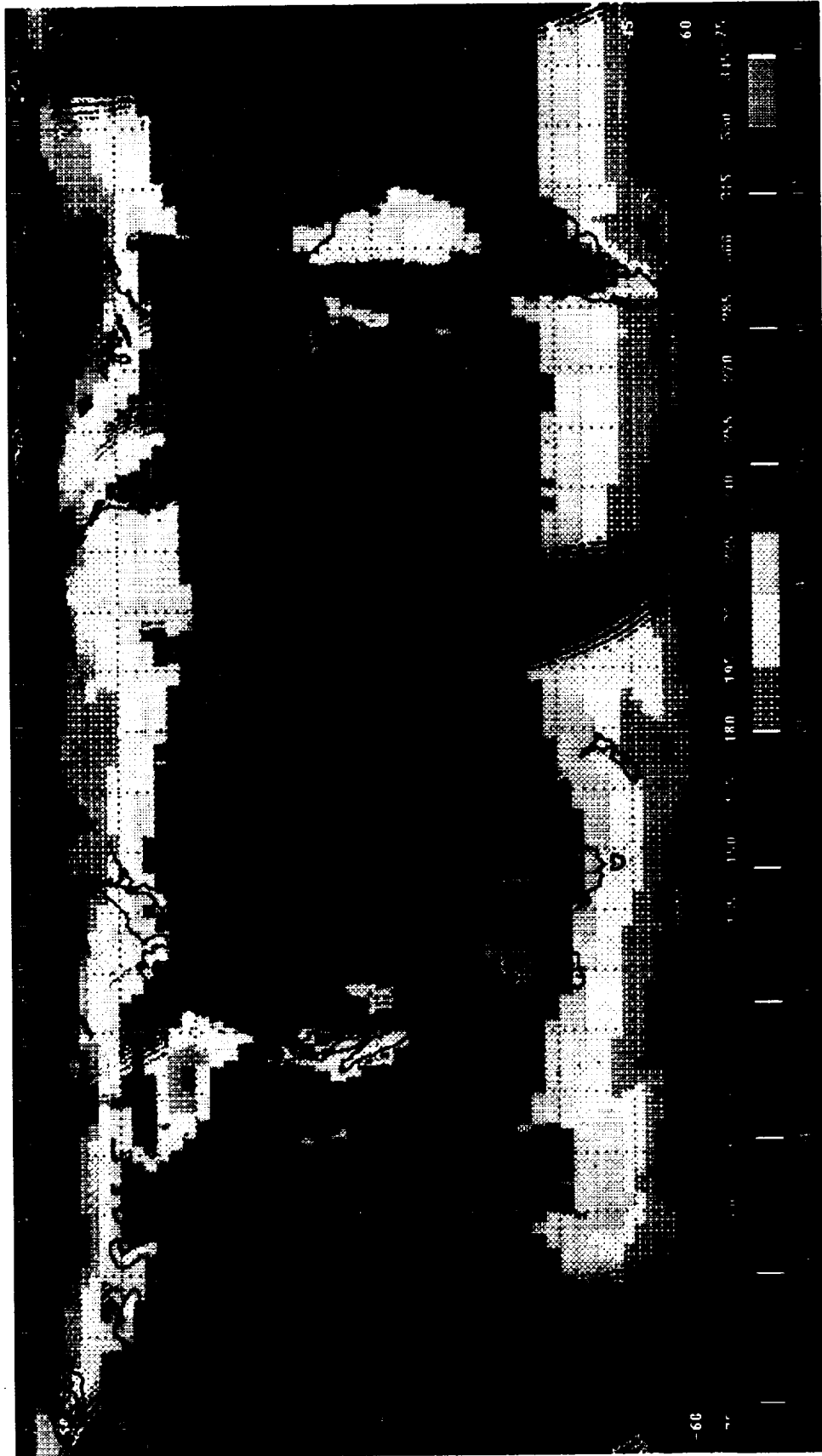


Figure 4.1-9. ISCCP clear-sky temperature (K), Oct. 22, 1986. (See section 4.1.6.1.)



To isolate the relevant shadow (or cloud) edge pixels, a thresholding procedure is used which is based on a restricted histogram, called the Max/Min histogram. This is constructed from the  $3 \times 3$  neighborhood surrounding the potential edge pixels. The intention is to capture the modes of the transition pixels generating the edge elements. Generally, there are three distinctive peaks, due to (1) shadows, (2) background, and (3) clouds.

A weighted averaging of the peak values of the Max/Min histogram is used to determine the appropriate threshold between shadow and background (and between cloud and background). This is accomplished by taking into account the size of the distributions. The procedure is iterated to convergence. When water is present in the scene, then a four-mode Max/Min histogram is produced. The same iterative procedure is used to eliminate the background pixels, retaining both shadow and water pixels. The ancillary percent water data set is used to identify probable regions of water.

#### 4.1.7.2. Nighttime Polar Classification

Nighttime polar cloud/surface classification is an extremely difficult problem. Yamanouchi et al. (1987) describe a nighttime polar (Antarctic) cloud/surface discrimination algorithm based upon brightness temperature differences between the AVHRR 3.7- and 10.8- $\mu\text{m}$  channels and between the 10.8- and 12- $\mu\text{m}$  channels. Their cloud/surface discrimination algorithm was more effective over water surfaces than over inland snow-covered surfaces. A number of problems arose over inland snow-covered surfaces. First, the temperature contrast between the cloud and snow surface became especially small, leading to a small brightness temperature difference between the two infrared channels. Second, the AVHRR channels are not well-calibrated at extremely low temperatures ( $<200$  K). As noted in their study, the temperature resolution of channels 4 (10.8- $\mu\text{m}$ ) and 5 (12- $\mu\text{m}$ ) are approximately 0.6 K at 180 K, while the temperature resolution of channel 3 (3.7- $\mu\text{m}$ ) is about 3.5 K at 220 K, and only 7.5 K at 210 K. Therefore, the channel 3 data are not generally useful for cloud detection at the low temperatures expected at the Antarctic. Additionally, the AVHRR data have a digitization problem at extremely low temperatures due to mechanical noise and also because of the nonlinear temperature dependence of the Planck function. The brightness temperature differences between AVHRR channels 4 and 5 offer the most hope for discriminating clouds from a snow- or ice-covered surface. Much further work needs to be done in this area.

#### 4.1.8. References

- Allen, Robert C., Jr.; Durkee, Philip A.; and Wash, Carlyle, H. 1990: Snow/Cloud Discrimination With Multispectral Satellite Measurements. *J. Appl. Meteorol.*, vol. 29, pp. 994–1004.
- Berendes, Todd; Sengupta, Sailes K.; Welch, Ron M.; Wielicki, Bruce A.; and Navar, Murgesh 1992: Cumulus Cloud Base Height Estimation From High Spatial Resolution Landsat Data—A Hough Transform Approach. *IEEE Trans. Geosci. & Remote Sens.*, vol. 30, no. 3, pp. 430–443.
- Brooks, D. R.; Harrison, E. F.; Minnis, P.; Suttles, J. T.; and Kandel, R. S. 1986: Development of Algorithms for Understanding the Temporal and Spatial Variability of the Earth's Radiation Balance. *Rev. Geophys.*, vol. 24, pp. 422–438.
- Chen, D. W.; Sengupta, S. K.; and Welch, R. M. 1989: Cloud Field Classification Based upon High Spatial Resolution Textural Features. Part II—Simplified Vector Approaches. *J. Geophys. Res.*, vol. 94, pp. 14749–14765.
- Coakley, J. A., Jr.; and Bretherton, F. P. 1982: Cloud Cover from High-Resolution Scanner Data—Detecting and Allowing for Partially Filled Fields of View. *J. Geophys. Res.*, vol. 87, pp. 4917–4932.
- Davis, P.; Stowe, L. L.; and McClain, E. P. 1993: Development of a Cloud Layer Detection Algorithm for the Clouds From AVHRR (CLAVR) Phase II Code. *Proceedings of SPIE Symposium*, SPIE.
- Ebert, Elizabeth 1987: A Pattern Recognition Technique for Distinguishing Surface and Cloud Types in the Polar Regions. *J. Climat. & Appl. Meteorol.*, vol. 26, pp. 1412–1427.
- Ebert, Elizabeth 1989: Analysis of Polar Clouds From Satellite Imagery Using Pattern Recognition and a Statistical Cloud Analysis Scheme. *J. Appl. Meteorol.*, vol. 28, pp. 382–399.

- Garand, Louis 1988: Automated Recognition of Oceanic Cloud Patterns. Part I—Methodology and Application to Cloud Climatology. *J. Climat.*, vol. 1, pp. 20–39.
- Giarratano, Joseph C.; and Riley, Gary 1989: *Expert Systems: Principles and Programming*. PWS-Kent Publ. Co.
- Gutman, G.; Tarpley, D.; and Ohring, G. 1987: Cloud Screening for Determination of Land Surface Characteristics in a Reduced Resolution Satellite Data Set. *Int. J. Remote Sens.*, vol. 8, pp. 859–870.
- Haralick, R. M.; Dinstein, I.; and Shanmugam, K. 1973: Textural Features for Image Classification. *IEEE Trans. Syst., Man, & Cybern.*, vol. SMC-3, pp. 610–621.
- Hecht-Nielsen, Robert 1990: *Neurocomputing*. Addison-Wesley Publ. Co.
- Inoue, Toshiro 1987: A Cloud Type Classification with NOAA 7 Split-Window Measurements. *J. Geophys. Res.*, vol. 92, pp. 3991–4000.
- Inoue, Toshiro 1989: Features of Clouds Over the Tropical Pacific During Northern Hemispheric Winter Derived From Split Window Measurements. *J. Meteorol. Soc. Japan*, vol. 67, pp. 621–637.
- Key, J.; and Barry R. G. 1989: Cloud Cover Analysis With Arctic AVHRR Data. I—Cloud Detection. *J. Geophys. Res.*, vol. 94, pp. 18521–18535.
- Kidwell, K. B., 1991: NOAA Polar Orbiter User's Guide, NOAA Climate Data Center, Satellite Data Services Division, Washington, D. C.
- Kriebel, K. T. 1978: Measured Spectral Bidirectional Reflection Properties of Four Vegetated Surfaces. *Appl. Opt.*, vol. 17, pp. 253–259.
- Lee, Jonathan; Weger, Ronald C.; Sengupta, Sailes K.; and Welch, Ronald M. 1990: A Neural Network Approach to Cloud Classification. *IEEE Trans. Geosci. & Remote Sens.*, vol. 28, pp. 846–855.
- Luger, George F.; and Stubblefield, William A. 1989: *Artificial Intelligence and the Design of Expert Systems*. Benjamin/Cummings Publ. Co.
- Matthews, Elaine; and Rossow William B. 1987: Regional and Seasonal Variations of Surface Reflectance From Satellite Observations at 0.6 micron. *J. Climat. & Appl. Meteorol.*, vol. 26, pp. 170–202.
- McClain, E. P. 1993: *Evaluation of CLAVR Phase-I Algorithm Performance—Final Report*. U.S. Department of Commerce/NOAA/NESDIS, Report 40-AAANE-201-424.
- Minnis, P.; and Harrison, E. F. 1984a: Diurnal Variability of Regional Cloud and Clear-Sky Radiative Parameters Derived From GOES Data. Part I—Analysis Method. *J. Climat. & Appl. Meteorol.*, vol. 23, pp. 993–1011.
- Minnis, P.; and Harrison, E. F. 1984b: Diurnal Variability of Regional Cloud and Clear-Sky Radiative Parameters Derived from GOES Data. Part II—November 1978 Cloud Distributions. *J. Climat. & Appl. Meteorol.*, vol. 23, pp. 1012–1031.
- Minnis, P.; and Harrison, E. F. 1984c: Diurnal Variability of Regional Cloud and Clear-Sky Radiative Parameters Derived From GOES Data. Part III—November 1978 Radiative Parameters. *J. Climat. & Appl. Meteorol.*, vol. 23, pp. 1032–1051.
- Minnis, Patrick; Harrison, Edwin F.; and Gibson, Gary G. 1987: Cloud Cover Over the Equatorial Eastern Pacific Derived From July 1983 International Satellite Cloud Climatology Project Data Using a Hybrid Bispectral Threshold Method. *J. Geophys. Res.*, vol. 92, pp. 4051–4073.
- Rossow, William B. 1989: Measuring Cloud Properties From Space—A Review. *J. Climat.*, vol. 2, pp. 201–213.
- Rossow, William B.; and Garder, Leonid C. 1993: Cloud Detection Using Satellite Measurements of Infrared and Visible Radiances for ISCCP. *J. Climat.*, vol. 6, no. 12, pp. 2341–2369.
- Rumelhart, D. E.; Hinton, G.; and Williams, R. 1986: Learning Internal Representations by Error Propagation. In *Parallel Distributed Processing—Exploration in the Microstructure of Cognition*. D. Rumelhart and J. McClelland, eds., MIT Press, pp. 318–362.
- Saunders, R. W.; and Kriebel K. T. 1988: An Improved Method for Detecting Clear Sky and Cloudy Radiances From AVHRR Data. *Int. J. Remote Sens.*, vol. 9, pp. 123–150.
- Seze, Genevieve; and Desbois, Michel 1987: Cloud Cover Analysis From Satellite Imagery Using Spatial and Temporal Characteristics of the Data. *J. Climat. & Appl. Meteorol.*, vol. 26, pp. 287–303.
- Seze, Genevieve; Rossow, William B. 1991a: Time-Cumulated Visible and Infrared Radiance Histograms Used as Descriptors of Surface and Cloud Variations. *Int. J. Remote Sens.*, vol. 12, pp. 877–920.

- Seze, Genevieve; and Rossow, William B. 1991b: Effects of Satellite Data Resolution on Measuring the Space/Time Variations of Surfaces and Clouds. *Int. J. Remote Sens.*, vol. 12, pp. 921–952.
- Stowe, L. L.; McClain, E. P.; Carey, R.; Pellegrino, P.; and Gutman, G. G. 1991: Global Distribution of Cloud Cover Derived From NOAA/AVHRR Operational Satellite Data. *Adv. Space Res.*, vol. 11, no. 3, pp. 51–54.
- Stowe, L. L.; Vemury, S. K.; and Rao, A. V. 1994: AVHRR Clear Sky Radiation Data Sets at NOAA/NESDIS. *Adv. Space Res.*, vol. 11, pp. 113–116.
- Suttles, J. T.; Green, R. N.; Minnis, P.; Smith, G. L.; Staylor, W. F.; Wielicki, B. A.; Walker, I. J.; Young, D. F.; Taylor, V. R.; and Stowe, L. L. 1988: *Angular Radiation Models for Earth-Atmosphere System. Volume I: Shortwave Radiation*. NASA RP-1184.
- Tarpley, J. D. 1979: Estimating Incident Solar Radiation at the Surface From Geostationary Satellite Data. *J. Appl. Meteorol.* vol. 18, pp. 1172–1181.
- Tovinkere, V. R.; Penaloza, M.; Logar, A.; Lee, J.; Weger, R. C.; Berendes, T. A.; and Welch, R. M. 1993: An Intercomparison of Artificial Intelligence Approaches for Polar Scene Identification. *J. Geophys. Res.*, vol. 98, no. D3, pp. 5001–5016.
- Welch, R. M.; Sengupta, S. K.; Goroch, A. K.; Rabindra, P.; Rangaraj, N.; and Navar, M. S. 1992: Polar Cloud and Surface Classification Using AVHRR Imagery—An Intercomparison of Methods. *J. Appl. Meteorol.*, vol. 31, no. 5, pp. 405–420.
- Welch, Ronald M.; Kuo, Kwo-Sen; and Sengupta, Sailes K. 1990: Cloud and Surface Textural Features in Polar Regions. *IEEE Trans. Geosci. & Remote Sens.*, vol. 28, pp. 520–528.
- Welch, R. M.; Navar, M. S.; and Sengupta, S. K. 1989: The Effect of Spatial Resolution Upon Texture-Based Cloud Field Classifications. *J. Geophys. Res.*, vol. 94, pp. 14767–14781.
- Yamanouchi, Takashi; Kawaguchi, Sadao; and Suzuki, Kazuya 1987: Detection of Clouds in Antarctica From Infrared Multi-spectral Data of AVHRR. *J. Meteorol. Soc. Japan*, vol. 65, pp. 949–962.

**Clouds and the Earth's Radiant Energy System (CERES)**

**Algorithm Theoretical Basis Document**

***Imager Cloud Height Determination***

***(Subsystem 4.2)***

**CERES Science Team Cloud Retrieval Working Group**

Bryan A. Baum<sup>1</sup>  
Patrick Minnis<sup>1</sup>  
James A. Coakley, Jr.<sup>2</sup>  
Bruce A. Wielicki<sup>1</sup>

**MODIS Science Team Cloud Retrieval Working Group**

Paul Menzel<sup>3</sup>

**Algorithm Implementation, Data Analysis, and Data Management**

James Titlow<sup>4</sup>  
Vasanth Tovinkere<sup>4</sup>  
Pat Heck<sup>5</sup>  
Shalini Mayor<sup>5</sup>

<sup>1</sup>Atmospheric Sciences Division, NASA Langley Research Center, Hampton, Virginia 23681-0001

<sup>2</sup>Department of Atmospheric Sciences, Oregon State University, Corvallis, Oregon 97331-2209

<sup>3</sup>Space Science and Engineering Center, University of Wisconsin, Madison, Wisconsin

<sup>4</sup>Science Applications International Corporation (SAIC), Hampton, Virginia 23666

<sup>5</sup>Analytical Services & Materials, Inc., Hampton, Virginia 23666

## 4.2. Imager Cloud Height Determination

### 4.2.1. Introduction

Section 4.1 discussed methodologies to provide two functions:

1. A global cloud mask
2. Scene classification using automated artificial intelligence schemes

Additionally, a scheme was outlined to update the clear-sky values for all five AVHRR channels depending on the results of the cloud-masking process. This section discusses the next two steps in the cloud-retrieval process, namely detection of cloud layers and determination of cloud-top pressure for each layer present. Several approaches are examined for use in the Version 1 CERES (Clouds and the Earth's Radiant Energy System) cloud-retrieval algorithm, such as spatial coherence (Coakley and Bretherton, 1982), multispectral techniques such as the layered bispectral threshold method (LBTM; Minnis et al., 1993), and artificial intelligence methods such as the fuzzy logic expert system approach. Additionally, the CO<sub>2</sub> slicing method will be used to determine mid- to high-level cloud-top pressures. A strength of spatial coherence and CO<sub>2</sub> slicing techniques is that they both work with infrared (IR) narrowband channels (at wavelengths between 11 and 15  $\mu\text{m}$ ) and thus are applied the same for both daytime and nighttime viewing conditions. The spatial coherence technique was designed to work for retrieval of low clouds, such as stratus and stratocumulus. Section 4.2.2 discusses the framework for the spatial-coherence algorithm. The LBTM daytime multispectral methods are discussed in section 4.2.3, the CO<sub>2</sub> slicing technique is outlined in section 4.2.4, and the fuzzy logic classifier in 4.2.5. The CERES Version 1 approach to inferring cloud-top pressures under conditions involving overlapping cloud layers is briefly outlined in section 4.2.5.

### 4.2.2. The Spatial Coherence Method

#### 4.2.2.1. Identification of Cloud Layers from Satellite Imagery Data

Everyday observations of clouds suggest that many cloud systems form well-defined layers. Surveys of satellite imagery data for the global oceans suggest that as many as 20 to 30% of all 250-km scale regions contain single cloud layers. At smaller observational scales (60 km), the isolation of single cloud layers may be as high as 50% (Coakley and Baldwin, 1984). Observations for the First ISCCP Regional Experiment (FIRE) II Cirrus Intensive Field Observations (IFO) suggest that as many as 50% of all 100-km scale regions are either single-layered or cloud-free (Lin and Coakley, 1993). Although cloud systems are often presumed to obey the physical relationships associated with a plane-parallel, homogeneous cloud, as is the case in ISCCP (International Satellite Cloud Climatology Project), clearly layered cloud systems might be expected to exhibit such behavior more closely than would more complex cloud systems. Because of their pervasiveness and to the relative abundance of theoretical tools that can be used to analyze them, layered cloud systems deserve special attention in observations of the earth's cloud systems. Effective optical properties of layered cloud systems should generally be more readily measurable than the macrophysical and microphysical properties of individual clouds. Changes in clouds brought about by changes in the climate system might well be noted first in the properties of layered clouds.

Experience with imagery data during the 1980's leads to the conclusion that layered cloud systems are relatively easy to identify. Here the spatial-coherence method is described as one approach to identifying the layers. The spatial-coherence method uses the pixel-to-pixel variability in emitted radiances to identify pixels that appear to be overcast by clouds that form a layer. Optical properties of cloud layers can be deduced from the overcast pixels. Various degrees of quality control can be applied to the analysis to ensure that the pixels so identified are indeed overcast. The increase in quality, however, is at the

expense of the number of such systems that meet the criteria of being part of a well-defined layer. The algorithm will be applied to groups of pixels that have a similar surface type (e.g., water).

#### *4.2.2.2. Historical Perspective*

In the early 1980's, as is the case today, the favored approach for obtaining cloud properties from satellite observations was the application of thresholds to imagery data (Minnis and Harrison, 1984; Rossow et al., 1985; Rossow and Garder, 1993). Although multispectral, clustering methods were also used to attempt an automated identification of cloud structures, the final estimate of cloud properties was still derived assuming that each of the imagery pixels belonging to a certain cluster was completely covered by the cloud system represented by the cluster (Debois et al., 1982). Everyday experience, however, leads to expectations that the occurrence of broken clouds on scales that are smaller or comparable to the spatial resolution typical of imagers (i.e. ~4 to 8 km) is rather common. Furthermore, when the breaks occur, it is unlikely that the clouds align themselves to fall exactly within the footprint of an imager pixel. This type of spatial sampling problem leads to the conclusion that the errors associated with threshold estimates of cloud cover may be sizable, as early work on threshold methods foretold (Shenk and Salomonson, 1972) and recent work confirms (Wielicki and Parker, 1992; Chang and Coakley, 1993).

In anticipation of these errors, a number of methods were proposed to obtain the fractional coverage within imager fields of view. Platt (1983) proposed a modified version of the visible-infrared bispectral method introduced by Reynolds and Vonder Haar (1977). The method used plane-parallel radiative transfer theory to identify fields of view that were overcast with clouds having a given liquid water or ice water column amount from those that contained broken clouds. The method has been extended and refined by Minnis and Harrison (1984) and by Minnis et al. (1993a, b). Arking and Childs (1985) adopted a similar scheme but added radiances observed at 3.7  $\mu\text{m}$  to allow for effects caused by droplet size in the plane-parallel radiative-transfer calculations. A third approach, the spatial-coherence method (Coakley and Bretherton, 1982), relied on the observation that many of the global cloud systems come in layers and that these layers extend over tens of kilometers, maintaining a fairly constant emission temperature over these scales. Where the region being observed is cloud-free or where it is overcast, the emitted radiances achieve a high degree of spatial uniformity at the pixel scale. Where the clouds are present but fail to completely cover the imager pixels, the emitted radiances vary erratically from pixel to pixel. While the spatial-coherence method explicitly seeks to identify the cloud layers, the retrieval of cloud properties employed in the bispectral and multispectral schemes relied on the assumption that the clouds being observed were part of a layer. The challenge is to develop an algorithm that identifies layers when present.

The spatial-coherence method identifies layers by identifying the portions of the region that exhibit a high degree of local uniformity in the emitted radiances. The purpose of this section is to outline a relatively simple approach to solving this problem. The solution is both a generalization and simplification of the earlier approaches (Coakley and Bretherton, 1982; Coakley and Baldwin, 1984). In the description given here, the method depends primarily on a single parameter—the difference in radiances expected for cloud-free and overcast fields of view. The dependence of the retrieved properties, namely the radiances associated with cloud-free and overcast portions of the region, is relatively insensitive to the choice of this parameter.

#### *4.2.2.3. Theory Behind the Spatial-Coherence Method*

The starting point for spatial-coherence analysis is the model of a well-defined, single-layered system of clouds over a relatively uniform background. What is meant by the term “well-defined” and

“relatively uniform” will be explained below. The emitted radiance observed by a radiometer viewing such a system is given by

$$I = (1 - C)I_{cs} + C(\epsilon_{cld}I_{cld} + t_{cld}I_{cs}) \quad (4.2-1)$$

where  $I$  is the emitted radiance,  $C$  is the fractional cloud cover for the field of view,  $I_{cs}$  is the radiance associated with the cloud-free portion of the field of view, i.e. the radiance observed when  $C = 0$ .  $\epsilon_{cld}$  is the mean effective emissivity associated with the cloud layer,  $t_{cld}$  is the mean transmissivity, and  $I_{cld}$  is the radiance that would be observed for overcast regions, i.e.  $C = 1$ , if the clouds were black at the wavelength of observation. In (4.2-1), the radiance is assumed to be at an infrared (IR) window wavelength so that downward emission above the cloud can be neglected. Likewise, the surface is assumed to be black at the wavelength of observation so that all radiation incident on the surface is absorbed, especially that emitted downward by the cloud. No radiation is reflected by the surface.

Over relatively small regions, i.e.  $\sim 100 \text{ km} \times 100 \text{ km}$  to  $500 \text{ km} \times 500 \text{ km}$  scale, the emission of the clear-sky background,  $I_{cs}$ , and the height of the cloud layer, and therefore  $I_{cld}$ , are assumed to have little variance. That is, the effects of variations in the thermal emissions associated with the clear-sky background and the height of the cloud layer are small when compared with effects caused by variations in the fractional cloud cover and the cloud optical properties. If these conditions are met, the background is said to be relatively uniform and the layer is said to be well-defined. From (4.2-1), the variance of the radiances under such conditions is given by

$$(I - \bar{I})^2 = [(C - \bar{C})I_{cs} + (C\epsilon_{cld} - \bar{C}\epsilon_{cld})I_{cld} + (Ct_{cld} - \bar{C}t_{cld})I_{cs}]^2 \quad (4.2-2)$$

The variances of emitted radiances over small areas spanning several imager pixels is the key to identifying the portions of a region that are cloud-free or overcast by clouds in a well-defined layer. Clearly, the variance becomes zero when the mean cloud cover in a region approaches zero. If the mean cloud cover is zero, then, of course, the fractional cover in every pixel  $i$  is also zero, i.e.  $C = \bar{C} = 0$ . Where the clouds become sufficiently extensive so that several imager pixels are overcast then, for analogous reasons, the variance approaches zero because  $C = \bar{C} = 1$ . Often when cloud systems become sufficiently extensive that they cover several imager pixels, they also become opaque. A notable exception, of course, is cirrus. For opaque, overcast clouds the variance again becomes zero because  $t_{cld}^i = t_{cld} = 0$  and  $\epsilon_{cld}^i = \bar{\epsilon}_{cld} = \epsilon_{cldmax}$ , where  $t_{cld}$  is the cloud transmissivity and  $\epsilon_{cldmax}$  is the emissivity that the clouds obtain when they become opaque, i.e.  $\epsilon_{cldmax} = 1 - r_{cldmax}$ , where  $r_{cldmax}$  is the reflectivity. To simplify notation,  $I_{cld}$  will be used to represent  $\epsilon_{cldmax}I_{cld}$  in the remainder of the text. It will be understood that  $I_{cld}$  is taken to be the emission observed for pixels overcast by opaque clouds. When pixels become overcast with opaque clouds, the variance in emitted radiances also becomes zero. When pixels become overcast by semitransparent clouds, like cirrus, pixel-to-pixel variations in the cloud optical properties, i.e.  $\epsilon_{cld}$  and  $t_{cld}$ , prevent the variance from dropping to zero.

Because clouds appear to vary incoherently on the  $\sim 1 \text{ km} \times 1 \text{ km}$  scale available to current satellite imagers, (4.2-2) indicates that variances in the emitted radiances for regions that are covered by several imager pixels will be nonzero when the region contains broken cloud. The variability will be caused partly by differences in the fractional cloud cover from pixel to pixel and partly by variations in the average cloud optical properties from pixel to pixel. The spatial-coherence method identifies pixels that are overcast by layered clouds where the clouds become opaque and pixels that are cloud-free by relying on the near-zero variances in emitted radiances for localized collections, or clusters, of the pixels. Collections of pixels that are partly covered by clouds or are overcast by clouds that are semitransparent invariably exhibit relatively larger variances.

It would appear that a simple threshold on the variance of emitted radiances would suffice to identify pixels that are overcast layered cloud systems. To a first approximation, the application of a simple threshold suffices; however, although fractional cloud cover and cloud optical properties tend to vary

incoherently on the  $\sim 1 \text{ km} \times 1 \text{ km}$  scale, they can at times conspire to produce near-zero variances in emitted radiances while only partly covering a collection of pixels. Regular arrays of clouds arising from regular patterns of convection or mesoscale circulations will produce such instances. These conditions appear to be met only rarely. As a guard against these relatively rare occurrences, the spatial-coherence method relies not only on the low variances in the emitted radiances observed for cloud-free and opaque-overcast regions, but also on the clustering in the radiance domain of the pixels identified as cloud-free and overcast. The clustering must occur within a region that is, on average, rarely overcast or cloud-free, i.e. regions with scales of  $\sim 250 \text{ km} \times 250 \text{ km}$ .

#### 4.2.2.4. Spatial Considerations

**4.2.2.4.1. Local scale,  $4 \text{ km} \times 4 \text{ km}$  to  $8 \text{ km} \times 8 \text{ km}$ .** In the spatial-coherence method, the variability of the radiances is usually calculated for small arrays of adjacent pixels. Typically  $2 \times 2$  (scan line  $\times$  scan spot) pixel arrays are used for  $4 \text{ km} \times 4 \text{ km}$  AVHRR Global Area Coverage (GAC) data. The variability within each array is called the local variability. In the case of the  $2 \times 2$  arrays of GAC pixels, the local variability is associated with  $8 \text{ km} \times 8 \text{ km}$  portions of the region. The size of the array over which the variability is calculated is not critical. It is reasonable to select a scale between  $4 \text{ km} \times 4 \text{ km}$  and  $8 \text{ km} \times 8 \text{ km}$  for the variance scale because the cloud-free and overcast portions of  $250 \text{ km} \times 250 \text{ km}$  regions are often several times the  $4 \text{ km} \times 4 \text{ km}$  to  $8 \text{ km} \times 8 \text{ km}$  scales. If the local standard deviations of the emitted radiances are plotted as a function of the local means for the pixel arrays covering a  $250 \text{ km} \times 250 \text{ km}$  region, an arch plot, typical of the spatial-coherence method, results (see Fig. 4.2-1). The figure shows the local means and standard deviations of the emitted  $11\text{-}\mu\text{m}$  radiances for a  $250 \text{ km} \times 250 \text{ km}$  region over the Atlantic Ocean. The data points are from  $4 \times 4$  arrays of  $1 \text{ km} \times 1 \text{ km}$  AVHRR observations collected during the 1992 Atlantic Stratocumulus-Transition Experiment (ASTEX). Figure 4.2-1 shows an arch that is typical of a single-layered system of marine stratocumulus. Radiances of  $11 \mu\text{m}$  at the foot of the arch near  $96 \text{ mWm}^{-2}\text{sr}^{-1}\text{cm}$  are associated with the cloud-free background. Radiances at the foot near  $81 \text{ mWm}^{-2}\text{sr}^{-1}\text{cm}$  are associated with overcast pixels. In Figure 4.2-1, each point represents a  $4 \text{ km} \times 4 \text{ km}$  portion of the  $250 \text{ km} \times 250 \text{ km}$  region. There are approximately 1000 points in the plot. Every other  $4 \text{ km} \times 4 \text{ km}$  sample has been skipped.

For comparison, Figure 4.2-2a shows the same observations with the region divided to form  $8 \times 8$  arrays of the  $1 \text{ km} \times 1 \text{ km}$  pixels. Each point in the figure now represents an  $8 \text{ km} \times 8 \text{ km}$  portion of the region. Again there are about a 1000 points in the figure. The similarity in radiances of the overcast and cloud-free feet with those in Figure 4.2-1 illustrate the lack of sensitivity to spatial scale. Figure 4.2-2b shows the same observations again but in this case the region was divided to form  $2 \times 2$  arrays of  $4 \text{ km} \times 4 \text{ km}$  pixels. The  $4 \text{ km} \times 4 \text{ km}$  radiances were obtained by taking the corresponding averages of the  $1\text{-km}$  radiances. As in Figure 4.2-2a, each point represents an  $8 \text{ km} \times 8 \text{ km}$  portion of the  $250 \text{ km} \times 250 \text{ km}$  scale region. The results in Figure 4.2-2b are like those obtained with  $4 \text{ km} \times 4 \text{ km}$  AVHRR GAC data. Although the radiances associated with the cloud-free and overcast feet differ little from those shown in Figures 4.2-1 and 4.2-2a, the arch in Figure 4.2-2b appears to be less well-defined than those in Figures 4.2-1 and 4.2-2a. The loss in clarity is produced by points dropping from the body of the arch towards the abscissa. This change in arch structure is consistent with the concept that clouds, when broken, populate adjacent  $1 \text{ km} \times 1 \text{ km}$  scale pixels incoherently. Because of this incoherence and the relative lack of sensitivity of the derived cloud-free and overcast radiances to the size of the array used, there appears to be some advantage to using large arrays of small pixels when possible rather than  $2 \times 2$  arrays as has been used traditionally.

**4.2.2.4.2. Frame scale,  $250 \text{ km} \times 250 \text{ km}$ .** Like the size of the array used to calculate the local variance, the size of the region for which the spatial-coherence analysis is performed is not critical. The scale is arbitrarily chosen using the following guidelines. The region must be sufficiently large that cloud-free and overcast pixels occur relatively frequently. Furthermore, the spatial-coherence method uses a clustering method to distinguish between low local variances in the emitted radiances that

LAC 4 X 4 N115816A

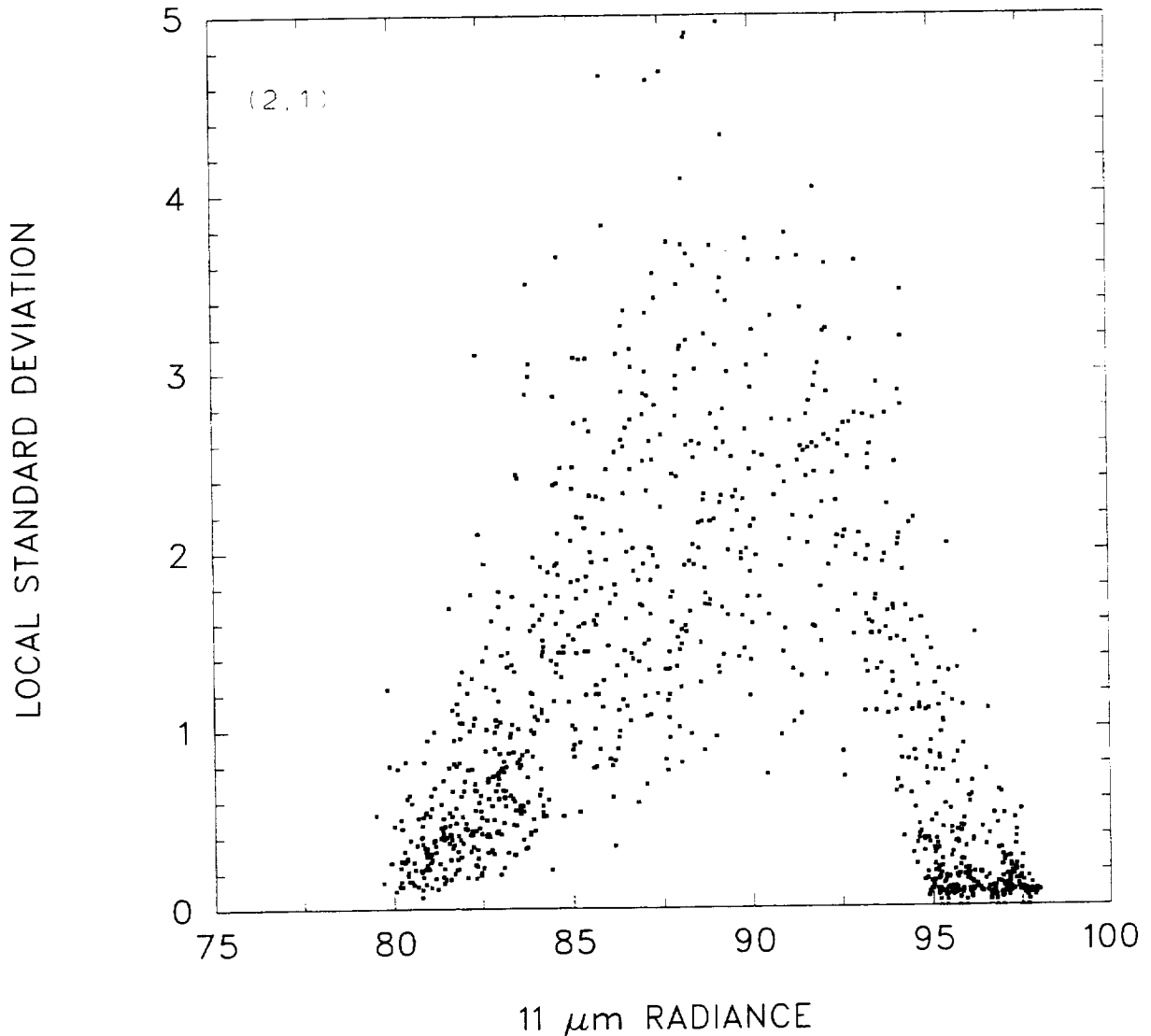


Figure 4.2-1. Local means and standard deviations for 250 km  $\times$  250 km region of the North Atlantic. Each point in the figure represents a 4  $\times$  4 array of pixels constructed from 1-km AVHRR data. Each point represents a 4 km  $\times$  4 km portion of the 250 km  $\times$  250 km region. There are approximately 1000 points in the figure. These points were obtained by skipping every other 4  $\times$  4 pixel array.

indicate cloud-free or overcast pixels from those that occur when pixels contain a repetitious pattern of broken clouds. Consequently, the region must be sufficiently large that it contains a substantial number of pixel arrays, i.e.  $\sim$ 1000 pixel arrays. It must be large enough that simple tests can be constructed to identify clustering within relatively narrow ranges of the emitted radiances against the null hypothesis that the radiances were randomly and uniformly distributed among the partly cloudy pixels. At the same time the region cannot be too large because variations of the radiances associated with cloud-free and overcast portions of the regions must remain small compared with the variability caused by variations in cloud cover and cloud optical properties. Experience with the spatial-coherence method has indicated that the 250 km  $\times$  250 km scale seems to satisfy these conditions. The 250 km  $\times$  250 km regions are termed frames in this analysis.

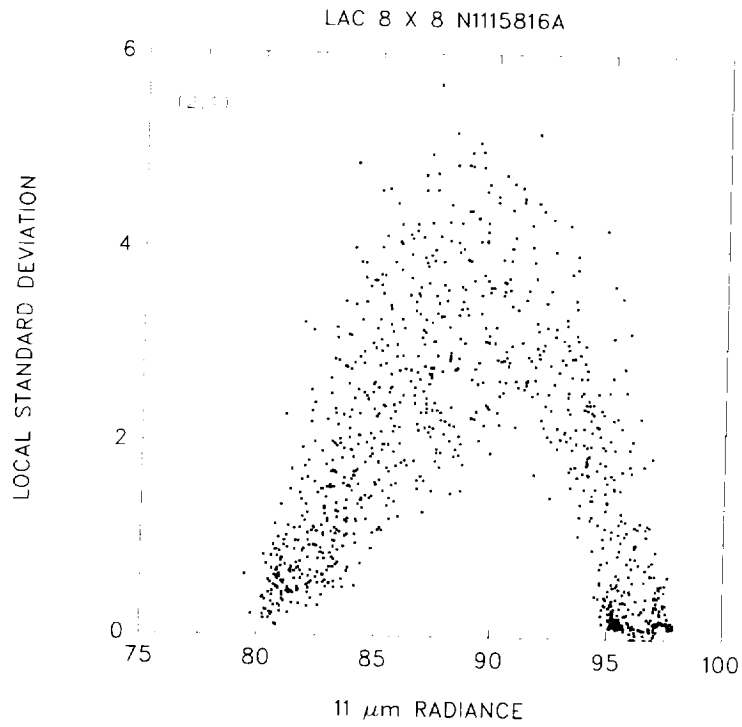


Figure 4.2-2a. Same as figure 1, but each point represents an  $8 \times 8$  array of 1-km pixels, thereby representing an  $8 \text{ km} \times 8 \text{ km}$  portion of the  $250 \text{ km} \times 250 \text{ km}$  region. There are approximately 1000 points in the image. All  $8 \times 8$  pixel arrays were used.

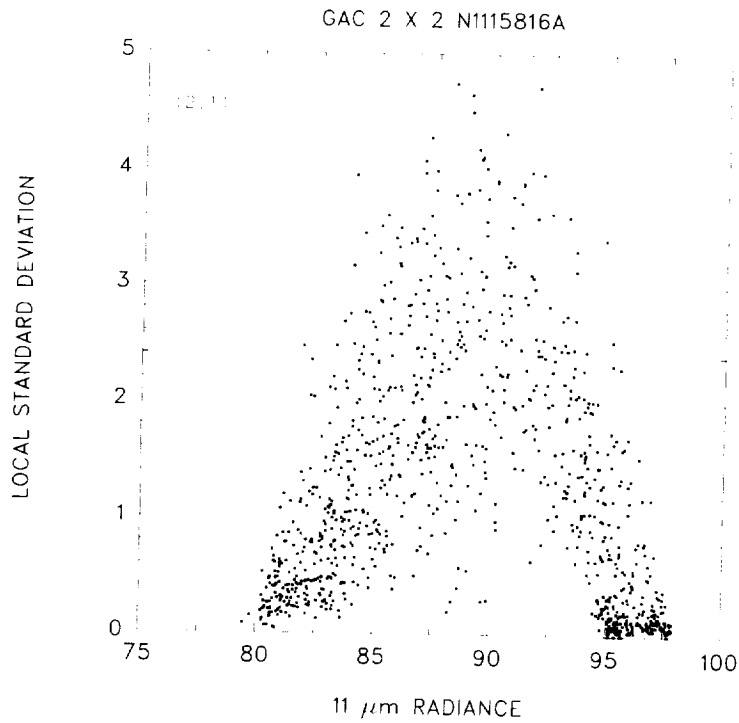


Figure 4.2-2b. Same as Figure 2a, but each point represents an  $2 \times 2$  array of 4-km pixels.

**4.2.2.4.3. Subframe scale, 50 km × 50 km.** Once pixels within a 250 km × 250 km frame have been identified as being overcast or cloud-free, they are mapped to smaller subframes of ~50 km × 50 km that constitute the larger frame. The size of the smaller subframe is again immaterial. It is chosen to be sufficiently large to contain a relatively large number of pixels (~10<sup>5</sup>) so that percentiles can be relied upon to be stable estimators of the range of radiances encountered in the subframes. Mapping the pixels to the subframes allows the construction of geographic gradients in the cloud-free background and overcast-opaque cloud radiative properties within the 250 km × 250 km frames. It also helps to isolate single-layered systems, for which simple plane-parallel theory applies, from more complex systems, for which suitable theories have yet to be developed.

#### **4.2.2.5. Mathematics of Spatial Coherence Cluster Analysis**

**4.2.2.5.1. 250 km × 250 km frame scale analysis.** This section addresses the problem of identifying which points in the arch diagram are associated with the feet of the arches (i.e. which are associated with cloud-free radiances); which are associated with overcast radiances for opaque, layered clouds; and which are associated with the body of the arch and thus with pixels that are either partly cloud covered or may be overcast with semitransparent clouds. The observations shown in Figure 4.2-3 will be used to illustrate the method for identifying the points that belong to the feet. The observations are for a 250 km × 250 km frame over the Atlantic Ocean. Like those in Figure 4.2-1, they were taken during the 1992 ASTEX experiment. Each point in the figure represents a 4 km × 4 km portion of the 250 km × 250 km scale frame. The observations indicate that the frame contains low-level and upper-level cloud layers. Because there are few pixels in the body of the arches associated with these layers, most of the pixels in this case are filled by either low-level or upper-level overcast cloud layers, or the pixels are cloud-free. Cases in which few pixels contain what appear to be broken clouds are rare (cf. Fig. 4.2-1).

It should be noted at the outset that the procedures presented here are somewhat arbitrary. The procedures are clearly not optimal in that they do not make use of any statistical description of how cloud systems actually populate imager pixels. Such a description would, for example, explain the different appearances of the arches shown in Figure 4.2-2. How broken cloud systems populate imager-scale pixels remains a subject of investigation. Nevertheless, while not optimal, the procedures presented here were designed with numerical efficiency and effectiveness in mind.

The identification of cloud-free and overcast fields of view involves the identification of pixel arrays exhibiting uniform emission. The first step is to decide on the magnitude of variability that will be allowed before a pixel array will be identified as containing broken clouds. There is, of course, a small but finite probability that pixel arrays containing broken cloud will also exhibit low spatial variability in emitted radiances. Subframes that are cloud-free or overcast by opaque clouds from a single layer cannot avoid exhibiting locally uniform emission. The locally uniform emission that is to be identified with a cloud layer or with cloud-free frames must exhibit emission within a narrow range of radiances, and the range over which the radiances are to be clustered must be defined.

The determination of the maximum standard deviation allowed for points in the feet of the arch and also for the range of radiances over which the points in a single foot are allowed to span is made by considering the effect of the variability in the radiances on the uncertainty in the cloud cover estimated from the spatial-coherence method. For a single-layered system of opaque clouds, (4.2-1) becomes

$$I = (1 - C)I_{cs} + CI_{cld} \quad (4.2-3)$$

The cloud cover is obtained by inverting (4.2-3). The uncertainty in the estimated cloud cover is thus given by

$$\Delta C = \sqrt{\frac{(1 - C)^2 \Delta I_{cs}^2 + C^2 \Delta I_{cld}^2}{(I_{cs} - I_{cld})}} \quad (4.2-4)$$

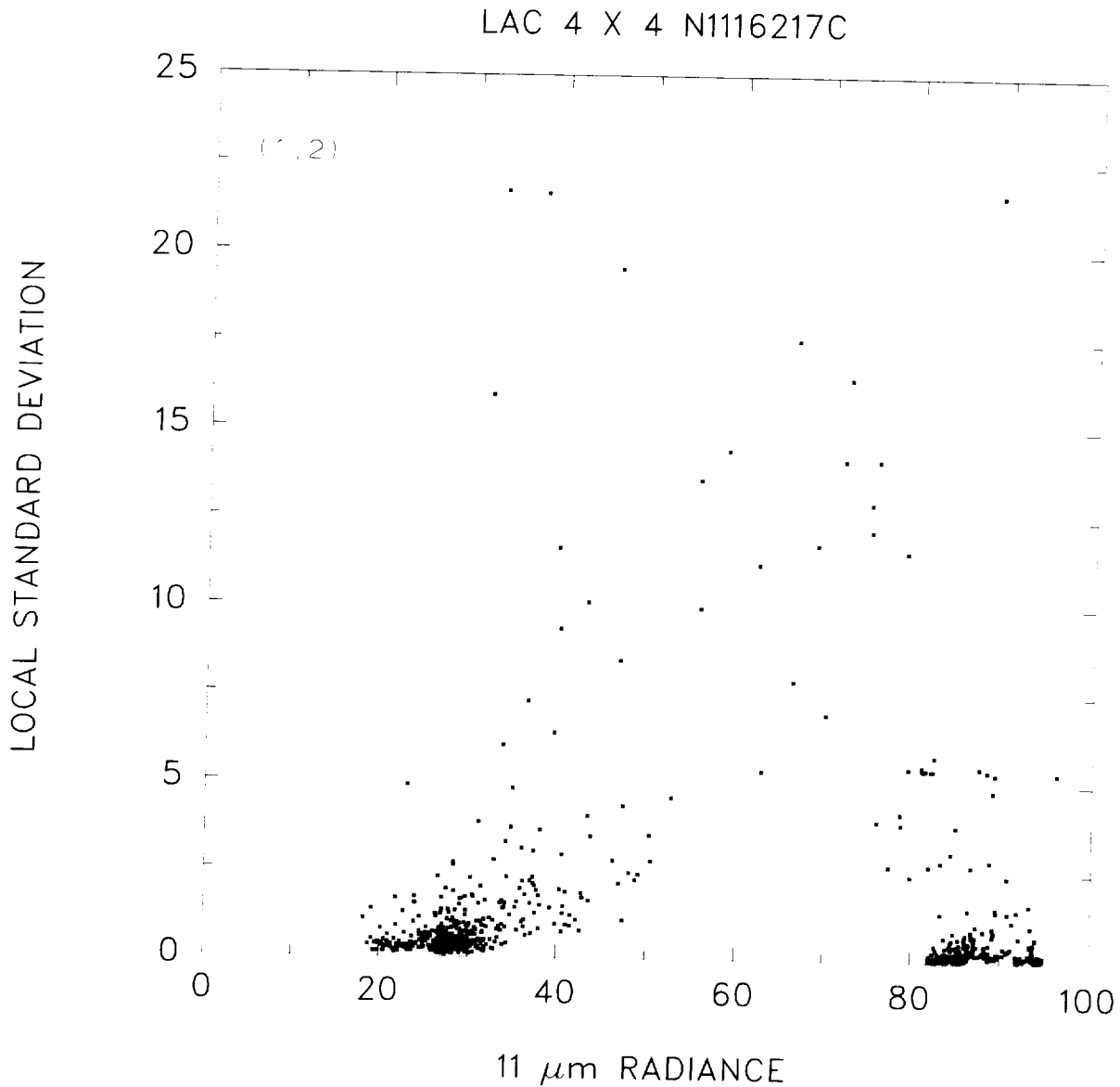


Figure 4.2-3. Same as Figure 1, but for a two-layered system.

The standard deviations of the radiances,  $\Delta I_{cs}$  for the cloud-free and  $\Delta I_{cld}$  for the overcast pixels, are taken to estimate the uncertainties in these radiances. Whether for overcast frames, ( $C = 1$ ) or for cloud-free frames ( $C = 0$ ), the uncertainty in the cloud cover associated with an array of pixels is given by

$$\Delta C = \frac{\sigma}{I_{cs} - I_{cld}} \quad (4.2-5)$$

where  $\sigma$  is the standard deviation of the radiances for the array. If  $\chi$  is taken to be an upper limit to the uncertainty in cloud cover to be tolerated, then in order for an array to be part of an arch foot, its standard deviation must satisfy

$$\sigma \leq \chi(I_{cs} - I_{cld}) \quad (4.2-6)$$

Of course, there is no prior knowledge of  $(I_{cs} - I_{cld})$ . Examination of spatial-coherence results for oceans spanning the globe and differences between ninetieth and tenth percentiles of the emitted

radiances observed for  $\sim 250 \text{ km} \times 250 \text{ km}$  frames over the globe suggests that  $(I_{cs} - I_{cld})$  is the value associated with low-level marine stratocumulus. For  $11\text{-}\mu\text{m}$  radiances this value  $(I_{cs} - I_{cld \text{ low-level}})$  appears to be about  $20 \text{ mWm}^{-2} \text{sr}^{-1} \text{cm}$ . Due to the larger variability of the cloud-free background, over land  $(I_{cs} - I_{cld \text{ low-level}}) \sim 60 \text{ mWm}^{-2} \text{sr}^{-1} \text{cm}$  is used. The smallest value of the cutoff is taken to be

$$\sigma_{cutoff} \leq \chi(I_{cs} - I_{cld \text{ low-level}}) \quad (4.2-7)$$

where  $\sigma$  is the smallest value of the cutoff and the acceptable uncertainty in the cloud cover is taken to be  $\chi = 0.03$ . As discussed below, the results of spatial-coherence analysis are insensitive to the actual choice of  $\sigma_{cutoff}$ .

The cutoff given in (4.2-7) is used for identifying pixels that are either cloud-free or overcast by **low-level** clouds. Obviously, for mid- and upper-level clouds the same equation applies with suitable values of  $I_{cld \text{ mid-level}}$  and  $I_{cld \text{ upper-level}}$  replacing  $I_{cld \text{ low-level}}$ . For constant uncertainty in the fractional cloud cover,  $\chi$ , these changes indicate that the allowable cutoff in the standard deviation can grow as  $(I_{cs} - I_{cld})$  grows. This growth in  $\sigma_{cutoff}$  is implemented as follows: because  $I_{cs}$  is generally not known and is to be produced by the retrieval, the algorithm begins by replacing  $I_{cs}$  with the 90<sup>th</sup> percentile of the  $11\text{-}\mu\text{m}$  radiances ( $I_{90}$ ) for the frame of interest. The cutoff associated with a particular value of the array mean intensity  $I$  is assumed to be

$$\sigma_{cutoff}(I) \leq \chi \text{INTEGER} \left( \frac{I_{90} - I}{\gamma} \right) \quad (4.2-8)$$

where  $\gamma = (I_{cs} - I_{cld \text{ low-level}})$ , which is taken to be  $20 \text{ mWm}^{-2} \text{sr}^{-1} \text{cm}$  over oceans and  $60 \text{ mWm}^{-2} \text{sr}^{-1} \text{cm}$  over land and  $\text{INTEGER}(x)$  is the integer value of  $x$  with the condition that  $\text{INTEGER}(x) \geq 1$ .

In order to determine whether the points that survive the cutoff are clustered, as they appear to be in a foot, some method of measuring the number of points per unit radiance interval is required. The simplest measure is that given by the number of pixels per unit radiance interval. The intervals into which the radiances are divided are given by (4.2-8), i.e.

$$\Delta I = \chi \text{INTEGER} \left( \frac{I_{90} - I}{\gamma} \right) \quad (4.2-9)$$

Figure 4.2-4a shows the distribution of radiances for the pixel arrays shown in Figure 4.2-3 and Figure 4.2-4b shows the distribution of radiances for the arrays that survive the standard deviation cutoff given by (4.2-8) for the radiance intervals given by (4.2-9). Note the following: first, the presence of the layers is revealed by peaks in the distribution of  $11\text{-}\mu\text{m}$  radiances. Such peaks are uncommon. The norm is that the majority of pixels are partly cloud covered and so the radiances are randomly distributed over their range (Chang and Coakley, 1993). Second, note the shift in the width of the radiance intervals used in Figs. 4.2-4a and 4.2-4b. The intervals in Figure 4.2-4b at low values of the  $11\text{-}\mu\text{m}$  radiance are larger than those used in Figure 4.2-4a. The shift is given by (4.2-9).

Clearly, the interval width used to determine the density of pixel-scale radiances will ultimately influence the uncertainty in the estimated cloud cover. The choice of the interval width is arbitrary. The interval width must be large enough that the number of pixels with radiances that fall within any given interval, were the radiances to be distributed uniformly over the range of radiances, is expected to be sufficiently large, i.e. 10. At the same time the interval must be sufficiently small that the distribution of radiances within a scene is approximated sufficiently well by the numbers of pixels in the various radiance intervals. That is, the intervals should be sufficiently small that a foot representing either the cloud-free background or an overcast layer is represented by arrays spanning several adjacent intervals.

In Figure 4.2-4b, each point that survived the cutoff was given equal weight. Clearly, points with smaller standard deviations are likely to have less cloud contamination for the cloud-free foot, or fewer

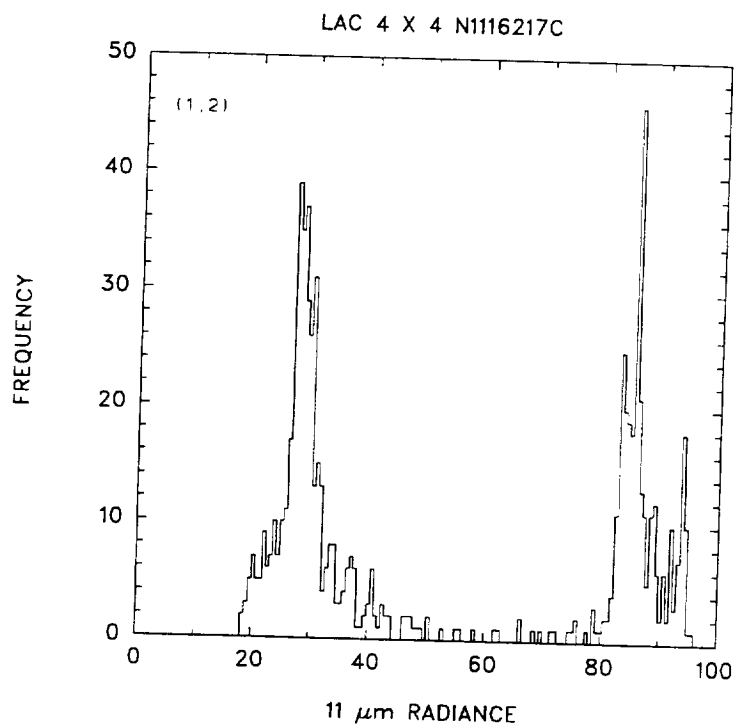


Figure 4.2-4a. Distribution of radiances for the observations shown in Figure 4.2-3.

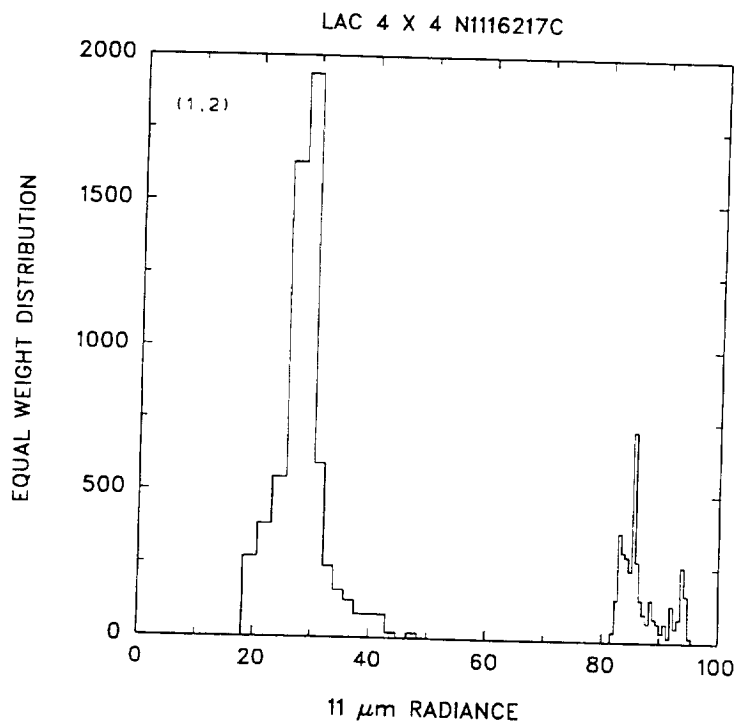


Figure 4.2-4b. Distribution of radiances for pixel arrays satisfying the cutoff in standard deviation given by Equation 4.2-8 for the radiance intervals given by Equation 4.2-9.

breaks in the clouds for the overcast foot than do points with larger standard deviations. Points with smaller standard deviations thus deserve more weight than those with larger standard deviations when estimating the radiance to be associated with the foot of an arch. By taking the radiances associated with each array to be uniformly distributed a new distribution function is created,  $\rho(I)$ , in which the contribution from a pixel array is approximately given by

$$\Delta\rho(I) = \frac{M\Delta I}{3\sigma} \quad (4.2-10)$$

where  $\Delta I$  is the width of the interval associated with radiance  $I$ ,  $I$  is the mean radiance of the array,  $M$  is the number of pixels in the pixel array,  $\sigma$  is the standard deviation of the radiances for the array, and  $3\sigma$  approximates the relationship between the standard deviation of a uniform distribution and its domain. The allocation of contributions in each intensity interval are made symmetrically about the interval associated with the mean intensity, i.e. the interval itself,  $i$ , its nearest neighbor intervals,  $i + 1$  and  $i - 1$ , and its next nearest neighbor intervals,  $i + 2$  and  $i - 2$ , etc. within the range of the intensities associated with the pixel array. The new distribution  $\rho(I)$  obtained by summing the contributions for all arrays in each of the radiance intervals is illustrated in Figure 4.2-5. The peaks of the distribution are clearly associated with the feet of the arches in Figure 4.2-3.

The next step involves determining the location and width of the peaks. The distribution is searched for local maxima. Once a maximum is found, the points in the interval and those on either side of the peak are used to calculate a mean and standard deviation of the radiances associated with the peak. The calculations are begun using the interval containing the peak,  $i$ , and the intervals on either side,  $i + 1$  and  $i - 1$ . A second standard deviation of the radiances is calculated using the two adjacent intervals,  $i + 2$  and  $i - 2$ , on either side of the original three-interval group. If the second estimate of the standard deviation is within 20% of the first, i.e.  $\sigma_1 \geq 0.8\sigma_2$ , then the width of the peak is taken to be given by the three intervals of the original group. For comparison, a Gaussian distribution gives  $\sigma_1 \geq 0.74\sigma_2$  where  $\sigma_1$  is the estimate of the standard deviation using the domain within one standard deviation of the mean and  $\sigma_2$  is the estimate of the standard deviation using the domain within two standard deviations of the mean. If the condition is not met by the two estimates of the standard deviation, then the interval is expanded to the five-interval group and the next two adjacent intervals are added and a new standard deviation for the seven interval group is calculated and compared with that of the five interval group. This process is repeated until either the standard deviations for the two ranges agree within 20%, or in expanding the interval a peak in the  $\rho(I)$  distribution is encountered that has a higher density of points, i.e. larger  $\rho(I)/\Delta I$  than that of the original group. If the latter case is true, the original peak is dropped from further consideration and the test is transferred to the new, denser peak. In Figure 4.2-5 the peaks of  $\rho(I)$  and their associated widths are indicated by dashed lines.

Once the peaks are located and their widths determined, neighboring peaks are examined to determine whether they overlap each other. The domain of a peak is taken to be the radiance intervals that lie within three standard deviations of the mean radiance associated with arrays forming the peak. If the domains of two peaks overlap, then the peaks are combined and the mean radiance and new standard deviation associated with the combined peak are calculated based on the arrays with mean radiances falling within the two standard deviation test intervals for the two separate peaks.

Once overlapping peaks are combined, they are tested for a minimum number of pixels. As can be seen in Figure 4.2-4b, some pixel arrays exhibit locally uniform emission, like that exhibited by the points in the feet of the arch, but are not themselves part of a foot. Experience has shown that such points are eliminated by demanding that the foot of the arch must contain at least 20 pixels. As is shown in the Appendix, this minimum number of pixels can be explained through manipulation of an analog model in which the criterion is that the points associated with the foot of an arch must exhibit a tightly clustered distribution of radiances. Arrays that appear to satisfy the local uniformity condition but are not in the foot of an arch are randomly scattered over the range of emitted radiances observed for the

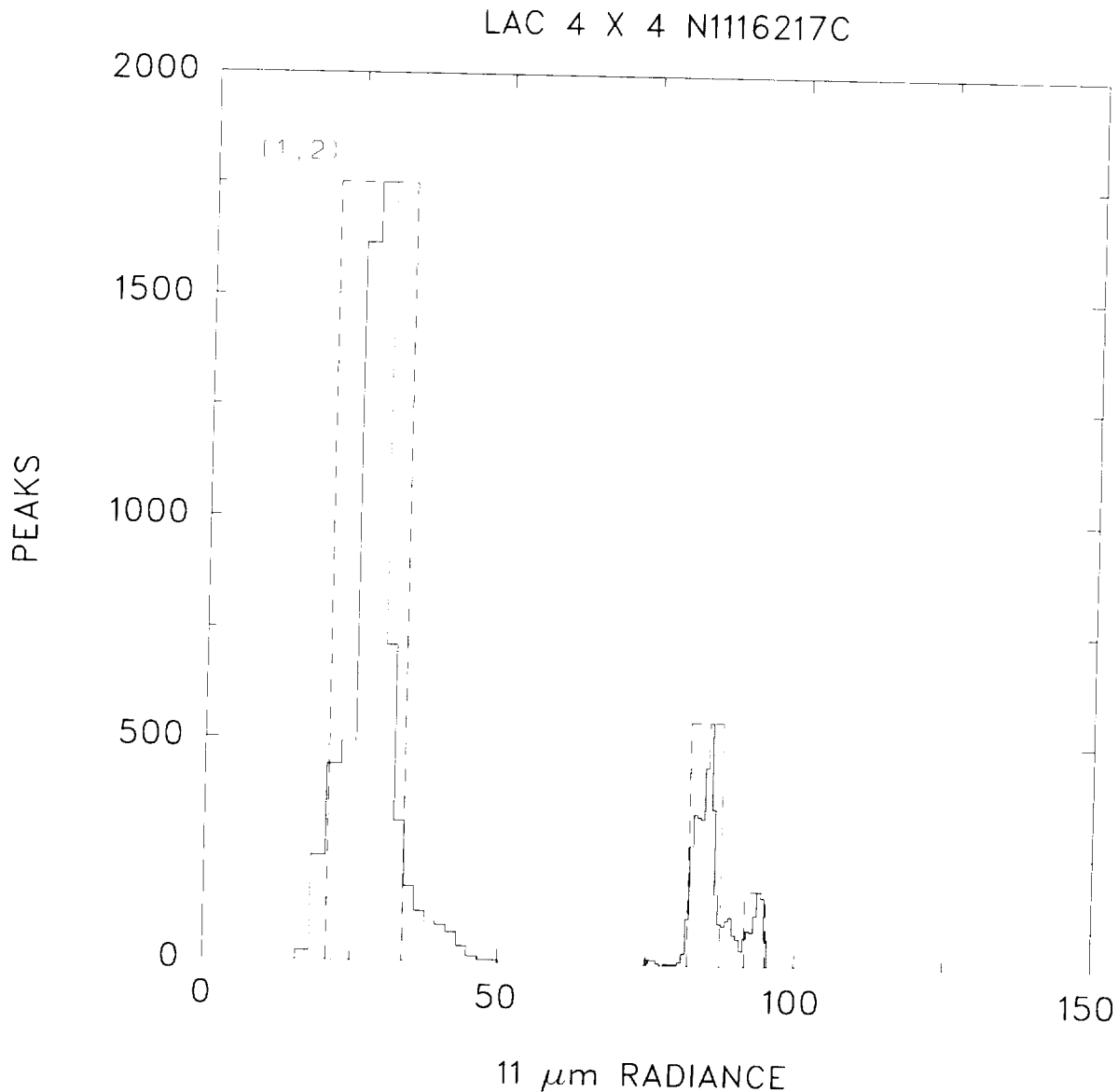


Figure 4.2-5.  $\rho(I)$  distribution for observations shown in Figure 3. The dashed lines indicate the radiance domains associated with the two layers and the cloud-free background.

frame. They fail to cluster around a specific radiance value as happens in the case of a foot. Experience with the spatial-coherence method indicates that employing this minimum number of pixels proved to be sufficient to eliminate the points that survived the uniformity cutoff but were not part of an arch foot in all but a few percent of the cases analyzed. In Figure 4.2-6, pixel arrays that were identified as being in the feet of the arches in Figure 4.2-3 are indicated by large dots; those that do not belong to a foot are indicated by small dots. Figure 4.2-6a shows the effect of the variable cutoff. The cutoff in the standard deviation is larger for the upper-level cloud deck (lower 11- $\mu\text{m}$  emission). The figure also shows that the random pixel arrays exhibiting standard deviations similar in value to those in the feet have been eliminated. Figure 4.2-6b shows a scatter plot of 0.63- $\mu\text{m}$  reflectivities and 11- $\mu\text{m}$  radiances. Not surprisingly, the pixels identified as being cloud-free and overcast have bispectral properties that would be expected of cloud-free and overcast pixels. As discussed below, multispectral consistency checks might be developed to confirm the results obtained through spatial coherence analysis.

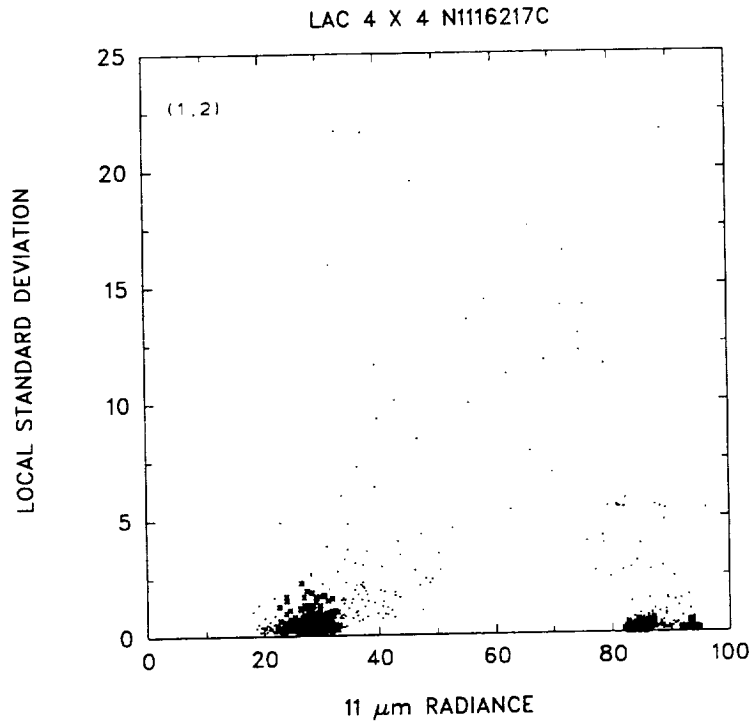


Figure 4.2-6a. Same as Figure 3, but pixel arrays identified as being cloud-free or overcast by clouds in a well-defined layer are indicated by large dots. Pixel arrays with broken or semitransparent clouds are indicated by small dots.

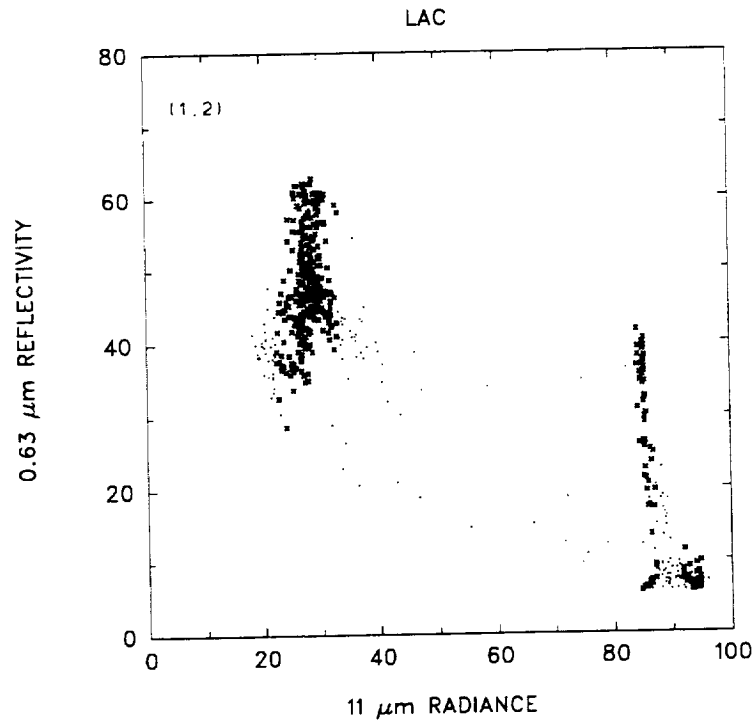


Figure 4.2-6b. 0.63- and 11- $\mu\text{m}$  radiances for the observations shown in Figure 6a.

The variables used in the identification of pixels exhibiting locally uniform emission were

1. The difference between the radiances expected for cloud-free and overcast fields of view,  $\gamma = (I_{cs} - I_{cld \text{ low-level}})$ ,
2. The 90<sup>th</sup> percentile of the emitted radiances, which was used in place of the cloud-free radiance to obtain  $\sigma_{cutoff}$
3. The two-standard-deviation test used to determine the width of a peak in the  $\rho(I)$  distribution
4. The use of three standard deviations to represent the domain of an isolated peak

Clearly, the choices for these parameters, while not without reason, were arbitrary. Fortunately, numerous arch feet obtained for 250 km  $\times$  250 km scale frames contain contributions from many pixel arrays and these arrays are often tightly clustered in the radiance domain. The outcome of the foot identification, namely the mean and standard deviation of the radiances for the pixels associated with the foot, is relatively insensitive to the variables chosen. The results differ little if  $\gamma$  is halved or doubled, if the 95<sup>th</sup> or 85<sup>th</sup> percentile is used in place of the 90<sup>th</sup>, or if three standard deviations rather than two are used to determine the width of a  $\rho(I)$  distribution peak and two standard deviations used to represent its domain.

**4.2.2.5.2. 50 km  $\times$  50 km subframe scale analysis.** As noted above, once identified on the 250 km  $\times$  250 km scale, the locations of the pixel arrays identified as being overcast and cloud-free are mapped to smaller regions of  $\sim$ 50 km  $\times$  50 km, or subframes. This mapping retains information on gradients in the radiative properties of cloud-free and overcast pixels across the 250 km  $\times$  250 km frame and better isolates, when possible, single-layered systems. Often on this smaller scale, however, no pixels are found to be either overcast or cloud-free. So, even though a single-layer system may span a 250 km  $\times$  250 km frame, it cannot be clearly identified as a single-layered system on the basis of the spatial structure of the 11- $\mu$ m radiances found in some of the 50 km  $\times$  50 km scale subframes that make up the larger frame. This problem is illustrated in Figures 4.2-7 through 4.2-9. The figures show that although overcast pixels for a given cloud layer may not reside in a particular 250 km  $\times$  250 km frame, they often reside in surrounding frames. The finding suggests that when evidence for a layer is missing in one frame, surrounding frames should be examined for the missing evidence. While the example uses observations for the 250 km  $\times$  250 km scale, but clearly inferences made based on observations over a domain become more reliable as the size of the domain decreases.

Figure 4.2-7 shows means and standard deviations of 11- $\mu$ m radiances and figure 4.2-8 shows the relationship of 0.63- $\mu$ m reflectivities and 11- $\mu$ m radiances for a 250 km  $\times$  250 km frame that, on the basis of the 0.63- and 11- $\mu$ m scatter plot, contains two distinct layers. The spatial-coherence analysis in this case fails to identify either of the layers. Figures 4.2-8 and 4.2-9 show observations for the 250 km  $\times$  250 km scale frame shown in Figure 4.2-7 as well as for the surrounding 250 km  $\times$  250 km scale frames. The incipient layered structures not found in Figure 4.2-7 are now revealed in the surrounding frames. Coakley and Baldwin (1984) proposed analyzing the properties in mesoscale-sized regions called "subframes." They used 16  $\times$  16 arrays of 4 km  $\times$  4 km AVHRR pixels, or a  $\sim$ 64 km  $\times$  64 km region for a subframe. If the subframe contained overcast pixels, or if the nearest neighbor subframes contained overcast pixels that explained the range of the emitted radiances, as defined by the 10<sup>th</sup> and 90<sup>th</sup> percentiles of the 11- $\mu$ m radiances in the subframe of interest, then the subframe was taken to contain the layer. "Explaining" the range of radiances meant satisfying the following conditions:

$$(I_{cld} - 2\Delta I_{cld}) < I_{10} \quad (4.2-11)$$

and

$$I_{cld} + 2\Delta I_{cld} > I_{90} \quad (4.2-12)$$

where  $I_{cld}$  and  $\Delta I_{cld}$  are the means and standard deviations associated with the overcast pixels in the frame surrounding the subframe in question. Values of the radiances are geographically interpolated to

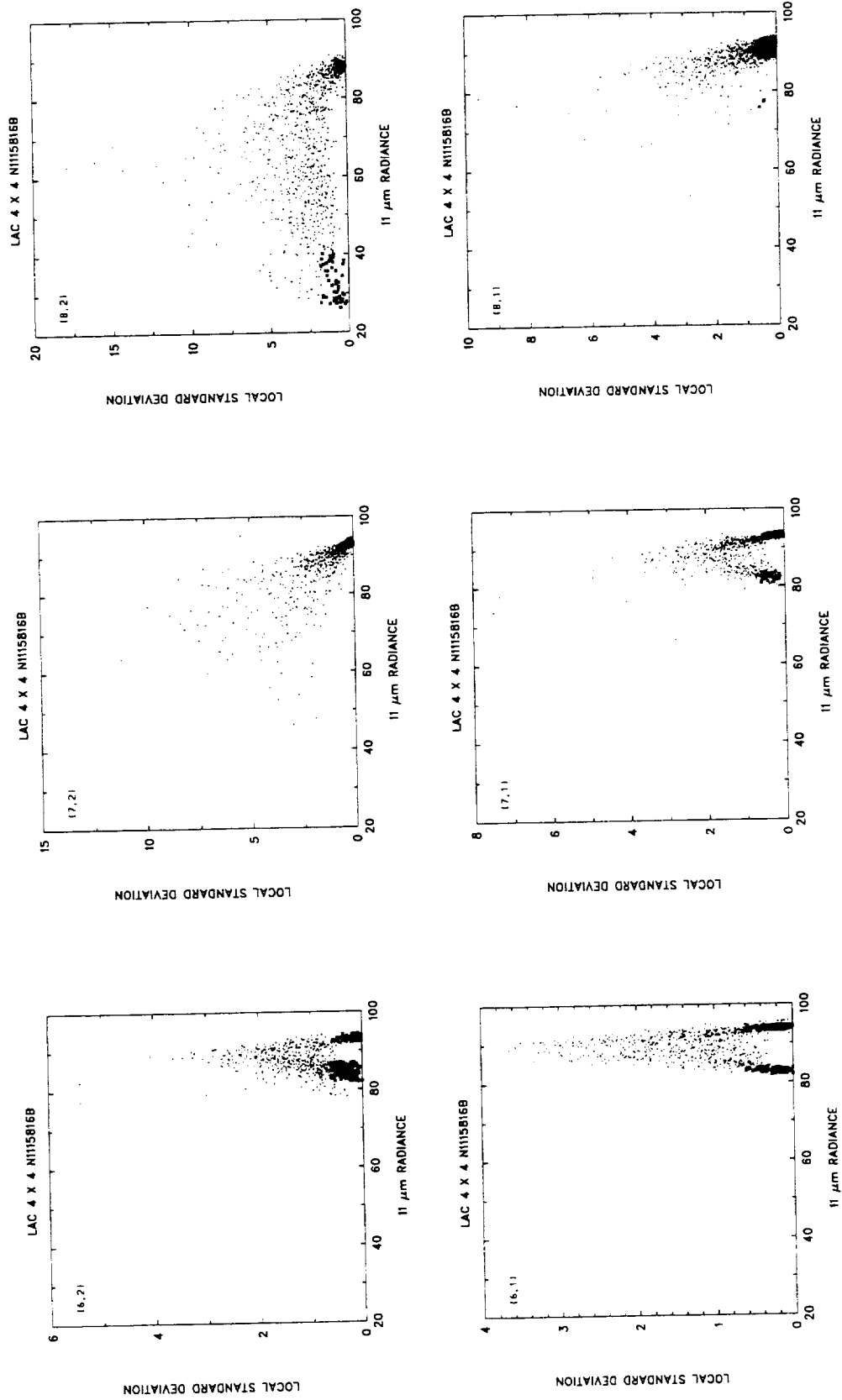


Figure 4.2.7. 3 × 2 array of adjacent 250-km scale frames. Each point represents a 4 × 4 array of 1-km AVHRR pixels. Large dots represent points found to be either overcast by layered clouds or cloud-free. The geographic orientation of the arrays are indicated by the (x,y) coordinates in the upper left corner of each frame. Frame (m + 1, l + 1) is the frame immediately to the west and north of frame (m,l).

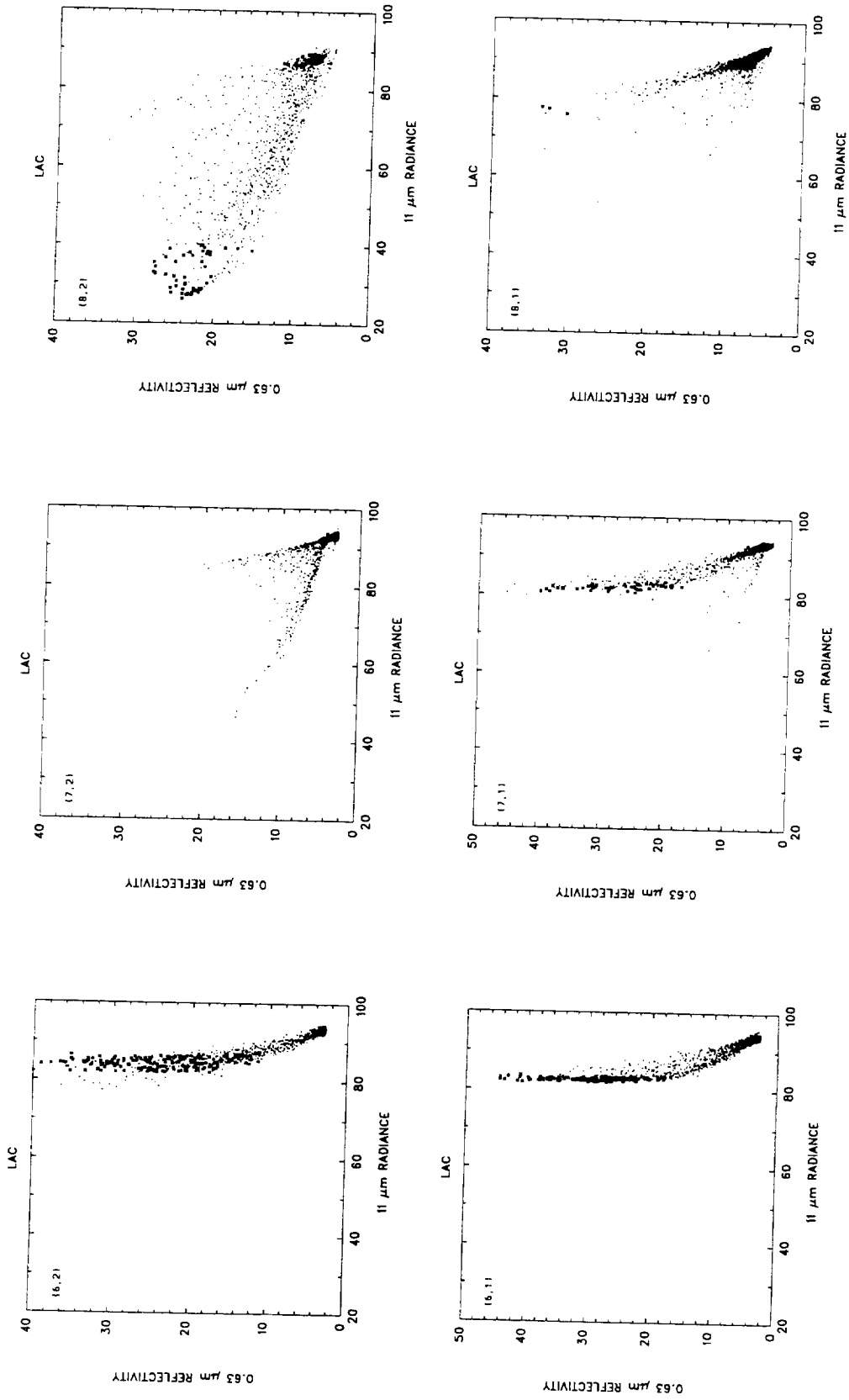


Figure 4.2-8. Same as Figure 7, but for 0.63- and 11-μm radiances.

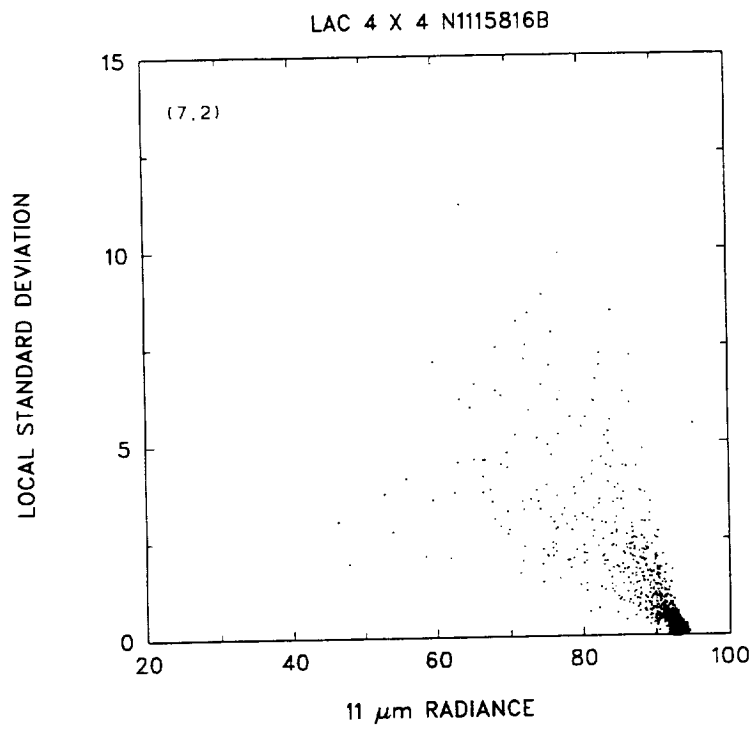


Figure 4.2-9a. Same as Figure 6a, but different two-layered system.

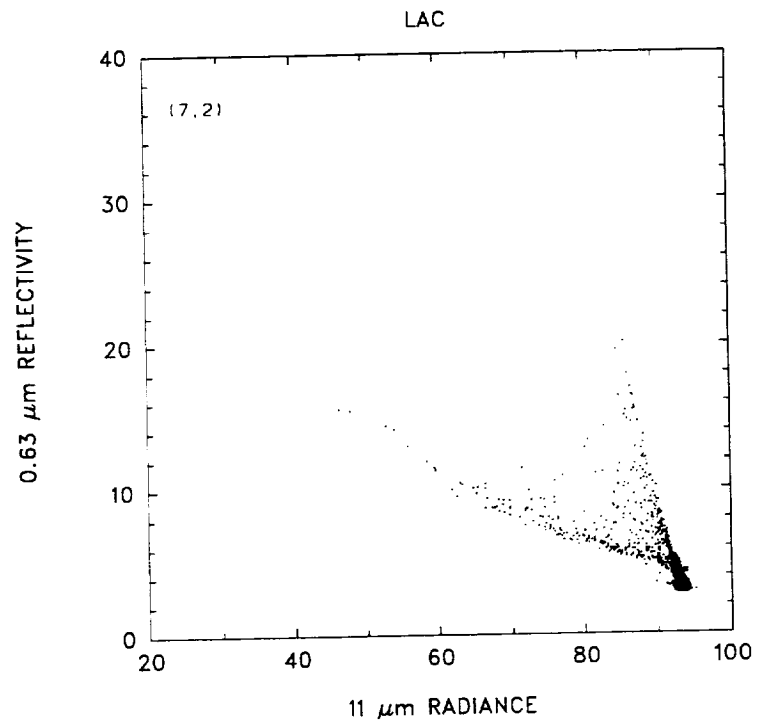


Figure 4.2-9b. 0.63- and 11-μm radiances for the observations shown in Figure 9a.

form estimates of the mean and standard deviation that would be achieved by overcast pixels in the subframe of interest were overcast pixels present.

Coakley and Baldwin (1984) followed a two-step procedure in implementing this search and interpolation of overcast radiances. First, all overcast pixels in a region containing the frame and the surrounding subframes (see Fig. 4.2-10) were classified into layers. The classification routine follows the same algorithm as that used to determine the feet of the arch with the exception that the range of  $11\text{-}\mu\text{m}$  radiances was divided into equal intervals,  $\Delta I$ , as opposed to variable-width intervals following (4.2-9). Up to three cloud layers were allowed. If more layers appeared to be present in the frame, then the layers that were nearest each other,  $|I_{cl d1} - I_{cl d2}| = \text{minimum value}$ , were combined into one layer with the properties of the layer calculated to be the average of the properties for the contributing layers. In the averaging, each layer in each subframe was given equal weight. Once the layers in the frame were classified, the range of radiances in a particular subframe was examined to determine whether layers identified in the frame but not in the subframe were needed to explain the range. If so, the nearest neighbor subframes were searched for the overcast pixels associated with the appropriate layers. If overcast pixels were found in the surrounding subframes, then the radiances associated with the overcast pixels were geographically interpolated to the subframe of interest as discussed in Coakley and Baldwin (1984).

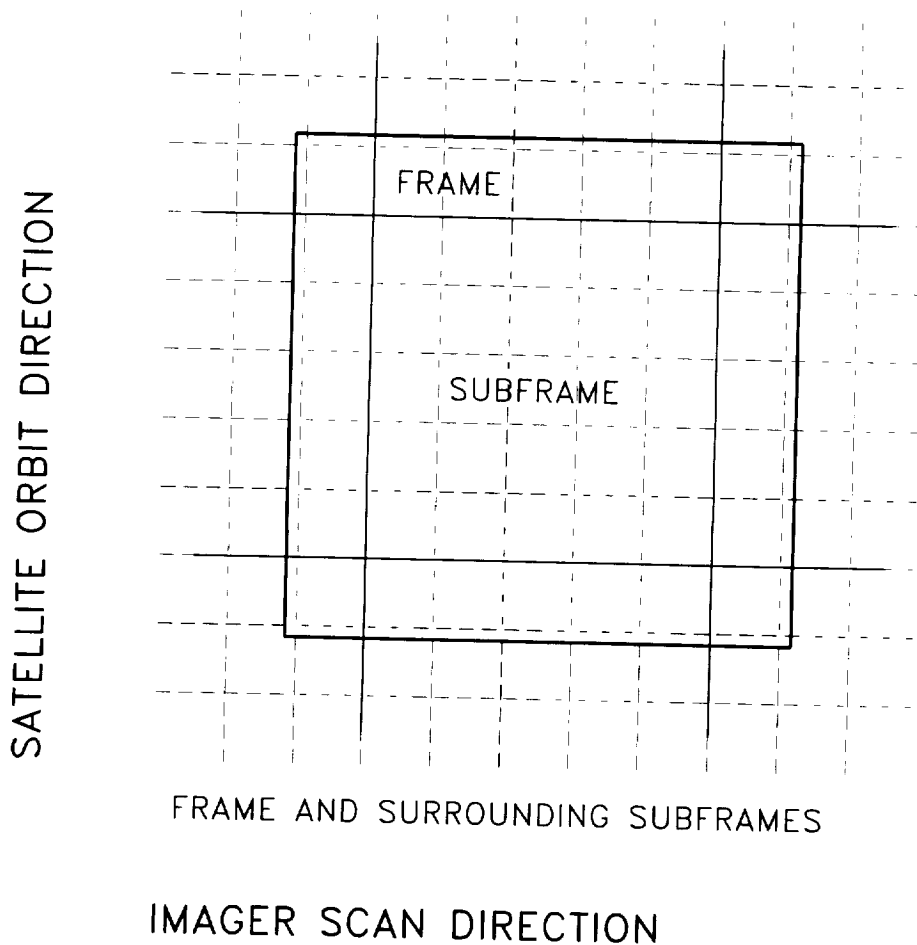


Figure 4.2-10. 50-km scale subframes and 250-km scale frames used in spatial coherence analysis. Each subframe represents the imager pixels mapped into a CERES footprint. Overcast and cloud-free  $11\text{-}\mu\text{m}$  radiances for all subframes in a frame and its surrounding subframes are classified (as described in the text) to determine the layered structure of clouds for the subframes constituting the frame.

The extent to which this interpolation strategy would have to be implemented is unclear. Experience with the spatial-coherence method indicates that a substantial portion (somewhere between 30 and 60%) of all layers on the subframe scale are interpolated, even though the search for missing layers is limited to nearest neighbor 50 km × 50 km subframes. How far the search for missing layers can be extended, whether 50 or 100 km or further, has not been explored.

#### 4.2.2.6. *Uncertainties*

This section discusses the uncertainties in the properties of the overcast pixels identified as being part of a well-defined cloud layer. In the following section, uncertainties arising through errors in layer identification, e.g. identifying a layer that doesn't exist or failing to identify a layer that does exist, are discussed.

The uncertainties associated with an identified layer are defined in terms of the standard deviations of the 11- $\mu\text{m}$  radiances,  $\Delta I_{cld}$ , obtained for the pixels identified as being overcast by opaque cloud. The standard deviation is used as a measure of the uncertainty in the retrieved layer properties. Included in this measure would be effects caused by gradients within the frame. Of course, because the probability is low that pixels overcast by opaque cloud will uniformly distribute themselves over a frame that is not itself overcast, the probability is likewise low that the standard deviation of radiances for the overcast pixels represents the range of layer properties within the frame.

As was noted in the introduction, a well-defined layer is by definition one for which the uncertainty in the properties, as indicated by the standard deviation of the 11- $\mu\text{m}$  radiances for the overcast pixels, is small compared with the variability in the radiances that would result from variations in fractional cloud cover. Thus a well-defined layer has the property that  $\Delta I_{cld} \ll I_{cs} - I_{cld}$ . Clearly, this condition can be satisfied within rather arbitrary limits. The application of arbitrarily strict criteria will, of course, arbitrarily limit the population of well-defined layers. The degree to which various criteria affect the population of layers identified as being well-defined remains to be established. As a rule of thumb, however, requiring that the parameter given by

$$\xi = \frac{\sqrt{\Delta I_{cs}^2 + \Delta I_{cld}^2}}{I_{cs} - I_{cld}} \leq 0.1 \quad (4.2-13)$$

would provide reasonably well-defined layers.

As discussed in the next section, cases exist in which layers may be identified as being present when in fact they are not. For example, the clouds in a layer congregate in regular arrays so that the observed emission satisfies the condition of low, local standard deviation, but the pixels are only partly cloud covered. Such occurrences appear to be rare. Nevertheless, they can probably be largely eliminated by demanding that the number of pixels identified as overcast and part of a well-defined layer must exceed a certain fraction of the area viewed, say 10%. This criteria is meant to apply only to those ~50 km × 50 km subframes that contain overcast pixels, not those for which layer information must be interpolated as described in Section 4.2.2.5.2. Interpolated properties are presumed to have the quality of the properties from which the interpolated values were obtained. Clouds can form regular arrays, but these arrays are fostered by mesoscale circulations which by their nature break down on the 100- to 200-km scale. The extent to which limiting the identification of well-defined layers by such a criteria and the likely dependence of such a criteria on spatial scales has not been explored.

#### 4.2.2.7. *Practical Considerations*

Not all cloud systems are layered. Some layered cloud systems, like cirrus, rarely achieve optical depths that allow them to be detected as a layer by the spatial-coherence method. Systems of opaque layered clouds can also be everywhere broken so that nowhere do they extend to form overcast clouds over several imager pixels, thereby avoiding identification by the spatial-coherence method. Coastlines

and background heterogeneity over land areas may mask the presence of layers. This section outlines the limitations inherent in the spatial-coherence method and suggests strategies for dealing with them.

#### **4.2.2.7.1 Limitations in Applying Spatial Coherence.**

**4.2.2.7.1.a. Errors caused by incorrect identification of cloud layers.** Clouds don't always form opaque layers that span several imager pixels. Even if the clouds were in such a layered system, they would not give rise to the local uniformity in the emitted radiances that would allow detection by the spatial-coherence method. The variance in emitted radiances, as given by (4.2-2) for a single-layered system, could be relatively high. In the case of cirrus, even when the layer is extensive so that numerous pixels are overcast, the pixel-to-pixel variation in emissivity and transmissivity gives rise to large local variances in emitted radiances. Opaque, low-level clouds may form a layer in which the clouds are nowhere extensive enough to cover several adjacent imager pixels. An example of such a situation was shown in Figure 4.2-7.

There are three strategies for dealing with situations like those shown in Figure 4.2-7. The first, proposed by Coakley and Baldwin (1984), is to seek evidence for the presence of a well-defined layer in neighboring frames. That approach was discussed in Section 4.2.2.5.2. The second is to use relationships among various wavelengths. It constitutes an alternative to the spatial coherence method and is discussed in the subsequent section. The third is to use two-dimensional texture analyses to detect the presence of the separate systems. That approach likewise represents an alternative.

**4.2.2.7.1.b. Errors caused by heterogeneous backgrounds.** Land is a more heterogeneous background than oceans. As noted earlier, the identification of layers over land uses a cutoff in the standard deviation of the pixel arrays for land scenes that is three times the value used for ocean scenes. The increase in background heterogeneity over land, of course, diminishes the ability to identify well-defined layers. Nevertheless, experience with retrievals performed for the 1992 FIRE II IFO over the central U.S. indicates that the use of the higher cutoff provides satisfactory results (Lin and Coakley, 1993).

Contrasts between land and water at coastlines, of course, must be dealt with by separating the analysis for the land and water portions of the scene. Pixel arrays that include the coastline should not be used in the identification of the layer. Indeed, as the results in Figures 4.2-1 and 4.2-2 indicate, limited sampling over a 250 km × 250 km frame appears to provide overcast and cloud-free identifications that are indistinguishable from those obtained using all pixel arrays. Consequently, a perimeter of arrays bracketing coastlines can be safely ignored in the identification of cloud layers. Such a strategy, however, has yet to be implemented.

#### **4.2.2.8. Proposal for Validation**

Well-defined layers seemed to be readily identified by eye, but obtaining the properties of well-defined layers, even from instrumented surface sites and aircraft is difficult and not a well-posed problem. Consequently, finding evidence that a particular remote sensing technique produces a useful characterization of cloud systems is likewise difficult.

Two strategies for validation have already been proposed. Perhaps the best approach would be to use active aircraft or space-borne lidars to identify layers simultaneously with the information being retrieved from imagery data. The vertical sounding of the atmosphere with lidars often reveals layered structures. When clouds are thin and diffuse, it is difficult to assign a height to the layer; nevertheless, for optically thick clouds, the soundings produce what appear to be layers with reasonably well-defined altitudes.

A weakness of lidar retrievals is that they are typically limited to the nadir track of the aircraft or orbiting platform. The flight path will occasionally miss layered structures that are revealed through the two-dimensional sampling available to imagers. Consequently, comparisons between lidar cloud

boundaries and imager inferences of layered structure must be made on the basis of representative ensembles of cases, as opposed to a case-by-case basis. An opportunity for such comparisons is forthcoming with the LITE mission in September 1994 (McCormick et al., 1993).

The second strategy for validation proposed earlier was to demand that inferences of layered structure based on the spatial-coherence method be verified by independent inferences based on the relationships between radiances at various wavelengths. For example, Figure 4.2-6a clearly shows a two-layered structure as deduced from spatial-coherence analysis, and the visible-IR relationship shown in Figure 4.2-6b produces a consistent multiwavelength interpretation. Of course, such confirmation is bound to work for simple, layered cloud systems, i.e. when there is little overlap between the two systems in the frame of interest. When there is overlap, as may be the case in frame [2,1] of Figures 4.2-11 and 4.2-12, visible-IR observations will not necessarily provide the desired confirmation. Use of other multiwavelength emissions may alleviate some of the problems. Emission at 8 and 13  $\mu\text{m}$  might reveal the branches associated with two-layered systems not revealed in the visible-IR scatter plots. Nevertheless, observations of thermal emission will capture only the highest and lowest layers present and not detected by the spatial coherence method, and they will miss intervening layers. As with lidar observations, the multispectral observations can be used to provide confirmation in a certain fraction of the cases, but not all cases.

Surveys with the spatial-coherence method suggest that single-layered cloud systems can be isolated on the  $\sim 50 \text{ km} \times 50 \text{ km}$  scale approximately 50% of the time. Of the remaining 50%, many of these systems are two-layered systems that should be amenable to confirmation through multispectral approaches and lidar soundings. Complex cloud systems, i.e. those that defy description in terms of layered structure, appear to constitute only 15 to 25% of the observations at the  $50 \text{ km} \times 50 \text{ km}$  scale.

#### **4.2.2.9. Quality Control**

As was noted in an earlier section, arbitrary levels of quality control may be applied to the spatial-coherence identification of layered cloud systems. The quality of the layer indentifications may be measured in terms of the confidence limits with which the radiances associated with the layer might be specified. The rule-of-thumb criteria noted earlier, as given by (4.2-11) and (4.2-12), combined with the demand that a reasonable number of overcast pixels reside in the frame, say at least 10%, produces an acceptable number of layered systems when layers interpolated from adjacent subframe layers are counted. A requirement is that the adjacent subframe layers satisfy the conditions of (4.2-11) and (4.2-12). As noted earlier, tradeoffs between numbers of samples and uncertainties in layer definitions have not been studied.

The second approach to quality control is to demand that the layers identified through spatial-coherence analysis also be revealed in the relationships among various wavelengths. Perhaps the most revealing set of wavelengths for such confirmation would be 8 and 13  $\mu\text{m}$ . Again, methods for identifying multiple layer structure on the basis of the relationships between various wavelengths have yet to be developed.

#### **4.2.2.10. Numerical and Programming Considerations**

The application of the spatial-coherence method for identifying layered structure places several requirements on the structure of the imager data stream. First, as was noted in Section 4.2.2.5.1, the identification of overcast pixels is performed on  $250 \text{ km} \times 250 \text{ km}$  scale frames. Second, because  $50 \text{ km} \times 50 \text{ km}$  subframes may lack overcast pixels for any of the layers present, some means are required for interpolating layer properties from one subframe to the next. Interpolation among nearest neighbor subframes each of order  $50 \text{ km} \times 50 \text{ km}$  scale was suggested. This frame and subframe scale analysis suggests a nested structure for the data stream as illustrated in Figure 4.2-10.

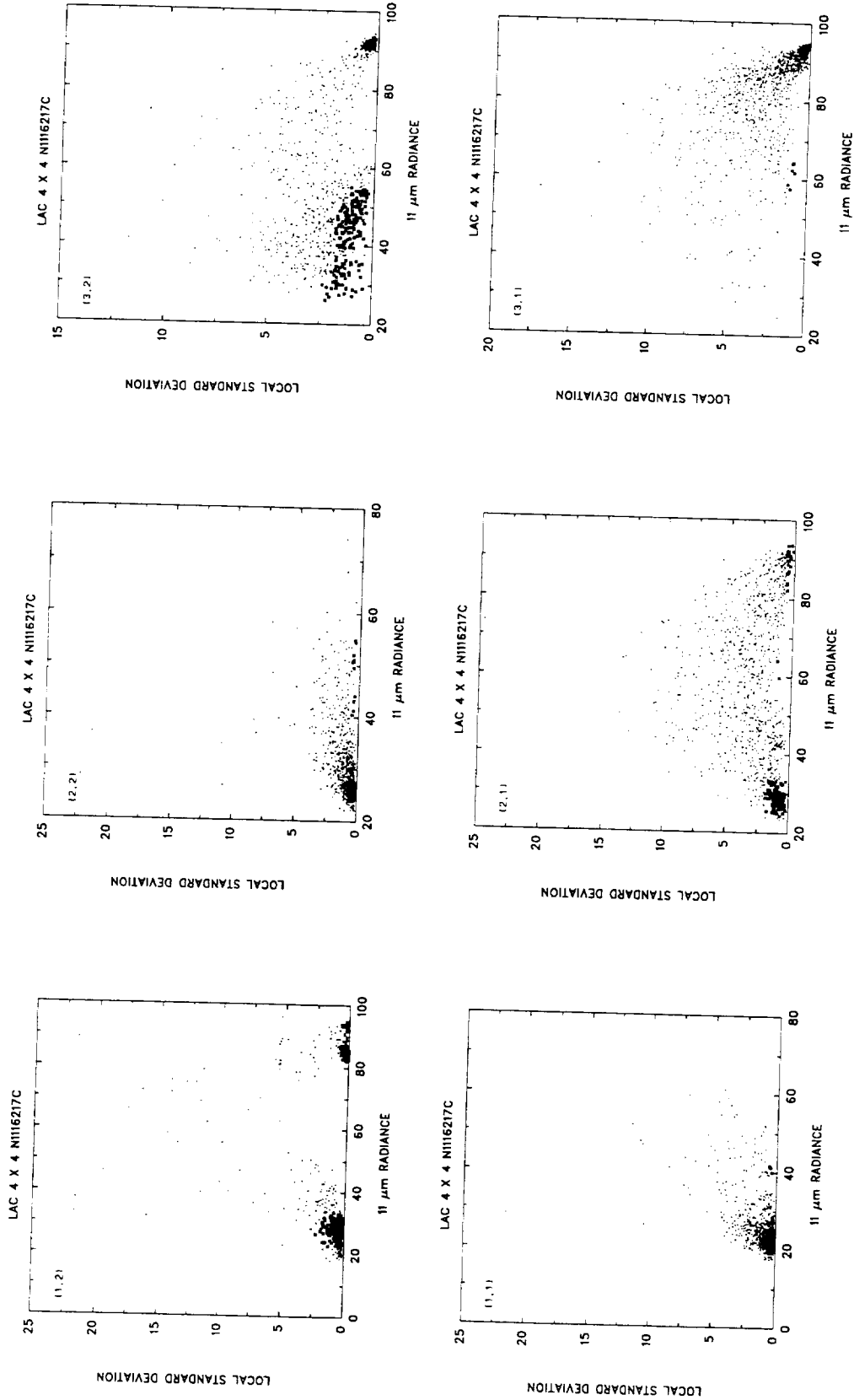


Figure 4.2-11. Same as Figure 7, except for different system.

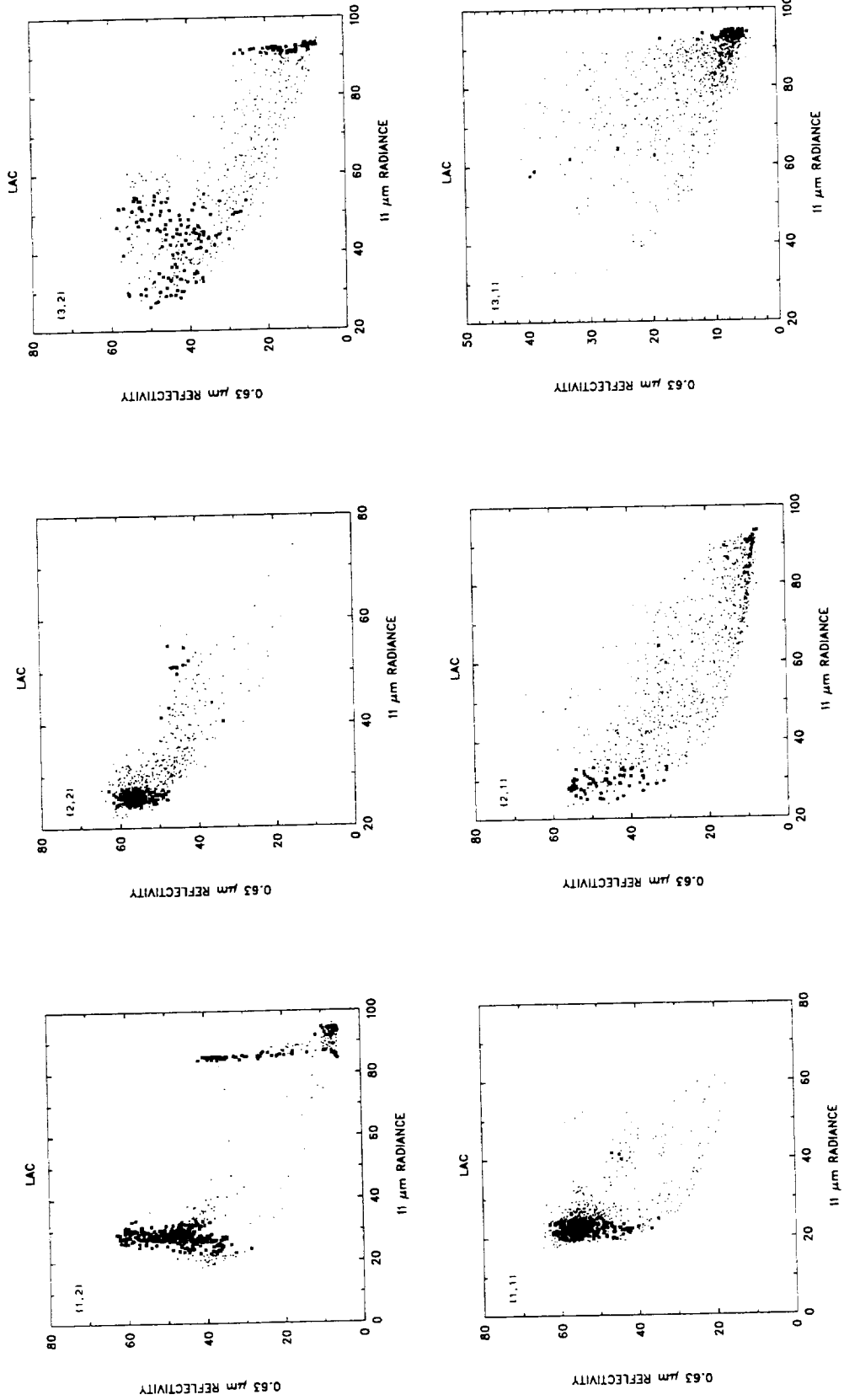


Figure 4.2-12. Same as Figure 11, but for 0.63- and 11-μm radiances.

The spatial coherence identification of layers would be undertaken as follows:

1. Overcast and cloud-free pixels would be identified in each  $250 \text{ km} \times 250 \text{ km}$  scale frame.
2. Overcast pixels within a frame and its surrounding  $50 \text{ km} \times 50 \text{ km}$  scale subframes would be classified to identify the overcast pixels with the various well-defined layers and assign the overcast pixels to specific layers.
3. Layers within the subframes constituting a frame would be determined on the basis of the layer identification of the overcast pixels within the subframe and its surrounding subframes.

These steps dictate the following structure. Spatial-coherence analysis is performed on imager scan lines sufficient to form a  $250 \text{ km} \times 250 \text{ km}$  scale frame. The analysis is performed for all  $250 \text{ km} \times 250 \text{ km}$  scale frames across the scan. Pixel radiances and layer identifications is retained in memory for a set of imager scan lines sufficient to form two adjacent sets of frames, i.e.  $500 \text{ km} \times 500 \text{ km}$  along the orbital track. In addition,  $50 \text{ km} \times 50 \text{ km}$  subframe scale layer properties are retained from the analysis of scan lines analyzed just prior to those currently in memory. Once the frame scale analysis is complete, the subframe scale analysis can begin with the first subframe of the scan lines residing in memory and end with the set of subframes that complete the first  $250 \text{ km} \times 250 \text{ km}$  scale frames spanned by the scan lines residing in memory. The results of the analysis for the subframes making up these  $250 \text{ km} \times 250 \text{ km}$  scale frames can be scrolled out of memory with the last set retained for the subsequent analysis of the subframes constituting the next  $250 \text{ km} \times 250 \text{ km}$  block of scan lines. New scan lines are read into memory forming a new  $250 \text{ km} \times 250 \text{ km}$  scale block and the spatial coherence analysis is applied to these new scan lines. The process is repeated.

Numerical efficiency has, to some extent, been addressed in the design proposed for the analysis. The design uses a uniform distribution to characterize the distribution of radiances within a spatial-coherence pixel array. This choice was intentional. It reduces numerical burdens incurred by using other distributions, such as Gaussian. It also is easier to implement than using the actual distribution of the pixel scale radiances. There is no point in resorting to the actual distribution of the pixel radiances, because, in order to identify clustering, the density of pixel-scale radiances must be measured and the measure used is somewhat arbitrary. Fortunately, as was noted earlier, the natural clustering of points about a well-defined range of emitted radiances forms a robust feature that can be readily characterized by any number of methods. The outcome, namely the means and standard deviations of the radiances associated with overcast pixels, will be relatively insensitive to the method used to identify clusters of locally uniform emitted radiances. The strategy proposed here is thought to be a simple, efficient, and effective means of seeking those results.

#### 4.2.3. Multispectral Approaches

A second strategy for identifying layers missed by spatial-coherence analysis is to use multispectral histogram methods. Figure 4.2-7 clearly showed branches in the visible-infrared scatter plots associated with distinct layers, both of which were missed by the spatial-coherence method. Similar branches are observed at night for emission at  $3.7$  and  $11 \mu\text{m}$  (Coakley, 1983). Fitting procedures, like those developed by Lin and Coakley (1993) for the multispectral analysis of single-layered systems might be generalized to identify branches associated with distinct layers. Alternatively, a variation of the hybrid bispectral threshold method (HBTM) of Minnis and Harrison (1984) and Minnis et al. (1987) or the layered bispectral threshold method (LBTM; Minnis et al., 1993) could be used to analyze such systems. A second set of multiregion, multilayer observations are shown in Figures 4.2-11 and 4.2-12. Here the upper-level system is clearly defined in frame [2,1], but there is no indication of lower-level systems that are prevalent nearby in frames [1,2] and [3,2]. Without additional logic, the HBTM or LBTM may divide the system shown in [2,1] into three distinct layers with predefined properties: high, middle and low. Thus, this multispectral approach may place multiple layers where only single layers exist. Some

simple modifications to the LBTM, however, can eliminate much of the ambiguity associated with single and overlapping layers.

#### 4.2.3.1. Daytime Methodology

The LBTM is similar to the ISCCP algorithm in that it compares the 11- $\mu\text{m}$  temperature  $T$  and reflectance  $\rho$  for each pixel to simple thresholds to determine if a pixel is cloudy or not. Instead of retrieving a visible optical depth  $\tau$  and cloud temperature  $T_{cld}$  for each cloudy pixel, the LBTM groups some pixels together before deriving  $T_{cld}$  and  $\tau$ . The LBTM nominally divides a visible-infrared histogram into three layers defined by hypothetical cloud temperatures at 2 and 6 km. Low clouds are those below 2 km, mid-level clouds are between 2 and 6 km, and high clouds are those above 6 km. When no  $\tau$ - and  $T_{cld}$ -solutions are possible for a nominal pixel grouping (discussed below), the LBTM attempts to reach a solution for a group of pixels by adding other pixels to the group until a solution is obtained. The LBTM also computes the mean layer cloud temperature  $T_k$  and optical depth  $\tau_k$  as well as their respective standard deviations  $\sigma_{T_k}$  and  $\sigma_{\tau_k}$  where  $k = 1, 3$  from low to high. Other differences between the two methods include ice-crystal reflectance models for high clouds, bidirectional reflectance models for clear scenes, and a parameterization of the Earth-atmosphere system reflectance.

The reflectance is parameterized in terms of  $\tau$ , the cloud altitude, clear-sky reflectance  $\rho_{cs}$ , the cloud particle size, the solar zenith angle  $\theta_o$ , the viewing zenith angle  $\theta$ , and the relative azimuth angle  $\psi$ . The 11- $\mu\text{m}$  emittance is a function of  $\tau$ ,  $\mu (= \cos \theta)$ , and the difference between the clear-sky temperature  $T_{cs}$  and the cloud temperature  $T_{cld}$ . For liquid water clouds, it is assumed that the cloud consists of spherical droplets having an effective radius of 10  $\mu\text{m}$ . Ice clouds are assumed to be composed of randomly oriented hexagonal ice crystals representing a cirrostratus size distribution (Takano and Liou, 1989). The ice model is used for  $T_{cld} < 253\text{K}$  and the water-droplet model is applied for warmer cloud temperatures. The parameterizations of reflectance and emittance are detailed in section 4.3.

Given the relationships between cloud reflectance and emittance, it is possible to define the variation of  $\rho$  and  $T$  for a given value of  $T_{cld}$ . The variation in brightness temperature for a given value of  $\tau$  or  $\rho$  is

$$T_{\epsilon} = T_{\epsilon}(\rho, T_{cld}) = B^{-1}\{\epsilon(\rho)B(T_{cld}) + [1 - \epsilon(\rho)]B(T_{cs})\} \quad (4.2-14)$$

where  $T_{\epsilon}$  is a model-defined emittance-dependent brightness temperature and  $B$  is the Planck function. The emittance  $\epsilon$  and  $\rho$  are computed from the emittance and reflectance parameterizations at various values of  $\tau$ . Thus, a value of  $T_{\epsilon}$  corresponding to a cloud having  $T_{cld}$  can be defined for any given reflectance and microphysical model.

Figure 4.2-13 shows an AVHRR visible-infrared histogram for an area over the southwestern tropical Pacific. The numbers plotted in the histogram represent the number of occurrences of the particular  $T$ - $\rho$  pair. The AVHRR 11- $\mu\text{m}$  sensor is channel 4, so the brightness temperatures are indicated with the subscript 4. As currently formulated, the LBTM histogram is divided into five areas: clear, low cloud, middle cloud, high cloud, and dark pixel or stratospheric cloud. The clear area incorporates all pixels having  $T > T_{cs} - \Delta T$  and  $\rho \leq \rho_t$  where  $\rho_t$  is the reflectance threshold value and the cloud threshold difference  $\Delta T$  has values of 6 K over land and 3 K over water. The clear-sky visible threshold reflectance is  $\rho_t$  as defined by Minnis et al. (1987). All other pixels are assumed to be overcast. Low-cloud pixels are all those having values of  $\rho > \rho_t$  and  $T > T_{\epsilon}(\rho, T_{12})$ . The temperature  $T_{12}$  corresponds to an altitude of 2 km. Similarly, the high-cloud pixels are those having  $T \leq T_{\epsilon}(\rho, T_{23})$ , where  $T_{23}$  corresponds to 6-km height. All nonclear pixels with temperatures and reflectances between the low- and high-cloud pixels are middle-cloud pixels. An upper boundary,  $T_{\epsilon}(\rho, T_p)$ , is computed to correspond to the tropopause temperature  $T_p$  minus 2 K. The 2K subtraction accounts for uncertainty in the tropopause temperature. These cloud-layer boundaries are shown as the solid curves in Figure 4.2-13 and labeled as  $P_{12}$ ,  $P_{23}$ ,

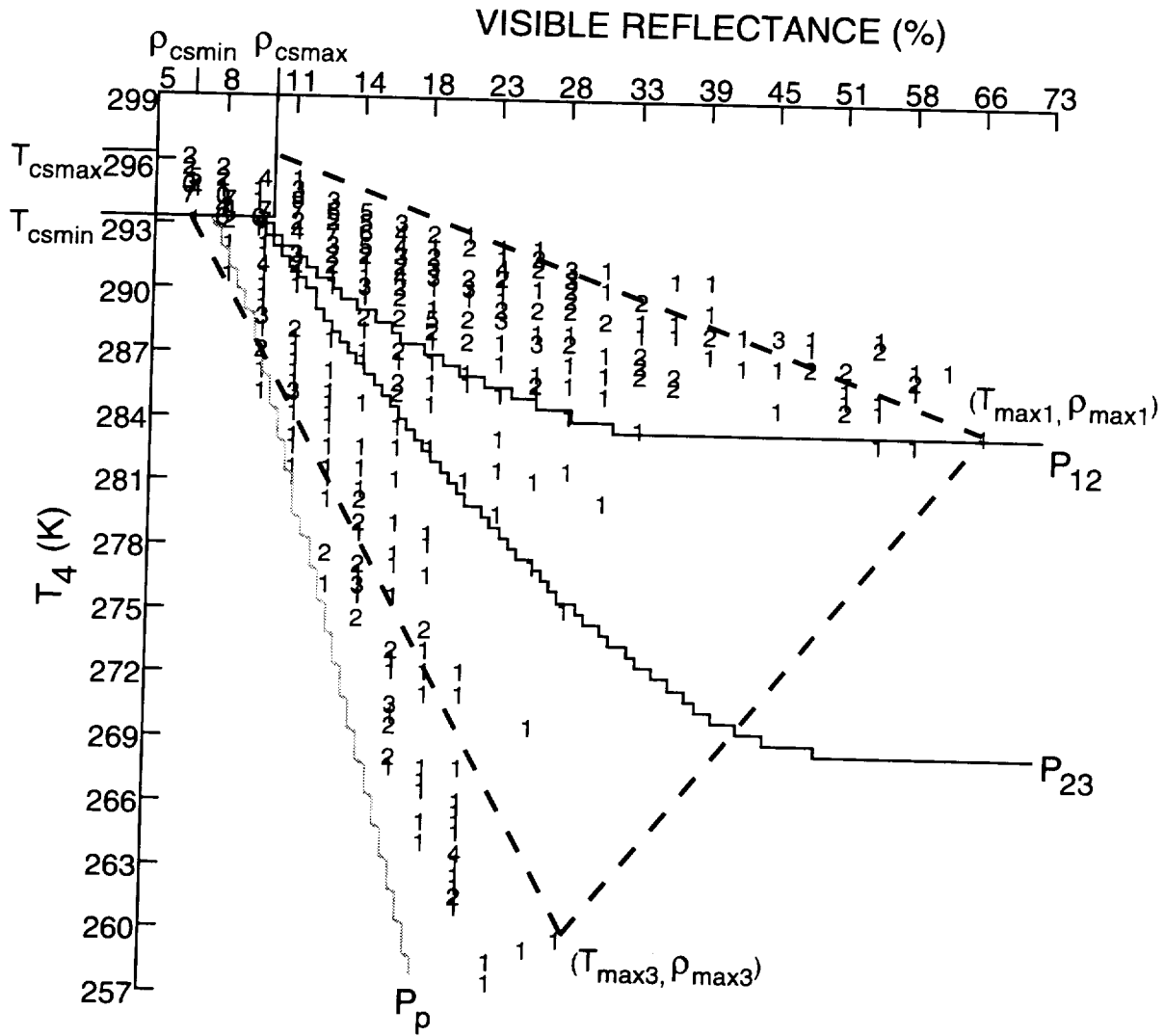


Figure 4.2-13. AVHRR VIS-IR histogram over 17.4°S at 153.3°E at 5.9 UTC, January 18, 1993.

and  $P_p$ . Pixels that are darker and colder than the respective reflectances and temperatures defining  $P_p$  are designated dark cloud pixels. These pixels are treated in a special manner described below.

The number of pixels in a scene assigned to a given layer,  $N_k$ , is

$$N_k = \sum_{ij} n(T_i, \rho_j) \tag{4.2-15}$$

Here,  $n$  is the number of pixels having  $T_i$  and  $\rho_j$  and the limits  $i$  and  $j$  are defined only for layer  $k$ . The temperatures in a given layer are averaged for each visible reflectance. Thus, for  $\rho_j$ ,

$$T_{kj} = B^{-1} \left[ \sum_i \frac{B(T_i) n(T_i, \rho_j)}{N_{kj}} \right] \tag{4.2-16}$$

where

$$N_{kj} = \sum_i n(T_i, \rho_j) \tag{4.2-17}$$

The emittance,  $\epsilon_j = \epsilon(\rho_j)$  is computed for each reflectance. The value of  $T_{kj}$  is substituted for  $T_\epsilon$  in (4.2-14) and used with the emittance to solve for  $T_{cld}(kj)$ . The pressure in the middle of the layer is used in the reflectance parameterization to compute Rayleigh scattering for all clouds in the layer.

If  $\rho_j$  is in the dark-pixel area of the histogram,  $\epsilon_j$  is indeterminate. It is assumed that dark pixels result from shadowing effects, other finite cloud effects, variations in  $\rho_{cs}$ , and inadequacies in the microphysical scattering models. When dark pixels are encountered, high-cloud pixels having greater reflectances are included in the calculation of  $T_{kj}$  to raise the mean, combined reflectance to a value of  $\rho > \rho_{cs}$  so that  $\epsilon$  can be computed. If there are no low- or middle-cloud pixels having  $\tau > 1$ , then high- or middle-layer pixels having the same temperature as the dark pixels are included in the summation. The summation continues with the next greatest visible reflectance until the mean reflectance is greater than  $\rho_{cs}$ . Pixels having temperatures lower than the coldest dim pixels are included in the summation only if the mean value of  $\rho$  remains in the dark-pixel area of the histogram. If the summation process does not result in a nondark mean value of  $\rho$ , it is assumed that the dark pixels are clear, but shadowed.

If the initial value of  $T_{cld}(kj)$  for any  $kj$  is less than  $T_p$ , then the summation process used for the dark pixels is invoked until  $T_{cld}(kj) \geq T_p$ . If this condition cannot be satisfied for the data, then it is assumed that the cloud is located at the tropopause. The mean emittance and optical depths are then adjusted to force this solution. Finally, the average temperature for layer  $k$  is

$$T_k = B^{-1} \left\{ \sum_j \frac{B[T_{cld}(kj)] N_{kj}}{N_k} \right\} \quad (4.2-18)$$

where  $T_j$  is the mean temperature for each  $\rho_j$ . The standard deviation  $\sigma_{Tk}$  is computed in the standard fashion using the values of  $T_j$ . In the exceptions noted above, the index and values of  $\rho_j$  are adjusted to reflect the change in summation. No pixel values are ever used twice.

The LBTM cloud-layer definitions, used to associate altitude with the cloud classifications given by surface observers, provide a convenient way to vertically slice up the troposphere. Clouds do not necessarily fall exactly into those altitude ranges, so a cloud deck may straddle the layer boundaries giving the appearance of two layers. Furthermore, high and low layers may overlap and produce radiance pairs that appear to be in the middle layer. To minimize misdetection and to find distinct layers, the following modifications are applied to the LBTM. This procedure is applicable to scenes with horizontal dimensions of 50 km or greater.

To find distinct layers, it is assumed that there is an envelope of temperatures and reflectances that bound the pixels belonging to a given layer. This envelope must account for the variations in both the clear-sky radiances in the scene and the cloud height within the layer. The variations in  $T_{cs}$  and  $\rho_{cs}$  can be represented by the extreme values. The clear-sky extremes are defined as the coldest and warmest clear temperatures,  $T_{csmin}$  and  $T_{csmax}$ , respectively, and the smallest and greatest clear-sky reflectances,  $\rho_{csmin}$  and  $\rho_{csmax}$ , respectively. The respective temperature and reflectance for the brightest pixel in a given layer are  $T_{maxk}$  and  $\rho_{maxk}$ . The histogram is searched for layers beginning with the highest layer containing an observation. Pixel values falling to the cold and dim side of the line defined by  $(T_{csmax}, \rho_{csmax})$  and  $(T_{max3}, \rho_{max3})$  can be explained by clouds in the high layer. If no pixels are observed on the warm and bright side of this line, then it may be concluded that there is probably only one distinct layer present. This layer is defined by  $T_{cldk}$  and  $\sigma_{Tk}$ .

If there are pixels on the warm, bright side then the same process is repeated for the next level down. For midlevel clouds, the line would be given by  $(T_{csmax}, \rho_{csmax})$  and  $(T_{max2}, \rho_{max2})$ . If there are low clouds derived from the LBTM and there are pixels warmer and brighter than this new line, then it is concluded that there is a distinct layer of low clouds. These low clouds may be scattered cumulus or a deck of stratus or stratocumulus. If no pixels are observed to the warm, bright side of this line, it is likely that there is a distinct midlevel deck in the scene.

This algorithm is based on the dependence of reflectance and emittance on cloud optical depth. Emittance increases toward unity at a greater rate than reflectance approaches its asymptotic value. This feature produces the curvature seen in the coldest, dimmest pixels in Figures 4.2-8, 4.2-9, and 4.2-12. For a given cloud deck, there will be a spread in the observed temperature for a given reflectance because of the variations in  $T_{cs}$ ,  $T_{cld}$ , and the particle sizes in the cloud. Pixels between the dimmest, coldest curve and the straight line defined above can also be explained by pixels that are partially filled with the upper cloud or by overlap between some lower cloud and the upper cloud. It is necessary to have lower clouds to obtain pixels on the warm, bright side of that line. In other words, the high cloud cannot be that reflective and still be that warm.

To distinguish overlapped pixels from those belonging to a single deck, a similar analysis is applied using lines between the extreme cloud values. Given the presence of both low and high clouds and pixels that fall in the middle layer, it is possible to determine if some of the midlevel pixels are actually overlapped or represent a distinct layer. A line is drawn between  $(T_{max3}, \rho_{max3})$  and  $(T_{max1}, \rho_{max1})$ . If there are midlevel pixels to the cold, bright side of this line, then it is highly probable that there is a distinct midlevel deck. Otherwise, the midlevel clouds are probably overlapped high and low clouds.

This process is illustrated in Figure 4.2-13 for data similar to that seen in Figure 4.2-9b. The LBTM found three cloud layers in this histogram. The line extending from  $(T_{csmin}, \rho_{csmin})$  to  $(T = 259\text{K}, \rho = 0.28)$  indicates that there must be clouds lower than the high-cloud deck. Similarly, the line from  $(T_{csmax}, \rho_{csmax})$  to  $(T = 284\text{K}, \rho = 0.66)$  indicates a distinct low layer. The lack of pixels brighter than those defined by the line  $(T = 259\text{K}, \rho = 0.28) - (T = 284\text{K}, \rho = 0.66)$  suggests that the pixels in the middle layer do not form a distinct layer. Instead, they are formed by the overlap of the high and low layers.

If there are two layers in adjacent levels or if there is only one distinct layer  $k$ , but there are some pixels in layer  $k-1$ , then the cloud temperatures are compared to determine if they are part of the same cloud deck. As in the spatial coherence method, the cloud deck is allowed to have a finite thickness or altitude range. This permitted layer range  $\Delta T_{lcl}$  varies with height because, in a given system, high cloud tops tend to vary over a greater vertical range than low clouds and retrieved high cloud altitudes are subject to more error than low clouds. Marine boundary layer cloud heights, for example, can be determined to within a few hundred meters (e.g., Minnis et al., 1992), while the typical instantaneous error in the derived thin cirrus heights is  $\sim \pm 1$  km (e.g., Minnis et al., 1993). For low clouds, i.e.,  $T_{cld} > 280\text{K}$ ,  $\Delta T_{lcl} = 2$  K. For high clouds, i.e.,  $T_{cld} < 220$  K,  $\Delta T_{lcl} = 6$  K. In between these extremes,

$$\Delta T_{lcl} = 2 + 0.67(280 - T_{cld}) \quad (4.2-19)$$

The allowed temperature range bounds the layer values. Thus, if  $2\sigma_{Tk} > \Delta T_{lcl}$ , then the layer is too diffuse to be designated as a distinct layer. If, however,  $2\sigma_{Tk}$  and  $2\sigma_{T_{k-1}}$  are both less than  $\Delta T_{lcl}$ , then it may be possible to combine the layers. The layers are combined if  $T_{k-1} < T_k + 2\sigma_{Tk}$  or if  $T_k > T_{k-1} - 2\sigma_{T_{k-1}}$  and the resulting standard deviation is less than  $0.5\Delta T_{lcl}$ .

Application of this process to the scatter plots in Figure 4.2-8 would yield single low-level decks for [1,1] and [2,1], and low and high decks with overlapped pixels for the remaining plots. In Figure 4.2-12, the technique would identify a low and a high deck for [1,1], a mid and high deck for [1,2], a low deck for [1,3], a mid and high deck for [2,10] a high deck for [2,2], and possibly a high deck for [2,3]. The high layers in [1,3], [2,2], and [2,3], the midlayers in [2,2] and [2,3] and the low layer in [2,3] may be too diffuse to pass the layer bounds test although they would pass the simple linear tests. Some layering of the high clouds in [1,3], [2,2], and [3,3] may be detectable with a greater vertical resolution of layers rather than the three used here. However, these scenes may contain convective clouds in various stages of development so that no extensive layers exist. Figure 4.2-14 shows an example of a diffuse situation over the tropical Pacific. The low-mid, mid-high, tropopause, and clear boundaries are drawn to illustrate how the histogram is sliced for a convective case. Application of the technique would yield only one distinct cloud layer in the middle levels with  $T_2 = 278.6$  K. The high layer would not satisfy the

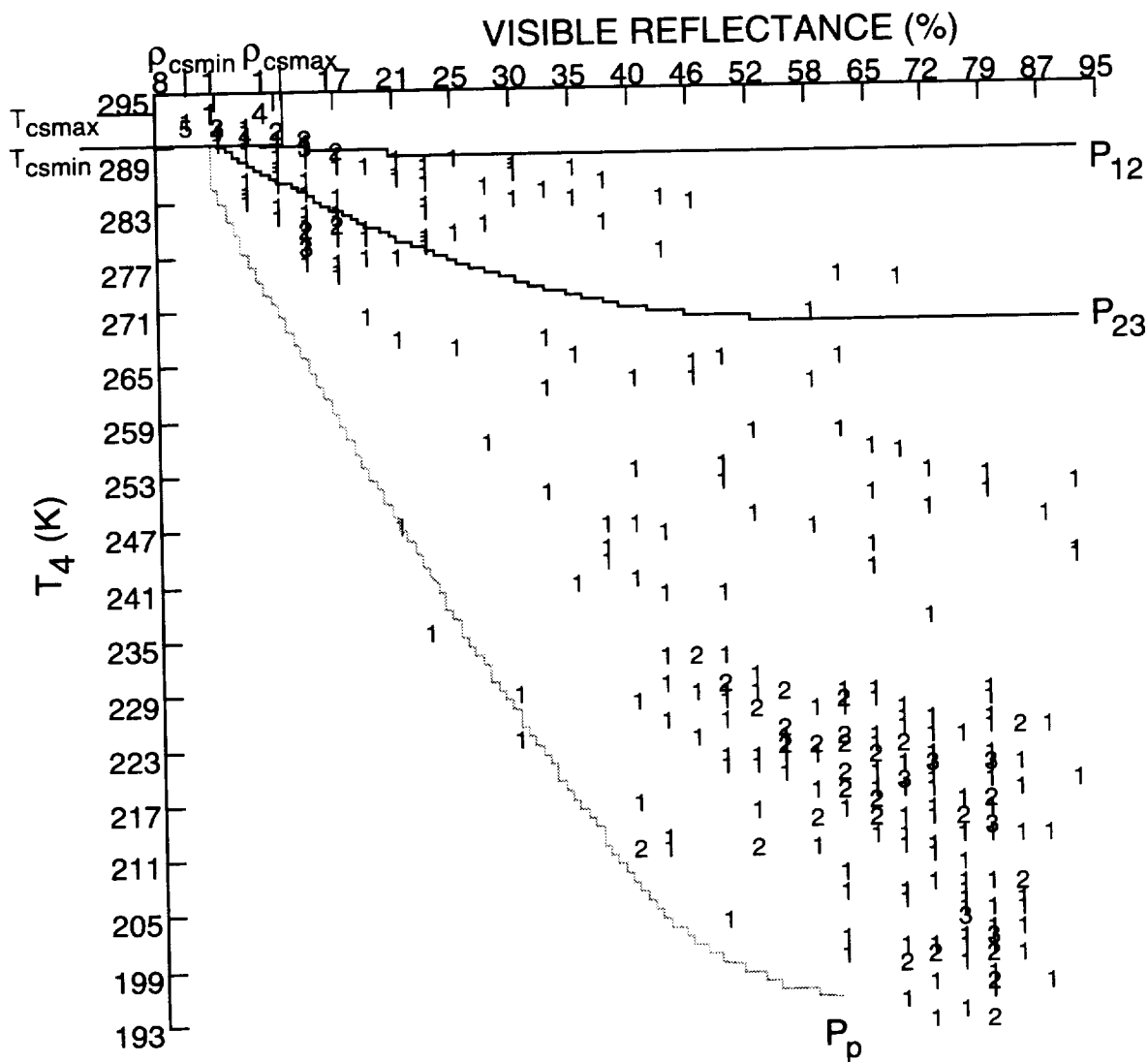


Figure 4.2-14. AVHRR VIS-IR histogram over 10.7°S at 143.2°E at 5.9 UTC, January 18, 1993.

temperature range rules. Some low-cloud pixels near the clear boundary would not constitute a layer because they fall to the cold, dim side of the mid-cloud  $\rho_{max}$  line.

For scenes containing more than one layer, it is possible to estimate which pixels are overlapped and which belong to a single layer. Given  $T_k$  and  $\sigma_{Tk}$  for layer  $k$ , the pixels that belong to the layer are those enveloped by the two curves defined by the model calculations of  $T$  and  $\rho$  for a range of optical depths. The computations use  $(T_{csmax}, \rho_{csmax})$  for the clear conditions and  $T_k + 2\sigma_{Tk}$  as the cloud temperature to determine the curve for the warm side of the cloud deck and  $(T_{csmin}, \rho_{csmin})$  for the clear conditions and  $T_k - 2\sigma_{Tk}$  as the cloud temperature to determine the cold curve. Pixels having values of  $T$  and  $\rho$  between those two curves are assigned to the layer. Figure 4.2-15 shows an example of a three-layer case. The boundary lines are shown as before with a crude approximation of the envelopes for each layer. The envelope overlap near the clear boundaries is typical, but will be somewhat diminished when the actual calculations are applied. The  $T$  and  $\rho$  for each pixel in the envelope overlap are compared to the central curve of the envelopes. This central curve is defined by  $T_k$  and  $(T_{cs}, \rho_{cs})$ . The pixel is assigned to the layer for which the difference between  $T$  and  $T_k(\rho)$  is minimal. The pixels that fall between the envelopes are considered to be overlapped pixels.

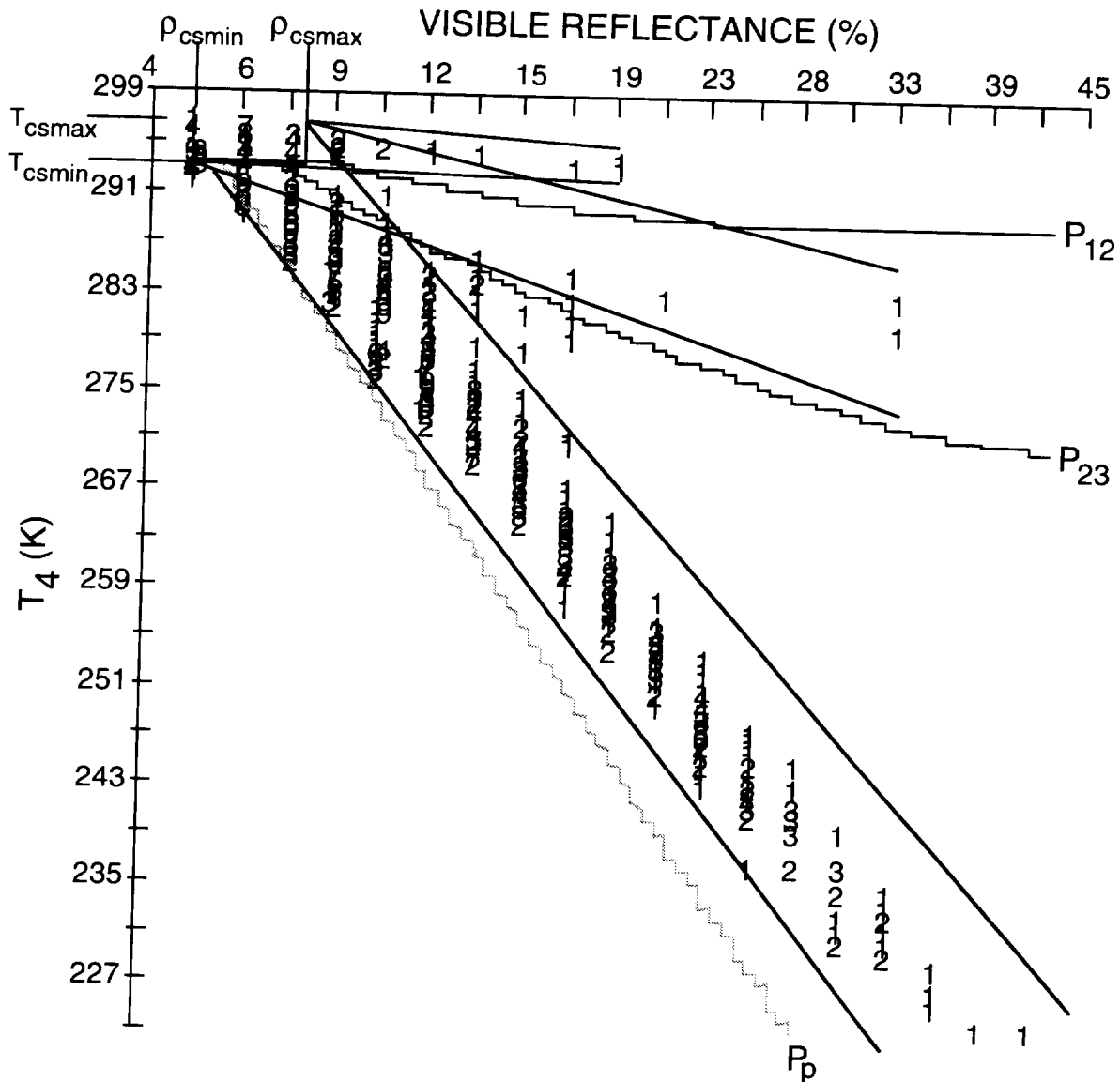


Figure 4.2-15. AVHRR VIS-IR histogram over 13.3°S at 149.4°E at 5.9 UTC, January 18, 1993.

This approach to cloud layering can detect more cloud layers than the spatial-coherence technique. It cannot detect three layers unless the reflectance of the middle layer exceeds that of either the low or high layer. The increased detectability may raise the level of uncertainty in the cloud layer properties. This bispectral approach is currently under development and will be altered to accommodate additional layers. The allowed layer temperature range, interpretation of the overlapped pixels, and techniques for defining the range in clear-sky temperature and reflectance are among the issues that are being examined.

#### 4.2.3.2. Nighttime Layer Pressure Retrieval

At night, a different approach is needed. Figure 4.2-16a shows  $T_4$  and the AVHRR channel 3 ( $3.7 \mu\text{m}$ ) brightness temperatures  $T_3$  for a layer of altostratus clouds over an area in the tropical Pacific. The value of  $T_{cs4}$  is  $\sim 293\text{K}$ . The brightness temperature differences  $BTD_{3-4}$  for channels 3 and 4, plotted

against  $T_4$  in Figure 4.2-16b, are more informative. For a given value of  $T_{cld}$ ,  $BTD_{3-4}$  increases as the optical depth increases up to a value of  $\tau \sim 4$ . As  $\tau$  continues to increase,  $BTD_{3-4}$  decreases rapidly until it is less than the clear-sky value. Thus, whenever  $BTD_{3-4}$  for cloudy pixels is less than the clear value, a nearly opaque cloud is indicated. The variation in  $BTD_{3-4}$  arises from variations in  $T_{cs}$ ,  $T_{cld}$ , and particle size. If there is a cluster of nearly opaque pixels around a given value of  $T_4$ , it is highly probable that a layer exists at  $T_4$ . The methods for determining these layers are the same as prescribed for the daytime case. The low, middle, and high boundaries are established for an optically thick cloud (e.g.,  $T_{12} = T[z = 2 \text{ km}]$  for all values of  $T_3$ ). The values of  $T_k$  and  $\sigma_{Tk}$  are computed using only the pixels having  $BTD_{3-4}$  less than the clear-sky value. The same criteria applied during the daytime are used at night for defining a layer and combining adjacent layers. In the case of Figure 4.2-16b, a layer would be determined at  $\sim 258\text{K}$ .

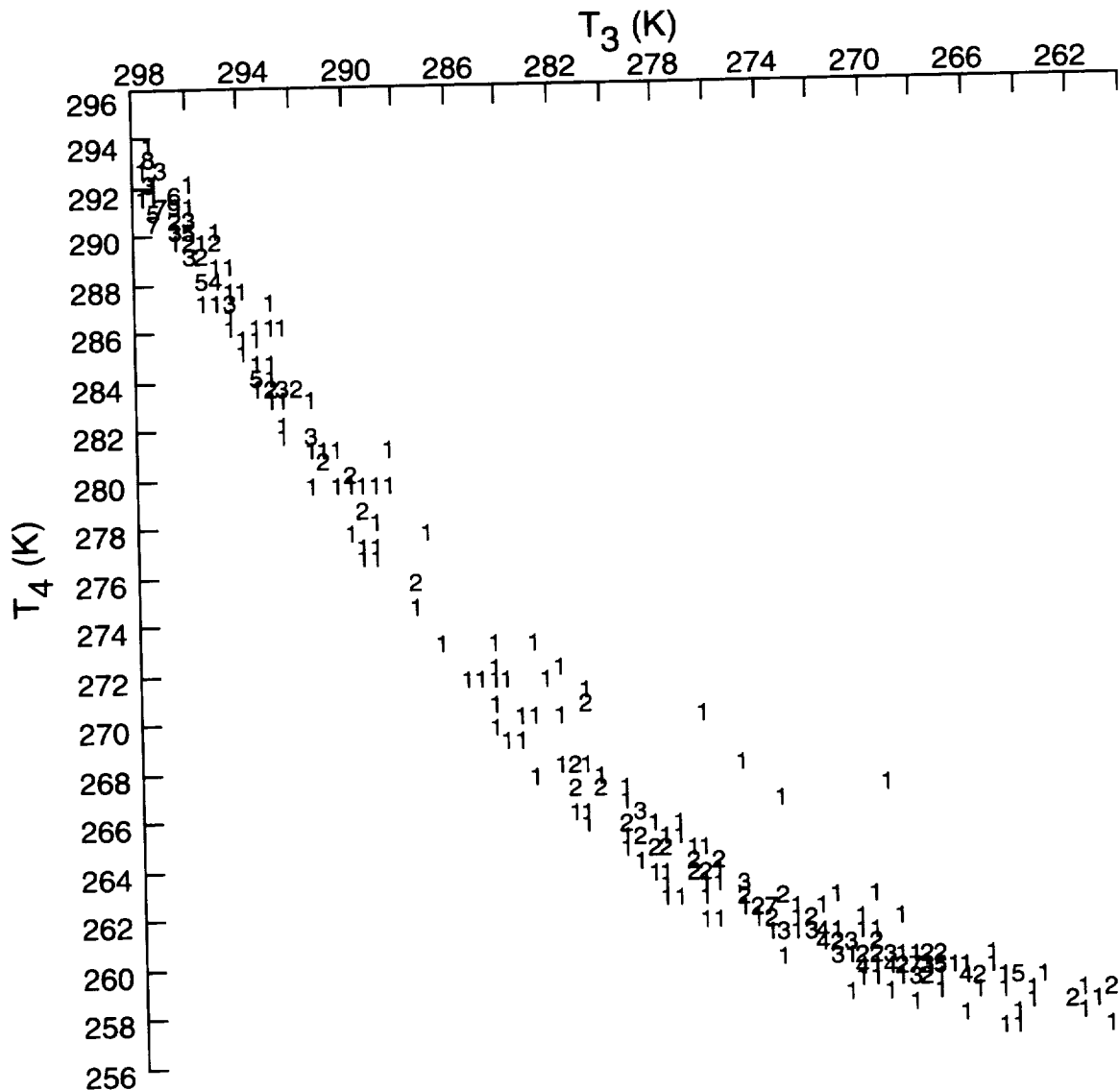


Figure 4.2-16a. AVHRR NIR-IR histogram over 5.9°S at 133.6°E at 18.8 UTC, January 26, 1993.

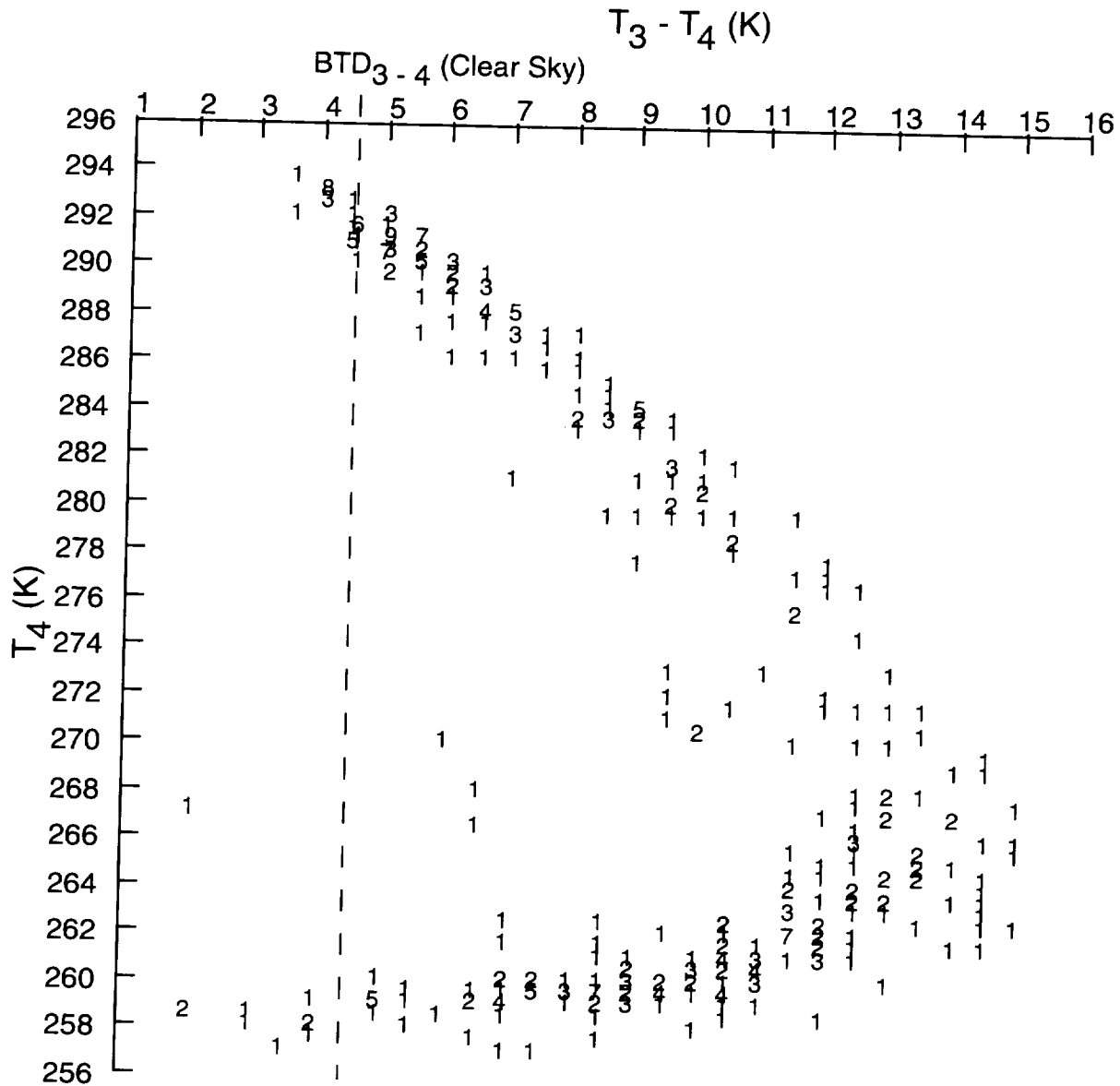


Figure 4.2-16b. AVHRR BTD-IR histogram over 5.9°S at 133.6°E at 18.8 UTC, January 26, 1993.

A layer analysis of the histogram in Figure 4.2-17 would yield a layer near 221 K. The solid line in Figure 4.2-17 corresponds to a parameterization calculation of  $BTD_{3-4}$  using a cirrostratus microphysical model,  $T_{cs4} = 293.5\text{K}$ , and  $T_{cld} = 221\text{K}$  (see section 4.3 for details). The model fit is consistent with a single layer of clouds having relatively uniform particle sizes. The more complex histogram in Figure 4.2-18 is typical of a two- or three-layer system. The clear portion of the scene is at approximately 291 K; a distinct middle layer is found at 273 K, and a diffuse high layer is found near 228 K. An additional low layer may be at ~288 K. This combination of clear, single-layer, and overlapping layers would probably only yield a single layer at ~273 K. The high-cloud layer would be too diffuse to pass the temperature range tests using  $T_{cs}$  as the background temperature. Because most of the high-cloud pixels are probably overlapping middle-cloud pixels, the background temperature should be the middle-cloud temperature. The result would be a high cloud at ~228 K.

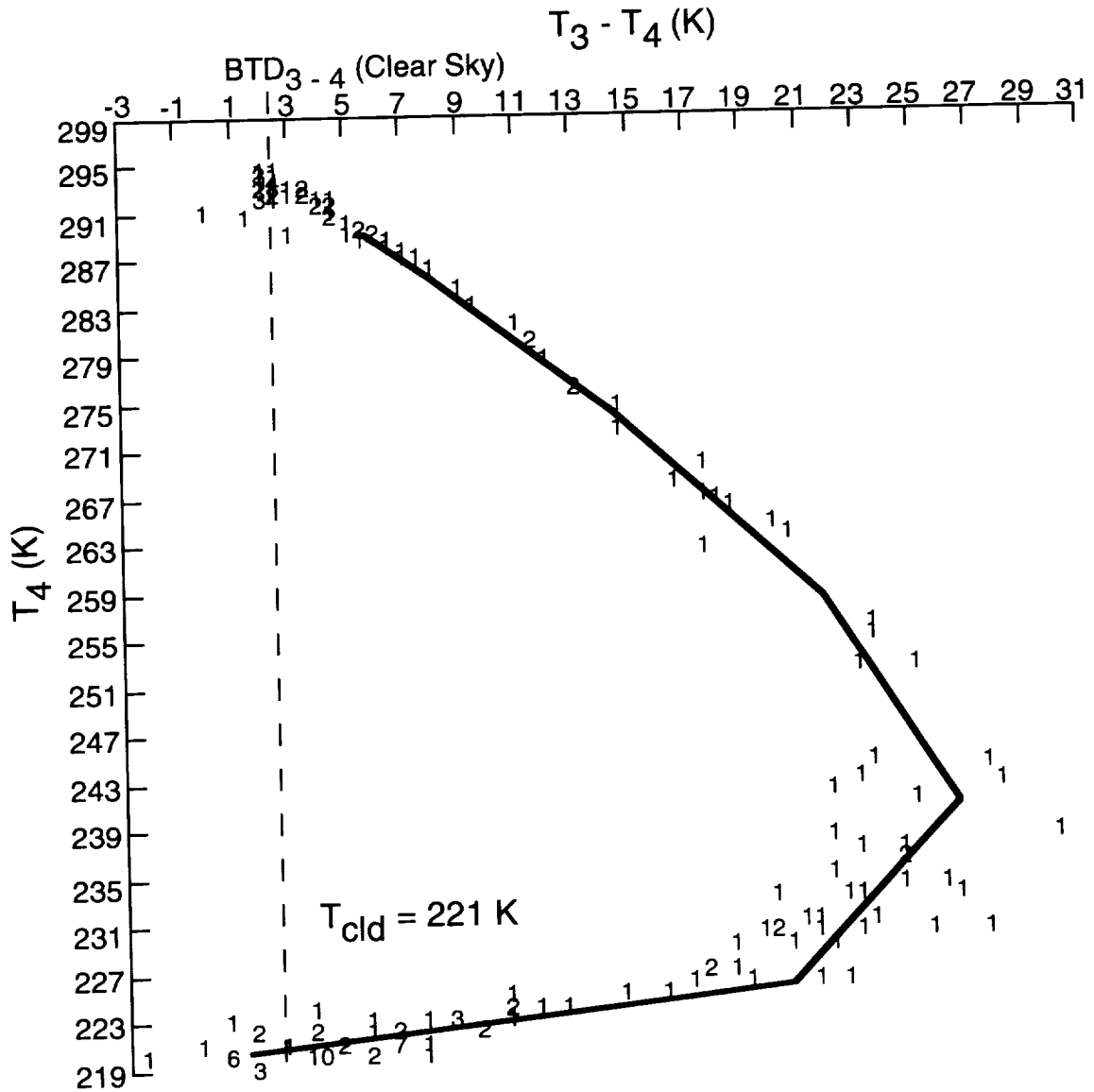


Figure 4.2-17. AVHRR BT-D-IR histogram over 7.1°S at 171.3°E at 16.3 UTC, January 30, 1993.

The examples shown here suggest that layers can be identified at night using a bispectral histogram approach. This method is currently under development. Issues that are being addressed include the detection of overlapped pixels, the determination of the appropriate background temperature, prescription of layer envelopes based on assumptions about particle size, detection of layers with no opaque pixels, and the determination of layers in overlapped conditions.

#### 4.2.3.3. Practical Considerations

For CERES, the LBTM histogram will be divided into six areas: clear, low (surface to 700 hPa), lower middle (700–500 hPa), upper middle (500–300 hPa), and high (<300 hPa), and the dark pixel area. The CERES LBTM will require the input variables: clear-sky radiances and their standard deviations for each channel, vertical profiles of temperature, surface type, pixel radiances, surface elevation, and ozone optical depth at 0.65  $\mu\text{m}$ . The output comprises the number of distinct layers, the means and standard deviations for  $\tau_k$  and  $T_k$ , and an index indicating whether it is overlapped or not. The methodologies described in this section will be validated using several different approaches. The layer cloud

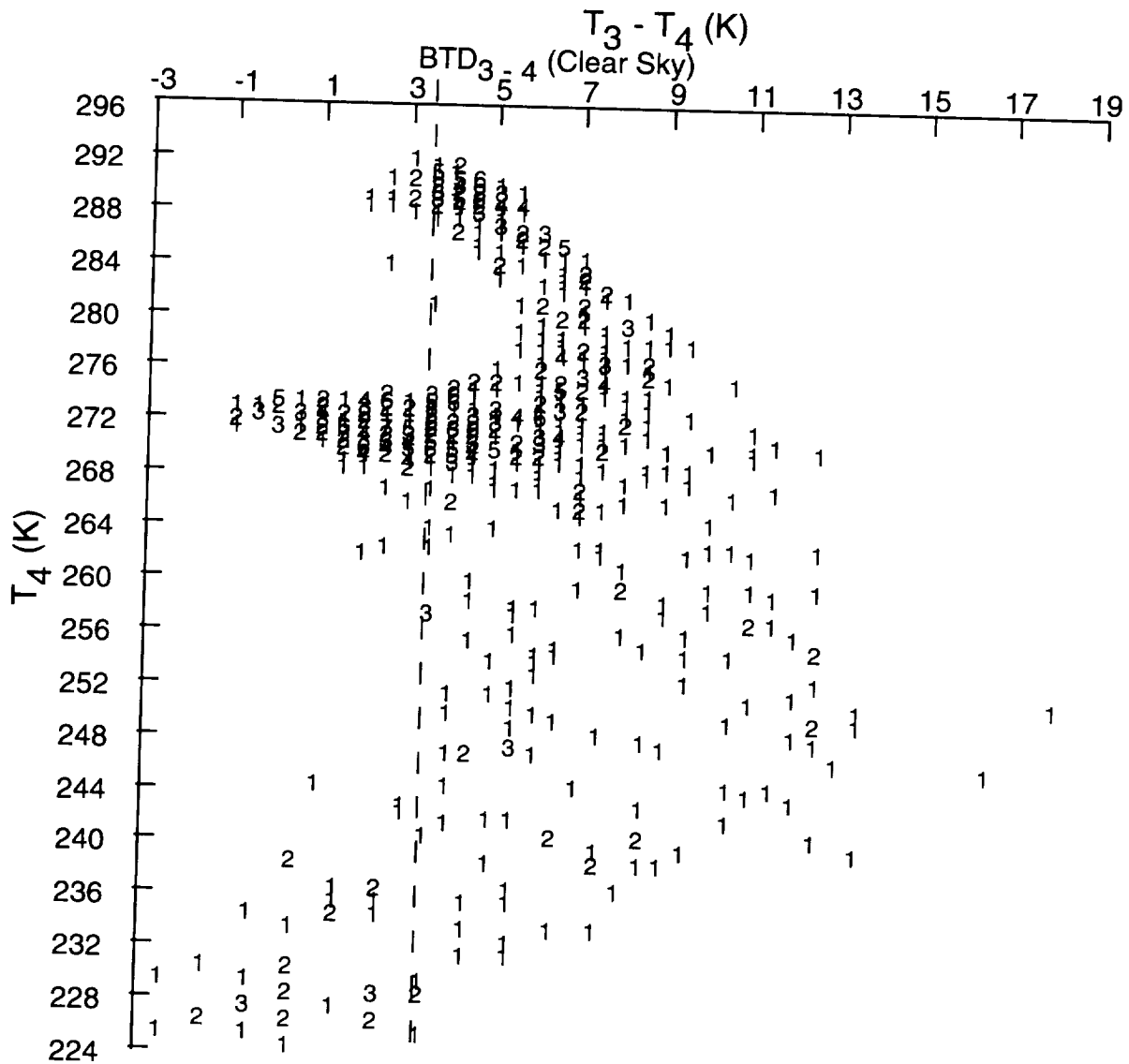


Figure 4.2-18. AVHRR BT-D-IR histogram over 4.3°S at 134.7°E at 18.8 UTC, January 26, 1993.

properties will be compared to those derived from the other satellite-retrieval methods to determine how much additional information can be gained by applying this methodology. Aircraft and surface lidar and radar data will be used to verify the detection of layers and their altitude determination. These validation efforts will use historical FIRE and ECLIPS datasets as well as active remote sensing data from ARM and future FIRE observations. Such field data taken over a wide variety of cloud types are essential for verification and development of these layer-detection techniques.

#### 4.2.4. The CO<sub>2</sub> Slicing Method

##### 4.2.4.1. Introduction

The CO<sub>2</sub> slicing methods (e.g., McCleese and Wilson, 1976; Smith and Platt, 1978; Chahine, 1974) have been shown to provide an accurate means of inferring cirrus cloud altitude from passive infrared radiance measurements. The methods take advantage of the fact that each of the sounding channels within the 15- $\mu$ m CO<sub>2</sub> band have varying opacity to CO<sub>2</sub>, thereby causing each channel to be sensitive

to a different layer in the atmosphere. The techniques have been shown to be effective for single-layered, nonblack, mid- to high-level clouds such as cirrus, but are generally applied operationally to any given cloud occurrence. The algorithms are most accurate for clouds that occur in a single, well-defined layer, or for multilayered cloud cases in which the uppermost cloud layer is nearly black. The derived cloud pressure is expected to be near cloud center for optically thin clouds (those with extinction optical depths less than 1). The cloud pressure is expected to decrease to cloud top for more nearly opaque cloud when the extinction optical depth is greater than 1.

This algorithm calculates cloud top pressure,  $p_{cld}$ , and effective cloud amount,  $\epsilon C$  (emittance  $\epsilon$  times cloud fraction  $C$ ), given one or more pairs of 15- $\mu\text{m}$  narrowband radiances. The method relies upon having significant pressure level differences between the peaks of the weighting functions for a given pair of channels. The algorithm specification includes suggested strategies for handling:

1. Temperature inversions (ambiguity in  $p_{cld}$ )
2. Lack of sensitivity in the weighting functions
3. Consistency in multichannel retrievals
4. Various problems relating to instrument noise, transmission function errors, and input data errors

This algorithm has been applied to data from the High Resolution Infrared Radiation Sounder (HIRS/2, henceforth HIRS for simplicity) (Wylie and Menzel, 1989; Menzel et al., 1992; Wylie et al., 1994), the Geostationary Operational Environmental Satellite (GOES) VISSR (Visible Infrared Spin Scan Radiometer) Atmospheric Sounder (VAS) (e.g. Menzel et al., 1983), and most recently to the High Resolution Interferometer Sounder (HIS) (Smith and Frey, 1990). The Moderate Resolution Imaging Spectroradiometer (MODIS) (King et al., 1992) under development for the Earth Observing System (EOS) has four channels in the 15- $\mu\text{m}$  region that are similar to the HIRS channels. The central wavenumbers and other characteristics of the appropriate channels for the HIRS and MODIS instruments are provided in Table 1. Error analyses based upon the CO<sub>2</sub> slicing method have been reported by Wielicki and Coakley (1981), Menzel et al. (1992), and Baum and Wielicki (1994). Sources of error for this algorithm will be discussed in greater detail later in this document. Retrieval errors will arise from instrument noise, errors in temperature and humidity profiles, errors in the clear-sky radiance, geometrically thick but optically thin clouds, radiative transfer calculation assumptions, and the presence of more than one cloud layer in the field-of-view (FOV).

#### 4.2.4.2. Basic Equations and Derivations

The clear-sky spectral radiance  $I_{cs}(v^i, p_s)$  for a black surface (surface emissivity,  $\epsilon_s^i = 1$ ,  $i$  is channel number) is given by

$$I_{cs}(v^i, p_s) = B(v^i, T_s)t(v^i, p_s) + \int_{P_s}^0 \frac{dt(v^i, p)}{d \ln p} B[v^i, T(p)] d \ln p \quad (4.2-20)$$

where  $B(v^i, T)$  is the Planck radiance at temperature  $T$ ,  $v^i$  is the wavenumber of channel  $i$ ,  $t(v^i, p)$  is the transmission from atmospheric pressure level  $p$  to the satellite at  $p = 0$ , and the subscripts  $s$  and  $cs$  denote surface and clear-sky, respectively. If the cloud is opaque (cloud emissivity,  $\epsilon_{cld}^i = 1$ ) at wavenumber  $v^i$  and completely fills the FOV, the radiance for an overcast black cloud ( $ob$ ) at pressure level  $p_{cld}$  is given by

$$I_{ob}(v^i, p_{cld}) = B(v^i, T_{cld})t(v^i, p_{cld}) + \int_{P_{cld}}^0 \frac{dt(v^i, p)}{d \ln p} B[v^i, T(p)] d \ln p \quad (4.2-21)$$

Table 4.2-1. HIRS and Anticipated MODIS Channels, Central Wavelengths, Principal Absorbing Components, and Approximate Pressure Level Corresponding to the Peak in the Individual Channel Weighting Functions; Central Wavelengths and Weighting Function Peaks May Change Slightly for Each Instrument.

Instrument	Channel number	Central wavelength, $\mu\text{m}$	Principal absorbing component	Approximate peak in weighting function, hPa
HIRS	4	14.21	CO <sub>2</sub>	300
HIRS	5	13.95	CO <sub>2</sub>	500
HIRS	6	13.66	CO <sub>2</sub> ; H <sub>2</sub> O	750
HIRS	7	13.34	CO <sub>2</sub> ; H <sub>2</sub> O	900
HIRS	8	11.10	H <sub>2</sub> O	Surface
MODIS	31	11.03	H <sub>2</sub> O	Surface
MODIS	32	12.02	H <sub>2</sub> O	Surface
MODIS	33	13.335	CO <sub>2</sub> ; H <sub>2</sub> O	900
MODIS	34	13.635	CO <sub>2</sub> ; H <sub>2</sub> O	750
MODIS	35	13.935	CO <sub>2</sub>	500
MODIS	36	14.235	CO <sub>2</sub>	300

The theoretical upwelling radiance  $I$  for a partially cloud-filled FOV is given by

$$I(\nu^i, p_{cld}, \epsilon_{cld}^i C) = I_{cs}(\nu^i, p_s) + \epsilon_{cld}^i C [I_{ob}(\nu^i, p_c) - I_{cs}(\nu^i, p_s)] \quad (4.2-22)$$

In this formulation, the cloud emittance  $\epsilon_{cld}^i$  of channel  $i$  is multiplied by the cloud fractional coverage  $C$ , and the quantity  $\epsilon_{cld}^i C$  is referred to as the effective cloud amount or effective cloud emittance in the literature.

**4.2.4.2.1. Transmittance functions.** The calculation of the transmission functions used to generate the theoretical upwelling radiances are based on a model developed by McMillin and Fleming (1976) and used by Weinreb et al. (1981) for HIRS transmittance calculations. Eyre and Woolf (1988) developed a newer model primarily for work with microwave channels. When the Eyre and Woolf (1988) model was tested on HIRS channels, it was found to have poor accuracy for channels with strong water vapor absorption. This shortcoming was addressed in the model reported by Eyre (1991), which improves the treatment of water vapor and has the added benefit of providing code that is much easier to vectorize than the model used by Weinreb et al. (1981). The model currently used is based on Eyre (1991) with code developed initially by Woolf (personal communication, 1993).

For HIRS analysis, the transmittance model is evaluated at 40 discrete pressure levels (0.1, 0.2, 0.5, 1, 1.5, 2, 3, 4, 5, 7, 10, 15, 20, 25, 30, 50, 60, 70, 85, 100, 115, 135, 150, 200, 250, 300, 350, 400, 430, 475, 500, 470, 620, 670, 700, 780, 850, 920, 950, and 1000 hPa). For a midlatitude spring/fall temperature profile shown in Figure 4.2-19a, transmittance profiles for HIRS 15- $\mu\text{m}$  channels 4 through 7 are shown in Figure 4.2-19b. Channels 4 and 5 have extremely low transmittances at the surface, showing that these channels are relatively insensitive to errors in clear-sky temperature. Channels 6 and 7 have

transmittances greater than 10% near the surface and are more sensitive to surface temperature than channels 4 or 5. Weighting functions for HIRS channels 4 through 8 are shown in Figure 4.2-20.

For MODIS 15- $\mu\text{m}$  radiometric data analysis, it is anticipated that the transmission model will be discretized at 50-hPa increments in the troposphere, and have an additional surface term for cases in which the surface pressure is greater than 1000 hPa. There has been some discussion as to whether 25-hPa pressure increments will be necessary.

#### 4.2.4.3. Radiance Ratio Method

Cloud-top pressure may be determined using the radiance ratio method, as discussed in Smith and Platt (1978), Wylie and Menzel (1989), Smith and Frey (1990), Menzel et al. (1983), and Wielicki and Coakley (1981). The change in radiance at a particular wavenumber caused by the presence of cloud is called the cloud signal. In the radiance-ratio method, a ratio is taken of the cloud signals for two channels spaced closely in wavenumber. For two spectral channels at wavenumbers  $\nu^i$  and  $\nu^j$  that are looking at the same FOV, the ratio for a single cloud layer is derived as

$$G(p_{cld}) = \frac{I_{meas}(\nu^i) - I_{cs}(\nu^i)}{I_{meas}(\nu^j) - I_{cs}(\nu^j)} = \frac{I_{ob}(\nu^i, p_{cld}) - I_{cs}(\nu^i, p_{cs})}{I_{ob}(\nu^j, p_{cld}) - I_{cs}(\nu^j, p_{cs})} \quad (4.2-23)$$

where  $G$  is the ratio of cloud signal for two different channels and  $I_{meas}(\nu^i)$  and  $I_{meas}(\nu^j)$  denote the measured radiance of channels  $i$  and  $j$ . We make the assumption that the emittances are the same for both channels. The function  $G$  is independent of both cloud opacity and effective cloud amount. However,  $G$  is dependent on the weighting function of the two channels, the cloud height, and the atmospheric temperature profile.

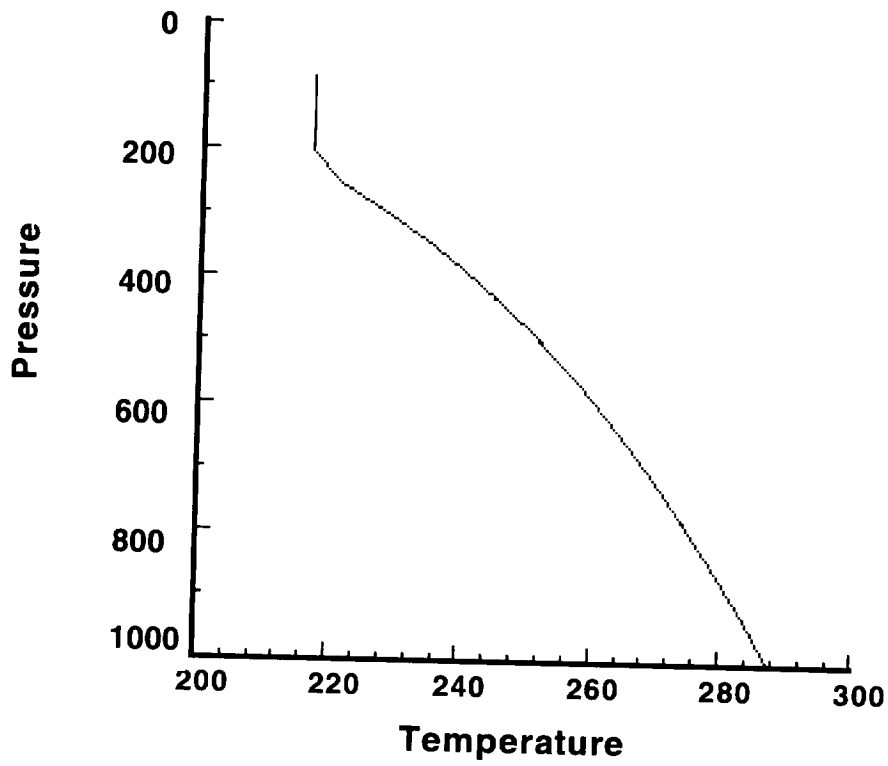
#### 4.2.4.4. Root-mean-square (RMS) Method

The implementation of the rms method requires a knowledge of temperature and humidity profiles. The rms radiance difference  $I_{rms}$  for  $N$  channels (Chahine, 1974; Wielicki and Coakley, 1981) is determined from

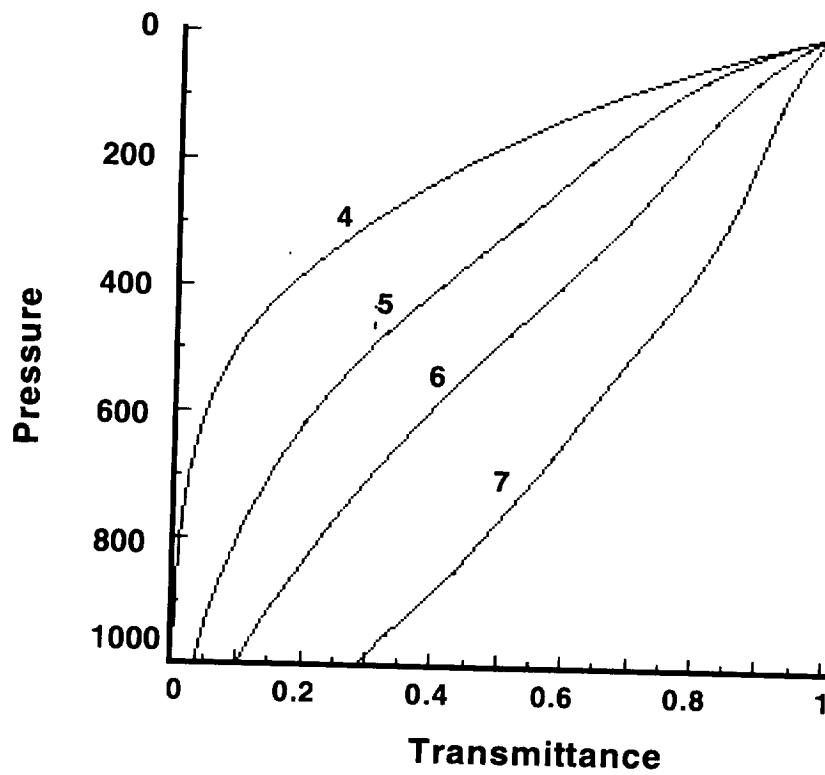
$$I_{rms}(p_{cld}, \epsilon_{cld}^i C) = \left\{ \sum_1^N [I_{meas}(\nu^i) - I^i(\nu^i, p_{cld}, \epsilon_{cld}^i C)]^2 \right\}^{1/2} \quad (4.2-24)$$

where  $I_{rms}$  is the rms radiance and  $I^i(\nu^i, p_{cld}, \epsilon_{cld}^i C)$  is determined from (4.2-22). For multilayer cloudiness, the retrieved cloud pressure errors will be the result of using a clear-sky radiance instead of the radiance of a lower cloud layer to compute the theoretical upwelling radiances when more than one cloud layer is present in an FOV. The atmosphere between 200 and 950 hPa is divided into 25-hPa intervals for the rms calculations. Thus, the derived cloud pressure will correspond to the rms minimum at a predefined interval.

The rms method, as stated in (4.2-25), has no provision for weighting the cloud signal from the various channels. The cloud signal for any particular channel increases with surface transmission so that the largest cloud signal will be recorded for the channel whose weighting function peaks closest to the surface, and the smallest cloud signal for the channel whose weighting function peaks farthest from the surface. The rms method as currently applied tends to weight the results toward the channels with greater transmittance.



(a) Average midlatitude temperature profile.



(b) NOAA-11 HIRS transmittances for channels 4, 5, 6, and 7.

Figure 4.2-19. Temperature and transmittance profiles.

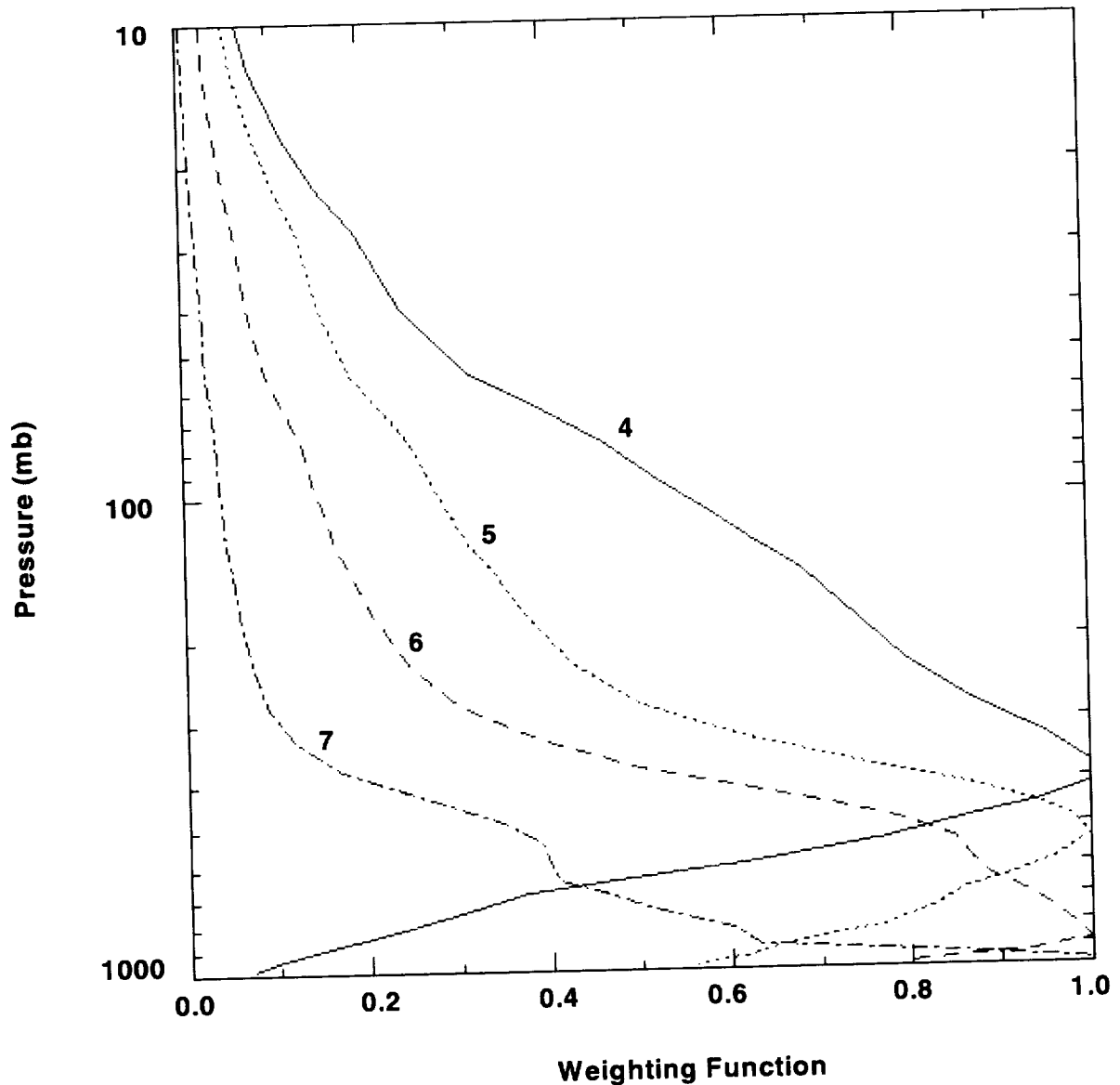


Figure 4.2-20. NOAA-11 HIRS weighting function  $dI/d \ln P$  for channels 4, 5, 6, and 7 for nadir viewing conditions.

#### 4.2.4.5. Calculation of Effective Emittance

Once a cloud height has been determined, an effective cloud amount (also referred to as effective emittance) can be evaluated from the infrared window channel data (usually  $11 \mu\text{m}$ ). For a single-level cirrus layer, the effective emittance is derived by rearranging (4.2-23):

$$\epsilon C = \frac{I(v^i, p_c) - I_{cs}(v^i, p_s)}{I_{ob}(v^i, p_c) - I_{cs}(v^i, p_s)} \quad (4.2-25)$$

When the effective emittance is less than unity, the sensor may be observing broken cloud ( $C < 1$ ;  $\epsilon_{cld} = 1$ ), overcast transmissive cloud ( $C = 1$ ;  $\epsilon_{cld} < 1$ ), or broken transmissive cloud ( $C < 1$ ;  $\epsilon_{cld} < 1$ ). With a HIRS FOV of  $\sim 18 \text{ km}$  at nadir, it is not reasonable to assume that the cloud completely covers the field of view except for large scale synoptic regimes. For the MODIS  $1 \text{ km} \times 1 \text{ km}$  pixel size, we can assume that high clouds fill the field of view ( $C = 1$ ) so that we obtain a direct estimate of  $\epsilon$  using (4.2-30)

or (4.2-31). For the large HIRS footprint,  $C$  is determined from AVHRR higher resolution data, assuming  $C = 1$  for the AVHRR pixel.

#### 4.2.4.6. Estimation of Clear-Sky Radiance

To calculate the  $G$  function for the single cloud-layer case, an estimate must be determined for the representative clear-sky radiance appropriate for the FOV. Clear-sky radiance/brightness temperature estimates are to be used from the CRH ancillary data set.

#### 4.2.4.7. Error Estimates for Cloud Property Retrieval

Retrieval errors will arise from instrument noise, errors in temperature and humidity profiles, errors in the clear-sky radiance, geometrically thick but optically thin clouds, radiative transfer calculation assumptions, and the presence of more than one cloud layer in the FOV. Because all of these issues have been reported in the literature, a brief summary will be presented here.

**4.2.4.7.1. Errors associated with the assumption of constant emissivity.** Spectrally close channels are used to minimize differences in the real and imaginary parts of the index of refraction for ice crystals and water droplets. Calculations by Jacobowitz (1970) indicate that negligible errors occur for the  $\text{CO}_2$  channels between 13.3 and 14.2  $\mu\text{m}$  for water and/or ice cloud determinations. This phenomenon is not deemed to be an error source in the  $\text{CO}_2$  slicing algorithm.

**4.2.4.7.2. Errors associated with the assumption of a thin cloud layer.** The  $\text{CO}_2$  slicing algorithm assumes that all of the radiative effects of the cloud occur as if the cloud were a thin layer at a single temperature. This makes the mathematics tractable. If the methodology to calculate radiative properties of a nonopaque cloud were to include a cloud term where the cloud has finite depth, then knowledge of the vertical structure of the cloud would be required. There are an infinite variety of combinations of cloud depths and vertical combinations that could produce the same integrated radiative signature; a unique solution is not possible. Any initial assumption of cloud structure biases the cloud top and bottom solution derived in the radiative transfer formulation.

Wielicki and Coakley (1981) discussed the consequences of the thin-layer cloud approximation. They concluded that the algorithm solution for cloud-top pressure would be near the center of the cloud for thin clouds and near the top of the cloud for opaque clouds. For an optically thick cloud, the equation would yield the correct cloud-top pressure. For an optically thin cloud, however, the radiative effects of the cloud are forced into one layer. This is similar to a center of mass concept. The algorithm solution will be close to the radiative center of the cloud. The retrieved cloud-top pressure is somewhere between the cloud top and its center, varying with the density of the cloud.

Cirrus height errors are also discussed in Wylie and Menzel (1989), where comparisons were made to cloud tops measured by lidars and by the stereo parallax observed from the images of two satellites at two different viewing angles. In the lidar comparison, the VAS-inferred cloud-top pressure over an observation area was compared to the highest lidar observation in the same area. The clouds had to be radiatively thin for the lidars to see through to the tops without complete signal attenuation. Definition of a single cloud top was often difficult within a cloud layer; the lidar heights varied considerably (by more than 50 hPa) from one cloud element to another in the same cloud layer. On the average, the VAS  $P_{cld}$  was found to be approximately 70 hPa larger (lower cloud altitude) than the lidar-derived cloud-top heights. The  $\text{CO}_2$  slicing algorithm was sensing the mean height; the VAS heights were comparable to the lidar cloud-top heights to within half the cloud thickness. In the comparisons to stereo parallax measurements for thin transmissive clouds, the VAS heights showed little bias. It was often difficult to measure parallax for thin transmissive clouds, as they appeared fuzzy with poorly defined boundaries in the images. Because the image of the clouds is more indicative of the center of the diffuse cloud mass than its outer boundaries, the parallax method is sensitive to the radiative center of mass rather than the

physical tops of these clouds. Thus, in these intercomparisons of actual measurements, the retrieved  $P_{cld}$  values were found to be within the accuracy suggested by theoretical considerations.

**4.2.4.7.3. Errors associated with the assumption of a lower cloud layer.** McCleese and Wilson (1976) have shown that the retrieved cloud height for the case of multiple cloud layers is a weighted average of the cloud heights actually present. They performed numerical simulations of cloud configurations for the Nimbus-5 sounding channels. However, no quantitative information was provided to aid in estimating the errors in cloud pressure retrieval one should expect for common multilevel cloud situations, like cirrus over stratus. Menzel et al. (1992) presented an error analysis performed for the GOES VAS. The errors in high-cloud pressure retrieval associated with the presence of a lower cloud layer were found to result in a maximum error in retrieved upper-cloud pressure of approximately 100 hPa. The GOES VAS has three CO<sub>2</sub> sounding channels that are similar to those of HIRS, but HIRS has more sounding channels.

Baum and Wielicki (1994) presented multilevel cloud-retrieval errors for the HIRS instrument. The effect of opaque lower-cloud contamination at 850 mb on cloud pressure retrieval for a HIRS FOV is shown in Figure 4.2-21 for four two-channel combinations implementing the ratio method. Calculations are performed for a range of  $P_{uc}$  where the subscript  $uc$  represents the upper cloud layer, ranging from 250 to 850 mb and a range of  $\epsilon_{uc}^i C_{uc}$  between 0.1 and 1.0. The implementation of either the rms or the ratio methods will result in a single derived cloud pressure for a chosen FOV and channel combination. For the case in which a FOV has two distinct cloud layers, the difference in retrieved minus actual cloud pressure is positive in all cases. A positive difference means that the retrieved upper-cloud height is lower than the actual upper-cloud height. An error in retrieved cloud pressure results in an error in the calculation of  $\epsilon_{uc}^i C_{uc}$ . For the pressure errors presented in Figure 4.2-21, corresponding  $\epsilon_{uc}^i C_{uc}$  errors are shown in Figure 4.2-22 for the same conditions. The retrieved  $\epsilon_{uc}^i C_{uc}$  are calculated by using the lowest sounding channel of the pair of channels chosen for the ratio method. The error in  $\epsilon_{uc}^i C_{uc}$  is defined to be the retrieved value minus the true value. Because this quantity is positive, the retrieved value will be too high for cases in which there is lower-cloud contamination in a HIRS FOV.

The conclusions from these studies are as follows. The position of the lower cloud layer affects the accuracy of the height estimate of the upper cloud layer. Opaque clouds located near the surface underneath high cirrus have little effect on the retrieved cirrus  $P_{cld}$ . As the low-level opaque cloud increases in height above the surface, and thus has a colder cloud-top temperature, the errors in upper-cloud retrieved  $P_{cld}$  increase. The errors in cloud pressure and effective cloud amount caused by the presence of a lower overcast, black cloud layer are greatest for the CO<sub>2</sub> slicing techniques that use the lowest sounding channel and least for those channels whose weighting functions peak higher in the atmosphere. Baum and Wielicki (1994) also found that the errors depend upon the temperature lapse rate between the low-level cloud top and the surface. The retrieved upper-cloud pressure bias increases with increased lapse rate between the low cloud and the surface. The choice of the optimal channel selection depends on the type of study being performed. While the HIRS channels whose weighting functions peak between 700 and 1000 hPa minimize random errors, the use of the sounding channels whose weighting functions peak at 300 to 500 hPa minimize bias errors. For a cloud climatology the bias errors are most critical.

**4.2.4.7.4. Errors associated with instrument noise.** Instrument noise produces two types of error into the cloud-top pressure retrieval. Random instrument noise leads to an rms error and a bias error. The rms error is a variation of retrieved cloud pressure about the retrieved mean cloud pressure, whereas the bias errors were caused by differences between actual mean and retrieved mean cloud pressures. The primary source of bias is limiting effective cloud amount to the range (0,1) and cloud-top pressure to the range between the surface and the tropopause.

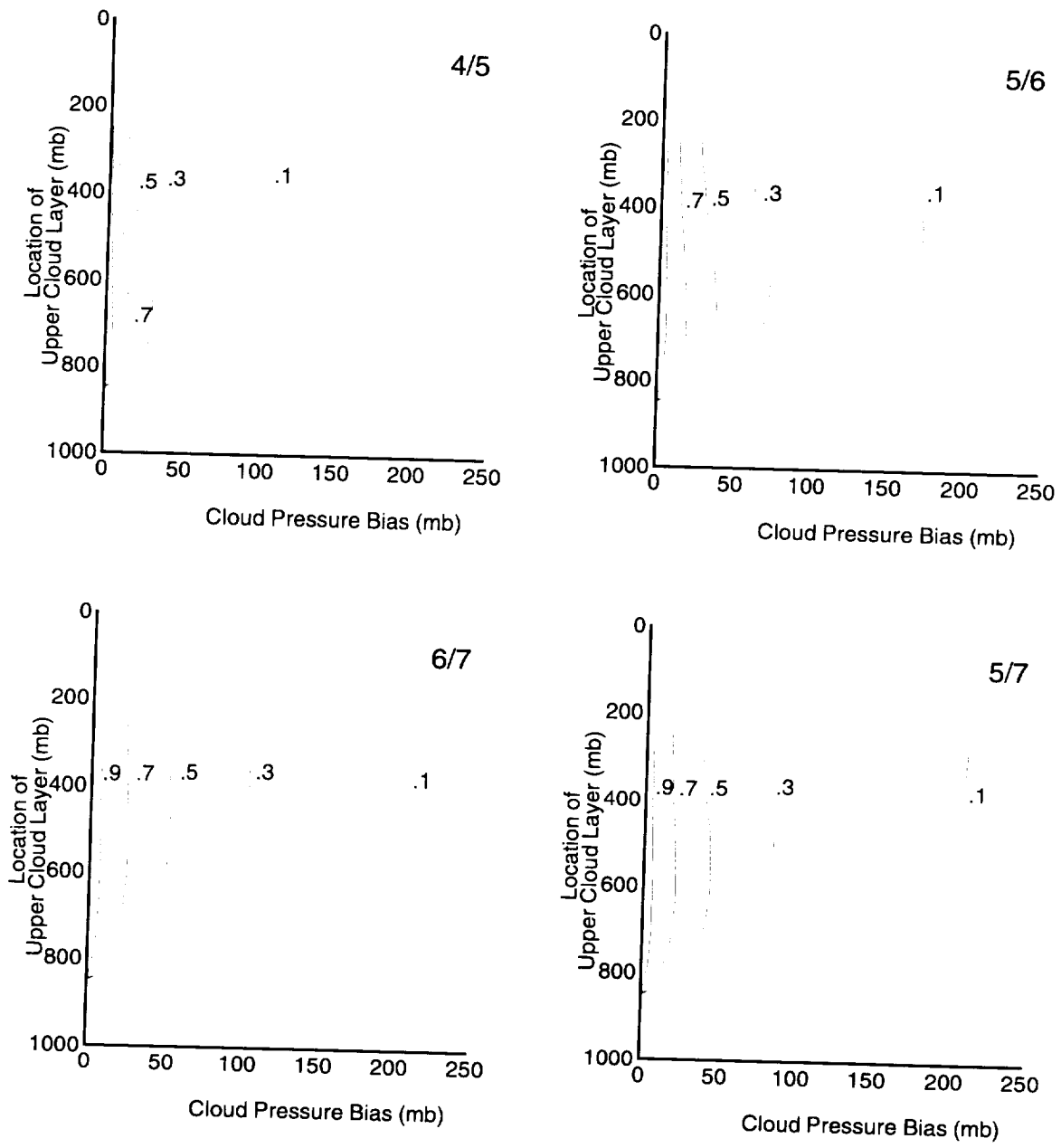


Figure 4.2-21. Multilevel cloud pressure retrieval bias errors (mb) for several  $\epsilon_{uc} C_{uc}$  as a function of the pressure of the upper transmissive cloud layer. Results are presented for the HIRS 4/5, 5/6, 6/7, and 5/7 channel ratio combinations. The opaque lower cloud-top pressure is held constant at 850 mb.

Wielicki and Coakley (1981) examined the rms and bias errors in cloud-top pressure retrieval for single-level clouds. In their study, the instrument noise was assumed to be Gaussian with zero mean and a standard deviation of  $0.22 \text{ mWm}^{-2}\text{sr}^{-1}\text{cm}$  for the HIRS  $15\text{-}\mu\text{m}$  channels. It is anticipated that the instrument noise should be significantly lower (by more than a factor of 2) for the MODIS instrument. The VAS instrument, by comparison, has a much higher instrument noise of approximately  $1.0 \text{ mWm}^{-2}\text{sr}^{-1}\text{cm}$ .

The  $\text{CO}_2$  slicing technique cannot measure the properties of clouds where the contrast of radiation from cloud-free and cloud-obscured observations is too small for reliable discrimination in the satellite

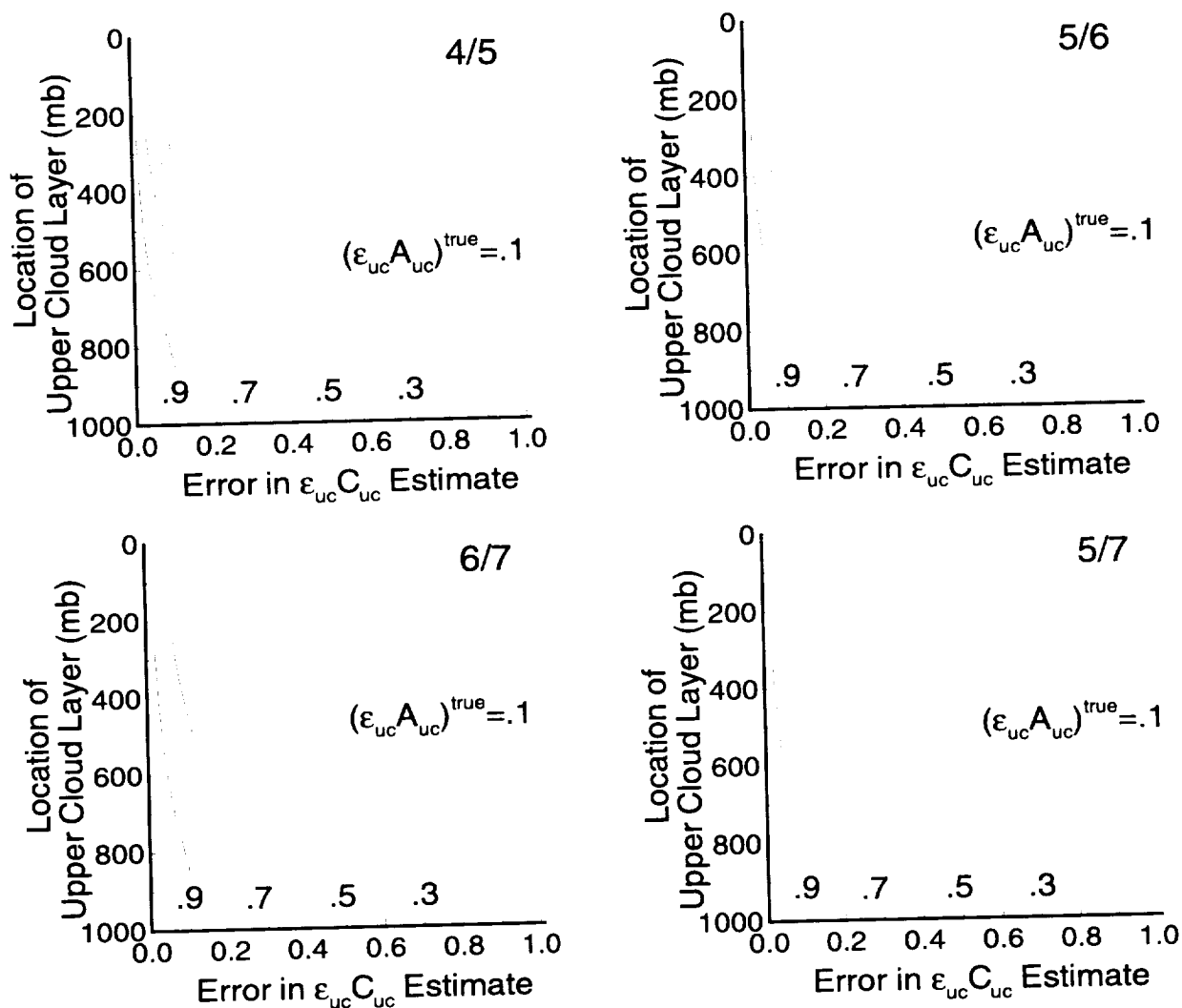


Figure 4.2-22. Upper-cloud effective cloud amount retrieval bias errors for several  $\epsilon_{uc} C_{uc}$  as a function of the pressure of the upper transmissive cloud layer. These results, derived from the pressure biases presented in Figure 4.2-21 are presented for the HIRS 4/5, 5/6, 6/7, and 5/7 channel ratio combinations. The opaque lower cloud-top pressure is held constant at 850 mb.

CO<sub>2</sub> spectral radiances. One could assign a threshold of perhaps 5 or 10 times the instrument noise as a threshold for further calculations, so that if the cloud signal falls below this threshold, the pixel is assumed clear (no clouds are retrievable). This threshold will not allow detection of very thin cirrus, such as subvisual cirrus, or low clouds below approximately 700 hPa.

**4.2.4.7.5. Errors caused by uncertainties in temperature profiles and water vapor profiles.** For single-level mid- to high-level clouds, the retrieval methods under study must first specify both clear-sky radiances,  $I_{cs}$ , and overcast black radiances,  $I_{ob}(P_{cld})$ , before cloud properties can be retrieved. Temperature errors affect the Planck functions  $B(T)$  and to a lesser extent the weighting functions  $dt/d \ln P$ . Water vapor errors affect only the weighting functions  $dt/d \ln P$ . Wielicki and Coakley (1981) evaluated errors caused by profile uncertainties by assuming the errors were Gaussian with zero mean. Errors were specified independently for each pressure level. Water vapor errors were specified as a percent of the correct mixing ratio at any level. Temperature error was found to dominate the retrieval error. Errors caused by uncertainties in temperature profiles and water vapor profiles dominated errors caused by instrument

noise for temperature rms errors of greater than or equal to 1.5 K for the HIRS 6/7 channel combination, for example. The errors were similar for all channel combinations. Retrieval errors were linearly proportional to temperature error and were inversely proportional to the cloud signal. For instrument noise, the lowest sounding channels (HIRS 6/7) give the smallest errors (Wielicki and Coakley, 1981).

#### 4.2.4.8. Practical Considerations

**4.2.4.8.1. Data dependencies of CO<sub>2</sub> slicing algorithm.** The CO<sub>2</sub> slicing algorithm requires calibrated, navigated, co-registered radiances from the channels listed in Table 1. Navigation implies knowledge of the surface terrain, which will be available from other sources such as the Defense Mapping Agency's Digital Chart of the World. Characteristics required of the surface include surface elevation, land/water percentage, and vegetation type. These data sets are described more fully in section 4.1. The MODIS, GOES, or HIRS viewing angles must be known. The NMC global model estimates of surface temperature, pressure, and profiles of temperature and moisture will be used in the calculation of the upper cloud-top height and effective emittance.

#### 4.2.4.9. Strategic Concerns

There are several concerns (or assumptions) in the CO<sub>2</sub> slicing cloud-retrieval method. First, the temperature and humidity estimates will be obtained from the NMC operational product on a fairly coarse horizontal grid (probably about 100 km) at fixed time intervals of 6 or 12 hours. Second, we assume that the frame is likely to have clouds with relatively stable cloud top altitudes, with at least some possibilities of seeing the ground nearby. Under these assumptions, both the clear-sky and cloudy-sky radiance profiles may be precomputed for each 1.25° grid cell once the temperature and humidity data are received and quality checked. This procedure may be performed for each of the potential channels and for the range of viewing zenith angles. If data are available from a simultaneous satellite swath of temperature and humidity retrievals, such as from AIRS/AMSU, then these computations could be performed at more frequent space and time points. Even with AIRS, the temperature and humidity points will be widely spaced with respect to the high-resolution imager data available for cloud retrieval.

We can list a number of sources of difficulty with this algorithm:

1. Temperature inversions induce an ambiguity in  $p_{cld}$ .
2. Height of cloud should not be far below the peak of the upper channel weighting function for the ratio method.
3. Algorithm does not work when signal/noise ratio becomes too small (a signal less than 10 times the signal noise is a reasonable initial estimate of this threshold).
4. Multichannel retrievals may not produce consistent values of  $p_{cld}$  or  $\epsilon_{cld}^i C$ .
5. Multilevel clouds in a given FOV are not included in the assumptions of this method.
6. Presence of nonuniform cloud in FOV (e.g., some black clouds mixed with thin, low-emittance cloud) will cause ambiguities in  $p_{cld}$  and  $\epsilon_{cld}^i C$ .
7. Algorithm assumes cloud is in a thin layer, so that the retrieval of cloud-top pressure is problematic for an optically thin cloud that has a large geometric thickness.
8. Instrument calibration errors cause some systematic shifts in cloud property retrievals.
9. Instrument spectral bandpass shifts will create errors.
10. Algorithm assumes that the emittances of clouds in any two closely spaced channels in the ratio method have nearly equal values.

11. Algorithm assumes clouds do not scatter in the IR.
  12. Weighting functions depend on the input temperature and humidity profiles and upon the assumed mixing ratios of trace gases.
  13. The accuracy of the retrieved cloud pressure depends on accuracy of the clear-sky radiance.
- These potential error sources have been discussed in previous sections and, although it is important to understand and minimize them, they are generally well-known and accepted in the field of study. The implementation of the algorithm will have exception-handling logic to handle potential problems.

#### **4.2.5. Other Strategies for Detection and Analysis of Multilayered Clouds**

##### **4.2.5.1. Overview**

Most of the current validation studies being performed from FIRE, ASTEX, TOGA-COARE, etc. are mainly concerned with analyzing clouds that appear in a single layer. Unfortunately, the analysis of overlapping cloud layers remains largely unexplored. Surface observations and satellite imagery show that multilayered cloud systems are commonly found in frontal areas where cirrus overlaps altostratus or stratus cloud. A summary of 12 years (1965–1976) of ship-reported synoptic observations (Hahn et al., 1982), over the North Atlantic Ocean shows that cirrus clouds have a frequency of occurrence between 20% and 45%, depending on season and location. The frequency of stratus co-occurrence with cirrus is often greater than 50% between 30°N and 60°N, also depending upon season and location. In the same latitude band, the probability of finding cirrus over ocean with no other cloud present is usually less than 20%. These findings are supported by Tian and Curry (1989) in a study of cloud overlap statistics performed using Air Force three-dimensional nephelometry during January 1979 over the North Atlantic Ocean. Given the relatively high probability of finding cirrus with other cloud types and the low probability of finding cirrus alone, we must develop methodologies to infer the vertical cloud structure prevalent over both land and oceans. This work has been initiated using data from the HIRS and AVHRR instruments aboard the National Oceanic and Atmospheric Administration (NOAA) operational satellite platforms (Kidwell 1991).

Another approach we will use for the Version 1 CERES cloud retrieval algorithm is to apply automated feature recognition techniques as described in Subsystem 4.1. Automated artificial intelligence techniques, principally the fuzzy logic cloud classifier, will be applied to the imager data to place the clouds in a larger context than would be gained from application of the algorithms described previously in this document. Another approach to classifying certain cloud types is provided by Phase II of the CLAVR algorithm. CLAVR-II will have some logic designed to type clouds as belonging to low stratus, thin cirrus, deep convective, or middle mixed. The middle mixed category is where cloud types will be placed that do not belong to the low stratus, thin cirrus, or deep convective categories. As new techniques are developed, they will be tested along with the other typing approaches to determine the strengths and weaknesses of each approach.

##### **4.2.5.2. Midlatitude Multiple Layer Cloud Classification**

Preliminary work has been initiated on classifying cloud scenes that contain overlapping cloud layers using a fuzzy logic classification system. Data used for the study (Baum et al. 1995) were taken from the First ISCCP Regional Experiment (FIRE) experiment held in Kansas during the fall of 1991. The daytime midlatitude scene classification system currently separates pixel subarrays into the following classes:

1. Water
2. Land
3. Low cloud

4. Mid-level cloud
5. High cloud
6. Multiple cloud layers

Snow is currently not included in this scheme. The training of the classifier was performed using 1-km resolution AVHRR data and has not been modified yet for the lower 4-km resolution GAC data. Future work will concentrate on developing the classification methodology for nighttime imagery, snow/ice covered surfaces and classification over desert regions. Present work concentrates on determining whether the broad cloud classes can be broken into more classes. For instance, we need to determine whether the low cloud class can be split into uniform stratus and stratocumulus classes; whether the mid-level cloud class may be split into altostratus and altocumulus classes, etc. It may also be useful to determine whether a cloud type is deeply convective or precipitating. The textural and spectral features used in Baum et al. (1995) for midlatitude cloud classification are shown in Table 4.1-2.

A description of the features may be found in Volume 4.1, section 4.1.3. This set of features was developed using data collected during the First ISCCP Regional Experiment held in Kansas in the fall of 1991. There was an extensive set of surface observations, rawinsondes, and other ancillary data to aid in scene analysis. This classification system has been applied to clouds embedded in air masses ranging from tropical to subpolar, but has yet to be modified and tested thoroughly to determine how robust the technique is for cloud layers occurring at other locations and during other seasons.

#### **4.2.5.3. Determination of Cloud Height for Overlapping Cloud Layers**

Imager pixels are identified as cloudy and clear as per Section 4.1. Uniform cloud layer properties such as temperature, pressure, and height are derived using such techniques as spatial coherence and CO<sub>2</sub> slicing. Imager data swath analysis occurs on several spatial scales. For example, the spatial coherence scheme discussed in Section 4.3 first operates on approximately a 250 km × 250 km scale, then on a smaller 50 km × 50 km scale. The HBTM scheme typically operates on groups of pixels on the 64 km × 64 km scale. The CO<sub>2</sub> slicing technique as used with the HIRS 15-μm data typically operates on each FOV, or about every 40 km (accounting for the distance between individual FOVs). In this section, we discuss a method to assign a cloud pressure for each of up to two cloud layers in each imager pixel from the analysis performed with these varying spatial scales.

When the cloud in an imager pixel is opaque, only one cloud layer is assigned to that pixel. The difficulties arise when cloud layers are transmissive, such as cirrus. Once the well-defined cloud layers have been identified using the methodologies outlined in the previous sections, the task is now to assign cloud pressures for the pixels that have more than one layer of cloud or in which the cloud layer is not opaque. Recall that textural classification occurs for 32 × 32 or 16 × 16 pixel arrays, and that the classification suggested by Stowe et al. (1991) operates on 2 × 2 arrays. In neither case is classification performed on the scale of an individual pixel. If, however, the classification procedures indicate the possibility of there being more than one cloud layer, each pixel within the classification subarray will be tagged as containing overlapping cloud layers. The upper and lower layer cloud-top pressures assigned to each pixel will be derived over a scale ranging from 40 km to 250 km, depending on the algorithm.

Baum et al. (1992) describe a multispectral, multiresolution (MSMR) methodology for analyzing collocated AVHRR and HIRS data. The CO<sub>2</sub> slicing technique called the ratio method (Smith and Platt 1978; Wielicki and Coakley 1981; Menzel et al. 1992) was applied to HIRS 15-μm radiometric data to infer mid- to high-level cirrus cloud pressure and effective emittances,  $\epsilon C$ . In a subsequent case study analysis of nighttime cirrus overlying a stratus layer over the mid-Atlantic Ocean, Baum et al. (1994) incorporated a spatial coherence technique (Coakley and Bretherton 1982; Coakley 1983) into the MSMR method for the retrieval of stratus cloud-top heights. Further detailed description of the CO<sub>2</sub> slicing and spatial coherence techniques are provided in sections 4.2.2 and 4.2.4 of this document.

Table 4.2-2. Spectral and Textural Features Chosen for Daytime Classification of NOAA-11 and NOAA-12 1-km Radiometric Data (Baum et al. 1995); Descriptions of Features are Provided in Text; for Channel 3, Further Specification is Made Between Measured Radiances (Converted to Brightness Temperature  $T_{B3}$ ) and Reflectances ( $\rho_3$ ) Determined by Subtracting Thermal Emission.

Feature	Type
Contrast $\rho_1$	Textural
Contrast $\rho_2$	Textural
Contrast $T_{B3}$	Textural
Contrast $\rho_3$	Textural
Homogeneity $\rho_1$	Textural
Mean $\rho_3$	Textural
Band difference [ $\rho_1 - \rho_2$ ]	Spectral
Band difference [ $T_{B3} - T_{B4}$ ]	Spectral
Band difference [ $\rho_2 - \rho_3$ ]	Spectral
Ratio [ $\rho_1/\rho_2$ ]	Spectral
Ratio [ $T_{B3}/T_{B4}$ ]	Spectral
Ratio [ $T_{B4}/T_{B5}$ ]	Spectral
Ratio [ $\rho_1/T_{B4}$ ]	Spectral
Overlay [ $\rho_1, T_{B3}, T_{B4}$ ]	Spectral
Low $\rho_3$	Spectral
High $\rho_3$	Spectral
Spatial coherence $\rho_2$	Spectral
Spatial coherence $T_{B4}$	Spectral

A schematic of the MSMR processing method is shown in Figure 4.2-23. There are three input data streams consisting of satellite data, temperature and relative humidity profiles, and a global geomap as described in Subsystem 4.1, section 4.1.4.1. The geomap provides surface elevation and land/water percentage at 10-minute resolution (approximately 18 km in the midlatitudes). To reduce the remote sensing errors, two modules have been incorporated into the MSMR method. The first module provides meteorological analysis based upon rawinsonde data and/or gridded NMC model analyses. The second module is an automated cloud classification method. The cloud classification process provides additional insight as to whether one or more cloud layers are present in a  $32 \times 32$  AVHRR array. For the multilayered cloud case study reported in Baum et al. (1995), the cloud heights calculated from application of the MSMR methodology agreed reasonably well with coincident lidar, radar, and aircraft data. For those  $32 \times 32$  AVHRR arrays that are tagged as containing more than one cloud class, each of the pixels will be tagged as belonging possibly to an overlapping cloud layer. Further resolution of the degree or nature of the overlapping clouds will be resolved by comparing the measured radiances with theoretical calculations as outlined in Subsystem 4.3. This work is in its beginning stages, and much more progress is anticipated between now and the TRMM launch.

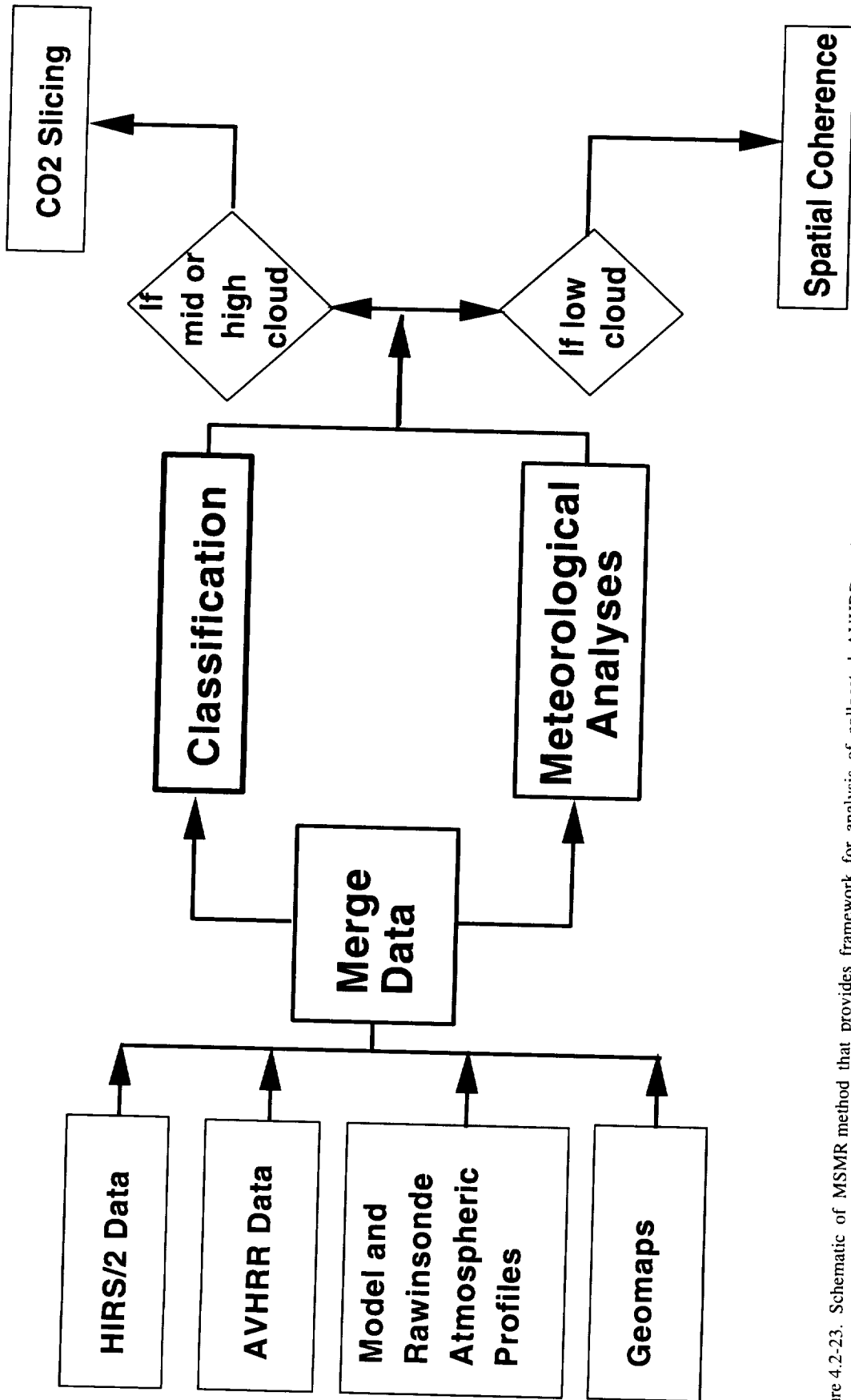


Figure 4.2-23. Schematic of MSMR method that provides framework for analysis of collocated AVHRR and HIRS data. The scheme has been developed to detect and analyze multiple cloud layers

## Appendix

### Analog Model for Pixel Clustering

The minimum number of points required in a peak of the  $\rho(l)$  distribution for the set of points to be characterized as being clustered is established as follows. A Gaussian distribution is taken to be an example of a distribution that is sharply peaked and clearly nonuniform. The null hypothesis is that the points distributed according to a Gaussian distribution are indistinguishable from those distributed according to a uniform distribution. The interval over which the test is applied is divided into three equal parts. For a distribution of points to be classified as being nonuniform or highly concentrated, the number of points within the center interval must satisfy the condition given by

$$N > \frac{M}{3} + \sqrt{2M} \quad (\text{A1})$$

where  $M$  is the number of points within the three intervals. In (A1),  $N$  is greater than three times the number of points that would be expected in the central interval were the points to be uniformly distributed over the three intervals. If the points are distributed according to a gaussian distribution so that the central interval spanned one standard deviation on either side of the mean and the outer intervals spanned an additional two standard deviations, then the above criteria would be satisfied when

$$\text{erf}(y) > \frac{1}{3}\text{erf}(3y) + \sqrt{\frac{2\text{erf}(3y)}{M}} \quad (\text{A2})$$

where

$$y = \frac{1}{2\sqrt{2}} = 0.354 \quad (\text{A3})$$

The condition is satisfied when  $M > 18.03$ . Thus, there must be ~20 pixels within three standard deviations on either side of a peak for the peak to satisfy the condition. If there are fewer pixels within the interval, then the number within one standard deviation of the mean, as given by a gaussian distribution, would not be more than three standard deviations above the number expected from a uniform distribution.

## References

- Arking, A.; and Childs, J. D. 1985: Retrieval of Cloud Cover Parameters From Multispectral Satellite Images. *J. Climat. & Appl. Meteorol.*, vol. 24, pp. 322–333.
- Baum, B. A.; Uttal, T.; Poellot, M.; Ackerman, T. P.; Alvarez, J.; Intrieri, J.; Starr, D. O'C; Titlow, J.; Tovinkere, V.; and Clothiaux, E. 1995: Satellite Remote Sensing of Multiple Cloud Layers. *J. Atmos. Sci.*, vol. 52, no. 23, pp. 4210–4230.
- Baum, Bryan A.; and Wielicki, Bruce A. 1994: Cirrus Cloud Retrieval Using Infrared Sounding Data—Multilevel Cloud Errors. *J. Appl. Meteorol.*, vol. 33, no. 1, pp. 107–117.
- Baum, Bryan A.; Wielicki, Bruce A.; Minnis, Patrick; and Parker, Lindsay 1992: Cloud-Property Retrieval Using Merged HIRS and AVHRR Data. *J. Appl. Meteorol.*, vol. 31, pp. 351–369.
- Chahine, M. T. 1974: Remote Sounding of Cloudy Atmospheres. I—The Single Cloud Layer. *J. Atmos. Sci.*, vol. 31, pp. 233–243.
- Chang, Fu-Lung; and Coakley, James A., Jr. 1993: Estimating Errors in Fractional Cloud Cover Obtained With Infrared Threshold Methods. *J. Geophys. Res.*, vol. 98, no. D5, pp. 8825–8839.
- Coakley, J. A., Jr.; and Bretherton, F. P. 1982: Cloud Cover From High-Resolution Scanner Data—Detecting and Allowing for Partially Filled Fields of View. *J. Geophys. Res.*, vol. 87, pp. 4917–4932.
- Coakley, J. A., Jr. 1983: Properties of Multilayered Cloud Systems From Satellite Imagery. *J. Geophys. Res.*, vol. 88, pp. 10818–10828.
- Coakley, J. A., Jr.; and Baldwin, D. G. 1984: Towards the Objective Analysis of Clouds From Satellite Imagery Data. *J. Climat. & Appl. Meteorol.*, vol. 23, pp. 1065–1099.
- Debois, M.; Seze, G.; and Szejwach, G. 1982: Automatic Classification of Clouds on METEOSAT Imagery—Application to High-Level Clouds. *J. Appl. Meteorol.*, vol. 21, pp. 401–412.
- Eyre, J. R. 1991: *A Fast Radiative Transfer Model for Satellite Sounding Systems*. ECMWF Tech. Memo. No. 176.
- Eyre, Jonathan R.; and Menzel, W. Paul 1989: Retrieval of Cloud Parameters From Satellite Sounder Data—A Simulation Study. *J. Appl. Meteorol.*, vol. 28, pp. 267–275.
- Eyre, Jonathan R.; and Woolf, Harold M. 1988: Transmittance of Atmospheric Gases in the Microwave Region—A Fast Model. *Appl. Opt.*, vol. 27, pp. 3244–3249.
- Hahn, C. J. 1982: *Atlas of Simultaneous Occurrence of Different Cloud Types Over the Ocean*. NCAR Tech. Note TN-201.
- Jacobowitz, Herbert 1971: Emission, Scattering and Absorption of Radiation in Cirrus Cloud Layers. Ph.D Thesis, Massachusetts Inst. Tech.
- Kidwell, K. B. 1991: *NOAA Polar Orbiter Data Users Guide*. NOAA National Climatic Data Center, Satellite Data Services Div.
- King, Michael D.; Kaufman, Yoram J.; Menzel, W. Paul; and Tanre, Didier D. 1992: Remote Sensing of Cloud, Aerosol, and Water Vapor Properties From the Moderate Resolution Imaging Spectrometer (MODIS). *IEEE Trans. Geosci. & Remote Sens.*, vol. 30, pp. 2–27.
- Lin, X; and Coakley, J. A. 1993: Retrieval of Properties for Semitransparent Clouds From Multispectral Infrared Imagery Data. *J. Geophys. Res.*, vol. 98, pp. 18,501–18,514.
- McCleese, D. J.; and Wilson, L. W. 1976: Cloud Top Heights From Temperature Sounding Instruments. *Q. J. R. Meteorol. Soc.*, vol. 102, pp. 781–790.
- McCormick, M. P.; Winker, D. M.; Browell, E. V.; Coakley, J. A.; Gardner, C. S.; Hoff, R. M.; Kent, G. S.; Melfi, S. H.; Menzies, R. T.; and Platt, C. M. R. 1993: Scientific Investigations Planned for the Lidar In-Space Technology Experiment (LITE). *Bul. Am. Meteorol. Soc.*, vol. 74, no. 2, pp. 205–214.
- McMillin, L. M.; and Fleming, H. E. 1976: Atmospheric Transmittance of an Absorbing Gas—A Computationally Fast and Accurate Transmittance Model for Absorbing Gases With Constant Mixing Ratios in Inhomogeneous Atmospheres. *Appl. Opt.*, vol. 15, pp. 358–363.
- Menzel, W. P.; Smith, W. L.; and Stewart, T. R. 1983: Improved Cloud Motion Wind Vector and Altitude Assignment Using VAS. *J. Climat. Appl. Meteorol.*, vol. 22, pp. 377–384.

- Menzel, W. P.; Wylie, D. P.; and Strabala, K. L. 1992: Seasonal and Diurnal Changes in Cirrus Clouds as Seen in Four Years of Observations With the VAS. *J. Appl. Meteorol.*, vol. 31, pp. 370–385.
- Minnis, P.; and Harrison, E. F. 1984: Diurnal Variability of Regional Cloud and Clear-Sky Radiative Parameters Derived From GOES Data. Part I: Analysis Method. Part II: November 1978 Cloud Distributions. Parts I–III, *J. Climat. & Appl. Meteorol.*, vol. 23, pp. 993–1051.
- Minnis, Patrick; Harrison, Edwin F.; and Gibson, Gary G. 1987: Cloud Cover Over the Equatorial Eastern Pacific Derived From July 1983 International Satellite Cloud Climatology Project Data Using a Hybrid Bispectral Threshold Method. *J. Geophys. Res.*, vol. 92, pp. 4051–4073.
- Minnis, Patrick; Harrison, Edwin F.; and Heck, Patrick W. 1990: The 27–28 October 1986 FIRE IFO Cirrus Case Study—Cloud Parameter Fields Derived From Satellite Data. *Mon. Weather Rev.*, vol. 118, pp. 2426–2446.
- Minnis, Patrick; Heck, Patrick W.; Young, David F.; Fairall, C. W.; and Snider, J. B. 1992: Stratocumulus Cloud Properties Derived From Simultaneous Satellite and Island-Based Instrumentation During FIRE. *J. Appl. Meteorol.*, vol. 31, pp. 317–339.
- Minnis, Patrick; Liou, Kuo-Nan; and Takano, Yoshihide 1993: Inference of Cirrus Cloud Properties Using Satellite-Observed Visible and Infrared Radiances. I—Parameterization of Radiance Fields. *J. Atmos. Sci.*, vol. 50, no. 9, pp. 1279–1304.
- Minnis, Patrick; Heck Patrick W.; and Young, David F. 1993: Inference of Cirrus Cloud Properties Using Satellite-Observed Visible and Infrared Radiances. II—Verification of Theoretical Cirrus Radiative Properties. *J. Atmos. Sci.*, vol. 50, no. 9, pp. 1305–1322.
- Platt, C. M. R. 1983: On the Bispectral Method for Cloud Parameter Determination From Satellite VISSIR Data—Separating Broken and Semitransparent Cloud. *J. Climat. Appl. Meteorol.*, vol. 22, pp. 429–439.
- Reynolds, D. W.; and Vonder Haar, T. H. 1977: A Bi-Spectral Method for Cloud Parameter Determination. *Mon. Weather Rev.*, vol. 105, pp. 446–457.
- Rossow, W. B.; Mosher, F.; Kinsella, E.; Arking, A.; and Harrison, E. 1985: ISCCP Cloud Algorithm Intercomparison. *J. Climat. & Appl. Meteorol.*, vol. 24, pp. 877–903.
- Rossow, William B.; and Garder, Leonid C. 1993: Cloud Detection Using Satellite Measurements of Infrared and Visible Radiances for ISCCP. *J. Climat.*, vol. 6, no. 12, pp. 2341–2369.
- Shenk, W. E.; and Salomonson, V. V. 1972: A Simulation Study Exploring the Effects of Sensor Spatial Resolution on Estimates of Cloud Cover From Satellites. *J. Appl. Meteorol.*, vol. 11, pp. 214–220.
- Smith, W. L.; and Platt, C. M. R. 1978: Comparison of Satellite-Deduced Cloud Heights With Indications From Radiosonde and Ground-Based Laser Measurements. *J. Appl. Meteorol.*, vol. 17, pp. 1796–1802.
- Smith, W. L.; and Frey, R. 1990: On Cloud Altitude Determinations From High Resolution Interferometer Sounder (HIS) Observations. *J. Appl. Meteorol.*, vol. 29, pp. 658–662.
- Stowe, L. L.; McClain, E. P.; Carey, R.; Pellegrino, P.; and Gutman, G. G. 1991: Global Distribution of Cloud Cover Derived From NOAA/AVHRR Operational Satellite Data. *Adv. Space Res.*, vol. 11, no. 3, pp. 51–54.
- Takano, Yoshihide; and Liou, Kuo-Nan 1989: Solar Radiative Transfer in Cirrus Clouds. I—Single-Scattering and Optical Properties of Hexagonal Ice Crystals. *J. Atmos. Sci.*, vol. 46, pp. 3–20.
- Tian, Lin; and Curry, Judith A. 1989: Cloud Overlap Statistics. *J. Geophys. Res.*, vol. 94, pp. 9925–9935.
- Weinreb, M. P. 1981: *Transmittances for the TIROS Operational Vertical Sounder*. NOAA Tech. Rep. No. NESS-85.
- Wielicki, B. A.; and Coakley, J. A., Jr. 1981: Cloud Retrieval Using Infrared Sounder Data—Error Analysis. *J. Appl. Meteorol.*, vol. 20, pp. 157–169.
- Wielicki, Bruce A.; and Parker, Lindsay 1992: On the Determination of Cloud Cover From Satellite Sensors—The Effect of Sensor Spatial Resolution. *J. Geophys. Res.*, vol. 97, no. D12, pp. 12799–12823.
- Wyle, D. P.; and Menzel, W. P. 1989: Two Years of Cloud Cover Statistics Using VAS. *J. Climat.*, vol. 2, pp. 380–392.

**Clouds and the Earth's Radiant Energy System (CERES)**

**Algorithm Theoretical Basis Document**

***Cloud Optical Property Retrieval***

***(Subsystem 4.3)***

Patrick Minnis<sup>1</sup>

David P. Kratz<sup>1</sup>

James A. Coakley, Jr.<sup>2</sup>

Michael D. King<sup>3</sup>

Donald Garber<sup>4</sup>

Patrick Heck<sup>4</sup>

Shalini Mayor<sup>4</sup>

W. L. Smith, Jr.<sup>4</sup>

David F. Young<sup>4</sup>

Robert Arduini<sup>5</sup>

<sup>1</sup>Atmospheric Sciences Division, NASA Langley Research Center, Hampton, Virginia 23681-0001

<sup>2</sup>Oregon State University, Corvallis, Oregon 97331-2209

<sup>3</sup>Goddard Space Flight Center, Greenbelt, Maryland 20771

## Abstract

*Cloud physical and optical properties determine how clouds affect the radiance and flux fields at the surface, within the atmosphere, and at the top of the atmosphere. In this subsystem, CERES analyzes individual pixel radiances to derive the cloud properties that influence the radiation fields. For each pixel, state-of-the-art methods are used to ascertain the temperatures and pressures corresponding to the cloud top, base, and effective radiating center; the phase and effective size of the cloud particles; the cloud optical depth at a wavelength of 0.65  $\mu\text{m}$ ; the cloud emittance at 10.8  $\mu\text{m}$ ; and the cloud liquid or ice water path. During daytime, three different techniques will be used to account for deficiencies in any one of the individual methods. The first method uses 0.65-, 3.75-, and 10.8- $\mu\text{m}$  data from VIRS, AVHRR, or MODIS data. It iteratively solves for phase, particle size, optical depth, and effective cloud temperature. Emittance is computed from the optical depth. Cloud top and base temperatures and pressures are estimated using empirical formulae based on field experiment data. The water path is computed from the particle size. The second technique uses the similarity principle with a combination of 0.65-, 1.6-, and 2.12- $\mu\text{m}$  reflectance data to derive phase, particle size, and optical depth. Cloud temperature is determined by correcting the observed 10.8- $\mu\text{m}$  brightness temperature for semitransparency using the retrieved optical depth. The other parameters are computed in the same manner used for the first method. This approach will be partially implemented for VIRS and AVHRR and will be fully operational for MODIS. VIRS and AVHRR lack the 2.12- $\mu\text{m}$  channel that is available on MODIS. The third technique uses 3.75-, 10.8-, and 12.0- $\mu\text{m}$  data to determine cloud temperature, optical depth, phase, and particle size for optically thin clouds. This last daytime method will be used mainly for shadowed clouds and thin clouds over highly reflective backgrounds. It also forms the primary method for nighttime analyses. A second nighttime analysis is used for estimating an effective size and temperature for pixel clusters. Optical depth and cloud fraction are computed for individual pixels. All of the methods currently in development will become operational for application to CERES/TRMM. Results of this subsystem will be validated using coincident datasets from field programs. The required correlative data for validation include surface and aircraft measurements of the subsystem parameters using lidars, radars, in situ microphysical probes, microwave radiometers, and sunphotometers.*

### 4.3. Cloud Optical Property Retrieval Subsystem

#### 4.3.1. Introduction

Cloud microphysics, phase and particle shape and size distribution determine the cloud optical depth and ice or liquid water path when integrated over the cloud thickness. These properties affect the emittance and bidirectional reflectance of the cloud. Cloud microphysics and macrophysics (areal extent, thickness, and altitude) determine the amount of radiation transmitted to the surface or to a lower atmospheric layer and the amount of absorption within the cloud layer. Therefore, the conversion of the

CERES radiances to flux, especially for the solar channel, depends on the cloud microphysics. Computation of the transmitted fluxes for the CERES estimation of atmospheric radiative divergence or surface heating also requires a quantification of the microphysical parameters.

From a climate perspective, it is important to know the global and climatological variability of cloud microphysical properties and to be able to relate them to radiative fluxes and cloud macrophysical properties. As an example, there is considerable interest in determining whether anthropogenic sources of cloud condensation nuclei significantly change the Earth radiation balance by altering the microphysical characteristics of clouds (e.g., Twomey 1977; Charlson et al. 1987; Wigley 1989). Such issues and how they may affect future climates can only be addressed through modeling studies. In climate models, such as GCM's, water vapor is condensed or frozen in a given time step. This mass of water releases latent heat and alters the radiative flux fields. The cloud particle size distribution, phase, and shapes determine how the cloud affects the flow of radiation. The particle size distribution, which can be expressed in terms of an effective radius or diameter, primarily affects the scattering and absorption efficiencies of the cloud particles (van de Hulst 1957) and defines the cross section normal to the incident flux. Particle shape primarily affects the scattering phase function which ultimately determines how radiation is reflected from the cloud. Water phase governs the basic absorption properties and affects the scattering phase function through its relation to particle shape and through the index of refraction. To produce realistic clouds and radiation fields, a GCM must condense or freeze water in the proper locations and then must distribute the mass into the correct particle sizes and shapes. Some current GCM's employ parameterizations of radiation dependence on cloud particle size (e.g., Slingo 1989). The CERES measurements, the most complete simultaneous global observations of cloud microphysics and radiative fluxes yet proposed, will serve as an essential ground truth set to ensure that climate models accurately perform this critical function.

The CERES Cloud Optical Property Retrieval Subsystem (COPRS) will employ state-of-the-art methods to analyze the relevant spectral radiances available from the VIRS, MODIS, and AVHRR instruments operating during the CERES era. The primary goal of COPRS is to determine the phase, effective particle size, optical depth, liquid or ice water path, radiating temperature, pressure, and thickness of the cloud within a given CERES pixel. Although there are a wide variety of methods available, there is no single technique for deriving the COPRS products that applies in all cases. This subsystem uses state-of-the-art procedures to arrive at the most accurate values for each product. Thus, it will combine several algorithms to cover as many cases as possible. The composite algorithm described herein is a fluid entity subject to change as new research and/or limiting factors warrant.

#### 4.3.2. Background

There are numerous approaches to the satellite remote sensing of cloud phase, optical depth, and particle size. All of the methods are based on the assumption of radiative transfer in a plane-parallel cloud. These techniques exploit the spectral dependence of water and ice extinction, using wavelengths at which absorption by water vapor and other gases is minimal. The parameters used to characterize these variations include the wavelength  $\lambda$ , the spectral single-scattering albedo  $\tilde{\omega}_o = Q_s/Q_e$ , the asymmetry parameter  $g$ , the spectral optical depth  $\tau_\lambda$ , and the particle radius  $r$ . The extinction efficiency is  $Q_e = Q_s + Q_a$ . The scattering efficiency  $Q_s$  depends on the imaginary refractive index  $m_i$  and the size parameter  $x = 2\pi r/\lambda$ . For spherical particles and a given  $\lambda$ ,  $Q_s$  increases monotonically with  $x$  from zero to a maximum value near  $x = 6$ , then oscillates asymptotically to a smaller constant value. The oscillations are smoothed out when  $Q_s$  is integrated over a typical cloud droplet size distribution  $n(r)$ , in which  $r$  may vary from 2 to 100  $\mu\text{m}$ . The absorption efficiency  $Q_a$  and  $\tilde{\omega}_o$  follow a similar variation without the oscillations for  $m_i < 0.25$  (Hansen and Travis 1974), values held by water for  $\lambda < 12.5 \mu\text{m}$  (Hale and Querry 1973). The variation with  $x$  becomes more monotonic for larger values of  $m_i$ . The asymptotic values of  $Q_e$  and  $\tilde{\omega}_o$  for large particles are 2.0 and 0.53, respectively. The single-scattering albedo is

essentially 1.0 and  $Q_s$  varies by less than 20% for typical cloud particle sizes at the nearly conservative-scattering wavelengths spanning the visible spectrum ( $\lambda < 1.0 \mu\text{m}$ ). For near-infrared wavelengths ( $\lambda \sim 3 \mu\text{m}$ ) ice and liquid water become moderately absorbing and  $x$  ranges from about 3 to 150. Thus, there are significant changes in both  $Q_e$  (~50%) and  $\bar{\omega}_o$  (~26%) with changing particle size. At longer wavelengths, absorption is stronger, though still variable with particle size and wavelength.

The asymmetry parameter, which summarizes the scattering phase function, ranges from  $-1$  to  $1$ . Zero indicates isotropy,  $g = -1$  corresponds to backscattering, and  $g = 1$  denotes complete forward scattering. For any given particle shape,  $g$  generally increases with increasing particle size because of the narrowing diffraction peak. Smaller particles tend to scatter a greater portion of the incident radiation back into the source direction. The asymmetry parameter, which depends on both the real and imaginary refractive indices, varies nonmonotonically in a fashion similar to  $Q_s$ . There is a relative minimum in  $g$  for  $10 < x < 20$  and a relative maximum for  $4 < x < 10$ . Hansen and Travis (1974) may be consulted for additional details of the radiative properties of water droplets.

The spectral optical depth for a given size distribution over some distance is

$$\tau_\lambda = \pi Q_e \int_{z_1}^{z_2} N r_e^2 dz \quad (4.3-1)$$

where the effective radius is

$$r_e = \frac{\int_{r_1}^{r_2} r \pi r^2 n(r) dr}{\int_{r_1}^{r_2} \pi r^2 n(r) dr} \quad (4.3-2a)$$

$n(r)$  is the number density of droplets with radius  $r$ , and  $N$  is the total particle number density. To distinguish between water and ice clouds,  $r_e$  will be used for water clouds and the equivalent diameter

$$D_e = \frac{\int_{L_1}^{L_2} D(L) \pi A_e(L) n(L) dL}{\int_{L_1}^{L_2} \pi A_e(L) n(L) dL} \quad (4.3-2b)$$

will be used for ice clouds. The variable  $D(L)$  is the volume equivalent diameter of the hexagonal ice crystal of length  $L$  and width  $d$ . It is assumed that there is a monotonic relationship between  $L$  and  $d$  for the hexagonal ice columns defined by Takano and Liou (1989). This yields a unique relationship between the cross-sectional area  $A_e$  of these randomly oriented columns (Takano and Liou 1989) and  $L$ . The parameters,  $\tau_\lambda$ ,  $r_e$  or  $D_e$ ,  $\bar{\omega}_o$ , and  $g$  affect the radiation absorbed, reflected, transmitted, and emitted by a given cloud. The dependence of the radiation field on these variables can be simulated using radiative transfer calculations. Cloud effective particle size, optical depth, phase, and cloud temperature can be determined from satellite-measured multispectral radiances by matching the radiances to the computed radiative transfer results.

The basic techniques for determining cloud phase, optical depth, and effective particle size can be divided into two groups that overlap: reflection and emission techniques. The former applies during daytime and only employs solar wavelengths. Emission techniques generally are applicable during any time of day because they rely primarily on radiation emitted at infrared and near-infrared wavelengths.

### 4.3.2.1. Solar Reflectance Methods

The spectral bidirectional reflectance or, simply, reflectance is

$$\rho_{\lambda}(\tau_{\lambda}; \mu_o, \mu, \phi) = \frac{I_{\lambda}(\mu_o, \mu, \phi)}{\mu_o \pi E_o \lambda} \quad (4.3-3)$$

where  $E_{o\lambda}$  is the spectral solar irradiance and  $\mu_o$ ,  $\mu$ , and  $\phi$  are the solar zenith and viewing zenith angle cosines and the relative azimuth angles, respectively. Optical depth can be determined directly from the reflectance data in the absence of particle size information, if a particle size is specified. Rossow et al. (1985) assumed that all clouds can be interpreted as having  $r_e = 10 \mu\text{m}$ , an approach later used in the ISCCP analyses (Rossow et al. 1988) and in pre-ISCCP analyses of NOAA-5 SR data (Rossow et al. 1990). In those analyses, a value of  $\tau_{0.65}$  is determined by matching the 0.65- $\mu\text{m}$  (visible) reflectance to a set of model-generated reflectance tables developed for different cloud heights, surface albedos, and optical depths. Later analyses using FIRE data (Baum et al. 1992; Minnis et al. 1993a) indicated that significant improvement is obtained in the accuracy of the derived optical depths by using the hexagonal ice crystal phase functions of Takano and Liou (1989) for cirrus clouds. Minnis et al. (1993b) developed a parameterization that incorporated surface albedo and cloud height so that reflectance tables were only needed to account for optical depth. The gained computer storage space could be used to accommodate models with variable particle size.

A more accurate estimate of  $\tau_{\lambda}$  can be made if the particle size, shape, and phase are known. One of the earliest applications of a reflection method for this purpose was performed by Hansen and Pollack (1970) who attempted to explain the spectral variation in aircraft reflectivity measurements (Blau et al. 1966) in terms of phase and particle size using theoretical computations. Twomey and Seton (1980) showed theoretically that mean radius and optical depth could be determined for optically thick clouds using the scaled optical depth  $\tau_{\lambda}' = (1 - \tilde{\omega}_o' g) \tau_{\lambda}$  and the scaled single-scatter albedo  $\tilde{\omega}_o' = \tilde{\omega}_o (1 - g) / (1 - \tilde{\omega}_o g)$ . A measurement of reflectance at a conservative-scattering wavelength could be used to determine  $\tau_{\lambda}'$ , while  $r_e$  could be estimated using simultaneous measurements of reflectance at  $\lambda = 1.6$  or  $2.2 \mu\text{m}$ . Later comparisons of aircraft reflectance measurements and calculations at  $\lambda = 0.75, 1.0, 1.2,$  and  $2.25 \mu\text{m}$  were relatively unsuccessful in matching the data with theory at all four wavelengths simultaneously (Twomey and Cocks 1982). Twomey and Cocks (1989) utilized an improved instrument and a multispectral minimum difference method to match theory and measurements much more closely for the same wavelengths plus  $\lambda = 1.66 \mu\text{m}$ .

Coakley et al. (1987) and Radke et al. (1989) showed that reflectance measurements at  $3.7 \mu\text{m}$  could be used to detect ship tracks in marine stratus clouds because the droplet radii decreased in the portion of the cloud affected by the ship's exhaust. They also showed that an increase in the reflectance ratio,  $\rho_{0.74}/\rho_{2.2}$ , accompanied the decrease in radius measured with in situ probes. Using theoretical calculations at  $0.75, 1.65, 2.16,$  and  $3.70 \mu\text{m}$  and a minimum difference method employing the scaled optical depth  $\tau' = (1 - g)\tau$  and the similarity parameter  $s = [(1 - \tilde{\omega}_o)/(1 - \tilde{\omega}_o g)]^{1/2}$ , Nakajima and King (1990) showed that measurements of reflectance at  $0.75 \mu\text{m}$  and at either of the other wavelengths could be used to solve for  $r_e$  and  $\tau_{\lambda}$ . However, a third channel was found to be desirable for removing ambiguities arising from the nonmonotonic variation of  $\tilde{\omega}_o$  with  $r_e$ . They also found that the retrieved value of  $r_e$  corresponds to the effective radius for some upper portion of the cloud that depends on the cloud thickness. Thus,  $r_e$  requires some adjustment to estimate the effective radius for the entire cloud. Later analyses of aircraft observations at  $0.75, 1.65,$  and  $2.16 \mu\text{m}$  (Nakajima et al. 1991) over stratocumulus clouds produced excellent correlation between the remotely sensed, center-adjusted effective radii and the in situ particle sizes (Fig. 4.3-1). Although the remotely sensing analysis apparently overestimated  $r_e$ , the results clearly demonstrated the potential of this method. Further examination of the results indicated that the water vapor absorption at  $1.65$  and  $2.16 \mu\text{m}$  needed additional study and that there are some significant disagreements between the aircraft probes used to measure particle sizes in the clouds. Wielicki et al. (1990) estimated particle sizes for water and ice clouds from Landsat observations at

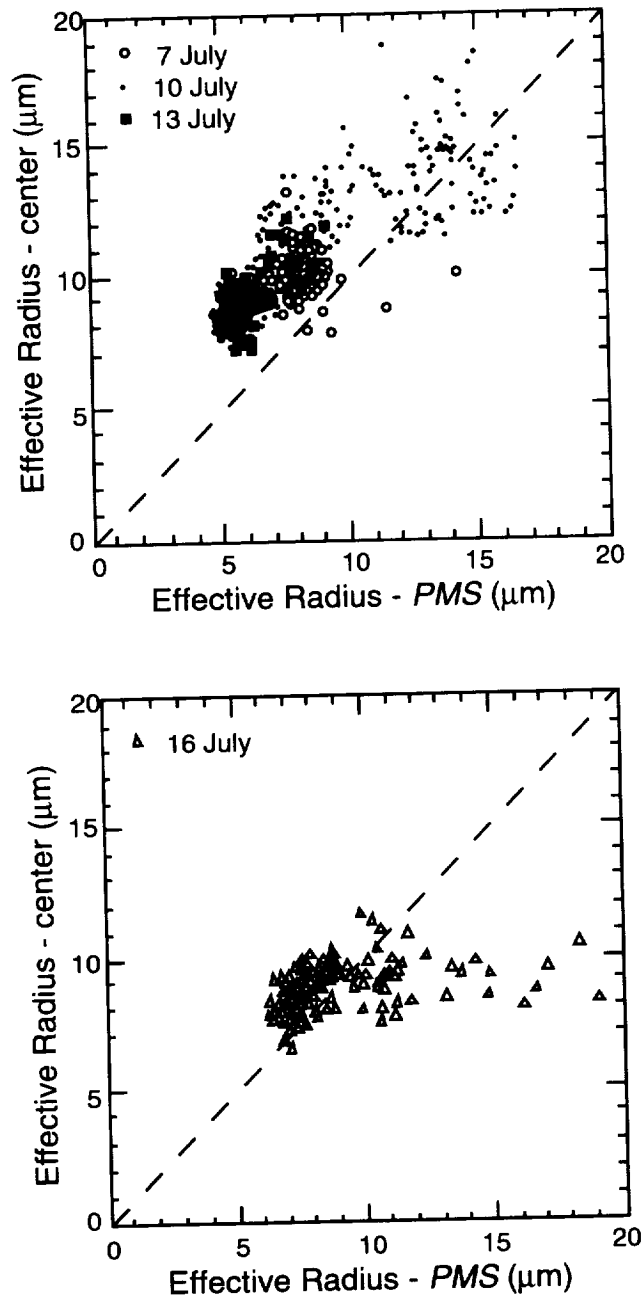


Figure 4.3-1. Effective radius derived from remote sensing and adjusted to center of cloud compared with values obtained from in situ measurements obtained using all three PMS probes. The top panel is based on ER-2 MCR measurements, while the bottom panel is from LANDSAT-5 TM data. All measurements were taken during 1987 off the coast of California during the FIRE Marine Stratocumulus Intensive Observing Period (adapted from Nakajima et al. 1991).

$\lambda = 0.83, 1.65, \text{ and } 2.21 \mu\text{m}$  by matching ratios of the reflectances to theoretical calculations. For water clouds, they found good agreement between the values of  $r_e$  derived from in situ data and the  $0.83\text{-}\mu\text{m}/2.21\text{-}\mu\text{m}$  reflectance ratios. Rawlins and Foot (1990) used reflectances from aircraft measurements at  $\lambda = 1.04, 1.24, 1.55, 2.01 \mu\text{m}$  to derive values of  $r_e$  that were 20% to 50% greater than their in situ counterparts. Differences between the in situ and remotely sensed data have not yet been entirely resolved as there are uncertainties in the instrumental results related to detection capabilities and in the remotely sensed data because of the effects of the vertical variation of  $r_e$  within the cloud.

Cloud phase can be determined by comparing the ratios of reflectances at two wavelengths: one that is a conservative scatterer for both ice and water and one that has strong absorption for ice and weak absorption for water. This type of approach was suggested by the theoretical calculations of Hansen and Pollack (1970) and other researchers. Curran and Wu (1982) used this approach to determine the presence of supercooled water clouds from Skylab measurements of reflectance at 1.61  $\mu\text{m}$ . Masuda and Takashima (1990) demonstrated theoretically that a combination of measurements at 0.63 or 0.86 and 1.61  $\mu\text{m}$  would be best for determining phase. Wielicki et al. (1990) found that the 2.21- $\mu\text{m}$ /0.83- $\mu\text{m}$  and the 1.65- $\mu\text{m}$ /0.83- $\mu\text{m}$  Landsat reflectance ratios could effectively distinguish between ice and water clouds when used together. King et al. (1992) showed that distinctly different 1.63- $\mu\text{m}$ /0.75- $\mu\text{m}$  reflectance ratios are measured over water and ice clouds. The water cloud reflectance ratio is about half that of the ice cloud. The ratio techniques are continually being improved and developed. They will be useful for the TRMM/VIRS and MODIS instruments but not for AVHRR.

#### 4.3.2.2. Thermal Infrared Emittance Techniques

The simple model of brightness temperature usually employed in satellite remote sensing of clouds is that the observed radiance is

$$B_{\lambda}(T_{\lambda}) = [1 - \epsilon_{\lambda}(\mu, \tau_{\lambda})][(1 - \epsilon_{s\lambda})B_{\lambda}(T_{D_s}) + \epsilon_{s\lambda}B_{\lambda}(T_s)] + \epsilon_{\lambda}(\mu, \tau_{\lambda})B_{\lambda}(T_{cld}) \quad (4.3-4)$$

where  $T_{\lambda}$  is the equivalent blackbody temperature,  $T_s$  is the surface temperature,  $T_{cld}$  is the cloud temperature,  $T_{D_s}$  is the equivalent blackbody temperature of the downwelling radiance at the surface,  $B$  is the Planck function,  $\epsilon_{s\lambda}$  is the surface emittance, and the effective cloud emittance  $\epsilon_{\lambda}$  approaches unity as the cloud becomes optically thick. If scattering is neglected,

$$\epsilon_{\lambda} = 1 - \exp(-\tau_{a\lambda}/\mu) \quad (4.3-5)$$

where the absorption optical depth  $\tau_{a\lambda} = (1 - \bar{\omega}_o)\tau_{\lambda}$ . The quantity  $\epsilon_{s\lambda}B_{\lambda}(T_s)$  can be replaced in many instances with  $B_{\lambda}(T_{cs\lambda})$ , where  $T_{cs\lambda}$  is the clear-sky temperature. It includes the attenuation of the atmosphere which is not explicitly included in (4.3-4). For semitransparent clouds, it is possible to estimate  $\epsilon_{\lambda}$  and  $T_{cld}$  from simultaneous measurements at two different wavelengths  $\lambda_1$  and  $\lambda_2$ , if  $T_{cs\lambda}$  and the relationship between  $\epsilon_{\lambda_1}$  and  $\epsilon_{\lambda_2}$  is known and  $\epsilon_{\lambda_1} \neq \epsilon_{\lambda_2}$ . The surface emittance is generally assumed to be unity for longer wavelengths. It may be as low as 0.9 for some surfaces at the near-infrared wavelengths. If  $\epsilon_{\lambda}$  is known, then  $\tau_{\lambda}$  can be determined from either (4.3-5) or some other function that relates the two quantities. If  $T_{cld}$  is known—from some other source or a third wavelength—it is theoretically possible to determine  $r_e$  and  $\tau_{\lambda}$ . As in the case for reflectance methods, the optical properties of clouds need to be different at each of the involved wavelengths. Hunt (1973) showed that the cloud emittance at 3.7  $\mu\text{m}$  is more sensitive to changes in optical depth and particle size than at longer wavelengths such as 11 or 12  $\mu\text{m}$ . Liou (1974) demonstrated that the optical properties of cirrus varied between 11 and 12  $\mu\text{m}$ . These three spectral channels have been used on meteorological satellites and, therefore, have received much of the attention for deriving cloud properties. Some techniques make use of the brightness temperature difference  $BTD_{i,j}$  between  $T_i$  and  $T_j$  to provide some information about the particle size and optical depth. The subscripts  $i$  and  $j$  can refer to sensor channel numbers or their nominal wavelengths. The AVHRR channels 3, 4, and 5 have nominal wavelengths of 3.73, 10.8, and 12.0  $\mu\text{m}$ .

Inoue (1985) developed a method using  $BTD_{4,5}$  and an implicit mean particle size to determine  $\epsilon_4$  and, therefore,  $\tau_4$  from AVHRR channels 4 and 5 taken over semitransparent cirrus clouds. Wu (1987) developed an algorithm to derive cirrus effective cloud fraction  $\epsilon_{11}C$  and  $T_{cld}$  using the HIRS2 3.7-, 4.0-, and 11- $\mu\text{m}$  data. d'Entremont (1986) exploited the variation of AVHRR  $BTD_{3,4}$  with particle size to determine the presence of low clouds and fog at night. Ackerman and Stephens (1987) further explained the phenomena that permit the estimation of particle size from measurements of radiation simultaneously at two wavelengths: one strongly absorbing and one weakly absorbing. Prabhakara et al. (1988) used  $BTD_{10.8,12.6}$  from the 10.8- and 12.6- $\mu\text{m}$  IRIS data taken by the Nimbus-4 satellite as

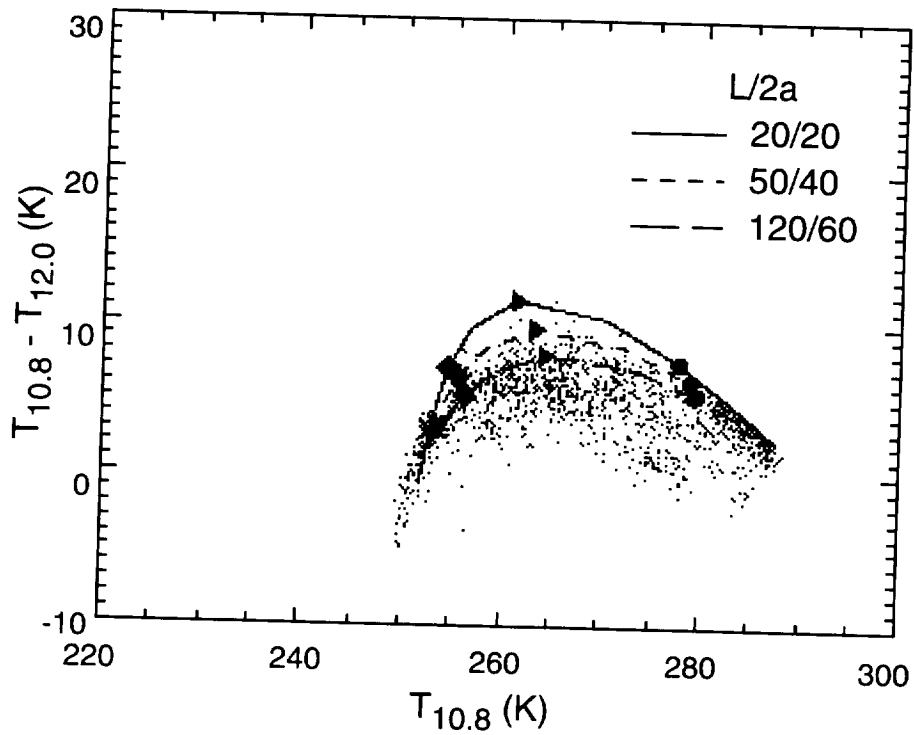
indices for the distribution of optically thin cirrus clouds. Ackerman et al. (1990) used ratios of the mass absorption coefficients derived from 10.1- and 12.0- $\mu\text{m}$  HIS measurements to estimate cirrus cloud particle sizes in terms of ice-sphere effective radius. Liou et al. (1990a) used an iterative technique to estimate cloud temperature and optical depth from 6.5- and 11- $\mu\text{m}$  radiances taken over high-altitude cirrus clouds. From theoretical calculations using spheres and cylinders to represent cirrus particles, Parol et al. (1991) concluded that the AVHRR  $BTD_{4-5}$  depends significantly on particle shape but not so much on phase. They found that scattering should be taken into account in the interpretation of the  $BTD$ 's. Takano et al. (1992) developed a parameterization to compute the optical properties of cirrus clouds at any infrared wavelength using a combination of hexagonal ice crystals and spheroids to represent the cirrus cloud particles. The latter are used for large size parameters  $x$ , while the former are invoked for small  $x$ . The Takano et al. (1992) model matched observations of  $BTD_{11-12}$  much more closely than the spherical representations. Lin and Coakley (1993) advanced a method to derive a particle size index for single-layer cloud decks using radiative transfer model fits to clusters of collocated AVHRR channel 4 and 5 pixels. Their method simultaneously solved for the emittance and cloud fraction by computing an envelope of solutions based on a single effective radius and cloud temperature for the pixel cluster. Ou et al. (1993) developed a method to derive  $\tau_{0.67}$ ,  $T_{cld}$ , and  $D_e$  from nighttime AVHRR measurements of  $T_{3.7}$  and  $T_{10.9}$ . They assumed that particle size depended on cloud temperature according to the parameterization of Heymsfield and Platt (1984) and developed a parameterization of  $B_{11}(T)$  in terms of  $B_{3.7}(T)$ . Baum et al. (1994) successfully modeled  $BTD_{3.7-11}$  and  $BTD_{11-12}$  values from AVHRR observations taken over oceanic cirrus, stratocumulus, and a cirrus-stratocumulus mix. Their models are based on the results of Takano et al. (1992), Liou et al. (1990b), Minnis et al. (1993b), and Mie scattering calculations. They found that a combination of all three channels may be used to determine  $T_{cld}$ ,  $\tau_\lambda$ , and  $r_e$  or  $D_e$  simultaneously.

Infrared spectra may be used to determine cloud phase, though not as easily as solar spectra. Ackerman et al. (1990) demonstrated that  $BTD_{11-12}$  and  $BTD_{8-11}$  may be used to determine the cloud phase for optically thin clouds, at least. The analyses of Baum et al. (1994) showed that a combination of  $BTD_{3.7-11}$  and  $BTD_{11-12}$  has the potential for separating ice and water clouds for many particle sizes for  $\tau_{0.65} < 6$ . Figures 4.3-2 and 4.3-3 adapted from Baum et al. (1994) show the  $BTD$ 's from AVHRR observations for a cloud deck with  $T_{cld} = 250$  K. The theoretical values of  $BTD_{3.7-11}$  for ice clouds, shown as the curves in Figure 4.3-2(a), are generally greater than those for water clouds (Fig. 4.3-3(a)) while the opposite is true for  $BTD_{11-12}$  (Figs. 4.3-2(b) and 4.3-3(b)). This potential for phase determination is currently under study.

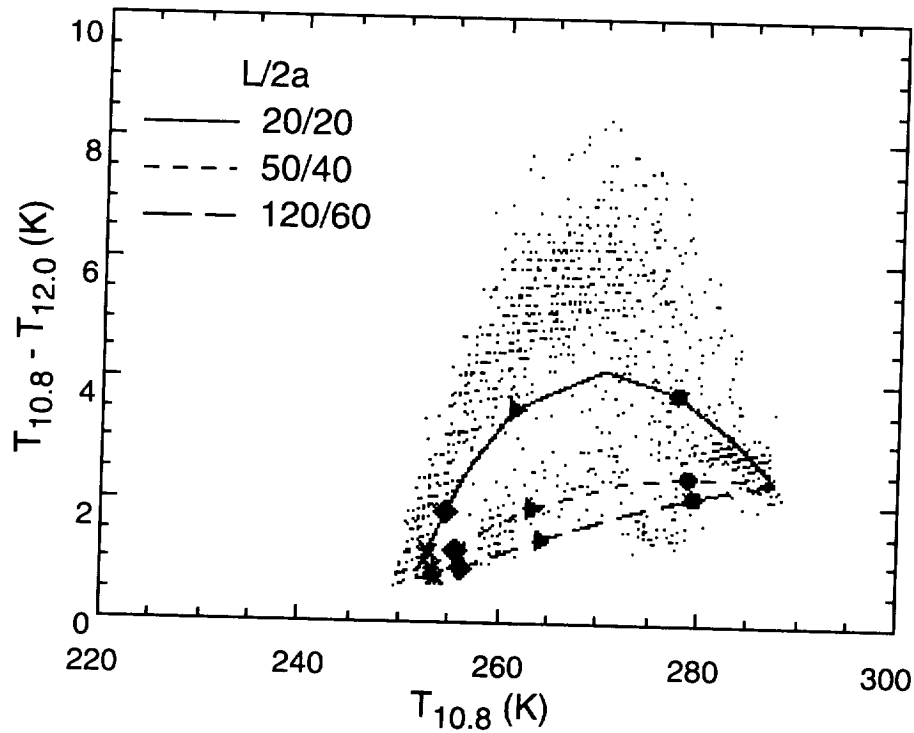
#### 4.3.2.3. Combined Thermal Emittance-Solar Reflectance Methods

There are mixed methods that use both thermal and solar channels and, sometimes, an overlapped solar-thermal channel. The simplest of the mixed techniques, a bispectral visible-infrared analysis, is the form most widely used. In this approach, optical depth is derived from the visible reflectances using an implicit or explicit model of the cloud radiative properties. The infrared (11  $\mu\text{m}$ ) emittance, derived from the visible optical depth, is used to correct the observed  $T_{11}$  using (4.3-4) to obtain  $T_{cld}$ . Reynolds and Vonder Haar (1977) used an empirical model that represents an implicit cloud model to relate cloud albedo to  $\epsilon_{11}$ . Rossow and Lacis (1990) used a theoretical-empirical approach and a single cloud microphysical model, a method also used by the ISCCP (Rossow et al. 1988). Minnis et al. (1993b) employed a purely theoretical method using various cloud microphysical models. Those bispectral methods are relatively effective and applicable to most operational satellite datasets. They do not, however, yield any information about particle size or phase other than what is assumed. To obtain particle size, a third channel or some other type of information is needed.

Arking and Childs (1985) pioneered the use of visible, infrared, and the 3.7- $\mu\text{m}$  data to retrieve cloud fraction  $C$ ,  $\tau_{0.65}$ ,  $r_e$ , and  $T_{cld}$  for each pixel. Their method uses a pixel clustering technique to determine  $T_{cld}$  for a scene. All pixels outside the cluster are assumed to have a cloud temperature equal

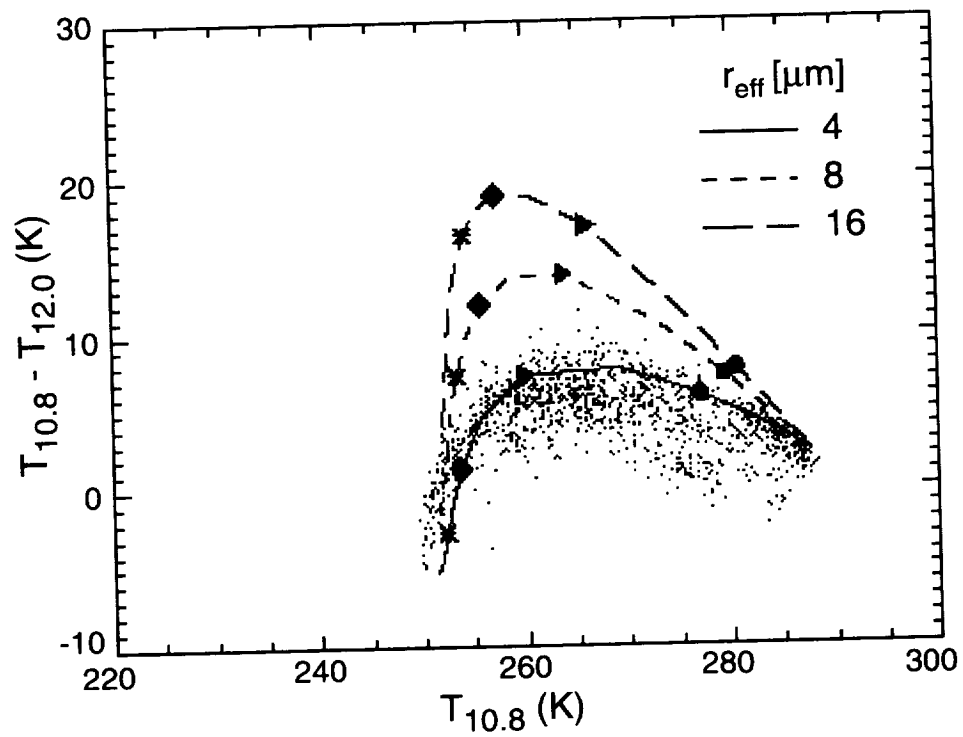


(a)  $BTD_{3.7-11}$ .

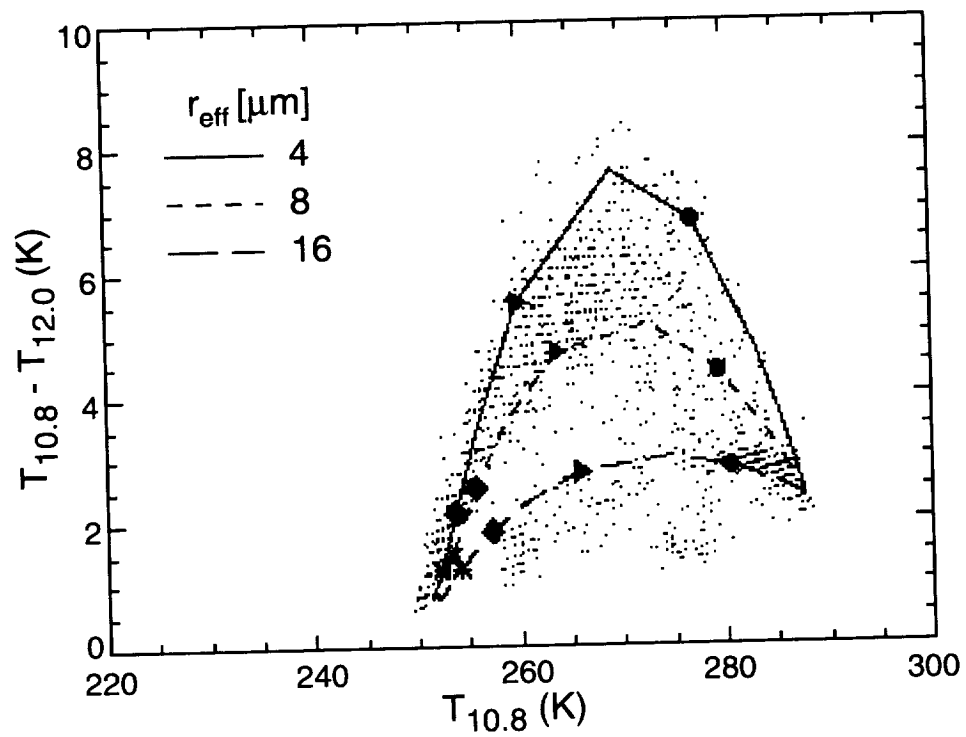


(b)  $BTD_{11-12}$ .

Figure 4.3-2. Comparison of theoretical results assuming cloud composed entirely of hexagonal ice crystals with AVHRR data taken over the northwest Atlantic at 0606 UTC, April 16, 1989. The ice crystal length-to-width ratios  $L/2a$  are given in  $\mu\text{m}/\mu\text{m}$ . The circles, triangles, diamonds, and asterisks refer to the  $10.8\text{-}\mu\text{m}$  optical depths of 0.5, 2, 4, and 6, respectively (adapted from Baum et al. 1994).



(a)  $BTD_{3.7-11}$ .



(b)  $BTD_{11-12}$ .

Figure 4.3-3. Same as Figure 4.3.2, except assuming cloud composed entirely of supercooled water droplets in the model calculations (adapted from Baum et al. 1994).

to the scene value of  $T_{cld}$ . The difference between the observed  $T$  and  $T_{cld}$  for each pixel outside the cluster is interpreted as a cloud fraction  $C < 1$ , so  $C$  is computed for each pixel. The optical depth and spherical particle size category are determined for each pixel using the visible and 3.7- $\mu\text{m}$  radiances with  $T_{cld}$  and  $C$ . The use of the 3.7- $\mu\text{m}$  data during the day complicates (4.3-4) because there is some solar reflectance at that wavelength. The observed radiance has an additional term

$$B(T) = \epsilon(\tau, r_e; \mu)B(T_{cld}) + [1 - \epsilon(\tau, r_e; \mu)]\epsilon_s B(T_{cs}) + \frac{\mu_o E_o}{\pi} \left\{ \rho(\tau, r_e; \mu_o, \mu, \phi) + \frac{[1 - \alpha_c(\tau, r_e; \mu)][1 - \alpha_c(\tau, r_e; \mu)]\rho_s(\mu_o, \mu, \phi)}{1 - \alpha_{sd}\alpha_{cd}(\tau, r_e)} \right\} \quad (4.3-6)$$

where the subscript  $\lambda$  has been dropped for simplicity. The effective emittance includes both the absorption and scattering effects of the cloud. The surface bidirectional reflectance and diffuse albedo are  $\rho_s$  and  $\alpha_{sd}$ , respectively. The cloud directional and diffuse albedos are  $\alpha_c$  and  $\alpha_{cd}$ , respectively. These terms are formally defined by Minnis et al. (1993b). Atmospheric absorption and scattering effects are neglected in equation (4.3-6), which can be used for any wavelength since  $E_o$  and  $\epsilon$  approach zero for infrared and visible wavelengths, respectively.

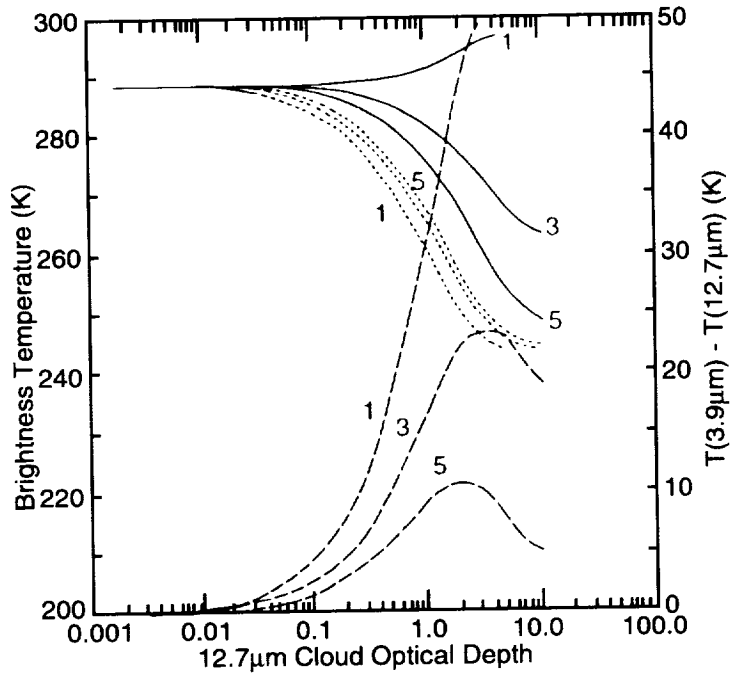
Stone et al. (1990) continued the development of the technique using *BTD*'s between infrared window (10–12.7  $\mu\text{m}$ ) and near-infrared (3.5–4.0  $\mu\text{m}$ ) radiances by comparing model calculations of daytime *BTD*'s for various sizes of ice spheres to GOES and AVHRR data. Figure 4.3-4 shows the Stone et al. (1990) model calculations of  $T_{3.9}$ ,  $T_{12.7}$ , and  $BTD_{3.9-12.7}$  for three different effective ice sphere sizes (as defined by Stone et al. 1990, model 1:  $D_e = 8 \mu\text{m}$ ; model 3:  $D_e = 32 \mu\text{m}$ ; model 5:  $D_e = 128 \mu\text{m}$ ). The daytime  $BTD_{3.9-12.7}$  values (Fig. 4.3-4(a)) are more sensitive to changes in  $D_e$  than their nocturnal counterparts (Fig. 4.3-4(b)) because of the reflected component in the 3.9- $\mu\text{m}$  radiances. This increased sensitivity is also found for liquid water clouds. Han (1992) exploited the daytime sensitivity of  $T_3$  to particle size to construct the first semiglobal survey of  $r_e$  for water clouds using ISCCP AVHRR data. His method explicitly solves (4.3-6) through an iterative technique for  $\tau_{0.67}$ ,  $T_{cld}$ , and  $r_e$  using  $\rho_{0.67}$ ,  $T_{3.73}$ , and  $T_{10.8}$  and a set of lookup tables derived from radiative transfer calculations. The lookup tables are limited to  $\mu > 0.9$ ,  $\mu_o > 0.2$ , and liquid water droplets. The method is applied only to pixels having  $T_{cld} > 273 \text{ K}$ . This technique has produced reasonable results over the middle and low latitudes where it was applied to a set of AVHRR data.

Young et al. (1993) and Young et al. (1994) expanded on the approach of Han (1992) by using models of reflectance and emittance developed by Minnis et al. (1994) for all angles, cloud and surface temperatures, cloud phase, optical depths, and particle sizes. Their iterative scheme is similar to that of Han (1992) but it contains some additional features. The Young et al. (1994) method selects an ice or water model automatically using the initial comparison of the computed  $T_{3.73}$  with the observed value. Mie scattering calculations are used for the water droplets. The ice cloud models are based on the hexagonal crystal and spheroid parameterizations of Takano and Liou (1989), Minnis et al. (1993b), and Takano et al. (1992). The initial applications of this methodology compare well with in situ and ground-based radar measurements of particle size taken during FIRE II and ASTEX.

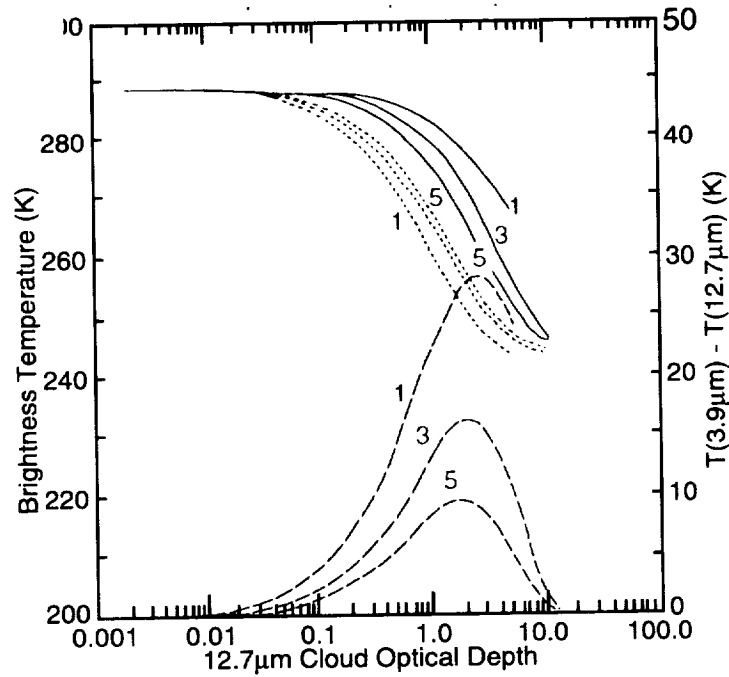
Another mixed technique, applicable only to water clouds over ocean in daylight, involves the simultaneous use of microwave radiances to infer liquid water path  $W_{liq}$  and visible radiances to derive optical depth. Minnis et al. (1992) used radiative transfer models of visible reflectance in terms of  $\tau_{0.65}$  and  $r_e$  and

$$r_e = \frac{3Q_e W_{liq}}{4\delta_{liq}\tau_{0.65}(\rho, r_e)} \quad (4.3-7)$$

to obtain  $r_e$  from surface-based microwave measurements of  $W_{liq}$  and GOES visible data. The density of liquid water is  $\delta_{liq}$ . This equation is a generalized version of an approximation by Stephens (1978) in



(a) Daytime.



(b) Nighttime.

Figure 4.3-4. Composite plots of 3.9- $\mu\text{m}$  and 12.7- $\mu\text{m}$  brightness temperature and their differences as functions of the 12.7- $\mu\text{m}$  optical depths for model cirrus clouds during (a) daytime and (b) nighttime situations. The numbers next to each curve relate to model values of effective particle size. Models 1, 3, and 5 refer to effective ice-sphere radii of 4, 16, and 64  $\mu\text{m}$ , respectively. The solid and short-dashed curves are for the 3.9- $\mu\text{m}$  and 12.7- $\mu\text{m}$  temperatures, respectively. The long-dashed curves relate to the temperature differences (adapted from Stone et al. 1990).

which  $Q_e$  is assumed to have a value of 2 for visible wavelengths. The extinction efficiency actually varies from 2.3 to 2 for  $r_e$  ranging from 2 to 32  $\mu\text{m}$ . Minnis et al. (1992) found excellent agreement between their derived effective radii assuming  $Q_e = 2$  and the available in situ data taken off the coast of California during the July 1987 FIRE stratocumulus experiment. Young et al. (1992) applied this visible-microwave approach to derive  $r_e$  from nearly coincident DMSP SSM/I microwave data and GOES visible radiances. The resulting mean value of  $r_e$  was 9.2  $\mu\text{m}$ , identical to that derived using the technique of Young et al. (1994) applied to nearly coincident AVHRR data. The values from the visible-microwave method, however, ranged from 6 to 14  $\mu\text{m}$  compared to 7 to 11  $\mu\text{m}$  from the AVHRR data. The most likely cause of the range differences may be the sensitivity of the reflectance techniques to the droplets in the top of the cloud (cf. Nakajima and King 1990). Further, the visible-microwave method must simultaneously account for the reflectance and liquid water path of the entire cloud. In nonprecipitating conditions, stratiform clouds tend to have smaller droplets at the bottom. The opposite situation is likely to occur for precipitating clouds. Additional research is required to reconcile the discrepancies between the two methods.

### 4.3.3. Data and Model Database

The primary input data to COPRS include the following elements from a CERES cloud-algorithm unit data block ( $16 \times 16$  imager pixels): mean  $T_{cs\lambda}(L)$ ,  $\rho_{cs\lambda}(L)$ ,  $\alpha_{sd\lambda}(L)$ ,  $T_{cs\lambda}(S)$ ,  $\alpha_{sd\lambda}(S)$ , and  $\rho_{cs\lambda}(S)$ ,  $T(p)$ ,  $\tau_{H_2O\lambda}(p)$ ,  $\tau_{aer}$ ,  $\tau_{O_3}$ ,  $E_{o\lambda}$  and  $\mu_o$ ,  $\mu$ , and  $\phi$  for the center of the block. The parenthetical  $L$  and  $S$  refer to land and sea, respectively. The clear-sky albedo is  $\alpha_s(\mu_o)$  and the clear-sky diffuse albedo is  $\alpha_{sd}$ . The spectral water vapor optical depth is  $\tau_{H_2O\lambda}(p)$ , and the visible aerosol and ozone optical depths are  $\tau_{aer}$  and  $\tau_{O_3}$ , respectively. The spectral radiances and geoclassification for each pixel in the data block are also included. These input elements have been described in detail in section 4.1. Other inputs derived in the section 4.2. subsystem are the clear, single-layer, or multiple-layer indices for each pixel and the values for the cloud layer temperatures for all layers detected for the eight surrounding data blocks.

To maintain a standard reference, optical depth is reported in terms of the visible channel optical depth,  $\tau_{0.65}$ . The optical depth at a given wavelength  $\lambda_1$  for any effective particle size can be related to the optical depth at any other wavelength  $\lambda_2$  by

$$\tau_{\lambda_1} = \tau_{\lambda_2} \frac{Q_{e\lambda_1}}{Q_{e\lambda_2}} \quad (4.3-8)$$

For simplicity, the wavelength subscript is dropped for the visible optical depth. It will continue to be used for other wavelengths. The AVHRR channel numbers 3, 4, and 5 will hereafter replace the wavelength designations for  $\lambda = 3.7$ , 10.9, and 11.9  $\mu\text{m}$ , respectively.

The cloud solar radiance model database consists of lookup tables giving the spectral cloud reflectance  $\rho_\lambda(r_e \text{ or } D_e; \tau; \mu_o, \mu, \phi)$ , cloud albedo  $\alpha_c(r_e \text{ or } D_e; \tau; \mu_o)$ , and diffuse cloud albedo  $\alpha_{cd}(r_e \text{ or } D_e; \tau)$  for the relevant channels: 0.63, 1.60, and 3.75  $\mu\text{m}$  for VIRS and AVHRR (Minnis et al. 1993b; Minnis et al. 1994) plus 2.12  $\mu\text{m}$  for MODIS. The lookup tables were constructed for  $r_e = 2, 4, 6, 8, 12, 16$ , and 32  $\mu\text{m}$  and  $D_e = 23, 37, 64, 108$ , and 180  $\mu\text{m}$  with  $\tau = 0.25, 0.5, 1, 2, 3, 4, 8, 16, 32, 64, 96$ , and 128;  $\mu_o = 1, 0.95, 0.85, \dots, 0.05$ ;  $\mu = 1, 0.9, 0.8, \dots, 0.1$ ; and  $\phi = 0, 7.5, 15, 30, 45, \dots, 165, 172.5, 180^\circ$ . The optical depth range for 3.75  $\mu\text{m}$  ends at  $\tau = 32$  because the reflectance is essentially constant for greater optical depths. For bright backgrounds, a set of lookup tables giving the 0.65- $\mu\text{m}$  reflectance at the top of the atmosphere has been developed for the same sets of angles. These lookup tables were computed for all of the water and ice clouds using surface albedos ranging from 0.20 to 0.80 in increments of 0.15 for  $\tau = 0.25, 0.5, 1, 2, 3, 4$ , and 8 and  $p = 1000, 700, 400$ , and 100. No water vapor or ozone absorption was included in these calculations.

Figure 4.3-5 shows examples of the cloud reflectance lookup tables normalized to the cloud albedo [i.e., the ratio  $\rho_\lambda(\mu_o, \mu, \phi)/\alpha_c(\mu_o)$ ] for  $r_e = 16 \mu\text{m}$  (Fig. 4.3-5(a)) and  $D_e = 37 \mu\text{m}$  (Fig. 4.3-5(b)) for channel 3 with  $\tau = 4$  and  $\mu_o = 0.55$ . The effective volume of these two particle distributions are close, but the diffuse albedos are 0.13 and 0.06, respectively. Although the reflectance patterns (Fig. 4.3-5) are somewhat similar, they show some distinct features typical of the differences between scattering from spheres and hexagonal crystals. The relative reflectance patterns for the visible channel (Fig. 4.3-6) are different than those in Figure 4.3-5, but the discrepancies between the ice and water reflectances are quite noticeable. In contrast to the 3.75- $\mu\text{m}$  results, the visible-channel liquid-cloud diffuse albedo of 0.31 is less than the value of 0.42 for ice-cloud model. Cloud albedo  $\alpha_c$  increases with decreasing particle size for both channel 3 and the visible channel as demonstrated in the reflectance plots of the models for  $r_e = 4, 8, \text{ and } 16 \mu\text{m}$  in Figures 4.3-7 and for  $D_e = 23, 41, \text{ and } 124 \mu\text{m}$  in Figures 4.3-8.

The cloud emittance models comprise a set of 75 coefficients for channels 3, 4, or 5 for the VIRS and AVHRR (Minnis et al. 1994) plus the 8.55- $\mu\text{m}$  channel of MODIS. The following regression formula was fitted to effective emittances computed using (4.3-4) and radiances calculated with the adding-doubling radiative transfer model of Minnis et al. (1993b).

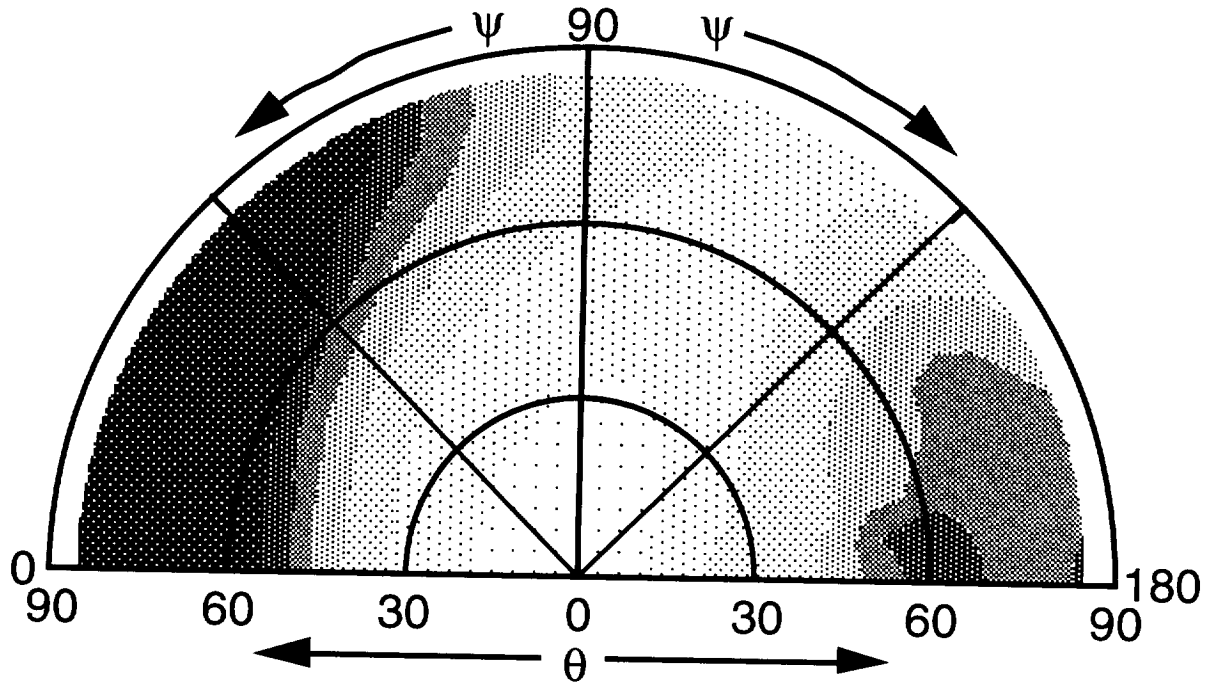
$$\varepsilon(\lambda, r_e) = a_0 + a_1 \{1/\ln(\Delta T)\} + a_2 \{1/\ln(\Delta T)\}^2 \quad (4.3-9)$$

where  $\Delta T = T_{cs} - T_{cld}$ ,  $a_i = \sum b_j \tau^j$ , and  $b_j = \sum c_k \mu^k$ , ( $j = 0, 4$  and  $k = 0, 4$ ). The visible optical depth is used in all cases. The standard error of this parameterization is  $\leq 3\%$  for most of the particle distributions. Figure 4.3-9 shows the  $BTD_{3-4}$  and  $BTD_{4-5}$  computed using the effective emittances from (4.3-9) for hypothetical nocturnal clouds viewed from  $\theta = 45^\circ$  at a temperature  $T_{cld} = 255 \text{ K}$  over a clear scene having a brightness temperature of  $T_{cs} = 300 \text{ K}$ . Four clouds are represented, two comprising water droplets with effective radii  $r_e = 6$  and  $16 \mu\text{m}$  and the other two consisting of randomly oriented hexagonal ice crystals having effective diameters  $D_e = 37$  and  $180 \mu\text{m}$ . As  $\tau$  increases, the 10.8- $\mu\text{m}$  temperature approaches  $T_{cld}$ . It is clear that, for both the water droplet and ice crystal models,  $BTD_{3-4} > BTD_{4-5}$ . This greater difference is typical for most cold clouds, and the ice models are obviously distinguishable from the water droplet models. Differences between  $BTD_{3-4}$  for  $D_e = 37$  and  $180 \mu\text{m}$  are smaller than those between  $BTD_{4-5}$  at the smaller optical depths (warmer brightness temperatures), while the reverse is true for larger optical depths. During the daytime, the  $BTD_{3-4}$  for  $D_e = 37$  and  $180 \mu\text{m}$  are always greater than  $BTD_{4-5}$  because of the solar contribution to the channel-3 radiance.

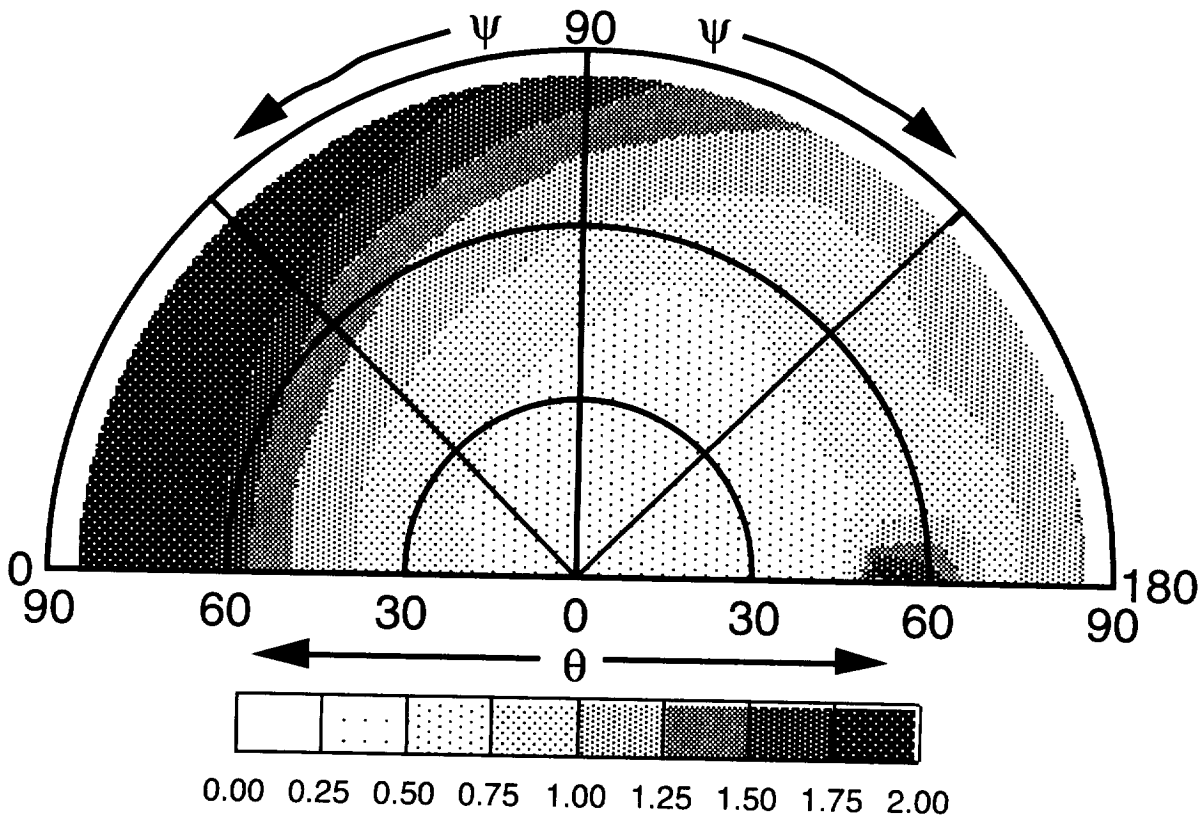
Atmospheric corrections for the solar channel are performed using the models and methods of Minnis et al. (1993b). Corrections for atmospheric water vapor are applied to the infrared and near-infrared channels using correlated-k fits (Kratz 1995; see also Appendix). When the models are applied, reflectances are computed for each appropriate channel at  $\mu_o$ ,  $\mu$ , and  $\phi$  for the center latitude and longitude of the data block over a range of particle sizes and optical depths for both land and ocean. Emittances are computed for the same particle sizes and optical depths at  $\mu$  using the initial guess of  $T_{cld}$ . The model results are then corrected for atmospheric attenuation. A clear-sky bidirectional reflectance model and spectral surface emittance are required in the analyses.

#### 4.3.4. Methodologies

The multispectral reflectance techniques are sensitive to a wide range of particle sizes but are limited to daytime. Emittance methods are applicable at all times, but they are sensitive to a smaller range of  $r_e$  and can be used only when the cloud is semitransparent. The 3-channel mixed methods are the only techniques available using current global satellite data and are applicable to a wide range of optical depths. They cannot be used at night, however, and are sensitive to a smaller range of particle sizes than the solar methods. There are also many other situations in which one or all of the techniques will fail to retrieve the desired parameters (see section 4.3.5.2.). To overcome these deficiencies, the COPRS will utilize all three approaches to arrive at the most reliable estimates of the cloud properties in as many situations as possible. For application to CERES/VIRS, the 3-channel reflectance-emittance techniques

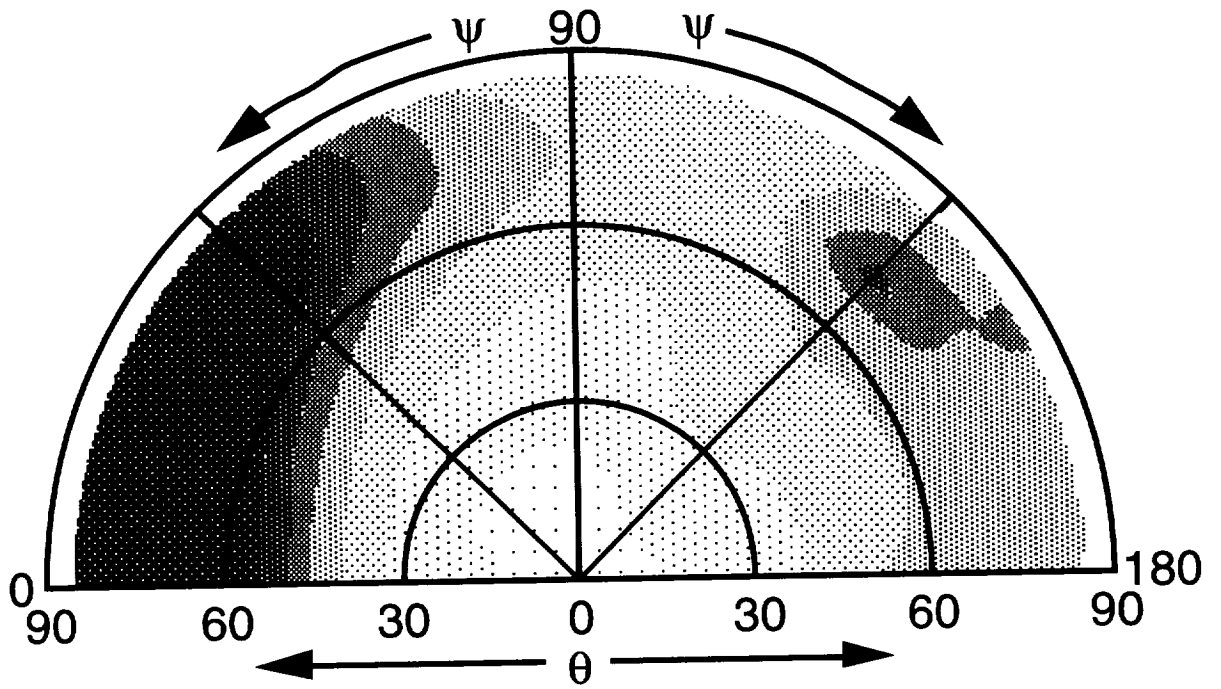


(a)  $r_e = 16 \mu\text{m}$ .

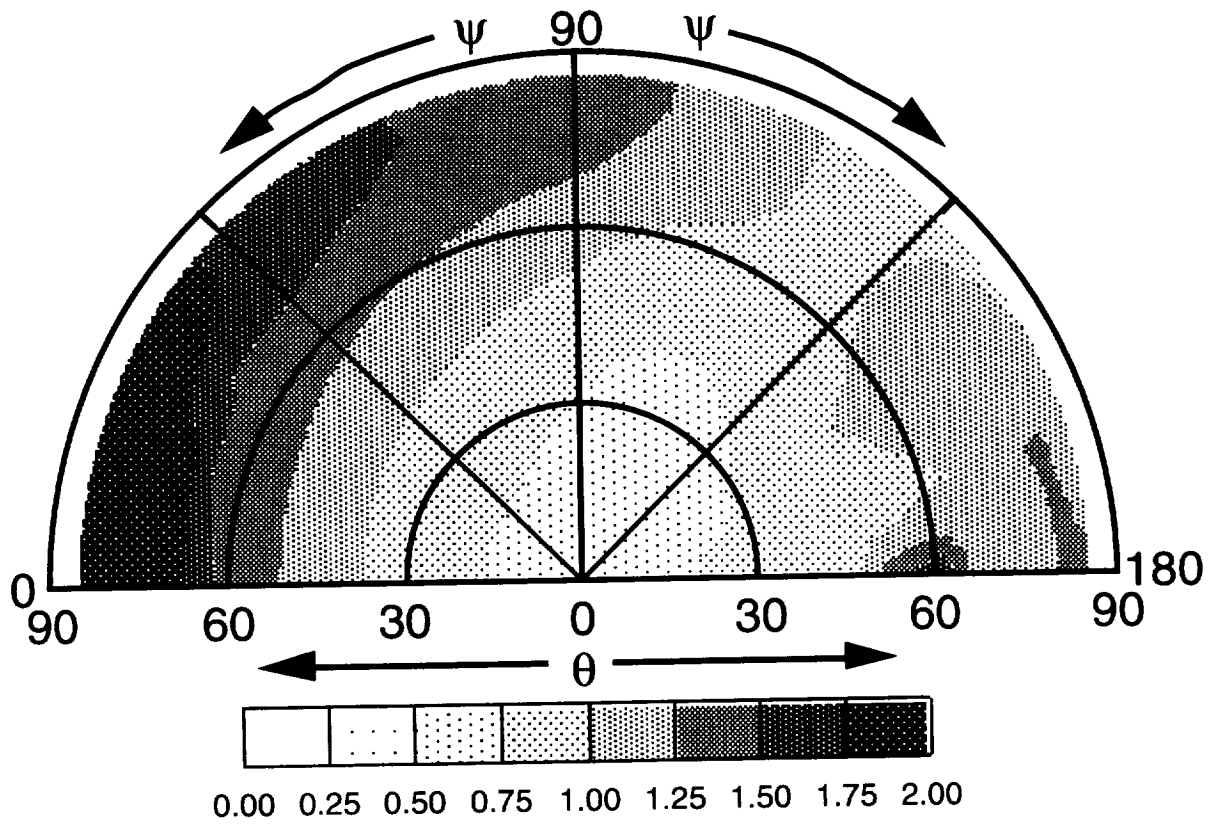


(b)  $D_e = 37 \mu\text{m}$ .

Figure 4.3-5. Normalized theoretical anisotropic reflectance values for  $\tau = 4$ ,  $\mu_o = 0.55$ , and  $\lambda = 3.75 \mu\text{m}$ .

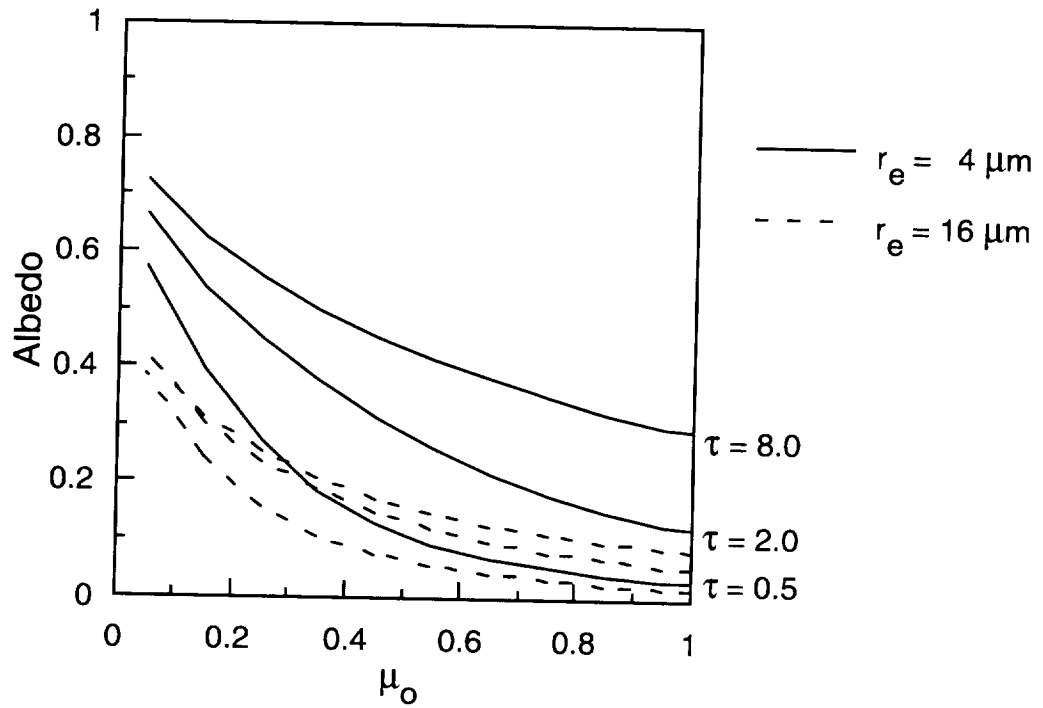


(a)  $r_e = 16 \mu\text{m}$ .

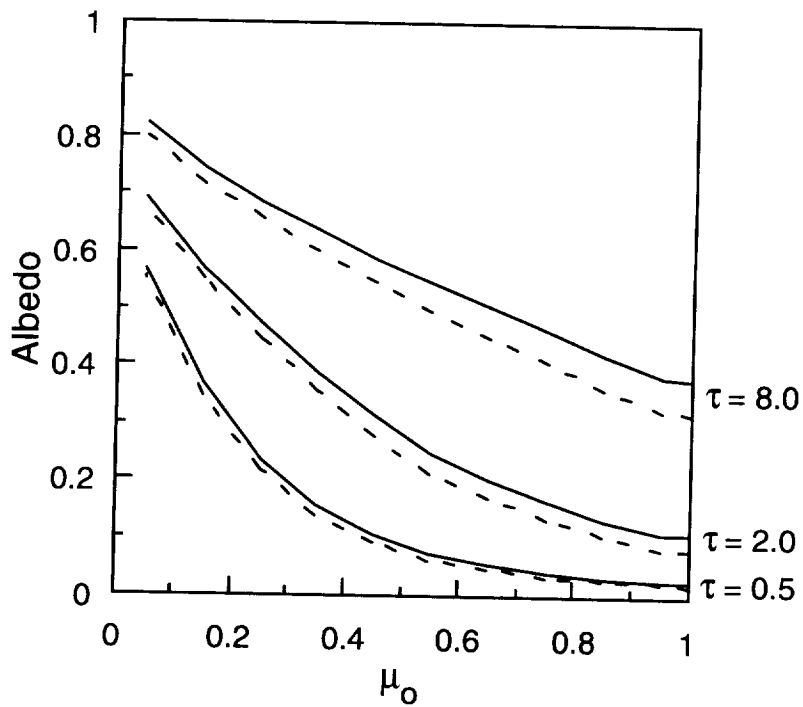


(b)  $D_e = 37 \mu\text{m}$ .

Figure 4.3-6. Normalized theoretical anisotropic reflectance values for  $\tau = 4$ ,  $\mu_o = 0.55$ , and  $\lambda = 0.65 \mu\text{m}$ .

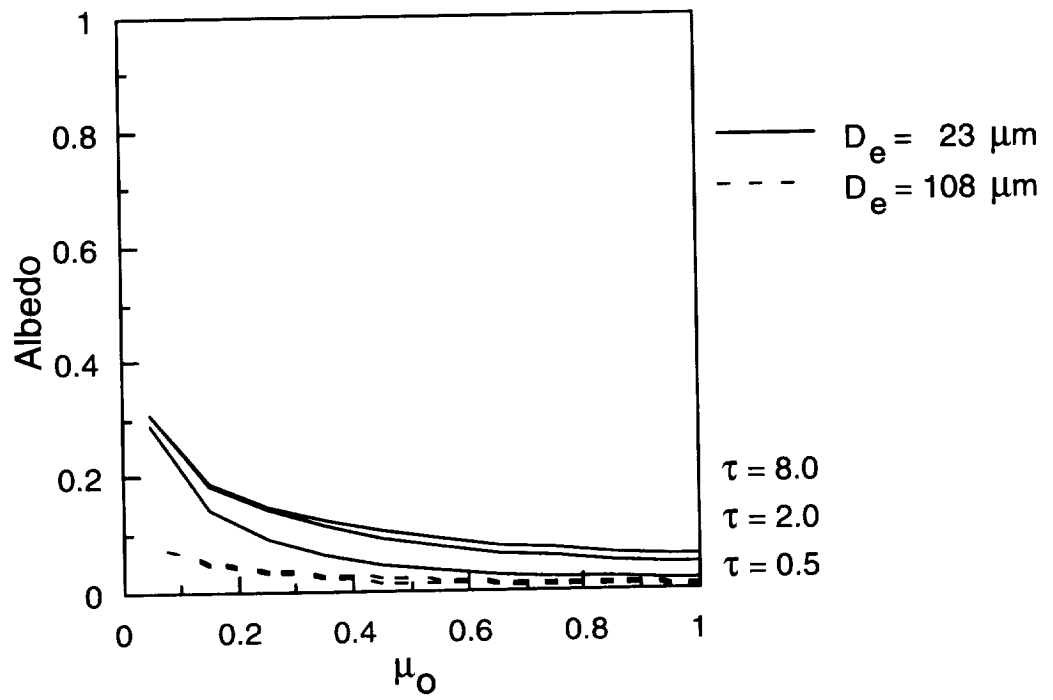


(a)  $\lambda = 3.75 \mu\text{m}$ .

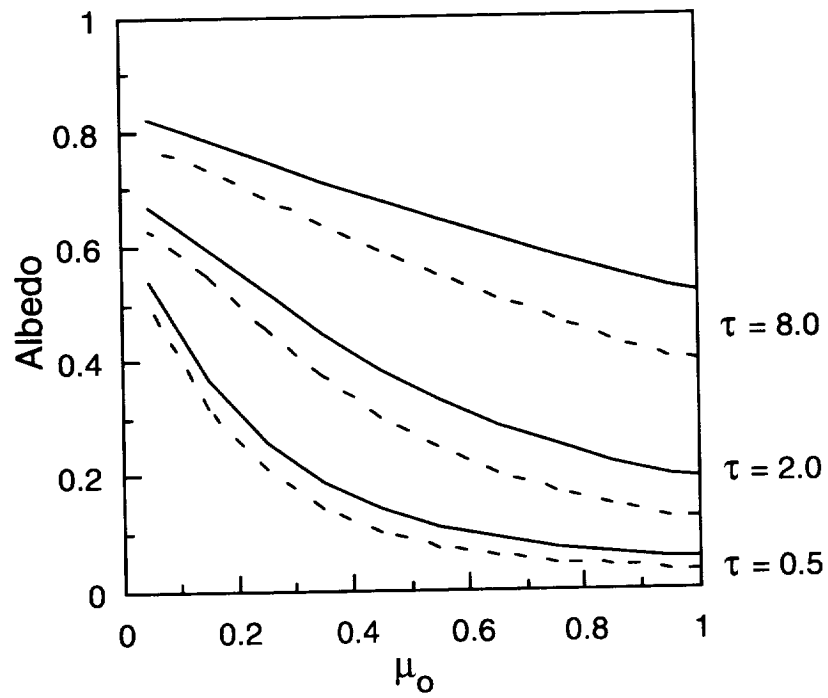


(b)  $\lambda = 0.65 \mu\text{m}$ .

Figure 4.3-7. Theoretical albedos for 4- $\mu\text{m}$  and 16- $\mu\text{m}$  water droplets.



(a)  $\lambda = 3.75 \mu\text{m}$ .



(b)  $\lambda = 0.65 \mu\text{m}$ .

Figure 4.3-8. Theoretical albedos for 23- $\mu\text{m}$  and 108- $\mu\text{m}$  ice particles.

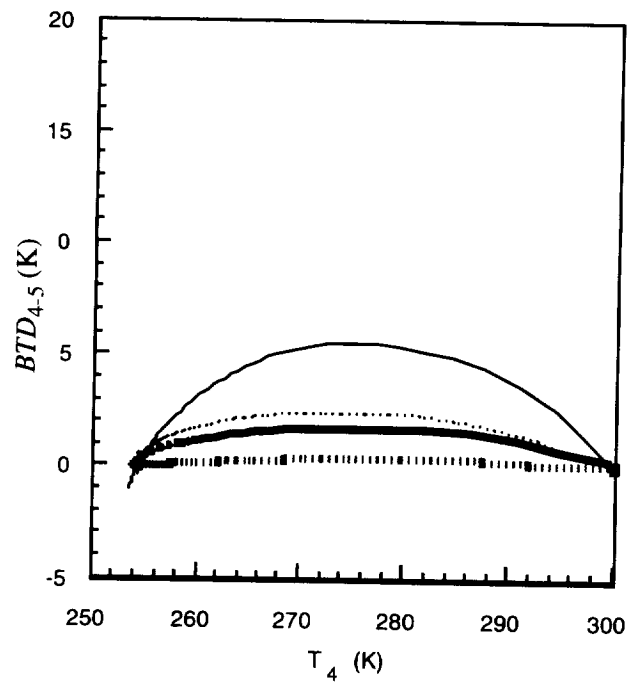
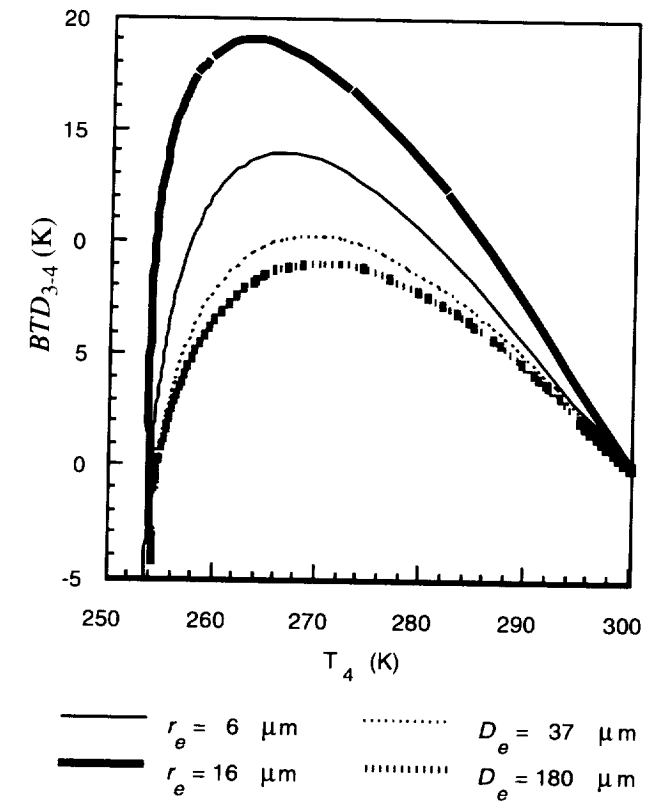


Figure 4.3-9. Theoretical brightness temperature differences for  $T_{cld} = 255$  K,  $\Theta = 45^\circ$ .

will serve as the primary methods for simultaneous retrieval of optical depth, effective particle size, and phase. The reflectance methods generally rely on a 2.13- $\mu\text{m}$  channel to determine particle size. This channel will be unavailable on VIRS. There is some skill in the reflectance methods, however, to determine particle size and phase using only the visible and 1.61- $\mu\text{m}$  channels. Therefore, the reflectance method will be applied during the daytime to verify phase and whenever a solution is unavailable from the 3-channel method. When the MODIS is operating, it will be possible to apply a full-scale reflectance technique because of the wide choice of channels. Whenever the primary and secondary methods fail, a 3-channel infrared method is applied during the daytime. The same 3-channel infrared method is applied at night in most cases. For the Release-1 algorithm using VIRS, the three channels are 3.75, 10.8, and 12  $\mu\text{m}$ . For MODIS, a 4-channel method will be possible because of the additional 8.55- $\mu\text{m}$  sensor. In all cases, both day and night, the results derived from each method will be compared for consistency and to arrive at a single result. The decision-tree selecting the final values will incorporate information regarding the reliability of each technique for the given conditions.

#### 4.3.4.1. Daytime Cloud Optical Depth, Particle Size, and Cloud Temperature

**4.3.4.1.1. 0.65-3.75-10.9- $\mu\text{m}$  method.** Given  $\rho_{cs}$  (0.65),  $\rho_{cs}$  (3.75),  $T_{cs4}$ , and  $T_{cs3}$ , the phase, particle size, optical depth, and cloud temperature are evaluated for each pixel by iteratively solving first for  $\tau$  using the observed visible reflectance  $\rho_{0.65}$ , second for  $T_{clid}$  using  $T_4$  in (4.3-4), and finally using  $T_3$  in (4.3-6) to obtain  $r_e$ . The optical depth is obtained by matching the observed reflectance to a parameterization of radiative transfer calculations of reflectance in terms of cloud optical depth. This model is

$$\rho_{0.65} = (\Sigma \rho_i / (1 - \zeta)), \quad i = 1, 5 \quad (4.3-10)$$

where  $\zeta$  is a regression correction parameter, and the  $\rho_i$  are parameterizations of the multiple scattering and absorption by the atmosphere, scattering by the cloud, and reflectance by the surface Minnis et al. (1993b). The reflectance parameterization is described briefly below.

The visible-channel reflectance contributed by the cloud and the atmosphere above it is

$$\rho_1 = t_{a1} \rho_{c1} = t_{a1} \rho_{c1}(\tau, \tau_{R1}) \quad (4.3-11a)$$

where the transmittance,

$$t_{a1} = \exp[-\tau_{O_3}(1/\mu_o + 1/\mu)]$$

and the Rayleigh optical depth above the cloud is  $\tau_{R1}$ . The beam reflectance by the surface is

$$\rho_2 = t_c \downarrow t_c \uparrow \rho_s \quad (4.3-11b)$$

where the downward and upward cloud transmittances are

$$t_c \downarrow = \exp[-(1 - f_D)\tau/\mu_o]$$

and

$$t_c \uparrow = \exp[-(1 - f_D)\tau/\mu]$$

respectively, and  $f_D$  is the fraction of the beam that is forward scattered because of diffraction or direct transmission through the droplet or crystal. Its value is generally greater than or equal to 0.5 at visible wavelengths. The proportion of the radiation that is scattered out of the forward direction, reflected by the surface, and transmitted diffusely back through the cloud to space is approximated as

$$\rho_3 = \alpha_{sd}(1 - \alpha_{cd})(1 - t_c \uparrow - \alpha_c) \quad (4.3-11c)$$

The fourth term,

$$\rho_4 = \left[ \rho_{R2}(1 - \alpha_c^{0.5}) - \alpha_{R1}\alpha_c^2 \right] (1 - \alpha_{cd}) \quad (4.3-11d)$$

accounts for the relative thickness of the Rayleigh layers above and below the cloud. The effects of the two Rayleigh layers are included by using the direct Rayleigh reflectance term for the bottom layer,  $\rho_{R2}$ , and the Rayleigh albedo for the top layer,  $\alpha_{R1}$ . The fifth term,

$$\rho_5 = a_0 + a_1 \left( \frac{\tau}{1 + \tau} \right)^2 \mu_o^2 \alpha_s + a_2 \alpha_{sd} \quad (4.3-11e)$$

accounts for an overestimate in the surface contribution to the reflectance by  $\rho_2$  for small cloud optical depths. The coefficients,  $a_i$ , depend on the microphysical model. The denominator in (4.3-11) uses the parameter

$$\zeta = b_0 + b_1 \ln \tau + b_2 \alpha_{sd} \ln \tau + b_3 \alpha_{sd} \quad (4.3-12)$$

to minimize biases in the parameterization. The coefficients,  $b_i$ , also vary with the microphysical model. Details of this parameterization are given by Minnis et al. (1993b).

The model represented by (4.3-11) yields relatively accurate optical depths over dark surfaces for all optical depths (Minnis et al. 1993b). For brighter surfaces, such as deserts, clouds, and snow, the optical depth errors can be greater than 50% for relatively thin clouds. Therefore, the lookup tables for top-of-the-atmosphere reflectance are used if  $\alpha_{sd} > 0.20$  and  $\tau \leq 8$ . The lookup table values are first multiplied by  $t_{a1}$  to account for ozone variability and then interpolated to obtain the top-of-the-atmosphere reflectances corresponding to the observed or expected clear-sky albedo and the specified cloud and angular conditions. These values replace the results of (4.3-11) for the thin clouds over bright scenes.

The three equations (4.3-4), (4.3-6), and (4.3-11) are solved using the iterative process outlined in Figure 4.3-10 for each cloudy pixel. An initial guess solves (4.3-11) for  $\tau$  assuming a water-droplet model with  $r_e = 8 \mu\text{m}$ . Cloud emittance is computed for channels 3 and 4 using (4.3-9);  $T_{cld}$  is then determined from (4.3-4) at  $11 \mu\text{m}$ . If  $T_{cld} > 253 \text{ K}$ , then it is used in (4.3-6) with  $\tau$  to compute  $BTD_{3-4}(r_e)$  for the full range of particle sizes in the water droplet model. Otherwise,  $BTD_{3-4}(D_e)$  is calculated for the ice crystal models. Finally, a new estimate of particle radius,  $r_e'$ , or  $D_e'$ , is determined by matching the observed  $BTD_{3-4}$  with the model output. For the water droplet case, if  $BTD_{3-4}$  is less than the value of the greatest model radius and  $T_{cld} < 273 \text{ K}$ , the process is repeated using the ice crystal models beginning with an initial guess of  $D_e = 37 \mu\text{m}$ . Otherwise,  $r_e$  is set equal to  $r_e'$  and the process is repeated until the two values are within  $0.1 \mu\text{m}$  of each other. Likewise, in the ice crystal case, if  $T_{cld} > 233 \text{ K}$  and  $BTD_{3-4}$  is greater than that of the smallest ice crystal model, the process is repeated using the water droplet models. The test for phase is executed only after the first iteration. An additional 10 iterations are allowed before the process is ended and no solution is obtained. Most cases require fewer than six iterations. In some instances, the ice and water droplet models will produce overlapping results so that the small ice crystals may occasionally be mistakenly identified as large water droplets. Overlapped cirrus and liquid water clouds and mixed-phase clouds can produce radiances that fall between the ice and liquid models.

This approach is illustrated using 1-km AVHRR data taken near Coffeyville, Kansas during the November-December 1991 FIRE Cirrus field experiment. Figure 4.3-11(a) plots the observed  $BTD_{3-4}$  against  $T_4$  for a small area at 1900 UTC, November 22, 1991. The plotted numerals correspond to the number of pixels having the given pair of  $BTD_{3-4}$ - $T_4$  values. The curves represent the ice and water droplet model results for  $T_{cld} = 264 \text{ K}$ . Figure 4.3-11(b) is a histogram of  $r_e$  derived using the process described above for the data in Figure 4.3-11(a). In this case, the cloud is diagnosed as being a

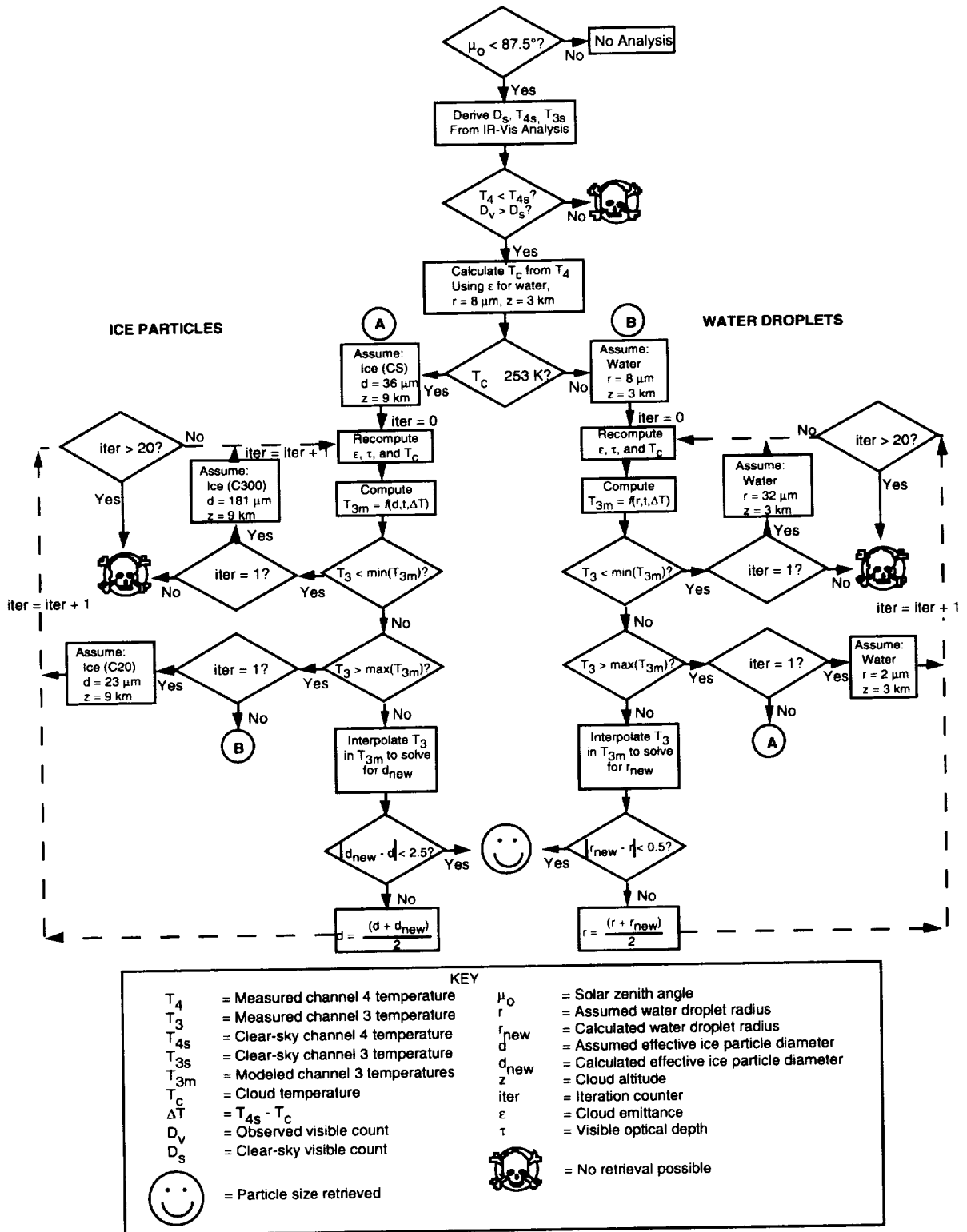
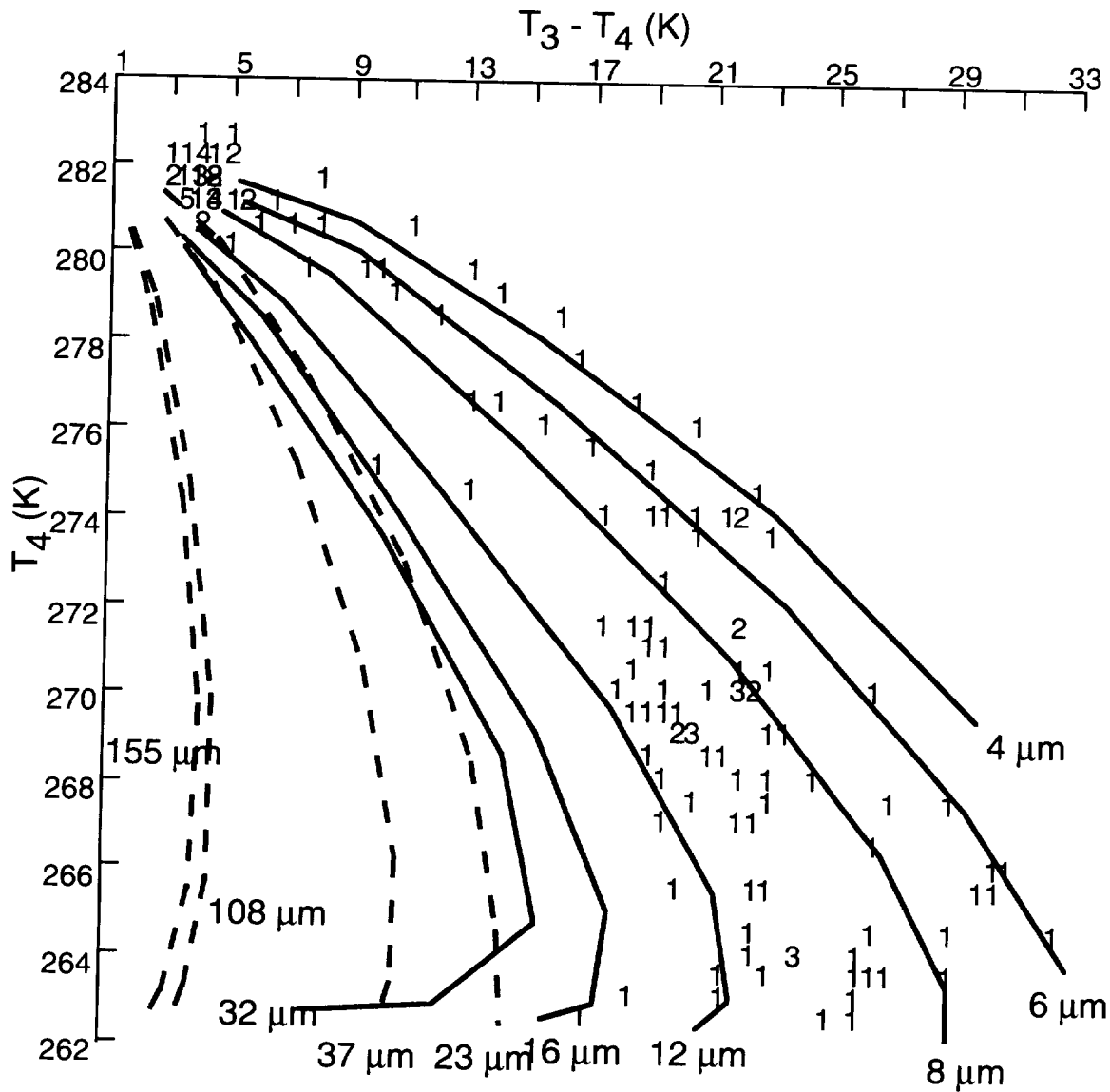
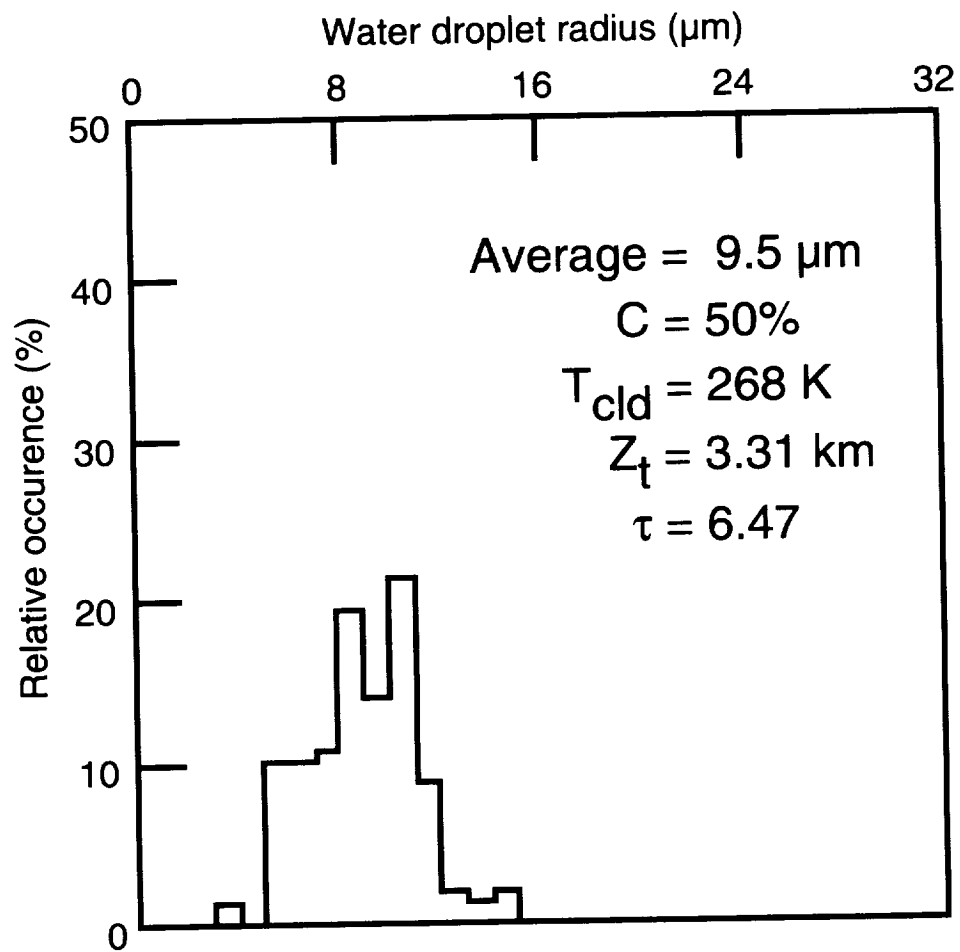


Figure 4.3-10. Flow diagram of channels 1, 3, and 4 cloud property retrieval algorithm. Effective diameter is denoted with  $d$ ; effective radius is  $r$ .



(a) Observed  $BT_{D_{3-4}}$  plotted against  $T_4$ .

Figure 4.3-11. AVHRR  $BT_{D-IR}$  histogram and water cloud retrieval in AVHRR data over  $39.3^\circ\text{N}$ ,  $98.1^\circ\text{W}$  at 2054 UTC, November 26, 1991.



(b) Histogram of  $r_e$ .

Figure 4.3-11. Concluded.

supercooled water cloud with mean  $r_e$ ,  $\tau$ , and  $T_{cld}$  values of 9.5  $\mu\text{m}$ , 6.5, and 268 K, respectively. A case where nonoverlapped high- and low-level clouds are present is shown in Figure 4.3-12 for data taken at 2042 UTC, November 28, 1991. The figure shows two-dimensional histograms of  $\rho_{vis}$  versus  $T_4$  (Fig. 4.3-12(a)) and  $BTD_{3-4}$  versus  $T_4$  (Fig. 4.3-12(b)) with a subjective estimate of the model that would best fit the histograms using the LBTM-derived (section 4.2.2.) values of  $T_{cld}$  from Figure 4.3-12(a). The full pixel-by-pixel analyses yielded the distribution of particle sizes given in Figure 4.3-13. The low-cloud top height of 1.6 km is 0.2 km higher than that derived from radar data taken at Coffeyville. The high-cloud altitude is at 9.0 km, midway between the base and top heights observed with the radar. The ice water path of the cirrus cloud is

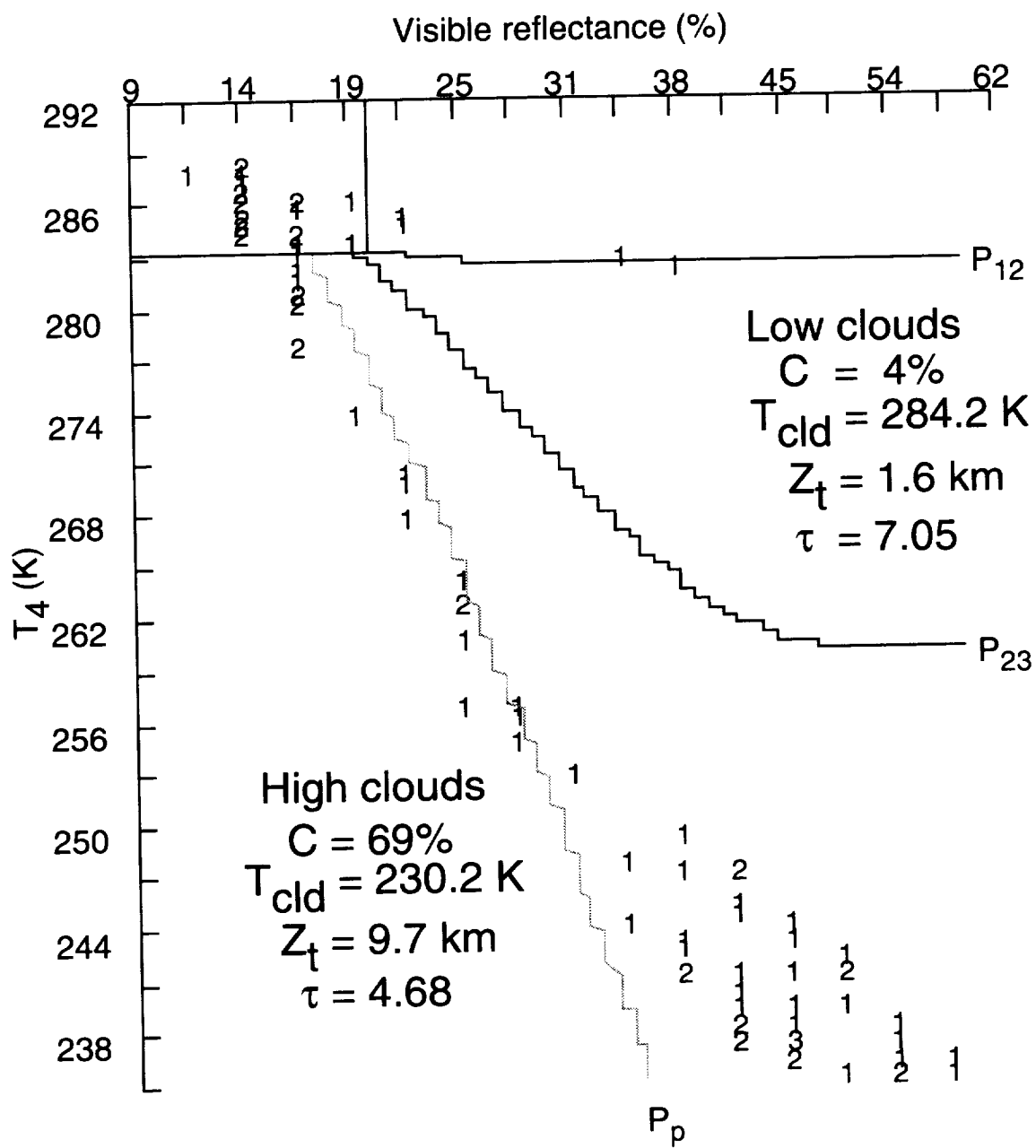
$$W_{ice} = \delta_{ice} \Sigma(V_i N_{oi}) \tau / \Sigma 2A_i N_{oi} \quad (4.3-13)$$

where  $V$  and  $A$  are the volume and cross-sectional areas, respectively, of the randomly oriented hexagonal crystal  $i$  in a specified distribution defined by the normalized number of crystals  $N_{oi}$ , and  $\delta_{ice}$  is the density of ice. The ice water path derived from the distribution in Figure 4.3-13(b) is 132  $\text{gm}^{-2}$  a value within 5% of the 139  $\text{gm}^{-2}$  derived from the surface radar. This result indicates the mean particle size is a reasonable estimate for the cloud. The high-cloud fraction is reduced from the LBTM analysis (Fig. 4.3-12(a)) because the cloud pixels with  $T_4 > 276$  K were too dim in the visible channel to solve for  $\tau$  and  $r_e$ . The mean value of  $r_e$  in Figure 4.3-13(a) yields  $W_{liq} = 47 \text{ gm}^{-2}$ , a value twice that of the half-hour-long surface microwave measurement; but it was derived using only four pixels or  $\sim 10$  minutes. Evaluation of a larger area of nearby low clouds provides a more appropriate comparison because it represents a longer time interval and the scene contains only one cloud layer. The results are  $r_e = 11.9 \mu\text{m}$  and  $W_{liq} = 30 \text{ gm}^{-2}$ . Comparisons of data taken during the FIRE II cirrus experiment found that the satellite-derived particle sizes from this method were within 15% of coincident ground-based, radar-derived ice particle sizes. These initial validations indicate that this technique can yield relatively accurate estimates of particle size and liquid water path.

Another example (Fig. 4.3-14) taken from AVHRR data near Coffeyville shows the difficulties arising from overlapped clouds. Here the retrieval for overlapped cirrus and low stratus yields large water droplets  $r_e = 16 \mu\text{m}$  and clouds at 4.0 km (Fig. 4.3-15(a)) in addition to the high clouds at 7.4 km with  $D_e = 58 \mu\text{m}$  (Fig. 4.3-15(b)). Nearby analyses of single layer stratus and cirrus yielded  $r_e = 10 \mu\text{m}$  and  $D_e = 46 \mu\text{m}$ , respectively. The surface instruments and soundings showed no indication of clouds in the middle layers but did show the two layers. Some of the clouds are apparently nonoverlapped because there are peaks in the size distributions at  $r_e = 10 \mu\text{m}$  (Fig. 4.3-15(a)) and at  $D_e = 40 \mu\text{m}$  (Fig. 4.3-15(b)). The overlapped clouds yield overestimates of particle size. This example shows that without knowledge of the overlap, the method will return errant values of  $T_{cld}$  and  $r_e$  for cases involving an optically thin cirrus over a lower cloud.

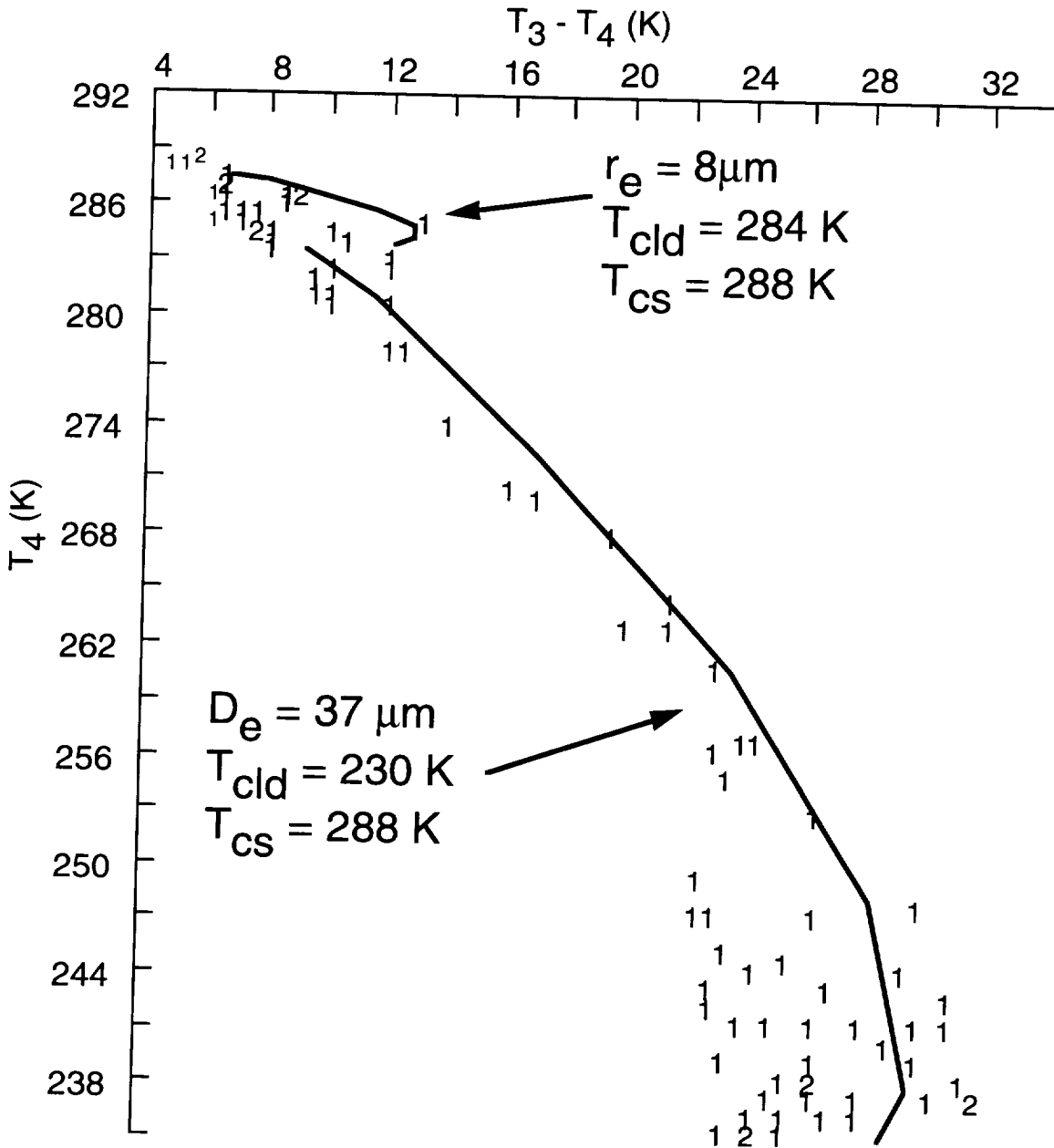
**4.3.4.1.2. Reflectance technique.** The reflectance approach uses the ratio  $\rho_{0.65}/\rho_{1.65}$  to determine the phase of the clouds by comparing the ratio to model calculations for thick ice and water droplet clouds. For each single-layer pixel, the phase will be determined by comparing the reflectance ratio to an ice-water threshold computed for  $\mu_o$ ,  $\mu$ , and  $\phi$  using the models discussed earlier. If the ratio exceeds the greatest model ice ratio, the cloud will be designated as liquid water; otherwise, the phase is ice.

After determination of the phase, a least squares approach is applied to match the multispectral radiances to a set of model calculations simulating the reflectances for clouds having a range of particle sizes and optical depths. This approach, the models to apply it, the expected errors, and current limitations are discussed in detail by King and Tsay (1993). This technique will use the VIRS 0.65-, 3.75-, and 1.60- $\mu\text{m}$  data during CERES/TRMM. It is anticipated that CERES/EOS will use the 3-channel reflectance method employing the 2.13- $\mu\text{m}$  MODIS channel. In the Release 2 software design for the COPRS, the reflectance method may serve as the primary particle size retrieval method.

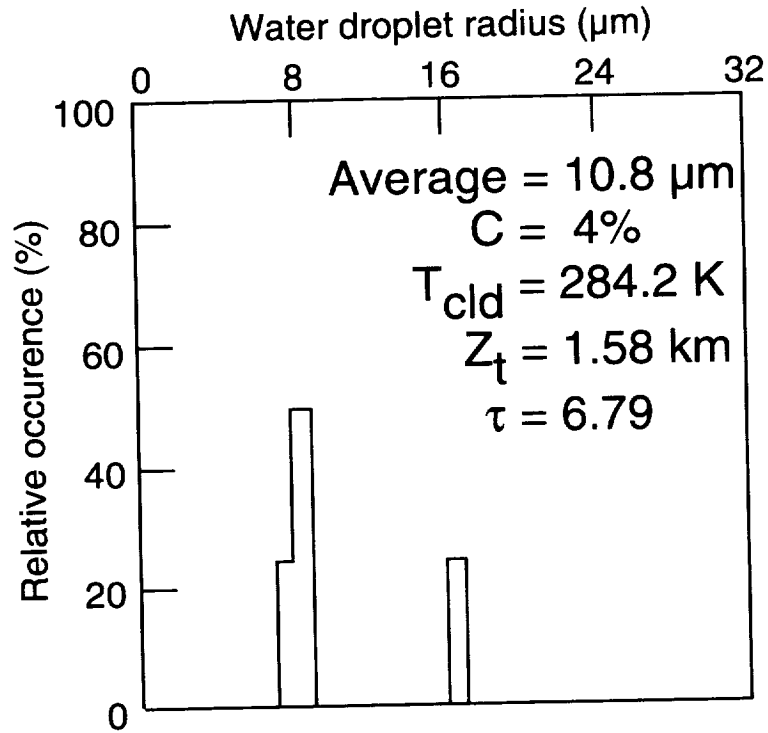


(a) VIS-IR histogram.

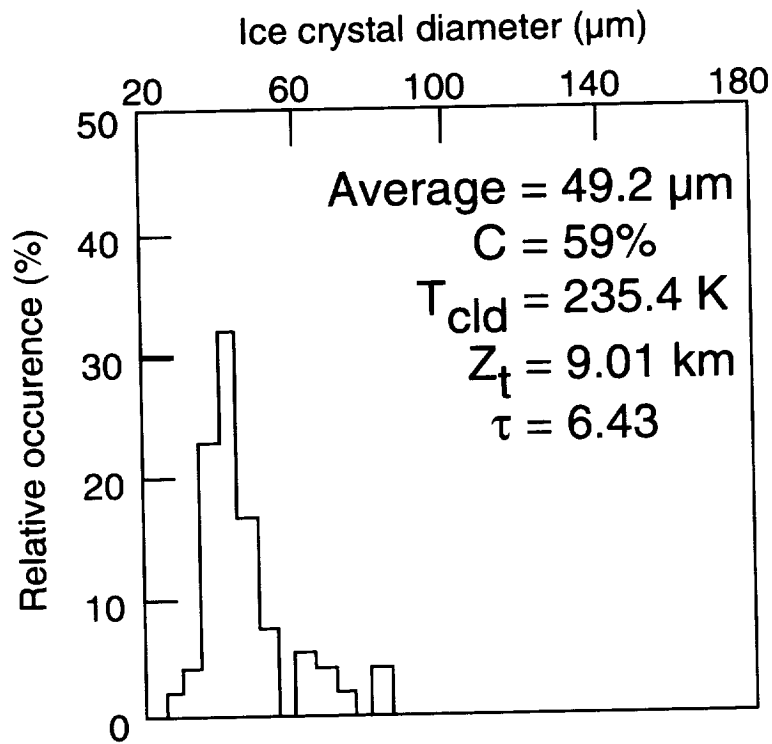
Figure 4.3-12. AVHRR histograms over 37.3°N, 95.1°W at 2042 UTC, November 28, 1991.



(b) BTD-IR histogram.  
 Figure 4.3-12. Concluded.



(a) Water cloud retrieval.



(b) Ice cloud retrieval.

Figure 4.3-13. Retrieval in AVHRR data over  $37.3^\circ\text{N}$ ,  $95.1^\circ\text{W}$  at 2042 UTC, November 28, 1991.

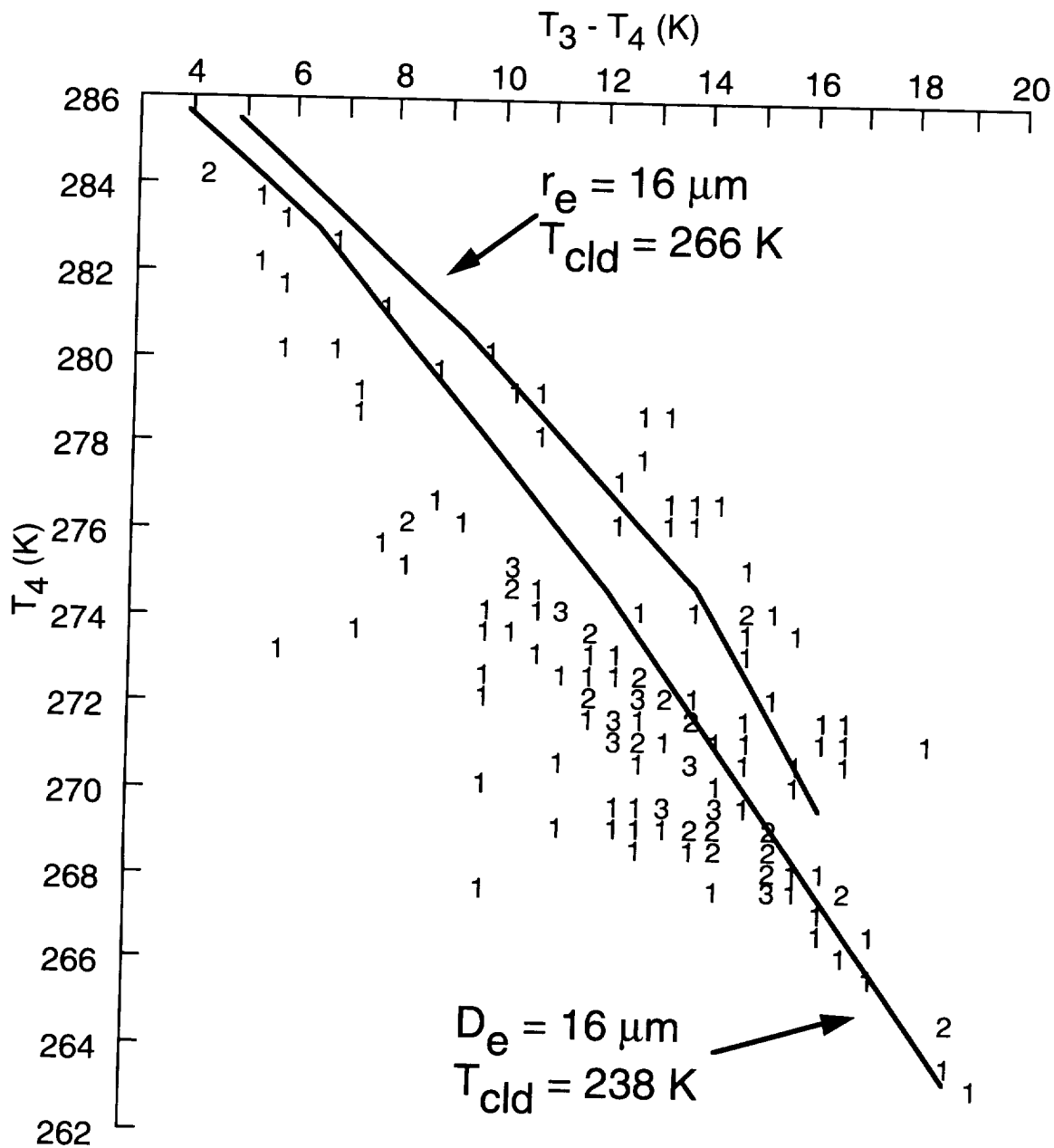
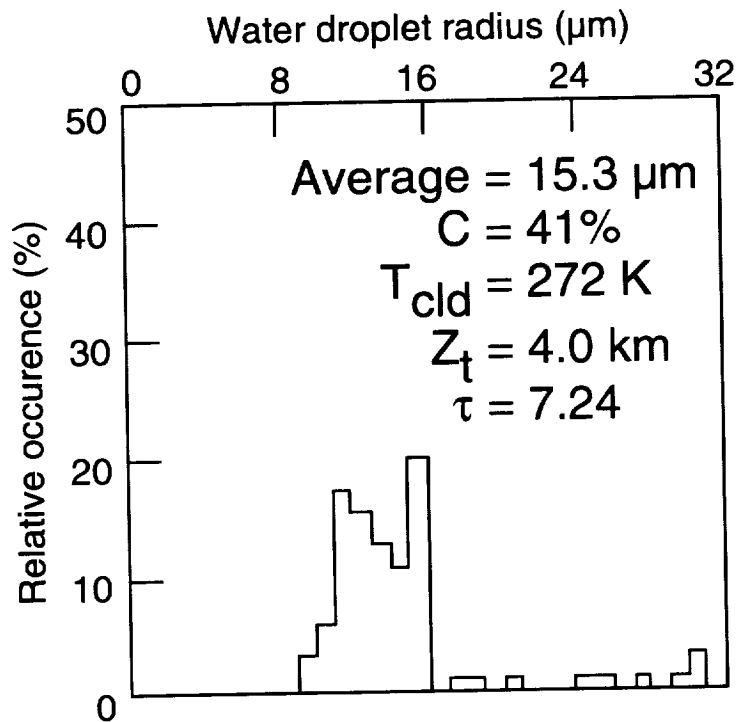
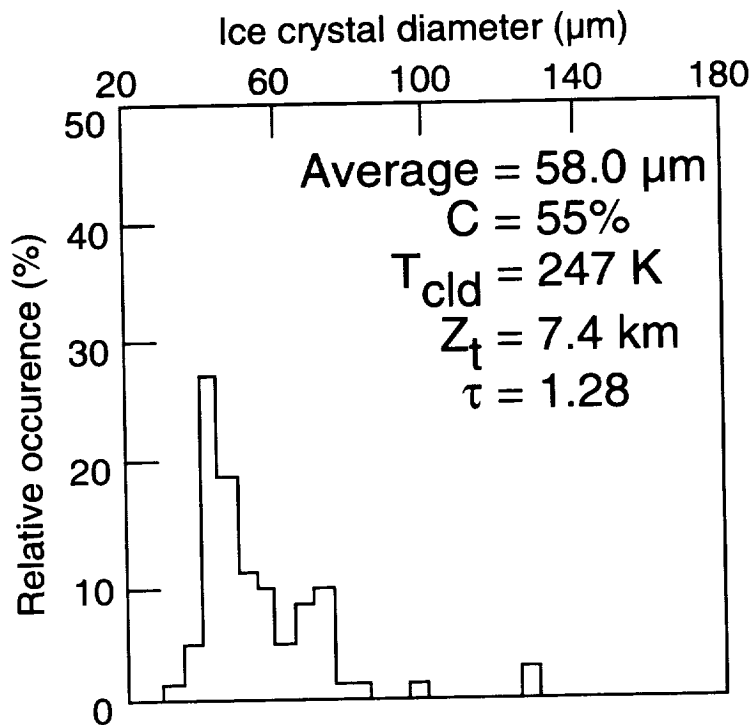


Figure 4.3-14. AVHRR BT-D-IR histogram over 37.1°N, 95.6°W at 2036 UTC, November 28, 1991.



(a) Water cloud retrieval.



(b) Ice cloud retrieval.

Figure 4.3-15. Retrieval in AVHRR data over 37.1°N, 95.6°W at 2036 UTC, November 28, 1991.

#### 4.3.4.2. Nighttime Cloud Optical Depth, Particle Size, and Cloud Temperature

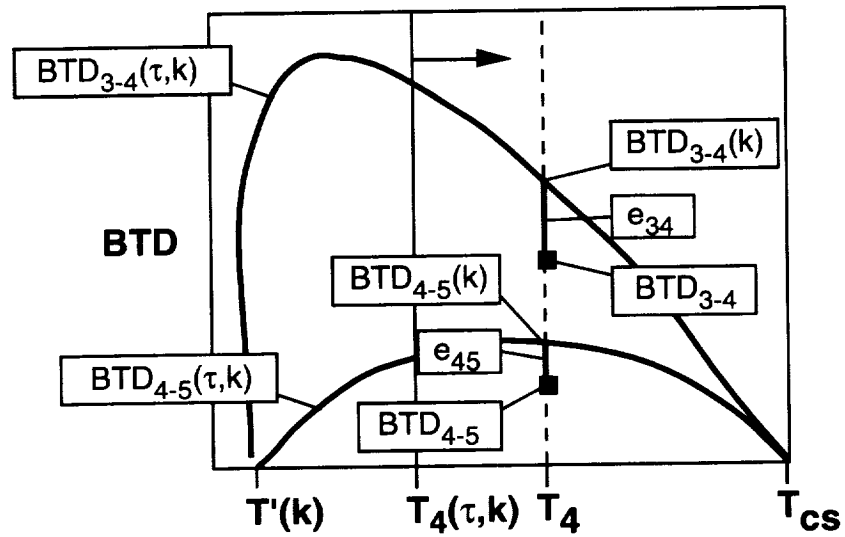
The cumulative experience of remotely sensing particle size and optical depth at night is much less than that for the daytime. The available techniques are either in early development or in a conceptual stage at this time. The primary shortcoming to the nocturnal methods is the lack of a relatively independent optical depth channel. When the sun is shining, it is usually possible to obtain a close approximation of optical depth using the visible channel because of its relative insensitivity to particle size (Fig. 4.3-6) and its independence from  $T_{cld}$ . This facilitates the determination of  $T_{cld}$  and, ultimately,  $r_e$ . At night, the problem is less tractable because all three channels are highly sensitive to  $T_{cld}$  and  $\tau$  for small optical depths ( $\tau < 6$ ). Although  $T_{cld}$  is well defined for larger optical depths, there is minimal information available regarding  $\tau$  and  $r_e$ . For those clouds having small optical depths, particle size and  $\tau$  can be determined using one of the approaches described below.

**4.3.4.2.1. Iteration-interpolation.** Given an optically thin cloud ( $\tau < 6$ ),  $\mu$ , and the background (clear-sky or cloudy) temperatures for channels 3, 4, and 5, it is assumed that a given pair of  $BTD_{3-4}$  and  $BTD_{4-5}$  at a particular value of  $T_4$  uniquely define a cloud characterized by  $T_{cld}$ ,  $r_e$  or  $D_e$ , and  $\tau$ . These parameters can be determined by matching the three measured quantities as closely as possible to the same parameters calculated using each of the microphysical models defined for the COPRS. Each observed quantity will fall between the corresponding pair of discrete theoretical calculations for a given phase. The distance in  $BTD$  from the model value to the observed value is used to interpolate between each model for each parameter to assign a value of cloud temperature, optical depth, and particle size to the pixel for both channels 3 and 5. In the absence of temperature indications, the phase is selected based on how closely the channel 3 and 5 parameters agree with each other. The final values of  $T_{cld}$ ,  $r_e$  or  $D_e$ , and  $\tau$  are determined by averaging the channels 3 and 5 results for the selected phase.

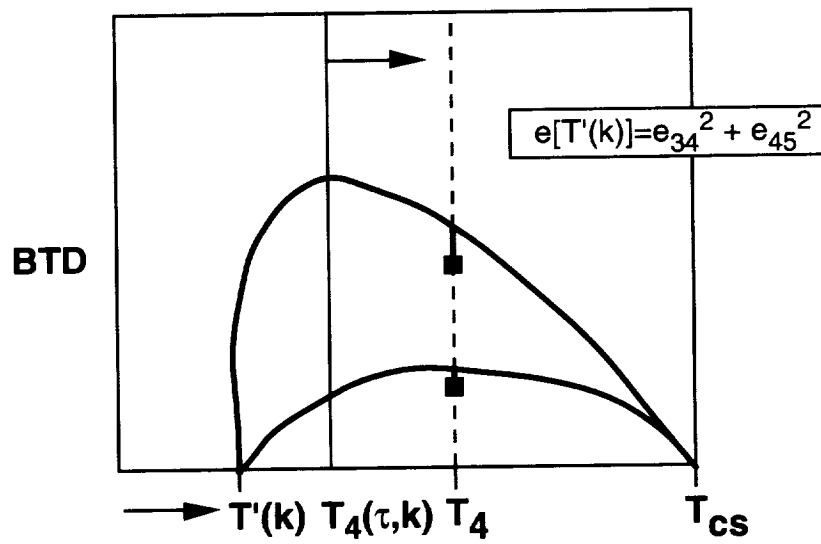
This technique attempts to determine  $\tau$ ,  $T_{cld}$ , and particle size through an iterative process that minimizes the differences between model-derived and observed values of  $BTD_{3-4}$  and  $BTD_{4-5}$  for the observed  $T_4$ . This procedure, illustrated schematically in Figure 4.3-16, begins with values given for  $\mu$  and  $T_{cs}$  and assumes an initial value of  $T_{cld} = T'(k)$ , where  $T'(k) < T_4$  and  $k$  is an emittance model index corresponding to a particular particle size and phase. The tropopause temperature is the initial value of  $T_{cld}$  unless the layer analysis (section 4.2.) indicates only a single layer is present or  $BTD_{3-4} < BTD_{3-4cs}$ . In the former case, the initial cloud temperature is the layer temperature minus 5 K. If  $BTD_{3-4} < BTD_{3-4cs}$ , the starting temperature is  $T_4 - 5$  K. For each of the channel-4 emittance models (4.3-8),  $\tau[T'(k), k]$  is determined using a secant iteration method to match  $T_4$ . This process is represented by the arrow in Figure 4.3-16(a). The resulting value of  $\tau$  is used to compute  $T_3$  and  $T_5$  using the channels 3 and 5 emittance models in (4.3-4). The model values of  $BTD_{3-4}[T'(k), k]$  and  $BTD_{4-5}[T'(k), k]$ , shown as the intersections of the model curves and the dashed line in Figure 4.3-15(a), are calculated from the model-derived temperatures and the observed  $T_4$ . Difference errors,  $e_{34} = BTD_{3-4} - BTD_{3-4}[T'(k), k]$  and  $e_{45} = BTD_{4-5} - BTD_{4-5}[T'(k), k]$ , are computed for each model. A composite error,

$$e[T'(k), k] = e_{34}^2 + e_{45}^2 \quad (4.3-14)$$

becomes the parameter to minimize. These operations are repeated varying  $T'(k)$  as illustrated in Figure 4.3-16(b) until  $e(T_{new}, r_e)$  is minimized yielding the best estimate of cloud temperature for model  $k$ . In the first iteration,  $T'(k)$  is increased by 10 K for each step until  $e$  begins to increase. Figure 4.3-17(a) depicts how  $e$  can vary with increasing  $T'(k)$ . Subsequent iterations repeat the error calculations using increasingly smaller temperature increments bounded by the last two temperatures used in the preceding iteration. The iterations continue until the increment is less than 0.1 K. For the case in Figure 4.3-17(a), the value of  $T_{cld}(k)$  corresponds to the minimum error. This entire procedure is repeated again for each model producing final values of  $e[T'(k), k]$  as shown in Figure 4.3-17(b). In practice, the algorithm begins with the smallest model for the phase and continues until  $e_{34}$  and  $e_{45}$

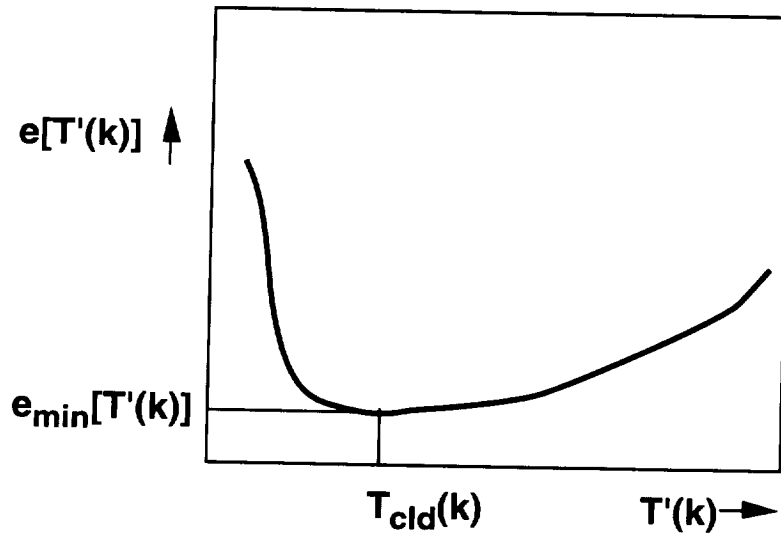


(a) First step of iteration process; compute errors for model k using first guess temperature.

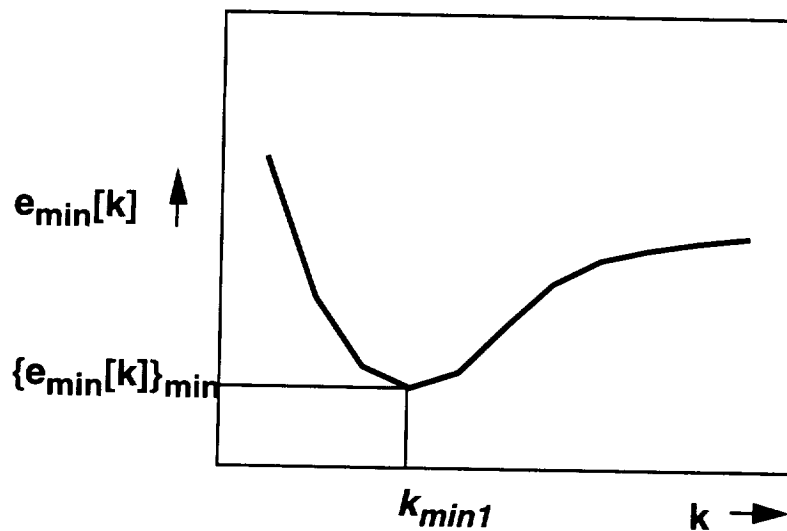


(b) Second step of iteration process; compute errors for second cloud-temperature guess.

Figure 4.3-16. Schematic illustration of emittance iteration process for nighttime cloud property retrievals.



(a) Determination of the minimum error in a given particle size model.



(b) Determination of model having minimum error.

Figure 4.3-17. Schematic diagram of minimum error estimation to determine most appropriate particle size models.

switch signs. The sign change in these error values indicates that the observation is between the last two models. One of the two models,  $k_{\min 1}$ , will have the smallest value of  $e$  for the particular phase, while the other model,  $k_{\min 2}$ , should also have a relatively low error. These two models are then selected for interpolation. If  $T_{cld} > 273$  K, only the water-droplet models are used. Conversely, if  $T_{cld} < 233$  K, only the ice-crystal models are considered further.

Final values of  $r_e$  or  $D_e$ ,  $T_{cld}$ , and  $\tau$  are computed for channel 3 by linearly interpolating between  $r_e(k_{\min 1})$  and  $r_e(k_{\min 2})$ ,  $T_{cld}(k_{\min 1})$  and  $T_{cld}(k_{\min 2})$ , and  $\tau(k_{\min 1})$  and  $\tau(k_{\min 2})$ , respectively, using  $e_{34}[T'(k_{\min 1}), k_{\min 1}]$  and  $e_{34}[T'(k_{\min 2}), k_{\min 2}]$  as the independent variables. The same interpolation is repeated for channel 5. The resultant values for the two channels are averaged to obtain the best estimate

of each parameter. If both phases are considered, then the results for the phase having the smallest uncertainty,

$$e_{35} = \left( \frac{T_{cld3} - T_{cld5}}{T_{cld3}} \right)^2 + \left( \frac{\tau_3 - \tau_5}{\tau_3} \right)^2 + \left( \frac{r_{e3} - r_{e5}}{r_{e3}} \right)^2 \quad (4.3-15)$$

are selected for the final parameter values. The subscripts 3 and 5 refer to the parameter values derived using channel 4 with channels 3 and 5, respectively. The most accurate estimates of  $T_{cld}$  are obtained for the larger optical depths ( $\tau > 6$ ), while the most accurate values of  $\tau$  and  $r_e$  should occur for ( $1 < \tau < 6$ ). There is little variation in *BTD* with particle size for small and large optical depths. This method was tested using a limited set of simulated data with superimposed noise. In these cases, the retrieved particle sizes were within 0.1  $\mu\text{m}$  of the simulated cloud values and the phase was chosen correctly. Testing of this method with actual data is underway.

**4.3.4.2.2. Single-layer, fixed-size technique.** An alternate method that may be included in the COPRS is the technique of Lin and Coakley (1993) that interprets the pixel radiances for a single-layer cloud deck as

$$B(T) = (1 - C)B(T_{cs}) + C(\epsilon B(T_{cld}) + tB(T_{cld})) \quad (4.3-16)$$

where wavelength is implied and  $C$  and  $\epsilon$  are the pixel-scale fractional cloud cover and cloud emittance, respectively. The cloud temperature and particle size index are determined iteratively from the group of pixels constituting the cloud deck. The emittance models described earlier will be used to determine particle size and phase. A single cloud temperature and effective radius are assumed for the entire deck. Those two parameters define a set of solutions to (4.3-16) that envelope most of the pixels representing the cloud deck. The emittance and cloud fraction for each pixel within the envelope are obtained through simultaneous solution of (4.3-16) for channels 4 and 5. Details of this method are given by Lin and Coakley (1993).

This technique is limited to those conditions where a single layer is easily discernible. It allows no variation of particle size and radiating temperature within the deck. The particle size derived for the deck tends to be the smallest observable particle size for the given set of pixels because it is defined by those pixels essentially having the greatest  $BTD_{4,5}$  for a given  $T_4$ . The cloud temperature also tends to be the coldest observed brightness temperature. This method, however, requires no iteration and is relatively simple to implement. Refinement of the technique is continuing.

#### 4.3.4.3. Multiple Cloud Layer Retrievals

The discussion above generally applies to single layer clouds or to overlapped clouds that include an optically thick upper cloud layer. In either case, the pixel index will probably denote a single layer cloud. For data blocks with multiple cloud layer pixels, a slightly different approach is taken. The first step for a given data block is to determine the particle sizes for all of the single-layer pixels. When available, the mean particle sizes and temperatures are computed for each layer. If single-layer particle size is not available, only the layer temperatures are available from the subsystem input dataset. Two approaches are taken for these cases.

When the layer temperatures and particle sizes are available, optical depth is the remaining unknown quantity if the background temperature is specified. In the case of multiple layers, the background temperature may vary with the emittance or optical depth of the lower cloud. The range of the background temperature is simply  $T_{cs} - T_{lc}$ , where  $T_{lc}$  is the lower-cloud temperature. An envelope of  $T_4$  and  $BTD_{3,4}$  can be constructed using the upper cloud temperature  $T_{uc}$  as  $T_{cld}$ , and  $T_{lc}$  and  $T_{cs}$  as the temperatures used to compute the clear radiance term in (4.3-4) and (4.3-9). Multilevel pixels falling outside this envelope will be treated as single-layer pixels and the particle size and cloud temperature

retrieval will be executed in the normal fashion. Those pixels with values within the envelope will be analyzed for particle size and background or “clear-sky” temperature. The initial background temperature is found by linear interpolation between the lower and upper bounds of  $BTD_{3-4}$  at the observed  $T_4$ . The optical depth of the upper cloud is found using (4.3-4). The final values of the lower and upper cloud optical depths are found by iterating this process. The mean particle sizes and temperatures for the upper and lower clouds are assigned to all of the pixels in the envelope.

When layer temperatures are the only parameters available, it is assumed that the lower cloud is optically thick so that  $T_{lc}$  is the only value substituting for  $T_{cs}$ . The 3-channel infrared method is then applied to find optical depth and cloud particle size. If particle sizes can be retrieved, they are used to compute mean values for the upper layer. The first approach is then invoked for the remaining pixels if they are available. If no particle sizes are retrieved, the particle size is specified using default values for water and ice. Optical depths are then computed using the visible reflectance. A technique for using the MODIS 1.38- $\mu\text{m}$  channel will also be explored for estimating the high cloud optical depth. The methods for processing multilayer pixels are in the development stage.

#### 4.3.4.4. Water Path

Rearranging (4.3-7) gives the liquid water path,

$$W_{liq} = \frac{4\delta_{liq}r_e\tau}{3Q_e} \quad (4.3-17)$$

for a given effective droplet radius and optical depth. Using the model distributions in (4.3-13) in a regression fit yields the ice water path,

$$W_{ice} = \delta_{liq}\tau D_e(0.304 + 0.00124D_e) \quad (4.3-18)$$

for the retrieved ice-crystal size and optical depth.

#### 4.3.4.5. Cloud Top and Base Altitudes

Cloud-top height  $Z_t$  is the lowest altitude from the sounding corresponding to  $T_{cld}$ . Because the value of  $T_{cld}$  may correspond more closely to the center of the cloud in optically thin cases, it will be adjusted in some cases to account for semitransparency. The adjustment uses the approach of Minnis et al. (1990a) for cirrus clouds. The channel-4 cloud-top emittance is defined as

$$\epsilon_t = \epsilon_4(2.97 - 0.00914T_{cld}) \quad (4.3-19)$$

The cloud-top temperature  $T_t$  is computed using the observed value of  $T_4$  and  $T_{cs4}$  in (4.3-4). This approach is used only for  $T_{cld} < 253$  K. For warmer clouds,  $\epsilon_t = 0.98\epsilon_4$ . No adjustment is made for water clouds because the correction is usually less than 0.1 km, the precision of the height determination. Cloud base is given as  $Z_b = Z_t - \Delta Z$ . The cloud thickness  $\Delta Z$  is computed using empirical formulae. For clouds below 4 km,  $\Delta Z = 0.08\tau^{1/2} - 0.04$  (Minnis et al. 1992). When  $\Delta Z < 0.02$  km,  $\Delta Z$  is set to 0.02 km. For other clouds,

$$\Delta Z = 7.5 - 0.026T_c + 0.85 \ln \tau \quad (4.3-20)$$

(Smith et al. 1993). The minimum thickness for these clouds is also 0.02 km, with a maximum of 8 km. Cloud base and top pressures correspond to  $Z_b$  and  $Z_t$  in the vertical profiles of  $Z(p)$  and  $T(p)$ .

### 4.3.5. Practical Considerations

#### 4.3.5.1. Computer Requirements

**4.3.5.1.1. Model input.** The bidirectional reflectance models have been computed for 13 particle sizes. They are discretized at 12 optical depths. The last four optical depths are not included for the 3.75- $\mu\text{m}$  channel since the reflectance is essentially invariant for larger optical depths. The arrays for each particle size require 0.25, 0.25, and 0.19 megabytes of storage, respectively, for the 0.65-, 1.61-, and 3.75- $\mu\text{m}$  channels. The emittance models for each particle size have been computed for 3.75, 11, and 12  $\mu\text{m}$ . A total of 75 coefficients are used for each emittance model.

**4.3.5.1.2. Subsystem output.** The output comprises a set of 16-bit integer values that define the cloud properties for each pixel in the analysis block. The parameters are phase (dimensionless), particle size (units of  $\mu\text{m} \times 10$ ), cloud visible optical depth (dimensionless  $\times 10$ ), channel-4 zenith emittance (dimensionless  $\times 100$ ), cloud liquid or ice water path ( $\text{kg}/\text{m}^2 \times 1000$ ), cloud-top pressure (hPa), cloud effective pressure or  $p(T_{\text{clid}})$  (hPa), cloud-base pressure (hPa), cloud effective temperature ( $\text{K} \times 10$ ), cloud effective altitude ( $\text{km} \times 10$ ), and cloud effective cloud particle size ( $\mu\text{m} \times 10$ ). In addition, there will be a quality flag and methodology flag to indicate the uncertainty and source of the retrieval for each pixel.

**4.3.5.1.3. Data processing requirements.** The processing requirements for the reflectance method are given by King and Tsay (1993). The processing needs for the other algorithms are substantial and will be determined.

#### 4.3.5.2. Strategic Concerns

There are many situations that can prevent or diminish the accuracy of a given parameter retrieval. Some situations can be handled through the application of alternative methods, others by using default options. Solutions to all of the problems noted below, as well as others that will inevitably arise in the development of this global methodology, will be examined in current and future research.

**4.3.5.2.1. Potential problems.** There are many situations that can foil the algorithms outlined above. A listing of all such conditions would be superfluous. Some of the more important potential problems confronting the COPRS are noted below.

In most daytime cases, a reliable retrieval of cloud optical depth, particle size, and temperature can be obtained for optically thick clouds. However, thick low or midlevel clouds can be shadowed by nearby high clouds voiding the plane-parallel assumption in all retrievals using solar reflectance. Shadows also can affect thin-cloud retrievals in variable thickness, single-layer fields (Minnis et al. 1990b). Clouds affected by shadows frequently are darker than the clear-sky pixels so that their properties cannot be obtained with reflectance models. Even when optically thick, ice clouds may not produce reflectances that conform to the model configurations because of the wide variety and potential orientations of the particles in cirrus clouds. Particle size retrievals for clouds containing very large particles will be constrained because of the limited sensitivity of the mixed and emittance methods.

Thin-cloud properties will be severely diminished in accuracy for pixels taken over relatively bright backgrounds such as desert, snow, or other clouds. It may not be possible to obtain a solution in many of these instances. Thin-cloud retrievals near coastlines will also be subject to errors in the clear-sky radiances because of slight mislocations. All of the retrievals are based on plane-parallel radiative transfer models. Thus, for scattered or broken cloud fields or for clouds with internal variations in their optical properties, there may be significant errors in the retrieval of particle size and optical depth (e.g., Stackhouse and Stephens 1994; Duda et al. 1994). Cloud thickness estimates are based on a limited amount of empirical data so that the global applicability of these formulas is highly uncertain. As discussed earlier,

nocturnal retrievals of  $\tau$  and  $r_e$  are not possible for optically thick clouds. During both day and night, retrievals for overlapped clouds will be much less certain than those for single layer clouds. Near the terminator, the geometry and the atmospheric path lengths diminish the variability in the reflected radiance fields and, essentially, negate the plane-parallel cloud assumption. Retrievals that depend on reflectances become much more uncertain. There is still some solar contamination of the channel-3 radiances at the high solar zenith angles so that an emittance-based retrieval must account for the solar reflectance component which is highly uncertain.

**4.3.5.2.2. Solutions.** Accounting for these various situations presents a challenge to the development of a comprehensive global analysis system. A first-order solution to the problem of shadowed cloud pixels is to tag them as such and assign them the mean values of the nearest cloud layer. If the shadowing is particularly heavy, it can be assumed that the reflected portion of the channel-3 radiance is negligible. In that case, the 3-channel iteration-interpolation method can be implemented. At this time, there is no technique available for finding ice particle shape and orientation using passive satellite measurements. If no solution can be obtained for a single-layer cloud during the daytime using the mixed technique because the particles are too large, the reflectance method using the 1.61- $\mu\text{m}$  channel will be applied. If no solution is obtained, the pixel particle size will be assigned using either the closest extreme model value or the average of all the adjacent pixels. A similar approach is used for optical depth and cloud temperature.

For thin clouds over bright scenes, it may be necessary to use the iteration-interpolation method since the channel-3 surface albedo is relatively small compared to the visible albedo. Similarly, clouds are much more reflective at visible rather than near-infrared wavelengths. In the bright background instances, the channel-3 solar component will be calculated for each of the models and optical depths. The iteration-interpolation method would proceed as usual. This daytime application of the 3-channel emittance method can also be used to determine the consistency between the day and night cloud property retrievals. The use of the 3-channel emittance technique during the day needs further evaluation.

The difficulties of the near-terminator geometry are less manageable than many of the other problems. It may be possible to assume a particle size and derive the cloud temperature and optical depth using channels 4 and 5. When MODIS is operating, the problem is somewhat mitigated because three thermal window channels will be available. At night, when the optical depth and radius retrievals are limited to  $\tau \sim 10$ , a default value will be assigned.

#### **4.3.5.3. Calibration and Validation**

The derived parameters for each pixel are critically dependent on the absolute calibration of the sensors. Although comprehensive sensitivity studies have not been performed for all of the COPRS algorithm components, some estimates of the dependence of particle size on the channel-3 radiance have been made by Han (1992). For example, he found that a precision of  $0.0017 \text{ W}\cdot\text{m}^{-2}\cdot\text{sr}^{-1}$  in the channel 3 radiances translates into uncertainties as low as 2% for  $r_e < 20 \mu\text{m}$ ,  $\tau > 3$  and as great as 10% in  $r_e$  for  $\tau \leq 1$ . Similar uncertainties in the channel 3 calibration would probably produce particle size errors of the same magnitude. The filter functions of the channel-3 sensor must also be accurately known to derive an accurate value of the spectral solar constant for the calculation of the solar component of the observed radiances. Further sensitivity studies are needed to evaluate the full impact of calibration on the derived quantities.

Validation efforts before, during, and after the CERES flights are essential to understanding the accuracy of the retrieved quantities. Before the initial launches, datasets taken during FIRE, ASTEX, ARM, and TOGA/COARE will be used to verify the optical depths, particle phases and sizes, water path, and cloud temperatures using the developmental code and substitute satellite (i.e., historical AVHRR and GOES) and aircraft data. After launch, FIRE III, SHEBA, and ARM data will be used to assess the operational algorithms. In situ measurements and active remote sensing of cloud

microphysics are needed to estimate the uncertainties in phase and particle size. During TRMM, the VIRS-derived droplet radii over water may also be compared for consistency to  $r_e$  retrieved with the microwave liquid-water-path/visible reflectance approach discussed in section 4.3.2.3. Radar and lidar data from aircraft and surface sites are needed to evaluate the particle sizes, cloud-top and cloud-base temperatures, and the ice water paths. Sunphotometers, radar, and lidar data are needed to verify optical depths. Microwave radiometers are needed to assess liquid water path. Other instruments, such as nephelometers, are needed to ensure that the scattering phase functions used in the model calculations are reasonably accurate. All of these types of instruments should be available in part or in total during each of the noted experiments. High-altitude radiometric measurements using wavelengths similar to VIRS or MODIS are needed for calibration checks and for model validation. The ER-2 MODIS Airborne Simulator and the Multispectral Pushbroom Imaging Radiometer (MPIR) proposed for unmanned aircraft by the DOE should be valuable assets for those purposes. Those data will also be useful for determining the sensitivity of the retrievals to the viewing conditions.

#### 4.3.5.4. Quality Control and Diagnostics

The initial quality control occurs within the basic algorithms. Constraints are also applied to ensure that no physically unreasonable values are passed to the next subsystem. Particle sizes are not allowed to fall outside of prespecified limits that depend on phase. Cloud temperatures are not allowed to exceed the warmest temperature in the sounding or at the surface, whichever is greatest. Cloud temperatures must be warmer than the tropopause temperature minus 5 K. As a consistency check, the cloud temperatures will also be compared to the values derived for the layer clouds. Liquid water path and optical depths will be capped to prevent unrealistic values. In all cases, a new value, from adjacent pixels or the nearest cloud layer or from a default value set, will replace the suspect pixel value. A quality flag will be set to indicate what bound was violated. A flag will also be set to denote which methodology or replacement technique produced the final cloud property values. Other diagnostics and quality checks will be implemented as needed.

#### 4.3.5.5. Numerical Computation Considerations

The code as currently developed processes up to 275 pixels per second on a 300 *Mflop* CPU. While the speed is less than real time, the operational algorithms will perform at higher rates as a result of code optimization.

#### 4.3.6. References

- Ackerman, Steven A.; and Stephens, Graeme L. 1987: The Absorption of Solar Radiation by Cloud Droplets—An Application of Anomalous Diffraction Theory. *J. Atmos. Sci.*, vol. 44, pp. 1574–1588.
- Ackerman, Steven A.; Smith, W. L.; Revercomb, H. E.; and Spinhirne, J. D. 1990: The 27–28 October 1986 FIRE IFO Cirrus Case Study—Spectral Properties of Cirrus Clouds in the 8–12 Micron Window. *Mon. Weather Rev.*, vol. 118, pp. 2377–2388.
- Arking, A.; and Childs, J. D. 1985: Retrieval of Cloud Cover Parameters From Multispectral Satellite Images. *J. Climat. & Appl. Meteorol.*, vol. 24, pp. 322–333.
- Baum, Bryan A.; Arduini, Robert F.; Wielicki, Bruce A.; Minnis, Patrick; and Si-Chee, Tsay 1994: Multilevel Cloud Retrieval Using Multispectral HIRS and AVHRR Data: Nighttime Oceanic Analysis. *J. Geophys. Res.*, vol. 99, no. D3, pp. 5499–5514.
- Baum, Bryan A.; Wielicki, Bruce A.; Minnis, Patrick; and Parker, Lindsay 1992: Cloud-Property Retrieval Using Merged HIRS and AVHRR Data. *J. Appl. Meteorol.*, vol. 31, pp. 351–369.
- Blau, H. H., Jr.; Espinola, R. P.; and Reifensstein, E. C., III 1966: Near Infrared Scattering by Sunlit Terrestrial Clouds. *Appl. Opt.*, vol. 5, pp. 555–564.
- Charlson, Robert J.; Warren, Stephen G.; Lovelock, James E.; and Andreae, Meinrat O. 1987: Oceanic Phytoplankton, Atmospheric Sulphur, Cloud Albedo and Climate. *Nature*, vol. 326, pp. 655–661.

- Coakley, James A., Jr.; Bernstein, Robert L.; and Durkee, Philip A. 1987: Effect of Ship-Stack Effluents on Cloud Reflectivity. *Science*, vol. 237, pp. 1020–1022.
- Curran, R. J.; and Wu, M.-L. C. 1982: Skylab Near-Infrared Observations of Clouds Indicating Supercooled Liquid Water Droplets. *J. Atmos. Sci.*, vol. 39, pp. 635–647.
- d'Entremont, Robert P. 1986: Low- and Mid-Level Cloud Analysis Using Nighttime Multispectral Imagery. *J. Climat. & Appl. Meteorol.*, vol. 25, pp. 1853–1869.
- Duda, D. P.; Stephens, G. L.; and Cotton, W. R. 1994: Impact of Enhanced CCN Concentrations on the Radiative Properties of a 3D Marine Stratocumulus Cloud. *Eighth Conference on Atmospheric Radiation*, AMS, pp. 262–264.
- Fu, Qiang; and Liou, K. N. 1992: On the Correlated  $k$ -Distribution Method for Radiative Transfer in Nonhomogeneous Atmospheres. *J. Atmos. Sci.* vol. 49, no. 22, pp. 2139–2156.
- Hale, G. M.; and Querry, M. R. 1973: Optical Constants of Water in the 200-nm to 200-Micron Wavelength Region. *Appl. Opt.*, vol. 12, pp. 555–563.
- Han, Q. 1992: Global Survey of Effective Particle Size in Liquid Water Clouds. Ph.D. Diss., Columbia University, New York.
- Hansen, J. E.; and Travis, L. D. 1974: Light Scattering in Planetary Atmospheres. *Space Sci. Rev.*, vol. 16, pp. 527–610.
- Hansen, J. E.; and Pollack, J. B. 1970: Near-Infrared Light Scattering by Terrestrial Clouds. *J. Atmos. Sci.*, vol. 27, pp. 265–281.
- Heck, Patrick W.; Mayer, Shalini; Young, David F.; Minnis, Patrick; Takano, Yoshihide; Liou, Kuo-Nan; and Spinhirne, James D. 1993: Comparison of Radiation and Cloud Parameters Derived From Satellite and Aircraft Measurements During FIRE 2 Cirrus IFO. *The FIRE Cirrus Science Results 1993*, David S. McDougal, ed., NASA CP-3238, pp. 24–27.
- Heymsfield, A. J.; and Platt, C. M. R. 1984: A Parameterization of the Particle Size Spectrum of Ice Clouds in Terms of the Ambient Temperature and the Ice Water Content. *J. Atmos. Sci.*, vol. 41, pp. 846–855.
- Hunt, G. E. 1973: Radiative Properties of Terrestrial Clouds at Visible and Infra-Red Thermal Window Wavelengths. *Q. J. R. Meteorol. Soc.*, vol. 99, pp. 346–369.
- Inoue, T. 1985: On the Temperature and Effective Emissivity Determination of Semi-Transparent Cirrus Clouds by Bi-Spectral Measurements in the 10 Micron Window Region. *Meteorol. Soc. Japan*, vol. 63, pp. 88–99.
- King, Michael D.; Kaufman, Yoram J.; Menzel, W. Paul; and Tanre, Didier D. 1992: Remote Sensing of Cloud, Aerosol, and Water Vapor Properties From the Moderate Resolution Imaging Spectrometer (MODIS). *IEEE Trans. Geosci. & Remote Sens.*, vol. 30, pp. 2–27.
- King, M. D.; and Tsay, S. C. 1993: Theoretical Basis of Cloud Retrieval Algorithms for MODIS: Cloud Cover, Thermodynamic Phase, Optical Thickness and Effective Particle Radius. *MODIS Algorithm Theoretical Basis Document*, p. 32.
- Kneizys, F. X.; Shettle, E. P.; Abreu, L. W.; Chetwynd, J. H.; Anderson, G. P.; Gallery, W. O.; Shelby, J. E. A. and Clough, S. A. 1988: *Users Guide to LOWTRAN 7*. AFGL-TR-88-0197, U.S. Air Force. (Available from DTIC as AD A206 773.)
- Kratz, D. P. 1995: The Correlated  $k$ -Distribution Technique as Applied to the AVHRR Channels. *J. Quant. Spectrosc. Radiat. Transfer*, vol. 53, pp. 501–507.
- Lin, Xijian; and Coakley, James A., Jr. 1993: Retrieval of Properties for Semitransparent Clouds From Multispectral Infrared Imagery Data. *J. Geophys. Res.*, vol. 98, no. 10, pp. 18,501–18,514.
- Liou, K. 1974: On the Radiative Properties of Cirrus in the Window Region and Their Influence on Remote Sensing of the Atmosphere. *J. Atmos. Sci.*, vol. 31, pp. 522–532.
- Liou, K. N.; Ou, S. C.; Takano, Y.; Valero, F. P. J.; and Ackerman, T. P. 1990a: Remote Sounding of the Tropical Cirrus Cloud Temperature and Optical Depth Using 6.5 and 10.5-Micron Radiometers During STEP. *J. Appl. Meteorol.*, vol. 29, pp. 716–726.
- Liou, K. N.; Takano, Y.; Ou, S. C.; Heymsfield, A.; and Kreiss, W. 1990b: Infrared Transmission through Cirrus Clouds—A Radiative Model for Target Detection. *Appl. Opt.*, vol. 29, pp. 1886–1896.
- Masuda, Kazuhiko; and Takashima, Tsutomu 1990: Deriving Cirrus Information Using the Visible and Near-IR Channels of the Future NOAA-AVHRR Radiometer. *Remote Sens. Environ.*, vol. 31, pp. 65–81.
- Minnis, P.; Young, D. F.; Garber, D. P.; Takano, Y.; and Liou, K. N. 1994: Effects of Cloud Particle Size and Shape on Satellite Remote Sensing of Cloud Properties. *Eighth Conference on Atmospheric Radiation*, AMS, pp. 418–420.

- Minnis, Patrick; Heck, Patrick W.; and Young, David F. 1993a: Inference of Cirrus Cloud Properties Using Satellite-Observed Visible and Infrared Radiances. II—Verification of Theoretical Cirrus Radiative Properties. *J. Atmos. Sci.*, vol. 50, no. 9, pp. 1305–1322.
- Minnis, Patrick; Heck, Patrick W.; Young, David F.; Fairall, C. W.; and Snider, J. B. 1992: Stratocumulus Cloud Properties Derived From Simultaneous Satellite and Island-Based Instrumentation During FIRE. *J. Appl. Meteorol.*, vol. 31, pp. 317–339.
- Minnis, Patrick; Liou, Kuo-Nan; and Takano, Yoshihide 1993b: Inference of Cirrus Cloud Properties Using Satellite-Observed Visible and Infrared Radiances. I—Parameterization of Radiance Fields. *J. Atmos. Sci.*, vol. 50, no. 9, pp. 1279–1304.
- Nakajima, Teruyuki; and King, Michael D. 1990: Determination of the Optical Thickness and Effective Particle Radius of Clouds From Reflected Solar Radiation Measurements. I—Theory. *J. Atmos. Sci.*, vol. 47, pp. 1878–1893.
- Nakajima, Teruyuki; King, Michael D.; Spinhirne, James D.; and Radke, Lawrence F. 1991: Determination of the Optical Thickness and Effective Particle Radius of Clouds From Reflected Solar Radiation Measurements. II—Marine Stratocumulus Observations. *J. Atmos. Sci.*, vol. 48, pp. 728–750.
- Ou, S. C.; Liou, K. N.; Gooch, W. M.; and Takano, Y. 1993: Remote Sensing of Cirrus Cloud Parameters Using Advanced Very-High-Resolution Radiometer 3.7- and 10.9- $\mu\text{m}$  Channels. *Appl. Opt.*, vol. 32, no. 12, pp. 2171–2180.
- Parol, F.; Buriez, J. C.; Brogniez, G.; and Fouquart, Y. 1991: Information Content of AVHRR Channels 4 and 5 With Respect to the Effective Radius of Cirrus Cloud Particles. *J. Appl. Meteorol.*, vol. 30, pp. 973–984.
- Prabhakara, C.; Fraser, R. S.; Dalu, G.; Wu, Man-Li C.; and Curran, R. J. 1988: Thin Cirrus Clouds—Seasonal Distribution Over Oceans Deduced From Nimbus-4 IRIS. *J. Appl. Meteorol.*, vol. 27, pp. 379–399.
- Radke, Lawrence F.; Coakley, James A., Jr.; and King, Michael D. 1989: Direct and Remote Sensing Observations of the Effects of Ships on Clouds. *Science*, vol. 246, pp. 1146–1149.
- Rawlins, F.; and Foot J. S. 1990: Remotely Sensed Measurements of Stratocumulus Properties During FIRE Using the C130 Aircraft Multi-Channel Radiometer. *J. Atmos. Sci.*, vol. 47, pp. 2488–2503.
- Reynolds, D. W.; and Vonder Haar, T. H. 1977: A Bispectral Method for Cloud Parameter Determination. *Mon. Weather Rev.*, vol. 105, pp. 446–457.
- Rossow, William B.; and Lacis, Andrew A. 1990: Global, Seasonal Cloud Variation From Satellite Radiance Measurements. II—Cloud Properties and Radiative Effects. *J. Climat.*, vol. 3, pp. 1204–1253.
- Rossow, William B.; Garder, Leonid, C.; Lu, Pei-Jane; and Walker, Alison 1992: *International Satellite Cloud Climatology Project (ISCCP): Documentation of Cloud Data*. Centel Federal Services Corp., New York.
- Rossow, W. B.; Mosher, F.; Kinsella, E.; Arking, A.; and Harrison, E. 1985: ISCCP Cloud Algorithm Intercomparison. *J. Climat. & Appl. Meteorol.*, vol. 24, Sept. 1985, pp. 877–903.
- Slingo, A. 1989: A GCM Parameterization for the Shortwave Radiative Properties of Water Clouds. *J. Atmos. Sci.*, vol. 46, pp. 1419–1427.
- Smith, William L., Jr.; Minnis, Patrick; Alvarez, Joseph M.; Uttal, Taneil; Intrieri, Janet M.; Ackerman, Thomas P; and Clothiaux, Eugene 1993: Development of Methods for Inferring Cloud Thickness and Cloud Thickness and Cloud-Base Height From Satellite Radiance Data. *The FIRE Cirrus Science Results 1993*, David S. McDougal, ed., NASA CP-3238, pp. 32–35.
- Stackhouse, Paul W., Jr.; and Stephens, Graeme L. 1994: Investigation of the Effects of the Macrophysical and Microphysical Properties of Cirrus Clouds on the Retrieval of Optical Properties—Results for FIRE 2. *The FIRE Cirrus Science Results 1993*, David S. McDougal, ed., NASA CP-3238, pp. 189–192.
- Stamnes, Knut; Tsay, S.-Chee; Jayaweera, Kolf; and Wiscombe, Warren 1988: Numerically Stable Algorithm for Discrete-Ordinate-Method Radiative Transfer in Multiple Scattering and Emitting Layered Media. *Appl. Opt.*, vol. 27, pp. 2502–2509.
- Stephens, G. L. 1978: Radiation Profiles in Extended Water Clouds. Part I—Theory. Part II: Parameterization Schemes. *J. Atmos. Sci.*, vol. 35, pp. 2111–2132.
- Stone, Robert S.; Stephens, Graeme, L.; Platt, C. M. R.; and Banks, S. 1990: The Remote Sensing of Thin Cirrus Cloud Using Satellites, Lidar and Radiative Transfer Theory. *J. Appl. Meteorol.*, vol. 29, pp. 353–366.
- Takano, Yoshihide; and Liou, Kuo-Nan 1989: Solar Radiative Transfer in Cirrus Clouds. I—Single-Scattering and Optical Properties of Hexagonal Ice Crystals. *J. Atmos. Sci.*, vol. 46, pp. 3–36.

- Takano, Y.; Liou, K. N.; and Minnis, P. 1992: The Effects of Small Ice Crystals on Cirrus Infrared Radiative Properties. *J. Atmos. Sci.*, vol. 49, no. 16, pp. 1487–1493.
- Twomey, S. 1977: The Influence of Pollution on the Shortwave Albedo of Clouds. *J. Atmos. Sci.*, vol. 34, pp. 1149–1152.
- Twomey, S.; and Cocks, T. 1982: Spectral Reflectance of Clouds in the Near-Infrared—Comparison of Measurements and Calculations. *J. Meteorol. Soc. Japan*, vol. 60, pp. 583–592.
- Twomey, S.; and Cocks, T. 1989: Remote Sensing of Cloud Parameters From Spectral Reflectance in the Near-Infrared. *Beitr. Phys. Atmos.*, vol. 62, no. 3, pp. 172–179.
- Twomey, S.; and Seton, K. J. 1980: Inferences of Gross Microphysical Properties of Clouds From Spectral Reflectance Measurements. *J. Atmos. Sci.*, vol. 37, pp. 1065–1069.
- Van De Hulst, Hendrik Christoffel 1957: *Light Scattering by Small Particles*. John Wiley & Sons, 1957.
- Wielicki, Bruce A.; Suttles, J. T.; Heymsfield, Andrew J.; Welch, Ronald M.; Spinhirne, James D.; Wu, Man-Li C.; and Starr, David O'C. 1990: The 27–28 October 1986 FIRE IFO Cirrus Case Study—Comparison of Radiative Transfer Theory With Observations by Satellite and Aircraft. *Mon. Weather Rev.*, vol. 118, pp. 2356–2376.
- Wigley T. M. L. 1989: Possible Climate Change Due to SO<sub>2</sub>-Derived Cloud Condensation Nuclei. *Nature*, vol. 339, pp. 365–367.
- Wu, Man-Li C. 1987: A Method for Remote Sensing the Emissivity, Fractional Cloud Cover and Cloud Top Temperature of High-Level, Thin Clouds. *J. Climat. & Appl. Meteorol.*, vol. 26, pp. 225–233.
- Young, D. F.; Mayor, S.; Minnis, P.; Intrieri, J. M.; Matrosov, S.; and Snider, J. 1994: Comparison of Satellite and Surface-Based Remote Sensing of Cloud Microphysical Properties During FIRE Cirrus Phase II. *Eighth Conference on Atmospheric Radiation*, AMS, pp. 231–233.
- Young, D. F.; Minnis, P.; Katsaros, K.; Dybbroe, A.; and Mileta, J. 1992: Comparison of Techniques for Deriving Water-Cloud Microphysical Properties From Multiple Satellite Data. *Proceedings of the 11th International Conference Clouds and Precipitation*, pp. 1053–1056.
- Young, D. F.; Minnis, P.; Snider, J. B.; Uttal, T.; Intrieri, J. M.; and Matrosov, S. 1993: Comparison of Cloud Microphysical Parameters Derived From Surface and Satellite Measurements During FIRE Phase II. *Proceedings of the FIRE Cirrus Science Conference*, pp. 52–55.

## Appendix

### Correction for Gaseous Absorption

Numerous cloud property retrieval techniques require knowledge of the absorption properties of the atmosphere as an integral part of the analysis. Complementary analysis of satellite data with radiative transfer theory improves not only our ability to analyze and understand the data, but our understanding of the physics of the processes modeled. To this end, the absorption by molecular species in the clear-sky pixels is accomplished by means of the correlated  $k$ -distribution technique.

#### *Correlated $k$ -Distribution Technique*

Various modeling techniques are available to account for the observed absorption of electromagnetic radiation by the molecules which are present in planetary atmospheres. The line-by-line, or monochromatic, procedure is very precise and has an accuracy that is limited only by the extent of our knowledge of the interactions of matter with energy. Such precision, however, is only obtained at the cost of very intensive routines which are not practical in production calculations. To overcome the computational burden of the line-by-line procedure, narrowband and broadband techniques have been devised. While these band models can be made arbitrarily accurate for a homogeneous (constant temperature, pressure, etc.) atmosphere, they require a scaling procedure to account for the inhomogeneity found in realistic atmospheres. In essence, the scaling procedure transforms the inhomogeneous pathlength found in a realistic atmosphere into an equivalent homogeneous pathlength. While entirely satisfactory for the case where only absorption is present, such a transformation is not acceptable for cases where scattering is involved. Nevertheless, a technique, known as the correlated  $k$ -distribution, has been devised to accurately and efficiently calculate molecular absorption for a inhomogeneous path without a scaling approximation.

Taking for a moment any arbitrary spectral interval, if the absorption coefficient ( $k$ ) is plotted against wavenumber  $\omega$ , a highly nonmonotonic plot will be obtained. The line-by-line procedure resorts to retracing this plot with sufficient spectral resolution so as to accurately reproduce the spectrum of absorption coefficients. An examination of this plot of  $k$  versus  $\omega$  will reveal that similar values of  $k$  occur many times. Thus arises the concept of the  $k$  distribution. If a transformation of coordinates is made from wavenumber space to cumulative probability space  $g(k)$ , it will be observed that the highly nonmonotonic plot of  $k$  versus  $\omega$  will become a monotonic plot of  $k$  versus  $g(k)$ . To this point, the only information which has been discarded is the precise spectral location of a particular  $k$ ; however, no gain in speed has been obtained. Recall that only the terms of the integration have been reordered. It is noted, however, that the monotonic distribution of  $k$  versus  $g(k)$  can have far fewer (often 3 to 5 orders of magnitude) terms, yet retain very high accuracy for the calculation of the absorption for the specified spectral interval. This reduction in the number  $k$  values needed leads to the increased efficiency necessary for any production calculations. To account for a inhomogeneous path, an additional assumption is required. Given any pressure or temperature encountered in the atmosphere, it is assumed that any particular absorption coefficient will always have the same cumulative probability. Thus, the location in cumulative probability space of any absorption coefficient at any given pressure or temperature will be correlated with that of the absorption coefficient at a specified reference pressure and temperature. This leads to the concept of the correlated  $k$ -distribution. Fu and Liou (1992) have demonstrated conclusively that the assumption of correlation is sufficiently accurate for most purposes. Since the  $k$ 's are assumed to be correlated for any pressure and temperature, the correlated  $k$ -distribution procedure can be calculated through an inhomogeneous atmosphere in the same manner as a monochromatic calculation. Thus, the correlated  $k$ -distribution allows for an efficient and accurate calculation which is compatible with most scattering routines.

**Clouds and the Earth's Radiant Energy System (CERES)**  
**Algorithm Theoretical Basis Document**

*Convolution of Imager Cloud Properties With  
CERES Footprint Point Spread Function  
(Subsystem 4.4)*

Richard Green<sup>1</sup>  
Bruce A. Wielicki<sup>1</sup>

<sup>1</sup>Atmospheric Sciences Division, NASA Langley Research Center, Hampton, Virginia 23681-0001

## Abstract

*CERES will determine the Earth Radiation Budget (ERB) at the top of the atmosphere (TOA) and at the surface of the Earth. To determine the surface ERB we must know the cloud properties over the CERES footprint. We use imager data at high resolution to get the necessary cloud properties. First, we locate the imager pixels that are within the CERES footprint. Since CERES has a rotating azimuth plane scanner, the collocation algorithm must be capable of handling an elongated and skewed footprint. We then determine the cloud statistics over the footprint with the cloud properties from the high-resolution imager cloud properties. Our statistics are weighted means and standard deviations where the weighting is the value of the point spread function (PSF). The major input and output data are defined in Appendixes A and B of section 4.0.*

### 4.4. Convolution of Imager Cloud Properties With CERES Footprint Point Spread Function

#### 4.4.1. Introduction

The general process is to analyze a large swath (approximately 500 km) of imager data as a unit and define cloud properties at each imager observation point (approximately 2 km grid). This requires multiple auxiliary data and various algorithms working in conjunction with one another. Once the 500-km swath of imager data is analyzed, the cloud statistics are determined over the CERES footprint. This footprint is defined by the CERES point spread function which gives the appropriate weighting of the field with respect to the optical axis. In other words, we form a CERES “cookie cutter” and cut out the cloud properties from the larger and higher resolution imager swath. This process continues with successive CERES footprints organized spatially along the satellite groundtrack until we are within 100 km of the end of the 500-km swath. If we proceed beyond this point, part of the CERES footprint could fall beyond the 500-km swath. At this point we drop the last 300 km of imager data, retain 200 km of data in the current area of convolution, and add a new 300-km swath at the beginning. Thus, we have a new 500-km swath and continue as before.

#### 4.4.2. Algorithm Description

##### 4.4.2.1. CERES Point Spread Function

The CERES scanning radiometer is an evolutionary development of the ERBE scanning radiometer. It is desired to increase the resolution as much as possible, using a thermistor bolometer as the detector. As the resolution is increased, the sampling rate must increase to achieve the desired resolution. When the sampling rate becomes comparable to the response time of the detector, the effect of the time response of the detector on the point spread function (PSF) must be considered. Also, the signal is usually filtered electronically prior to sampling in order to attenuate electronic noises and to remove high-frequency components of the signal which would cause aliasing errors. The time response of the filter together with that of the detector will cause a lag in the output relative to the input radiance, so that the time response causes the centroid of the PSF to be displaced from the centroid of the optical field-of-view. Thus, the signal as sampled is coming not only from where the radiometer is pointed, but includes a “memory” of the input from where it had been looking. Another effect of the time response is to broaden the PSF, which will reduce the resolution of the measurement, increase blurring errors, and decrease aliasing errors.

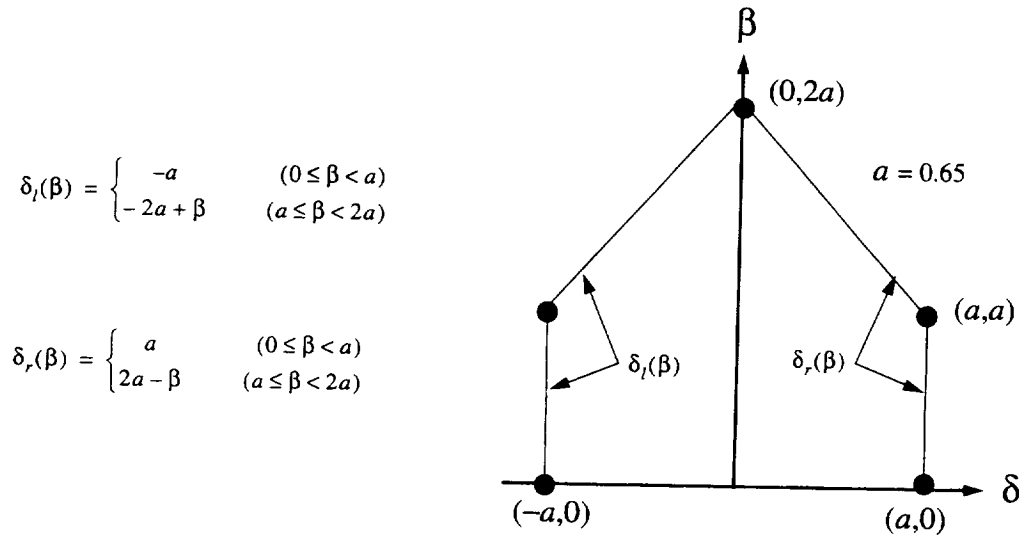


Figure 4.4-1. Optical FOV.

A full discussion of the point spread function and its development are given in Smith (1994) and a graph of the function is given in Figure 1-5. We will only define the function here. In Figure 4.4-1, we redraw half of the optical field of view (FOV) from Figure 4.4-2 where  $\delta$  is the along-scan angle and  $\beta$  is the cross-scan angle. The left and right boundaries are given by  $\delta_l(\beta)$  and  $\delta_r(\beta)$ , respectively. With these definitions we write the PSF as

$$P(\delta, \beta) = \begin{cases} 0 & (|\beta| > 2a) \\ 0 & (\delta < \delta_l(\beta)) \\ F[\delta - \delta_l(\beta)] & (\delta_l(\beta) \leq \delta < \delta_r(\beta)) \\ F[\delta - \delta_l(\beta)] - F[\delta - \delta_r(\beta)] & (\text{Otherwise}) \end{cases} \quad (4.4-1)$$

where

$$F(\xi) = 1 - (1 + a_1 + a_2)e^{-c_1\xi} + e^{-6.35465\xi}[a_1 \cos(1.90282\xi) + b_1 \sin(1.90282\xi)] + e^{-4.61598\xi}[a_2 \cos(5.83072\xi) + b_2 \sin(5.83072\xi)] \quad (4.4-2)$$

and

$$a_1 = 1.84205 \quad a_2 = -0.22502$$

$$b_1 = 1.47034 \quad b_2 = 0.45904$$

$$c_1 = 1.98412$$

The centroid of the PSF is derived in Smith (1994) and is approximately  $1.0^\circ$ . This shift is denoted in Figure 4.4-3. Note that positive  $\delta$  is opposite the scan direction.

#### 4.4.2.2. Geometry of the Point Spread Function

The scanner footprint geometry is given in Figure 4.4-2. The optical FOV is a truncated diamond (or hexagon) with  $Y'$  denoting the optical axis. The optical FOV is  $1.3^\circ$  in the along-scan direction and

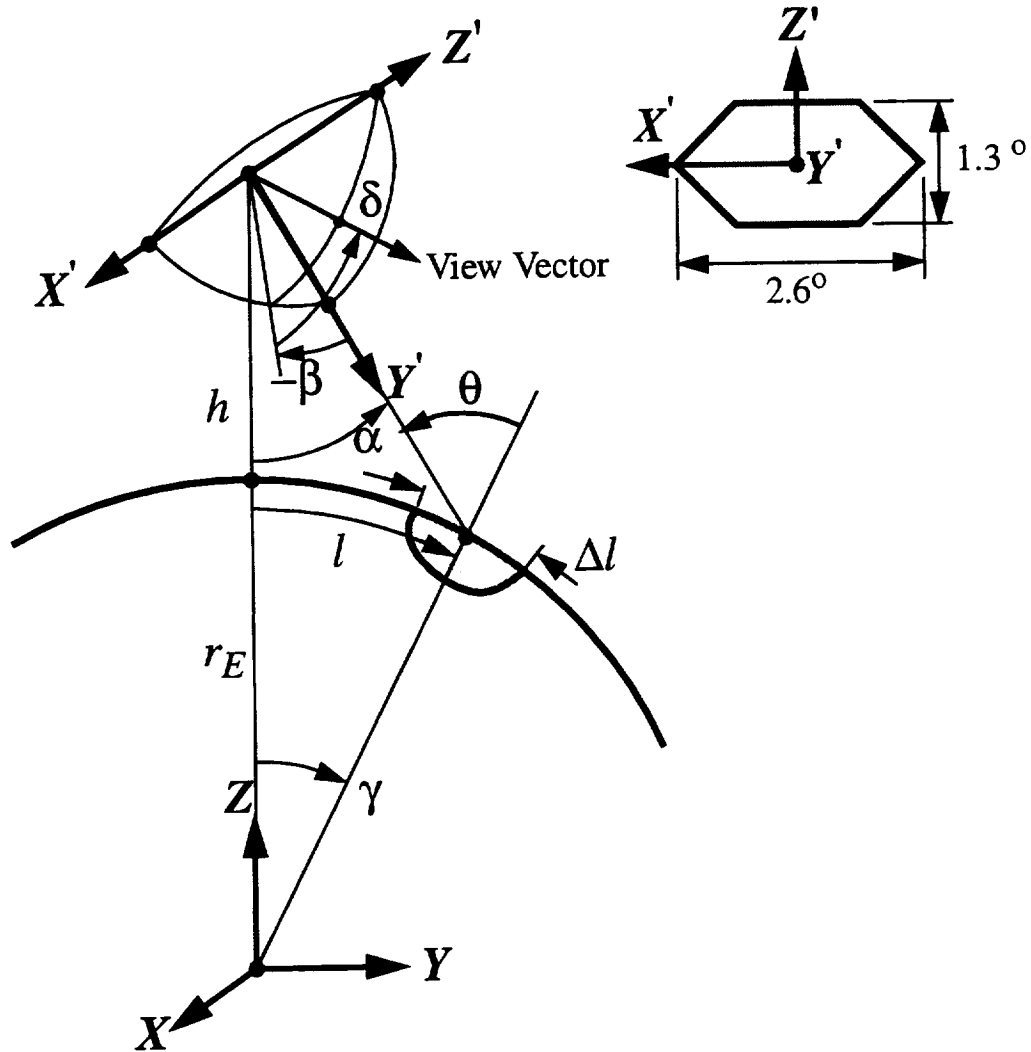


Figure 4.4-2. Scanner footprint geometry.

2.6° in the across-scan direction. A point within the FOV is located by  $\beta$  and  $\delta$ . The cone angle  $\alpha$  (or nadir angle) determines the location of the footprint on the Earth. If  $\alpha = 0$ , the footprint is at nadir. The viewing zenith angle  $\theta$  is a direct result of the satellite altitude  $h$ , the Earth radius  $r_E$ , and the cone angle  $\alpha$ . The surface distance  $l$  and the Earth central angle  $\gamma$  between nadir and the optical axis at the surface are also a result of the viewing geometry. Once this geometry is established we can determine the projection of the optical FOV on the curved surface of the Earth. In Figure 4.4-2, we have denoted the length of the FOV by  $\Delta l$ .

Figure 4.4-3 gives three CERES FOV's. The shaded area is the optical FOV. Note that only half of the FOV is given since it is symmetrical about the scan line. We have placed the origin at the centroid of the PSF which is about 1.0° behind the optical axis. This is the lag that is inherent in the system. About the PSF centroid we have drawn the outlines of the half-power cutoff and the full 95-percent energy cutoff. All of the pertinent dimensions are given.

Tables 4.4-1 and 4.4-2 give numerical values for the TRMM and EOS satellites. Table 4.4-1 presents the orbital characteristics and a summary of the footprint sizes. The largest footprint determines how close we can get to the end of the 500-km swath of imager data before we need to stop and extend the imager data. For TRMM the optical FOV projected onto the surface at nadir is 8 km long in the scan

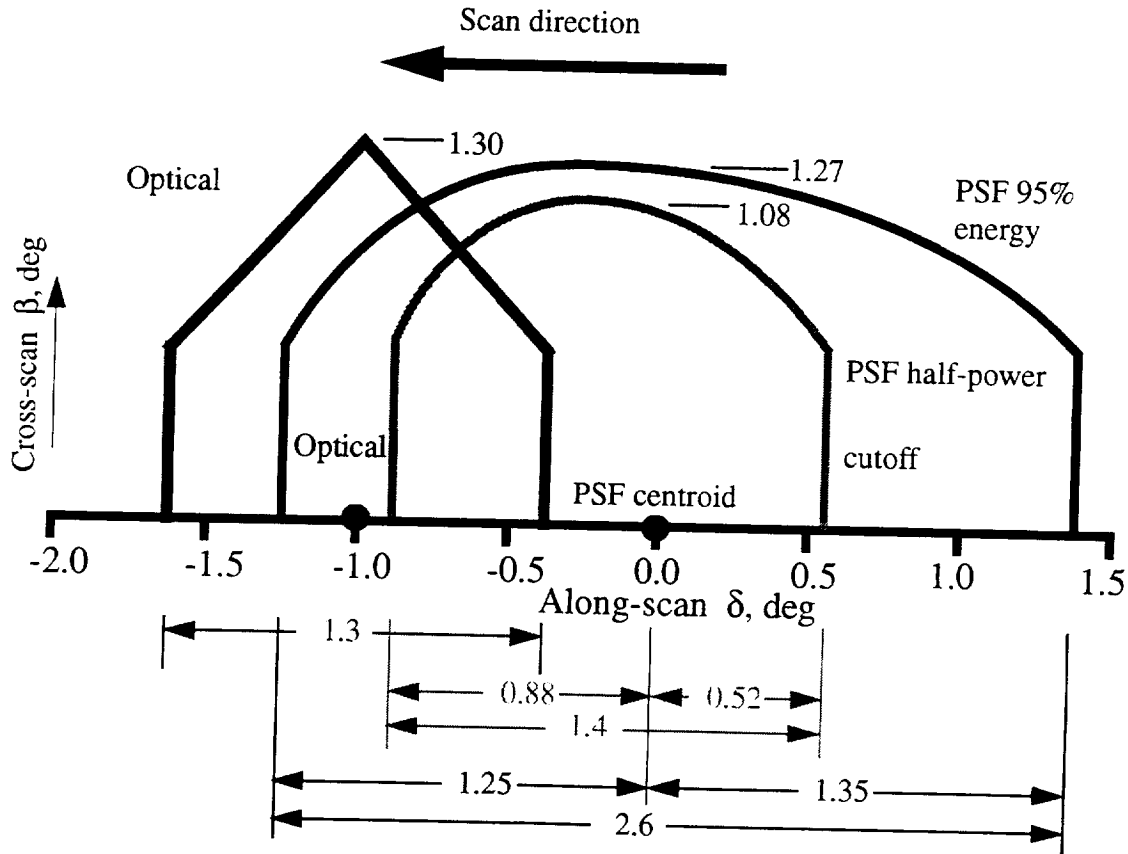


Figure 4.4-3. CERES fields-of-view.

Table 4.4-1. Orbital and CERES FOV Characteristics

		TRMM	EOS
$h$	Altitude of spacecraft, km	350	705
$r_E$	Radius of surface, km	6367	6367
$\alpha_h$	Cone angle at horizon, deg	71.4	64.2
$\gamma_h$	Earth central angle (ECA) at horizon, deg	18.6	25.8
$P$	Period, minute	91.4	98.7
Optical hexagonal footprint. Center at nadir.		$8 \times 16^*$	$16 \times 32$
PSF half-power cutoff. Centroid at nadir.		$9 \times 13$	$17 \times 27$
PSF 95% energy cutoff. Centroid at nadir.		$16 \times 16$	$32 \times 31$
PSF 95% energy cutoff. Centroid at $\theta^\# = 70^\circ$ .		$116 \times 38$	$212 \times 71$
PSF 95% energy cutoff. Centroid at $\theta = 75^\circ$ .		$186 \times 47$	$328 \times 82$
PSF 95% energy cutoff. Limit of Earth view at horizon.		$507 \times 63$	$660 \times 97$

\*Footprint size in along-scan length  $\times$  perpendicular-to-scan width in km.  
 $\#$  $\theta$  is viewing zenith at the surface.

direction and 16 km wide. Frequently this footprint is referenced by its equivalent area circle with a diameter of approximately 10 km. The optical FOV, however, is spread over the surface according to the point spread function as discussed above. We can also project the PSF on the surface at nadir. If we truncate the PSF at the half-power point, then the footprint is  $9 \times 13$  km. If we truncate the PSF so that 95-percent energy is retained, then the footprint grows to  $16 \times 16$  km. Normally radiance measurements

Table 4.4-2. Footprint Sizes

TRMM					EOS				
$\delta$	$\beta$	$\theta$	$l$	$\Delta l$	$\delta$	$\beta$	$\theta$	$l$	$\Delta l$
Optical hexagonal footprint at nadir, $\alpha = 0^\circ$					Optical hexagonal footprint at nadir, $\alpha = 0^\circ$				
0.65	0	0.7	4.0		0.65	0	0.7	8.0	
-0.65	0	0.7	-4.0	8	-0.65	0	0.7	-8.0	16
0	1.30	1.4	7.9	16	0	1.30	1.4	16.0	32
PSF half-power cutoff at nadir, $\alpha = 0^\circ$					PSF half-power cutoff at nadir, $\alpha = 0^\circ$				
0.88	0	0.9	5.4		0.88	0	1.0	10.8	
-0.52	0	0.5	-3.2	9	-0.52	0	0.6	-6.4	17
0	1.08	1.1	6.6	13	0	1.08	1.2	13.3	27
PSF 95% energy cutoff at nadir, $\alpha = 0^\circ$					PSF 95% energy cutoff at nadir, $\alpha = 0^\circ$				
1.25	0	1.3	7.6		1.25	0	1.4	15.4	
-1.35	0	1.4	8.2	16	-1.35	0	1.5	16.6	32
0	1.27	1.3	7.8	16	0	1.27	1.4	15.6	31
PSF 95% energy cutoff Centroid at $\theta = 70^\circ$ , $\alpha = 62.96^\circ$					PSF 95% energy cutoff Centroid at $\theta = 70^\circ$ , $\alpha = 57.78^\circ$				
1.25	0	71.8	841.8		1.25	0	72.2	1468.7	
0	0	70.0	781.6		0	0	70.0	1357.7	
-1.35	0	68.1	725.6	116	-1.35	0	67.7	1256.7	212
0	1.27	70.0	19.4	38	0	1.27	70.0	35.3	71
PSF 95% energy cutoff Centroid at $\theta = 75^\circ$ , $\alpha = 66.29^\circ$					PSF 95% energy cutoff Centroid at $\theta = 75^\circ$ , $\alpha = 60.42^\circ$				
1.25	0	77.1	1067.7		1.25	0	77.9	1800.9	
0	0	75.0	967.8		0	0	75.0	1621.1	
-1.35	0	72.9	881.7	186	-1.35	0	72.3	1472.6	328
0	1.27	75.0	23.3	47	0	1.27	75.0	40.9	82
PSF 95% energy cutoff Limit of Earth view at horizon $\alpha = \alpha_h - 1.65^\circ = 69.75^\circ$					PSF 95% energy cutoff Limit of Earth view at horizon $\alpha = \alpha_h - 1.65^\circ = 62.55^\circ$				
1.25	0	85.9	1660.6		1.25	0	85.3	2387.0	
0	0	81.8	1338.5		0	0	80.3	1971.4	
-1.35	0	78.8	1153.5	507	-1.35	0	76.7	1726.8	660
0	1.27	81.8	31.4	63	0	1.27	80.3	48.5	97
PSF half power cutoff at $\theta = 75^\circ$ , $\alpha = 66.29^\circ$					PSF half power cutoff at $\theta = 75^\circ$ , $\alpha = 60.42^\circ$				
0.88	0	76.5	1035.6		0.88	0	77.0	1741.8	
0	0	75.0	967.8		0	0	75.0	1621.1	
-0.52	0	74.2	932.5	103	-0.52	0	73.9	1559.6	182
0	1.08	75.0	19.8	40	0	1.08	75.0	34.8	69

are inverted to flux at the TOA only out to a viewing zenith angle of  $70^\circ$ . At this point the TRMM scanner FOV has grown to  $116 \times 38$  km. The along-scan direction increases much more rapidly than the cross-scan direction because of the shallow angles. Table 4.4-2 gives footprint sizes for various viewing geometries for both the TRMM and EOS satellites.

#### 4.4.2.3. Spatial Ordering of CERES Pixel Data

The CERES data have been spatially ordered to facilitate the collocation of the imager data and the CERES footprint. The rotating azimuth plane scanner has the capability of viewing 1000 km forward along the groundtrack and 3.3 seconds later viewing 1000 km backward along the groundtrack. This distance plus the size of the footprints would require about 2500 km of imager data to be available for collocating at one time. To circumvent this problem, the CERES data have been spatially ordered along the groundtrack according to their along-track angle.

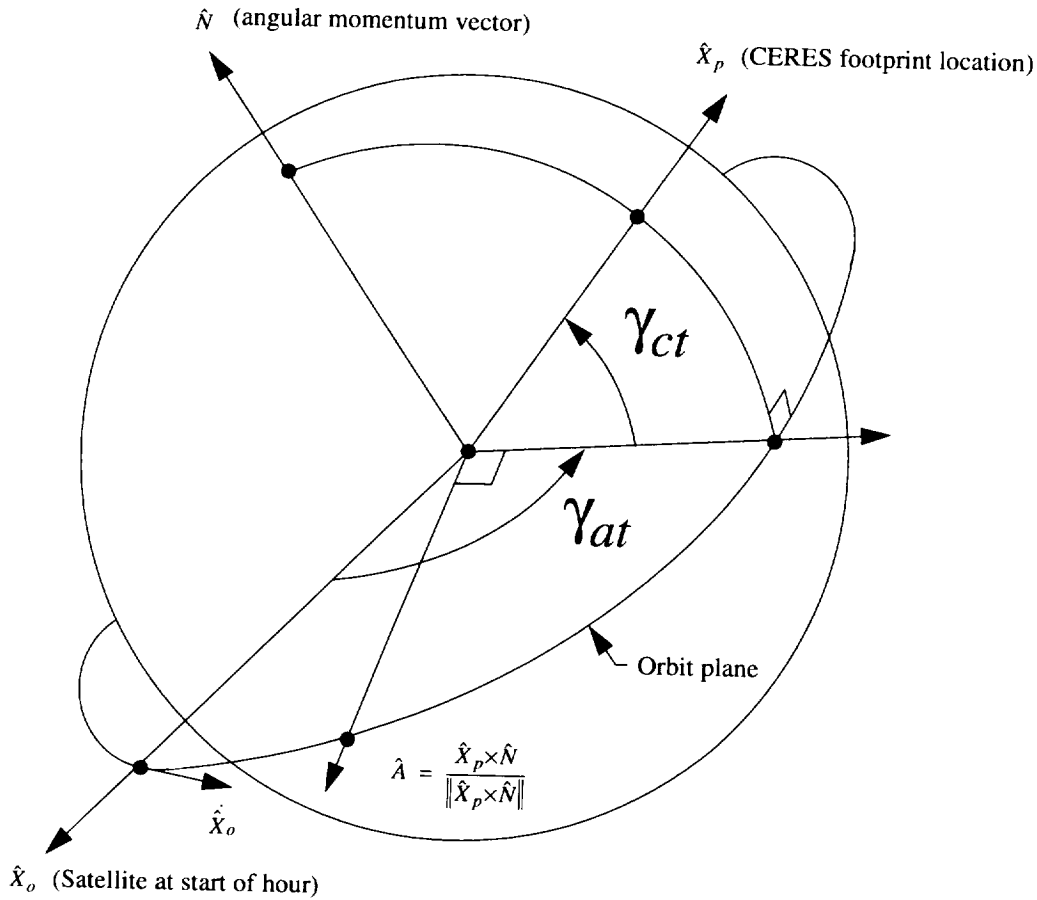


Figure 4.4-4. Along-track and cross-track angles.

The along-track angle  $\gamma_{at}$  and the cross-track angle  $\gamma_{ct}$  define the location of the CERES footprint relative to the orbit plane and relative to the start of the 1-hour SSF product (see Fig. 4.4-4). These footprint location angles are determined from the orbital geometry. Let us define the time at the start of the 1-hour SSF product as  $t_o$ . The position of the satellite at  $t_o$  is defined as  $\hat{X}_o$ . The colatitude and longitude of the satellite at  $t_o$  are defined by  $\Theta_o$  and  $\Phi_o$  as in Figure 4.4-5 so that the position components are

$$\begin{aligned} x_o &= \sin \Theta_o \cos \Phi_o \\ y_o &= \sin \Theta_o \sin \Phi_o \\ z_o &= \cos \Theta_o \end{aligned} \quad (4.4-3)$$

where  $\hat{X}_o$  is expressed in the Earth equator, Greenwich meridian coordinate system at the hour start,  $t_o$ . We freeze this coordinate system at  $t_o$  so that it does not rotate. This will be our basic coordinate system. The satellite inertial velocity at  $t_o$  is given by ephemeris data  $\dot{x}_o, \dot{y}_o, \dot{z}_o$ . The unit angular momentum vector is perpendicular to the orbit plane and is given by

$$\hat{N} = \frac{\hat{X}_o \times \dot{\hat{X}}_o}{\|\hat{X}_o \times \dot{\hat{X}}_o\|} \quad (4.4-4)$$

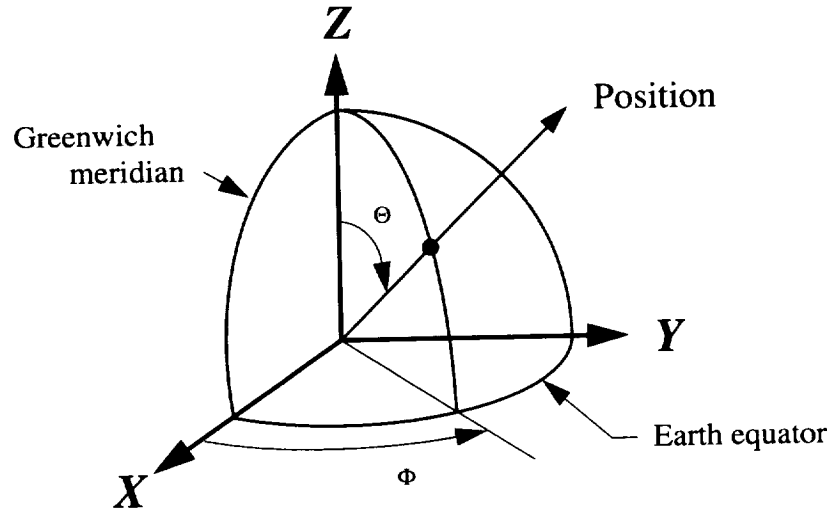


Figure 4.4-5. Colatitude and longitude angles.

where  $\|\hat{X}\|$  denotes the magnitude of  $\hat{X}$ , or

$$\|\hat{X}\| = \sqrt{x^2 + y^2 + z^2} \quad (4.4-5)$$

The position of a pixel  $\hat{X}_p$  at time  $t$  is given by  $\Theta_p, \Phi_p$ . This position is in the Earth equator, Greenwich meridian coordinate system at time  $t$ . The position in our basic coordinate system is

$$\begin{aligned} \Delta t &= t - t_o \\ \Delta \Phi &= \omega_E \Delta t \end{aligned} \quad (4.4-6)$$

$$\begin{aligned} x_p &= \sin \Theta_p \cos(\Phi_p + \Delta \Phi) \\ y_p &= \sin \Theta_p \sin(\Phi_p + \Delta \Phi) \\ z_p &= \cos \Theta_p \end{aligned} \quad (4.4-7)$$

where the rotational rate of the Greenwich meridian is  $\omega_E = 0.004178$  deg/sec.

The cross-track angle is given by

$$\hat{X}_p \cdot \hat{N} = \cos(90^\circ - \gamma_{ct})$$

or

$$\sin \gamma_{ct} = \hat{X}_p \cdot \hat{N} \quad (-90^\circ \leq \gamma_{ct} \leq 90^\circ) \quad (4.4-8)$$

The along-track angle is given by

$$\begin{aligned} \hat{A} &= \frac{\hat{X}_p \times \hat{N}}{\|\hat{X}_p \times \hat{N}\|} \\ \hat{A} \cdot \hat{X}_o &= \cos(\gamma_{at} - 90^\circ) \\ \hat{X}_o \times \hat{A} \cdot \hat{N} &= \sin(\gamma_{at} - 90^\circ) \end{aligned}$$

or

$$\left. \begin{aligned} \sin \gamma_{at} &= \hat{A} \cdot \hat{X}_o \\ \cos \gamma_{at} &= -\hat{X}_o \times \hat{A} \cdot \hat{N} \end{aligned} \right\} \quad (0^\circ \leq \gamma_{at} < 360^\circ) \quad (4.4-9)$$

The SSF product contains 1 hour of CERES footprint data for one scanning radiometer. Each footprint is a separate record and is organized spatially along the groundtrack with increasing along-track angle. The start of the data on the 1-hour SSF is the nadir position of the satellite on the groundtrack when the hour starts. This point is defined as  $0^\circ$  along-track angle. Measurements made prior to this “initial time” can be included on the SSF if their along-track angle is positive, or downtrack. Measurements made after this “initial time” that look backwards and have footprints with along-track angle near  $360^\circ$  are included on the previous SSF hour product. Thus, the SSF contains all footprints with an along-track angle between the nadir point at hour start and the nadir point at hour end.

#### 4.4.2.4. Geometry of Collocation

The time of observation and the size of the CERES footprint will vary greatly, but the locations of the CERES footprints are well behaved. Figure 4.4-6 illustrates this geometry. Consider the three contiguous numbered footprints. The first footprint represents the maximum size footprint. According to Table 4.4-2, a CERES footprint directed forward along the groundtrack from the TRMM orbit and at a shallow viewing zenith angle of  $75^\circ$  extends from 100 km forward of the PSF centroid to 86 km backwards of the centroid and is 47 km wide. The measurement is made when the satellite is 968 km back from the centroid and 2.2 minutes away. Therefore our field of imager data must be at least 186 km in length. A reasonable swath length of imager data is 500 km, which will allow many CERES footprints to be collocated. After all of the imager pixels within this footprint are located and the cloud statistics determined, we move to the next CERES footprint denoted by “2.” This footprint was obtained by viewing off the groundtrack when the satellite was beyond the area of interest. Its shape is skewed, which makes the collocation more complex. The next CERES footprint denoted by “3” is a nadir viewing footprint. From Figure 4.4-6 we see that spatial ordering gives varying footprint sizes and times of observation, but has footprints that are close to each other.

We proceed along the groundtrack and collocate footprints until we are within about 100 km of the end to the 500-km swath of imager data. At that point we drop data at the back of the swath and add new data on the forward part of the swath, analyze this new swath, and then start the collocation process where we left off. This continues until we are again within 100 km of the end of the swath.

The geometry of the process of locating the actual imager pixels within the CERES footprint is shown in Figure 4.4-7. Knowing the along-track and cross-track angle of the centroid of a CERES footprint (represented by the open circle in Fig. 4.4-7), we can easily locate the nearest imager pixel (denoted by the number 1 solid circle). Since the CERES measurement time  $t_c$  and the imager measurement time  $t_i$  are different, the CERES footprint will have moved from its original location due to the rotation of the Earth. For the moment we will assume pixel 1 is within the footprint at time  $t_i$ . The test for a pixel to be within the footprint is to determine the value of the PSF and test against the 95-percent energy value. Next, we move outward to pixel 2 and evaluate the PSF at this point to determine if the pixel is within the footprint. We proceed in this manner until we reach pixel 12 that is outside the footprint. We then return to pixel 1 and proceed inward until pixel 14 is reached. This completes one row of imager pixels. We find the center pixel 5 and step to the next row. This is denoted by pixel 15. By finding the center pixel we stay within the footprint even for the skewed case. From pixel 15 we step outward and then inward until we complete the row. This process is continued until the step from center is outside the footprint, shown as pixel 257. Returning to the center of the first row, we step to pixel 258 and continue until all the imager pixels are located. It is possible for the PSF centroid at  $t_c$  to be outside

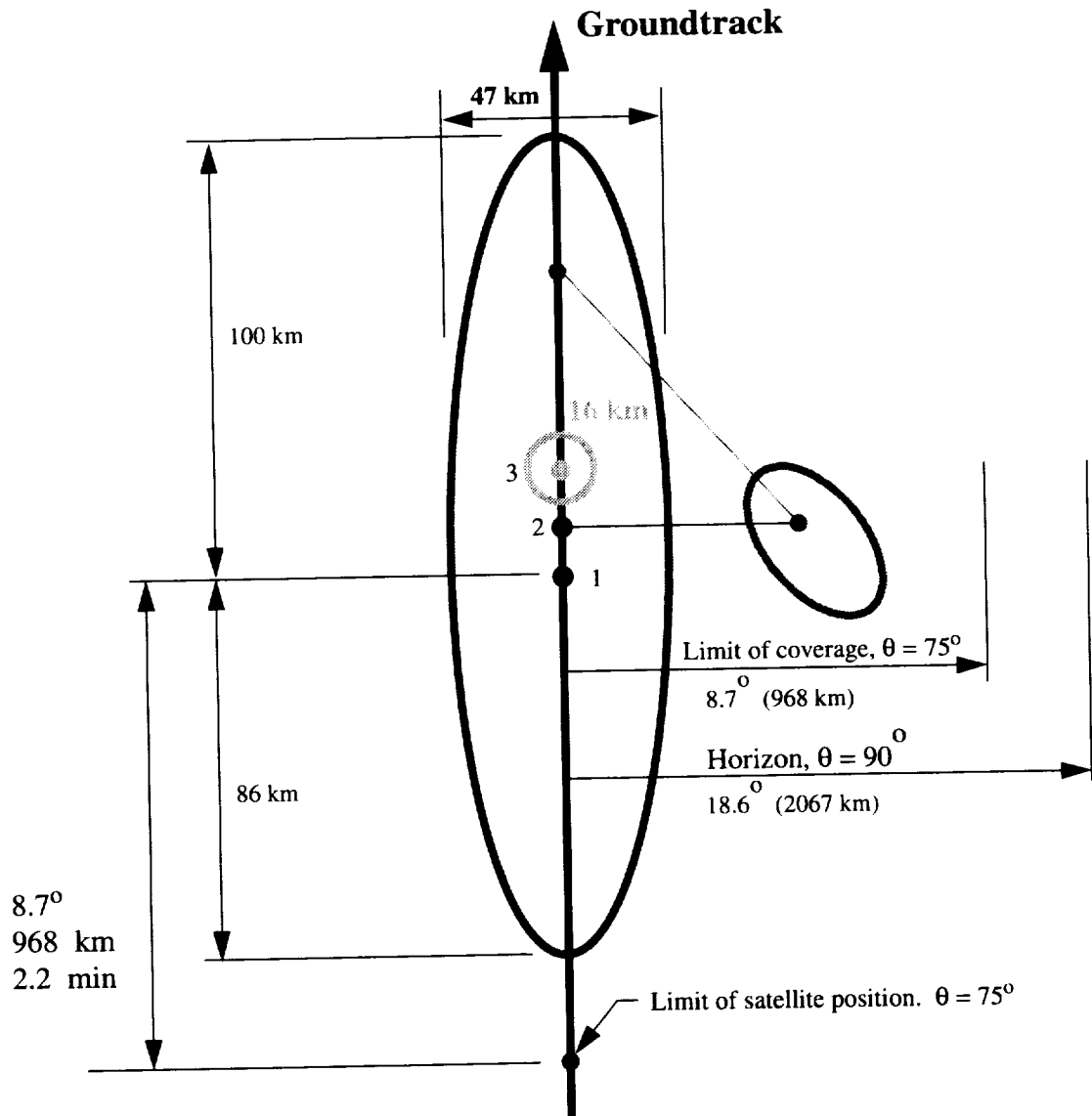


Figure 4.4-6. Spatial ordering of CERES footprints.

the footprint at  $t_i$ . In this case we search eastward for an imager pixel with a colatitude and longitude that is near the PSF centroid. If  $t_c < t_i$ , search eastward. Otherwise, search westward.

In general the imager does not scan to the horizon but restricts its scan to a swath along the groundtrack. Thus, we will encounter the case where the CERES footprint is only partially covered by imager pixels. In this case we integrate the PSF over the area of the footprint that is covered and accept the partial coverage if the energy is 75 percent or greater instead of the normal 95-percent energy.

At each imager pixel we must evaluate the PSF to determine whether the pixel is within the CERES footprint of equivalently whether the value of the PSF at the pixel is greater than the 95-percent energy cutoff. We now examine the geometry of this calculation. The colatitude and longitude of the PSF centroid is recorded on the SSF product with the CERES footprint data along with other necessary parameters. Also recorded is the cone angle  $\alpha_{\text{cen}}$  and the clock angle  $\kappa_{\text{cen}}$  of the centroid (Fig. 4.4-8) along with the satellite position and velocity. Recall that we need to determine the along-scan angle  $\delta$  and the cross-scan angles  $\beta$  of the imager pixel to evaluate the PSF. Referring to Figure 4.4-2, we need to form an axis

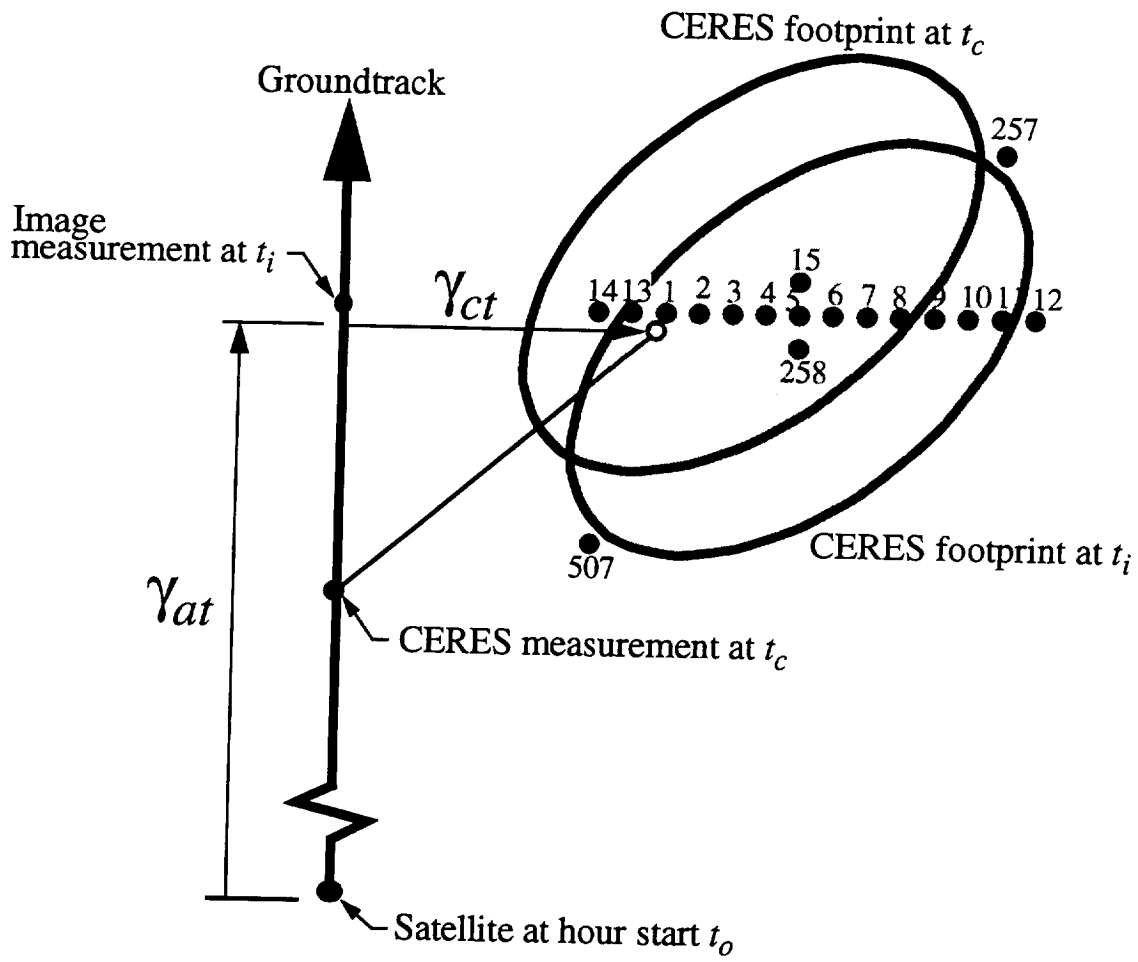


Figure 4.4-7. Collocating imager pixels and CERES footprints.

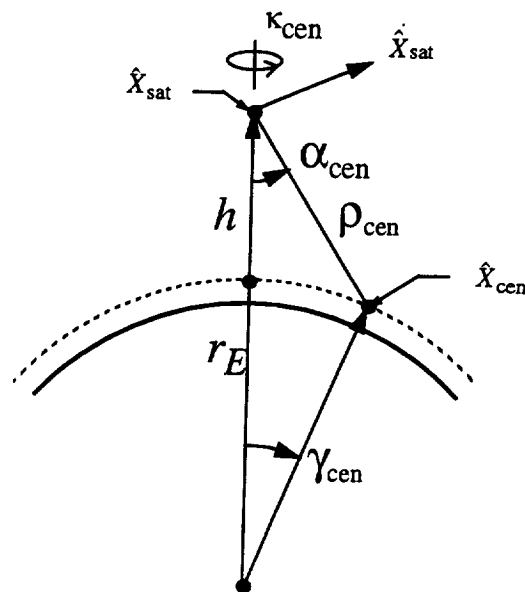


Figure 4.4-8. Viewing geometry.

system at the satellite with the  $Y'$ -axis pointing toward the centroid and the  $X'$ -axis perpendicular to the  $Y'$ -axis and  $\hat{X}_{\text{sat}}$ . We then determine  $\delta$  and  $\beta$  of the imager view vector relative to the  $Y'$ -axis.

The colatitude and longitude of the imager pixel is available with the imager data. Working in the Greenwich meridian earth equator coordinate system (Fig. 4.4-5), we have from (4.4-3)

$$\begin{aligned}x_{\text{imag}} &= \sin \Theta_{\text{imag}} \cos \Phi_{\text{imag}} \\y_{\text{imag}} &= \sin \Theta_{\text{imag}} \sin \Phi_{\text{imag}} \\z_{\text{imag}} &= \cos \Theta_{\text{imag}}\end{aligned}\quad (4.4-10)$$

The unit vector to the satellite  $\hat{X}_{\text{sat}}$  and to the PSF centroid  $\hat{X}_{\text{cen}}$  are also determined from their colatitude and longitude in the same way.

The viewing geometry for the centroid of the PSF is given in Figure 4.4-8. The Earth central angle  $\gamma_{\text{cen}}$  between the satellite and the centroid is

$$\cos \gamma_{\text{cen}} = \hat{X}_{\text{sat}} \cdot \hat{X}_{\text{cen}} \quad (0 \leq \gamma_{\text{cen}} \leq 90^\circ) \quad (4.4-11)$$

The range  $\rho_{\text{cen}}$  is from the law of sines or

$$\rho_{\text{cen}} = \frac{r_E \sin \gamma_{\text{cen}}}{\sin \alpha_{\text{cen}}} \quad (4.4-12)$$

From Figures 4.4-2 and 4.4-8 we have

$$(r_E + h)\hat{X}_{\text{sat}} + \rho_{\text{cen}}\hat{Y}' = r_E\hat{X}_{\text{cen}}$$

or

$$\hat{Y}' = \frac{r_E\hat{X}_{\text{cen}} - (r_E + h)\hat{X}_{\text{sat}}}{\rho_{\text{cen}}} \quad (4.4-13)$$

and

$$\begin{aligned}\hat{X}' &= \frac{\hat{Y}' \times \hat{X}_{\text{sat}}}{\|\hat{Y}' \times \hat{X}_{\text{sat}}\|} \\ \hat{Z}' &= \hat{X}' \times \hat{Y}'\end{aligned}\quad (4.4-14)$$

It follows that

$$\hat{X}_{\text{imag}} \cdot \hat{Z}' = \cos(90^\circ - \delta)$$

and

$$\frac{\hat{Z}' \times \hat{X}_{\text{imag}}}{\|\hat{Z}' \times \hat{X}_{\text{imag}}\|} \cdot \hat{Y}' = \cos(90^\circ + \beta)$$

or

$$\begin{aligned}\sin \delta &= \hat{X}_{\text{imag}} \cdot \hat{Z}' & (-90^\circ \leq \delta \leq 90^\circ) \\ \sin \beta &= -\frac{\hat{Z}' \times \hat{X}_{\text{imag}}}{\|\hat{Z}' \times \hat{X}_{\text{imag}}\|} \cdot \hat{Y}' & (-90^\circ \leq \beta \leq 90^\circ)\end{aligned}\quad (4.4-15)$$

and finally we calculate  $P(\delta, \beta)$  from (4.4-1). If  $P(\delta, \beta) \leq P_{95\%}$ , then the imager pixel is within the CERES footprint. This formulation assumes  $\alpha < 0$  and the scan is toward nadir. If  $\alpha > 0$  and the scan is outward, set  $\delta = -\delta$  to reverse the PSF tail.

We have evaluated the PSF at the imager pixel starting with its surface colatitude and longitude. The CERES centroid is also located at the surface by its colatitude and longitude in the same way as the imager. Thus, for cross-track scanning the locations align well. However, there is a location error when the imager is scanning cross-track and the CERES is scanning at another azimuth. The scanners actually sense the radiation along the slant path defined by its viewing zenith angle. Although both instruments view the same surface point, they will view different points at an altitude above the surface. Thus, the observed cloud fields will be slightly different and the error will be a function of cloud height and spatial autocorrelation. This problem is minimal since the azimuth scanning data is mainly for the angular distribution model (ADM) development. If the location errors are random with mean zero, then the errors will not cause an ADM bias error but only an increase in variance which will require slightly more data to overcome.

#### 4.4.2.5. Cloud Statistics Over a CERES FOV

For every imager pixel, the parameters listed in Table 4.4-3 are determined (see Subsystems 4.1, 4.2, 4.3). If the number of cloud layers (parameter #1) is 0, then the pixel is clear and #8–#31 are meaningless. If there is one cloud layer, then #8–#19 contain the cloud properties. If there are two layers, then all parameters have meaning and cloud layer 1 is the lower cloud and cloud layer 2 is the higher cloud. And finally, if #1 is  $-1$  (which is a special use of the parameter), then we disregard the pixel altogether.

Table 4.4-3. Imager Pixel Parameters

General	Cloud layer 1 (low)	Cloud layer 2 (high)
1. Number of cloud layers (-1, 0, 1, or 2)	8. Cloud fraction (0-1.0)	20. Cloud fraction (0-1.0)
2. Imager viewing zenith angle	9. Visible optical depth	21. Visible optical depth
3. Imager relative azimuth angle	10. Infrared emissivity	22. Infrared emissivity
4. Current CERES footprint PSF value	11. Water path	23. Water path
5. Imager radiance 0.6 $\mu\text{m}$	12. Top pressure	24. Top pressure
6. Imager radiance 3.7 $\mu\text{m}$	13. Effective* pressure	25. Effective pressure
7. Imager radiance 11.0 $\mu\text{m}$	14. Effective temperature	26. Effective temperature
	15. Effective height	27. Effective height
	16. Bottom pressure	28. Bottom pressure
	17. Particle radius	29. Particle radius
	18. Particle phase (0-ice or 1-water)	30. Particle phase (0-ice or 1-water)
	19. Vertical aspect ratio	31. Vertical aspect ratio

\*Effective as viewed from space or cloud top if optically thick and cloud center if optically thin.

The parameter #4 is different from the other parameters that are independent of the CERES footprints. It is dynamic in that it changes, depending on the current CERES footprint being processed. Recall that the pixels within a footprint are located by evaluating the point spread function (4.4-1) and testing against the 95-percent energy cutoff. This value of the PSF is saved as #4 and used in the weighted averages.

The most general CERES footprint contains clear areas and clouds in four height categories (Fig. 4.4-9). Category 1 (low clouds) corresponds to a cloud pressure greater than 700 hPa, category 2 (lower middle clouds) corresponds to a cloud pressure between 700 and 500 hPa, etc. The cloud data in every imager pixel within the CERES footprint is categorized by its effective pressure #13 and #25. An imager pixel with two layers #1 will contain cloud data in two height categories. Thus, all imager cloud

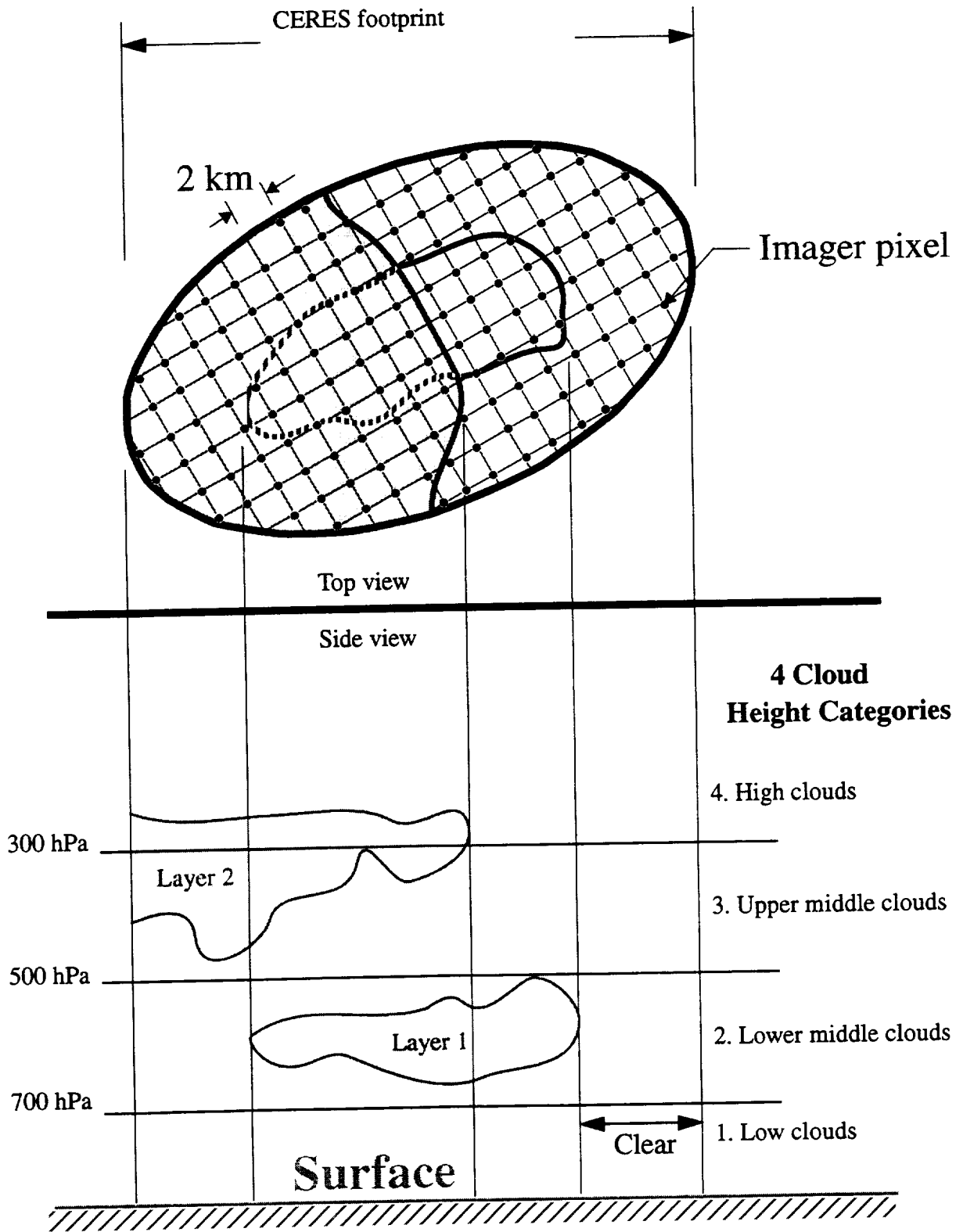


Figure 4.4-9. CERES cloud geometry.

Table 4.4-4. Eleven Cloud Overlap Conditions

Index	Definition	Symbol	
No layer			
1	Clear (no clouds)	CLR	0
One layer			
2	Low cloud only (cloud effective pressure > 700 hPa)	L	1
3	Lower middle cloud only (700 ≥ eff. pressure > 500 hPa)	LM	2
4	Upper middle cloud only (500 ≥ eff. pressure > 300 hPa)	UM	3
5	High cloud only (eff. pressure ≤ 300 hPa)	H	4
Two layers			
6	High cloud over upper middle cloud	H/UM	43
7	High cloud over lower middle cloud	H/LM	42
8	High cloud over low cloud	H/L	41
9	Upper middle cloud over lower middle cloud	UM/LM	32
10	Upper middle cloud over low cloud	UM/L	31
11	Lower middle cloud over low cloud	LM/L	21

data is assigned to one of four cloud height categories. We also define the cloud overlap condition of the cloud layers according to Table 4.4-4. Although clear areas have no clouds, we still define clear as 1 of the 11 cloud overlap conditions, or the condition of no clouds.

The cloud statistics are determined from the set of imager pixels within the CERES footprint and recorded as the SSF product (Table 4.4-5). For the “Full Footprint Area” we record the number of height categories containing cloud data over the footprint, which can be from 0 to 4. Next, we record the total number of imager pixels within the footprint. We also average and record the mean viewing zenith and relative azimuth angles for the imager pixels, which are different from the CERES angles. Recall that the imager is a cross-track scanner while the CERES can scan at any azimuth. Thus, the imager and CERES have different viewing geometries. The radiances from the 0.6-, 3.7-, and 11.0- $\mu\text{m}$  imager channels are each ordered and the mean, 5 percentile, and 95 percentile are recorded.

For the “Clear Footprint Area” we first record the number of clear pixels. Next, we have the weighted area fraction. A clear area will be more effective if it is near the PSF centroid and less effective if it is near the boundary of the footprint. Therefore, we determine the weighted area fraction where the weights are the PSF value #4 for each pixel, or

$$f_{\text{clear}} = \frac{\sum \text{PSF}}{\sum_{\text{All pixels}} \text{PSF}} \quad (4.4-16)$$

If we neglect the weighting, then the area fraction is simply the number of clear pixels ratioed to the total number of pixels. The SSF records the number of imager pixels in each area so that various areas can be defined, assuming the imager pixels are uniformly spaced over the CERES footprint. A “fraction” value on the SSF product always relates to the entire footprint.

In general, we determine a weighted mean as

$$\bar{x} = \frac{\sum_{i=1}^N w_i x_i}{\sum_{i=1}^N w_i} \quad (4.4-17)$$

Table 4.4-5. CERES Footprint Data on the SSF Product

<p><b>Footprint Geometry</b></p> <p>Time of CERES measurement  Earth-Sun distance  Sun position (colat, long)  Satellite position (colat, long, radius)  Satellite velocity (<math>\dot{x}</math>, <math>\dot{y}</math>, <math>\dot{z}</math>)  View position at TOA (colat, long)  (along-track, cross-track)  View position at surface (colat, long)  View position at satellite (cone, clock, index)  View velocity at satellite (cone rate, clock rate)  Angles at TOA (V.Zen, S.Zen, R.Az, N.Az)  Surface type fraction (10 land types,  3 sea types, altitude)  Scene type (clear flag, inversion type)</p> <p><b>Footprint Radiation</b></p> <p>Radiance filtered (TOT, SW, WN)  Radiance filtered flag (TOT, SW, WN)  Radiance unfiltered (SW, LW, WN)  Flux at TOA (SW, LW, WN)  Flux at surface (SW, LW, NetSW, NetLW)  Parameters at surface (emissivity,  photoactive, direct/diffuse ratio)</p> <p><b>Full Footprint Area</b></p> <p>Number of cloud height categories  Number of imager pixels  Radiance 0.6 <math>\mu\text{m}</math> (5%, mean, 95%)  Radiance 3.7 <math>\mu\text{m}</math> (5%, mean, 95%)  Radiance 11.0 <math>\mu\text{m}</math> (5%, mean, 95%)  Bidirect reflect or brightness temperature  Precipitable water  Angles at TOA (mean V.Zen, mean R.Az)  Flags (general, algorithm: texture, cloud layer,  S.Cohr, IR sounder, threshold, optical depth,  emissivity, particle radius, water path)</p> <p><b>Clear Footprint Area</b></p> <p>Number of imager pixels (see overlap condition 1)  PSF weighted area fraction (see overlap condition 1)  Radiance 0.6 <math>\mu\text{m}</math> (mean, std)  Radiance 3.7 <math>\mu\text{m}</math> (mean, std)  Radiance 11.0 <math>\mu\text{m}</math> (mean, std)  Stratospheric aerosol (optical depth, radius)  Total aerosol (optical depth, radius)</p>	<p><b>Cloudy Footprint Areas</b>  <b>(for each of 4 height categories)</b></p> <p>Number of imager pixels  Number of overcast pixels  PSF weighted area fraction  PSF weighted overcast fraction  PSF weighted broken cloud fraction  Radiance 0.6 <math>\mu\text{m}</math> (mean, std)*  Radiance 3.7 <math>\mu\text{m}</math> (mean, std)  Radiance 11.0 <math>\mu\text{m}</math> (mean, std)  Visible optical depth (mean, std)  IR emissivity (mean, std)  Liquid water path (mean, std)  Ice water path (mean, std)  Top pressure (mean, std)  Effective<sup>#</sup> pressure (mean, std)  Effective temperature (mean, std)  Effective height (mean, std)  Bottom pressure (mean, std)  Water particle radius (mean, std)  Ice particle radius (mean, std)  Particle phase (mean, std)  Vertical aspect ratio (mean, std)  Visible optical depth / IR emissivity (13 percentiles)</p> <p><b>Cloud Overlap Condition</b>  <b>(for each of 11 conditions)</b></p> <p>Number of imager pixels  PSF weighted area fraction</p> <p><b>Abbreviations</b></p> <p>LW - longwave channel  N.Az - azimuth angle wrt North  NetLW - net longwave  NetSW - net shortwave  PSF - point spread function  R.Az - relative azimuth angle  S.Cohr - spatial coherence  SW - shortwave channel  S.Zen - solar zenith angle  TOA - top of atmosphere  TOT - total channel  V.Zen - viewing zenith angle  WN - window channel</p>
--	---

\*All means and standard deviations are PSF weighted.

<sup>#</sup>Effective as viewed from space or cloud top if optically thick and cloud center if optically thin.

and the associated weighted standard deviation as

$$S = \left[ \frac{\sum_{i=1}^N w_i x_i^2}{\sum_{i=1}^N w_i} - \bar{x}^2 \right]^{1/2} \quad (4.4-18)$$

where the weights  $w_i$  are the PSF values and  $x$  is the parameter of interest. From (4.4-17) and (4.4-18) we determine the weighted means and standard deviations for the 0.6-, 3.7-, and 11.0- $\mu\text{m}$  imager channels over the clear pixels.

For the “Cloudy Footprint Areas” we record the parameters listed in Table 4.4-5 for each of the four height categories. First, the number of pixels in each category is recorded. Since a single imager pixel with two layers is counted in two different height categories, the sum of pixels in the four categories plus the number of clear pixels can exceed the total number of pixels as recorded under “Full Footprint Area.” Next, the number of overcast pixels within each category is recorded. The cloud fraction in Table 4.4-3 (#8 and #20) is determined from a high resolution (250 m) cloud mask (0 or 1) and averaged over the imager grid. The imager grid is defined by the 11- $\mu\text{m}$  imager channel which at nadir is 4 km for AVHRR, 2 km for VIRS, and 1 km for MODIS. The cloud fraction is a measure of cloud brokenness and ranges continuously from 0 to 1. We define overcast as a cloud fraction greater than 0.95. The number of pixels with overcast clouds is recorded on the SSF product.

The weighted area fractions for the height categories are a function not only of count but also a function of the pixel cloud fraction (#8 and #20). We define the area fraction of the  $i$ th category ( $i = 1, 2, 3, 4$ ) as

$$f_i = \frac{\sum_{\text{Category } i \text{ pixels}} \text{PSF} \times \text{cloud fraction}}{\sum_{\text{All pixels}} \text{PSF}} \quad (4.4-19)$$

The overcast area fraction is obtained by restricting the summation in (4.4-19) to only the overcast pixels. And finally, the broken cloud fraction is simply the area fraction minus the overcast cloud fraction.

The next 16 parameters result from determining the mean (4.4-17) and the standard deviation (4.4-18) of the cloud parameters in Table 4.4-3. The water path (#11 and #23) is sorted into two separate parameters according to particle phase (#18 and #30) so that we can form statistics on both liquid water path and ice water path. The same is true for particle radius.

In addition to the means and standard deviations we record the visible optical depth frequency distribution during daytime. For each category we order the imager pixel visible optical depths (#9 and #21) and record the following 13 percentiles: 1, 5, 10, 20, 30, 40, 50, 60, 70, 80, 90, 95, 99. Because of the large spatial variability of cloud optical depth, the frequency distribution is determined by using the highest resolution visible channel data available which for MODIS is 250 m. Thus, for MODIS #9 and #21 are vectors of the visible optical depth at the higher imager resolution. At night the optical depth distribution is replaced by a frequency distribution of 11  $\mu\text{m}$  infrared emissivity.

We also record on the SSF product the number of pixels and area fraction for each of the 11 cloud overlap conditions as defined by Table 4.4-4. These area fractions are determined by (4.4-16) where “clear” is replaced by “condition 1,” “condition 2,” etc. Note that the area fraction for the 4 categories incorporates cloud fraction (4.4-19) and the area fraction for the 11 overlap conditions does not use

cloud fraction. It follows that the 11 overlap condition area fractions sum to unity. A more complete listing of the parameters in the SSF product are given in Appendix B of section 4.0.

#### 4.4.3. Implementation Issues

##### 4.4.3.1. How much computer memory do we need to process the 500-km swath of imager data?

As stated in section 4.4.2.5., the imager grid is defined by the spacing of the 11- $\mu\text{m}$  imager channel data. For MODIS this is a 1-km grid, by which we mean that at nadir two consecutive 11- $\mu\text{m}$  measurements are approximately 1 km apart. The angular spacing or cone angle between measurements remains constant during the scan, which implies that two measurements near the limb will be more than 1 km apart. Nevertheless, we still refer to the measurement spacing or imager grid as a 1-km by 1-km grid or simply a 1-km grid.

The imager cloud parameters in Table 4.4-3 are defined on the imager grid. However, the frequency distribution percentiles of cloud optical depth in Table 4.4-5 are defined from the visible channel at its resolution. For AVHRR and VIRS, these two grids are the same at 4 km and 2 km, respectively. For MODIS the 11- $\mu\text{m}$  channel grid is 1 km and the visible channel grid is 250 m. Thus, each MODIS imager grid will contain 16 optical depth measurements which are associated with its central imager grid point. This will double the amount of imager data over the 500-km swath that is held in computer memory at one time.

Table 4.4-3 in section 4.4.2.5. shows 31 parameters that are defined at each imager grid point. For MODIS the 500-km swath of imager data is about 2000 km wide so that we have  $500 \times 2000 = 10^6$  grid points at 1 km spacing. If each of the 31 parameters is 4 bytes, then we need to process approximately 120 MB in memory at one time. When we go to the higher 250-m resolution for the optical depth frequency distribution, then each optical depth parameter in Table 4.4-3 becomes a vector of 16 parameters and our 31-parameter list goes to 61 parameters. And, it follows that our memory requirements go from 120 MB to 240 MB. This will be a future requirement on the processing system. The initial release 1 requirements using AVHRR with both IR and visible channels at a 4-km grid are  $120 \div 4^2 = 7.5$  MB.

#### 4.4.4. Reference

Smith, G. Louis 1994: Effects of Time Response on the Point Spread Function of a Scanning Radiometer. *Appl. Opt.*, vol. 33, no. 30, pp. 7031–7037.

**Clouds and the Earth's Radiant Energy System (CERES)**  
**Algorithm Theoretical Basis Document**

***CERES Inversion to Instantaneous TOA Fluxes***  
***(Subsystem 4.5)***

R. N. Green<sup>1</sup>  
B. A. Wielicki<sup>1</sup>  
J. A. Coakley, Jr.<sup>2</sup>  
L. L. Stowe<sup>3</sup>  
P. O'R. Hinton<sup>4</sup>

<sup>1</sup>Atmospheric Sciences Division, NASA Langley Research Center, Hampton, Virginia 23681-0001

<sup>2</sup>Oregon State University, Corvallis, Oregon 97331-2209

<sup>3</sup>NOAA/NESDIS/E/RALL, 5200 Auth Road, Camp Springs, Maryland 20233

<sup>4</sup>Science Applications International Corporation (SAIC), Hampton, Virginia 23666

## Abstract

*The CERES-measured radiances at satellite altitude are inverted to instantaneous fluxes at the top of the atmosphere (TOA). The observed scene is identified by its surface type and cloud parameters. For each scene type, a corresponding angular distribution model (ADM) is used to convert from radiance to flux. The scene identification is discussed in Subsystems 4.0–4.4. This subsystem discusses inversion with the current ERBE ADM's and the development of a new generation of CERES ADM's.*

*The inputs necessary to invert the CERES radiances to fluxes are as follows: orbital geometry and filtered scanner radiances recorded in the IES product, spectral correction coefficients, and the Angular Distribution Models (see Appendix A of section 4.0). The outputs of this process are the unfiltered radiances, scene type, and TOA fluxes. These computed values are recorded in the SSF product (see Appendix B of section 4.0).*

### 4.5. Ceres Inversion to Instantaneous TOA Fluxes

#### 4.5.1. Introduction

The unfiltered radiances are inverted to the top of the atmosphere (TOA) by

$$\hat{F}_j = \frac{\pi I_j}{R_i(\Omega)} \quad (4.5-1)$$

where  $I_j$  ( $j = \text{SW, LW, WN}$ ) are the CERES radiances,  $\hat{F}_j$  are the corresponding flux estimates at the TOA, and  $R_i(\Omega)$  are the angular distribution models (ADM) that relate radiance to flux. The viewing geometry is represented by  $\Omega$  and the index  $i$  denotes different scene types. The longwave radiance ADM's (limb-darkening models) are a function of viewing zenith whereas the shortwave radiance ADM's (bidirectional models) are a function of three angles: viewing zenith, solar zenith, and relative azimuth. Thus, the inversion of radiances to fluxes at the TOA involves determining the scene type ( $i$ ), evaluating  $R_i(\Omega)$ , and applying equation (4.5-1).

CERES will require a new generation of ADM's. The best available set of ADM's is the ERBE (Barkstrom 1984) production ADM's (Suttles et al. 1988 and 1989) based on 12 scene types. These models are not adequate for CERES for two reasons. First, the ERBE models describe all the cloud anisotropic effects with only four coarse cloud-cover classes. This choice was dictated in part by scene identification that was based only on the ERBE radiances (Wielicki and Green 1989). The ERBE processing system was self-sufficient and used no ancillary data. Second, the ERBE models are not adequate for CERES because they are biased. The purpose of the ADM's is to correct for the anisotropy so that the flux can be estimated independent of the viewing geometry. However, postflight analysis (Suttles et al. 1992) has shown that the estimated shortwave albedo systematically increases with viewing zenith and the estimated longwave flux decreases with viewing zenith. It is generally accepted that the ERBE ADM models underestimate both longwave limb darkening and shortwave limb brightening.

The ERBE biases could be the result of either the Nimbus-7 ERB data from which the models were constructed or the SAB algorithm (Sorting by Angular Bins) that produced the models. Because the ERBE models produce a bias even when applied to the Nimbus-7 data from which they were derived (Suttles et al. 1992), the SAB seems to be the problem and not the data. Specifically, the assumptions

needed to apply the SAB (section 4.5.2.4) may not hold. Another possibility is FOV size. Ye (1993) has shown that on ERBE the increasing FOV size from nadir to limb can cause systematic differences in estimated fluxes. In any case, CERES is developing a totally new approach to constructing ADM's from radiance data. This next generation algorithm searches for radiance pairs that view the same area at the same time. Constructing the ADM's with radiance pairs eliminates the questionable SAB assumptions.

The goal of CERES is to reduce the ADM errors on ERBE by a factor of four. This reduction would imply that a reasonable number of CERES scene types is about 200. Whereas ERBE modeled only cloud cover, CERES will model cloud cover plus visible optical depth, particle size, and cloud height for shortwave models. For longwave, CERES will model cloud cover plus cloud emissivity, cloud height, column water vapor, lapse rate, and surface emittance. The 200 scene types for CERES will represent a discretization of these cloud parameters.

The new CERES ADM's will be developed with CERES radiance data. This procedure follows from the fact that radiance data must be classified and sorted according to the cloud types within its field of view (FOV) so that scene-dependent ADM can be constructed. This full cloud characterization will only become available on CERES, where a full complement of ancillary data together with a library of remote sensing algorithms will be used to identify the scene (Subsystems 4.1–4.3). Once the FOV is identified, the data are sorted into scene types and accumulated over a period of time to determine the mean models in the presence of natural variation. The 12 ERBE models were built with 205 days of Nimbus-7 data and constructed over a 4-year period. The CERES models will require 2 to 3 years to collect the data and construct the 200 models.

During this 2- to 3-year period, the CERES radiances will be inverted to the TOA with the best available set of ADM's. Releases 1 and 2 will map the CERES extensive cloud properties into the 12 ERBE scene types. Although inadequate for the CERES advanced goals, the ERBE models applied to the CERES data will still yield better results than for ERBE. The main improvement comes from the CERES cloud characterization, which will eliminate much of the misidentification on ERBE. In addition the cloud contamination in the clear scenes will be greatly reduced. The cloud cover classes will be more exact and the smaller CERES FOV will increase the resolution and sharpen the results. After the new CERES ADM's are constructed and tested for validity, the CERES radiances will be inverted to the TOA with the full set of 200 ADM's.

This CERES inversion subsystem and the ERBE-like inversion (Subsystem 2) are very different. ERBE-like processing uses no ancillary data, identifies the scene with the MLE algorithm, and inverts the radiances with the 12 ERBE scene types for the duration of the mission. The CERES inversion will make extensive use of ancillary data to characterize the cloud parameters and invert the radiances with 200 CERES scene types.

This subsystem describes the conversion of the CERES cloud parameters on the SSF product to the 12 ERBE scene types. It discusses the 200 CERES scene types and how they will be determined. The assumptions associated with the SAB algorithm for constructing ADM's are established and a new algorithm RPM (Radiance Pairs Method) is derived.

## **4.5.2. Algorithm Description**

### **4.5.2.1. The 12 CERES Scene Types**

The 12 ERBE scene types and their corresponding ADM's will be used initially for CERES inversion until the new comprehensive set of CERES ADM's are validated and ready for use. The 12 ERBE scene types were derived by combining 5 surface types (ocean, land, snow, desert, mixed, or coastal) with 4 cloud conditions (clear, partly cloudy, mostly cloudy, and overcast). These four cloud conditions are defined by clear (0%–5% cloud cover), partly cloudy (5%–50% cloud cover), mostly

Table 4.5-1. ERBE Scene Types

Index	Scene types
1	Clear ocean
2	Clear land
3	Clear snow
4	Clear desert
5	Clear land-ocean mix (coastal)
6	Partly cloudy over ocean
7	Partly cloudy over land or desert
8	Partly cloudy over land-ocean mix
9	Mostly cloudy over ocean
10	Mostly cloudy over land or desert
11	Mostly cloudy over land-ocean mix
12	Overcast

cloudy (50%–95% cloud cover), and overcast (95%–100% cloud cover). The surface types and cloud conditions were combined to give the scene types in table 4.5-1.

Each CERES measurement must be classified as one of the 12 scene types based on the cloud parameters on the SSF product (table 4.4-6). First, we define the surface type. The SSF records the area fraction for 3 sea types and 10 land types that sum to 1.0. The sum of the three sea types will be our ocean fraction, and the entire CERES FOV is defined as ocean if this fraction is greater than 0.67. One or more of the 10 land type fractions are summed to define the fraction of snow and the fraction of desert. If the snow fraction is greater than 0.50, then the entire FOV is classified as snow, and similarly for desert. The land fraction is (1 – ocean fraction). If the land fraction is greater than 0.67, then the FOV is classified as land. Otherwise the FOV is mixed or coastal.

Next, we define the cloud cover over the CERES FOV. The SSF records the clear area fraction from which we define the cloud cover as (1 – clear area fraction). With cloud cover we can define the FOV as clear, partly cloudy, mostly cloudy, or overcast as given above. Finally, surface type and cloud cover define one of the 12 CERES scene types.

#### 4.5.2.2. The 200 CERES Scene Types

One of the major tasks is to define the 200 CERES scene types so that the maximum amount of anisotropic variance is explained. In general this is a clustering problem. In practice we must define an initial set of parameters that define reasonable scenes and iterate on their definitions. The parameters with the strongest effect on anisotropy will receive further discretization while the parameters with weak or no effect will be grouped together. First, however, the ADM scene types must be matched for inversion and directional model scene types for time and space averaging. Thus, our first division is the four cloud height categories (Fig. 4.4-9). For shortwave radiation we further hypothesize the following sensitivity of cloud parameters to anisotropy in decreasing order of effect:

1. Cloud height categories (four intervals in hPa: >700, 700–500, 500–300, <300)
2. Cloud optical depth (three intervals)
3. Cloud amount (five intervals on %: 1–25, 25–50, 50–75, 75–99, 99–100)
4. Cloud particle size (two intervals)
5. Surface type (five types: ocean, land type 1, land type 2, snow, desert)

Thus, the initial set of shortwave scenes is  $4 \times 3 \times 5 \times 2 \times 5 = 600$  models plus 5 clear models (a clear scene has <1% cloud cover). Obviously, this exceeds our 200-model goal. These 605 models will be examined for sensitivity and adjusted accordingly until our 200-model limit is satisfied. For long-wave radiation we hypothesize the following sensitivity of cloud parameters:

1. Cloud height categories (four intervals in hPa: >700, 700–500, 500–300, <300)

2. Infrared emissivity (three intervals: <0.6, 0.6–0.8, 0.8–1.0)
3. Cloud amount (five intervals on %: 1–25, 25–50, 50–75, 75–99, 99–100)
4. Column water vapor (precipitable water) (three intervals in cm: 0–2, 2–4, >4)
5. Lapse rate (three intervals in [(temp. at 200 hPa – temp. at surface) / (alt. at 200 hPa – alt. at surface)] in K/km: 0–3, 3–6, >6)
6. Surface emittance at 11  $\mu\text{m}$  (three intervals: <0.90, 0.90–0.95, 0.95–1.00)
7. Surface type (five types: ocean, land type 1, land type 2, snow, desert)

Thus, the initial set of longwave scenes is  $4 \times 3 \times 5 \times 3 \times 3 \times 3 \times 5 = 8100$  models plus five clear models. Because each shortwave model has 810 angular bin values and each longwave models has only 9, we may be able to increase the number of longwave models beyond 200.

#### 4.5.2.3. Formulation of Angular Distribution Model (ADM)

For simplicity we will formulate only the longwave ADM. The shortwave ADM involves three directional angles instead of one, but is formulated similarly. The outgoing longwave radiance  $I$  at a point in  $\text{W}\cdot\text{m}^{-2}\text{sr}^{-1}$  is

$$I(\theta) = \pi^{-1}FR(\theta) \quad (4.5-2)$$

where  $F$  is the flux in  $\text{W}\cdot\text{m}^{-2}$  and  $R(\theta)$  is the longwave ADM as a function of the zenith angle  $\theta$ . Integrating both sides of (4.5-2) over the hemisphere defined by the zenith and azimuth angles, we get the normalization condition for  $R$  as

$$2 \int_0^{\pi/2} R(\theta) \sin\theta \cos\theta d\theta = 1 \quad (4.5-3)$$

Let us model the longwave limb-darkening function as

$$R(\theta) = \sum_{i=1}^N \beta_i f_i(\theta) \quad (4.5-4)$$

where  $f_i(\theta)$  are basis functions, and  $\beta_i$  are the parameters of the model, which are estimated from radiance measurements. Substituting (4.5-4) into (4.5-3) gives the normalization condition as

$$\sum_{i=1}^N \beta_i C_i = 1 \quad (4.5-5)$$

where

$$C_i = 2 \int_0^{\pi/2} f_i(\theta) \sin\theta \cos\theta d\theta \quad (4.5-6)$$

In this subsystem we will use the piecewise constant basis set given by

$$f_i(\theta) = \begin{cases} 1 & \theta_{i-1} \leq \theta \leq \theta_i \\ 0 & \text{otherwise} \end{cases} \quad (i = 1, 2, \dots, N) \quad (4.5-7)$$

where the  $\theta_i$ 's span the space  $0 \leq \theta \leq 90^\circ$ . From (4.5-6) and (4.5-7) we have

$$C_i = \sin^2 \theta_i - \sin^2 \theta_{i-1} \quad (i = 1, 2, \dots, N) \quad (4.5-8)$$

#### 4.5.2.4. Sorting by Angular Bins (SAB)

The sorting of observed radiances into angular bins was the technique used by Taylor and Stowe (1984) to develop the current ERBE angular distribution models. Radiances are sorted into angular bins, averaged, and numerically integrated to determine the mean flux. Dividing the average bin radiance by the mean flux yields the anisotropy for the angular bin. We define the SAB method as follows:

$$\hat{\beta}_i = \frac{\pi \bar{I}_i}{\bar{F}} \quad (4.5-9)$$

where

$$\bar{I}_i = \frac{1}{K_i} \sum_{r=1}^{K_i} I_i^r \quad (4.5-10)$$

$$\bar{F} = \pi \sum_{n=1}^N C_n \bar{I}_n \quad (4.5-11)$$

where  $I_i^r$  is the  $r^{\text{th}}$  measured radiance in the  $i^{\text{th}}$  angular bin and  $\theta_{i-1} \leq \theta < \theta_i$ .

Let us define the characteristics of the SAB. From (4.5-2), (4.5-4), and (4.5-7) we model the radiance as

$$I_i^r = \pi^{-1} F_i^r \beta_i^r + \varepsilon_i^r \quad (4.5-12)$$

where  $F_i^r$ ,  $\beta_i^r$ , and  $\varepsilon_i^r$  are random variables. We define the means and standard deviations as  $F_i^r \sim [\mu_F, \sigma_F]$ ,  $\beta_i^r \sim [\beta_i, \sigma_{\beta_i}]$ , and  $\varepsilon_i^r \sim [0, \sigma_\varepsilon]$ , respectively. The main characteristics of the SAB are the expected values and variances of  $\hat{\beta}_i$ . We will need three assumptions to proceed:

$$\begin{aligned} E[F_i^r] &= E[F_i^r] = \mu_F \\ E[F_i^r \beta_i^r] &= E[F_i^r] E[\beta_i^r] \\ E[\bar{F} \hat{\beta}_i] &= E[\bar{F}] E[\hat{\beta}_i] \end{aligned} \quad (4.5-13)$$

The first assumption is a statement of uniform sampling or the expected flux observed over the  $i^{\text{th}}$  angular bin is the same for all bins. This assumption is necessary to determine  $\bar{F}$ . The second and third assumptions state that the anisotropy  $\beta$  and field strength  $F$  are uncorrelated or an increase in flux does not change the scene type's anisotropy. Both of these assumptions are questionable and seen as weaknesses of the SAB. With these assumptions, however, we can show that  $E[I_i^r] = E[\bar{I}_i] = \pi^{-1} \mu_F \beta_i$  and  $E[\bar{F}] = \mu_F$ . Furthermore, taking the expected value of (4.5-9), we have

$$\left. \begin{aligned} E[\bar{F} \hat{\beta}_i] &= E[\pi \bar{I}_i] \\ E[\hat{\beta}_i] &= \beta_i \end{aligned} \right\} \quad (4.5-14)$$

and the estimate is unbiased.

The variance of the estimate is determined by

$$\left. \begin{aligned} \text{Var}[\bar{F}\hat{\beta}_i] &= \text{Var}[\pi\bar{I}_i] \\ E^2[\bar{F}]\text{Var}[\hat{\beta}_i] + E^2[\hat{\beta}_i]\text{Var}[\bar{F}] + \text{Var}[\hat{\beta}_i]\text{Var}[\bar{F}] &= \pi^2\text{Var}[\bar{I}_i] \\ \text{Var}[\hat{\beta}_i] &= \frac{\pi^2\text{Var}[\bar{I}_i] - \beta_i^2\text{Var}[\bar{F}]}{\mu_F^2 + \text{Var}[\bar{F}]} \end{aligned} \right\} \quad (4.5-15)$$

We can approximate this variance from data by  $\text{Var}[\bar{I}_i] \approx S_{I_i}^2$ ,  $\beta_i \approx \hat{\beta}_i$ , and  $\mu_F^2 \approx \bar{F}$ , or

$$\text{Var}[\hat{\beta}_i] \approx \frac{\pi^2 S_{I_i}^2 - \hat{\beta}_i^2 S_{\bar{F}}^2}{\bar{F}^2 + S_{\bar{F}}^2} \quad (4.5-16)$$

It is instructive to simplify the variance further with the following assumptions: (1)  $\beta_i$  is constant, (2)  $\mu_F^2 \gg \text{Var}[\bar{F}]$ , (3)  $\sigma_\varepsilon = 0$ , (4)  $K_i = K_j = K$ . These assumptions result in

$$\sigma_{\hat{\beta}_i} \approx \frac{\beta_i \left( \frac{\sigma_F}{\mu_F} \right)}{\sqrt{K_i}} \left[ 1 - \sum_{n=1}^N C_n^2 \beta_n^2 \right]^{\frac{1}{2}} \quad (4.5-17)$$

Thus, the SAB must average out the field variance  $\sigma_F/\mu_F$  with  $\sqrt{K_i}$  where  $\frac{\sigma_F}{\mu_F} \approx \frac{S_{I_i}}{\bar{I}_i}$ .

#### 4.5.2.5. Radiance Pairs Method (RPM)

The Radiance Pairs Method searches the radiance data to find radiances that view approximately the same area at approximately the same time. The purpose of a radiance pair is to eliminate flux between the two measurements. By dividing one radiance by the other, we eliminate the influence of flux and form the ratio of anisotropies. In contrast, a single radiance measurement gives the product of flux and anisotropy, which cannot be separated without questionable assumptions. The SAB assumes uniform sampling to isolate the anisotropy. In this section we will derive the Radiance Pairs Method.

We can consider (4.5-5) a constraint on the admissible  $\beta$ 's, or we can eliminate one of the  $\beta$ 's. We choose to eliminate  $\beta_N$ . Thus, (4.5-4) becomes

$$R(\theta) = \sum_{i=1}^{N-1} \beta_i f_i(\theta) + \left[ \frac{1 - \sum_{i=1}^{N-1} \beta_i C_i}{C_N} \right] f_N(\theta) \quad (4.5-18)$$

We now define a new set of basis functions  $G_i(\theta)$  so that

$$R(\theta) = \sum_{i=1}^{N-1} \beta_i G_i(\theta) + G_N(\theta) \quad (4.5-19)$$

where

$$\left. \begin{aligned} G_N(\theta) &= \frac{f_N(\theta)}{C_N} \\ G_i(\theta) &= f_i(\theta) - C_i G_N(\theta) \end{aligned} \right\} \quad (i = 1, 2, \dots, N-1) \quad (4.5-20)$$

Although we chose to eliminate  $\beta_N$  from the estimation process, the above equation can be generalized to eliminate any one of the  $\beta$ 's. Note that  $R(\theta)$  in (4.5-19) satisfies the normalization (4.5-3) independent of the  $\beta_i$ 's, which can take on any value including all zeros. We will estimate the values of  $\beta$  from satellite data.

A useful data type to estimate the  $\beta$ 's is scanner radiance  $I$ . We model the radiance measurement from (4.5-2) as

$$I(\theta) = \pi^{-1} F R(\theta) + \eta \quad (4.5-21)$$

where  $F$  is the true instantaneous flux,  $R(\theta)$  is a random variable because it varies for different scenes, and  $\eta$  is a random measurement error with mean 0 and standard deviation  $\sigma_\eta$ . Normally with satellite radiance data we assume a model of  $R(\theta)$ , and estimate the flux  $F$ . Here we want to estimate  $R(\theta)$  which necessitates a value for  $F$ . If we pair two radiance measurements ( $I^1$  and  $I^2$ ) observing about the same area at about the same time so that  $F$  is common to both measurements, then we can ratio the radiance measurements and eliminate  $F$ . The measurement equation is

$$m_k = \frac{I_k^1}{I_k^2} = \frac{\pi^{-1} F_k R(\theta_k^1) + \eta_k^1}{\pi^{-1} F_k R(\theta_k^2) + \eta_k^2} \quad (4.5-22)$$

or

$$m_k = \frac{R(\theta_k^1) + \eta_k^1 / (\pi^{-1} F_k)}{R(\theta_k^2) + \eta_k^2 / (\pi^{-1} F_k)} \quad (4.5-23)$$

where  $\theta_k^1$  and  $\theta_k^2$  are the two viewing zenith angles for the  $k^{\text{th}}$  measurement pair. However, it can be shown that the measurement equation is biased, or the expected value of  $m_k$  is not the desired ratio of anisotropies, that is

$$E[m_k] = \frac{R(\theta_k^1)}{R(\theta_k^2)} \xi \quad (4.5-24)$$

where  $\xi$  is the bias. Thus, we redefine the measurement statistic as

$$m_k \equiv \left( \frac{1}{\xi} \right) \frac{I_k^1}{I_k^2} \quad (4.5-25)$$

where  $\xi$  can be estimated from the radiance data ratios. We then model this measurement as

$$m_k = \frac{R(\theta_k^1)}{R(\theta_k^2)} + \epsilon_k \quad (4.5-26)$$

Since (4.5-25) is unbiased, we model  $\epsilon_k$  as a random measurement error where  $E[\epsilon_k] = 0$  and  $E[\epsilon_k^2] = \sigma_\epsilon^2$ .

We now write the measurement in terms of the parameters to be estimated. Substituting (4.5-19) into (4.5-26) gives

$$\begin{aligned}
 m_k &= \frac{\sum_{i=1}^{N-1} \beta_i G_i(\theta_k^1) + G_N(\theta_k^1)}{\sum_{i=1}^{N-1} \beta_i G_i(\theta_k^2) + G_N(\theta_k^2)} + \varepsilon_k \\
 &= Q(\theta_k^1, \theta_k^2, \beta) + \varepsilon_k
 \end{aligned} \tag{4.5-27}$$

It will be expeditious to use linear estimation theory. Because the measurement equation (4.5-27) is a nonlinear function of  $\beta$ , we linearize about an initial estimate  $\hat{\beta}^o$ . Thus,

$$m_k = Q(\theta_k^1, \theta_k^2, \hat{\beta}^o) + \sum_{i=1}^{N-1} \frac{\partial Q}{\partial \beta_i}(\theta_k^1, \theta_k^2, \hat{\beta}^o)(\beta_i - \hat{\beta}_i^o) + \text{H.O.T.} + \varepsilon_k \tag{4.5-28}$$

and retaining only the linear terms

$$\Delta m_k = \sum_{i=1}^{N-1} \frac{\partial Q}{\partial \beta_i} \Delta \beta_i + \varepsilon_k \tag{4.5-29}$$

where

$$\begin{aligned}
 \Delta m_k &= m_k - Q(\theta_k^1, \theta_k^2, \hat{\beta}^o) \\
 \Delta \beta_i &= \beta_i - \hat{\beta}_i^o
 \end{aligned} \tag{4.5-30}$$

and

$$\frac{\partial Q}{\partial \beta_i} = \frac{R(\theta_k^2, \hat{\beta}^o)G_i(\theta_k^1) - R(\theta_k^1, \hat{\beta}^o)G_i(\theta_k^2)}{R(\theta_k^2, \hat{\beta}^o)^2} \tag{4.5-31}$$

If we have  $K$  measurements ( $k = 1, 2, \dots, K$ ), then we can form a matrix measurement equation and estimate the  $\Delta \beta$  vector with the Gauss-Markoff Theorem. Let us define

$$\Delta m = \begin{bmatrix} \Delta m_1 \\ \Delta m_2 \\ \vdots \\ \Delta m_K \end{bmatrix} \quad \varepsilon = \begin{bmatrix} \varepsilon_1 \\ \varepsilon_2 \\ \vdots \\ \varepsilon_K \end{bmatrix} \quad \Delta \beta = \begin{bmatrix} \Delta \beta_1 \\ \Delta \beta_2 \\ \vdots \\ \Delta \beta_{N-1} \end{bmatrix} \tag{4.5-32}$$

$$X = \begin{bmatrix} \frac{\partial}{\partial \beta_1} Q(\theta_1^1, \theta_1^2, \hat{\beta}^o) & \frac{\partial}{\partial \beta_2} Q(\theta_1^1, \theta_1^2, \hat{\beta}^o) & \dots & \frac{\partial}{\partial \beta_{N-1}} Q(\theta_1^1, \theta_1^2, \hat{\beta}^o) \\ \frac{\partial}{\partial \beta_1} Q(\theta_2^1, \theta_2^2, \hat{\beta}^o) & \frac{\partial}{\partial \beta_2} Q(\theta_2^1, \theta_2^2, \hat{\beta}^o) & \dots & \frac{\partial}{\partial \beta_{N-1}} Q(\theta_2^1, \theta_2^2, \hat{\beta}^o) \\ \vdots & \vdots & & \vdots \\ \frac{\partial}{\partial \beta_1} Q(\theta_K^1, \theta_K^2, \hat{\beta}^o) & \frac{\partial}{\partial \beta_2} Q(\theta_K^1, \theta_K^2, \hat{\beta}^o) & \dots & \frac{\partial}{\partial \beta_{N-1}} Q(\theta_K^1, \theta_K^2, \hat{\beta}^o) \end{bmatrix} \quad (4.5-33)$$

The matrix measurement equation is given by

$$\Delta m = X \Delta \beta + \epsilon \quad (4.5-34)$$

and the weighted estimate is (Liebelt, p.148)

$$\Delta \hat{\beta} = (X^T W X)^{-1} X^T W \Delta m \quad (4.5-35)$$

and the covariance of  $\Delta \hat{\beta}$  is

$$\text{Cov}[\Delta \hat{\beta}] = (X^T W X)^{-1} \quad (4.5-36)$$

where  $W$  is the weighting matrix or

$$W = \text{Cov}^{-1}[\epsilon \epsilon^T] \quad (4.5-37)$$

It follows from (4.5-30) that  $\hat{\beta} = \hat{\beta}^o + \Delta \hat{\beta}$  and from (4.5-19) that the estimate of  $R$  is

$$\hat{R}(\theta) = \sum_{i=1}^{N-1} \hat{\beta}_i G_i(\theta) + G_N(\theta) \quad (4.5-38)$$

Finally, the variance of the estimate is

$$\text{Var}[\hat{R}(\theta)] = G^T(\theta) \text{Cov}[\Delta \hat{\beta}] G(\theta) \quad (4.5-39)$$

### 4.5.3. Implementation Issues

#### 4.5.3.1. Spectral Correction

A general discussion of converting from filtered radiances to unfiltered radiances is given in section 2.2.1. The ERBE-like spectral correction will use the shortwave and total channels to derive the unfiltered shortwave and longwave radiances. The unfiltered window radiance will be a function of only the window channel. The CERES spectral correction, in comparison, will use all three channels to define each unfiltered radiance of shortwave, longwave, and window.

### 4.5.4. References

- Barkstrom, B. R. 1984: The Earth Radiation Budget Experiment. *Bul. Am. Meteorol. Soc.*, vol. 65, pp. 1170–1185.
- Liebelt, Paul B. 1967: *An Introduction to Optimal Estimation*. Addison-Wesley Publ. Co.
- Suttles, J. T.; Green, R. N.; Minnis, P.; Smith, G. L.; Staylor, W. F.; Wielicki, B. A.; Walker, I. J.; Young, D. F.; Taylor, V. R.; and Stowe, L. L. 1988: *Angular Radiation Models for Earth-Atmosphere System. I—Shortwave Radiation*. NASA RP-1184.

- Suttles, J. T.; Green, R. N.; Smith, G. L.; Wielicki, B. A.; Walker, I. J.; Taylor, V. R.; and Stowe, L. L. 1989: *Angular Radiation Models for Earth-Atmosphere System. II—Longwave Radiation*. NASA RP-1184.
- Suttles, John T.; Wielicki, Bruce A.; and Vemury, Sastri 1992: Top-of-Atmosphere Radiative Fluxes—Validation of ERBE Scanner Inversion Algorithm Using Nimbus-7 ERB Data. *J. Appl. Meteorol.*, vol. 31, no. 7, pp. 784–796.
- Taylor, V. R.; and Stowe, L. L. 1984: Reflectance Characteristics of Uniform Earth and Cloud Surfaces Derived From Nimbus-7 ERB. *J. Geophys. Res.*, vol. 89, pp. 4987–4996.
- Wielicki, Bruce A.; and Green, Richard N. 1989: Cloud Identification for ERBE Radiative Flux Retrieval. *J. Appl. Meteorol.*, vol. 28, pp. 1133–1146.
- Ye, Q. 1993: The Spatial-Scale Dependence of the Observed Anisotropy of Reflected and Emitted Radiation. Ph.D. Thesis, Oregon State Univ.



**Clouds and the Earth's Radiant Energy System (CERES)**

**Algorithm Theoretical Basis Document**

*Empirical Estimates of Shortwave and Longwave Surface*

*Radiation Budget Involving CERES Measurements*

*(Subsystem 4.6.0)*

B. R. Barkstrom<sup>1</sup>

R. D. Cess<sup>2</sup>

A. K. Inamdar<sup>3</sup>

V. Ramanathan<sup>3</sup>

S. K. Gupta<sup>4</sup>

N. A. Ritchey<sup>4</sup>

A. C. Wilber<sup>4</sup>

W. L. Darnell<sup>1</sup>

<sup>1</sup>Atmospheric Sciences Division, NASA Langley Research Center, Hampton, Virginia 23681-0001

<sup>2</sup>Institute for Terrestrial and Planetary Atmospheres, Marine Sciences Research Center, State University of New York at Stony Brook, Stony Brook, New York 11794-5000

<sup>3</sup>Center for Clouds, Chemistry, and Climate, Scripps Institution of Oceanography, University of California, San Diego, California

<sup>4</sup>Analytical Services & Materials, Inc., Hampton, Virginia 23666

## Abstract

*This portion of the CERES processing system is intended to produce the shortwave and longwave flux components of the surface radiation budget based on empirical relationships between the CERES TOA fluxes and measured surface radiation budget components. The input to this processing consists of three major kinds of data: CERES footprint cloud properties, CERES TOA fluxes for each footprint, and meteorological data. When this system finishes, the output data are the shortwave and longwave flux components at the Earth's surface. There are three kinds of algorithms that we use for the first release of the CERES processing system: net shortwave flux based on the CERES TOA net flux (Li-Leighton), clear-sky longwave fluxes based on relationships derived by Inamdar and Ramanathan, and cloudy-sky longwave fluxes based on relationships derived by Gupta et al.*

### 4.6.0. Empirical Estimates of Shortwave and Longwave Surface Radiation Budget Involving CERES Measurements

#### 4.6.0.1. Introduction

At this point in the CERES processing, we have determined the cloud properties within CERES footprints and we have inverted the CERES radiances to produce TOA fluxes. We also have available the atmospheric constituents and temperatures with modifications that provide what corrections are needed to agree with the basic cloud properties. What we need to do next is to estimate the component fluxes at the Earth's surface.

We often think of these surface radiative fluxes in terms of the two broad spectral bands that we have discussed before: shortwave fluxes and longwave fluxes. Each of these bands have upwelling and downwelling components. Historically, there have been a number of different philosophies regarding the best way to measure the fluxes at the surface and the best way to estimate them from satellite measurements.

In the case of the shortwave fluxes, the classic instrument for measuring the surface flux has been the solar pyranometer, which determines the downwelling flux from all directions. Some observation stations use a shaded pyranometer to measure diffuse flux. An inverted pyranometer can also measure the upwelling flux. However, such instrumentation has difficulties, including thermal convection within the instruments and angular and spectral sensitivities, that make it difficult to accurately characterize it. These problems are compounded by the fact that the angular and spectral radiances emerging from the surface depend both upon the surface properties and upon the radiances coming from the atmosphere. For example, under clear skies the radiance field has a very large value near the Sun's location in the sky and also exhibits considerable limb-brightening in the downwelling diffuse radiance. Blue parts of the shortwave radiance are more diffuse than are the red parts of that spectral band. Given this kind of variability, there have been adherents to measuring the radiance field and integrating radiances to derive fluxes.

The same kind of bifurcation in the measurement community appears in the longwave spectral interval. Here, some measurement devices obtain downwelling fluxes separately from upwelling ones, while other devices obtain the net radiation. Some instruments also measure radiances and use data reduction to produce fluxes.

What is encouraging is the advance of the surface measurement community that is beginning to develop the means for providing reliable surface measurements over at least some portion of the Earth's

surface. Such systems as the Baseline Surface Radiation Network (BSRN) and the measurements from the Atmospheric Radiation Measurement (ARM) program of the Department of Energy offer excellent opportunities to develop empirical relationships between the TOA fluxes from CERES and the surface radiation budget. In this portion of the processing system, we emphasize techniques that use the CERES measurements directly or that have the potential for doing so. In the Surface and Radiation Budget portion of the processing, given in ATBD subsystem volume 5.0 and subsidiary volumes, we discuss methods that depend explicitly upon radiative transfer calculations. In the sections below, we discuss the Li-Leighton shortwave calculation and the longwave calculations of Inamdar and Ramanathan, as well as those of Gupta.

#### 4.6.0.2. Shortwave Net Flux at the Surface

The first approximation to the shortwave spectrum's radiative transfer is that it has two spectral subdivisions: a conservative scattering portion that extends from a wavelength of about 0.4  $\mu\text{m}$  to about 0.7  $\mu\text{m}$ , and a completely absorbing portion that covers both the region shortward of 0.4  $\mu\text{m}$  and longward of 0.7  $\mu\text{m}$ . Under this assumption, the net flux at the Earth's surface is related to the net flux at the top of the atmosphere:

$$F_{SFC}^{\uparrow\downarrow} = F_{TOA}^{\uparrow\downarrow} - B \quad (4.6-1)$$

$F^{\uparrow\downarrow}$  represents the net flux at whichever surface we are considering.  $B$  represents the solar energy absorbed in the opaque part of the solar spectral range.

In practice, of course, the shortwave radiative transfer is somewhat more complicated. There is ozone absorption across the middle of the "conservative" part of the spectrum, and the near-infrared water vapor bands are not completely black. There are also concerns in the community that clouds are not completely conservative scatterers, as well. Nonetheless, Cess et al. (1991) pursued the possibility of slightly altering the linear relationship between the top of the atmosphere net flux and the surface net flux in the previous equation (4.6-1):

$$F_{SCF}^{\uparrow\downarrow} = AF_{TOA}^{\uparrow\downarrow} - B \quad (4.6-2)$$

If equation (4.6-1) is not too bad an approximation, then equation (4.6-2) should have a value of  $A$  that is near 1. Cess et al. (1991) used data from net shortwave radiometers on towers together with instantaneous, simultaneous, and collocated ERBE data to verify that this linear relationship was reasonable. They found that  $A$  was about 0.9, and that  $B$  was about  $50 \text{ W}\cdot\text{m}^{-2}$ , with each coefficient having a slight dependence on water vapor. Interestingly, the numerical values of  $A$  and  $B$  were independently derived from a theoretical radiative transfer model and from a regression of the satellite data against the surface net flux measurements. Cess et al. (1991) suggest that the linear relationship appears to be accurate to within about 1%, particularly if the data period extends to a 1-month average to remove some of the noise in the system.

Li and Leighton (1993) extended this simple linear relationship to allow a more accurate inclusion of water vapor and solar zenith angle. They applied this algorithm to the 5-year, global ERBE data set based on the ERBE scanner monthly averages. Li et al. (1993) provide a comparison of this algorithm against a more extensive set of tower measurements of net shortwave flux and direct comparisons with the ERBE data. Their algorithm is discussed in ATBD subsystem 4.6.1.

#### 4.6.0.3. Longwave Fluxes at the Surface

The development of satellite techniques to estimate the longwave radiative fluxes at the Earth's surface has proceeded more slowly. In some ways this problem is more difficult because the downwelling longwave flux responds to both water vapor and to cloud properties. In the tropics, the water vapor is so opaque in the longwave part of the spectrum that most experts believe that clouds are likely to have a

comparatively small positive effect on the downwelling flux. However, this is not the case in other parts of the Earth.

Toward the beginning of the CERES investigation, Ramanathan (Raval and Ramanathan 1989) began pursuing a number of studies related to the greenhouse effect and longwave fluxes at the Earth's surface. They were particularly attracted to the simple picture that longwave radiation escapes nearly unimpeded in the atmospheric window, whereas it is blocked in most of the other parts of the spectrum. The first approximation to the upwelling longwave flux relates this flux directly to the surface temperature,  $T_{SFC}$ :

$$F_{LW}^{\uparrow}(SFC) = \sigma T_{SFC}^4 \quad (4.6-3)$$

Ramanathan would then describe the greenhouse effect in terms of the difference

$$G \equiv F_{LW}^{\uparrow}(SFC) - F_{LW}^{\uparrow}(TOA) \quad (4.6-4)$$

Raval and Ramanathan (1989) ascribed the rapid rise in greenhouse effect to water vapor continuum absorption in the atmospheric window, an effect they called the *super greenhouse effect*. Hallberg and Inamdar (1993) used sensitivity studies to confirm the effect. The confirmation led to the suggestion that variability in the window component of the greenhouse effect could be used as a signature of lower tropospheric water vapor. The absorption of this gas dominates the downward emission at the surface.

In looking for a simple way to obtain the downwelling flux at the surface, Ramanathan began to explore possible relationships between the window flux between 8  $\mu\text{m}$  and 12  $\mu\text{m}$  and the downwelling flux. Further work by Inamdar and Ramanathan (1994) has extended this work. For clear-sky conditions, these explorations led to the algorithm suggested in ATBD subsystem volume 4.6.2. Ramanathan's suggestion also led to the decision by the CERES Science Team to replace the ERBE longwave channel (which was not spectrally flat over the longwave spectral range) with a reasonably flat spectral channel to capture just the window region radiation. Stephens et al. (1994) have independently suggested similar relations that could be used to derive longwave flux at the surface from broadband measurements.

Under cloudy conditions, more work is needed to derive longwave flux at the Earth's surface. In ATBD subsystem volume 4.6.3, Gupta et al. (cf. also Gupta 1989; Gupta et al. 1992; Darnell et al. 1983) provide a description of an algorithm that uses the CERES broadband fluxes, together with data about the atmosphere and the cloud properties derived from CERES to compute the longwave fluxes at the Earth's surface.

In the figure 4.6-1 on the following page, we show the decomposition of the three empirically based algorithms for surface flux that we apply in subsystem 4.0. The input and output data for each of these algorithms is not identical, so some care in reading this diagram is needed. In addition, each of these algorithms operates on the data in one CERES footprint. Because of the simplicity of the algorithms, these output fields contribute to both the surface radiation branch of the CERES processing, where these data provide the only source of surface radiation budget data, and in the atmosphere branch of processing. Intercomparison of the two, independently produced, fields will provide an important source of validation and quality control information in the future. The algorithms are described in subsystems 4.6.1, 4.6.2, and 4.6.3.

#### 4.6.0.4. Implementation Issues

There appear to be no major implementation issues at this point. The interfaces between these algorithms and the available data within this subsystem are readily available. The Li-Leighton algorithm uses the CERES TOA fluxes and atmospheric water vapor. The Inamdar-Ramanathan algorithm uses CERES TOA fluxes, the CERES window channel radiance, surface temperature, and precipitable water.

The Gupta et al. algorithm uses data similar to the Inamdar-Ramanathan algorithm, with the addition of the other cloud properties available from the CERES footprint cloud properties.

#### 4.6.0.5. References

- Cess, Robert D.; Dutton, Ellsworth, G.; Deluisi, John J.; and Jiang, Feng 1991: Determining Surface Solar Absorption From Broadband Satellite Measurements for Clear Skies—Comparison With Surface Measurements. *J. Climat.*, vol. 4, pp. 236–247.
- Darnell, Wayne L.; Gupta, Shashi K.; and Staylor, W. Frank 1983: Downward Longwave Radiation at the Surface From Satellite Measurements. *J. Climat. & Appl. Meteorol.*, vol. 22, no. 11, pp. 1956–1960.
- Gupta, Shashi K. 1989: A Parameterization for Longwave Surface Radiation From Sun-Synchronous Satellite Data. *J. Climat.*, vol. 2, pp. 305–320.
- Gupta, Shashi K.; Darnell, Wayne L.; and Wilber, Anne C. 1992: A Parameterization for Longwave Surface Radiation From Satellite Data—Recent Improvements. *J. Appl. Meteorol.*, vol. 31, no. 12, pp. 1361–1367.
- Hallberg, Robert; and Inamdar, Anand K. 1993: Observations of Seasonal Variations in Atmospheric Greenhouse Trapping and Its Enhancement at High Sea Surface Temperature. *J. Climat.*, vol. 6, no. 5, pp. 920–931.
- Inamdar, A. K.; and Ramanathan, V. 1994: Physics of Greenhouse Effect and Convection in Warm Oceans. *J. Climat.*, vol. 7, no. 5, pp. 715–731.
- Li, Z.; and Leighton, H. G. 1993: Global Climatologies of Solar Radiation Budgets at the Surface and in the Atmosphere From 5 Years of ERBE Data. *J. Geophys. Res.*, vol. 98, pp. 4919–4930.
- Li, Zhanqing; Leighton, H. G.; and Cess, Robert D. 1993: Surface Net Solar Radiation Estimated From Satellite Measurements—Comparisons With Tower Observations. *J. Climat.*, vol. 6, no. 9, pp. 1764–1772.
- Raval, A.; and Ramanathan, V. 1989: Observational Determination of the Greenhouse Effect. *Nature*, vol. 342, pp. 758–761.
- Stephens, G. L.; Slingo, A.; Webb, M. J.; Jones, A.; and Randall, D. A. 1994: A New Method for Deriving the Atmospheric Greenhouse Effect From Satellite Observations, submitted to *Nature*.



**Clouds and the Earth's Radiant Energy System (CERES)**

**Algorithm Theoretical Basis Document**

***Estimate of Shortwave Surface Radiation Budget From CERES***

***(Subsystem 4.6.1)***

David P. Kratz<sup>1</sup>

Zhanqing Li<sup>2</sup>

<sup>1</sup>Atmospheric Science Division, NASA Langley Research Center, Hampton, Virginia 23681-0001

<sup>2</sup>Canada Centre for Remote Sensing, Ottawa, Ontario, Canada

## Abstract

*A concise review is presented for the algorithm that has been tentatively selected to produce simulated net shortwave surface fluxes from measured TOA radiances. There exists, however, an intense controversy concerning the applicability of this shortwave radiative transfer algorithm. The acquisition of planned correlative surface and TOA measurements may soon resolve the existing disagreement.*

### 4.6.1. Estimate of Shortwave Surface Radiation Budget From CERES

#### 4.6.1.1. Shortwave Net Flux at the Surface

For shortwave radiation,  $\lambda < 3.3 \mu\text{m}$ , evidence has been presented (see e.g., Cess et al. 1991; Li et al. 1993a) that a straightforward relation exists between TOA and surface fluxes. More recent studies (see e.g., Cess et al. 1995; Ramanathan et al. 1995), however, indicate that important physical processes may have been overlooked with the consequence that significant contributions to the radiation field may have been neglected. Specifically, Cess et al. (1995) and Ramanathan et al. (1995) present evidence that for cloudy-sky conditions shortwave absorption occurs in excess of that predicted theoretically. The conclusions of Cess et al. (1995) and Ramanathan et al. (1995) are further supported by aircraft measurements of shortwave fluxes made within the cloudy tropical atmosphere by Pilewski and Valero (1995). Nevertheless, recent studies by Li et al. (1995a) and Chou et al. (1995) have been unable to obtain similar shortwave flux enhancements and thus do not support the conclusions of Cess et al. (1995) and Ramanathan et al. (1995). A resolution of this issue may soon be forthcoming from the ARM Enhanced Shortwave Experiment (ARESE). The principal objective of ARESE is to measure the absorption of solar radiation directly for both clear-sky and cloudy-sky conditions and to determine the uncertainties on these measurements. It is hoped that ARESE will lead to a determination of the processes that appear to cause absorption in excess of model predictions. Until a comprehensive determination is made, however, a reasonable course of action is to retain the existing Li et al. (1993a) shortwave algorithm, at least for the early stages of the validation study.

Li et al. (1993a) derived a parameterization of the net shortwave surface flux in terms of the reflected shortwave flux at the top of the atmosphere, the column water vapor amount (precipitable water), and the cosine of the solar zenith angle. This empirical transfer algorithm was deduced exclusively from radiative transfer calculations and is entirely independent of surface observations. Hence, the Li et al. (1993a) algorithm requires no information about either the surface conditions or the presence or absence of clouds. The algorithm has been tested by comparing the net surface flux deduced from broadband radiance measurements from ERBS against surface data from two sets of tower measurements (Li et al. 1993b). The results indicate that one should anticipate errors in the monthly-mean surface insolation to have biases near zero with RMS errors between 8 and 28  $\text{W}\cdot\text{m}^{-2}$  (Li et al. 1995b). The RMS errors are associated principally with poor representation of surface observations within a grid-cell, and thus, with a sufficient number of surface observations, it is estimated that the RMS errors will be within 5  $\text{W}\cdot\text{m}^{-2}$ . Thus, it is reasonable to expect the uncertainty in the global climatology of the surface solar radiation budget to be well within 10  $\text{W}\cdot\text{m}^{-2}$  (Li et al. 1993b). The net shortwave flux at the surface in  $\text{W}\cdot\text{m}^{-2}$  is determined from the Li et al. (1993a) algorithm as follows:

$$SW_{\text{surf}}^{\text{net}} = E_o d^{-2} \mu \left\{ 1 - \frac{C}{\mu} - \frac{D}{\sqrt{\mu}} + \frac{1 - \exp(-\mu)}{\mu} (0.0699 - 0.0683 \sqrt{p}) \right. \\ \left. - [1 + A + B \ln(\mu) - 0.0273 + 0.0216 \sqrt{p}] \alpha_{\text{TOA}} \right\}$$

where

$$E_o = \text{solar constant} = 1365 \text{ W}\cdot\text{m}^{-2}$$

$d$  = Earth-Sun distance in astronomical units

$p$  = precipitable water in cm

$\theta_o$  = solar zenith angle

$$\mu = \cos \theta_o$$

$$\alpha_{TOA} = \text{albedo at TOA} = F_{TOA}/(E_o d^{-2} \mu)$$

$F_{TOA}$  = satellite-derived reflected shortwave flux at TOA,  $\text{W}\cdot\text{m}^{-2}$

$$A = 0.0815$$

$$B = 0.0139$$

$$C = -0.01124$$

$$D = 0.1487$$

The algorithms for the downward shortwave flux at the surface are still under development.

#### 4.6.1.2. References

- Cess, Robert D.; Dutton, Ellsworth G.; Deluisi, John J.; and Jiang, Feng 1991: Determining Surface Solar Absorption From Broadband Satellite Measurements for Clear Skies—Comparison With Surface Measurements. *J. Climat.*, vol. 4, pp. 236–247.
- Cess, R. D.; Zhang, M. H.; Minnis, P.; Corsetti, L.; Dutton, E. G.; Forgan, B. W.; Garber, D. P.; Gates, W. L.; Hack, J. J.; Harrison, E. F.; Jing, X.; Kiehl, J. T.; Long, C. N.; Morcrette, J.-J.; Potter, G. L.; Ramanathan, V.; Subasilar, B.; Whitlock, C. H.; Young, D. F.; and Zhou, Y. 1995: Absorption of Solar Radiation by Clouds: Observations Versus Models. *Science*, vol. 267, pp. 496–499.
- Chou, M.-D.; Arking, A.; Otterman, J.; and Ridgway, W. L. 1995: The Effects of Clouds on Atmospheric Absorption of Solar Radiation. Accepted by *GRL*.
- Li, Zhanqing; Leighton, H. G.; Masuda, Kazuhiko; and Takashima, Tsutomu 1993a: Estimation of SW Flux Absorbed at the Surface From TOA Reflected Flux. *J. Climat.*, vol. 6, no. 2, pp. 317–330.
- Li, Zhanqing; Leighton, H. G.; and Cess, Robert D. 1993b: Surface Net Solar Radiation Estimated From Satellite Measurements—Comparisons With Tower Observations. *J. Climat.*, vol. 6, no. 9, pp. 1764–1772.
- Li, Z.; Barker, H. W.; and Moreau, L. 1995a: The Variable Effect of Clouds on Atmospheric Absorption of Solar Radiation. *Nature*, vol. 376, pp. 486–490.
- Li, Z.; Whitlock, C. H.; and Charlock, T. P. 1995b: Assessment of the Global Monthly Mean Surface Insolation Estimated From Satellite Measurements Using Global Energy Balance Archive Data. Accepted by *J. Climat.*
- Pilewski, P.; and Valero, F. P. J. 1995: Direct Observations of Excess Solar Absorption by Clouds. *Science*, vol. 267, pp. 1626–1629.
- Ramanathan, V.; Subasilar, B.; Zhang, G. J.; Conant, W.; Cess, R. D.; Kiehl, J. T.; Grassl, H.; and Shi, L. 1995: Warm Pool Heat Budget and Shortwave Cloud Forcing: A Missing Physics? *Science*, vol. 267, pp. 499–503.



**Clouds and the Earth's Radiant Energy System (CERES)**

**Algorithm Theoretical Basis Document**

***Estimation of Longwave Surface Radiation Budget From CERES***

***(Subsystem 4.6.2)***

**CERES Science Team Surface Radiation Budget Working Group**

**Principal Investigators**

A. K. Inamdar<sup>1</sup>

V. Ramanathan<sup>1</sup>

<sup>1</sup>Center for Clouds, Chemistry and Climate, Scripps Institution of Oceanography, University of California, San Diego, California

## Abstract

*This paper describes the status of the studies underway for the development of algorithms for surface longwave radiation budget using CERES instrumentation. The algorithm reported here uses a combination of TOA longwave fluxes measured by CERES and other correlated meteorological variables. CERES will estimate longwave fluxes in two spectral regions: broadband (4 to 500  $\mu\text{m}$ ) and window (8 to 12  $\mu\text{m}$ ).*

*A radiative transfer model was used to simulate the TOA and surface longwave fluxes and choose the algorithm. The input to the model is sondes launched from ships. The complete algorithm relates the longwave down flux at the surface in terms of four parameters: TOA broadband and window flux, the total column water vapor, the surface temperature, and the near-surface atmospheric temperature. The rms errors in the predicted surface fluxes (pole to pole) range between 3 and 4.5  $\text{W}\cdot\text{m}^{-2}$ . The model and algorithm have been validated with field data collected during the Central Equatorial Pacific Experiment (CEPEX) and ARM Probe sites.*

### 4.6.2. Estimation of Longwave Surface Radiation Budget From CERES

#### Symbols

$F_0^+$	surface black body emission $\approx \sigma T_s^4$
$F_0^-$	downward longwave flux at the surface, $\text{W}\cdot\text{m}^{-2}$
$*F_\infty^+$	longwave flux at TOA, $\text{W}\cdot\text{m}^{-2}$
$f_0^-$	normalized $F_0^-$ where $f_0^- = F_0^-/F_0^+$
$f_\infty^+$	normalized $F_\infty^+$ where $f_\infty^+ = F_\infty^+/F_0^+$
$G_a$	clear-sky greenhouse effect of the atmosphere where $G_a = F_0^+ - F_\infty^+$
$g_a$	normalized $G_a$ where $g_a = G_a/F_0^+ = 1 - f_\infty^+$
$I_0^-$	downwelling radiance in the 500 to 2000 $\text{cm}^{-1}$ range, $\text{W}\cdot\text{m}^{-2}\cdot\text{sterad}^{-1}$
$T_a$	atmospheric temperature, subscript indicates the pressure level
$T_s$	surface temperature, K
$w_{tot}$	total column precipitable water, $\text{g}\cdot\text{cm}^{-2}$
$\tau_{vis}$	aerosol optical depth in the visible (0.55 $\mu\text{m}$ )

#### 4.6.2.1. Introduction

The methods used for deriving the surface longwave radiation budget can be classified as physical, empirical, or statistical. The physical methods are based on the application of the full radiative transfer theory (Frouin et al. 1988; Darnell et al. 1983; Wu and Cheng 1989) using the profiles of temperature, humidity, and molecular species in the atmosphere. These profiles are retrieved from satellite (NOAA

\*The second subscripts "win" and "nw" for any flux parameter denote the corresponding quantities integrated over the window (8–12  $\mu\text{m}$ ) and nonwindow spectral intervals, respectively.

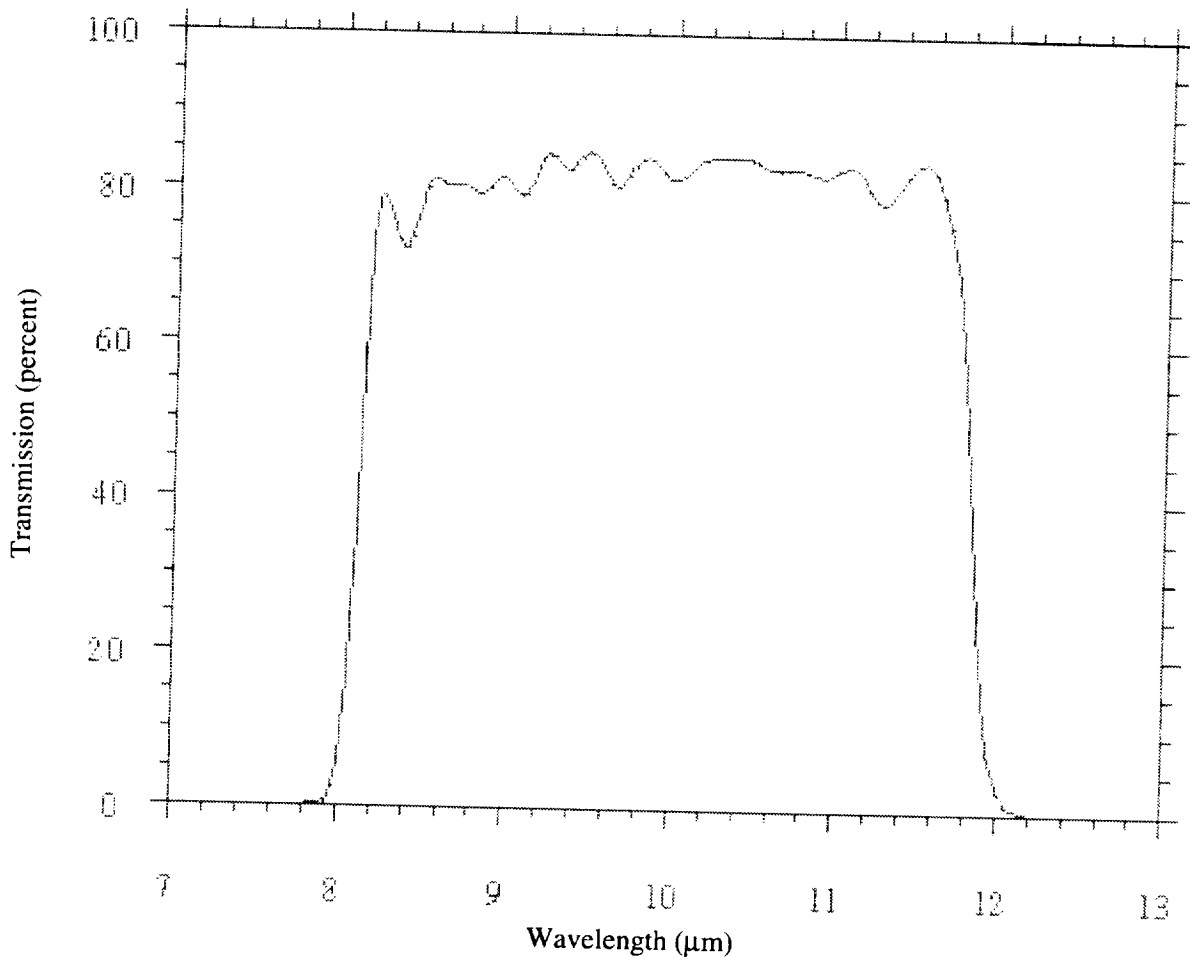


Figure 1. Combined longwave filter transmission (average of both front and rear filters).

TOVS) radiance data. Errors in the retrieved parameters limit the accuracy of the surface fluxes. Numerous simple empirical relationships (Brutsaert 1975; Idso 1981; Schmetz et al. 1986; Tuzet, 1990) have employed an effective sky-emittance temperature to predict the downward flux. These relationships depend on the temperature and partial pressure of water vapor (Idso 1981) near the surface, but a drawback is that they apply to only a selected range of surface temperatures. Statistical methods, on the other hand, use a combination of top-of-the-atmosphere spectral radiances measured by AVHRR/HIRS-2-type instruments and obtain surface fluxes through regression techniques (Schmetz 1986; Gupta 1989).

Our method is a variant of the statistical technique and is developed for the CERES instrument. Because our method is geared toward CERES instruments, a brief description of CERES longwave measurement will be given first.

**4.6.2.1.1. CERES longwave measurements.** CERES uses a pair of broadband scanning radiometers. The radiometers have a total band (shortwave + longwave) and shortwave and longwave window channels. The broadband (4 to 500  $\mu\text{m}$ ) longwave flux is obtained from a combination of all of the three channels. The spectral response characteristic of the longwave window channel is shown in figure 1. For reference, the atmospheric transmittance is shown in figure 2. The sensor has a nominal optical spectral bandpass from 8 to 12 microns that is formed by a filter of multilayer dielectric interference stacks. A combination of two filters is used.

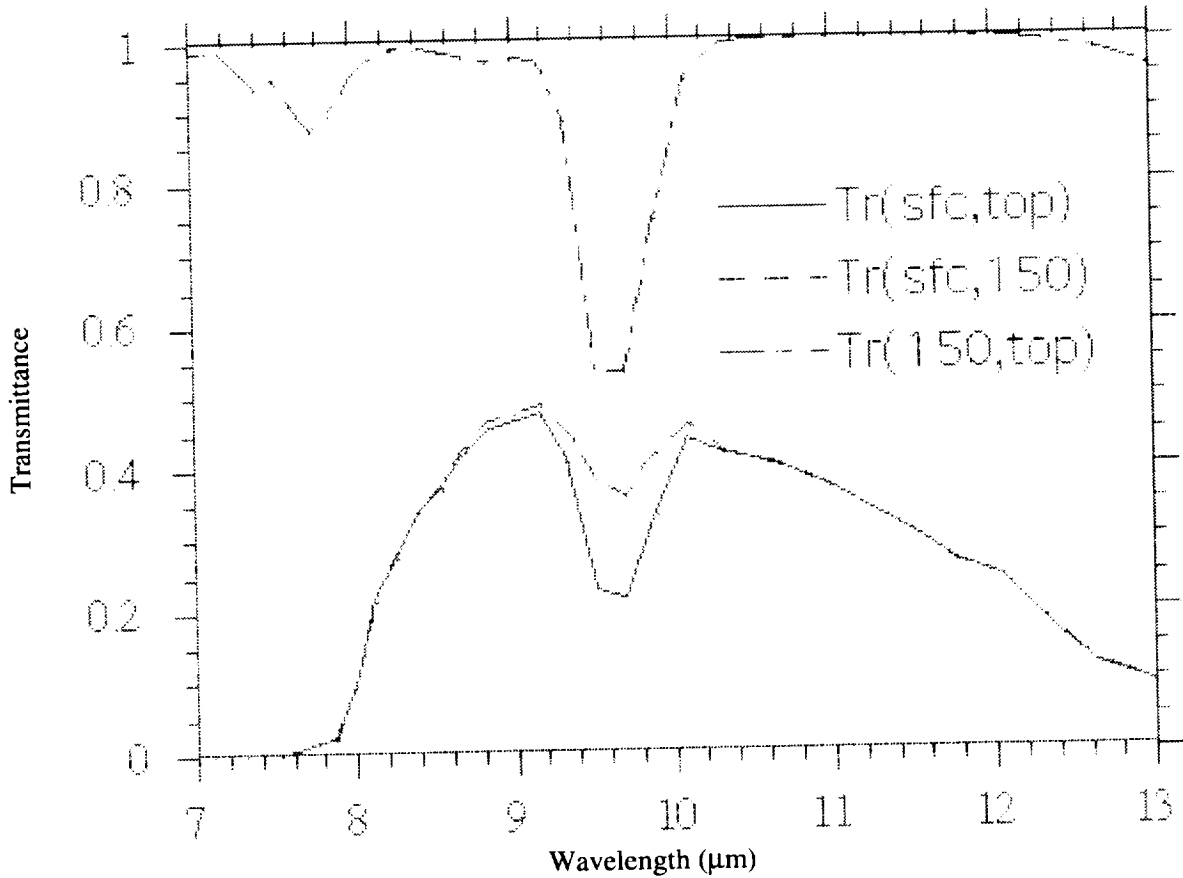


Figure 2. Atmospheric transmittances from 7 to 13  $\mu\text{m}$  (sfc, top, and 150 refer to the surface, top of atmosphere, and 150-mb levels, respectively).

#### 4.6.2.2. Clear-Sky Downward Surface Flux

The basis of our algorithm is model calculation of longwave fluxes (both broadband and window) at the TOA and the surface. These calculations use soundings deployed from ships.

**4.6.2.2.1. Model simulation and data.** The greenhouse effect and the downward flux density at the surface can be expressed by using the integral form of the solution to the equation of radiative transfer as

$$G_a = \int_{z_{\text{top}}}^0 A(z_{\text{top}}, z') \frac{dB(z')}{dz'} dz' \quad (1)$$

$$F_a^- = B(z_{\text{top}})A(z_{\text{top}}, 0) - \int_0^{z_{\text{top}}} A(0, z') \frac{dB(z')}{dz'} dz' \quad (2)$$

where  $z$  is the altitude,  $B(z')$  is the Planck blackbody function,  $A(z, z')$  is the atmospheric absorptance between the levels specified in the arguments, and  $z_{\text{top}}$  is the altitude at the top of atmosphere. The absorptance  $A$ , and hence  $F_a^-$ , is the result of absorption and emission by water vapor,  $\text{CO}_2$ , ozone,  $\text{CH}_4$ ,  $\text{N}_2\text{O}$ , and trace gases and scattering by aerosols and water droplets in the entire atmospheric column. It

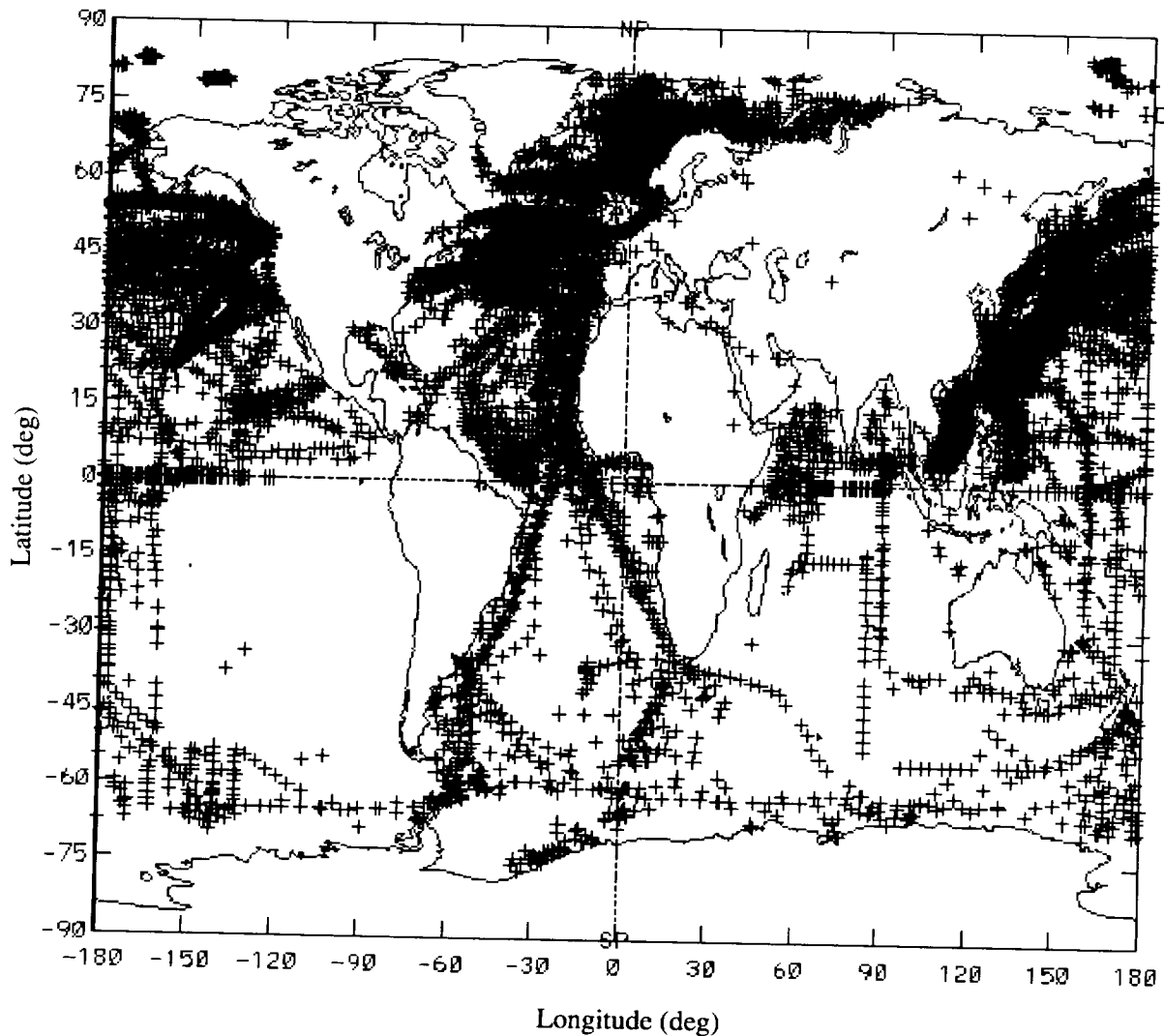


Figure 3. Ship data locations (1985 to 1989) over the global oceans used in this study.

depends on the vertical distribution of temperature, as well as molecular species, including water vapor, in the atmosphere. The transmittances have been computed using the  $20\text{ cm}^{-1}$  LOWTRAN 7 (Kneizys et al. 1988) transmittance code. However, the continuum model used in LOWTRAN 7 has been updated including a revised version (May 1994) of the Clough-Kneizys-Davies (CKD) model (Clough et al. 1989). Revisions effected in both the self- and foreign-continuum coefficients (Clough and Brown 1995) to the data of Burch in the  $1300\text{ cm}^{-1}$  region have been validated against HIS spectra downlooking from 20 km and uplooking from the surface. Equations (1) and (2) are evaluated using a quadrature scheme and a high vertical resolution equivalent to a vertical layer spacing ranging from a minimum of 1 mb to a maximum of  $1/4\text{ km}$ . Agreement of the boundary fluxes using the ICRCCM standard atmospheres (Ellingson 1991) as input is within  $2\text{ to }3\text{ W}\cdot\text{m}^{-2}$ .

The input data used for this study consist of the ship rawinsondes for the years 1985 to 1989—to coincide with the Earth Radiation Budget Experiment (ERBE) observations for the same period—obtained from the NCAR NMC upper air data base. The locations of ship data over the entire globe used in this study is shown in figure 3. There is a fair distribution of data points to exclude any sampling-related problems in the analysis. The poor quality of humidity values above 5 to 6 km

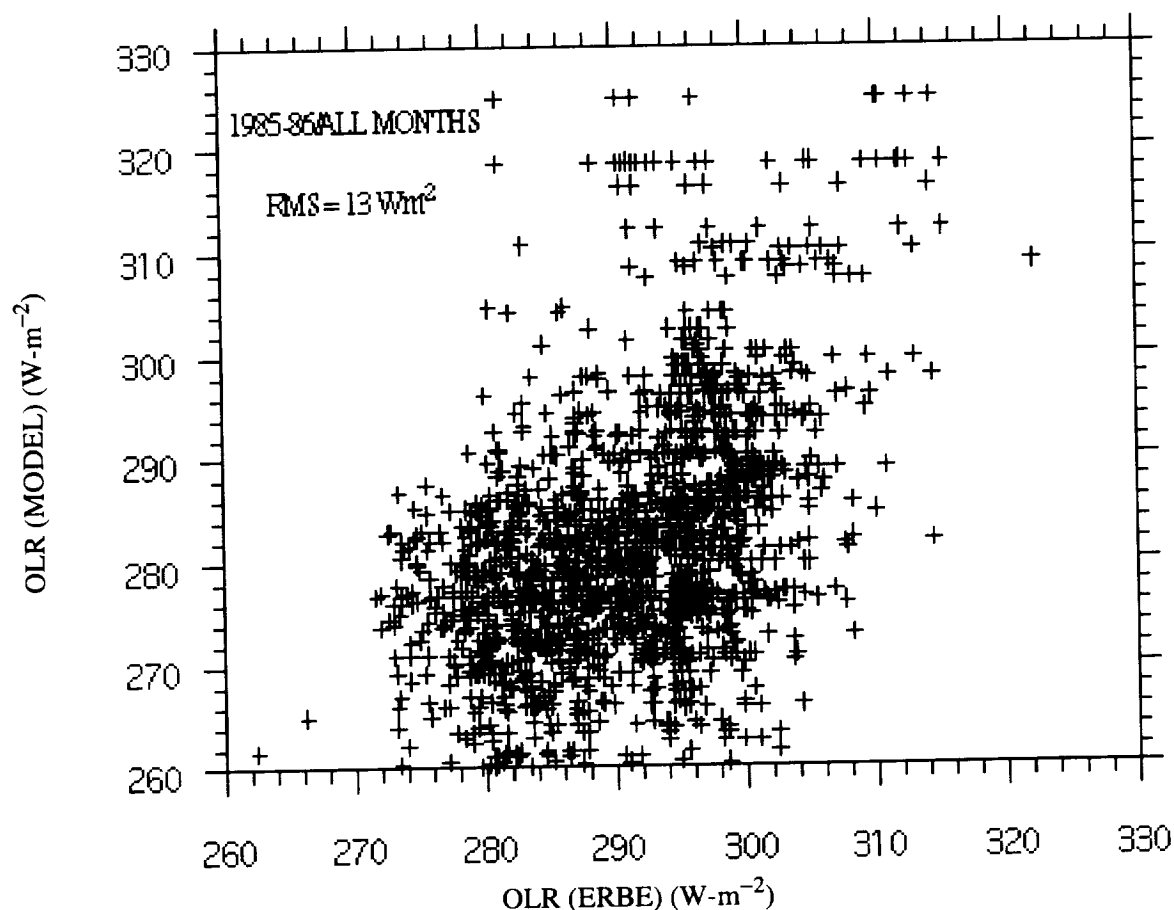


Figure 4. Comparison of model-derived longwave fluxes at TOA for 1985 ship data with collocated ERBE measurements.

reported from soundings is well known (Elliot and Gaffen 1991). An error analysis, using the standard deviation of errors as reported by field tests of radiosonde instruments (Inamdar and Ramanathan 1994), showed the error to be distributed between 6% near the surface to nearly 13% at about 200 mb. Humidity data above 200 mb have not been used. To establish the fidelity of sonde data, an independent validation has been performed by employing the Earth Radiation Budget Experiment (ERBE) data. We use the daily clear-sky ERBE OLR data for 1985 extracted from the hour-box record in the same time window (within 24 hr) and location as the ship data. The comparison shown in figure 4 in the form of a scatter plot between ERBE and model TOA fluxes is within the uncertainty limits of the former.

**4.6.2.2.2. Parameterization.** We begin the process of parameterization by first performing the radiative transfer simulations through equations (1) and (2) and employing ship sondes as input, to derive the TOA and surface longwave fluxes. We first fit the window and nonwindow components of downward flux in terms of the respective components of greenhouse effect as

$$f_{0,win}^- = a_0 g_{a,win} + a_1 \quad (3)$$

$$f_{0,nw}^- = b_0 g_{a,nw} + b_1 \quad (4)$$

and next focus on seeking an optimum combination of parameters,  $P_i$  (see table 1), that best fit the deviations of window and nonwindow fluxes as predicted from (3) and (4) from the actual fluxes:

Table 1. Parameterization Equations

Model	Equation	Comments
Tropics (30°S to 30°N)	$\bar{f}_{0,win} = 3.2504g_{a,win} + [0.1377w_{tot} + 3.46305\ln(f_{\infty,win}^+/f_{0,win}^+) + 0.13866(T_s/300) + 1.12813(T_{950}/300)]f_{\infty,win}^+ - 0.24155$	Window rms error 3.3 W-m <sup>-2</sup>
	$\bar{f}_{0,nw} = 0.25878g_{a,nw} + [0.07363\ln(w_{tot}) - 1.09875(T_s/300) + 1.442(T_{950}/300)]f_{\infty,nw}^+ + 0.45445$	Nonwindow rms error 1.7 W-m <sup>-2</sup>
	$\bar{f}_0 = \bar{f}_{0,win} + \bar{f}_{0,nw}$	Total rms error 4.4 W-m <sup>-2</sup>
Extra Tropics (30° to Pole)	$\bar{f}_{0,win} = 1.6525g_{a,win} + [0.15385w_{tot} + 2.0074\ln(f_{\infty,win}^+/f_{0,win}^+) - 0.29873(T_s/300) + 0.52062(T_{950}/300)]f_{\infty,win}^+ - 0.01875$	Window rms error 1.7 W-m <sup>-2</sup>
	$\bar{f}_{0,nw} = 0.12284g_{a,nw} + [0.07748\ln(w_{tot}) - 1.52282(T_s/300) + 1.81629(T_{950}/300)]f_{\infty,nw}^+ + 0.52066$	Nonwindow rms error 2.0 W-m <sup>-2</sup>
	$\bar{f}_0 = \bar{f}_{0,win} + \bar{f}_{0,nw}$	Total rms error 3.2 W-m <sup>-2</sup>

$$\bar{f}_{0,win} - a_0g_{a,win} = c_0 + f_{\infty,win}^+ \sum_i c_i P_i \quad (5)$$

$$\bar{f}_{0,nw} - b_0g_{a,nw} = d_0 + f_{\infty,nw}^+ \sum_i d_i P_i \quad (6)$$

where the  $c_i$  and  $d_i$  are constants to be determined through regression analyses. The combination of parameters,  $P_i$ , have been chosen after a careful investigation of the physics of the problem and extensive sensitivity studies (described briefly below) to identify the parameters contributing most to the variability of the downward flux.

The physics of radiative transfer in the window and nonwindow spectral regions forms the basis of our algorithm. The close correlation between the atmospheric greenhouse effect ( $G_a$ ) and the downward emissions (Inamdar and Ramanathan 1994) leads us to choose the window and nonwindow components of  $G_a$  as the key radiometric quantities in the parameterization. Note that a two-step procedure is followed [the pair of equations (3), (5) and (4), (6)] in predicting each component of the downward flux. Although a single step regression could have yielded a similar or even better accuracy, this two-step procedure forces the coefficients of the window and nonwindow components of greenhouse effect to bear the bulk of the burden in variability associated with atmospheric temperature and water vapor. This procedure partially alleviates problems related to the contamination of clear-sky TOA fluxes with thin cirrus. For instance, a direct regression would assign a higher weight to the coefficients of temperature terms, and application of the algorithm could be misconstrued to interpret any lower values of OLR as emanating from a colder atmosphere.

In the opaque nonwindow spectral regions, the atmospheric absorption attains saturation close to the surface, and hence it is the near-surface emissions that determine the down flux. In fact more than 95% of the total downward flux originates in the first few kilometers. Further, following the work of Cess and Tiwari (1972), the column absorption resulting from vibration-rotation bands in the non-window can be best described in the logarithmic limit. The column absorption in the window is highly sensitive to the vertical distribution of moisture and can be expressed as a combination of a linear limit and a temperature-dependence factor. Because transmittance in the window is very nearly exponential,

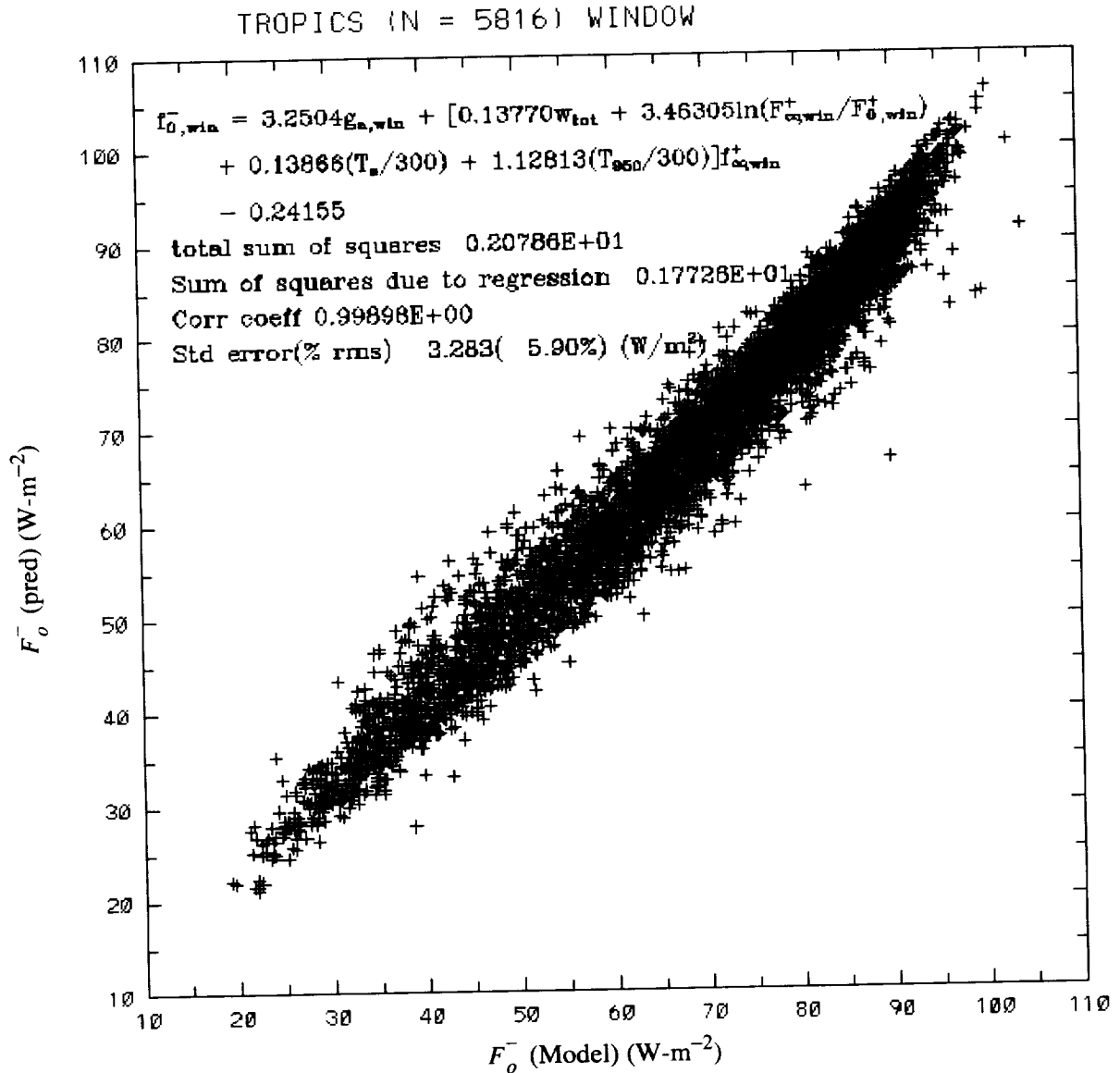


Figure 5. Comparison of clear-sky downward longwave fluxes predicted from the parameterized model 1 (recommended) with those from the detailed radiative transfer calculations over the tropics.

the ratio of window component of top-of-atmosphere to surface emissions yields an approximate measure of the optical depth. The surface temperature and the air temperature in the vicinity of the surface (950 mb in this case), were chosen to account for the flux variances that were not explained by the flux and water vapor terms.

In summary, we propose our standard model in terms of the window and nonwindow components of  $g_a$ ,  $\ln(w_{tot})$ ,  $w_{tot}$ ,  $\ln(F_{\infty,win}^+/F_{0,win}^+)$ ,  $T_s$ , and  $T_a$ . All of the radiative flux parameters have been normalized (Raval and Ramanathan 1989) with the surface blackbody emission to eliminate the surface temperature dependence. Regression analysis of the radiative transfer-simulated fluxes has been performed separately for the tropics (30°S to 30°N) and extratropics (30° to poles) to accommodate the different physics and thus achieve better accuracy. Table 1 and figures 5 to 10 present a summary of the recommended models. Inputs for the model are, in addition to the CERES broadband and window channel information, data on temperature and the total column water vapor,  $w_{tot}$  (g·cm<sup>-2</sup>) derived either

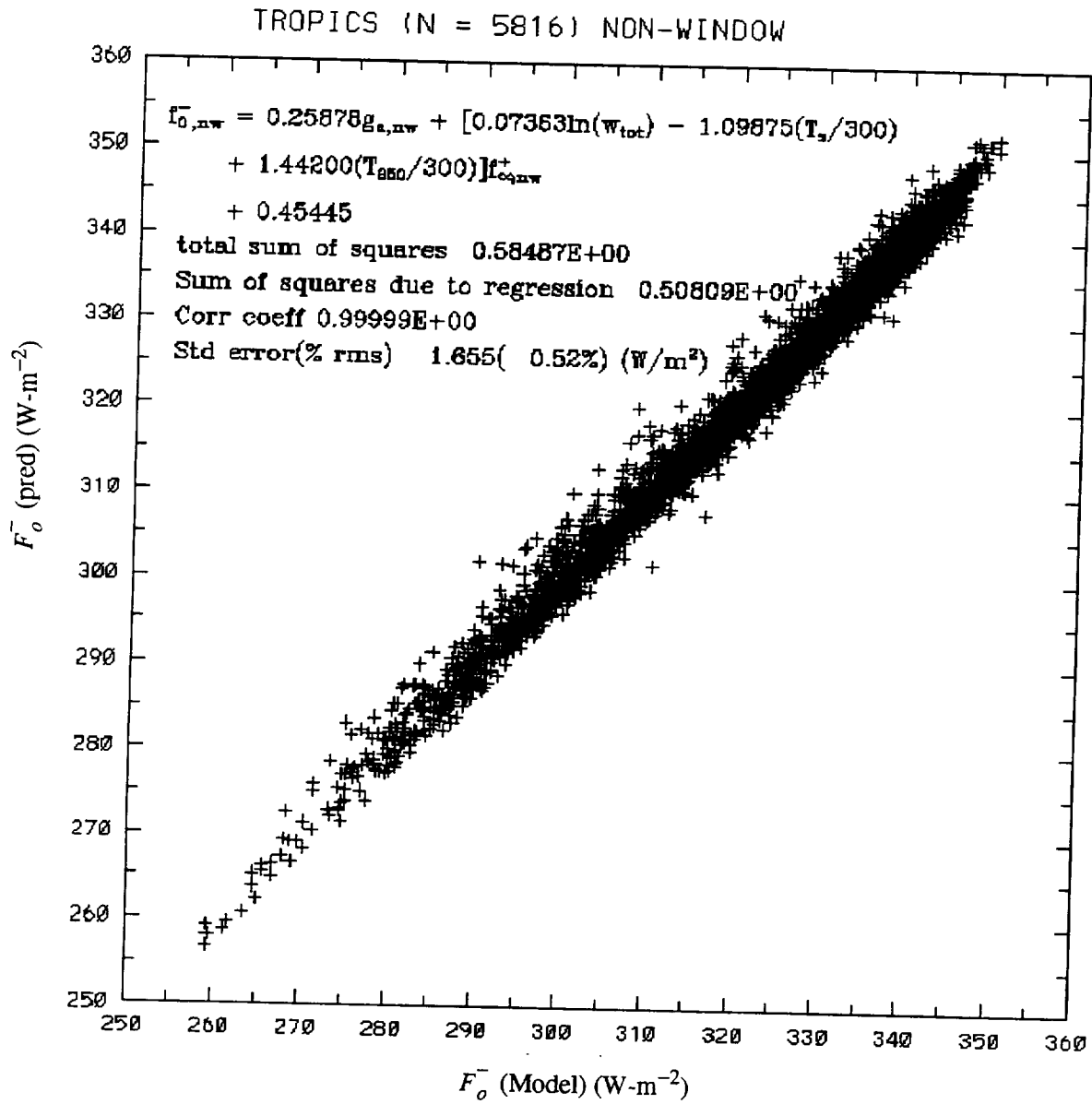


Figure 6. Same as in figure 5, but for extratropics.

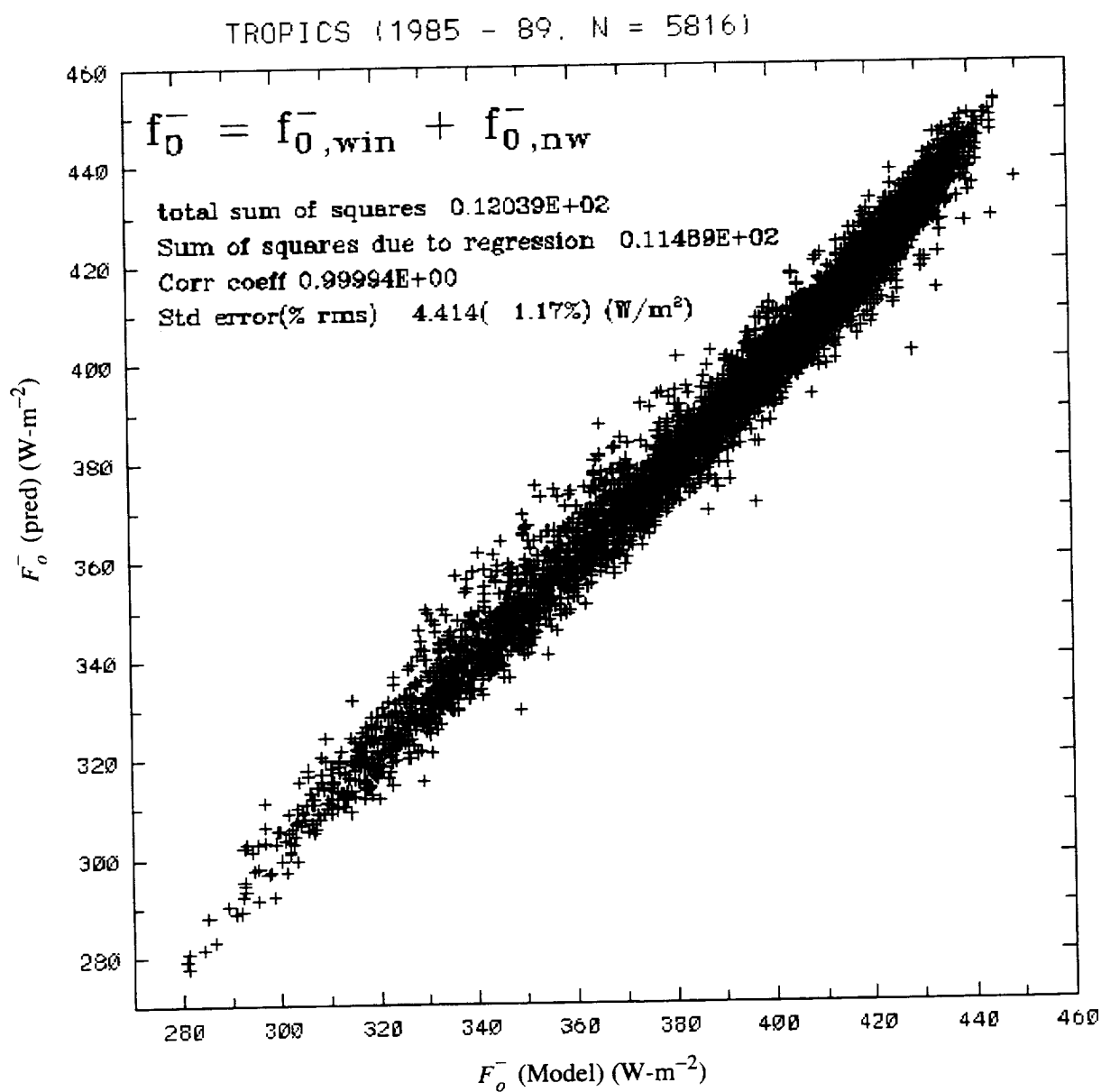


Figure 7. Same as in figure 5, but for model 2 (table 1).

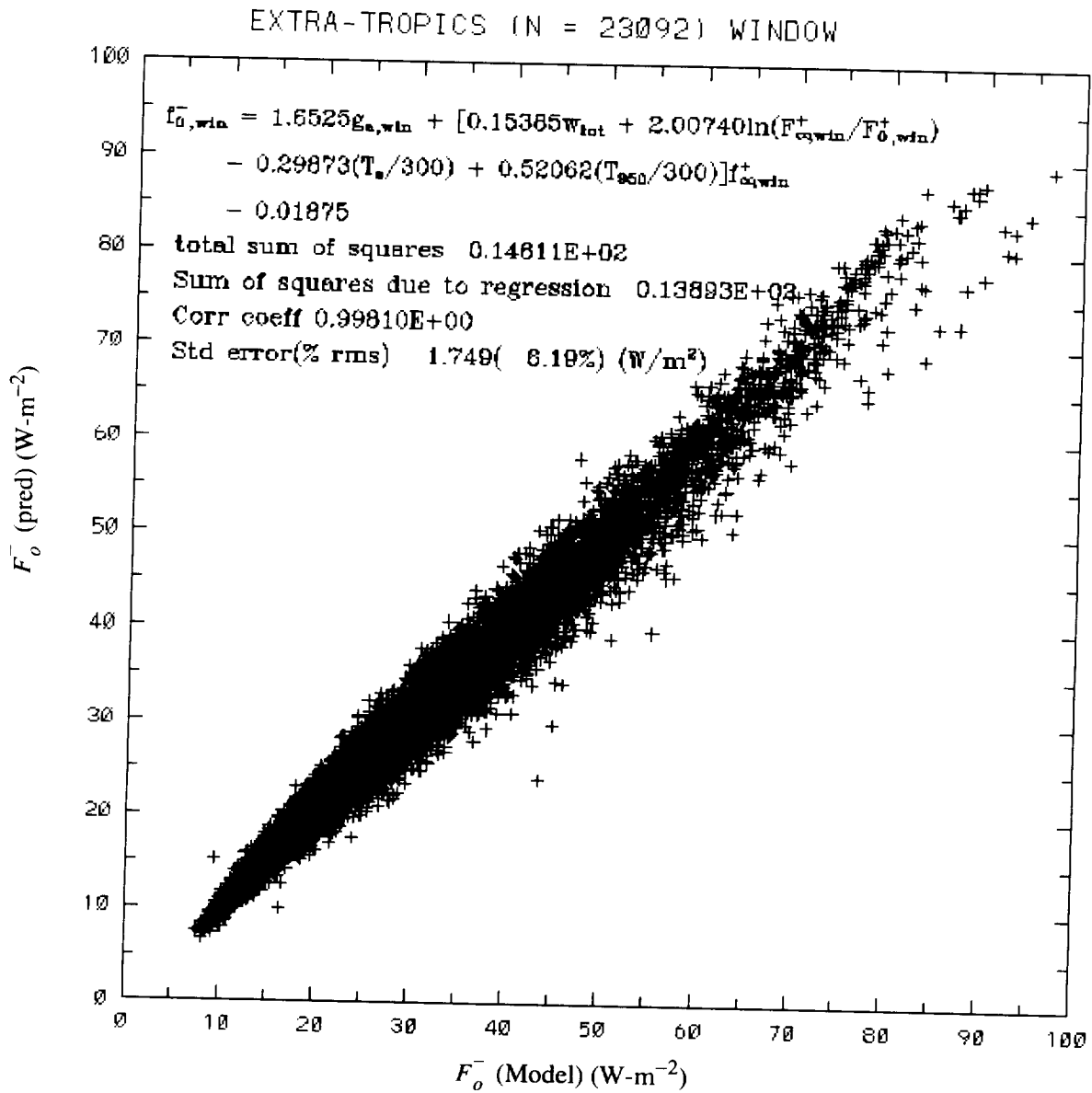


Figure 8. Same as in figure 7, but for the extratropics.

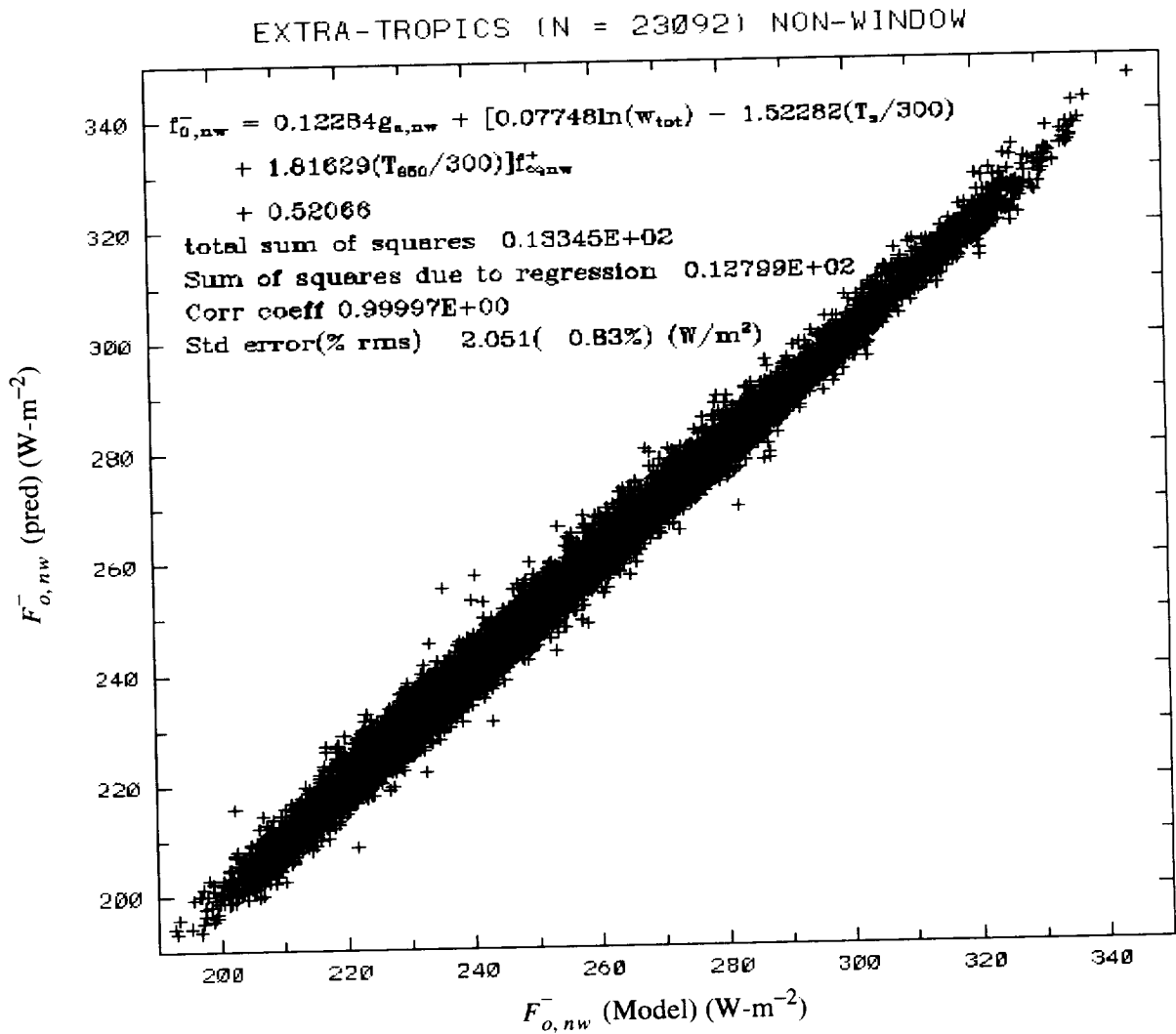


Figure 9. Same as in figure 6, but for the extratropics.

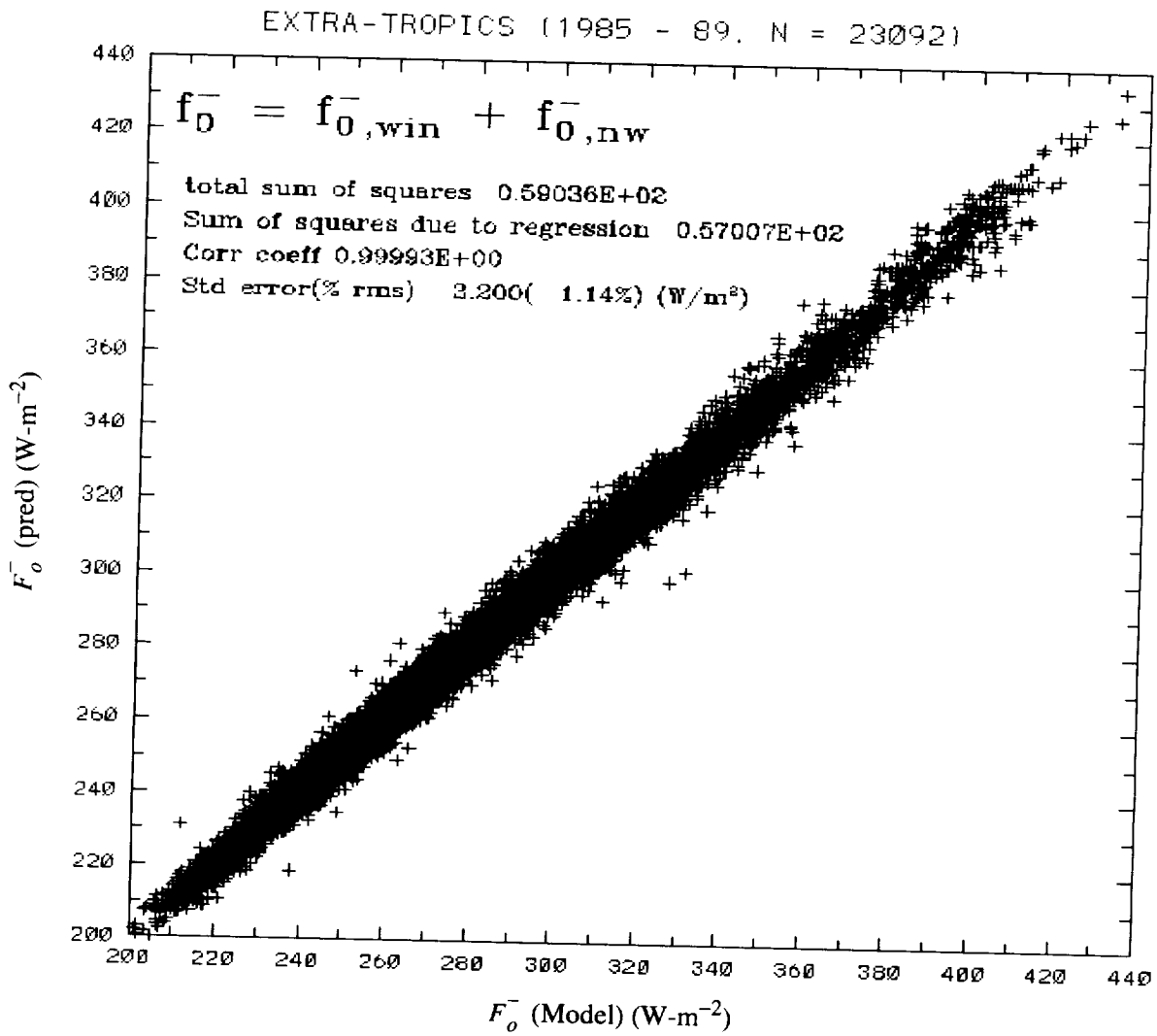


Figure 10. Same as in figure 7, but for the extratropics.

through instruments such as the Special Sensor Microwave Imager (SSM/I) measurements over the oceans, microwave sensors aboard the Defense Meteorological Space Program (DMSP) satellite, or from detailed water vapor profiles derived from the TOVS data products. It is to be noted from figures 5 to 10 that the coefficients of  $g_{a,win}$  and the window flux ratio term dominate in the tropics and explain the bulk of the variability. The combination of residual parameters of water vapor, temperature, and window flux ratio appearing in brackets are multiplied by the respective components of outgoing longwave flux to explain the nonlinear variability in  $g_a$  at higher temperatures. The standard error between the radiative fluxes derived from the full radiative transfer model [ $F_0^-$  (Model) in fig. 5] and that predicted by the parameterization [ $F_0^-$  (pred)], is about  $4.4 \text{ W}\cdot\text{m}^{-2}$  for the tropics and  $3.2 \text{ W}\cdot\text{m}^{-2}$  for the extratropics. The terms “total sum of squares,”  $\Sigma[f_0^-(\text{model}) - \bar{f}_0]^2$ ; “sum of squares due to regression,”  $\Sigma[f_0^-(\text{pred}) - \bar{f}_0]^2$ , where  $\bar{f}_0$  is a mean value of  $\bar{f}_0^-$  (model); and correlation coefficient shown in figures 5 to 10 represent statistical measures of the goodness of fit. A comparison of the former two terms reveals how closely the chosen parameters explain the total variance of the predicted quantity. The correlation between the model and predicted fluxes is very high (0.9998) and the regression line is extremely close to the 45° line, indicating the absence of any bias in the parameterized flux estimates.

#### 4.6.2.3. Validation

The data sources used in the validation exercise come from the Central Equatorial Pacific Experiment (CEPEX) conducted in March/April 1993, which was a multiplatform endeavor, and also measurements made during the Intensive Observation Period (November 1992 to February 1993) at the Kavieng island site as part of the TOGA/ISS program.

The research vessel Vickers, with a cruise track along the equator starting from Honiara (160°E, 10°S) to the Christmas islands (160°W, 5°N), made state-of-the-art measurements of temperature, humidity, and ozone mixing ratios between March 8 and 21, 1993. The ship also had aboard a Fourier Transform Infrared Spectroradiometer (FTIR) measuring the narrow field of view (Lubin 1994) incoming longwave radiance in the 5- to 20- $\mu\text{m}$  region, and in addition an Eppley Pyrgeometer to measure the broadband longwave fluxes. The FTIR radiances are converted to broadband fluxes using the following procedure: Vickers soundings are used as input and equation (2) is used to simulate both the broadband longwave fluxes and the 5- to 20- $\mu\text{m}$  radiances under clear skies. A plot of these (fig. 11) indicated an excellent quadratic fit with a correlation coefficient of 0.999. The broad band fluxes derived from this relation are referred to as “FTIR fluxes” and form the basis of our comparison. The comparison is restricted to the days identified as “clear skies” by visual observations of overhead sky conditions aboard the ship. Top-of-atmosphere fluxes are derived from the infrared brightness temperatures measured by the Japanese Geostationery Meteorological Satellite (GMS) collocated with the Vickers ship. The infrared brightness temperatures have been converted after correcting for the limb-darkening effects to yield both the window (8- to 12-mm) channel and broadband flux using regression relations between the variables derived from model simulations. These GMS-derived window and broadband TOA fluxes and temperature and total precipitable water obtained from the Vickers sondes form the input to the algorithm. One must remember here the inherent limitations of the TOA fluxes as, in reality, both the flux components are derived from only one independent measure (namely the infrared brightness temperature). There is also evidence of contamination by thin cirrus clouds (see lower panel) as indicated by wide differences with the model simulations. Despite these shortcomings, the agreement of the algorithm-predicted fluxes is pretty good not only with the model, but also the FTIR and Pyrgeometer measurements (top panel). Although there is a systematic difference with the FTIR fluxes, the disparities between the FTIR and the collocated Pyrgeometer suggest a calibration-related uncertainty in FTIR of nearly 5 to 8  $\text{W}\cdot\text{m}^{-2}$ .

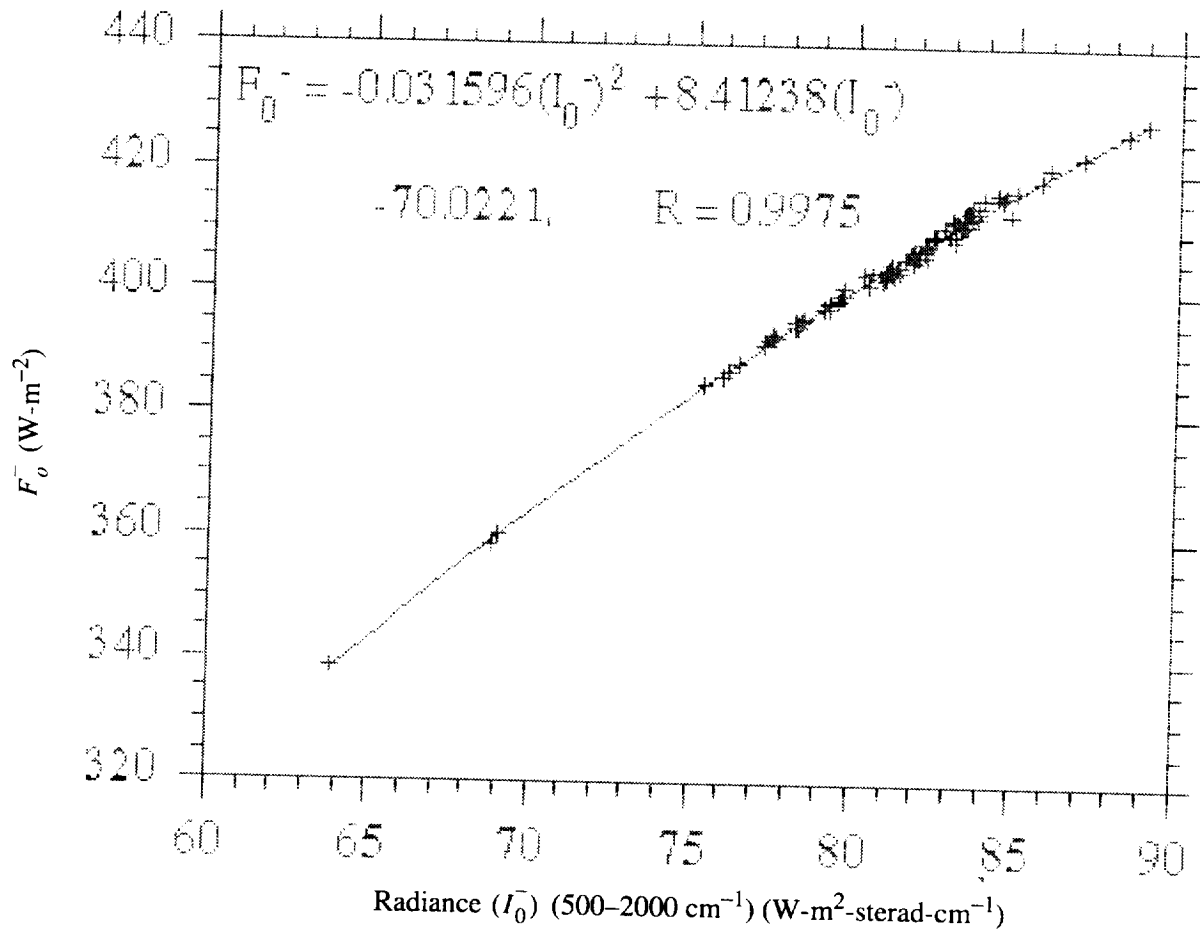
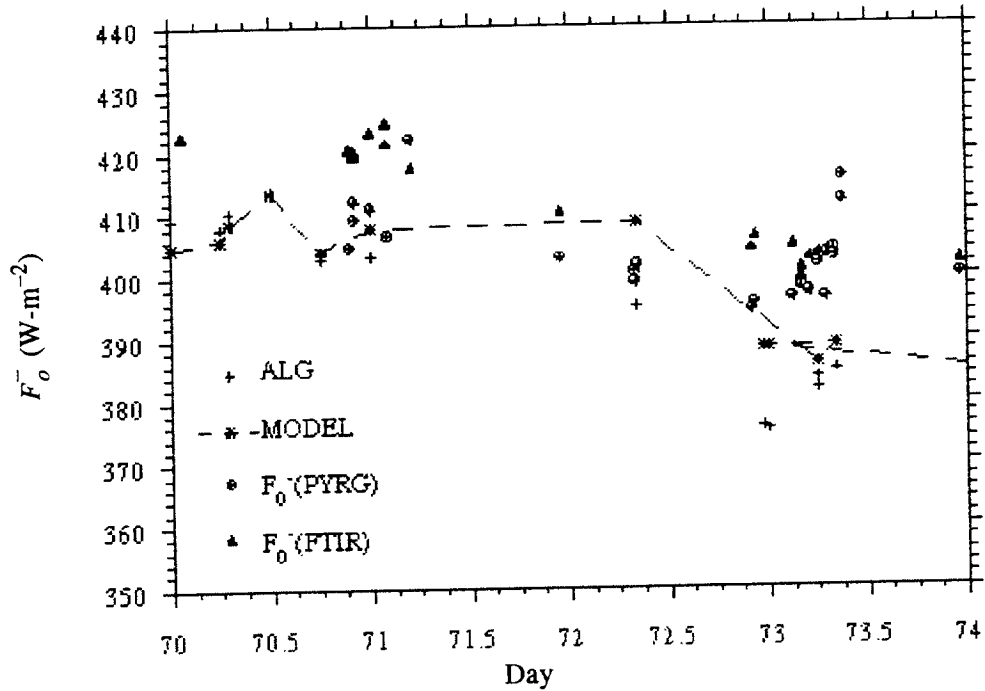
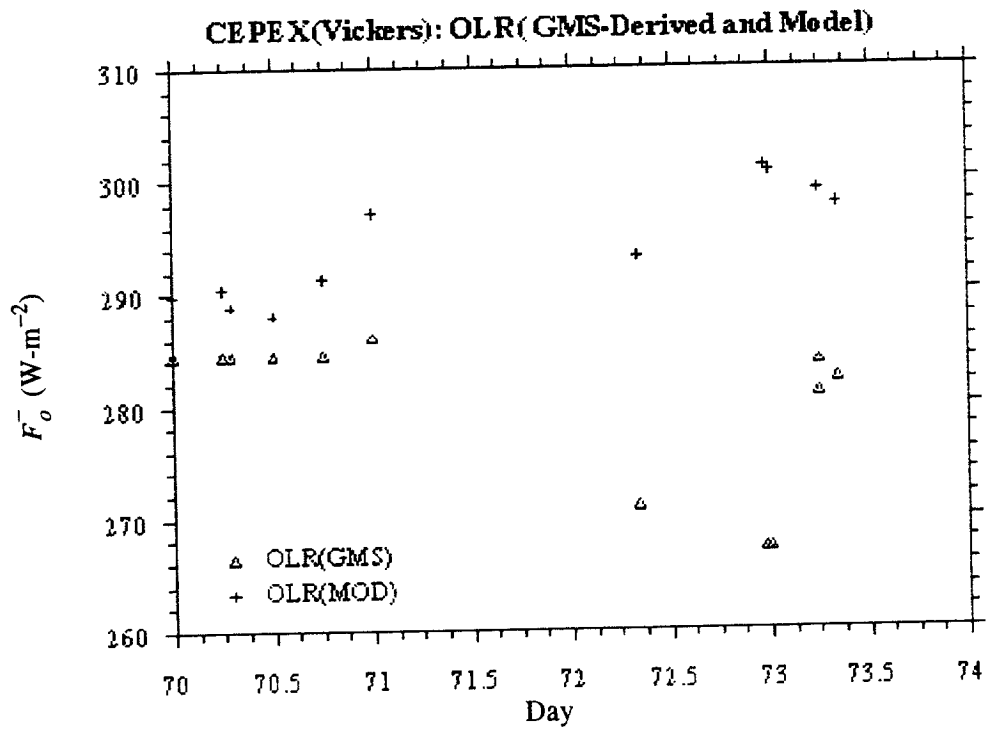


Figure 11. Model-simulated broadband fluxes and radiances for FTIR spectral range of 5 to 20  $\mu\text{m}$  for Vickers sondes.

The next data set used in our validation exercise is the broadband flux and sonde measurements at Kavieng island ( $151^\circ\text{E}$ ,  $2.5^\circ\text{S}$ ) in the western pacific. Unlike the CEPEX, the algorithm predictions are not constrained by the TOA flux measurements, and here we recourse to the model-derived outgoing longwave fluxes instead. Comparisons are restricted to the daytime only, where clear-sky scenes are identified through concurrent observations of shortwave radiation. The scheme followed for scene identification is based on choosing a threshold value (Chuck Long, personal communication) for the ratio of diffuse to global incident (direct + diffuse) solar flux at the surface. This threshold value is a function of the solar zenith angle and obtains from an empirical relationship derived from a statistical analyses of 5 minute bin-averaged data of shortwave radiation fluxes. An interesting observation from figures 12 and 13 is the opposite signs of the slight bias observed in the algorithm estimates of flux, reflecting the uncertainties related to the instrument calibration and also the quality or bias of sonde measurements in the two separate field experiments. The algorithm is seen to perform reasonably well (fig. 13) with the mean difference being  $3 \text{ W}\cdot\text{m}^{-2}$  and an rms difference of about  $10 \text{ W}\cdot\text{m}^{-2}$ .



(a) Downward fluxes computed from radiative transfer model (continuous dashed line), predicted by algorithm, derived from FTIR-measured radiances, and also broadband flux measured by pyrgeometer aboard Vickers ship.



(b) Model-simulated outgoing longwave fluxes and those derived from GMS-observed infrared brightness temperature. The latter were used in algorithm estimates of flux.

Figure 12. Computed, predicted, and derived fluxes.

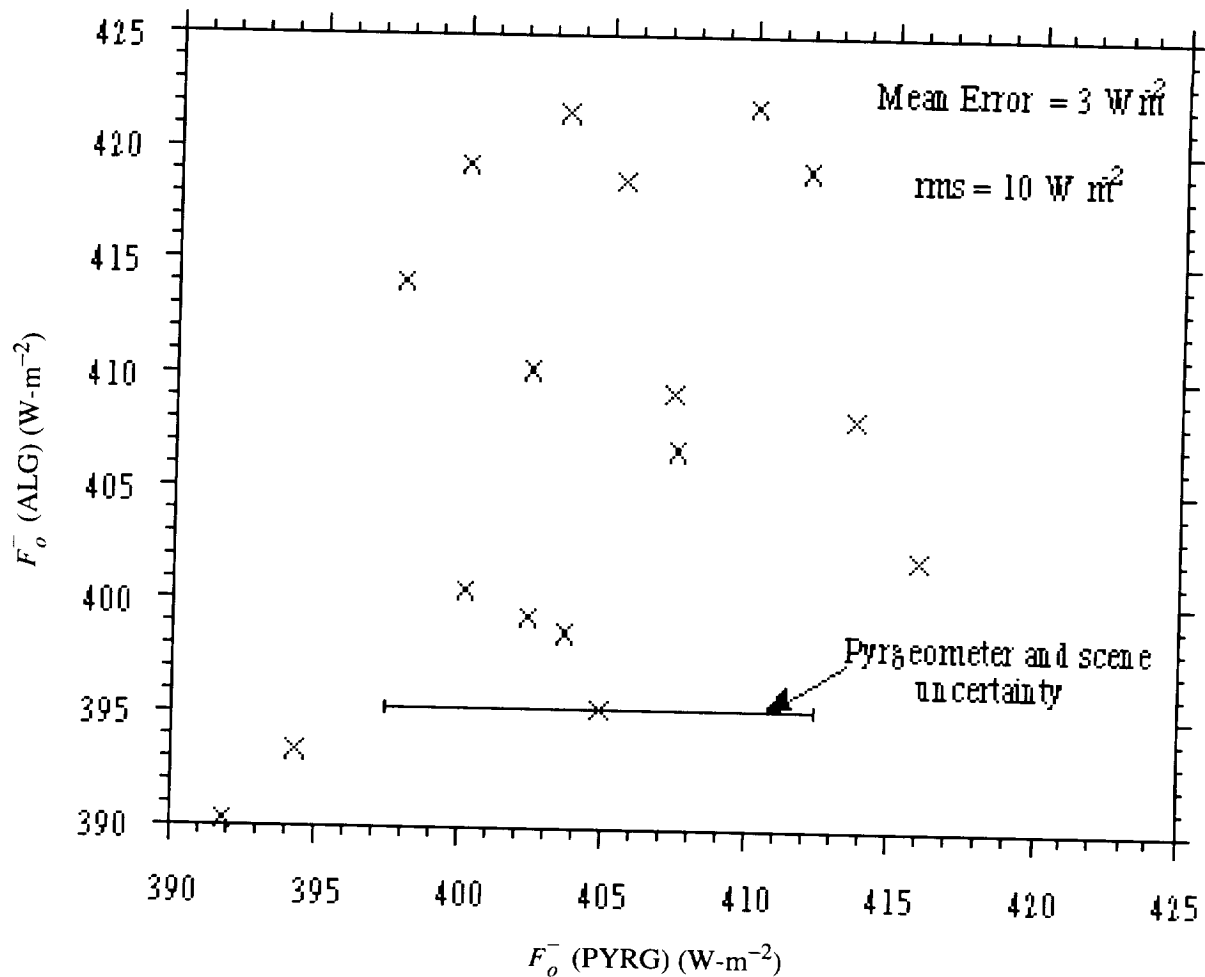


Figure 13. Time series of downward fluxes obtained from radiometer observations and algorithm at Kavieng Island (Nov. 1992 to Feb. 1993). TOA fluxes used in algorithm are from model.

#### 4.6.2.4. Conclusion

This work describes the methods to derive the clear-sky downward longwave flux at the surface from CERES broadband and window channel TOA flux measurements, atmospheric temperature data at 950 mb level, and total column water vapor information. The detailed radiative transfer simulations have been performed using 5 years (1985 to 1989) of ship sondes as input. The simulated outgoing longwave fluxes agree with the collocated ERBE data with an rms error of about  $13 \text{ W} \cdot \text{m}^{-2}$ , which is within the uncertainties of ERBE fluxes. The parameterizations exploit the physics of radiative transfer in the window and nonwindow spectral regions. Because of the close affinity of the downward flux with the greenhouse effect, the downward emissions in the window and nonwindow are first constrained in terms of their respective components of greenhouse effect, and in the second step the deviation of the predicted flux is explained in terms of the other residual variables. Column absorption in the nonwindow varies as the logarithm of the absorber amount, whereas the window component varies in the linear limit and is highly sensitive to the vertical distribution of moisture. The effect of continuum, which dominates in the tropics, is proportional linearly to the column water vapor and the logarithm of TOA and surface flux ratio in the window, the latter constituting a measure of the optical depth. The tropics ( $30^\circ\text{S}$  to  $30^\circ\text{N}$ ) and extratropics ( $30^\circ$  to poles) have been treated separately because of the differences in the physics and to achieve the best accuracy. The rms accuracies obtained range between 3 and

$4.5 \text{ W}\cdot\text{m}^{-2}$ , and the correlation coefficient between the radiative transfer-simulated fluxes and that predicted by the parameterization has been found to be very high (0.999).

Validation studies employing data from the CEPEX and ARM Probe sites indicate a reasonable agreement between the measurements and the parameterized flux estimates within the limits of uncertainties posed by the errors in scene identification, instrument calibration and/or aerosol emissions in the lower atmosphere, and modeling of the continuum absorption in the window. Sensitivity studies (not reported here) have revealed that thick haze in the atmospheric boundary layer (horizontal visibilities <15 km) could enhance the downward emissions by about  $3\text{--}5 \text{ W}\cdot\text{m}^{-2}$ . Measurements at the ARM sites at Oklahoma and Kavieng also support this fact. Although there have been few, if any, simultaneous measurements of aerosols and longwave fluxes in the atmosphere to validate, a proposal to add an additional parameter in the form of aerosol visible optical depth in the future is under consideration.

#### 4.6.2.5. References

- Brutsaert, W. 1975: On a Derivable Formula for Longwave Radiation From Clear Skies. *Water Resour. Res.*, vol. 11, pp. 742–744.
- Cess, R. D.; and Tiwari, S. N. 1972: Infrared Radiative Energy Transfer on Gasses. *Adv. Heat Transf.*, vol. 8, pp. 229–283.
- Clough, S. A.; and Brown, P. D. 1995: The Water Vapor Continuum and its Role in Remote Sensing. Abstract Volume of the 1995 OSA Tropical Meeting on the *Optical Remote Sensing of the Atmosphere*.
- Clough, S. A.; Kneizys, F. X.; and Davies, R. W. 1989. Line Shape and the Water Vapor Continuum. *Atmos. Res.*, vol. 23, pp. 229–241.
- Darnell, Wayne L.; Gupta, Shashi K.; and Staylor, W. Frank 1983: Downward Longwave Radiation at the Surface From Satellite Measurements. *J. Climat. & Appl. Meteorol.*, vol. 22, pp. 1956–1960.
- Ellingson, Robert G.; Ellis, James; and Fels, Stephen 1991: The Intercomparison of Radiation Codes Used in Climate Models—Long Wave Results. *J. Geophys. Res.*, vol. 96, pp. 8929–8953.
- Elliot, W. P.; and Gaffen, D. J. 1991: On the Utility of Radiosonde Humidity Archives for Climate Studies. *Bull. Am. Meteorol. Soc.*, vol. 72, pp. 1507–1520.
- Frouin, Robert; Gautier, Catherine; and Morcrette, Jean-Jacques 1988: Downward Longwave Irradiance at the Ocean Surface From Satellite Data—Methodology and in Situ Validation. *J. Geophys. Res.*, vol. 93, pp. 597–619.
- Gupta, Shashi K. 1989: A Parameterization for Longwave Surface Radiation From Sun-Synchronous Satellite Data. *J. Climat.*, vol. 2, pp. 305–320.
- Idso, S. B. 1981: On the Systematic Nature of Diurnal Patterns of Differences Between Calculations and Measurements of Clear Sky Atmospheric Thermal Radiation. *Q. J. R. Meteorol. Soc.*, vol. 107, pp. 737–741.
- Inamdar, A. K.; and Ramanathan, V. 1994: Physics of Greenhouse Effect and Convection in Warm Oceans. *J. Climat.*, vol. 7, no. 5, pp. 715–731.
- Kneizys, F. X.; Shettle, E. P.; Abreu, L. W.; Chetwynd, J. H.; Anderson, G. P.; Gallery, W. O.; Selby, J. E. A.; and Clough, S. A. 1988: *Users Guide to LOWTRAN 7*. AFGL-TR-88-0177, U.S. Air Force.
- Lubin, D. 1994: Infrared Radiative Properties of the Maritime Antarctic Atmosphere. *J. Climat.* vol. 7, pp. 121–140.
- Raval, A.; and Ramanathan, V. 1989: Observational Determination of the Greenhouse Effect. *Nature*, vol. 342, pp. 758–761.
- Schmetz, P.; Schmetz, J.; and Raschke, E. 1986: Estimation of Daytime Downward Longwave Radiation at the Surface From Satellite and Grid Point Data, *Theor. Appl. Climatol.*, vol. 37, pp. 136–149.
- Tuzet, Andree 1990: A Simple Method for Estimating Downward Longwave Radiation From Surface and Satellite Data by Clear Sky. *Int. J. Remote Sens.*, vol. 11, pp. 125–131.
- Wu, M. C.; and Cheng, C. P. 1989: Surface Downward Flux Computed by Using Geophysical Parameters Derived From HIRS 2/MSU Soundings. *Theor. Appl. Climatol.*, vol. 40, pp. 37–51.

**Clouds and the Earth's Radiant Energy System (CERES)**

**Algorithm Theoretical Basis Document**

***An Algorithm for Longwave Surface Radiation Budget for Total Skies***

***(Subsystem 4.6.3)***

Shashi K. Gupta<sup>1</sup>

Wayne L. Darnell<sup>2</sup>

Nancy A. Ritchey<sup>1</sup>

Anne C. Wilber<sup>1</sup>

<sup>1</sup>Analytical Services & Materials, Inc., Hampton, Virginia 23666

<sup>2</sup>NASA Langley Research Center, Hampton, Virginia 23681-0001

## Abstract

*The algorithm described here was developed for deriving global fields of downward and net LW radiative fluxes at the Earth's surface. It will be used to compute LW SRB, along with other algorithms which use the CERES LW window channel (subsystem 4.6.2) and full-column GCM-type radiative transfer computations (subsystem 5.0).*

*The main inputs for this algorithm are surface temperature and emissivity, atmospheric profiles of temperature and humidity, fractional cloud amounts, and cloud heights. The algorithm is flexible so as to be adaptable to the use of input data from a wide variety of sources.*

*The main output of the algorithm are the downward and net LW fluxes at the surface. The spatial and temporal resolution of the output parameters is the same initially as that of the inputs. Later on, the output parameters may be projected onto a different spatial grid and temporally averaged into daily, diurnally resolved monthly, and monthly averages.*

*This algorithm is based on parameterized equations developed expressly for computing surface LW fluxes in terms of meteorological parameters conveniently available from satellite and/or other operational sources. Also, these equations are soundly based in the physics of radiative transfer as they were developed from a large database of surface fluxes computed with an accurate narrowband radiative transfer model. This algorithm is currently being used with meteorological inputs from ISCCP-C1 data sets. For CERES processing with this algorithm, all meteorological inputs except clouds will be available from the MOA archival product. Cloud parameters will come from VIRS for CERES on TRMM and from MODIS-N for CERES on EOS-AM and EOS-PM.*

### 4.6.3. An Algorithm for Longwave Surface Radiation Budget for Total Skies

#### 4.6.3.1. Introduction

Net longwave radiative flux at the Earth's surface is a significant component of the surface energy budget. It affects, in varying measures, the surface temperature fields, the surface fluxes of latent and sensible heat, the atmospheric and oceanic general circulation, and the hydrological cycle (Suttles and Ohring 1986). In recognition, the WCRP has established the Surface Radiation Budget Climatology Project with the goal of developing long-term global climatologies of surface LW as well as SW radiative fluxes. Surface LW fluxes are also a highly desirable output product for the CERES Project.

#### 4.6.3.2. Background

In the framework of CERES processing, the most desirable method would be to derive surface radiative fluxes from the top of atmosphere (TOA) flux measurements, made directly by CERES instruments. Use of such schemes would confer on surface products the distinction of being based on direct observation. Such schemes have been quite successful in deriving surface SW flux, based on a strong correlation between net SW fluxes at the TOA and the surface (Cess et al. 1991; Li et al. 1993). Similar correlations between TOA and surface LW fluxes have not yet been established. Even though there has

been considerable effort in this direction (Ramanathan 1986), there are no accepted algorithms for retrieving surface LW fluxes from TOA LW fluxes alone. The situation becomes particularly difficult in the presence of clouds, because strong absorption of LW radiation in the clouds results in a complete decoupling of the LW radiation fields at the TOA and the surface (Stephens and Webster 1984).

An alternative approach for deriving surface LW fluxes is to compute them using radiative transfer models with meteorological data. Keeping in view the accuracy requirements and the volume of processing to be done for CERES, the radiative transfer model has to be computationally fast while maintaining high accuracy. The meteorological data have to be available on a global scale, preferably from operational sources. The algorithm described here meets the above requirements fully. It is based on a fast parameterized computation scheme developed from an accurate narrowband radiative transfer model (Gupta 1989).

#### 4.6.3.3. Input Sources and Outputs

The basic inputs to this algorithm are surface temperature and emissivity, temperature and humidity profiles, and cloud-top height. As described in the next section, a few secondary inputs are derived from the above parameters. The algorithm was structured originally to utilize TOVS products, which until the mid eighties were about the only operational source of global meteorological data (Gupta 1989). Starting in the late eighties, global ISCCP-C1 datasets (hereafter referred to as C1 data) which represent a synthesis of temperature and humidity profiles from TOVS and ISCCP's retrieval of cloud parameters became available (Rossow and Schiffer 1991). Since this algorithm works with basic meteorological parameters, it was quickly and easily adapted to the use of C1 data (Gupta et al. 1992).

For CERES data processing, all meteorological data except clouds will be available from the MOA archival product. Cloud parameters for CERES processing from TRMM will be retrieved from VIRS, and for EOS-AM and EOS-PM processing from MODIS-N. Surface emissivity data are also not available from any of the above sources. In the earlier work, a value of unity has been used for all surfaces. For CERES processing of EOS-AM and EOS-PM data, surface emissivity data may become available from MODIS-N, but for processing of TRMM data, surface emissivity data may come from the AVHRR Pathfinder data sets.

The outputs of this algorithm are the downward and net LW fluxes obtained initially at the same spatial and temporal resolution as the inputs. The outputs can be easily projected on other desirable spatial grids and averaged over other time intervals. An example of the results obtained with C1 inputs on the 2.5° equal-area grid and averaged monthly for October 1986 is shown in Plate 1.

#### 4.6.3.4. Algorithm Description

The downward longwave flux (DLF) at the surface, denoted as  $F_d$ , is computed as

$$F_d = C_1 + C_2 A_c \quad (1)$$

where  $C_1$  is the clear-sky DLF,  $C_2$  is the cloud forcing factor, and  $A_c$  is the fractional cloud amount. The net longwave flux (NLF), denoted as  $F_n$ , is computed as

$$F_n = F_d - \epsilon_s \sigma T_s^4 - (1 - \epsilon_s) F_d \quad (2)$$

where  $\sigma$  is the Stefan-Boltzman constant,  $\epsilon_s$  and  $T_s$  are the emissivity and temperature of the surface. Parameterizations described below were developed for  $C_1$  and  $C_2$  in terms of TOVS meteorological parameters which are a part of C1 data.

Clear-sky DLF ( $C_1$ ) is represented as

$$C_1 = (A_0 + A_1 V + A_2 V^2 + A_3 V^3) \times T_e^{3.7} \quad (3)$$

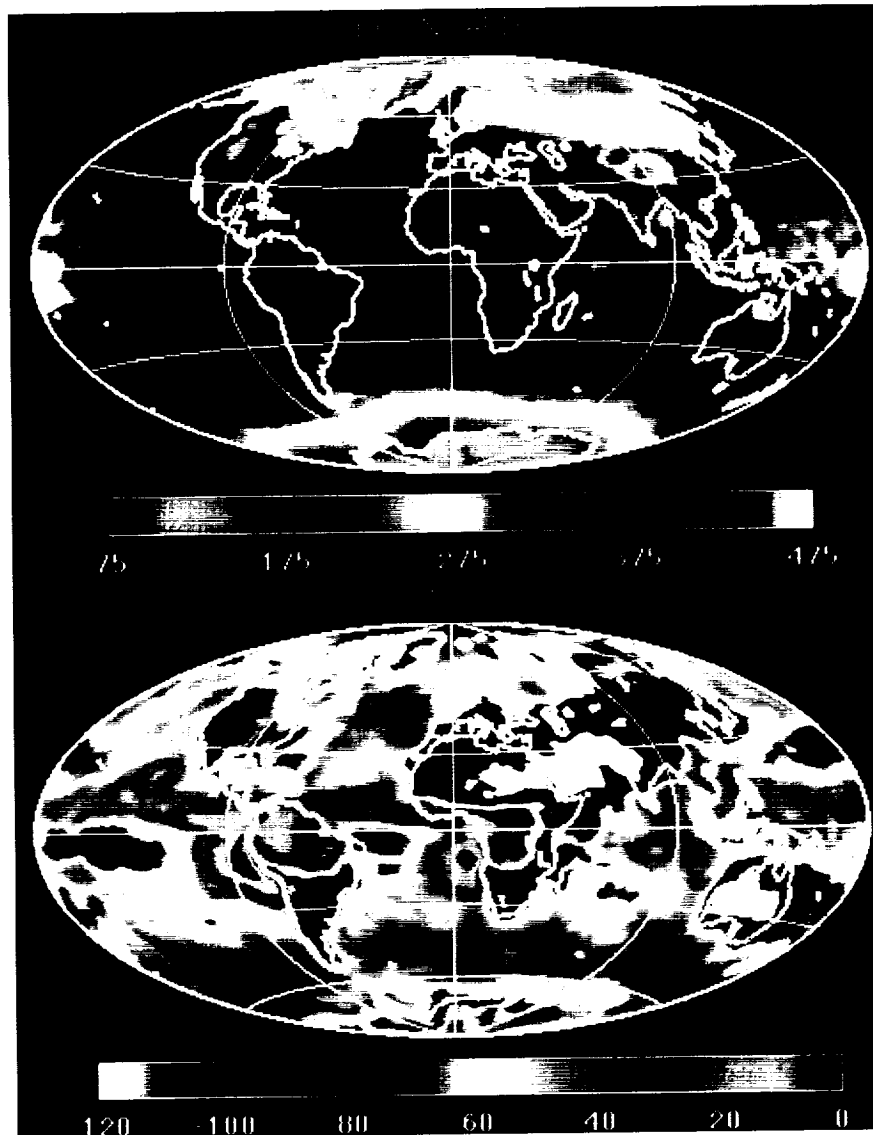


Plate 1. Surface longwave fluxes ( $\text{W}\cdot\text{m}^{-2}$ ) monthly averages for October 1986.

where  $V = \ln W$ ,  $W$  is the water vapor burden of the atmosphere,  $T_e$  is an effective emitting temperature of the atmosphere, and  $A_0$ ,  $A_1$ ,  $A_2$ , and  $A_3$  are regression coefficients.  $T_e$  is computed as

$$T_e = k_s T_s + k_1 T_1 + k_2 T_2 \quad (4)$$

where  $T_1$  and  $T_2$  are the mean temperatures of the first and second atmospheric layers next to the surface, which cover the surface–800 mb, and 800–680 mb regions. The values of the weighting factors  $k_s$ ,  $k_1$ , and  $k_2$  were determined from sensitivity analysis and found to be 0.60, 0.35, and 0.05 respectively. The values of the regression coefficients in equation (3) are

$$A_0 = 1.791 \times 10^{-7}$$

$$A_1 = 2.093 \times 10^{-8}$$

$$A_2 = -2.748 \times 10^{-9}$$

and

$$A_3 = 1.184 \times 10^{-9}$$

The cloud forcing factor ( $C_2$ ) is represented as

$$C_2 = T_{cb}^4 / (B_0 + B_1 W_c + B_2 W_c^2 + B_3 W_c^3) \quad (5)$$

where  $T_{cb}$  is the cloud-base temperature, and  $W_c$  is the water vapor burden below the cloud base. The values of the regression coefficients are

$$B_0 = 4.990 \times 10^7$$

$$B_1 = 2.688 \times 10^6$$

$$B_2 = -6.147 \times 10^3$$

and

$$B_3 = 8.163 \times 10^2$$

$T_{cb}$  and  $W_c$  are computed from available C1 data using the following procedure. A cloud-base pressure ( $P_{cb}$ ) is obtained by combining the available cloud-top pressure with climatological estimates of cloud thickness.  $T_{cb}$  is obtained by matching  $P_{cb}$  against the available temperature profile.  $W_c$  is computed from the five-layer water vapor distribution available from the C1 data. For details of the above procedure and the development of equations (3) and (5) from the results of detailed radiative transfer computations, the reader is referred to Gupta (1989). All temperature values are in K, and water vapor burden values in  $\text{kg-m}^{-2}$ .

It was found during the processing of global C1 data sets that the use of equation (5) resulted in significant overestimation of  $C_2$  in the presence of low-level clouds. As long as  $(P_s - P_{cb}) > 200$  mb (where  $P_s$  is the surface pressure), equation (5) yielded accurate results and was used as such. For  $(P_s - P_{cb}) \leq 200$  mb, significant overestimation of  $C_2$  occurred, and was remedied with the following procedure. The maximum value of  $C_2$  (denoted as  $C_{2\text{max}}$ ) is limited by the condition when the cloud base is located at the surface (i.e.,  $P_s - P_{cb} = 0$ ). This limit is used to constrain the values of the regression coefficients of equation (5). In practice, constraining the value of  $B_0$  was found to be quite adequate. The modified value of  $B_0$  (denoted as  $B'_0$ ) subject to the above constraint is represented as

$$B'_0 = T_s^4 / (\sigma T_s^4 - C_1) \quad (6)$$

The value of  $B'_0$  is much larger than  $B_0$ , and for  $(P_s - P_{cb}) = 0$ , it forces the value of  $C_2$  obtained from equation (5) to match the value of  $C_{2\text{max}}$ .  $B_0$  continues to yield satisfactory results when  $(P_s - P_{cb}) > 200$  mb. For values of  $(P_s - P_{cb})$  between 0 and 200 mb, the applicable value of this regression coefficient is obtained by linear interpolation (in pressure) between  $B'_0$  and  $B_0$ . For a detailed discussion of the steps described above, the reader is referred to Gupta et al. (1992).

#### 4.6.3.5. Accuracy/Error Analysis

Fluxes computed with the above algorithm are subject to random and systematic errors coming from the radiation models as well as the meteorological data. In the context of this algorithm, errors coming from the radiation models can be divided further into those coming from (i) the use of the parameterized equations (3) and (5), and (ii) the detailed radiation model from which those equations were derived.

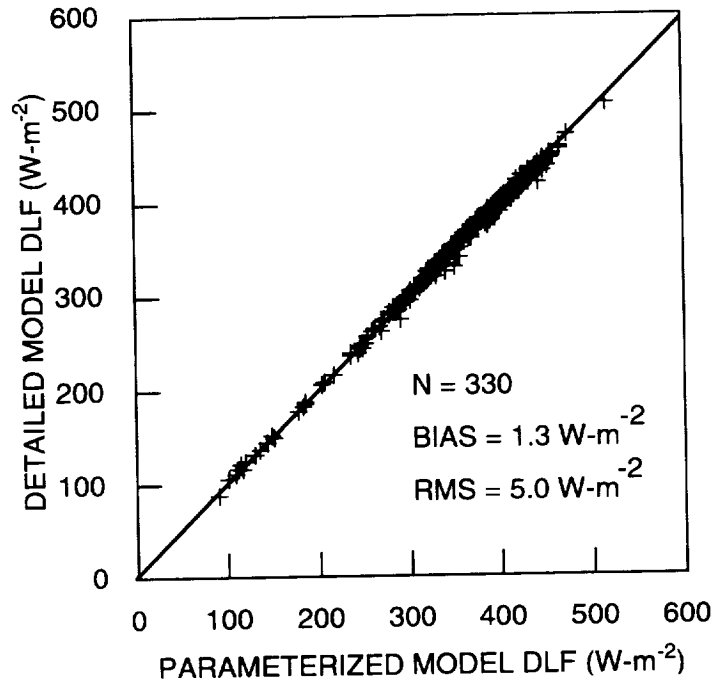


Figure 1. Scatter plot between DLF computed with parameterized model and detailed model for 330 soundings sampled from global C1 data for July 1983.

A reasonable estimate of the errors coming from equations (3) and (5) relative to the detailed model can be obtained by comparing the fluxes computed with the two methods, but with the same meteorological data. Figure 1 shows such a comparison of DLF values for a set of 330 soundings representing pole-to-pole meteorological conditions, sampled from the global C1 dataset for July 1983. It shows that the parameterized model DLF is  $1.3 \text{ W-m}^{-2}$  higher. The rms difference between the two sets (which includes the bias) is  $5.0 \text{ W-m}^{-2}$ .

The errors in the fluxes computed from the detailed model come from the spectral line parameters, and the various approximations made in the spectral, angular, and height integration of the radiative transfer equation. Reasonable estimates of the detailed model errors can be obtained in the framework of the ICRCCM (Ellingson et al. 1991). Figure 2 shows a comparison of DLF values obtained with the detailed model and other ICRCCM results for the five climatological profiles. The ordinate represents the ratio of the DLF values for a model to the line-by-line DLF values which are used as reference. Thus, the dashed line represents the reference line-by-line results, the “+” symbols the highest values, and the “x” symbols the lowest values from among the large number of results submitted to the ICRCCM. This comparison shows that the fluxes from the present detailed model (depicted as hollow circles) average about 1% higher than the line-by-line results. This difference is equivalent to a systematic error of about  $2\text{-}3 \text{ W-m}^{-2}$ , which is slightly higher than the difference between the detailed and parameterized model results.

A brief discussion of the random and systematic errors coming from the meteorological data is presented here. For details, the reader is referred to Gupta et al. (1993). Random errors arising from meteorological data errors on an individual sounding basis were found to be of the order of  $\pm 20 \text{ W-m}^{-2}$ . For monthly averages, these were reduced to about  $\pm 5 \text{ W-m}^{-2}$ . Systematic errors in the fluxes arise from the biases in the meteorological inputs. Biases in the cloud parameters were found to be one of the large

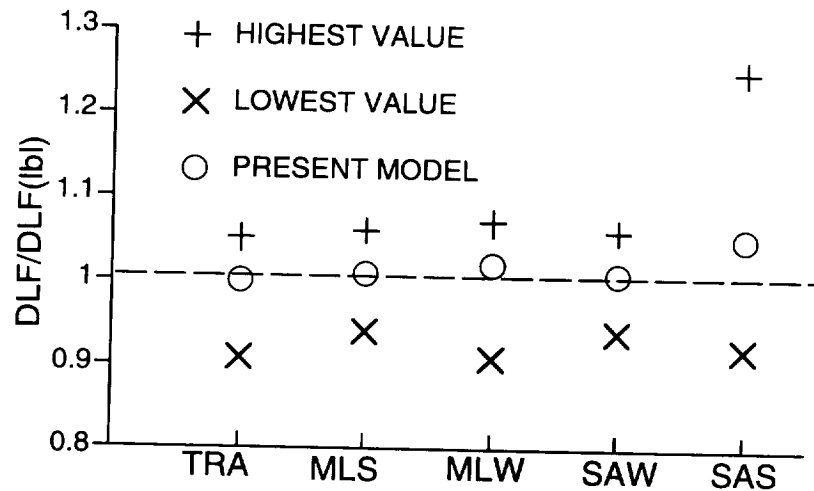


Figure 2. Comparison of clear-sky DLF obtained with detailed model and line-by-line and other ICRCCM results for five climatological profiles (TRA = tropical; MLS = midlatitude summer; MLW = midlatitude winter; SAS = subarctic summer; SAW = subarctic winter).

sources. Also, if  $\epsilon_s$  deviates significantly from unity and realistic values of  $\epsilon_s$  are not used, additional bias is incurred in the computation of  $F_n$ . The magnitude of this bias is given by

$$\Delta F_n = (1 - \epsilon_s)(F_d - \sigma T_s^4) \quad (7)$$

which can be quite large, especially over desert areas.

#### 4.6.3.6. Strategic Concerns and Remedies

The apparent weaknesses of the algorithm, e.g., the overestimation of  $C_2$  in the presence of low-level clouds, were remedied as described earlier. The weighting scheme of equation (4) is designed to minimize the errors in the presence of strong temperature discontinuities at the surface. Large uncertainties in surface temperature and emissivity over land areas are still important concerns, but have to await advances in retrieval algorithms for their resolutions. Satellite data sets sometimes have large gaps, and fill values (e.g., -999.) are frequently substituted in the data streams where real data are missing. Unchecked, this would generally result in absurd values for output parameters. The situation will be handled by checking all important input parameters against carefully chosen high and low limits. The limits are chosen to encompass the normal spatial and temporal variabilities of these parameters. When an input parameter falls outside the above limits, an attempt is made to generate a replacement (in place of the fill value) by interpolation or from climatology. When these attempts fail, the input and output data are rejected and excluded from the averages.

#### 4.6.3.7. Concluding Remarks

The algorithm described here is already operational with C1 data sets as inputs. Error analysis of the outputs shows that errors coming from the meteorological inputs are considerably larger than those coming from the parameterized equations. With improved meteorological inputs available from MOA, and cloud parameters from VIRS and MODIS-N, we expect the errors in CERES estimates of surface LW fluxes to be considerably lower than those achievable presently. This algorithm has recently been selected by the GEWEX SRB Project for producing a long time-series (up to 12 years) of surface LW fluxes. It is expected that under the auspices of GEWEX, this algorithm will undergo thorough evaluation against surface measurements available from around the globe. Surface LW fluxes obtained with this algorithm would constitute a valuable CERES product by themselves, and would also be useful for independently checking on the quality of the fluxes obtained from the GCM-type radiative transfer computations.

#### 4.6.3.8. References

- Cess, Robert D.; Dutton, Ellsworth G.; Deluisi, John J.; and Jiang, Feng 1991: Determining Surface Solar Absorption From Broadband Satellite Measurements for Clear Skies—Comparison With Surface Measurements. *J. Climat.*, vol. 4, no. 2, pp. 236–247.
- Ellingson, Robert G.; Ellis, James; and Fels, Stephen 1991: The Intercomparison of Radiation Codes Used in Climate Models—Long Wave Results. *J. Geophys. Res.*, vol. 96, no. D5, pp. 8929–8953.
- Gupta, Shashi K. 1989: A Parameterization for Longwave Surface Radiation From Sun-Synchronous Satellite Data. *J. Climat.*, vol. 2, no. 4, pp. 305–320.
- Gupta, Shashi K.; Darnell, Wayne L.; and Wilber, Anne C. 1992: A Parameterization for Longwave Surface Radiation From Satellite Data—Recent Improvements. *J. Appl. Meteorol.*, vol. 31, no. 12, pp. 1361–1367.
- Gupta, S. K.; Wilber, A. C.; Darnell, W. L.; and Suttles, J. T. 1993: Longwave Surface Radiation Over the Globe From Satellite Data—An Error Analysis. *Int. J. Remote Sens.*, vol. 14, no. 1, pp. 95–114.
- Li, Zhanqing; Leighton, H. G.; Masuda, Kazuhiko; and Takashima, Tsutomu 1993: Estimation of SW Flux Absorbed at the Surface From TOA Reflected Flux. *J. Climat.*, vol. 6, no. 2, pp. 317–330.
- Ramanathan, V. 1986: Scientific Use of Surface Radiation Budget for Climate Studies. *Surface Radiation Budget for Climate Applications*, J. T. Suttles and G. Ohring, eds., NASA RP-1169, pp. 58–86.
- Rossow, W. B.; and Schiffer, R. A. 1991: ISCCP Cloud Data Products. *Bull. Am. Meteorol. Soc.*, vol. 72, no. 1, pp. 2–20.
- Stephens, G. L.; and Webster, P. J. 1984: Cloud Decoupling of the Surface and Planetary Radiative Budgets. *J. Atmos. Sci.*, vol. 41, no. 4, pp. 681–686.
- Suttles, J. T.; and Ohring, G., eds. 1986: *Surface Radiation Budget for Climate Applications*. NASA RP-1169.



REPORT DOCUMENTATION PAGE			Form Approved OMB No. 0704-0188	
Public reporting burden for this collection of information is estimated to average 1 hour per response, including the time for reviewing instructions, searching existing data sources, gathering and maintaining the data needed, and completing and reviewing the collection of information. Send comments regarding this burden estimate or any other aspect of this collection of information, including suggestions for reducing this burden, to Washington Headquarters Services, Directorate for Information Operations and Reports, 1215 Jefferson Davis Highway, Suite 1204, Arlington, VA 22202-4302, and to the Office of Management and Budget, Paperwork Reduction Project (0704-0188), Washington, DC 20503.				
1. AGENCY USE ONLY (Leave blank)	2. REPORT DATE December 1995	3. REPORT TYPE AND DATES COVERED Reference Publication		
4. TITLE AND SUBTITLE Clouds and the Earth's Radiant Energy System (CERES) Algorithm Theoretical Basis Document. <i>Volume III—Cloud Analyses and Determination of Improved Top of Atmosphere Fluxes (Subsystem 4)</i>			5. FUNDING NUMBERS WU 148-65-41-01	
6. AUTHOR(S) CERES Science Team				
7. PERFORMING ORGANIZATION NAME(S) AND ADDRESS(ES) NASA Langley Research Center Hampton, VA 23681-0001			8. PERFORMING ORGANIZATION REPORT NUMBER L-17522	
9. SPONSORING/MONITORING AGENCY NAME(S) AND ADDRESS(ES) National Aeronautics and Space Administration Washington, DC 20546-0001			10. SPONSORING/MONITORING AGENCY REPORT NUMBER NASA RP-1376, Volume III	
11. SUPPLEMENTARY NOTES				
12a. DISTRIBUTION/AVAILABILITY STATEMENT Unclassified—Unlimited Subject Category 47 Availability: NASA CASI (301) 621-0390			12b. DISTRIBUTION CODE	
13. ABSTRACT (Maximum 200 words) The theoretical bases for the Release 1 algorithms that will be used to process satellite data for investigation of the Clouds and Earth's Radiant Energy System (CERES) are described. The architecture for software implementation of the methodologies is outlined. Volume III details the advanced CERES methods for performing scene identification and inverting each CERES scanner radiance to a top-of-the-atmosphere (TOA) flux. CERES determines cloud fraction, height, phase, effective particle size, layering, and thickness from high-resolution, multispectral imager data. CERES derives cloud properties for each pixel of the Tropical Rainfall Measuring Mission (TRMM) visible and infrared scanner and the Earth Observing System (EOS) moderate-resolution imaging spectroradiometer. Cloud properties for each imager pixel are convolved with the CERES footprint point spread function to produce average cloud properties for each CERES scanner radiance. The mean cloud properties are used to determine an angular distribution model (ADM) to convert each CERES radiance to a TOA flux. The TOA fluxes are used in simple parameterization to derive surface radiative fluxes. This state-of-the-art cloud-radiation product will be used to substantially improve our understanding of the complex relationship between clouds and the radiation budget of the Earth-atmosphere system.				
14. SUBJECT TERMS Earth Observing System; Clouds and the Earth's Radiant Energy System; Earth radiation budget; Clouds satellite measurements; Surface radiation; Atmospheric radiative divergence			15. NUMBER OF PAGES 259	
			16. PRICE CODE A12	
17. SECURITY CLASSIFICATION OF REPORT Unclassified	18. SECURITY CLASSIFICATION OF THIS PAGE Unclassified	19. SECURITY CLASSIFICATION OF ABSTRACT Unclassified	20. LIMITATION OF ABSTRACT	



